66TH ELECTRONIC MATERIALS CONFERENCE

JUNE 26-28, 2024 || THE UNIVERSITY OF MARYLAND, COLLEGE PARK || MARYLAND

EMC 2024

The 66th Electronic Materials Conference

CONFERENCE PROGRAM

Please visit our website for more information!

2024.emc-conference.org

WELCOME TO THE CONFERENCE!

It is with great pleasure that we welcome you to the 66th Electronic Materials Conference (EMC 2024) at the University of Maryland in College Park, USA! We expect this Conference to follow in EMC's long tradition of offering premier research on the preparation, characterization and use of electronic materials. Below, we have outlined highlights we believe will be of interest to you.

Conference Chair
Daniel Wasserman
The University of Texas at Austin

Program Chair
Adrienne Stiff Roberts
Duke University

CONFERENCE HIGHLIGHTS

The 66th EMC Program
Features over 300 oral/poster presentations and 38 technical sessions focused on Electronic Materials Science and Technology; Energy Storage and Conversion Materials; Nanoscale Science and Technology; Organic Materials, Thin Films and Devices; Oxide Semiconductors and Dielectrics; and Wide Bandgap Semiconductors.

EMC Awards Ceremony & Plenary Session
The 66th EMC kicks off Wednesday morning with the Awards Ceremony & Plenary Session. First, the 2023 Best Student Presentation Award winners will be announced and honored. The Plenary Lecture follows, where Joseph J. Berry, of the University of Colorado Boulder, will give his presentation, "A Perovskite Paved Pathway to Multi-Terawatt scale Photovoltaics"

Welcome Reception/Poster Session
Sponsor: Taiyo Nippon Sanso
Join us for a Welcome Reception on Wednesday evening from 6:00 pm to 8:00 pm in the Edward St. John (ESJ) building. During this time, poster authors will be available for in-depth discussions at the Poster Session, also located throughout the first floor. Both of these events are great for meeting with longtime colleagues, making new connections and sharing information. Light snacks and refreshments will be served.

Exhibit
Be sure to visit the EMC exhibitors Wednesday and Thursday on the First Floor of the ESJ Building to learn more about the latest products and services in the rapidly evolving world of electronic materials. See page 23 for exhibit hours.

Student Finalists for the Oral Presentation Award
Be sure to check out our student award finalists on Wednesday at 4:30 PM in rooms 0202 and 0224 in the Edward St. John (ESJ) building.

Panel Discussion: Future Careers in Electronic Materials
Join us on Thursday at 4:30 PM in room 0202 in the Edward St. John (ESJ) building to engage in a panel discussion.

Conference Dinner Reception
Don't miss this year's Conference Dinner Reception, Thursday evening at 6:00 PM, in the Stamp Student Union Building Grand Ballroom. Full Conference registration includes one Dinner Reception ticket. You can purchase additional Dinner Reception tickets at the EMC Registration Desk for $100 USD per person, subject to availability. This is an indoor event.

EMC is coordinated with the Device Research Conference (DRC), which will be held during the same week, from June 24-26, 2024. This recognizes the strong interaction between device and electronic materials research and provides fruitful exchange of information between attendees of both Conferences. Badges for DRC will be accepted for admittance to both conferences on Wednesday, June 26. DRC may not attend the EMC Welcome Reception/Poster Session.

SPECIAL THANKS!

CONFERENCE SUPPORT

NSF

WELCOME RECEPTION/POSTER SESSION SPONSOR

TAIYO NIPPON SANSO

REFRESHMENT BREAK SPONSOR

UMC
UNITED MINERAL & CHEMICAL CORP

TABLE OF CONTENTS

The 66th EMC has been managed by

Conference Catalysts

COMMITTEES

Executive Committee

Conference Chair
Daniel Wasserman
The University of Texas at Austin

Program Chair
Adrienne Stiff-Roberts
Duke University

Treasurer
Kevin Daniels
University of Maryland

Secretary
Stephanie Law
Penn State University

Ex-Officio Members
Lisa Porter, Carnegie Mellon University
Wojciech Jadwisienczak, Ohio University

Members at Large
Andrew Allerman, Sandia National Laboratories
Kris Bertness, National Institute of Standards and Technology
Suzanne Mohney, Penn State University
Jamie Phillips, University of Delaware
Christian Wetzel, Rensselaer Polytechnic Institute
Jerry Woodall, University of California, Davis

Members
Elaheh Ahmadi, University of California, Los Angeles
Ganesh Balakrishnan, University of New Mexico
Leonard Brillson, The Ohio State University
Mona Ebrish, Vanderbilt University
Daniel Ewing, Department of Energy's Kansas City National Security Campus
Susan Fullerton, University of Pittsburgh
Gerd Grau, York University
Michael Hamilton, Auburn University
Deidra Hodges, Florida International University
Anthony Hoffman, University of Notre Dame
David Janes, Purdue University
Sriram Krishnamoorthy, University of California, Santa Barbara
Patrick Lenahan, The Pennsylvania State University
Nadeemullah Mahadik, U.S. Naval Research Laboratory
Jay Mody, Intel Corporation
Parsian Mohseni, Rochester Institute of Technology
Becky Peterson, University of Michigan
Robert 'Chris' Roberts, University of Texas, El Paso
Jae-Hyun Ryou, University of Houston
Shayla Sawyer, Rensselaer Polytechnic Institute
Paul Simmonds, Tufts University
Michael Spencer, Morgan State University
Pawan Tyagi, University of the District of Columbia
Huili Grace Xing, Cornell University

Electronic Materials Science and Technology

Additive Manufacturing
Soaram Kim, Texas A&M University
Nathan Lazarus, University of Delaware
Robert C. 'Chris' Roberts, The University of Texas at El Paso
William Scheideler, Dartmouth College

Computational Electronic Materials Discovery
Anderson Janotti, University of Delaware
Sriram Krishnamoorthy, University of California, Santa Barbara
Tae-Yeon Seong, Korea University
Patrick Shea, Northrop Grumman Corporation
Angel Yanguas-Gil, Argonne National Laboratory

Contacts to Semiconductor Epilayers, Nanostructures and Organic Films
Leonard Brillson, The Ohio State University
Shadi Dayeh, University of California, San Diego
Suzanne Mohney, The Pennsylvania State University
Lisa Porter, Carnegie Mellon University
Tae-Yeon Seong, Korea University
Jerry Woodall, University of California, Davis
Eilam Yalon, Technion University of Science and Technology

Epitaxial Materials and Devices
Seth Bank, The University of Texas at Austin
Kurt Eyink, Air Force Research Laboratory
Mihee Ji, U.S. Army Research Laboratory
Rehan Kapadia, University of Southern California
Sriram Krishnamoorthy, University of California, Santa Barbara
Charles Lutz, Lumentum Operations LLC
Nadeemullah Mahadik, U.S. Naval Research Laboratory
Kyle McNicholas, Lincoln Laboratory, Massachusetts Institute of Technology
Aaron Muhowski, Sandia National Laboratories
Hari Nair, Cornell University
Leland Nordin, University of Central Florida
Siddharth Rajan, The Ohio State University
Shadi Shahedipour-Sandvik, State University of New York Polytechnic Institute
Stephanie Tomasulo, U.S. Naval Research Laboratory
Christine Wang, Lincoln Laboratory, Massachusetts Institute of Technology
Dan Wasserman, The University of Texas at Austin
Man Hoi Wong, Hong Kong University of Science and Technology

Hetero-Integration, Interconnects and Packaging
Guohai Chen, National Institute of Advanced Industrial Science and Technology
Mona Ebrish, U.S. Naval Research Laboratory
Daniel Ewing, Department of Energy's Kansas City National Security Campus
Michael Hamilton, Auburn University
Karl Hirschman, Rochester Institute of Technology

Materials for Memory and Computation
Alan Doolittle, Georgia Institute of Technology
Susan Fullerton, University of Pittsburgh
Eric Seabron, Howard University
Feng Xiong, University of Pittsburgh
Ke Xu, Rochester Institute of Technology
Eilam Yalon, Technion University of Science and Technology
Angel Yanguas-Gil, Argonne National Laboratory

Materials Processing and Integration
Daniel Ewing, Department of Energy's Kansas City National Security Campus
Mark Goorsky, University of California, Los Angeles
Doug Hall, University of Notre Dame
Karl Hirschman, Rochester Institute of Technology
Karl Hobart, U.S. Naval Research Laboratory
Becky (R.L.) Peterson, University of Michigan
Nate Quitoriano, McGill University
Steve Ringel, The Ohio State University
Robert C. 'Chris' Roberts, The University of Texas at El Paso
Patrick Shea, Northrop Grumman Corporation
Jerry Woodall, University of California, Davis

Materials for Quantum Applications
Matthew Doty, University of Delaware
Rachel Goldman, University of Michigan
Anthony Hoffman, University of Notre Dame
Stephanie Law, The Pennsylvania State University
Connie Li, U.S. Naval Research Laboratory
Jeremy Robinson, U.S. Naval Research Laboratory
Thomas Searles, University of Illinois at Chicago
Chakrakpani Varanasi, U.S. Army Research Office—Materials Science Division

Metamaterials and Materials for THz, Plasmonics and Polaritons
Joshua Caldwell, Vanderbilt University
Zizwe Chase, University of Illinois, Chicago
Kurt Eyink, Air Force Research Laboratory
Rachel Goldman, University of Michigan
Anthony Hoffman, University of Notre Dame
Stephanie Law, The Pennsylvania State University
Aaron Muhowski, Sandia National Laboratories
Leland Nordin, University of Central Florida
Eric Seabron, Howard University
Thomas Searles, University of Illinois at Chicago
Jason Valentine, Vanderbilt University
Daniel Wasserman, The University of Texas at Austin
Huili Grace Xing, Cornell University

Micro-LEDs and -Displays—Materials, Fabrication and Characterization
Karl Hirschman, Rochester Institute of Technology
Joon Seop Kwak, Korea Institute of Energy Technology
In-Hwan Lee, Korea University
Zetian Mi, University of Michigan
Tae-Yeon Seong, Korea University
William Wong, University of Waterloo
Jerry Woodall, University of California, Davis

Nanofabrication and Processing
Bruno Azeredo, Arizona State University
Kris Bertness, National Institute of Standards and Technology
Mona Ebrish, U.S. Naval Research Laboratory
Munho Kim, Nanyang Technological University, Singapore
Xiuling Li, The University of Texas at Austin
Parsian Mohseni, Rochester Institute of Technology
Angel Yanguas-Gil, Argonne National Laboratory

Narrow Bandgap Materials and Devices
Sadhvikas Addamane, Sandia National Laboratory
Ganesh Balakrishnan, The University of New Mexico
Suprem Das, Kansas State University
Shanti Iyer, North Carolina Agricultural and Technical State University
Sanjay Krishna, The Ohio State University
Andrej Lenert, University of Michigan
Kyle McNicholas, Lincoln Laboratory, Massachusetts Institute of Technology
Aaron Muhowski, Sandia National Laboratories
Kunal Mukherjee, Stanford University
Leland Nordin, University of Central Florida
Jamie Phillips, University of Delaware
Gregory Triplett, Saint Louis University
Christine Wang, Lincoln Laboratory, Massachusetts Institute of Technology
Daniel Wasserman, The University of Texas at Austin
Mark Wistey, Texas State University
Joshua Zide, University of Delaware

Point Defects, Doping and Extended Defects
Andrew Armstrong, Sandia National Laboratories
Ramon Collazo, North Carolina State University
Rachel Goldman, University of Michigan
Karl Hirschman, Rochester Institute of Technology
Lincoln Lauhon, Northwestern University
Kunal Mukherjee, Stanford University
Steve Ringel, The Ohio State University
Shadi Shahedipour-Sandvik, State University of New York Polytechnic Institute
Christian Wetzel, Rensselaer Polytechnic Institute
Jerry Woodall, University of California, Davis
Kin-Man Yu, City University of Hong Kong

Energy Storage and Conversion Materials

Electrochemical Energy Storage and Conversion
Susan Fullerton, University of Pittsburgh
Jung-Hyun Kim, The Ohio State University
Zetian Mi, University of Michigan
Edward Yu, The University of Texas at Austin

Energy Harvesting
Alan Doolittle, Georgia Institute of Technology
Deidra Hodges, Florida International University
Suzanne Mohney, The Pennsylvania State University
Jamie Phillips, University of Delaware
Shadi Shahedipour-Sandvik, State University of New York Polytechnic Institute

Solar Cell Materials and Devices
Rachel Goldman, University of Michigan
Mark Goorsky, University of California, Los Angeles
Andrej Lenert, University of Michigan
Steve Ringel, The Ohio State University
Jae-Hyun Ryou, University of Houston
William Scheideler, Dartmouth College
Christian Wetzel, Rensselaer Polytechnic Institute
Jerry Woodall, University of California, Davis
Heayoung Yoon, The University of Utah

Thermoelectrics and Thermal Transport
Kris Bertness, National Institute of Standards and Technology
Samuel Graham, University of Maryland
Ferdinand Poudeu, University of Michigan
Xiaojia Wang, University of Minnesota
Yaguo Wang, The University of Texas at Austin
Joshua Zide, University of Delaware

Nanoscale Science and Technology

Graphene, BN, MoS2 and Other 2D Materials and Devices
Thomas Beechem, Purdue University
Zizwe Chase, University of Illinois, Chicago
Kevin Daniels, University of Maryland
Mona Ebrish, U.S. Naval Research Laboratory
James Edgar, Kansas State University
Susan Fullerton, University of Pittsburgh
Jyoti Katoch, Carnegie Mellon University
Roland Kawakami, The Ohio State University
Manos Kioupakis, University of Michigan
Soaram Kim, Texas A&M University
Rachel Koltun, Guardian Industries
Lincoln Lauhon, Northwestern University
Suzanne Mohney, The Pennsylvania State University
Siddharth Rajan, The Ohio State University
Joan Redwing, The Pennsylvania State University
Eric Seabron, Howard University
Michael Snure, U.S. Air Force Research Laboratory
Michael Spencer, Morgan State University
Christine Wang, Lincoln Laboratory, Massachusetts Institute of Technology
Huili Grace Xing, Cornell University
Ke Xu, Rochester Institute of Technology
Fei Yan, North Carolina Central University

Low-Dimensional Structures—Quantum Dots, Wires and Wells
Sadhvikas Addamane, Sandia National Laboratory
Ganesh Balakrishnan, The University of New Mexico
Matthew Doty, University of Delaware
Kurt Eyink, Air Force Research Laboratory
Rachel Goldman, University of Michigan
Lincoln Lauhon, Northwestern University
Minjoo (Larry) Lee, University of Illinois at Urbana-Champaign
Zetian Mi, University of Michigan
Parsian Mohseni, Rochester Institute of Technology
Jamie Phillips, University of Delaware
Paul Simmonds, Tufts University
Daniel Wasserman, The University of Texas at Austin

Nanoscale Characterization—Scanning Probes, Electron Microscopy and Other Techniques
Thomas Beechem, Purdue University
Zizwe Chase, University of Illinois, Chicago
Rachel Goldman, University of Michigan
Lincoln Lauhon, Northwestern University
James LeBeau, Massachusetts Institute of Technology
Anders Mikkelsen, Lund University
Jay Mody, Intel Corporation
Volker Rose, Argonne National Laboratory
Eric Seabron, Howard University
Rainer Timm, Lund University
Heayoung Yoon, The University of Utah
Edward Yu, The University of Texas at Austin

Nanostructured Materials
Kris Bertness, National Institute of Standards and Technology
Matt Brubaker, National Institute of Standards and Technology
Xiuling Li, The University of Texas at Austin
Zetian Mi, University of Michigan
Anders Mikkelsen, Lund University
Parsian Mohseni, Rochester Institute of Technology
Roberto Myers, The Ohio State University
Nate Quitoriano, McGill University
Rainer Timm, Lund University
George Wang, Sandia National Laboratories
William Wong, University of Waterloo

Organic Materials, Thin Films, and Devices

Flexible, Printed and/or Dissolvable Thin Films
Suprem Das, Kansas State University
Daniel Ewing, Department of Energy's Kansas City National Security Campus
Gerd Grau, York University
Thomas Jackson, The Pennsylvania State University
Becky (R.L.) Peterson, University of Michigan
Robert C. 'Chris' Roberts, The University of Texas at El Paso
Jae-Hyun Ryou, University of Houston
William Scheideler, Dartmouth College
Jung-Hun Seo, University at Buffalo, The State University of New York
Sarah Swisher, University of Minnesota
William Wong, University of Waterloo

Organic Devices and Molecular Electronics
Canek Fuentes-Hernandez, Northeastern University
Gerd Grau, York University
Thomas Jackson, The Pennsylvania State University
David Janes, Purdue University
Ioannis Kymissis, Columbia University
Takhee Lee, Seoul National University
Curt Richter, National Institute of Standards and Technology
Adrienne Stiff-Roberts, Duke University
Pawan Tyagi, University of the District of Columbia
William Wong, University of Waterloo

Organic and Hybrid Optoelectronic Materials
Alexander Ayzner, University of California, Santa Cruz
Canek Fuentes-Hernandez, Northeastern University
Deidra Hodges, Florida International University
Adrienne Stiff-Roberts, Duke University
Darlene Taylor, North Carolina Central University

Wearable Electronics and Biosensors
Francesca Cavallo, The University of New Mexico
Buddhadev Paul Chaudhuri, Biolinq Inc.
Tzahi Cohen-Karni, Carnegie Mellon University
Shadi Dayeh, University of California, San Diego
David Estrada, Boise State University
Thomas Jackson, The Pennsylvania State University
David Janes, Purdue University
Soaram Kim, Texas A&M University
Robert C. 'Chris' Roberts, The University of Texas at El Paso
Jae-Hyun Ryou, University of Houston
Shayla Sawyer, Rensselaer Polytechnic Institute

Oxide Semiconductors and Dielectrics

Dielectrics, Ferroelectrics and Multifunctional Oxides
Alan Doolittle, Georgia Institute of Technology
Lauren Garten, Georgia Institute of Technology
Doug Hall, University of Notre Dame
Karl Hirschman, Rochester Institute of Technology
Anderson Janotti, University of Delaware
David Lederman, University of California, Santa Cruz
Patrick Lenahan, The Pennsylvania State University
Joseph Ngai, The University of Texas at Arlington
Becky (R.L.) Peterson, University of Michigan
Angel Yanguas-Gil, Argonne National Laboratory

Gallium Oxide and Other Ultra-Wide Bandgap Oxides
Elaheh Ahmadi, University of California, Los Angeles
Thaddeus J. Asel, U.S. Air Force Research Laboratory
Ramana Chintalapalle, The University of Texas at El Paso
Esmat Farzana, Iowa State University
Shizuo Fujita, Kyoto University
Chirag Gupta, University of Wisconsin - Madison
Masataka Higashiwaki, Osaka Metropolitan University
Karl Hirschman, Rochester Institute of Technology
Mihee Ji, U.S. Army Research Laboratory
Nidhin Kurian Kalarickal, Arizona State University
Sriram Krishnamoorthy, University of California, Santa Barbara
Shin Mou, Air Force Research Laboratory
Hari Nair, Cornell University
Becky (R.L.) Peterson, University of Michigan
Lisa Porter, Carnegie Mellon University
Siddharth Rajan, The Ohio State University
Marko Tadjer, U.S. Naval Research Laboratory
Man Hoi Wong, Hong Kong University of Science and Technology
Huili Grace Xing, Cornell University
Hongping Zhao, The Ohio State University

Oxide Semiconductors—Growth, Doping, Defects, Nanostructures and Devices
Leonard Brillson, The Ohio State University
Karl Hirschman, Rochester Institute of Technology
Thomas Jackson, The Pennsylvania State University
Anderson Janotti, University of Delaware
Mark Losego, Georgia Institute of Technology
Hari Nair, Cornell University
Becky (R.L.) Peterson, University of Michigan
Shayla Sawyer, Rensselaer Polytechnic Institute
William Scheideler, Dartmouth College
Sarah Swisher, University of Minnesota
Kin-Man Yu, City University of Hong Kong

Wide Bandgap Semiconductors

Diamond and Ultra-Wide Bandgap Materials
Mark Goorsky, University of California, Los Angeles
Andrew Koehler, U.S. Naval Research Laboratory
Nadeemullah Mahadik, U.S. Naval Research Laboratory
Mahesh R. Neupane, U.S. Army Research Laboratory
Lisa Porter, Carnegie Mellon University
Jung-Hun Seo, University at Buffalo, The State University of New York
Patrick Shea, Northrop Grumman Corporation
Michael Spencer, Morgan State University

Group III-Nitrides—Growth, Processing, Characterization, Theory and Devices
Elaheh Ahmadi, University of California, Los Angeles
Zakaria Y. Al Balushi, University of California, Berkeley
Andrew Allerman, Sandia National Laboratories
Srabanti Chowdhury, Stanford University
Theeradetch Detchprohm, Georgia Institute of Technology
Alan Doolittle, Georgia Institute of Technology
Russell Dupuis, Georgia Institute of Technology
Daniel Ewing, DOE Kansas City National Security Campus
Esmat Farzana, Iowa State University
Qhalid Fareed, Texas Instruments
Daniel Feezell, The University of New Mexico
Hiroshi Fujioka, The University of Tokyo
Chirag Gupta, University of Wisconsin - Madison
Matthew Hardy, U.S. Naval Research Laboratory
Jennifer Hite, U.S. Naval Research Laboratory
Mihee Ji, U.S. Army Research Laboratory
Andrew Koehler, U.S. Naval Research Laboratory
In-Hwan Lee, Korea University
Xiaohang Li, King Abdullah University of Science & Tech.
Shubhra Pasayat, University of Wisconsin - Madison
Siddharth Rajan, The Ohio State University
Shadi Shahedipour-Sandvik, SUNY Polytechnic Institute
Andrei Vescan, RWTH Aachen University
Christian Wetzel, Rensselaer Polytechnic Institute
Jonathan Wierer, North Carolina State University
Man Hoi Wong, Hong Kong University of Science & Tech.
Huili Grace Xing, Cornell University

Silicon Carbide—Growth, Processing, Characterization, Theory and Devices
Joshua Caldwell, Vanderbilt University
MVS Chandrashekhar, University of South Carolina
Sarit Dhar, Auburn University
Hemant Dixit, Wolfspeed
Michael Dudley, Stony Brook University, SUNY
Daniel Ewing, DOE Kansas City National Security Campus
Nadeemullah Mahadik, U.S. Naval Research Laboratory
Michael Spencer, Morgan State University

FLOOR PLANS & MAPS

The University of Maryland, College Park

Registration will be located in Edward St. John (ESJ) and open during the following times:

Wednesday: 7:30 AM - 7:30 PM
Thursday: 8:00 AM - 5:30 PM
Friday: 8:00 AM - 10:30 AM

Please pick up your badge upon arrival to the conference. Badges must be worn at all times to access conference activities.

The technical sessions will be located in Edward St. John except for the Wednesday morning award session and plenary. The Wednesday morning award session and plenary is located in the Grand Ballroom in the Stamp Student Union. Please note it takes approximately five minutes to walk between the buildings. The walking path can be found on the diagram.

Other Important Locations:
Daily Lunch: Yahentamitsi Dining Hall
Note: Pre-purchased ticket required

Exhibits: ESJ

Welcome Reception/Poster Session: ESJ

Conference Dinner: Stamp Student Union, Grand Ballroom

Those staying on campus should retrieve their rooming information at Annapolis Hall. Check in is Tuesday between 3 PM - 6 PM. If you arrive outside of these hours, an onsite attendant will be able to assist at Annapolis Hall. There will be no storage of your personal luggage in ESJ.

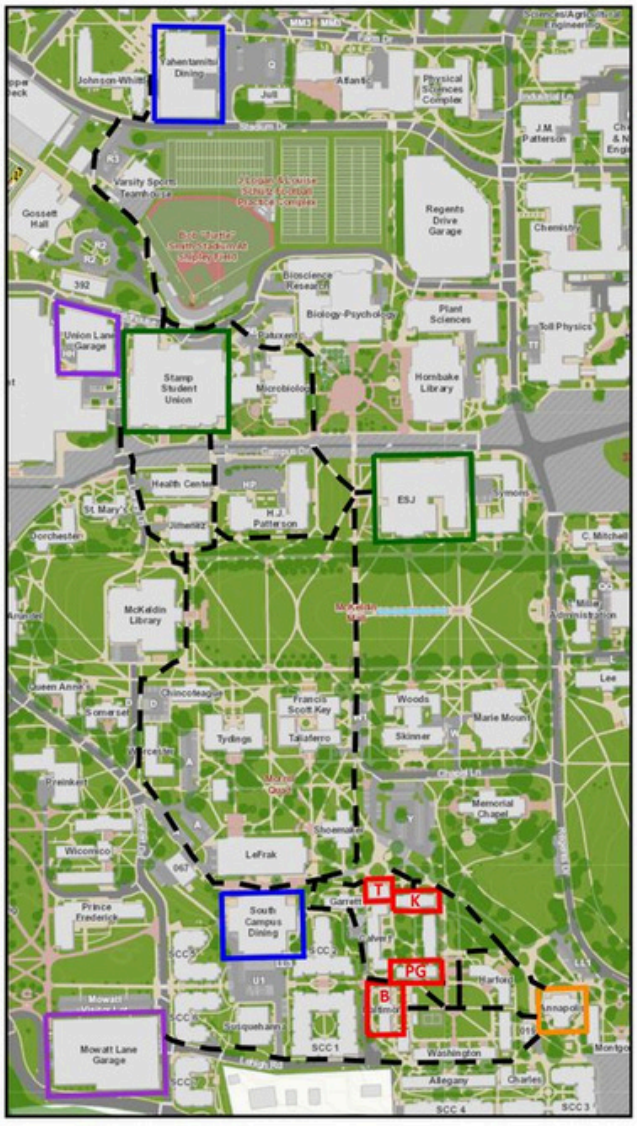

The University of Maryland, College Park, USA

Edward St. John will host the majority of the EMC 2024 conference events and technical sessions.

Edward St. John Learning and Teaching Center is on a hill, allowing street access to two floors. It is easiest to walk in the doors on Campus Drive.

The Ground Floor (rooms 0100-0300) can be accessed from McKeldin Mall and Campus Drive (doors facing Hornbake Library).

The First Floor (rooms 1100-1300) can be accessed from Campus Drive (doors facing HJ Patterson), and the columned historical entrance facing McKeldin Mall.

The Academy Loft 2101 is only accessible from the south (McKeldin Mall) side of the building. It is not connected to the rest of the second floor.

Please see the provided floor maps of the classrooms in ESJ.

Doors facing HJ Patterson along Campus Drive

Historical entrance facing McKeldin Mall

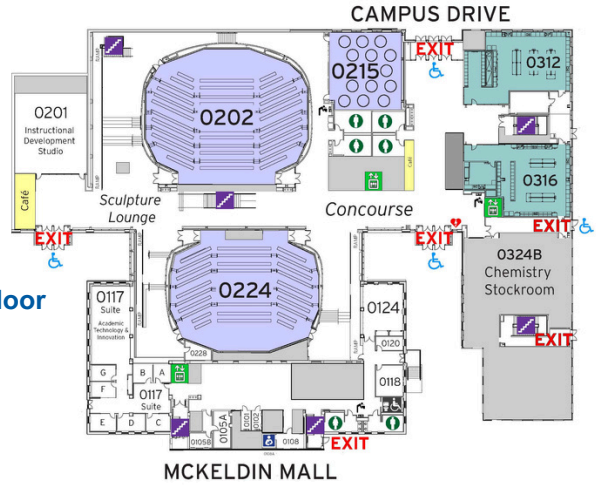

Ground Floor

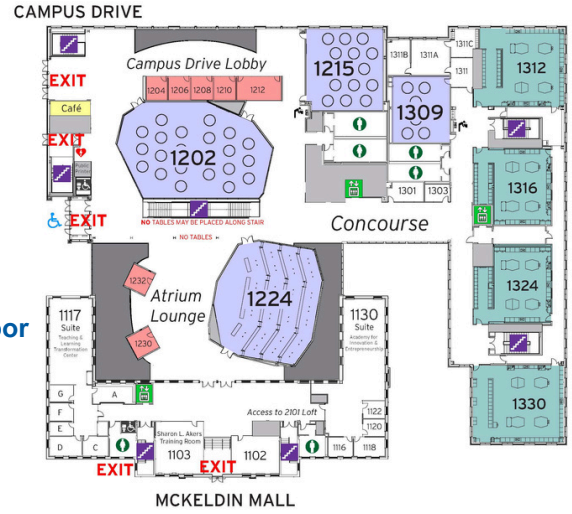

First Floor

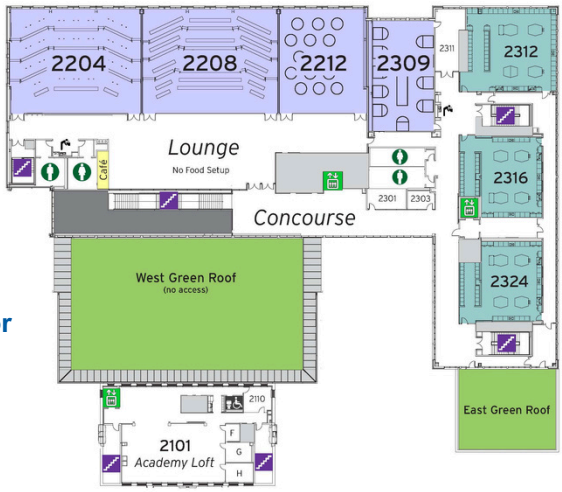

Second Floor

EMC AWARDS CEREMONY AND PLENARY SESSION

Wednesday, 8:15 AM - 9:30 AM
Stamp Student Union, Grand Ballroom

2023 STUDENT AWARDS

PLENARY SPEAKER

Joseph J. Berry
The University
of Colorado Boulder

Joseph J. Berry is a Senior Research Fellow and team lead for metal halide perovskite technologies at the National Renewable Energy Laboratory and an Associate Professor of Physics at the University of Colorado Boulder. He is a graduate of the Penn State Department of Physics, receiving his PhD for work on spin physics of magnetic II-VI, III-V and metallic/semiconductor systems. After his PhD work, he was awarded a National Research Council Fellowship at the National Institute of Standards and Technology (NIST/JILA), where he worked on the development and application of high-resolution spectroscopic techniques to solid-state electro-optical systems. Since joining NREL he has worked on a range of thin film photovoltaic materials and devices with an emphasis on relating basic interfacial properties to device level performance. He has worked on these issues in several Energy Frontier Research Centers (EFRCs) to connect basic science of materials, with an emphasis on semiconductors, to advances in energy technologies. His research interests have led to his current focus on metal-halide-perovskite enabled tandem PV technologies.

A Perovskite Paved Pathway to Multi-Terawatt scale Photovoltaics

This talk will consider the future of metal halide perovskite (MHP) photovoltaic (PV) technologies as photovoltaic deployment reaches the terawatt scale. The requirements for significantly increasing PV deployment beyond current rates and what the implications are for technologies attempting to meet this challenge will be addressed. In particular how issues of CO2 impacts and sustainability inform near and longer-term research development and deployment goals for MHP enabled PV will be discussed. To facilitate this, an overview of current state of the art results for MHP based single junction, and multi-junctions in all-perovskite or hybrid configurations with other PV technologies will be presented. This will also include examination of performance of MHP-PVs along both efficiency and reliability axes for not only cells but also modules placed in context of the success of technologies that are currently widely deployed.

Best Student Poster Award

Hansel Hobbie
"Zirconium Oxide Dielectric Thin Films Fabricated by Water-only Aerosol Jet Printing"
Advisor: Aaron Franklin, Duke University

DAILY SCHEDULE OF EVENTS

ESJ = Edward St. John Building
Stamp = Stamp Student Union

Wednesday	
7:30 AM	Registration Opens - ESJ Building, Ground Floor
8:15 AM	EMC and DRC Joint Plenary - The Grand Ballroom, Stamp Student Union Building
9:30 AM	Coffee Break
10:00 AM	Group III-Nitrides: Detectors - ESJ 0202
	Gallium Oxide Electronic Devices - ESJ 0224
	Metamaterials and Materials for THz, Plasmonics, and Polaritons - ESJ 2208
	Nano-Magnetic, Magnetic Memory and Spintronic Materials - ESJ 2204
	Computational Electronic Materials Discovery - ESJ 1224
11:30 AM	Lunch
1:00 PM	Nitride Electronic Devices - ESJ 0202
	Multifunctional Oxides: Characterization and Processing - ESJ 0224
	Nonlinear and Plasmonic Materials - ESJ 2208
	Graphene and Graphene Heterostructure Synthesis and Devices - ESJ 2204
	Growth and Characterization of Diamond and WBG-Nitride Materials - ESJ 1224
	Electrochemical Energy Storage - ESJ 1202
2:15 PM	Coffee Break
2:45 PM	Nitride Electronic Devices - ESJ 0202
	Multifunctional Oxides: Characterization and Processing - ESJ 0224
	Epitaxy of Dissimilar Materials - ESJ 2208
	Graphene and Graphene Heterostructure Synthesis and Devices - ESJ 2204
	Growth and Characterization of Diamond and WBG-Nitride Materials - ESJ 1224
	Advances in Thermal Co-Design and Solutions for Wide Bandgap Semiconductors - ESJ 1202
4:30 PM	Student Finalists Oral Presentation Award -- ESJ 0202 and 0224
	Student FInalists Oral Presentation Award - Part A - ESJ 0202
	Student Finalists Oral Presentation Award - Part B - ESJ 0224
6:00 PM	Welcome Reception and Poster Session - ESJ Building, Ground Floor

DAILY SCHEDULE OF EVENTS

ESJ = Edward St. John Building
Stamp = Stamp Student Union

Thursday	
8:00 AM	Registration Opens - ESJ Building, Ground Floor
8:30 AM	III-N Device and Material Characterization - ESJ 0202
	Oxide Semiconductor Thin Films and Devices - ESJ 0224
	Narrow Gap and Highly Mismatch Alloys - ESJ 2208
	Materials for Quantum Applications - ESJ 2204
	Doping and Impurities - ESJ 1224
	Wearable Electronics and Biosensors - ESJ 1202
	Epitaxial Materials - ESJ 1215
9:45 AM	Coffee Break
10:15 AM	III-N Device and Material Characterization - ESJ 0202
	Oxide Semiconductor Thin Films and Devices - ESJ 0224
	Epitaxy of Highly Mismatched Alloys - ESJ 2208
	Materials for Quantum Applications - ESJ 2204
	Doping and Impuritie - ESJ 1224
	Wearable Electronics and Biosensors - ESJ 1202
	Novel Integration and Material Processing - ESJ 1215
11:30 AM	Lunch
1:00 PM	III-Nitride: Ferroelectric Materials and Devices - ESJ 0202
	Gallium Oxide Epitaxy, Processing, and Characterization - ESJ 0224
	Printed Electronic Materials and Devices - ESJ 2208
	Nanofabrication and Processing - ESJ 2204
	SiC Materials, Characterization and Devices - ESJ 1224
	Materials for Memory and Computation - ESJ 1202
2:15 PM	Coffee Break
2:45 PM	Contacts to III-N Semiconductors - ESJ 0202
	Gallium Oxide Epitaxy, Processing, and Characterization - ESJ 0224
	Additive Manufacturing and 3D Devices - ESJ 2208
	Nanostructured Materials and Devices - ESJ 2204
	SiC Materials, Characterization and Devices - ESJ 1224
	Materials for Memory and Computation - ESJ 1202
	Heterointegration of WBG/UWBG semiconductors - ESJ 1215
4:30 PM	Panel Discussion: Future Careers in Electronic Materials, ESJ 0202
6:00 PM	EMC 2024 Conference Dinner - Stamp Student Union Building, Grand Ballroom

DAILY SCHEDULE OF EVENTS

ESJ = Edward St. John Building
Stamp = Stamp Student Union

Friday	
8:00 AM	Registration Opens - ESJ Building, Ground Floor
8:30 AM	Growth of Group III-Nitrides - ESJ 0202
	Optoelectronic Devices - ESJ 0224
	Hybrid Organic/Inorganic Devices and Molecular Electronics - ESJ 2208
	Transition Metal Dichalcogenide and h-BN Synthesis and Devices - ESJ 2204
	Ferroelectrics and Structural Defects - ESJ 1224
	Solar Cell Materials and Devices - ESJ 1202
9:45 AM	Coffee Break
10:15 AM	Growth of Group III-Nitrides - ESJ 0202
	Optoelectronic Devices - ESJ 0224
	Oxide UV Photodetectors and Other Devices - ESJ 2208
	Transition Metal Dichalcogenide and h-BN Synthesis and Devices - ESJ 2204
	Doping and Transport - ESJ 1224
	Solar Cell Materials and Devices - ESJ 1202
11:30 AM	EMC 2024 Complete

CONFERENCE BADGE

Badges must be worn at all times within the Conference venue, including all receptions.

RECORDING/PHOTO POLICY

Recording or photographing Conference presentations, posters or displays is strictly prohibited without prior permission of the presenter.

PROGRAM-AT-A-GLANCE

ESJ = Edward St. John Building
Stamp = Stamp Student Union

WEDNESDAY AM

7:30 AM	**Registration Opens**	
8:15 AM	**EMC and DRC Joint Plenary - The Grand Ballroom, Stamp Student Union Building**	
9:30 AM	**Coffee Break**	
10:00 AM	**Group III-Nitrides: Detectors ESJ 0202**	
	10:00 AM	Effects of Radiation and Operating Temperature in GaN and AlN Thin-Film Piezoelectric Sensors for Harsh Environment Applications
	10:15 AM	Improved Responsivity of GaN-based Avalanche Photodetectors through Implementation of AlGaN Windows
	10:30 AM	Development of N-polar InAlGaN for Cs-free photocathode structures
	10:45 AM	Device design and demonstration of an integrated AlGaN/GaN infrared detector with InGaN/GaN visible emitter
	11:00 AM	Lateral p-GaN/AlGaN/GaN Hybrid Anode Diodes (HADs) with Hydrogen Plasma Triangular Guard Array (TGA) Termination
	Gallium Oxide Electronic Devices ESJ 0224	
	10:00 AM	Effect of surface preparation on electrical characteristics of Ga2O3 vertical rectifiers
	10:15 AM	Characterization of temperature dependence of barrier height in Ni/β-Ga2O3 SBD over a wide temperature range and evaluation of valence band structure by XPS
	10:30 AM	β-(AlxGa1−x)2O3 Vertical SBD with a BN interlayer
	10:45 AM	Field Engineering for BTBT Leakage Current Suppression in NiOx/β-Ga2O3 PN and PiN Heterojunction diodes
	11:00 AM	Reliability studies of large-scale vertically stacked ultrawide bandgap oxides for CMOS IC
	11:15 AM	Systematic Investigation of Electrical Performance of β-Ga2O3 Schottky Barrier Diodes under High-Dose Gamma Irradiation
	Metamaterials and Materials for THz, Plasmonics, and Polaritons ESJ 2208	
	10:00 AM	Enhancing Light-Matter Interactions in the Long Wave Infrared
	10:15 AM	Lateral Cavity-Enhanced Guided Mode Resonance Structure for Mid-wave Infrared Photodetection
	10:30 AM	Temperature Dependent Properties of doped InAsSb/GaSb Hyperbolic Metamaterial Stacks
	10:45 AM	Anomalous diffraction in two-dimensional metacrystals from propagating surface modes
	11:00 AM	Hybrid Terahertz Photonic Structure of Al/Cd3As2 for Ultrastrong Coupling Applications
	11:15 AM	Realizing Molecular Optomechanics Induced Hybrid Properties in Soft Materials Filled Plasmonic Nanocavities
	Nano-Magnetic, Magnetic Memory and Spintronic Materials ESJ 2204	
	10:00 AM	Induced Magneto-Electric Properties of Fe3+ Doped Ruddlesden Popper Perovskite Nanocomposite Antennas for Bio-Compatible Sensor Devices
	10:15 AM	Efficient Voltage Control of Two-Dimensional Magnetic Insulators
	10:30 AM	Near Ideal Band-Insulator Behavior in Bi2(Te,Se)3/Bi2Te3 Superlattice Heterostructures
	10:45 AM	Spin-orbit torque facilitated switching of Bi2Se3/NiFe heterostructures
	11:00 AM	Efficient generation of spin-polarized light emission with 2D magnetic heterostructure
	11:15 AM	Magnetic Tunnel Junction Testbed based Molecular Spintronics Devices: A Method of Solving 70-Year-Old Challenge in Making Molecular Devices
	Computational Electronic Materials Discovery ESJ 1224	
	10:00 AM	Blackbox Machine Learning for Nonlinear Materials Design
	10:15 AM	Light-matter interaction in Fabry Perot interferometer made of MXene based Distributed Bragg Reflectors
	10:30 AM	Electronic structure and magnetism of titanium carbide MXenes
	10:45 AM	A Practical Simulation and Modeling Solution for Complex Magnetic Molecule and Magnetic Tunnel Junction-based Molecular Spintronics Devices: A Monte Carlo Method
	11:00 AM	The Monoclinic Beer-Lambert Law in Beta Gallium Oxide
	11:15 AM	Selective Incorporation of Group-V Elements in GaN
11:30 AM	**Lunch**	

PROGRAM-AT-A-GLANCE

ESJ = Edward St. John Building
Stamp = Stamp Student Union

WEDNESDAY PM

1:00 PM	**Nitride Electronic Devices ESJ 0202**	
	1:00 PM	High Forward Current Density in Si-doped AlN Schottky Barrier Diodes
	1:15 PM	Mitigation of Reverse Leakage Current and Charge Trapping in GaN Schottky Barrier Diodes
	1:30 PM	Monolithic Bidirectional GaN-on-Si HEMT with >1.5kV Breakdown Voltage
	1:45 PM	Ohmic and Schottky Contacts to High-Voltage GaN Photoconductive Semiconductor Switch
	2:00 PM	Charge-trap coupled ferroelectric gate ScAlN/ScN/AlGaN/GaN HEMT with normally off operation
	Multifunctional Oxides: Characterization and Processing ESJ 0224	
	1:00 PM	Proposal for a new evaluation method of relationship between the lifetime of ferroelectric capacitors and dielectric breakdown spot
	1:15 PM	In situ nondestructive spectromicroscopic analysis of dielectric breakdown in HfO2-based ferroelectric capacitors by laser-based photoemission electron microscope
	1:30 PM	Three-dimensional Characterization of Antiferroelectric Nanodomains Stabilized by Chemical Disorder with Multislice Electron Ptychography
	1:45 PM	Visualizing Polar Textures in 3D Using Multislice Electron Ptychography
	2:00 PM	Remote Hydrogen Plasma defect analysis of Ga2O3
	Nonlinear and Plasmonic Materials ESJ 2208	
	1:00 PM	Coupled Quantum Well Interface Quality and Second-Harmonic Generation Effects
	1:15 PM	Semiconductor quantum well structures with large third-order interband optical nonlinearities
	1:30 PM	Optical Structuring to Reliably Determine Interband Optical Nonlinearity via Second Harmonic Generation
	1:45 PM	Probing the Electric Dipole Approximation in Nonlocal Systems
	2:00 PM	Shadow Mask Molecular Beam Epitaxy
	Graphene and Graphene Heterostructure Synthesis and Devices ESJ 2204	
	1:00 PM	Mechanics of Ultra-High Sensitivity Epitaxial Graphene ELISA Sensors
	1:15 PM	High-Density and Responsivity NIP Axial-Core Shell GaAsSb Nanowire Photodetectors on Monolayer Graphene for Near-Infrared Applications
	1:30 PM	Investigation of Dry Transfer of Epitaxial Graphene from SiC(0001)
	1:45 PM	Ionic Sieve Based - Redox Gas Sensing via Layered Manganese Dioxide Epitaxial Graphene Heterostructures
	2:00 PM	Synthesis and Device Applications of Monolayer InO2 at the EG/n-SiC Interface
	Growth and Characterization of Diamond and WBG-Nitride Materials ESJ 1224	
	1:00 PM	Investigation of Mechanical and Electrical Properties of Polycrystalline Diamond Membranes and Devices
	1:15 PM	X-ray Topography and Scattering of Single Crystal (001) Diamond Substrates for Wafer Bonding Applications
	1:30 PM	Thermal Performance and Interfacial Mapping of a Compression Bonded GaN/diamond Interface for Vertical Power Devices
	1:45 PM	Codesigned III-Nitride Devices: Thermal Boundary Resistance in AlN Heat Spreaders on Sapphire, Bulk AlN, and Copper
	2:00 PM	MPCVD Growth of Polycrystalline Diamond on (010) β-Ga2O3 for Thermal Management
	Electrochemical Energy Storage ESJ 1202	
	1:00 PM	In-Operando Monitoring of V2O5 Interfacial Defects at Solid State Battery Interfaces
	1:15 PM	A nanoindentation platform for in-operando measurement of stress-electrochemical coupling in thin-film solid-state batteries
	1:30 PM	Tuning the composition and structure of high mobility NASICON-like thin films through atomic layer deposition
	1:45 PM	Deposition of LiPON solid-electrolyte onto V2O5 leads to intense lithiation
	2:00 PM	Models for Solid-Electrolyte Fracture during Li-Metal Plating require Consistent Electrochemical-Mechanical Couplings
2:15 PM	**Coffee Break**	

PROGRAM-AT-A-GLANCE

ESJ = Edward St. John Building
Stamp = Stamp Student Union

WEDNESDAY PM

2:45 PM	**Nitride Electronic Devices ESJ 0202**	
	2:45 PM	Probing the role of AlGaN's surface oxide in contacts to Al-rich AlGaN heterostructures
	3:00 PM	The Deposition Temperature Impact in Sputtered Magnesium Oxide on n-Type Gallium Nitride for Metal-Oxide-Semiconductor Capacitors Applications
	3:15 PM	Optimization of the BFoM: New Insights on the Power Performance of Wide- and Ultrawide-Bandgap Semiconductors
	3:30 PM	Enhancement Mode AlInN/GaN High Electron Mobility Transistors via Thermally Oxidized AlxIn1-xN Gates
	3:45 PM	Ti-Based Contact Optimization for Demonstration of AlN MOSFET
	Multifunctional Oxides: Characterization and Processing ESJ 0224	
	2:45 PM	Developing X-ray Diffraction Methods for Multilayer Thin-Film 128° Y-cut LiNbO3 on Sapphire
	3:00 PM	Nanomembrane Transfer based integration of High-k Crystalline SrTiO3 Thin Film with GaN
	3:15 PM	Characterization of ALD HfSiOx gate dielectric on β-Ga2O3 (001)
	3:30 PM	Rietveld refinement, Dielectric and Electrical response of DyFeO3 nanoparticles
	3:45 PM	Evolution of Insulator-Metal Transition and Magnetoresistance with Thickness in Oxygen deficient Strontium Titanate Thin Films
	Epitaxy of Dissimilar Materials ESJ 2208	
	2:45 PM	Defect Filtering at the Interface of III-V on Silicon though Templated Liquid Phase Growth
	3:00 PM	A Platform Method to Growth Epitaxial III-V on LiNbO3
	3:15 PM	Electron Microscopy based Characterization of GaSb Growth on Silicon for Fabrication of Quantum Dots
	3:30 PM	Room temperature 3 – 8 μm photoluminescence in heteroepitaxial Pb1-xSnxSe on GaAs
	3:45 PM	Altermagnetic α-MnTe Films Grown by Molecular Beam Epitaxy on Al2O3 (0001) Substrates
	Graphene and Graphene Heterostructure Synthesis and Devices ESJ 2204	
	2:45 PM	Mobility Enhancement in a 2D Electron Gas formed by a Topological Crystalline Insulator/Graphene Heterostructure
	3:00 PM	Emission Current Enhancement from Quasi-Freestanding Epitaxial Graphene Microstructure Electron Emitters Through Surface Layered Silicon Dioxide
	3:15 PM	Microwave photoexcited transport studies of graphene
	3:30 PM	Linear Stark shift of two-dimensional Ga via AC electric double layer gating
	Growth and Characterization of Diamond and WBG-Nitride Materials ESJ 1224	
	2:45 PM	High-Temperature AlN Schottky Barrier Diodes on Single-Crystal AlN Substrates
	3:00 PM	Growth of Cubic Boron Nitride by Plasma Assisted Chemical Vapor Deposition on Silicon and Diamond Substrate
	3:15 PM	Assessing the quality of h-BN single crystals by metal-flux method for developing phosphors for deep-UV AC-driven powder electroluminescent devices
	3:30 PM	Charge distribution and transport coefficients of mobile holes in gated diamond heterostructures.
	3:45 PM	Epitaxial AlN film with improved quality on Si (111) substrates realized by boron pretreatment via MOCVD
	Advances in Thermal Co-Design and Solutions for Wide Bandgap Semiconductors ESJ 1202	
	2:45 PM	Gallium Oxide Epitaxy and Devices For Enhanced Electro-thermal performance
	3:00 PM	Considerations and Strategies for Gallium Oxide Power Module Packaging
	3:15 PM	Enhancing Thermal Transport at Interfaces in Wide Bandgap Electronics
4:30 PM	**Student FInalists Oral Presentation Award - Part A ESJ 0202**	
	4:30 PM	GaAsSb/Si heterojunction photodiodes fabricated with epitaxial layer transfer
	4:45 PM	Molecular Beam Epitaxy Selective Area Regrowth of High Aspect Ratio Microstructures for Mid-Infrared Optoelectronics
	5:00 PM	Shadow Mask Molecular Beam Epitaxy
	5:15 PM	Bismuth Incorporation into InSb Towards Long-Wave Infrared Photodetectors
	Student Finalists Oral Presentation Award - Part B ESJ 0224	
	4:30 PM	Expanded stability of layered SnSe-PbSe alloys and evidence of displacive phase transformation from rocksalt in heteroepitaxial thin films
	4:45 PM	Lathe-based Aerosol Jet Printing: A New Additive Manufacturing Method for Fabricating Conformal Electronics on 3D Curvilinear Substrates
	5:00 PM	Exploring Form and Functionalization in Crystalline Nanocellulose Inks for Environmentally Sustainable Printed Electronics
	5:15 PM	Heteroepitaxial Integration of Embedded Visible InP Quantum Dot Lasers on SiN/Si Photonic Integrated Circuits
6:00 PM	**Welcome Reception and Poster Session - ESJ Building**	

POSTER SESSION

ESJ = Edward St. John Building
Stamp = Stamp Student Union

WEDNESDAY PM | ESJ Building

Poster Set Up
8:00 AM - 2:00 PM

General Viewing
Wednesday:
2:15 PM - 2:45 PM

Thursday:
9:45 AM - 10:15 AM
2:15 PM - 2:45 PM

Poster Tear Down
Thursday:
By 5:30 PM

All posters that remain hung up by this time will be thrown away

- **Poster boards are aligned in a horizontal format. Each poster should be no larger than 4ft x 4ft. Each poster board will be double-sided with two posters each side. The poster boards will have push pins available to you to use.**
- **All poster presenters are responsible for printing and bringing their own poster to hang. There are no large printers at the conference.**
- **Poster presenters should be standing with their poster.**
- **Student poster presenters must attend from 6:00 pm to 8:00 pm to present poster and answer questions to be eligible for the Best Student Poster Presentation Award.**

Poster 1	MXene-contacted Carbon Nanotube Thin-film Transistors Using Aerosol Jet Printing
Poster 2	TOWARDS P3HT INKJET PRINTABILITY OF SENSORS
Poster 3	Resolving Complex Surface Engineering Challenges by Taguchi Design of Optimization of Electroless Nickel Coating Parameters on Additively Manufactured Binder Jetted Composites*
Poster 4	Machine Learning-Enabled Quantitative Analysis of Optically Obscure Scratches on Nickel-Plated Additively Manufactured (AM) Samples
Poster 5	Investigating the Role of Machine Learning and Deep Learning for Determining the Performance of Perovskite-Based Solar Cells
Poster 6	Graphical User Interface and Data Visualization for Monte Carlo-based simulation of Molecular Tunnel Junction Spintronics Devices
Poster 7	Evaluation of Machine Learning Models for Monte Carlo Simulation study of Magnetic Tunnel Junction based Spintronic Devices (MTJMSDs).
Poster 8	Influence of Edge-Contact Formation Conditions on Monolayer MoS2 Transistors
Poster 9	Electrical and material characterization of ion beam-modified contact interfaces in WS2 field-effect transistors
Poster 10	Fabrication and Characterization of Exfoliated h-BN/Graphene Devices on prepatterned contacts
Poster 11	Supercapacitive Properties of Pulsed Laser Deposited Ba(Fe0.7Ta0.3)O3−δ Thin Films Deposited on Ni Foil
Poster 12	Growth Optimization and Characterization of Sn-doped Gallium Oxide Thin Films by Pulsed Laser Deposition for κ-Ga2O3 Stabilzation
Poster 13	Synthesis of 5,10,15,20-Tetrasulphonatophenyl Porphyrin Molecular Channels for Harnessing Magnetic Tunnel Junction based Molecular Spintronic Device for Fuel Cell Application
Poster 14	Photovoltaic effect on silicon-alumina-ferromagnet tunnel junction providing insights about spin-dependent molecular spintronics solar cells
Poster 15	Paramagnetic Molecules Lose Identity When Connected to Diverse Combinations of Metal Electrodes In MTJ Based Molecular Spintronics Devices
Poster 16	Photoluminescence maps of defects in β-Ga2O3
Poster 17	Fabrication and Characterization of SnO2 Electron transport Layer
Poster 18	Carrier Recombination Dynamics in Intrinsic and Alloyed β-Ga2O3 Thin Films on Sapphire Substrate
Poster 19	Structural characterization and surface morphology of thick homoepitaxial growth on miscut (100) β-Ga2O3 substrates by MOCVD
Poster 20	Studying Single Molecule Magnet (SMM) induced coupling effect on Magnetic Tunnel Junction (MTJ) using Electron spin resonance (ESR)
Poster 21	Correlation between Local chemistry, Bottleneck size, and Lithium conductivity in perovskite solid electrolytes
Poster 22	Improvement of CdTe Solar Cells Using Patterned Al2O3 Reflectors
Poster 23	Thermal Conductivity of High Al Content AlGaN Multiple Quantum Well Heterostructures
Poster 24	Benchmarking Diamond Surface Preparation via Inductively Coupled Plasma-Reactive Ion Etching (ICP-RIE)
Poster 25	In-situ annealing induced phase transition of α, κ, γ-Ga2O3 in different atmospheric conditions
Poster 26	Solution-Processed SnO2 Thin Film Transistor with Low Operating Voltage Enabled by Li2SnO3/SnO2 Stacked Gate Dielectric
Poster 27	Intercalation of Nanostructured Polyacrylonitrile Particles on Ti3C2 MXene Layers for Improved Supercapacitance

POSTER SESSION

ESJ = Edward St. John Building
Stamp = Stamp Student Union

WEDNESDAY PM | ESJ Building

Poster 28	Structural Profiling of SnO2 Aerogels for Electronic Applications
Poster 29	Effect of metal doping on topographic, microstructure, optical and thermal properties of ZONP
Poster 30	Multi-level Switching of ZnS-Based RRAM
Poster 31	Effect of Co-suppering NiO: V2O5 Thin Film for Hydrogen Sensing Application
Poster 32	Effect of Dzyaloshinskii -Moria interaction on Magnetic Tunnel Junction-Based Molecular Spintronics Devices (MTJMSDs)
Poster 33	Resistive-Switching characteristics in ALPO
Poster 34	Fabrication and Characterization of Flexible PVDF-TrFE/MnCoFe204 Nanocomposite Thin Film for Electrical Applications
Poster 35	Enhancing IGZO Thin Film Transistors: A Dual Treatment Approach
Poster 36	In situ growth of lead-free perovskite crystals on fine fibers for flexible fiber-based solar cell manufacturing
Poster 37	Structural Improvement in epitaxial NbN films grown on vicinal c-plane Sapphire
Poster 38	Rolled-up metamaterials (RUMMS) for infrared imaging
Poster 39	Engineering ErAs:InGaAlBiAs Photoconductive Switches for THz Emission and Detection: Material Design, Growth, and Characterization
Poster 40	Modeling the Optical Properties of Reconfigurable Phase Change Materials on Nanostructured Silicon
Poster 41	Fabrication of PDMS-based Piezoelectric Nanogenerator Using Indium Doped Zinc Stannate towards Energy Harvesting and Sensory Applications
Poster 42	DFT-Based Modeling of Epitaxial Silicon Growth from TCS-H2 systems
Poster 43	Morphology-Driven Magnetic Property Manipulation in Binary Particle Mixtures for Microscale Magnetic Control.
Poster 44	Impact of Mg Incorporation in Semipolar Planes of N-polar and Ga-polar 3D Microstructures on Photocathode Internal Quantum Efficiency

Journal of Electronic Materials

A special issue of the Journal of Electronic Materials (JEM)* will be published with peer-reviewed papers from the 66th Electronic Materials Conference.

- Article Submission Deadline: August 31, 2024 at 11:59 PM (Eastern)
- Contact the 2024 Special Issue Editors listed below

The Journal of Electronic Materials reports monthly on the science and technology of electronic materials, while examining new applications for semiconductors, magnetic alloys, dielectrics, nanoscale materials and photonic materials. The Journal welcomes articles on methods for preparing and evaluating the chemical, physical, electronic and optical properties of these materials. Specific areas of interest are materials for state-of-the-art transistors, nanotechnology, electronic packaging, detectors, emitters, metallization, superconductivity and energy applications. Review papers on current topics enable individuals in the field of electronics to keep abreast of activities in areas peripheral to their own.

Manuscripts for the EMC 2024 collection will be evaluated according to the same high standards as would be applied to any article submitted to the Journal. Authors are encouraged to read carefully and comply with the “Instructions for Authors” on springer.com/journal/11664. Submission of a manuscript implies that the work described has not been previously published and is not under consideration for publication elsewhere.

Questions?

Contact the 2024 Special Issue Editors:

Parsian K. Mohseni
pkmeen@rit.edu

Ganesh Balakrishnan
gunny@unm.edu

Wojciech M. Jadwisienczak
jadwisie@ohio.edu

PROGRAM-AT-A-GLANCE

ESJ = Edward St. John Building
Stamp = Stamp Student Union

THURSDAY AM

8:00 AM	**Registration Opens**	
8:30 AM	**III-N Device and Material Characterization ESJ 0202**	
	8:30 AM	Dependence of Minority Carrier Lifetime on Alpha Irradiation Fluence in n-type Free-Standing GaN
	8:45 AM	Temperature-dependent measurement of hole velocity vs. electric field in polarization-induced two-dimensional hole gases in GaN/AlN heterojunctions
	9:00 AM	Growth and Characterization of UV-A Light-Emitting Diodes
	9:15 AM	Epitaxially Grown N-polar GaN Quantum Dots for Short Wave Ultraviolet (UV-C) Applications
	9:30 AM	Hole Transport and Doping in Polarization-Graded p-type AlGaN
	Oxide Semiconductor Thin Films and Devices ESJ 0224	
	8:30 AM	Electrically Active Defects and Their Impact on Carrier Mobility and Density in Indium Tin Oxide (ITO)
	8:45 AM	Enhanced Charge Transport and Transistor Performance of α-IGZO Oxide Semiconductor via High-k/Low-k Bilayer Gate Dielectrics
	9:00 AM	Metastability Of Indium-Tungsten-Oxide Thin-Film Transistors And Associated Operational Dependence On Oxygen Partial Pressure
	9:15 AM	Kinetically Controlled Liquid Metal Printed Ternary 2D Semiconducting Oxides
	9:30 AM	Oxide Transistors on Gallium Nitride as a Platform for Monolithic MicroLED Displays
	Narrow Gap and Highly Mismatch Alloys ESJ 2208	
	8:30 AM	Bismuth Incorporation into InSb Towards Long-Wave Infrared Photodetectors
	8:45 AM	Analysis of Highly Mismatched Sb-based Alloys grown on InAs Substrates
	9:00 AM	Bismuth Incorporation in AlInSb for an Improved Barrier Layer Material
	9:15 AM	Negative Differential Resistance in Ultra-Thin Mid-Wave Infrared Detectors
	9:30 AM	Heteroepitaxial IV-VI semiconductor mid-infrared light-emitting diodes and detectors
	Materials for Quantum Applications ESJ 2204	
	8:30 AM	MBE grown site-templated quantum dot platforms with spectral control for quantum devices
	8:45 AM	Selective Area Regrowth for Chipscale Trapped Atom/Ion Quantum Systems
	9:00 AM	Quantum Sensing with Defects in Diamond and Wide Bandgap Semiconductors
	9:15 AM	Annealing Modulated Structural and Electrical Properties of Crystalline NbN Superconductor on GaN substrate by Sputter Deposition
	9:30 AM	Electron Spin Resonance of Defects in the Nb/a-Si/Nb Materials System
	Doping and Impurities ESJ 1224	
	8:30 AM	Optical Properties of β-Ga2O3 Due to Impurities and Electron Irradiation
	8:45 AM	Electrical and Optical Characteristics of Si- and Ge-implanted AlN annealed at 1500 ºC
	9:00 AM	Band gap luminescence of Si and Ge doped homoepitaxial AlN
	9:15 AM	Deterministic generation of optical defects in van der Waals materials
	9:30 AM	Adatom Surface Diffusion and Phase Separation in III-V Semiconductor Alloys
	Wearable Electronics and Biosensors ESJ 1202	
	8:30 AM	Eutectic Gallium-Indium (EGaIn) Electrodes for Wearable Electroencephalography (EEG)
	8:45 AM	Skin-Attachable Piezoelectric III-N Thin-Film Sensors for Continuous Monitoring of Cortisol and Glucose Levels from Sweat
	9:00 AM	Piezoelectric Flexible Pressure Sensor Array with Single-Crystalline III-N Thin Film for Practical Rehabilitation by Detection of Muscle Motions
	9:15 AM	Development of real-time wireless gait analysis system with wearable sensor
	9:30 AM	pH dependence of SARS-CoV-2 Detection using Graphene FET Array Biosensor
	Epitaxial Materials ESJ 1215	
	8:30 AM	Developing Piezoelectric Barium Nickelate for Catalysis
	8:45 AM	Correlation Between Optical Spectra and Dislocation Content in ZnS Epilayers
	9:00 AM	Statistical analysis of dislocation nucleation and growth on epitaxial ZnS
	9:15 AM	Expanded stability of layered SnSe-PbSe alloys and evidence of displacive phase transformation from rocksalt in heteroepitaxial thin films
	9:30 AM	Growth and Characterization of Ternary-Containing AlInAsSb Digital Alloys
9:45 AM	**Coffee Break**	

PROGRAM-AT-A-GLANCE

ESJ = Edward St. John Building
Stamp = Stamp Student Union

THURSDAY AM

10:15 AM	**III-N Device and Material Characterization ESJ 0202**	
	10:15 AM	Low Leakage GaN p-i-n Homojunction Avalanche Photodiodes via Shallow-Bevel-Mesa Edge Termination
	10:30 AM	A Linear Spectroscopy Method to Investigate Plasma Damage in GaN Films Grown on CTE Matched Substrates
	10:45 AM	Oxide interface characterization of n/p-GaN for power electronics
	11:00 AM	Ohmic Contact Improvement of AlN/Al0.8Ga0.2N Heterostructure by Atomic Layer Etching (ALE)
	11:15 AM	Decoupling semiconductor thermal and electrical properties for improved thermoelectric performance
	Oxide Semiconductor Thin Films and Devices ESJ 0224	
	10:15 AM	Application of Ion Energy Spectroscopy to Study the Plasma Kinetics during the Pulsed Laser Deposition of Strontium Titanate Thin Films
	10:30 AM	β-Ga2O3 self-switching diodes
	10:45 AM	Impact of Gate Roughness on the Field Effect Mobility of IGZO TFTs
	11:00 AM	Crystal orientation-dependent electronic properties of β-Ga2O3 surfaces
	Epitaxy of Highly Mismatched Alloys ESJ 2208	
	10:15 AM	Bandgap Evolution in B-III-V Alloys
	10:30 AM	Enhanced minority carrier lifetime in bulk Hydrogen-passivated InAsSbBi
	10:45 AM	Improvement in Optical Quality Upon Annealing in B-III-V Alloys
	11:00 AM	Influences of Carbon Tetrabromide (CBr4) and Tin Fluxes on GeCSn Growth
	11:15 AM	Observation of Low Resistance Al and Ni p-type Ohmic Contacts to Dilute GeC and GeCSn Alloys
	Materials for Quantum Applications ESJ 2204	
	10:15 AM	Kinetics of Native Oxide Formation in NbTiN Thin Films
	10:30 AM	Synthesis and characterization of SmB6 thin films by chemical vapor deposition
	10:45 AM	Electrical Transport Study of GeSn Films
	11:00 AM	Understanding the degradation of thin GaSe
	11:15 AM	Advancements in Time -Resolved Microwave Conductivity through Non-Resonant Coplanar Transmission Line and Interferometric Detection
	Doping and Impuritie ESJ 1224	
	10:15 AM	Precise Spatial Photodoping of Lateral Graphene p-n Interfaces
	10:30 AM	Analysis of Lattice Damage in Post-Annealed 4H-SiC Epiwafers Implanted with High Energy Al Ions at Elevated Temperatures
	10:45 AM	Rare-earth impurities in III-V semiconductors and their alloys
	11:00 AM	Vacancies and hydrogen-related defects in KTaO3
	11:15 AM	“No electron freezing out” in Si-doped β-Ga2O3 (010) down to 2 K
	Wearable Electronics and Biosensors ESJ 1202	
	10:15 AM	Optical Characterization of Coal Particulate on PETG Filters Between 375nm and 1500nm Light
	10:30 AM	Experimental ISFET Surface Modification Validation for Streptavidin-Biotin Binding
	10:45 AM	Paper-based Biosensors for the Detection of Creatinine Levels in Kidney Disease
	11:00 AM	Development of a Modular Bioelectronic Sensing Interface Using Escherichia coli and Dissimilatory Metal Reducing Bacteria Shewanella oneidensis MR-1
	11:15 AM	Tuning the Carbon Black content to switch Piezoelectric Behavior of P(VDF-TrFE) to Piezoresistive for Integrated Wearable Sensing Applications
	Novel Integration and Material Processing ESJ 1215	
	10:15 AM	GaAsSb/Si heterojunction photodiodes fabricated with epitaxial layer transfer
	10:30 AM	Study on the characteristics of Si channel layer formed by recrystallization with UV nanosecond pulsed laser annealing for monolithic 3D integration
	10:45 AM	Synthesis of Scandium Diboride Crystals Using the Laser-Diode Floating Zone Method
	11:00 AM	Enabling Material and Process Integration by Combining Thermal Scanning Probe Lithography and Soft Etching
	11:15 AM	Fabrication of Mixed-Dimensional Heterostructures through Micro-Transfer Printing of III-V Thin Films on Monolayer Nanomaterials
11:30 AM	**Lunch**	

PROGRAM-AT-A-GLANCE

ESJ = Edward St. John Building
Stamp = Stamp Student Union

THURSDAY PM

1:00 PM	**III-Nitride: Ferroelectric Materials and Devices ESJ 0202**	
	1:00 PM	Molecular Beam Epitaxy and Characterisation of Ferroelectric Quaternary Alloy ScAlGaN
	1:15 PM	Unraveling Atomic-Scale Polarization Switching in Single Crystalline Nitride Ferroelectrics
	1:30 PM	Uncovering Wurtzite ferroelectric domain walls
	1:45 PM	Unveiling Electronic Properties of Wurtzite Ferroelectric Domain Walls
	2:00 PM	Calculation of the Band Structure in Ferroelectric AlScN HEMTs
	Gallium Oxide Epitaxy, Processing, and Characterization ESJ 0224	
	1:00 PM	MOCVD Grown β-(Al,Ga)2O3/Ga2O3 2DEGs enabled by TEAl
	1:15 PM	Heteroepitaxy of β-Ga2O3 on GaN by MOCVD: The Impact of Nitride Polarity on β-Ga2O3 Crystalline Quality
	1:30 PM	Impact of Ga Beam Flux on Compensating Acceptors and Electron Mobility in Plasma-assisted MBE-grown β-Ga2O3
	1:45 PM	Epitaxial growth of β-(Al,Ga)2O3 films using TTBAl as Al source
	2:00 PM	Excellent Si Doping Control in β-Ga2O3 (010) Films by Pulsed Laser Deposition
	Printed Electronic Materials and Devices ESJ 2208	
	1:00 PM	Lathe-based Aerosol Jet Printing: A New Additive Manufacturing Method for Fabricating Conformal Electronics on 3D Curvilinear Substrates
	1:15 PM	Exploring Form and Functionalization in Crystalline Nanocellulose Inks for Environmentally Sustainable Printed Electronics
	1:30 PM	Printed Electrical Conductors: Aging and Reliability Scoping Study
	1:45 PM	Investigating Ag-Sn Transient Liquid Phase Sintering for Additive Manufacturing in Electronics
	2:00 PM	A Comprehensive Study of Dispense Printing: Unveiling Interactions Between Silver Flake Inks and Varied Substrates
	Nanofabrication and Processing ESJ 2204	
	1:00 PM	Fabrication and Characterization of High-Frequency n-type Si/SiGe Fin Bulk Acoustic Resonators
	1:15 PM	Focused Ion Beam Milling of Ta/Co/NiFe Magnetic Tunnel Junction based Molecular Spintronics Device
	1:30 PM	Development and Characterization of a Tunnel Junction Chemical Sensing (TJCS) device for Neurochemical Detection with a Focus on Dopamine Sensing.
	1:45 PM	The Effect Of The Dimension Of Ferromagnetic Electrodes On The Magnetic Properties Of The Magnetic Tunnel Junction Based Molecular Spintronics Devices
	2:00 PM	Low Interface Defects (~ 10^10 cm^-2eV^-1) Solution Processed Charge Trapping Oxide
	SiC Materials, Characterization and Devices ESJ 1224	
	1:00 PM	Comparison between epitaxial and implanted aluminum-doped 4H-SiC
	1:15 PM	Microstructural Analysis of Different Stacking Faults in 180um Thick SiC epitaxial layers
	1:30 PM	Analysis of Inclusions and Associated Dislocation Configurations in 4H-SiC Wafers through Synchrotron X-Ray Topography
	1:45 PM	Frank dislocations generation and behavior investigation in PVT-grown 4H-SiC crystals
	2:00 PM	Mitigation of BPD Faulting Using H2 Etches for Pulsed Power Applications
	Materials for Memory and Computation ESJ 1202	
	1:00 PM	Phase Change Chalcogenides for Functional Photonics and Electronics: Advanced Materials, Metrology, and Devices
	1:15 PM	Entropy-stabilized oxide memristors
	1:30 PM	Understanding the Interplay of Device Geometry on the Temporal Response of Lithium Intercalation Synapses for Enhanced Neural Computation Beyond the Cross-bar Architecture
	1:45 PM	Bit Error Rate Probability of Single and Multi Level Cell Flash Memory
	2:00 PM	Quantum Enhanced Josephson Junction Field-Effect Transistors for Logic Applications
2:15 PM	**Coffee Break**	

PROGRAM-AT-A-GLANCE

ESJ = Edward St. John Building
Stamp = Stamp Student Union

THURSDAY PM

2:45 PM	**Contacts to III-N Semiconductors ESJ 0202**	
	2:45 PM	Deconstructing the Zr/Al/Mo/Au Ohmic Contact to AlN-rich AlGaN
	3:00 PM	Evidencing Low Ohmic Contacts on n-type AlN with Contact Resistivity at 10-3 Ω·cm2 Level
	3:15 PM	Revolutionizing P-Type GaN: An Innovative Approach to Achieve High-Doping Efficiency and Low-Contact Resistance for GaN Devices
	3:30 PM	Schottky Diodes to GaN Prepared by Atomic Layer Deposition
	Gallium Oxide Epitaxy, Processing, and Characterization ESJ 0224	
	2:45 PM	In-situ Deep Patterned Etching of beta -Ga2O3 using Triethylgallium
	3:00 PM	Impact of Remote Hydrogen Plasma on Ga2O3 Carrier Density and Mobility
	3:15 PM	Cracking in β-(AlxGa1-x)2O3 films on (010) β-Ga2O3 substrates: Characterization and Modelling
	3:30 PM	Investigation of Thermal Stability and Phase Transitions of α-, κ(ε)-, and γ-Ga2O3 Epitaxial Films via Annealing and In-Situ XRD
	3:45 PM	Photoluminescence study on MgGa2O4 thin films grown by molecular beam epitaxy
	Additive Manufacturing and 3D Devices ESJ 2208	
	2:45 PM	3D Woven Liquid Metal Litz Wire for MHz Functionality
	3:00 PM	ANALYSIS OF DIFFERENT MICROFLUIDIC STRUCTURES IN PACKAGES FABRICATED USING METAL ADDITIVE MICROFABRICATION FOR THE THERMAL MANAGEMENT OF SEMICONDUCTOR DIES.
	3:15 PM	Electroless Nickel Plating Application on Additive Manufacturing Metal Components As-Built, ChemPolished (cp), and ElectroPolished (ep) Exploration.
	3:30 PM	INVESTIGATION OF POLYMER MICROSTRUCTURE PYROLYSIS FOR ROBUST 3D PRINTED CARBON MEMS
	3:45 PM	3D PolyJet-printed flexible coil for wireless power transfer application
	Nanostructured Materials and Devices ESJ 2204	
	2:45 PM	Electrolyte-Gated Junctionless III-V Nanowire Transistors: A TCAD-Based Evaluation
	3:00 PM	Rapid Material Characterization with Scanning Microwave Microscopy for High-Throughput Material Discovery
	3:15 PM	Functionalized Bioelectronic Materials for Multiplexed Leukocytes Enumeration Enabled by Machine Learning
	3:30 PM	Perovskite Nanofiber Developed as the Matrix of Electrochemical Amyloid β Immunosensor
	3:45 PM	Continuous Liquid Metal Printing of 2D Transparent Conductive Oxide Flexible Bioelectrodes
	SiC Materials, Characterization and Devices ESJ 1224	
	2:45 PM	Bulk 3C-SiC synthesis with Laser Diode Floating Zone
	3:00 PM	Using a Convolutional Neural Network with Ultraviolet Photoluminescence Images to Map Defects on SiC Wafers
	3:15 PM	Investigating CVD Graphene Barriers for Remote Epitaxy of SiC
	3:30 PM	Demonstration of Metal/3C-SiC/Silicon Bipolar UV Phototransistor
	3:45 PM	Investigation of high-order silane based SiGe epitaxy in ultra-high vacuum chemical vapor deposition process
	Materials for Memory and Computation ESJ 1202	
	2:45 PM	Enhancement hysteresis in transparent MOS device
	3:00 PM	Growth of Novel 2D Ferromagnet MnxSey by Chemical Vapor Deposition
	3:15 PM	Controlling the nanoscale heat flow in phase change memory with Sb2Te3/TiTe2 superlattices
	3:30 PM	Memory effect in CdTe nanoparticles
	3:45 PM	In-situ Growth of {-201} Fiber-textured β-Ga2O3 Semiconductor Tape for Flexible Thin-Film Transistor
	Heterointegration of WBG/UWBG semiconductors ESJ 1215	
	2:45 PM	Direct wafer bonding of GaN on AlN for thermal management and power device applications
	3:00 PM	Fabrication and characterization of heterogeneous pn and Schottky diodes made with bonded GaN membranes
	3:15 PM	Lapping and Chemical Mechanical Polishing of wide and ultra-wide bandgap semiconductors
	3:30 PM	Understanding the breakdown-field capability of narrow band gap (p-Si)/ultra-wide band gap (n-Ga2O3) heterojunction p-n diode
	3:45 PM	p-GaAsn-Ga2O3 heterojunction diode with breakdown voltage of ~800V
4:30 PM	**Panel Discussion: Future Careers in Electronic Materials, ESJ 0202**	
6:00 PM	**EMC 2024 Conference Dinner**	

PROGRAM-AT-A-GLANCE

ESJ = Edward St. John Building
Stamp = Stamp Student Union

FRIDAY AM

8:00 AM	**Registration Opens**	
8:30 AM	**Growth of Group III-Nitrides ESJ 0202**	
	8:30 AM	Electrical Conductivity of Si-doped AlN on Sapphire: Effects of Various Growth Conditions
	8:45 AM	Crack-Free AlN Film Exceeding 1-µm Thickness Epitaxially Grown on Si Substrate
	9:00 AM	Semi-metallic conductivity in N-polar Al-rich AlGaN on C-face 4H-SiC by Molecular Beam Epitaxy
	9:15 AM	Evolution of AlN: from 1 nm Nitridation to 2 µm of Molecular Beam Epitaxy
	9:30 AM	Strain Accumulation and Relaxation on Crack Formation in Epitaxial AlN Films on Si (111) Substrate
	Optoelectronic Devices ESJ 0224	
	8:30 AM	Suppressing AlInAsSb Avalanche Photodiode Dark Currents by Tuning the Absorption Region
	8:45 AM	Effect of Varying Period Structure on Tunneling Current in AlInAsSb Digital Alloys
	9:00 AM	The Electro-absorption effect in InGaAs and GaAsSb p-i-n photodiodes
	9:15 AM	Influence of Growth Temperature on Defect States in GaAs0.51Sb0.49 pin Diodes on InP
	9:30 AM	InGaAlAs/InAlAs on InP Avalanche Photodiodes For Near-Infrared LIDAR Imaging
	Hybrid Organic/Inorganic Devices and Molecular Electronics ESJ 2208	
	8:30 AM	Synthesis and Characterization of MAPbBr3 Perovskites for Radiation Detection Applications
	8:45 AM	Synthesis and characterization of yttrium ferrite nanoparticle incorporated PVDF-TPU composite
	9:00 AM	Trenched bottom electrode based molecular devices with gate electrode: Process and applications of promising spintronics molecular devices.
	9:15 AM	Modification of Conjugated Polymers with Indigo Dye to Enhance their Optoelectronic Properties: An Experimental and Computational Study
	9:30 AM	Realization of Self-poled, flexible P(VDF-TrFE) energy harvester using PDMS/Carbon Black Electrostatic Interaction Layer
	Transition Metal Dichalcogenide and h-BN Synthesis and Devices ESJ 2204	
	8:30 AM	Electrical Transport of High-Quality CVD-Grown MoSe2 Nanoribbons
	8:45 AM	Evaluating the Dielectric and Piezoelectric Response of 2D SnSe Thin Films
	9:00 AM	Seeking an Ion Beam Substitute for Neutron Irradiation in the Monolayer 2D Semiconductor MoS2
	9:15 AM	Self-limiting stoichiometry in SnSe thin films
	9:30 AM	Selective Area Epitaxy of van der Waals Materials on Semiconductor Substrates
	Ferroelectrics and Structural Defects ESJ 1224	
	8:30 AM	Exploring the Energetics of Domain Walls in Wurtzite Ferroelectrics
	8:45 AM	Imaging Point Defects and Implantation Damage in Silicon Carbide using Multislice Electron Ptychography
	9:00 AM	Controlling dislocation motion in semiconductors using an electric field
	9:15 AM	Probing qubits in silicon carbide using Multislice electron ptychography
	Solar Cell Materials and Devices ESJ 1202	
	8:30 AM	Growth of Hexagonal ScFeO3 for Bulk Photovoltaic Effect Optoelectronics
	8:45 AM	AlGaAsP distributed Bragg reflectors for GaAsP/Si solar cells
	9:00 AM	Preparation of the Alloys of the CuBiS2 – CuInS2 System and Their Characterization
	9:15 AM	Formation of off-stoichiometric AgGaTe2 and application to solar cells.
	9:30 AM	Translucent Solar Cells Fabricated with Nanosecond Pulsed Laser Beams
9:45 AM	**Coffee Break**	

PROGRAM-AT-A-GLANCE

ESJ = Edward St. John Building
Stamp = Stamp Student Union

FRIDAY AM

10:15 AM	**Growth of Group III-Nitrides ESJ 0202**	
	10:15 AM	Epitaxial Growth of Multichannel AlScN/GaN Heterostructures by Molecular Beam Epitaxy
	10:30 AM	Epitaxial Growth of High ScN Fraction ScAlN on (111) Si
	10:45 AM	Growth and Characterization of AlInN/GaN Superlattices
	11:00 AM	Misfit Dislocation Management in a 1D FACELO AlGaN/GaN Heterostructure
	Optoelectronic Devices ESJ 0224	
	10:15 AM	Heteroepitaxial Integration of Embedded Visible InP Quantum Dot Lasers on SiN/Si Photonic Integrated Circuits
	10:30 AM	Effects of Molecular Beam Epitaxy Selective Area Growth Techniques on III-V Optical Quality
	10:45 AM	Molecular Beam Epitaxy Selective Area Regrowth of High Aspect Ratio Microstructures for Mid-Infrared Optoelectronics
	11:00 AM	Demonstration of InAs Quantum Dots-in-a-Well Photonic Crystal Surface Emitting Lasers (PCSELs) by Epitaxial Regrowth
	11:15 AM	Optical and morphological study of local-droplet etched quantum dots
	Oxide UV Photodetectors and Other Devices ESJ 2208	
	10:15 AM	Significantly enhanced and dark current suppressed β-Ga2O3 based DUV self-powered photodetector by ion implantation process
	10:30 AM	Highly Textured Sn Doped β-Ga2O3 Epilayers for Economic Solar-Blind Ultraviolet Photodetectors with High Responsivity
	10:45 AM	Kappa/beta gallium oxide type-II phase heterojunction for self-powered deep ultraviolet photodetection.
	11:00 AM	Phase Transition and Bandgap Engineering of MgSnO Thin Films for Solar-blind Ultraviolet Photodetector Applications
	11:15 AM	Usage of Albrecht model for simulation of β-Ga2O3-/NiOx super junction devices for ultrawide bandgap electronics
	Transition Metal Dichalcogenide and h-BN Synthesis and Devices ESJ 2204	
	10:15 AM	Extraordinary tunnel electroresistance in layer-by-layer engineered van der Waals ferroelectric tunnel junctions
	10:30 AM	Electric-field-sensitive polymer electrolytes for non-volatile doping of two-dimensional field-effect transistors
	10:45 AM	Growth and characterization of two-dimensional hexagonal boron nitride on Ni (111) substrates by using diborane and ammonia in molecular beam epitaxy
	11:00 AM	Vibrational Characteristics of Rare Earth Element based Two Dimensional MXenes
	Doping and Transport ESJ 1224	
	10:15 AM	Hole transport analysis in p-type N-polar GaN
	10:30 AM	Enhanced Be Dopant Incorporation and the Role of In Surfactant in MOCVD GaN:Be
	10:45 AM	Mercury-probe based electrical characterization of β-Ga2O3
	11:00 AM	Using Near-Zero Field Magnetoresistance Measurements as a Tool for Defect Analysis in Silicon Photovoltaics
	11:15 AM	Nanoscale electrical conductance and leakage currents in etched and selective-area regrown GaAs pn junctions
	Solar Cell Materials and Devices ESJ 1202	
	10:15 AM	Transforming Magnetic Metal into Semiconductor: Spin Solar Cell Phenomenon on Single Molecule Magnet(SMM) Impacted CoFeB based Magnetic Tunnel Junctions
	10:30 AM	Optimization of Pb-free Highly Efficient Cs2AgInBr6 Double Perovskite Solar Cells: A Numerical Investigation using SCAPS
	10:45 AM	Investigation of a Simplified Metamorphic Buffer Approach in GaAs(y)P(1-y) Alloys
	11:00 AM	Thin Film Deposition of Two-Dimensional Hybrid Perovskite in Inert Gas by Resonant Infrared Matrix-Assisted Pulsed Laser Evaporation (RIR-MAPLE)
	11:15 AM	Photovoltaic-Powered Monarch Butterfly Migration Tracker
11:30 AM	**EMC 2024 Complete**	

EXHIBITOR PROFILES

Edward St. John (ESJ) Building

Set Up	Wednesday Exhibit	Thursday Exhibit
7:00 AM - 10:00 AM	10:00 AM - 8:00 PM	10:00 AM - 4:00 PM

United Mineral & Chemical Corp

umccorp.com/

Bringing the world's raw materials to you! A modern distributor, in a modern world, while keeping our family values.

NEOCERA

neocera.com

The Leading Manufacturer Of PLD/PED Systems

Neocera is a technology company that serves academia, government and multinational companies that designs thin-film development products. Neocera offers a full range of solutions for thin films including pulsed laser deposition (PLD) systems, pulsed electron deposition (PED) systems, components and in situ diagnostic tools.

NEXTRON

microprobesystem.com

With the pride and sense of vocation that we are able to contribute in even the smallest way towards executing NEXTRON's vision, "Science and technology that coexists with nature and humanity," we will do our very best to become a global, professional research equipment company.

GATAN

https://www.gatan.com/

There is always more to see. And when you're working with electron microscopy, the closer you can get to your sample, the more of its secrets it will reveal.

That's why at Gatan we have spent the last 60 years working with our customers to push the boundaries of what can be done with electron microscopy. Together, we have invented new approaches to problems that deliver fresh understanding.

With state of the art cameras, imaging energy filters, specimen preparation equipment and other EM products and solutions, we take the most powerful microscopy on earth and make it work even harder for you.

Gatan. Let's get closer.

TECHNICAL PROGRAM

WEDNESDAY

JUNE 26, 2024

Technical Program: Wednesday, June 26, 2024

7:30 AM
Registration Opens
ESJ Building, Ground Floor

8:15 AM
EMC and DRC Joint Plenary
Stamp Student Union, Grand Ballroom

10:00 AM
Group III-Nitrides: Detectors
Session Chairs: Mihee Ji (Army Research Laboratory), Russell Dupuis (Georgia Institute of Technology)
ESJ 0202

10:00 AM
Effects of Radiation and Operating Temperature in GaN and AlN Thin-Film Piezoelectric Sensors for Harsh Environment Applications
Dr. Nam-In Kim[1], Mr. Asad Ali[1], Mr. Muhammad Aqib[1], Dr. Mihee Ji[2], Dr. Vijay S. Parameshwaran[2], Dr. Wendy L. Sarney[2], Dr. Marc Litz[2], Prof. Jae-Hyun Ryou[1]
[1]University of Houston, [2]Army Research Laboratory

Current and next-generation energy, transportation, aerospace, and defense applications demand pressure, strain, and vibration sensing in extreme conditions such as high temperatures, exposure to corrosive media and radiation, and mechanical vibration. Among different techniques of sensing including piezoresistive sensors and fiber optic sensors, piezoelectric transducers offer the advantages of simple structure, robustness, insensitivity to electromagnetic radiation, fast response time, and low power consumption. However, most ferroelectric or piezoelectric transducers have shown limitations in operating temperatures. To address the technical challenges, including limited dynamic range, bandwidth, and lifetime, we developed single-crystalline Group-III-nitride (III-N) piezoelectric sensors. III-N materials have spontaneous and piezoelectric polarization and no solid-phase transformation at high temperatures. They are also thermally stable, chemically inert, mechanically hard, and radiation hardened, which makes them inherently suitable for extreme-environment applications. We recently demonstrated that single-crystalline wide bandgap GaN and ultra-wide bandgap AlN piezoelectric thin-film sensors showed stable output voltage characteristics up to 400 °C and 900 °C, respectively [Sens. Actuator. A 305, 111940 (2020); Adv. Funct. Mater. 33, 2212538 (2023)]. At all temperatures, the output voltage increases nearly linearly with input gas pressure both for AlN and GaN sensors, i.e., showing an excellent linearity of the sensor. However, the output voltages at the same pressure also slightly change with temperature, showing increased voltage then decreased voltage with higher temperature, resulting in maximum sensitivity at 800 °C and 300 °C for AlN and GaN, respectively. In this presentation, we will report possible mechanisms of sensitivity change which will be important for further calibration and design of the physical sensors. Furthermore, we will experimentally investigate the effect of radiation on the piezoelectric characteristics of the sensors. Both the GaN and AlN are more radiation hard than Si and GaAs due to their high bond strengths. However, the radiation effect on the piezoelectric properties has not been reported. Among different types of radiation, we will first investigate the effect of alpha radiation. The piezoelectric output voltage will be measured at room and high temperatures before and after the radiation with various doses and energies of the particle. For the samples with degraded performance characteristics, further material characterizations including transmission electron microscopy will be employed. We expect that these highly sensitive, reliable, and durable sensors flexible III-N piezoelectric sensors can tolerate such extreme environments for the efficiency, maintenance, and integrity of the aforementioned applications with proven performance and durability.

10:15 AM
Improved Responsivity of GaN-based Avalanche Photodetectors through Implementation of AlGaN Windows (Student)
Mr. Davide Balzerani[1], Ms. Alexandra Dolgashev[1], Ms. Zhiyu Xu[1], Prof. Nepomuk Otte[2], Prof. Shyh-Chiang Shen[1], Dr. Theeradetch Detchprohm[1], Prof. Russell Dupuis[1]
[1]Georgia Institute of Technology, School of Electrical and Computer Engineering, [2]Georgia Institute of Technology, School of Physics

Avalanche photodetectors (APDs) operating in the ultraviolet (UV) spectrum have multiple applications in astrophysics, high-energy physics [1], non-line-of-sight optical communications [2] and positron-emission tomography [3]. We have developed GaN-based UV APDs that implement AlGaN “windows” designed to increase the responsivity of the top-illuminated devices. Four structures were grown by metalorganic chemical vapor deposition (MOCVD) on low-threading-dislocation-density (0001) free-standing GaN:Si ([n]~1E18 cm-3) substrates in an AIXTRON close-coupling-showerhead 6x2 reactor. The studied structures have a common structure that consist of an 800 nm-thick n-GaN:Si ([n]~1E18 cm-3) layer, a 1 µm-thick n-GaN:Si ([n]=6E18 cm-3) layer and a 200 nm-thick multiplication layer unintentionally doped GaN:uid ([n]~2E16 cm-3). Four different p-type windows were grown on top of the multiplication layer: (1) a 100nm p-GaN:Mg layer grown at 1070°C, (2) a 100nm p-GaN:Mg layer grown at 980°C, (3) a graded-composition p-AlGaN:Mg window with a 200 nm-thick AlxGa1-xN:Mg layer (x linearly graded from 0.25 to 0.00) and (4) a 200 nm-thick p-doped AlGaN:Mg short period super lattice (SPSL) window with average x=0.13 and with a SL period of 5 nm. The four structures were completed with a heavily-doped 20 nm p+-GaN:Mg ([Mg] ~ 1×1020 cm-3) contact layer.

The grown structures were fabricated into top-illuminated APDs. Prior to mesa formation using inductively coupled plasma BCl3/Cl2/Ar etching, the regions around the intended mesa areas were implanted with nitrogen ions to prevent sidewall current leakage [4]. The n-type and p-type contacts were deposited with an e-beam evaporator and the devices were passivated with a SiO2 layer.

The forward- and reverse-bias characteristics of the fabricated APDs with a mesa diameter of 96 μm were measured. The two all-GaN APDs had similar breakdown characteristics while the APDs with AlGaN windows showed higher breakdown voltages (BVs) than those of the all-GaN devices. Under illumination at λ=355nm, their optical gains extracted from the J-V characteristics were about 4~7×105 at the compliance current density of 1 A/cm2. The photoresponsivities of the APDs with the four structures were also measured. The devices with the graded-composition p-AlGaN window and the p-AlGaN SPSL window exhibited an about 36% and 25% higher peak responsivity at 80% of their breakdown voltage with respect to the all-GaN devices with the p-doped layer grown at 1070°C and 980°C respectively. The temperature-dependent J-V characteristics were also measured and the predominancy of the avalanche behavior at the breakdown was confirmed by positive temperature coefficients which were extracted from the BV-T characteristics for all the four studied structures. Further details on materials and devices will be presented.
[1] F. Gramuglia et al. Front. Phys. 10, 849237 (2022).
[2] Z. Xu et al. IEEE Commun. Mag. 46, 67 (2008).
[3] V. Spanoudaki et al J. Instrum 2, P12002 (2007).
[4] M. Cho et al. IEEE Tran. Electron Devices 68, 2760 (2021).

10:30 AM
Development of N-polar InAlGaN for Cs-free photocathode structures
Dr. Vincent Meyers[1], Mr. Benjamin McEwen[1], Mr. Alireza Lanjani[2], Ms. Shadi Omranpour[1], Mr. Luca Cultrera[3], Mr. Siddharth Karkare[4], Prof. F. Shahedipour-Sandvik[1]
[1]Department of Nanoscale Science and Engineering, University at Albany, [2]College of Nanotechnology, Science, and Engineering, University at Albany, [3]Brookhaven National Laboratory, [4]Arizona State University

The utility of photocathode devices as electron beam sources for accelerator applications has grown in recent years. Particle colliders, electron coolers, free-electron lasers, and some electron microscope applications benefit from photoemitted electron beams from photocathodes. However, the low brightness, short coherence time, and low lifetimes of current devices hamper increased use. Currently, photocathodes in these applications are made predominantly from alkali antimonides [1] or cesiated III-V materials [2], which suffer from low lifetime and sensitivity to poor vacuum. An ideal photocathode for electron beam generation would exhibit photoresponsivity near the visible range (to avoid DUV laser requirement), minimal degradation in the presence of high fields/poor vacuum, high brightness, and high spin coherence lifetime. Design and operation of solar-blind GaN photocathodes has been explored extensively [3], however use of GaN for electron beam source is limited due to the relatively high work function of bare GaN (~7 eV). Recently, however, the ability to utilize the polarization charges inherent to InxAlyGa1-x-yN wurtzite system has resulted in GaN photocathodes with effective negative electron affinity at the surface, yielding stable photocathode quantum efficiencies (QE) up to 26% [4]. Band gap and lattice constant can be continuously tuned by controlling quaternary composition, indicating the possibility of efficient electron beam photocathode sources with visible-range photoresponsivity.

In this work, development of a new class of visible-range photocathode structures for use as electron beam generators is investigated. N-polar InxAlyGa1-x-yN:Mg films are grown by metalorganic chemical vapor deposition and their QE in the visible and near-UV is interrogated. The influence of metal precursor flow ratio, temperature, and the starting polarity of a (GaN) substrate on InxAlyGa1-x-yN alloy fractions x and y are documented. Surface and microstructural characterization indicate that smooth (RMS~3.5 nm) and crack-free N-polar In0.025Al0.975N can be achieved on GaN. Electrical characterization and internal quantum efficiency of films doped with Mg by Hall Effect and photoemission measurements are also presented. The resulting applicability to photocathode electron beam source applications is discussed.
[1] S. Schubert, et al. Apl Materials 1:3 (2013).
[2] C. Sinclair, et al. Phys. Rev. ST Accel. Beams 10.2 (2007): 023501.
[3] J. Marini, et al. J. Appl. Phys. 124, 113101 (2018)
[4] E. Rocco, et al. IEEE Photon J. 14.2 (2022): 1-12.

10:45 AM
Impact of Mg Incorporation in Semipolar Planes of N-polar and Ga-polar 3D Microstructures on Photocathode Internal Quantum Efficiency
Ms. Shadi Omranpour[1], Dr. Emma Rocco[1], Dr. Vincent Meyers[1], Mr. Benjamin McEwen[1], Mr. Alireza Lanjani[2], Dr. Lloyd Douglas Bell[3], Prof. F. Shahedipour-Sandvik[1]
[1]Department of Nanoscale Science and Engineering, University at Albany, [2]College of Nanotechnology, Science, and Engineering, University at Albany, [3]Jet Propulsion Laboratory, California Institute of Technology, Pasadena, USA

Photocathode detectors have practical utilization in astronomy and military for low signal photon detection and image intensifiers [1] [2]. The III-nitride material system is a noticeable candidate for photocathodes, with properties of wide and tunable bandgap energies and radiation hard [3] [4]. Previously, dopant incorporation studies of the p-type dopant incorporation, Mg, within GaN hillock structures indicated enhanced Mg incorporation efficiency on the semi-polar facets. This led to improved optical and electrical device performance. In addition, microstructures with stabilized semi-polar sidewalls in both Ga and N polarity were reported by a combination of V/III ratio and growth time optimization. N-polar and Ga-polar microstructures with semi-polar facets, achieved a maximum internal quantum efficiency (IQE) of 2.71% compared to polar planes. The higher QE is attributed to improved incorporation efficiency of Mg-dopants within the semi-polar facets [5]. Our previous work has demonstrated higher rates of MgGa and less Mg clustering in semi-polar facets than in c-plane films [5]. This suggests that the controlled growth of semi-polar GaN:Mg may enable enhanced p-type conductivity, and therefore IQE, of photocathode devices.

As previous studies have shown, conductivity of Ga-polar p-GaN films does not increase monotonically with [Mg] [6]. In this work we investigate the impact of varying Mg and Ga precursor molar flow ratio on photocathode IQE in response to increased semi-polar facet area relative to planar structures of both N and Ga polarity. We accomplish this by performing selective area growth (SAG) via metal-organic chemical vapor deposition (MOCVD) to create 3D p-GaN photocathode structures on (0001)- and ()-oriented GaN templates. Their IQE is compared to planar films at comparable growth conditions using photoemission spectroscopy. SAG structures on Ga- and N-polar substrates exhibit maximum IQE of 3.6% and 7.8% respectively. However, the precursor molar flow ratio at which these maxima occur varies drastically with differing polarity This suggests that the optimal precursor flow ratio for p-conductivity in semipolar planes relative to (0001) and () differs. The variation of IQE is discussed in the context of polarity dependence of Mg incorporation. The optical and structural characteristics of the designed photocathode microstructures will be presented through analysis of micro-photoluminescence and transmission electron microscopy (TEM).

[1] M. P. Ulmer, Quantum Sensing and Nanophotonic Devices VI, 2009.
[2] Peter D. Townsend, Contemporary Phys, vol. 44, no. 1, 2010.
[3] E Muñoz, et al, J. Phys, vol. 13, 2001.
[4] Carlos Rivera, Jet al," The Open Electrical & Electronic Engineering Journal, vol. 4, 2010.
[5] Emma Rocco, State University of New York, Polytechnic Institute, 2023.
[6] H. Obloh, et al," Journal of Crystal Growth, 1998.

11:00 AM
Device design and demonstration of an integrated AlGaN/GaN infrared detector with InGaN/GaN visible emitter (Student)

Mr. Alireza Lanjani[1], Mr. Benjamin McEwen[1], Dr. Vincent Meyers[1], Dr. Emma Rocco[1], Ms. Shadi Omranpour[1], Dr. David Hill[2], Dr. Winston K. Chan[2], Prof. F. Shahedipour-Sandvik[1]
[1]Department of Nanoscale Science and Engineering, University at Albany, [2]SRI International

Wide bandgap III-Nitride materials continue to be of great interest for applications in optoelectronic and power devices due in large part to their large and tunable bandgap energy. One such optoelectronic device is quantum well infrared photodetector (QWIP) which relies on intersubband transitions (ISBTs). These detectors are being used in optical telecommunication and thermal imaging applications. III-nitride materials have attracted much attention in the design of QWIPs owing to their large conduction band offset of nearly 2 eV [1] and valence band offset of nearly 0.8 eV [2] (between AlN/GaN) which makes them suitable for a variety of ISBT energies [3]. Due to the lack of inversion symmetry in the wurtzite crystal structure and lattice mismatch between AlxGa1-xN and GaN, this material exhibits strong polarization charges. This polarization charges offer additional design flexibility and permit further tuning of band offset and ISBT energies to target absorption wavelengths in a wider spectral range.

One of the challenges impeding the use of III-nitride QWIPs in some applications that require emission is visible range is the need for frequency up-conversion to permit emission of visible light. Without integrated up-conversion, QWIP must have an additional readout circuit, which increases device complexity and size. To overcome this challenge, monolithic integration of detector-emitter can be used which is based on photoexcitation of carriers from IR radiation in quantum well detector and transportation of excited carriers into an emitter for generation of light with higher energy [4].

In this work, we present a device design for a monolithically integrated AlxGa1-xN/GaN detector with InxGa1-xN/GaN multi quantum well (MQW) emitter with a target absorption wavelength of 1.55 μm and emission in the visible range. For the detector, a p-type (Mg-doped) QWIP was utilized to permit absorption of normal-incidence light, eliminating the need for optical couplers such as grating. Doping, thickness, and composition of layers were determined such a way to promote high carrier injection efficiency. The QWIP structure, consisting of 2.5 nm Al0.45Ga0.55N/4 nm GaN layers, and the MQW structure, consisting of 3 periods In0.3Ga0.7N/GaN were grown by MOCVD. Following the growth of the integrated structure, sample was characterized using atomic force microscopy (AFM), scanning transmission electron microscope (STEM), and x-ray diffraction (XRD) to assess surface morphology, crystalline quality, layer thickness, and interface mixing. Devices fabricated from the QWIP structure indicate low dark current density of ~10-7 A/cm2 at room temperature. Under illumination with an IR broadband light source (700–2000 nm), ~5 μA/W photoresponsivity, corresponding to ISBT energies in the valence band, is observed.

[1] A. N. Westmeyer et al., J Appl Phys, 99, 2006
[2] G. Martin et al., J Electron Mater, 24, 1995
[3] S. D. Gunapala et al., IEEE Journal of Selected Topics in Quantum Electronics, 20, 2014
[4] T. Rao et al., Coatings, 12, 2022

11:15 AM
Lateral p-GaN/AlGaN/GaN Hybrid Anode Diodes (HADs) with Hydrogen Plasma Triangular Guard Array (TGA) Termination

Mr. Dawei Wang[1], Mr. Dinusha Herath Mydiyanselage[1], Mr. Bingcheng Da[1], Mr. Ziyi He[1], Dr. Houqiang Fu[1]
[1]Arizona State University

Wide bandgap material GaN is promising in high-efficiency power conversion systems. To realize GaN power integrated circuits (ICs), peripheral logic circuits based on GaN are necessary, such as controllers, drivers, and protection circuits. By using the AlGaN/GaN high electron mobility transistors (HEMTs) platform, all these components can be integrated on a single chip, dramatically reducing parasitic effects, such as gate ringing and turn-on of power transistors. Lateral AlGaN/GaN hybrid anode diodes (HADs) consist of a cathode metal as ohmic contact, a 2DEG channel and a hybrid Schottky/ohmic anode that is composed of electrically connected ohmic contact and gate. The negative anode voltage can directly cut off the 2DEG channel, thus improving the reverse performance.

In this work, we perform the design and fabrication of p-GaN/AlGaN/GaN Hybrid Anode Diodes (HADs) with Hydrogen Plasma Guard Line Termination. The device epilayers were grown by metal-organic chemical vapor deposition (MOCVD) on a sapphire substrate, as shown in Fig. 1(a), consisting of a thick GaN buffer layer, a 300 nm UID-GaN layer, a 1 nm AlN space layer, a 20 nm Al0.2Ga0.8N layer and a 90 nm p-GaN layer with an acceptor Mg concentration of 3×1019 cm-3. The substrate was annealed at 800 ℃ for 30 minutes to break the Mg-H bond and activate the p-GaN layer. The metal stack Ti/Al/Ni/Au were deposited as cathode, followed by post-annealing at 850 ℃ for 30s. The p-GaN layer under the cathode was etched before metal deposition to for better ohmic contact. Then, several hydrogen plasma-treated pattered arrays termination, i. e., triangular guard array termination were fabricated that can eliminate high electric field crowding at the edge of anode, as shown in Fig. 1(b). For the pattern of the triangular guard arrays, as different from the traditional guard ring termination for vertical GaN devices, the guard array was formed by a series of discontinuous triangular dots for partially depleting the 2DEG channel so that the p-GaN will not cut off the 2DEG current along the whole device. The shape was designed for optimized electric field management. In addition, stripe edge termination structures were also introduced at the edge of anode. Hydrogen plasma treatment was applied to the surface for 5 minutes. The post annealing at 500 ℃ was processed for hydrogen diffusion. The pattern of H plasma treated area can be clearly noticed under SEM image, as shown in Fig. 1(c). Finally, the gate metal Ni/Au were deposited via e-beam evaporation. The electrical testing indicated that the p-GaN current can be fully passivated by hydrogen plasma treatment. The forward current density has slightly changed with the hydrogen plasma guard line termination structure, as shown in Fig. 2(a) and 2(b). The device shows temperature dependent characters, as shown in Fig. 3(a), and the C-V measurement was shown in Fig. 3(b). The device breakdown voltage was around 2 kV with an anode to cathode length (LAC) of 20 um. As shown in Fig. 4, the devices with triangular guard array design have higher breakdown voltage than the regular devices. The expected breakdown voltage of the devices with a LAC of 45 um and 95 um is 4-8 kV. These results can provide critical references for the future development of high breakdown voltage and etching-free termination in lateral p-GaN/AlGaN/GaN devices.

10:00 AM
Gallium Oxide Electronic Devices
Session Chairs: Marko Tadjer (U.S. Naval Research Laboratory), Becky Peterson (University of Michigan, Ann Arbor)
ESJ 0224

10:00 AM
Effect of surface preparation on electrical characteristics of Ga2O3 vertical rectifiers
Mr. Joseph Spencer[1], Dr. Alan Jacobs[1], Dr. Karl Hobart[1], Dr. Travis Anderson[1], Dr. Yuhao Zhang[2], Dr. Marko Tadjer[3]
[1]U.S Naval Research Laboratory, [2]Virginia Tech, [3]U.S. Naval Research Laboratory

As wide bandgap technology continues to advance, commercial power and defense industries are pushing the limits and operating conditions of electronic devices. High power electronics are being envisioned to operate in harsh environments while simultaneously supporting ever higher voltages with improved efficiency. Gallium oxide (Ga2O3) is an ultra-wide band gap (4.8 eV) semiconductor with the potential to meet those needs. Ga2O3 has seen a surge in popularity within the semiconductor research communities, propelled by advantageous material properties and growth conditions [1]. Still in the early stages of commercial development, Ga2O3 has already seen commercialization of 4” melt-grown substrates as well as the demonstration of 6” research grade substrates. High quality homoepitaxial growth results in thick, lowly doped drift regions capable of supporting the large projected critical electric field of 8 MV/cm. [2] This makes Ga2O3 a prime candidate semiconductor for vertical power devices where the drift region quality, doping, and thickness heavily influence the breakdown voltage and critical electric field.

The broad acceptance of Ga2O3 is currently hindered by an absence of p-type conductivity which primarily stems from a lack of dispersion within the valence band maximum. [3] Without the possibility of p-type Ga2O3 via impurity doping, the formation of PN and JBS diodes must rely on nickel oxide (NiO, EG = 3.7 eV). For the JBS diode, it is beneficial to embed the regions of p-type NiO into the epitaxial Ga2O3 to better shield the anode from areas of high critical electric field. This requires etching Ga2O3; however, Ga2O3 is susceptible to surface and sub-surface damage, as a result of the dry etching process. One report has been conducted on the impacts of etch damage and its mitigation on Schottky contacts. [4] However, the impact of etch damage and chemical treatments on the Ga2O3 NiO heterojunction have yet to be systematically explored. In this work, we compare the impact of plasma damage and subsequent chemical treatments on the performance of a NiO heterojunction with an etched Ga2O3 surface.
Four Ga2O3 epiwafers were patterned for BCl3 etching where one half of each sample was etched (800 W, 5 mT, 40 sccm BCl3) and the other half remained un-etched. Three of the samples were then treated in H3PO4 (80°C), HCl, and TMAH (70°C), respectively, while a fourth sample was left untreated for reference. Schottky barrier diodes and NiO/Ga2O3 PN diodes were then fabricated on the etched and un-etched surfaces of the epiwafers. I-V measurements across the etched/un-etched PN and SBDs reveal immediate impacts of the etch damage and chemical treatments. An HCl treated surface prior to NiO deposition resulted in superior reverse-bias blocking capabilities, compared to the other treatments, but suffered from increased forward bias on-resistance for both the PN and SBDs. This could signify poor damage mitigation or surface passivation. Temperature dependent I-V- measurements on the PN diodes reveal a negative linearity of the temperature coefficient (α) for the HCl acid treated PN diode. PN diodes treated with H3PO3 and TMAH show nonlinearity coupled with large α. H3PO4 treatment results in superior on-state performance but degrades the off-state blocking capabilities. This could signify an increase in defects rather than a removal. Variation in diode ideality and electrical performance reveal a need for further investigation into this heterojunction preparation, which serves to advance the performance of high voltage Ga2O3 NiO devices.

1) Spencer, JA., et al. Applied Physics Reviews (2022)
2)Higashiwaki, M., et al. Applied Physics Letters (2012).
3) Mock, A., et al. Physical Review B 96.24, (2017)
4) Yang, J., et al. JVST B 36(6), (2018)

10:15 AM
Characterization of temperature dependence of barrier height in Ni/β-Ga2O3 SBD over a wide temperature range and evaluation of valence band structure by XPS (Student)
Mr. Akihira Munakata[1], Dr. Kohei Sasaki[2], Dr. Kentaro Ema[2], Prof. Yoshiaki Nakano[1], Prof. Masaki Kobayashi[1], Prof. Takuya Maeda[1]
[1]The University of Tokyo, [2]Novel Crystal Technology, Inc.

Beta-phase Gallium oxide (β-Ga2O3) is a promising material for a power device with high breakdown voltage and low on-resistance. β-Ga2O3 devices with excellent characteristics have already been reported [1, 2]. However, the temperature dependence of the barrier height of metal/β-Ga2O3 SBD has not been investigated in detail. We reported that barrier height of Ni/β-Ga2O3 decreased with an increase in temperature, and the temperature coefficient ($d e\phi b/dT = -0.43$-0.50 meV/K) was consistently obtained by I-V and C-V measurements from 298 K to 473 K [3]. We pointed out that the thermionic emission-diffusion (TED) model should be used in the analysis to obtain precise values from the I-V characteristics. The value of $d e\phi b/dT$ is about one third of dEg/dT. In this study, we report the temperature dependence of the barrier height over a wider temperature range (55-573 K) obtained by three methods: current-voltage (I-V), capacitance-voltage (C-V), and internal photoemission (IPE) photocurrent measurements. The valence band structure of Ga2O3 was also evaluated by XPS to investigate the relevance between $d e\phi b/dT$ and dEg/dT .

Figure 1 shows the schematic cross section of a β-Ga2O3 Schottky barrier diode (SBD) investigated in this study. The epitaxial layer was grown by hydride vapor phase epitaxy (HVPE). Ti (50 nm)/Au (200 nm) was deposited on the backside as an Ohmic electrodes, and Ni (20 nm)/Au (200 nm) was deposited on the topside as Schottky electrodes. The Schottky electrodes have a square shape (1.6 mm × 1.6 mm). These measurements were performed in air above room temperature and in vacuum below room temperature, respectively. Figure 2 shows the C-V characteristics of the SBDs. In the 1/C2-V plots, the built-in potential decreases with increasing temperature. From the slope of the plots, the net donor concentration was found to be almost constant at 5.1×1015 cm-3 at all the temperature, which is uniformly distributed along the depth. Figure 3 shows the temperature dependence of the built-in potential (Vd), the voltage drop due to the diffusion distribution of electrons at the edge of the depletion region edge (kT), and the energy difference between the conduction band minimum and the Fermi level (Ec−EF). The barrier height, which was obtained as $e\phi b = Vd + (EC - EF) + kT$, decreases with increasing temperature, and its temperature coefficient is -0.51 meV/K above room temperature. Figure 4 shows the I-V characteristics of SBDs. The current increases with an increase in temperature. The ideality factor is very close to unity for above room temperature, but it deviated from unity as temperature decreased below room temperature. Figure 5 shows the temperature dependence of thermal velocity (vR) and effective diffusion velocity (vD). In the calculation of vD, the reported data of the Hall-effect measurements for β-Ga2O3 was used [4]. Above the room temperature, vD is smaller than vR and the current is also limited by the diffusion transport of electrons, thus a TED model-based analysis is required [5]. Below room temperature, on the other hand, vD is larger than vR, and the difference between TE and TED becomes smaller. Figure 6 show the temperature dependence of barrier height and ideality factor obtained by I-V measurements. Above room temperature, the temperature coefficient of barrier height obtained from TE model is -0.20 meV/K, that from TED model is -0.47 meV/K. The analysis based on TED model is consistent with the results of C-V measurements. Below room temperature, an accurate analysis was difficult due to underestimation of barrier height associated with non-ideal current transport such as defect-related leakage and/or inhomogeneity of barrier height. Figure 7 shows the temperature dependence of Fowler plots obtained by IPE measurements. With increasing temperature, the x-intercept of the linear extrapolation (corresponding to barrier height) shifts toward the lower energy. The temperature coefficient of barrier height obtained from IPE is -0.39 meV/K in the range of 296 K to 353 K. As shown in Figure 8, the temperature coefficients of barrier height obtained from I-V (TED), C-V, IPE were approximately −0.39-0.51 meV/K above room temperature and were consistent. Figure 9 shows the valence band spectra obtained by XPS. A clearer valence band structure was obtained compared to previous research [6]. It was obtained that VBM=EF−4.47 eV. In the future, we will perform the same measurements at different temperatures to identify the temperature dependence of the VBM to compare it with that of the barrier height.
[1] M. Higashiwaki et al., Appl. Phys. Lett. 108, 133503 (2016). [2] W. Li et al., IEDM 2019. [3] A. Munakata et al., LEC 2023. [4] A. Neal et al., APL 113, 062101 (2018). [5] T. Maeda et al., APEX 10, 051002 (2017). [6] L. Lyle et al., APL Mater. 9, 061104 (2021).

10:30 AM
β-(AlxGa1−x)2O3 Vertical SBD with a BN interlayer (Student)
Mr. Bingcheng Da[1], Mr. Dinusha Herath Mydiyanselage[1], Dr. Houqiang Fu[1]
[1]Arizona State University

Ultrawide bandgap (UWBG) semiconductors have attracted significant attention for their potential applications in power electronics, optoelectronics, and RF electronics. Among these materials, β-Ga2O3 emerges as a promising candidate for UWBG semiconductors owing to its notable properties such as a high breakdown field of 8 MV/cm and a wide bandgap ranging from 4.6 to 4.9 eV. Furthermore, it exhibits a high Baliga's figure of merit (BFOM) in comparison to GaN and SiC. By alloying Ga2O3 with Al2O3, (AlxGa1−x)2O3 is produced with a tunable bandgap (e.g., 4.8-6.2 eV for x = 0 to 0.71). This alloy is expected to possess a higher BFOM than Ga2O3, which makes it more suitable for power electronic applications. Recent research has shown optoelectronic and power devices utilizing β-(AlxGa1–x)2O3, yet most of these power devices operate laterally, which often underperforms compared to their theoretical limits. In contrast, vertical architectures dominate

commercial Si and SiC power devices, particularly in high-voltage and high-power applications. Vertical architectures offer advantages such as increased current and voltage handling capability, superior avalanche capability, absence of surface-related issues, enhanced heat dissipation, and reduced chip area. Various methods have been proposed to enhance the reverse leakage current performance of Schottky barrier diodes (SBDs). Additionally, metal–insulator–semiconductor (MIS) diodes have emerged as an appealing alternative to improve reverse performance. Introducing an ultrathin dielectric layer can effectively suppress reverse leakage current and mitigate electrical field effects at Schottky contact edges. Boron nitride (BN) is a promising candidate for MIS diodes due to its UWBG of 6 eV, high breakdown electric field of 10 MV/cm, high stability, and flat surface. This study successfully demonstrated β-(AlxGa1–x)2O3 metal–insulator–semiconductor (MIS) vertical diodes with a BN interlayer. β-(AlxGa1−x)2O3 epilayer with an Al composition of 21% and a nominal Si doping of 2 × 1017 cm, grown by molecular beam epitaxy. Boron nitride (BN) interlayer was directly deposited on the β-(AlxGa1–x)2O3 epilayer using pulsed laser deposition. Pt/Ti/Au was utilized on the BN layer as the top Schottky contact, while Ti/Au served as the bottom Ohmic contact. The structure of the devices is shown below (Fig 1). Forward and reverse I-V measurements were conducted, revealing excellent rectification with a high on/off ratio of ∼109, as shown in Fig 2 (a) and (b). The C-V measurement was done to extract the doping concentrate of AlGaO layer, as shown in Fig 2 (c). The temperature-dependent I-V measurement was done to extract the effective barrier height and ideality factor, these two both show excellent linear dependence with temperature. As shown in Fig 3. Remarkably, the insertion of the ultrathin BN layer led to a nearly two-order decrease in reverse leakage current compared to traditional vertical β-(AlxGa1−x)2O3 Schottky Barrier diodes, with the turn-on voltage increasing from 1.5V to ~2V. This approach presents a promising solution to address reverse leakage current issues in β-(AlxGa1–x)2O3-based vertical devices, paving the way for next-generation high-power electronics.

10:45 AM
Field Engineering for BTBT Leakage Current Suppression in NiOx/β-Ga2O3 PN and PiN Heterojunction diodes (Student)
Mr. Jose Manuel Taboada Vasquez[1], Mr. Saravanan Yuvaraja[2], Mr. Manoj Rajbhar[1], Ms. Ankita Mukherjee[3], Dr. Biplab Sarkar[3], Prof. Xiaohang Li[2]
[1]Advanced Semiconductor Laboratory, Electrical and Computer Engineering program, CEMSE Division, King Abdullah University of Science and Technology, Thuwal 23955-6900, Saudi Arabia., [2]King Abdullah University of Science and Technology, [3]Department of Electronics and Communication Engineering, Indian Institute of Technology Roorkee, Uttarakhand 247667, India

Devices based on wide bandgap semiconductors are crucial for the evolution of power electronics. GaN and SiC are extensively studied and commercially utilized in various applications. However, their cost of production is high. On the other hand, the availability of high crystalline quality β-Ga2O3 substrates grown using the Czochlarski growth technique is a promising aspect of developing low-cost power electronic devices. With its large bandgap (Eg: ∼4.8 eV), β-Ga2O3 yields a significantly larger critical field than other power semiconductor devices. This has been demonstrated in recent years, with some reports showing the fabrication of β-Ga2O3 devices exceeding breakdown voltages of 2 kVs. To achieve higher breakdown voltages, device engineering techniques such as adding a p-type layer to form a PN junction and consequently, a larger depletion region, should be implemented. However, the absence of p-type β-Ga2O3 has necessitated searching for potential alternatives, with NiOx emerging as a viable candidate. Recent reports show NiOx/β-Ga2O3 heterojunction-based diodes exceeding kilovolts of breakdown voltage and amps of ON current.

Conversely, NiOx and β-Ga2O3 form a type-II heterostructure with large conduction band (CB) and valence band (VB) offsets. This significantly reduces the distance between the VB maxima of NiOx and CB minima of β-Ga2O3 under high reverse bias conditions, facilitating direct and indirect band-to-band tunneling (BTBT) assisted OFF-state leakage current. This work shows a method to reduce BTBT-related leakage current in NiOx/β-Ga2O3 heterojunction bipolar diodes. PiN-configured NiOx / β-Ga2O3 bipolar diodes enhances electric field control, thereby minimizing OFF-state leakage. A PiN and a PN diode were fabricated to prove this, as shown in Figure 1. Figure 2 shows their I-V characteristics of them. Temperature-based I-V characteristics were performed to confirm the BTBT leakage current, as shown in Figure 3. The findings are verified through experiments and TCAD simulations, shown in Figure 4, the electric field distribution, and Table 1, the parameters used to perform the simulation

11:00 AM
Reliability studies of large-scale vertically stacked ultrawide bandgap oxides for CMOS IC (Student)
Mr. Saravanan Yuvaraja[1], Mr. Vishal Khandelwal[1], Dr. Shibin Chandroth[1], Dr. Yi Lu[1], Mr. Zhiyuan Liu[1], Mr. Mritunjay Kumar[1], Dr. Xiao Tang[1], Mr. Glen Isaac Maciel Garcia[1], Mr. Dhanu Chettri[1], Prof. Chehao Liao[1], Prof. Xiaohang Li[1]
[1]King Abdullah University of Science and Technology

This article highlights the enhanced performance of CMOS circuits using Ga2O3-based ambipolar transistors with HfO2/NiO/Ga2O3/NiO/HfO2 heterostructures and Ti/Au gate electrodes. These transistors achieve high electron and hole current on/off ratios of 109 and 107, respectively. Across 100 devices, they show a threshold voltage of -7.99 ± 0.92 V (p-channel) and 7.81 ± 0.81 V (n-channel), subthreshold swings of 0.59 ± 0.07 V/dec (p-channel) and 0.61 ± 0.06 V/dec (n-channel), and current densities of 0.99 ± 0.26 mA/mm (p-channel) and 58.23 ± 12.99 mA/mm (n-channel). These devices maintain long-term stability over 200 days with significant threshold voltage shifts after negative bias stressing. The n-channel on/off ratio significantly exceeds that of existing Ga2O3 unipolar transistors at 300 °C. The versatile polarity of these transistors enables their integration into CMOS inverters, NOR, and NAND gates with efficient switching speeds. This advancement in oxide-semiconductor-based CMOS technology is a key step toward future integrated electronics

11:15 AM
Systematic Investigation of Electrical Performance of β-Ga2O3 Schottky Barrier Diodes under High-Dose Gamma Irradiation (Student)
Mr. Saleh Ahmed Khan[1], Mr. Sudipto Saha[2], Prof. Uttam Singisetti[2], Prof. A F M Anhar Uddin Bhuiyan[3]
[1]Department of Electrical and Computer Engineering, University of Massachusetts Lowell, MA 01854, USA, [2]University at Buffalo, SUNY, [3]University of Massachusetts Lowell

β-Ga2O3, with its attractive properties such as an ultrawide bandgap energy (~4.8 eV) and high breakdown field strength (~8 MV/cm) holds significant promise for the development of high-power devices with robust radiation tolerance, suited for applications in extreme environments such as space and nuclear facilities. Given the demanding reliability requirements for stable operation in harsh conditions, the ability of these devices to withstand high radiation exposure presents an intriguing research area. A recent study on the gamma-ray (γ-ray) irradiation effect of β-Ga2O3 Schottky barrier diodes (SBDs) revealed high intrinsic irradiation hardness at a dose of 1 Mrad (Si) [1], prompting further investigation into their performance under high radiation doses. This study offers a systematic investigation into the influence of gamma-ray radiation on electrical performance of β-Ga2O3 SBDs exposed with different radiation doses, revealing an outstanding tolerance of up to 5 Mrad (Si). Importantly, minimal changes in electrical characteristics are observed, with the devices maintaining stable on-current, on-resistance, and reverse breakdown characteristics even after exposure to such high doses of irradiation. A Schottky barrier diode fabricated using commercially available halide vapor phase epitaxy (HVPE)-grown n- β-Ga2O3 (~10.8 μm thick, Sidoped, Nd ~2.1 × 1016 cm-3) film on (001) Ga2O3 substrate (Sn doped, ~5.4 × 1018 cm-3) was subjected to γray irradiations with energies of 1.173 MeV and 1.332 MeV, at a rate of 1 Mrad (Si)/hr for 1, 2, and 2 hours consecutively at room temperature, corresponding to cumulative absorbed doses of 1, 3, and 5 Mrad(Si), respectively. Electrical measurements were performed immediately between each radiation dose. The current-voltage characteristics (J-V) and specific on-resistance (Ron, sp) as shown in Figure 1(a) exhibited a significant decrease in on-current, dropping from 101.25 Acm-2 to 22.68 Acm-2 after the initial 1 Mrad exposure, with an increase in on-resistance from ~3 mΩ.cm2 to ~14 mΩ.cm2. However, with subsequent cumulative doses (3 and 5 Mrad), the on-current increased while the on-resistance decreased compared to the initial 1 Mrad dose. In the diode C-V characteristics shown in Figure 1(b), we noticed a similar trend where the capacitance dropped after exposure to 1 Mrad radiation. This decrease was likely caused by the formation of deep-level traps in the Schottky barrier interface. Conversely, for higher doses (3 and 5 Mrad), the capacitance tended to increase, indicating a possible radiation annealing effect [1] and the restoration of device performance after initial degradation. Furthermore, an increase in the built-in voltage from 0.95 V to 1.02 V was also observed after exposure to 1 Mrad irradiation as shown in Fig. 1(c), while subsequent higher radiation doses resulted in the restoration of the built-in potential to ~0.95 V. Additionally, analysis of the carrier concentration versus depth plot as shown in Fig. 1(d) extracted from the C-V profile revealed a slight decrease in carrier concentration from ~3.2×1016 cm-3 pre-radiation to ~3.1×1016 cm-3 after irradiation with different doses. Temperature-dependent J-V-T measurements performed after 5 Mrad irradiation at the temperature range of 25˚C to 250˚C indicated a reduction in both on-current and reverse leakage current for all temperatures tested as shown in in Fig. 2(a). A slight increase in the ideality factor (n) and barrier height (ΦB) was also observed after irradiation, along with an increase in Ron, sp for different temperatures (Fig. 2b,c). The reverse breakdown voltage increased slightly for all investigated devices after radiation exposure as shown in Fig. 2(d), consistent with previous observations for Ga2O3 SBDs postneutron irradiation [2]. In summary, this study offers valuable insights into the electrical performance of β-Ga2O3 SBDs under high dose γ-ray irradiation, paving the way for their potential application in extreme radiation environments.

10:00 AM
Metamaterials and Materials for THz, Plasmonics, and Polaritons
Session Chairs: Leland Nordin (Stanford University), Stephanie Law (Pennsylvania State University)
ESJ 2208

10:00 AM
Enhancing Light-Matter Interactions in the Long Wave Infrared
Dr. Brandon Durant[1], Dr. Patrick Yee[1], Dr. Adam Colbert[1], Dr. Madeleine Fort[1], Ms. Sabrina DeBreau[2], Prof. Joseph Tischler[3], Dr. Daniel Ish[1], Dr. Chase Ellis[1], Dr. Janice Boercker[1]
[1]U.S. Naval Research Laboratory, [2]Texas Tech University, [3]University of Oklahoma

Doped lead chalcogenide colloidal quantum dots (CQDs) support steady state intraband transitions in the long-wave infrared (LWIR).1,2 Similar to interband optical transitions (valence band to conduction band), intraband transitions (between states within the valence or conduction band, Figure 1a) show high absorption coefficients and follow quantum confinement models. This allows access to low-energy transitions much smaller than the bulk bandgap optical transitions while also providing tunability based on the size of colloidal quantum dots (Figure 1b). These transitions open possibilities for solution processed, LWIR absorbers/emitters at room temperature.

To enhance the interaction between infrared light and the quantum dots (diameter = 10.3 nm), we exploit plasmonic-like resonances that are supported by nanostructured surfaces of 4H-SiC. These nanostructures have been shown to confine LWIR to sub-wavelength dimensions, well beyond the diffraction limits.3 This has the potential to greatly enhance the coupling between free-space light and nanomaterials such as CQDs.
Intraband transitions in lead chalcogenide CQDs can be accessed by populating the 1Se energy level (or depopulating the 1Sh levels) through chemical modification of the surfaces, chemical oxidation/reduction reactions, or photogeneration of carriers. In this work, we use the latter technique, photogenerating carriers through excitation with a 532 nm above bandgap laser. To probe interactions, we measure the relative reflectance of CQD films on SiC nanostructures with and without continuous-wave laser excitation, essentially a steady-state pump-probe technique. By casting PbS CQDs onto arrays of SiC nanoresonators, we observe polarization-sensitive response of the combined metamaterial-CQD (Figure 2). Overall, we find that the absorption spectrum of the CQDs is strongly modified by the surface phonon polarition (SPhP) resonances supported by the nanostructured SiC surface. This interaction offers

exciting possibilities for the incorporation of LWIR active nanocrystals with the exceptionally high light confinement of SPhP resonators, such as high temperature LWIR detectors, light sources, and chemical sensors.

References
1Ramiro, I., et al, Nano Lett. 2020, 20 (2), 1003–1008
2Abelson, A., et al, Nat. Mat. 2020, 19 (1), 49–55
3Ellis, C. et al, Sci. Rep. 2016, 6 (1), 32959

10:15 AM
Lateral Cavity-Enhanced Guided Mode Resonance Structure for Mid-wave Infrared Photodetection (Student)

Mr. Noah Mansfield[1], Ms. Sreeja Purkait[2], Mrs. Yadviga Tischenko[1], Prof. Viktor Podolskiy[2], Prof. Daniel Wasserman[1]
[1]Department of Electrical and Computer Engineering, University of Texas at Austin, Austin, TX 78758,
[2]Department of Physics, University of Massachusetts, Lowell, MA, 01854

The dominant material system for mid-wave infrared (MWIR, 3-5μm) photodetectors has long been Mercury-Cadmium-Telluride (MCT), which offers wide wavelength flexibility (by control of alloy composition), low dark currents, and high responsivity. However, there is parallel interest in detectors leveraging conventional III-V materials, in part due to the uniformity afforded by III-V semiconductor epitaxy and the reduced toxicity of the III-V's when compared to MCT. Type-II superlattice (T2SLs) based detectors, first proposed by Smith and Mailhiot in 1987 [1], have shown promise due to their tunable effective bandgaps and reduced Auger recombination rates [2] compared to bulk ternary III-V's such as InAsSb. However, these improvements come at the cost of a substantially lower absorption coefficient, due to the reduced overlap between electron and hole wavefunctions in the superlattice. The impact of the T2SL's smaller absorption coefficient can be reduced by designing structures that leverage various optical resonances that enhance the overlap of incident light with the absorbing region of the respective detector structures. Our research group has previously demonstrated high-responsivity MWIR detectors that take advantage of a guided-mode-resonance (GMR) [3,4] to localize incident light in the absorbing region of a MWIR detector placed in a high-index waveguide core, clad by a degenerately-doped "n++" designer material below, and air above [5]. Incident light is resonantly coupled into the device active region via a patterned GaSb grating above the detector element. However, in order to achieve high performance (narrow bandwidth and strong mode confinement), a large number of grating periods are required to efficiently couple incident light into the detector and minimize finite-size effects. As such, incorporating the GMR detectors into conventional focal plane array architectures, with wavelength-scale pixels, is a significant challenge. However, there has been previous work demonstrating passive high-Q GMR filters by confining the guided modes to reduced lateral dimensions using effective index Bragg reflectors. These structures, first proposed in 2011 by Ura, et al., are known as cavity resonator integrated guided mode filters [6]. By using periodic Bragg gratings, the guided mode can be confined both laterally and vertically, drastically reducing the number of periods needed to achieve a strong, resonant response. By coupling such a design with existing MWIR GMR detectors, we can achieve small lateral area GMR detectors, bringing the required dimensions for a GMR-enhanced detector closer to those used by conventional focal plane arrays (FPAs) in the same wavelength range.

Our GMR detector structure [3] was first simulated for infinite periodicity and optimized for substrate-side illumination at 4.1μm through a GaSb substrate using rigorous coupled wave analysis [7]. The infinitely-periodic GMR detector structure was then reproduced in finite-element method (FEM) simulations to ensure simulation accuracy. Finite-size effects were then analyzed with FEM simulations for structures ranging from five to thirty grating periods. As expected, the simulated on-resonance external quantum efficiency of these detector structures drops significantly with reduced number of grating periods. We subsequently analyze a laterally-confined structure using a reflective gold coating on the mesa sidewalls to back-reflect the optical mode within the GMR cavity. We show that using this approach, the majority of the resonant response can be recovered, even for structures with few grating periods. The total width of the final pixel structure is approximately 8.1μm, dimensions compatible with modern MWIR FPAs. Finally, the optical response for a fabricated, super-periodic structure of repeated pixel elements was simulated, showing a pronounced dip in TE reflection at the design wavelength when compared to a planar, unpatterned region. Note that this structure neglects electrical isolation in favor of optical response, but mesa sidewall passivation can provide electrical isolation between the top and bottom contacts of the nBn structure.

The proposed photonic architecture provides a mechanism to recover high EQE in wavelength-scale pixels leveraging the guided mode resonance architecture. Even with as few as five grating periods, strong response is observed with the correct design of the lateral cavity. We will present designs showing resonant response as a function of grating period, mesa offset, and phase, and demonstrate the potential for integration with MWIR FPA architectures.

The authors acknowledge funding from the NASA ACT program (22-ACT22-0041).

[1] J. Appl. Phys, 62, 2545-2548 (1987)
[2] Appl. Phys. Lett., 107, 261104 (2015)
[3] IEEE Photonic. Tech. L., 34, 11, 615-618 (2022)
[4] Appl. Optics, 32, 14, 2606-2613 (1993)
[5] Opt. Express, 20, 11, 12155-12165 (2012)
[6] IEEE C. Trans. Opt. Netw., 1-4 (2011)
[7] From V. A. Podolskiy's research group, see http://viktor-podolskiy-research.wiki.uml.edu/RCWA

10:30 AM
Temperature Dependent Properties of doped InAsSb/GaSb Hyperbolic Metamaterial Stacks

Dr. KURT EYINK[1], Dr. Heather Haugan[1], Dr. Augustine Urbas[1]
[1]Air Force Research Laboratory

Hyperbolic metamaterials have been receiving considerable due to their large density of states, high spontaneous emission rates and tailorable properties[1],[2]. One way of forming these structures is through the combination of a degenerately doped semiconductor and undoped semiconductor to form stacks of these materials. Here the metallic component is the degenerately doped semiconductor and the metallic fraction is fixed from the ratio of the metallic region to the total thickness. We, as well as others, used a doped InAsSb in combination with undoped GaSb. The composition of the InAsSb was lattice matched to the GaSb to allow a wider range of topological structures. We have previously characterized Si:InAsSb/GaSb stacks and have found that the Si:InAsSb structures have the doped charge squeezed into the central region of the InAsSb[3]. We had found that the amount of squeezing was relatively independent of the size of the InAsSb region being consistently in the 3nm range. With Si doping concentrations

in the 1019/cm3, these semiconductor HMMs have been shown to produce both type I and II responses in infrared region. This suggests possible uses by combining these with InAs/GaSb SLS detectors. However many of detector applications require cooling well below room temperature to reduce dark current. Although these HMM have been characterized at room temperature, as far as we know, no temperature dependent studies have been performed. In this work, we extend previous research in these materials by looking at the temperature dependence of these stacks down to 77K. Stacks of InAsSb/GaSb were formed and subsequently characterized with spectroscopic ellipsometry as a function of temperature. These structure were subsequently fit using simple effective medium models to determine changes in doping and other structural changes as a function of temperature.

[1] Wenjie Ji, Jie Luo, and Yun Lai “Extremely anisotropic epsilon-near-zero media in waveguide metamaterials” Optics Express 2714, 19464 (2019).
[2] Iñigo Liberal and Nader Engheta, “Near-zero refractive index photonics” Nature Photonics 11, 150 (2017).
[3] K.G. Eyink, H.J. Haugan, A.T. Neal, K. Mahalingam, V. Pustovit, A. Urbas, “Determination of critical parameters for design of semiconductor hyperbolic metamaterials” Optical Materials 112, 110576 (2021).

10:45 AM
Anomalous diffraction in two-dimensional metacrystals from propagating surface modes (Student)
Mr. Ehsan Zahedi[1], Dr. Milan Palei[2], Dr. Anthony Hoffman[1]
[1]Department of Electrical Engineering, University of Notre Dame, [2]Department of Molecular Engineering, University of Chicago

We demonstrate anomalous diffraction from silver two-dimensional metacrystals (TDMCs)—optical materials that combine wavelength-scale and sub-wavelength engineering. In addition to diffraction peaks described by Bragg theory, we observe narrow peaks that are regularly spaced between the predicted Bragg orders. We present a model that relates these additional diffraction peaks to the propagation and decay of surface modes with hyperbolic dispersion. TDMCs have applications in super-resolution imaging.
Diffraction is a wave phenomenon important in the study of crystalline and periodic structures. It is the result of constructive and destructive interference of light with different optical path lengths. The far-field diffraction pattern can be described by Fraunhofer diffraction theory, which relates the intensity distribution to the Fourier transform of the diffracting object. For an array of rectangular scatterers, like the TDMC in this work, the far-field diffraction pattern resembles a sinc function, and each scatterer can be considered as an optical antenna. As the number of scatterers increases, the lobes in the radiation patterns begin to overlap, resulting in the distinct, narrow diffraction peaks described by Bragg's theory.
Here, we demonstrate that the far-field diffraction from TDMCs exhibits additional diffraction peaks between the Bragg diffraction orders, Fig. 1(a). This anomalous diffraction resembles diffraction from small photonic crystals [1], but arises from hyperbolic surface modes that efficiently couple to the far-field rather than a small number of fabricated scatterers. We design TDMCs by combining sub-wavelength features to engineer the dispersion of the surface modes with wavelength-scale features to engineer coupling to free space, Fig. 1(b). The TDMCs are fabricated on a silicon substrate using electron beam lithography, silver deposition via electron beam evaporation, and metal-liftoff, Fig. 1(b). The fabricated TDMC is an array comprising 500×100 nm ridges with 90 and 70 nm gaps along the longitudinal and lateral axes, respectively. The total array area measures 5×5 mm2 and contains 3,000,000 individual ridges.
We measure the diffraction patterns of the TDMCs under normal illumination using a two-axis rotary stage and lasers with different wavelengths (λ = 405, 532, and 633 nm), Fig. 1(a). The Bragg diffraction peaks for the measured TDMCs are given by: sin(theta_m)-sin(theta_i)=m*lambda/a, where 'a' is the lattice constant, 'lambda' is the free-space wavelength, 'theta_i' is the angle of incidence, and 'theta_m' is the angle of the mth diffracted mode. We observe the 1st order diffraction mode at 43º for λ = 405 nm and 64º for λ = 532 nm, which are in good agreement with the Bragg equation. We also observe additional diffraction peaks between the 0th and 1st order diffraction modes, indicated by the numbers in Fig. 1(a). Unlike the additional diffraction peaks from small photonic crystals, the additional diffraction peaks from our samples are narrow and bright.

To explain the anomalous diffraction, we develop a model that accounts for phase coupling across several ridges—referred to as optical domains—due to propagating modes. We show that the number of anomalous diffraction peaks is related to the number of coupled ridges in the optical domain, and their width is related to the number of optical domains that contribute to the far-field. The narrow width of these peaks results from the substantial number of optical domains within the TDMC. We model the propagation and decay of the surface modes using COMSOL and show good agreement between the number of coupled ridges and the anomalous diffraction peaks, Fig. 2. Our model agrees well with the number, angle, and width of the observed anomalous diffraction peaks, Fig. 3.

Our study demonstrates anomalous diffraction from TDMCs and explains the behavior in terms of propagating hyperbolic modes. Our model agrees well with experiment. This work not only opens avenues for potential applications in imaging and optical metrology but also underscores the complex relationship between structural parameters and hyperbolic modes.

Reference:
[1] Rybin et al., Sci. Rep. 6, 30773 (2016). https://doi.org/10.1038/srep30773

11:00 AM
Hybrid Terahertz Photonic Structure of Al/Cd3As2 for Ultrastrong Coupling Applications (Student)
Mr. Tenyu Aikawa[1], Prof. Thomas Searles[1], Prof. Zizwe Chase[1], Dr. Riad Yahiaoui[1], Prof. Pai-Yen Chen[1]
[1]University of Illinois at Chicago

Here the ultra strong coupling regime is investigated with a unique Dirac semimetal Cd3As2. Dirac semimetal thin films of Cd3As2 have been shown to have a linear energy dispersion along with ultra high mobility, which can support plasmons at the terahertz frequency.[1] Ultrastrong coupling will be important for the future quantum information technology. Devices that can ultra strongly couple light matter interactions will be critical for the computational speed of future of quantum computing architectures.[2,3] A meta surface can be used to enhance the coupling factor by N , where N is the “meta-atoms" in the array.[4] The unit cell of the metamaterial contains an aluminum ribbon and Cd3As2 cavity separated by a 100μm thick quartz substrate (Figure 1). The Cd3As2 cavity has a resonance at 1THz and the aluminum ribbon has a resonance frequency at 1THz as can be seen in Figure 2. When the cavity and the ribbon share the same resonant frequency they can resonantly couple together; creating a coupled state. This coupled state creates an upper and lower polariton, the difference between the two states defines the coupling strength η. When the

coupling strength is η > 0.1 it is in the ultrastrong coupling regime.[5] Coupling the cavity and ribbon together we are able to reach the ultrastrong coupling regime with a η ≡ 0.2. The evolution of the polariton system can be observed by tuning the ribbon and cavity in and out of resonance. The Rabi splitting or anti-crossing can be observed as a function of the ribbon width which tunes the resonant frequency of the ribbon. When ribbon and cavity share the resonant frequency it can be seen that these resonant frequencies avoid each other creating the upper and lower polariton that we observe in Figure 2.

11:15 AM
Realizing Molecular Optomechanics Induced Hybrid Properties in Soft Materials Filled Plasmonic Nanocavities (Student)
Mr. Bisweswar Patra[1], Dr. Bijesh Kafle[2], Prof. Terefe Habteyes[2]
[1]Center for High Technology Materials, University of New Mexico, Albuquerque, New Mexico, [2]Department of Chemistry and Chemical Biology, Center for High Technology Materials, University of New Mexico, Albuquerque

Recent advances indicate that enhanced light-matter interaction in plasmonic nanocavities can create hybrid properties in integrated plasmonic metal nanostructures and soft materials. Here, by integrating polyelectrolytes and surface ligands in gold nanorod-on-mirror nanocavities and detecting the nanocavity resonance and vibrational Raman scattering simultaneously, we found that the plasmon-vibration interaction modifies both the nanocavity and molecular responses. Large enhancement of Raman scattering accompanied by the plasmon resonance linewidth broadening are observed as the laser-plasmon detuning approaches the CH vibrational frequency of the molecular systems in the nanocavities. The experimental observations are consistent with the molecular optomechanics theory that predicts dynamical backaction amplification of the vibrational modes and high sensitivity of Raman scattering when the plasmon resonance overlaps with the Raman emission frequency. The results presented here suggests that molecular optomechanics coupling may be manipulated for creating hybrid properties based on quantum mechanical interaction of molecular oscillators and nanocavity electromagnetic optical modes.
(1) Albrecht, M. G.; Creighton, J. A., Anomalously Intense Raman-Spectra of Pyridine at a Silver Electrode. J. Am. Chem. Soc. 1977, 99, 5215-5217.
(2) Jeanmaire, D. L.; Vanduyne, R. P., Surface Raman Spectroelectrochemistry .1. Heterocyclic, Aromatic, and Aliphatic-Amines Adsorbed on Anodized Silver Electrode. J. Electroanal. Chem. 1977, 84, 1-20.

10:00 AM
Nano-Magnetic, Magnetic Memory and Spintronic Materials
Session Chairs: Michael Hamilton (Auburn University), Cheng Gong (University of Maryland)
ESJ 2204

10:00 AM
Induced Magneto-Electric Properties of Fe3+ Doped Ruddlesden Popper Perovskite Nanocomposite Antennas for Bio-Compatible Sensor Devices (Student)
Mr. Richard Harry[1], Prof. Shaik Zainuddin[2], Prof. Vijaya Rangari[3], Mr. Faruk Soso[1], Mr. Rifat Mahbub[1]
[1]Tuskegee University/University of Nebraska Lincoln, [2]Tuskegee University, [3]Department of Material Science and Engineering, Tuskegee University, AL, 36088, USA

The rush for automation and connectivity in today's age has focused on advancing technology toward developing novel sensors and actuators, bringing about the widely known concept of the Internet of Things (IoT). With this surge of innovation, there remains much opportunity to design devices that detect, measure, and control distinct electromagnetic field components using magnetoelectric (ME) coupling. This research focused on fabricating a multiferroic composite applicable within a multidirectional sensor system capable of such field control. In this study, multiferroic nanocomposite membranes were processed and characterized from their composition made from polyvinylidene – co – trifluoroethylene (P(VDF-TrFE)), a common fluoropolymer, as a matrix and K+- doped Ruddlesden-Popper perovskite (RPP), K2La2Ti3O10, nanoparticles (NPs) as filler. Modified intercalation techniques combining co-precipitation and sol-gel synthesis methods were performed to induce ME coupling in membranes by adding 90/10, 75/25, and 50/50 wt.% Fe3O4 in K2La2Ti3O10 to become K2La2TiFeO10 (FKLTO)and to optimize the ME coupling potential via variance of wt.% of RPP. X-ray diffraction (XRD), differential scanning calorimetry (DSC), vibrating sample magnetometry (VSM), and polarization vs. electric field hysteresis (P-E) loops were carried out to investigate the morphological, microscopic, and magnetoelectric behavior of P(VDF-TrFE)/RPP and added Fe3O4 by wt.% samples. Results have shown that the addition of 50 wt.% K+ RPP induces weak ferri-magnetic behavior hysteresis loops, indicating the presence of ionic interactions between K-Fe, Fe-Ti, and Fe-La metallic pairs, which were verified by peak shifts within the XRD profile. Breakdown strength was shown to decrease by 300 kV/cm as the wt.% of Fe3O4 added exceeded its saturation point of 50wt% Fe3O4. Target applications for magnetoelectric nanocomposite films are wearable electronics, automated power systems, skin prosthetics, and e-textiles.

10:15 AM
Efficient Voltage Control of Two-Dimensional Magnetic Insulators (Student)
Mr. Shanchuan Liang[1], Prof. Cheng Gong[1]
[1]University of Maryland, College Park

Magnetic insulators (MI), possessing long-range magnetic order while being electrically insulating, allow spin propagation without electrons' motion and thus promise a unique paradigm of next-generation dissipationless magnetoelectric and magneto-optical devices. While two-dimensional (2D) MIs usher the prospects into the atomic-thin region, efficient electrical control as an essential prerequisite for practical devices remains elusive; fundamental obstacles arise from the difficulty of electrostatically doping insulators and the inability of external electric fields to effectively modify materials' crystal fields. Here, by constructing a heterostructure consisting of a

functional thin film and a 2D magnetic insulator, we achieved a reversible and non-volatile electrical control of magnetism. The wavefunction overlaps at the heterostructure interface differs greatly under opposite voltages applied, leading to effective control of the coercivities in magnetic hysteresis loops of the 2D magnets. Our work opens up new avenues to usher 2D MIs towards future nanoscale spintronic, magnonic, and magneto-optical applications.

10:30 AM
Near Ideal Band-Insulator Behavior in Bi2(Te,Se)3/Bi2Te3 Superlattice Heterostructures
Dr. Patrick Taylor[1], Dr. Brandi Wooten[2], Prof. Joseph Heremans[2], Dr. Douglas Crane[3], Dr. Christopher Caylor[3], Dr. Lon Bell[3]
[1]Army Research Laboratory, [2]The Ohio State University, [3]DTP Thermoelectrics

Topological Insulator (TI) materials promise a wide variety of compelling new spintronics and integrated device technologies that could leverage the unique spin-polarized surface currents coupled with the complete absence of bulk transport. For applications such as these, the (Bi,Sb)2(Te,Se)3 class of topological insulators are attractive because their topological surface states display a robust Dirac-like energy-momentum dispersion. In practice, however, achieving true bulk insulation in this class of materials remains a significant challenge.
Of the (Bi,Sb)2(Te,Se)3 class of topological materials, the Bi2Te2Se1 composition is particularly interesting because 1) it offers one of largest bulk band gap values of known TIs so that the concentration of bulk intrinsic carriers can be small1, 2) the Dirac bands appear separated from bulk bands to minimize scattering, and 3) spin-orbit torque efficiency values are estimate to be among the highest in literature.2,3 For this work, we explore selenium-dilute Bi2(Te,Se)3 near the specific Bi2Te2Se1 composition in the form of a superlattice heterostructure with pure Bi2Te3. X-Ray diffraction shows well-defined superlattice satellite peaks about the (0015) reflection as shown in Fig. 1(b), and indicate excellent superlattice structure. We will present results from transport measurements, thermal measurements, and angle-resolved photoemission spectroscopy (ARPES) for these superlattice heterostructures.
The unusually large Seebeck coefficient values shown in Fig. 1(a) are evidence of near ideal band insulator behavior and that the Fermi level resides within the bulk band gap. This is also consistent with the ARPES band structure measurements, such as that of Figure 2, that show complete absence of conduction band states, and more explicitly show band insulator behavior.
Further, the transport measurements were analyzed with the method of four coefficients. Both compositions showed a reduced carrier concentration at lower temperatures, with the lower Se-doped sample achieving 1.1×1018 cm-3 at 80 K with a mobility of 2500 cm2/V-sec. Analysis of the Nernst coefficient suggested dominant interaction was impurity scattering. The effective mass of carriers determined from transport measurements ranged from ~0.4-0.6 me.
References:
1. S. Jia, H. Ji, E. Climent-Pascual, M. K. Fuccillo, M. E. Charles, J. Xiong, N. P. Ong, R. Cava, Phys. Rev. B 84, 235206 (2011)
2. Y. Wang, D. Zhu, Y. Wu, Y. Yang, J. Yu, R. Ramaswamy, R. Mishra, S. Shi, M. Elyasi, K. Teo, Y. Wu, H. Yang, Nature Communications, Vol. 8, Article number: 1364 (2017)
3. J. Han, A. Richardella, S. Siddiqui, J. Finley, N. Samarth, L. Liu, Phys. Rev. Lett. 119, 077702 (2017)

10:45 AM
Spin-orbit torque facilitated switching of Bi2Se3/NiFe heterostructures
Dr. Mehmet Noyan[1], Dr. Xiaohang Zhang[2], Dr. Olaf van 't Erve[1], Dr. Connie Li[1], Dr. Jisoo Moon[3], Dr. Enrique Cobas[1], Dr. Qiang Zou[4], Prof. Lian Li[4], Dr. Berend Jonker[1]
[1]U.S. Naval Research Laboratory, [2]Nova Research, [3]City College of New York, [4]West Virginia University

As worldwide demand for computing grows exponentially and processors become increasingly powerful, the need for memory technologies that are energy efficient, non-volatile and capable of ultrafast read/write operations is urgent. One promising technique is the use of materials with spin-orbit coupling to control magnetic layers using spin-orbit torque (SOT). [1] Topological insulators (TIs), materials with large spin-orbit coupling in which band inversion leads to the creation of spin-momentum locked surface states have been the subject of active research for use as sources of SOT. [2,3] However, TIs are often unintentionally doped, with Fermi energies in either the conduction or valence bands, creating a parallel bulk conducting channel that diverts current from the surface states, and potentially decreasing their SOT generation.
Here we present our group's ongoing work to leverage spin-momentum locking in topological insulators to manipulate magnetic layers. I will focus on recent results in which we have switched the in-plane moment of a NiFe layer in a Bi2Se3/NiFe heterostructure in which the Bi2Se3 has been specially engineered to be bulk insulating, as demonstrated in transport (Fig 1a) and angle-resolved photoemission spectroscopy (ARPES) measurements (Figure 1b). Using Kerr rotation measurements, we find that we are able to switch the NiFe layer four times more efficiently using a bulk-insulating versus a bulk-conducting Bi2Se3 layer (Figure 2), and with a current density more than an order of magnitude lower than required in heavy metals. I will contextualize these results with transport and second harmonic-hall measurements that provide insights into the competing contributions to the SOT from the bulk spin-hall effect and the spin-momentum locked surface states.
[1] R. Ramaswamy, J. M. Lee, K. Cai, and H. Yang, Appl. Phys. Rev. 5, 031107 (2018).
[2] Y. Wang, D. Zhu, Y. Wu, Y. Yang, J. Yu, R. Ramaswamy, R. Mishra, S. Shi, M. Elyasi, K.-L. Teo, Y. Wu, and H. Yang, Nat. Commun. 8, 1364 (2017).
[3] J. Han and L. Liu, APL Mater. 9, (2021).

11:00 AM
Efficient generation of spin-polarized light emission with 2D magnetic heterostructure
Dr. Xiao-Xiao Zhang[1]
[1]University of Florida

The advent of two-dimensional(2D) magnetic crystals has enabled both studies of fundamental magnetic interactions in reduced dimensions and novel compact designs for

spintronics devices. In this talk, I will present our recent results on a 2D spin-polarized light-emitting-diode composed of a monolayer semiconducting transition metal dichalcogenide (TMD) and few-layered CrI3. The valley and spin degrees of freedom are coupled in a monolayer TMD due to the broken inversion symmetry and the large spin-orbit coupling. The most common initiation method of the valley/spin index is through the valley-dependent optical selection rule, where the valley- and spin-polarized carriers are selectively excited with different circularly polarized light. Here, we demonstrate an efficient electrical injection of spin-polarized carriers and subsequent valley-polarized electroluminescence in monolayer TMD through the magnetic tunneling junction of CrI3. The magnetic field dependence of the electroluminescence helicity closely follows the overall magnetization of the few-layered CrI3, as shown in Fig. 1. By comparing the case of optical excitation, we conclude the electrical spin injection has an efficiency of > 70%. Furthermore, the electroluminescence helicity can be modulated and reversed electrostatically by varying the CrI3 doping level due to the doping-dependent interlayer exchange interactions in CrI3. Our results establish an efficient device scheme to achieve high efficiency and an electronically tunable spin-polarized 2D light-emitting diode and open up new directions for valleytronics and spintronics.

11:15 AM
Magnetic Tunnel Junction Testbed based Molecular Spintronics Devices: A Method of Solving 70-Year-Old Challenge in Making Molecular Devices
Dr. Pawan Tyagi[1]
[1]University of the district of Coulombia

Molecule-based devices may govern the advancement of logic and memory devices for next-generation computers and may be suitable for quantum computation. Molecules are unparalleled nanostructures that serve as device elements because chemists can mass-produce a variety of molecules with unique optical, magnetic, and transport characteristics. However, the biggest challenge is to connect two or three metal electrodes to the molecule (s) and develop a robust and versatile device fabrication technology that can be adopted for commercial-scale mass production. Utilizing tunnel junctions as a testbed for making molecular devices solves many critical problems [1]. We focused on producing magnetic tunnel junction-based molecular devices (MTJMSD). This talk will show that an MTJMSD evolves when molecules are bridged along the exposed side edges of a tunnel junction. With the MTJMSD approach, many unprecedented advantages become available to devise researchers. MTJMSD enables the connection between ferromagnetic electrodes and a variety of molecules with the spin state. For the first time, the MTJMSD approach enabled magnetic measurements and conventional transport studies[1]. Magnetic studies showed that molecules could transform the magnetic[2] and transport properties of the MTJs[3] at room temperature. Molecules' strong impact on ferromagnetic electrodes produced several orders of resistance changes at room temperature. An MTJMSD approach is a high-yield method and can be mass-produced with the conventional microfabrication tools present in typical labs. Our MTJMSD approach also allows numerous control experiments to provide a deep understanding of device mechanisms. This talk will demonstrate two types of control experiments to prove that we successfully made a molecular device. The first control experiment is the reversible impact of making and breaking molecular channels on the overall charge transport. We also performed ferromagnetic resonance before and after damaging the tunnel barrier and damaging the molecular channels by using the plasma. In addition, this talk will discuss how the MTJMSD approach is also suitable for making light sensors and biochemical sensors, as molecules are present in the open region.

10:00 AM
Computational Electronic Materials Discovery
Session Chairs: Angel Yanguas-Gil (Argonne National Laboratory), Sriram Krishnamoorthy (University of California)
ESJ 1224

10:00 AM
Blackbox Machine Learning for Nonlinear Materials Design (Student)
Mr. Patrick Devaney[1], Mr. Kevin Wen[1], Mr. Rithvik Ramesh[2], Mr. Nathaniel Irwin[1], Ms. Amberly Ricks[3], Prof. Sanjay Shakkottai[1], Prof. Seth Bank[1]
[1]University of Texas at Austin, [2]California Institute of Technology, [3]Department of Electrical and Computer Engineering, University of Texas at Austin, Austin, TX 78758

The increasing complexity of band-engineered electronic and photonic materials has radically advanced device performance and functionality. Traditional optimization techniques such as gradient ascent can identify globally optimal designs but require substantial knowledge about the objective function for both runtime performance and guarantees of approaching maxima. Blackbox optimizers (also referred to as zeroth-order or derivative-free optimizers) often make comparatively small assumptions about functions.
Here, we demonstrate materials design using multi-armed bandit-type online learning algorithms for blackbox optimization, which do not require a priori training sets, provide formal guarantees of finding the global optimal, scale well to high dimensionality problems, and can be applied to physical experiments [1] [2]. For this proof-of-principle study, we chose the maximization of the interband second-order optical nonlinear susceptibility, $\chi(2)$, of two coupled AlGaAs/GaAs quantum wells (QW) because of the well-developed theory and thoroughly explored design space to compare against [3]. In this study, we are only manipulating the total well width W, the sum of the widths of both wells, and an asymmetry parameter s describing the distribution of the well widths in the system, with all other parameters, including aluminum composition, fixed. We used a Schrödinger-Poisson solver to compute the wavefunctions and the energy levels of the first two bound electron and heavy hole states; these in turn are used to evaluate the $\chi(2)$ objective function for the material structure [3] [4].
The primary blackbox optimization algorithm applied, SequOOL, provides formal asymptotic guarantees for approaching a global maximum of a function given a local smoothness condition to that global maximum [1]. Most strikingly, it provides those guarantees while being parameter-free, so it does not need to have learning rates or similar parameters tuned before its use, making the

application of SequOOL simpler than competing approaches. For this fixed test system, χ(2) was maximized at 6.907 nm/V, with a total well width of 10.089 nm and an asymmetry parameter of 0.4267, reached at function evaluation 419. An informed brute-force solution to this problem reached approximately the same solution in 500 samples but with significantly restricted parameter space consisting of only 4 total well thicknesses. A naïve brute force approach necessitated 2440 function samples.
Despite the simplified two-parameter design space, blackbox methods identified the same global optimum as informed brute-force studies in fewer simulations; this computational advantage will grow markedly with increasing design complexity, with a particular future focus on true digital alloy material compositions. While we have only applied these blackbox optimizers to simulation thus far, they can also be applied to the actual experiments for automated science, especially with bandit optimizers like StroquOOL designed for operating under stochastic feedback [1]. These studies are in progress and will be reported at the conference.
This research was supported by a Multidisciplinary University Research Initiative from the Air Force Office of Scientific Research (AFOSR MURI Award No. FA9550-22-1-0307) and designing Materials to Revolutionize and Engineer our Future (NSF DMREF Award No. DMR-2118787).
[1] P. L. Bartlett, V. Gabillon, and M. Valko, “A simple parameter-free and adaptive approach to optimization under a minimal local smoothness assumption,” Proc. Machine Learning Research, vol. 98, pp. 1–23, 2019.
[2] W. Li, H. Li, J. Honorio, and Q. Song, “PyXAB – A Python Library for X-Armed Bandit and Online Blackbox Optimization Algorithms.” arXiv, 2023. doi: 10.48550/ARXIV.2303.04030.
[3] R. Ramesh, T. Hsieh, A.M. Skipper, Q. Meng, K.C. Wen, F. Shafiei, M.A. Wistey, M.C. Downer, J.B. Khurgin, and S.R. Bank, "Interband second-order nonlinear optical susceptibility of asymmetric coupled quantum wells," Applied Physics Letters, vol. 123, no. 25, Dec. 2023.
[4] S. Birner et al., “nextnano: General Purpose 3-D Simulations,” IEEE Trans. Electron Devices, vol. 54, no. 9, pp. 2137–2142, Sep. 2007, doi: 10.1109/TED.2007.902871.

10:15 AM
Light-matter interaction in Fabry Perot interferometer made of MXene based Distributed Bragg Reflectors
Dr. Chandra Adhikari[1], Dr. Dipendra Dahal[2], Dr. Bhoj Gautam[1]
[1]Department of Chemistry, Physics and Materials Science, Fayetteville State University, Fayetteville, NC 28301, USA, [2]Department of Physics and Astronomy, Hunter College of the City University of New York, NY 10065, USA

The study of light-matter interaction has been a crucial tool in understanding the intricate properties of matter in photonic and optoelectronic industries. The ability to analyze matter through its interaction with light has paved the way for fundamental research and advancements in the field of physics and engineering. Here, we semi-analytically study the reflection and transmission spectra of the Fabry Perot interferometer made up of silica sandwiched between two distributed Bragg reflectors (DBRs) made up of layered stacking of Titanium-based MXene alternatively with low refractive index materials such as Magnesium fluoride. We make use of Maxwell’s equation to theoretically investigate the relation of transmission and reflectance of the multilayer system and determine the transmission and reflection spectra of the DBRs in the system. The cavity formed between the two DBRs causes the formation of a transmission peak within the stop band in the transmission versus wavelength plot. The transmission coefficient is almost unity at that wavelength, indicating that the system becomes almost transparent to the incident light, and the light behaves as if there is no Fabry Perot interferometer at all. We reveal that the wavelength corresponding to the transmission peak also depends on the thickness of the cavity. Tuning of such resonance peaks varying the cavity lengths in the Fabry Perot interferometer is of great interest in optoelectronic device applications such as optical filters.
This work is supported by the Department of Energy BES-RENEW award number DE-SC0024611.

10:30 AM
Electronic structure and magnetism of titanium carbide MXenes (Student)
Mr. Joshua Abbott[1], Mr. Da'Shawn Morris[1], Ms. Saniya Lyles[1], Dr. Chandra Adhikari[1], Dr. Bhoj Gautam[1]
[1]Department of Chemistry, Physics and Materials Science, Fayetteville State University, Fayetteville, NC 28301, USA

A two-dimensional transition metal carbide, nitride or carbonitride, called MXenes have a wide range of applications due to their excellent electrical conductivity, mechanical strength, volumetric capacitance, larger surface area, high thermal conductivity, and chemical stability and show promise in electronic devices, sensors, energy storage devices, oxygen evolution reaction and hydrogen evolution reaction catalysts and so on. We theoretically study the stability, electronic structures, magnetism, optical properties, and applicability of various MXenes for electrode materials for energy storage applications. The wet method of synthesis of MXenes from the MAX phase results in the synthesized MXenes being surface terminated, making the preparation of pristine MXenes difficult. The surface termination strongly affects the electronic and magnetic properties of MXenes, such as pristine Ti3C2 showing metallic character, while Ti3C2 with fluoride group termination, which is the most common product in the wet synthesis method, shows semiconducting behavior. Our preliminary study shows Ti2C is a half-metallic ferromagnet in its ground state, with one spin channel metallic and the other spin channel insulating; however, Ti3C2 is a very weak antiferromagnet.
This work is supported by the Department of Energy BES-RENEW award number DE-SC0024611.

10:45 AM
A Practical Simulation and Modeling Solution for Complex Magnetic Molecule and Magnetic Tunnel Junction-based Molecular Spintronics Devices: A Monte Carlo Method
Mr. Christopher D'Angelo[1], Dr. Pawan Tyagi[2]
[1]University of the District of Columbia, [2]University of the district of Coulombia

Mass-producible and robust molecular spintronics devices (MSD) can revolutionize memory and logic devices to produce the next generation of computers. MSDs are also explored worldwide for their potential application in quantum

computers to harness the quantum properties of molecules[1]. MSD can be a testbed for producing novel materials where molecules serve as a catalyst to activate spin filtering-like phenomenon and impact the connected two ferromagnets or metal electrodes [2] (Fig.1a-c). Fabrication and systematically understanding MSD are two major hurdles in advancing this field. Tyagi et al. proposed a Magnetic tunnel junction-based molecular spintronics device (MTJMSD) to overcome fabrication difficulty and observed a number of unprecedented phenomena [2]. Numerous magnetic properties of MTJMSD could not be understood due to the lack of simulation and modeling methods for microscopic MSDs at room temperature. The biggest challenge in advancing the MSD field is the lack of simulation and modeling tools and methods that can successfully predict or explain the microscopic phenomenon of MSDs. Existing strategies are either not feasible due to the complexity of MSD or just focus on a particular part of MSD and are applicable to unrealistic environments (e.g. 0 K temperature) [3]. A Monte Carlo Simulation for MSD(MCSMSD) was invented to fill this technology gap (Fig.1). This program simplifies molecule structure and represents molecule interaction with configurable metallic leads using parametrically controllable variables. Interatomic interactions among molecules and metal electrodes and external stimuli such as magnetic field and thermal energies are also controlled parametrically to simulate a vast range of possibilities and subsequently correlate them with experimental observations if applicable. This talk will discuss the flow diagram of simulating several shapes of MSD by parametrically varying the interaction parameter and material properties such as anisotropy and inter-atomic Heisenberg coupling, as well as the analog of electron density. We will also discuss the new capabilities of the simulation program that can simulate complex molecule structures connected to the metal electrodes. A new graphical interface that enables our MCSMSD program to be used by high school and undergraduate students for STEM outreach will also be discussed. Metallic electrodes can be set to ferromagnetic, paramagnetic, nonmagnetic, and antiferromagnetic in nature. Our simulation program has successfully produced profound insights behind the experimentally observed intriguing phenomenon on MTJMSD that motivated us to build this simulation program[4-7].

References: [1] J. Lehmann, A. Gaita-Arino, E. Coronado, and D. Loss, "Quantum computing with molecular spin systems," J. Mater. Chem., vol. 19, pp. 1672-1677, 2009.
[2] P. Tyagi, "Trenched Bottom Electrode and Liftoff based Molecular Devices. U.S. Patent Application No. 16/102,732.," 10833162, Nov 10, 2020, 2020.
[3] V. M. Jie Liu, Michael C. Shaughnessy-Culver, Stephen Lee Smith. Yong-Seog Oh; Pratheep Balasingam Terry Sylvan; Kam-Chiu Ma, "Simulation scaling with DFT and non-DFT," 2020.
[4] P. Tyagi, C. Riso, U. Amir, C. Rojas-Dotti, and J. Martínez-Lillo, "Exploring room-temperature transport of single-molecule magnet-based molecular spintronics devices using the magnetic tunnel junction as a device platform," RSC Advances, vol. 10, pp. 13006-13015, 2020.
[5] P. Tyagi, C. Baker, and C. D'Angelo, "Paramagnetic Molecule Induced Strong Antiferromagnetic Exchange Coupling on a Magnetic Tunnel Junction Based Molecular Spintronics Device," Nanotechnology, vol. 26, p. 305602, 2015.
[6] M. Savadkoohi, C. D'Angelo, A. Grizzle, B. Dahal, and P. Tyagi, "Impact of ferromagnetic electrode length and thickness on Magnetic Tunnel Junction-Based Molecular Spintronic Devices (MTJMSD)," Organic Electronics, vol. 102, p. 106429, 2022.
[7] E. Mutunga, C. D'Angelo, A. Grizzle, V. Lamberti, and P. Tyagi, "Dramatic effect of electrode type on tunnel junction based molecular spintronic devices," Organic Electronics, vol. 106, p. 106526, 2022/07/01/ 2022.

11:00 AM

The Monoclinic Beer-Lambert Law in Beta Gallium Oxide (Student)

Mr. Md Mohsinur Rahman Adnan[1], Dr. Darpan Verma[1], Dr. Chris Sturm[2], Dr. Mathias Schubert[3], Dr. Roberto Myers[1]
[1]The Ohio State University, [2]Universitat Leipzig, [3]University of Nebraska-Lincoln

The highly anisotropic absorption and photoresponsivity in monoclinic crystal structure Beta Gallium Oxide near the optical absorption edge can be modeled with the help of a modified Beer-Lambert law having two effective absorption coefficients. At any given fixed photon energy, it is observed that the absorption coefficient associated with the incoming polarization state will always weaken to its smallest possible value beyond a critical penetration depth where this critical depth itself depends on the incoming polarization state. To understand this behavior, we have performed photon energy and penetration depth dependent Stokes vector analysis and plotted them on the Poincare sphere to track the changes in polarization state of the incoming light as it travels farther within the material. We find that the weakening of the absorption coefficient upon beam propagation manifests from apparent rotation of the incoming linear polarization state to align eventually with the least absorbing crystal direction in the plane tangential to the propagation direction. The presence of strong linear dichroism near the optical absorption edge in Beta Gallium Oxide causes this effective rotation. The least absorbing polarization direction has been identified to be aligned approximately parallel to the dipole excitation orientation of the a-exciton for incident electric field directions within the (010) plane and parallel to the orientation of the b-exciton , i.e., parallel to the b-axis for electric field directions within the (001) plane. Due to the monoclinic crystal structure, the linear dichroism in is a result of the anisotropy of physical absorbers, i.e., excitons and band-to-band transitions whose dipole excitation direction are not perpendicular to each other. As a result, polarization directions cannot be found anymore for which the absorption behavior follows the Beer-Lambert law, and modifications to the historic form derived from observation are required. Phenomena caused by low-symmetry structure materials might have been overlooked and need thorough investigation in other materials with anisotropic excitons in low symmetry systems such as monoclinic structure two dimensional materials and the entire class of monoclinic and triclinic semiconductors. The linear rotation of the incoming polarization state is accompanied by a circular rotation which arises from the birefringence property in Beta Gallium Oxide. The polarization angle and photon energy dependence of the critical penetration depth can be interpreted as a result of effective linear and circular birefringence and dichroism acting onto the incoming polarization state. Our observations

can be extended to photon energies beyond the range of interest i.e., further away from optical absorption edge under certain conditions.

11:15 AM
Selective Incorporation of Group-V Elements in GaN (Student)
Mr. Yujie Liu[1], Mr. Ishtiaque Navid[1], Prof. Zetian Mi[1], Prof. Emmanouil Kioupakis[1]
[1]University of Michigan

Dilute concentrations of group-V elements (As, Sb, and Bi) doping into GaN induce large band-gap bowing and tunable room-temperature photoluminescence from the UV to the green spectral regions. It is often assumed that the group-V elements preferentially are incorporated as anions (X3–) into the N sublattice. However, the incorporation mechanism of these highly mismatched ions into the host nitride material remains unclear.
In this work, we use first-principles calculations to explore the possibility that group-V elements may be incorporated as cations (X3+, X5+) into the metal sublattice. The analysis of bulk defect thermodynamics demonstrates that XGa becomes energetically comparable compared with XN under certain growth conditions. We also show that the incorporation of group-V elements both as cations and as anions group-V elements is further confirmed experimentally by the additional micro-Raman peaks observed in group-V elements doped samples [1-3]. Band structures of different types of group-V doped GaN and their agreement with experimental spectra also suggest the incorporation of cation-like group-V elements. Experimentally, secondary ion mass spectroscopy (SIMS) clearly indicates that low epitaxial growth temperature is favorable for the incorporation of the group-V elements into the GaN lattice. Micro-Raman characterization shows additional peaks due to the incorporation of group-V elements at the dilute levels, originating from both disorder-activated Raman scattering (DARS) and local vibrational modes (LVM). X-ray photoelectron spectroscopy (XPS) measurements are also used to deduce the electronic interaction between group-V dopant atoms and GaN nanostructure [4]. Our results shed light on the incorporation mechanism of dilute nitride alloys and its effects on material characteristics.
References:
[1] Chowdhury, F. A., et al. “Optically active dilute-antimonide III-nitride nanostructures for optoelectronic devices.” Applied Physics Letters 111.6 (2017).
[2] Chowdhury, F. A., and Zetian Mi. “Probing the large bandgap-bowing and signature of antimony (Sb) in dilute-antimonide III-nitride using micro-Raman scattering.” Journal of Applied Physics 126.8 (2019).
[3] Chowdhury, F. A., et al. “Dilute-antimonide GaSbN/GaN dots-in-wire heterostructures grown by molecular beam epitaxy: Structural and optical properties.” Applied Physics Letters 118.1 (2021).
[4] Ishtiaque A. Navid et al. “Structural and Optical Characterization of Dilute Bi-Doped GaN Nanostructures Grown by Molecular Beam Epitaxy.” Accepted by APL Materials. (2024).
[5] Sarney, W. L., et al. “GaN1−xSbx highly mismatched alloys grown by low temperature molecular beam epitaxy under Ga-rich conditions.” Journal of crystal growth 383 (2013): 95-99.

11:30
Lunch

1:00 PM
Nitride Electronic Devices
Session Chairs: Chirag Gupta (University of Wisconsin), Mona Ebrish (Vanderbilt University)
ESJ 0202

01:00 PM
High Forward Current Density in Si-doped AlN Schottky Barrier Diodes
Mr. Cris Quinones[1], Dr. Dolar Khachariya[2], Dr. Pramod Reddy[3], Mr. Jack Almeter[1], Dr. Pegah Bagheri[1], Dr. Ronny Kirste[3], Dr. Seiji Mita[3], Prof. Erhard Kohn[1], Prof. Ramón Collazo[1], Prof. Zlatko Sitar[1]
[1]North Carolina State University, [2]Adroit Materials Inc., [3]Adroit Materials

Aluminum Nitride (AlN) is an attractive material for extreme environment capable kV-class power devices due to its ultra-wide bandgap, high breakdown field, thermal conductivity, and temperature stability. Despite these exceptional properties, there are very few reports of devices fabricated on AlN.[1], [2] This is due to the difficulty in doping, which makes realizing practical devices very challenging. For example, AlN Schottky barrier diodes (SBDs) reported in the literature show poor performance, large ideality factors and low ON-state current. Particularly, the forward current in AlN SBDs has been limited by the resistivity of the AlN as well as poor ohmic contacts. In this work, we study the effect of the ohmic contact layer composition on the forward current in quasi-vertical, Si-doped AlN Schottky barrier diodes.
Using metalorganic chemical vapor deposition (MOCVD), three distinct quasi-vertical AlN SBD structures were grown on native AlN single-crystal substrates. All devices consisted of a 1 m thick n-AlN drift layer with [Si] = 1×1017 cm-3 on top of a 2 µm highly-doped contact layer (Fig. 2). The Ga composition was increased from 0% in device (a) to 20% and 30% in devices (b) and (c), respectively. In device (c), a compositionally graded layer was implemented between AlN and AlGaN for improved electron transport across the interface by reducing conduction band offsets. All devices were fabricated using standard photolithography and reactive-ion etching. Ohmic contacts were formed by depositing a large area Cr/Ti/Al/Ti/Au metal stack on the etched surface, followed by circular Ni Schottky contacts. The resulting electrical behavior of the Schottky diodes was analyzed using I-V measurements. In the forward bias, a 104× improvement in forward current density was achieved by managing the ohmic contact layer, as shown in Fig. 2. The current density was >3 kA/cm2 at 10 V for diode (c), a record for AlN Schottky diodes. A low ideality factor (η<1.3) current region was observed for all diodes, indicating

Schottky emission dominates. However, a series resistance was not observed. Instead, the current followed the Frenkel-Poole (FP) emission model in all diodes (Fig. 3). Using temperature dependent I-V, both the Schottky and FP barriers are extracted. In reverse bias, a maximum breakdown voltage of 770 V was observed for diode (b) (Fig. 4). These results represent significant progress towards understanding electronic devices on AlN and realizing high-performance power electronics on this material.
[1] H. Fu et al. IEEE Electron Device Letters 38(9), 1286–1289 (2017).
[2] T. Maeda et al, Appl. Phys. Express 15(6), 061007 (2022).

01:15 PM
Mitigation of Reverse Leakage Current and Charge Trapping in GaN Schottky Barrier Diodes
Dr. Amelia Peterson[1], Mrs. Kim Kropka[1], Dr. Anthony Rice[1], Dr. Albert Colon[1], Dr. Jason Neely[1], Dr. Greg Pickrell[1]
[1]Sandia National Laboratories

GaN Schottky barrier diodes (SBDs) are promising candidates for high voltage, fast-switching applications and have also attracted interest for their operation in harsh environments. However, their use in these applications is hindered by performance challenges such as high leakage current and premature breakdown which are driven by surface states, edge effects, and compensating trap states. Ion implantation and plasma treatments can passivate the GaN surface to reduce leakage current and increase breakdown voltages in GaN SBDs [1-2], but these high-energy treatments can also induce damage to the lattice. Studies have shown that ultraviolet light and ozone (UV/O3) processes, a low-energy alternative for surface passivation, can significantly reduce leakage current in GaN diodes [3] and GaN Schottky gates in AlGaN/GaN HEMTS [4-5]. In this study, we present a UV/O3 and HF wet etch method for the GaN SBD structure shown in Figure 1 to reduce perimeter leakage. Prior to deposition of the SiO2 passivation layer shown in Figure 1, the GaN surface around the Pd anode is treated using a 200C UV/O3 process, followed by an HF wet etch, followed by an additional UV/O3 treatment. The reverse bias leakage of the devices treated with the UV/O3 and HF process is measured and compared to a control wafer which did not receive a passivation treatment. Figure 2 shows the histograms of leakage current density measured on each device at -100V for both wafers and the three device sizes fabricated. Table 1 compares the devices with and without the passivation treatment by calculating the ratio of the current densities at their respective histogram peaks. Compared to devices processed with no surface passivation, the UV/O3 and HF process results on average in a 1000 times reduction in reverse bias leakage current at -100V for most diodes with a 250μm diameter and some diodes with a 500μm diameter. The histogram for the UV/O3 and HF treated wafer also shows that the left peaks on the 250μm and 500μm devices are independent of anode size, indicating the elimination of perimeter leakage current in some of the UV/O3 and HF treated devices. This dependence of anode size on leakage current implies that smaller devices have fewer defects along their perimeter, and therefore the passivation treatment can passivate all defects on these devices. In addition, this process mitigates a hysteretic increase of leakage current induced by deep trap states at large reverse biases. These results indicate that deep traps in GaN SBDs may increase leakage current and cause premature breakdown. We explore the mechanisms behind the interaction of perimeter defects, deep traps, and leakage current and discuss a refinement of the HF and UV/O3 treatment to control them.
[1] Han, S., et al. (2018). "High-Voltage and High- Ion/Ioff Vertical GaN-on-GaN Schottky Barrier Diode with Nitridation-Based Termination." IEEE Electron Device Letters 39(4): 572-575.
[2] Liu, Z., et al. (2019). "High-voltage vertical GaN-on-GaN Schottky barrier diode using fluorine ion implantation treatment." AIP Advances 9(5): 055016.
[3] K. Kim, D. Liu, J. Gong, and Z. Ma, "Reduction of Leakage Current in GaN Schottky Diodes Through Ultraviolet/Ozone Plasma Treatment," IEEE Electron Device Letters, vol. 40, no. 11, pp. 1796-1799, 2019, doi: 10.1109/LED.2019.2944353.
[4] S. Mazumder, S.-H. Li, Z.-G. Wu, and Y.-H. Wang, "Combined Implications of UV/O3 Interface Modulation with HfSiOX Surface Passivation on AlGaN/AlN/GaN MOS-HEMT," Crystals, vol. 11, no. 2, doi: 10.3390/cryst11020136.
[5] K. Kim et al., "AlGaN/GaN Schottky-Gate HEMTs with UV/O_3-Treated Gate Interface," IEEE Electron Device Letters, vol. 41, no. 10, pp. 1488-1491, 2020, doi: 10.1109/LED.2020.3019339.

01:30 PM
Monolithic Bidirectional GaN-on-Si HEMT with >1.5kV Breakdown Voltage (Student)
Mr. Md Tahmidul Alam[1], Mr. Jiahao Chen[1], Mr. Ruixin Bai[1], Prof. Shubhra Pasayat[1], Prof. Chirag Gupta[1]
[1]University of Wisconsin-Madison

For efficient and reliable extraction, storage, and conversion of renewable energy (e.g. solar, wind and hydro energy), novel power electronic converters with bidirectional current flow and blocking capability are required [1]. Multilevel T-type inverter [2], AC-AC matrix converter [3], DC-DC dual active bridge (DAB) [4] etc. are some examples of bidirectional power converters. These converters require bidirectional transistors that can allow and block current in both directions. The initial attempts of achieving bidirectional transistors were to cascade or parallel two unidirectional transistors in reverse direction [5], [6]. However, these types of implementations increased the on-resistance by ~2x and reduced reliability. Monolithic bidirectional transistors implemented by a single GaN HEMT can reduce these issues significantly [7]. However, there are little reports on >1.3kV monolithic bidirectional GaN HEMTs (MBGH), its detailed device structure and performance optimization strategies are also not available. In this study, we report >1.5kV MBGH with detailed description of device structure and a performance optimization strategy by multiple field plates.

MOCVD-grown GaN (2 nm)/Al 0.25Ga0.75N (20 nm)/AlN (1 nm)/GaN (1.5 μm)/ AlGaN (3.5 μm)/AlN buffer (200 nm)/Si (111) substrate was used to fabricate the MBGH (Fig. 1). Device fabrication started with ohmic metal deposition (Ti/Al/Ni/Au) (20/120/30/50nm) and subsequent annealing in 900°C for 45 seconds in N2 environment. Thereafter, a 200nm deep mesa isolation was etched. Then, TLM measurements were performed to extract contacts

resistance (Rc = 1.51 Ω.mm) and sheet resistance (Rsheet = 360 Ω/□). Following that 200nm thick Ni gates were deposited and the surface was passivated by PECVD Si3N4. After that, two field plate trenches (180nm and 300nm thick Si3N4 under first and second file plate respectively) were etched, and Ni was deposited as field plate metal. Each field plate was shorted to the nearest ohmic electrode.
The IV characteristics of the transistors were almost symmetrical in both directions (Fig. 2). RON was ~10 Ω.mm (or 2.54 mΩ. cm2) for Lgg =11μm, Lgs =2μm, Lg = 1μm. This value closely matched with the predicted RON from Rc and Rsheet (10.5 Ω.mm). The transfer curve shows that the device has a good on-off ratio of ~107 with a steep subthreshold slope of 88mV/dec, making it suitable for high frequency switching applications (Fig. 3). To optimize the breakdown voltage experimentally, both the field plate lengths were varied. It was found that the breakdown voltage was maximum when the total field plate length was close to a “critical length” (~3μm) (Fig. 4). Above the “critical length” breakdown voltage decreased possibly because of the higher impact ionization rate in the channel due to the proximity of the high voltage bias to the opposite gate. The highest breakdown voltage in these devices was 1360V (Fig.5).

To test if silicon substrate can be used to fabricate transistors with higher breakdown voltage, some two terminal breakdown measurements were done. Two ohmic electrodes were separated by 10μm, 30μm and 50μm with a 600nm mesa isolation in between. The breakdown voltage was found to saturate (~2kV) in these test structures (assuming 1mA/mm as the breakdown threshold) (Fig. 6). The HEMTs/sapphire samples showed almost linear increase in two-terminal breakdown voltage with electrode distance (850V, 2200V and >3kV for 10μm, 30μm and 50μm respectively). It was possibly due to the better insulating property of the sapphire substrate. Therefore, HEMTs-on-sapphire substrates may be used to get ultra-high voltage MBGH.

Another set of MBGH’s were fabricated both on silicon and sapphire substrates. The maximum breakdown voltage in the HEMT/silicon and HEMT/sapphire substrate were ~1600V (RON = 10.77 Ω.mm) and ~1400V (RON = 13.18 Ω.mm) respectively (with Lgg =17μm, other dimensions unchanged) (Fig. 7). During measurement these devices were unpassivated. This time Rc reduced to 1.13 Ω.mm and 0.76 Ω.mm in the HEMT/Si and HEMT/sapphire samples respectively due to more optimization of annealing conditions. Attempts are ongoing to further increase the breakdown voltage by tuning the Si3N4 thickness under the field plates, using high-k dielectric and implantation-based isolation. These advances will be presented at the conference.

Acknowledgment: The work was supported by NSF through MRSEC and NSF ASCENT program.
[1] Gorji SA et al. An overview. IEEE Access. 2019 [2] C. Kuring et al. International Exhibition and Conference for Power Electronics, Intelligent Motion, Renewable Energy and Energy Management, 2018. [3] Nagai S at al. IEEE International Solid-State Circuits Conference Digest of Technical Papers (ISSCC) 2014 [4] Zhou H et al. 2008 IEEE Industry Applications Society Annual Meeting 2008 [5] Waldron J et al. 25th International Symposium on Power Semiconductor Devices & IC's (ISPSD) 2013 [6] Wang H et al. IEEE Electron Device Letters. 2021 [7] T. Morita et al. IEEE International Electron Devices, 2007.

01:45 PM
Ohmic and Schottky Contacts to High-Voltage GaN Photoconductive Semiconductor Switch
Dr. Geoffrey Foster[1], Dr. Andrew Koehler[1], Dr. Karl Hobart[2], Dr. Travis Anderson[2]
[1]US Naval Research Laboratory, [2]Naval Research Lab

Photoconductive semiconductor switches (PCSSs) have the potential to outperform conventional unipolar semiconductor power devices. PCSS devices operate using photoconductivity, wherein the material becomes conductive after the absorption of light [1]. In recent years, wide bandgap photoconductive semiconductor switches, such as GaN PCSSs, have gained attention due to high critical electric field strength, high electron saturation velocity, and the ability to provide high power ultrafast devices. A PCSS can overcome the on-resistance vs. breakdown voltage limits of the drift layer in a unipolar power device by optically modulating the conductivity of the entire drift layer through high-density free-carrier injection. This mechanism of modulating channel-conductivity by optically injecting charge (electrons and holes) facilitates fast switching speeds while inherently providing optical isolation to the gate driver control circuitry to mitigate electromagnetic interference. While the holes will recombine quickly, it may be possible to collect a hole current in addition to the generated electron current. Schottky contacts, to n-type GaN, will be used to collect any hole current while also comparing their electrical properties versus an Ohmic contact.

Four microns of GaN was grown on a silicon carbide (SiC) substrate by metal organic chemical vapor deposition (MOCVD), with a carbon doping concentration of 7 x 1016 cm-3. In order to collect both an electron current and a hole current, two different contacts must be deposited. For electron collection, Ti/Al/Ni/Au contacts were deposited using a lift off technique with an 800C rapid anneal. For hole collection, Pd/Pt/Au contacts, were deposited alongside the Ti/Al/Ni/Au contacts. Contacts were arranged in two different configurations in a circular transmission line (CTLM) arrangement. Device 1 has Ti/Al/Ni/Au on sides of the TLM and Device 2 has Ti/Al/Ni/Au on one side and Pd/Pt/Au on the other side. The material was then characterized using photoionization spectroscopy with a monochromatic light source on Device 1. A strong photoresponse, with eight orders of magnitude on/off current, is seen at bandgap, and at 3.1eV, indicating a response from carbon-related defects. Off-state breakdown values, measured from Device 1 CTLM structures, range from 1553V at a gap of 50 microns to 7385V at a gap of 250 microns. A 3W 365nm 46.24mm2 light emitting diode (LED), focused through a 20x magnification near UV infinity corrected objective, was used to illuminate the PCSS for on-state measurements. The LED and objective are mounted on a micromanipulator to control the position and height of the optical power density. Maximum optical power density is measured to be 0.102 W/cm2. Device 1 is linear, while Device 2 shows a rectifying behavior with a rectification of 2.5 orders of magnitude, indicating unipolar (electron) transport with the Pd/Pt/Au forming a Schottky contact. Both device 1 and 2 have a similar linear

on-resistance, indicating that series resistance dominates both devices. Under the contact, the carbon doped GaN is shadowed, not allowing for optical carrier generation and remains highly resistive, leading to a high contact resistance. Conductive GaN can be grown under the contacts will likely reduce this sheet resistance and is the subject of further work.

References:
1 A. D. Koehler et al., “High Voltage GaN Lateral Photoconductive Semiconductor Switches,” ECS J. Solid State Sci. Technol., vol. 6, no. 11, pp. S3099–S3102, 2017, doi: 10.1149/2.0231711jss.

02:00 PM
Charge-trap coupled ferroelectric gate ScAlN/ScN/AlGaN/GaN HEMT with normally off operation (Student)

Mr. Jiangnan Liu[1], Dr. Ding Wang[1], Mr. Shubham Mondal[1], Prof. Zetian Mi[1]
[1]University of Michigan

The merits of wide bandgap, high electron saturation velocity enables gallium nitride (GaN) a good material platform for the next generation power electronics that can operate fast and endurably under high power and certain extreme environment. These superior properties lead to many efforts in developing high performance AlGaN/GaN-bsed high electron mobility transistors (HEMTs) that are ideally suited for high power and high frequency applications such as 6G communications and the automotive industry. Despite intense research conducted in the design and fabrication of AlGaN/GaN HEMTs, several challenges still remain and need to be addressed for a wider range of future commercial adoptions. One of the issues is that the safe operation of power electronics generally requires low leakage current and a normally-off, i.e., enhancement-mode (E-mode) operation. The normally off behavior would also benefit the circuit design by reducing the protection circuits, and multiple attempts on shifting the threshold voltage (Vth) to a positive value has been made. Initial effort was focusing on reducing the AlGaN barrier thickness to lower the Fermi-level to the level below the AlGaN conduction band and the 2DEG (2-dimensional electron gas) concentration would be reduced accordingly, yet it induced much higher series resistance. Further work on fluorine-treated surface technique was developed to inject more negatively charged ions to shift the Vth to achieve E-mode operation. However, this method exhibits poor thermal stability and larger gate current leakage. It also faces process variation issue due to it relies heavily on the fluorine plasma treatment step. Currently, the commercially adopted way is by incorporating a p-type GaN gate in the HEMT structure to extend the depletion region in the 2DEG layer but this method has limited Vth shifting and the breakdown voltage would be lowered.
In this work, we developed the AlGaN/GaN-based normally off HEMT device by building a complex gate structure with a ferroelectric scandium aluminum nitride (ScAlN) and a charge trapping layer scandium nitride (ScN). The ultrathin (monolayer) ScN acts as an electron reservoir to help trap and store the electrons from the 2DEG channel region, transitioning the operation from the depletion mode to the enhancement mode. In the meantime, the ferroelectric ScAlN with a switching polarization property would help with the charge trapping. To achieve the normally off operation, an initialization process by applying a positive gate bias (10 V) is performed to inject the carriers from the channel to the ScN trapping layer, shifting the threshold voltage from -1.2 V to +1.3 V. The fabricated device also shows a steep subthreshold swing (SS) as low as 65 mV/dec, close to the Boltzmann limit, which is beneficial for high-speed switching and low power consumption. Furthermore, within the tested cycles, the device performance, including the threshold voltage remains almost intact, showing a stable operation in the normally off state. Time scale analysis shows that the threshold voltage stays in the positive side for longer than 1000 seconds. These results show that an AlGaN/GaN HEMT device with a fully epitaxial monolayer charge-trap coupled ferroelectric gate provides a stable normally off operation for high performance power devices.

1:00 PM
Multifunctional Oxides: Characterization and Processing
Session Chairs: Lauren Garten (Georgia Institute of Technology), Patrick Lenahan (Penn State University)
ESJ 0224

01:00 PM
Proposal for a new evaluation method of relationship between the lifetime of ferroelectric capacitors and dielectric breakdown spot (Student)

Mr. Yuki Itoya[1], Dr. Hirokazu Fujiwara[2], Dr. Cédric Bareille[3], Prof. Shik Shin[4], Prof. Toshiyuki Taniuchi[2], Prof. Masaharu Kobayashi[1]
[1]Institute of Industrial Science, The University of Tokyo, [2]Material Innovation Research Center (MIRC), The University of Tokyo, [3]Institute for Solid State Physics, The University of Tokyo, [4]Office of University Professor, The University of Tokyo

To achieve high-density ferroelectric memories, ferroelectric HfO2 (FE-HfO2) has been paid attention because of its high CMOS compatibility, high scalability, and high coercive electrical field .However, the write endurance of FE-HfO2-based capacitors is still limited mainly by dielectric breakdown (DB). Time dependent dielectric breakdown (TDDB) measurements are performed to statistically evaluate the lifetime of FE-HfO2 memories.
Laser-based photoemission electron microscopy (laser-PEEM) is a promising tool for observing DB process. By using a continuous wave (CW) laser with a photon energy of 4.66 eV, a high spatial resolution and deep probing depth are achieved. Furthermore, by the in-situ laser-PEEM observation, the filament formation was visualized through the top electrode. The in-situ laser-PEEM is an effective tool for visualizing leakage paths inside capacitors without any destructive sample treatments.
In this study, we observe TDDB process of HfO2-based metal-ferroelectric-metal (MFM) capacitors by in-situ laser-PEEM. We observe DB spots of capacitors, which reveals that the position of the DB spot depends on the lifetime of the capacitors: they are broken near the edge for the short-lifetime capacitors, while broken near the center for the long-lifetime capacitors. This suggests that the lifetime is determined by the quality of the bottom-electrode edge for

the short-lifetime capacitors, while that is determined by the ferroelectric film quality for the long-lifetime capacitors.

01:15 PM
In situ nondestructive spectromicroscopic analysis of dielectric breakdown in HfO2-based ferroelectric capacitors by laser-based photoemission electron microscope
Dr. Hirokazu Fujiwara[1], Mr. Yuki Itoya[2], Prof. Masaharu Kobayashi[2], Dr. Cédric Bareille[3], Prof. Shik Shin[4], Prof. Toshiyuki Taniuchi[1]
[1]Material Innovation Research Center (MIRC), The University of Tokyo, [2]Institute of Industrial Science, The University of Tokyo, [3]Institute for Solid State Physics, The University of Tokyo, [4]Office of University Professor, The University of Tokyo

We have developed an in-situ laser-based photoemission electron microscope (laser-PEEM) to investigate characteristic modulations of ferroelectric devices [1]. Here, we report our laser-PEEM system with a Sawyer-Tower circuit and electronic structure of a conduction path formed by a dielectric breakdown (DB) event in a HfO2-based ferroelectric capacitor. We succeeded in visualizing a DB spot within the capacitor with the size of 40 μm × 40 μm without removing the top electrode. Furthermore, we revealed that the density of states responsible for electrical conduction formed after DB lies over an energy region of more than 1 eV below the Fermi level. The bandwidth is in line with that calculated by a first-principles calculation assuming a high oxygen-vacancy density [2]. Furthermore, we confirmed that the photoelectron-energy dependence of the intensity is consistent with the universal curve of inelastic mean free path of photoelectrons[3]. This indicates that the photoelectron signal from a deep area can be observed. This study demonstrates that laser-PEEM using a short wavelength continuous wave (CW) laser is a powerful tool for nondestructive observation of defect distribution in dielectrics in electronic devices. [1] H. Fujiwara et al., Appl. Phys. Lett. 123, 173501 (2023). [2] E. Pavoni et al., Materials 15, 4175 (2022). [3] M. P. Seah et al, Surf. Interface Anal. 1, 2 (1979).

01:30 PM
Three-dimensional Characterization of Antiferroelectric Nanodomains Stabilized by Chemical Disorder with Multislice Electron Ptychography
Dr. Menglin Zhu[1]
[1]Department of Materials Science and Engineering, Massachusetts Institute of Technology, Cambridge, MA 02139 USA

Antiferroelectric (AFE) perovskite oxides exhibit remarkable dielectric properties and offer extensive structural and chemical tunability, making them promising for applications such as high-energy-density capacitors and solid-state cooling [1,2]. However, tailoring AFE phase is challenging due to the complex structure and chemistry, requiring a thorough understanding of how the local chemical environment influences phase stability. While scanning transmission electron microscopy (STEM) is effective in quantifying atomic displacements (polarization) and chemistry in AFE materials [3,4], the projective nature of conventional techniques imposes limitations, which may not represent bulk material properties.

In this study, we overcome this limitation by using multislice electron ptychography to characterize an anti-phase boundary (APB) in a perovskite oxide in 3D [5]. As in Figure 1b, ptychographic recovers hidden information along the projection for every 1nm slice, revealing an inclined APB with chemical diffusion and the spatial proximity between the AFE phase and the chemical APB (Figure 1c).

Spatial statistics (Figure 1a) are integrated to determine the correlation between the local chemical environment and structural distortions. Contrary to the chemically ordered bulk, nanoregions within the chemically disordered APB is found to persist in their AFE state, reflecting a local elevation in Tc induced by chemical disorder. The study demonstrates that chemical disorder at an APB elevates the local Tc of the AFE-to-PE transition, emphasizing the importance of nanoscale characterization and the impact of nanoscale heterogeneities on phase stability. It provides a pathway for engineering the response of antiferroelectric materials through chemistry and defect control.

01:45 PM
Visualizing Polar Textures in 3D Using Multislice Electron Ptychography (Student)
Mr. Michael Xu[1], Dr. Menglin Zhu[1], Mr. Colin Gilgenbach[1], Ms. Bridget Denzer[1], Prof. James LeBeau[1]
[1]Department of Materials Science and Engineering, Massachusetts Institute of Technology

Relaxor ferroelectrics have been shown to display exceptional piezoelectric and dielectric properties, often attributed to their complex chemical and structural characteristics [1]. For example, the prototypical relaxor ferroelectric system, Pb(Mg1/3Nb2/3)O3-PbTiO3 (PMN-PT), has been the subject of many studies looking into the role of chemical and structural order/disorder on polar domain structure [1-4]. While direct imaging using scanning transmission electron microscopy (STEM) offers a local probe of these nanoscale features, projection of the three-dimensional (3D) sample can present challenges for unambiguously determining relationships between chemistry and polar structure [5-6]. To overcome many of these challenges and recover information from the projection, multislice electron ptychography has emerged as a powerful tool, in which the 3D sample information is iteratively reconstructed from overlapping convergent beam electron diffraction (CBED) patterns [6-8].

Here, we will demonstrate how multislice electron ptychography can help provide a comprehensive understanding of polar domain structures in the relaxor ferroelectric PMN-PT. First, we compare reconstructed phase images and conventional annular dark-field (ADF) images, highlighting the ability to determine depth-resolved polar displacements (Figure 1). A picture of the 3D domain structure can be obtained by quantifying these polar displacements across image stacks, offering insight into local features such as domain walls and polar nanodomains (PNDs) (Figure 2). Further, through comparison across multiple ptychographic reconstructions and film states, the

effect of epitaxial strain on domain structure is directly visualized. Analysis of local polar motifs in each strain state reveals complex textures correlated with B-site occupancy, with diminishing effect as compressive epitaxial strain is increased. These factors together are found to contribute to a relaxor-like to ferroelectric-like phase transition, consistent with prior X-ray and molecular dynamics-based studies [9]. Ultimately, these findings demonstrate how quantitative and statistical analysis of ptychographic reconstructions can offer direct nanoscale insights into polar domain structure and evolution [10].

[1] Liu, H. et al. Nat. Commun. 14, 1007 (2023)
[2] Takenaka, H., Grinberg, I., Liu, S. & Rappe, A. M. Nature 546, 391–395 (2017)
[3] Otoničar, M. et al. Adv. Funct. Mater. 30, 2006823 (2020)
[4] Kumar, A. et al. Nat. Mater. 20, 62–67 (2021)
[5] Calderon, S., Funni, S. D. & Dickey, E. C. Microsc. Microanal. 1–12 (2022)
[6] Harikrishnan, K. P. et al. Microsc. Microanal. 29, 1626–1627 (2023)
[7] Jiang, Y. et al. Nature 559, 343–349 (2018)
[8] Chen, Z. et al. Science 372, 826–831 (2021)
[9] Kim, J. et al. Nat. Phys. 18, 1502–1509 (2022)
[10] This work was supported by the Army Research Laboratory via the Collaborative for Hierarchical Agile and Responsive Materials (CHARM) under cooperative agreement W911NF-19-2-0119. This work made use of the MIT.nano Characterization Facilities.

02:00 PM
Remote Hydrogen Plasma defect analysis of Ga2O3
Mr. Carlos DeLeon[1]
[1]Graduate Student

Gallium Oxide (Ga2O3) is an increasingly important semiconductor for high power electronics due to its ultra-wide bandgap. The most commercially common growth technique to produce Ga2O3 is through Molecular Organic Chemical Vapor Deposition (MOCVD) in which one can produce high quality films at a fast growth rate. However, the presence of impurities such as carbon and hydrogen during MOCVD growth can negatively impact electrical properties [1]. The goal of this project is to identify effects of both C and H on the electrical properties of Ga2O3 [2,3,4] and to identify possible methods of controlling their effects. Remote Hydrogen Plasma (RHP) is a technique that can passivate, rearrange, and reconfigure defects within the film in a non-destructive fashion. Depth Resolved Cathodoluminescence (DRCLS) in conjunction with room temperature Hall measurements were used to measure Ga2O3 samples with differing C content that underwent RHP exposure with increasing time. Carrier density of both samples increased and then remained constant as exposure time increased while mobility in both samples were observed to decrease and remained constant with time.

From our previous studies, the 3.8 eV defect is thought to be H – related, results which are supported by our RHP studies. However, the difference in C content across different samples also reveals that the defect is likely C - related. After an hour of RHP exposure, the high C sample experienced a 14% increase near surface of the 3.8 eV defect, while the low C sample showed only a negligible percent change near surface. The carrier concentration increases by 20% for the high C sample while mobility decreases by 20%. The carrier concentration and mobility for low C sample has negligible change after 1 hour of RHP exposure. This suggests the 3.8 eV defect has a significant impact on electrical properties, while several other deep level defects we observed defects did not track with changes with electrical properties. When exposed to RHP for an additional 2 hours, the electrical properties of both samples experience negligible change while deep level defects we observed at hv = 2.5 eV, 3.6 eV, and 3.8 eV, changed significantly. This suggests a complex interplay between H incorporation and defect – H complex formation within Ga2O3. Further experiments are in progress to understand the exact role of H and C in Ga2O3 and to extend the RHP passivation of C through full Ga2O3 epilayer thicknesses. With complete optimization, RHP treatment on MOCVD grown Ga2O3 can increase conductivity that will result in better devices in power electronics.

1:00 PM
Nonlinear and Plasmonic Materials
Session Chairs: Aaron Muhowski (Sandia National Labs), Seth Bank (University of Texas at Austin)
ESJ 2204

01:00 PM
Coupled Quantum Well Interface Quality and Second-Harmonic Generation Effects (Student)
Ms. Amberly Ricks[1], Mr. Kevin Wen[2], Ms. Madeline Brown[2], Dr. Zarko Sakotic[2], Dr. Moaz Waqar[3], Prof. Xiaoqing Pan[3], Prof. Daniel Wasserman[1], Prof. Seth Bank[2]
[1]Department of Electrical and Computer Engineering, University of Texas at Austin, Austin, TX 78758, [2]University of Texas at Austin, [3]University of California Irvine

Materials that can exhibit nonlinear optical properties have been of increasing interest given their ability to improve device performance in optoelectronics. While traditional nonlinearities are engineered with intersubband transitions in material systems such as LiNbO3, the performance is limited to small wavelength windows and the devices are difficult to integrate with common semiconductor substrates.1 Leveraging the interband nonlinearities found in established quantum well (QW) materials allows for operation to be extended into the near-IR.2 In particular, structuring GaAs/AlGaAs into multiple asymmetric coupled QWs can enhance the existing interband nonlinearity; designing the QW structure, including the total QW width, barrier width, barrier composition, and overall QW asymmetry, allows for tuning of the wavelength at which nonlinear enhancement is found. In this work, we investigate the impact of the structural properties of as-grown structures on their second-order nonlinear response using a combination of electron microscopy and second harmonic generation (SHG) measurements.

We know from simulations that the thickness and composition of the thin tunneling barrier layer are of critical importance for SHG.3 Imperfections in this barrier layer, such as poor interfaces with the QWs, could also adversely affect the nonlinear response. It is well established that interface mixing and surface roughness in two-dimensional

electron gas and superlattice devices leads to decreased mobility and overall performance degradation.4,5 Thin QWs are particularly affected by even minimal heterointerface roughness.4 Known methods to remedy these issues include (1) the use of growth interruptions at interfaces, which aids in smoothing the surface epitaxial layer, and (2) growing binary-binary heterointerfaces (i.e. AlAs/GaAs) rather than binary-ternary heterointerfaces (i.e. AlxGa1-xAs/GaAs), where interface roughness effects are weaker.4,5
In this work, 16-period GaAs coupled QWs with 42% asymmetry were grown by solid-source molecular beam epitaxy on SI GaAs substrates. Samples were grown at 600°C, monitored by band-edge thermometry, and a 15 As overpressure was maintained. To explore if SHG would be enhanced with improved interfaces between the GaAs QWs and Al0.55Ga0.45As barriers, we first introduced 30-90 second growth pauses in between each interface. SHG measurements showed an enhanced nonlinear response for QW stacks that included growth pauses. In an effort to further improve the SHG response, we replaced the Al0.55Ga0.45As barriers with AlAs barriers and designed the coupled QWs to the same asymmetry specifications, with 30 second growth pauses included. To our surprise, the SHG response was dramatically reduced using AlAs barriers. Scanning transmission electron microscopy (STEM) images of analogous QW stacks revealed that the interface mixing was not very different between the AlAs and Al0.55Ga0.45As barriers and their GaAs QWs. Energy dispersive X-ray spectroscopy (EDS) measurements revealed similar Al concentration gradients between interfaces for both barrier materials, suggesting the interface mixing could be from another source, such as effusion cell transients. STEM images of GaAs/ Al0.55Ga0.45As QW stacks with 0-90 second growth pauses are underway to evaluate the effectiveness of growth pauses for interface smoothing. A similar growth pause study for GaAs/AlAs QW stacks is in progress in order to identify the source of interface mixing, and our future work will continue to optimize the barrier material quality to enhance the nonlinear response. This research was supported by a Multidisciplinary University Research Initiative from the Air Force Office of Scientific Research (AFOSR MURI Award No. FA9550-22-1-0307).
1M. M. Fejer et al., Phys. Rev. Lett., 62, 1989. 2J. Khurgin, Appl. Phys. Lett., 51, 1987. 3R. Ramesh et al., Appl. Phys. Lett., 123, 2023. 4H. Sakaki et al., Appl. Phys. Lett., 51, 1987. 5M. Wataya et al., Jpn. J. Appl. Phys., 28, 1989.

01:15 PM
Semiconductor quantum well structures with large third-order interband optical nonlinearities (Student)
Mr. Kevin Wen[1], Mr. Patrick Devaney[1], Mr. Rithvik Ramesh[2], Ms. Amberly Ricks[3], Ms. Qian Meng[4], Dr. Zarko Sakotic[1], Prof. Daniel Wasserman[3], Prof. Jacob Khurgin[5], Prof. Seth Bank[1]
[1]University of Texas at Austin, [2]California Institute of Technology, [3]Department of Electrical and Computer Engineering, University of Texas at Austin, Austin, TX 78758, [4]Microelectronics Research Center and ECE Dept., The University of Texas at Austin,[5]John Hopkins University

Materials with large third-order optical nonlinearities play important roles in photonic integrated circuits and optical signal processing. In particular, the third-order nonlinear susceptibility χ(3), and related phenomena such as the Kerr effect and the nonlinear index of refraction are responsible for the operation of electro-optic modulators and Kerr frequency combs. However, in many cases the nonlinear processes exhibited by conventional bulk semiconductors are not strong or fast enough for efficient photonic computation[1]. Previous approaches to address these challenges using engineered semiconductor heterostructures relied mainly on intersubband transitions, which restricted their operation to the long-wavelength infrared[2]. It has been recently shown that interband nonlinearities[3] contribute significantly to the second-order nonlinear susceptibility χ(2) of coupled quantum wells (QWs) at shorter wavelengths[4]. This motivates our study of their applicability to enhance the third-order susceptibility.
In this work, we report a new method for engineering materials with a large χ(3) in the visible and near-infrared ranges by leveraging the interband transitions of three coupled-QWs. We began by developing a general method to calculate the of the χ(3) coupled-QWs using the dipole matrix formalism. We solved for the eigenstates by separating the wavefunctions into the unit cell and envelope portions; these were determined using density functional theory (Vienna Ab initio Simulation Package with HSE06 hybrid functionals) and a self-consistent Schrodinger-Poisson solver, respectively.
We then studied the χ(3) nonlinearities that are accessible using the well-established GaAs/AlGaAs heterostructure system, which can be grown with high-quality via molecular beam epitaxy. Our coupled-QW structure consisted of three wells of varying widths (~5-10 nm) separated by two tunneling barriers that are fixed at 1 nm width. These wells were designed with inversion symmetry to suppress any second-order effects. We found that by altering the QW parameters, we can engineer wavefunctions with favorable energies and geometries that suggest large enhancements in the nonlinear index of refraction. The parameters we considered in this study were the total width of the QWs and the center well parameter, which quantifies how much larger the center well is relative to the outer wells. To simplify the calculations, we made use of wavefunction symmetry and orthogonality constraints to reduce the number of relevant electronic transitions. Finally, we identified the excitation schemes and transitions most responsible for this enhancement to propose a general method of designing third-order nonlinear materials. Experimental studies are underway, and results will be reported at the conference.
This research was supported by a Multidisciplinary University Research Initiative from the Air Force Office of Scientific Research (AFOSR MURI Award No. FA9550-22-1-0307).
[1] S. Takeda, A. Furusawa, Toward large-scale fault-tolerant universal photonic quantum computing, APL Photonics, 1, 4 (6): 060902 (2019)
[2] F. Capasso, C. Sirtori and A. Y. Cho, "Coupled quantum well semiconductors with giant electric field tunable nonlinear optical properties in the infrared," in IEEE Journal of Quantum Electronics, vol. 30, no. 5, pp. 1313-1326, May 1994, doi: 10.1109/3.303697.
[3] J. Khurgin, “Second-order nonlinear effects in asymmetric quantum-well structures,” Phys. Rev. B, vol. 38, no. 6, pp. 4056–4066, Aug. 1988, doi: 10.1103/PhysRevB.38.4056
[4] R. Ramesh, T. Hsieh, A.M. Skipper, Q. Meng, K.C. Wen, F. Shafiei, M.A. Wistey, M.C. Downer, J.B. Khurgin, and S.R. Bank, "Interband second-order nonlinear optical susceptibility of asymmetric coupled quantum wells," Applied

Physics Letters, vol. 123, no. 25, Dec. 2023.

01:30 PM
Optical Structuring to Reliably Determine Interband Optical Nonlinearity via Second Harmonic Generation (Student)
Mr. John Duncan[1], Mr. Rithvik Ramesh[2], Ms. Amberly Ricks[3], Dr. Shafiei Farbod[4], Mr. Félix Estévez[4], Dr. Zarko Sakotic[4], Ms. Madeline Brown[4], Dr. Michael Downer[4], Prof. Daniel Wasserman[3], Prof. Seth Bank[4]
[1]Chandra ECE Department, The University of Texas at Austin, [2]California Institute of Technology, [3]Department of Electrical and Computer Engineering, University of Texas at Austin, Austin, TX 78758, [4]University of Texas at Austin

While large intersubband nonlinearities from III-V coupled quantum wells are well established and technologically important, they are restricted in spectral coverage to the mid- and long-wavelength infrared by the available conduction band offsets. By contrast, interband nonlinearities leverage the bandgap energy, enabling access to shorter wavelengths. We recently demonstrated asymmetric AlGaAs/GaAs coupled quantum well interband nonlinear structures that enhance the production of visible second harmonic (390 nm) light under near infrared (780 nm) excitation. However, extracting the second order nonlinear susceptibility from these second harmonic generation (SHG) experiments is complicated by standing wave effects within the multi-quantum well structure. This results in anomalous variations in the observed SHG from samples containing different numbers of asymmetric coupled quantum wells due to differences in the local optical intensity felt by each pair, which must be removed through normalization to the relevant optical field strengths and introduces a key source of uncertainty.
We address this challenge by optimizing the placement of each set of asymmetric coupled quantum wells such that the standing wave intensity of the fundamental beam is nearly the same at each of these points. This is done through a greedy search algorithm, in which each set of quantum wells are placed one at a time within the next closest standing wave intensity available. This allows for quick calculations that should create an easily discernible second order nonlinear susceptibility by making the local optical intensity at each pair much closer.
Finite-difference time-domain (FDTD) simulations were used to calculate the electric field intensity and place each asymmetric quantum well accordingly. We find that using greedy search works well due to minimal variations in electric field intensity caused by the independent placement of the wells. Samples containing various numbers of coupled-QWs were grown by solid-source molecular beam epitaxy using typical AlGaAs growth conditions. Surface second harmonic generation experiments to experimentally validate this approach are in progress and results will be reported at the conference.

01:45 PM
Probing the Electric Dipole Approximation in Nonlocal Systems (Student)
Mr. Alexander Ware[1], Ms. Corey White[1], Mr. Jacob LaMountain[2], Prof. Seth Bank[1], Prof. Evgenii Narimanov[3], Prof. Viktor Podolskiy[2], Prof. Daniel Wasserman[1]
[1]Department of Electrical and Computer Engineering, University of Texas at Austin, Austin, TX 78758, [2]Department of Physics, University of Massachusetts, Lowell, MA, 01854, [3]Department of Electrical and Computer Engineering, Purdue University, West Lafayette, In, 47907

The electric-dipole approximation underlies much of our ability to model light-matter interactions and thus optoelectronic phenomena and devices. For example, intraband free electron response as well as interband and intersubband transitions can all be accurately understood using the dipole approximation [1]. Designing materials or optoelectronic systems where the electric dipole approximation no longer applies could enable investigations of new optical phenomena and potentially the development of optical structures and optoelectronic devices with new capabilities. These could include access to interband transitions typically disallowed due to wavefunction symmetry, more precise control of free carrier recombination states, or ultra-subwavelength device architectures leveraging new light-matter interactions.
A core assumption of the electric-dipole approximation is the negligible spatial variation of the electric field over the extent of the dipole with which the field is interacting. When considering interactions with an electron, for example, this approximation is valid if the spatial variation of the field is on the order of the extent of the electron wavefunction [2]. Hyperbolic metamaterials (HMMs) comprised of alternating layers of metals and dielectrics with thicknesses much smaller than the free-space wavelength can support modes with high gradient electric fields- as the length scale of the electric field variation is on the order of the material perturbation [3]. Integrating free carriers into the dielectric layers of these hyperbolic metamaterials provides a unique architecture to explore the interaction of free charge with strong electric field gradients and potentially light-matter interaction outside of the quasi-static assumption on which the electric-dipole approximation is based.
Modeling these hyperbolic metamaterials using a bulk material effective permittivity has been sufficient to reproduce the optical response in the vast majority of cases [4], but as the thicknesses of the metamaterial layers approach the nanometer scale, it becomes necessary to account for the nonlocal response of the material [5]. The nonlocal response is caused by excitation of carriers in the metal layers and the coupling of this excitation between adjacent metal layers [6-7]; this can be observed as enhanced absorption at energies greater than the plasma frequency [8-9]. Notably, the regime in which we expect these nonlocal effects to be significant is also where the electric-dipole approximation may no longer hold. Experimental demonstration of nonlocal response in these systems offers an ideal path for investigating less well-known phenomena beyond the bounds of the electric-dipole approximation.
We present a series of hyperbolic metamaterials designed to confine free carriers to regions of highly varying electric fields. These structures, grown by molecular beam epitaxy, consist of 5 periods of an 80nm degenerately doped InAs layer (metal) and 80nm AlAsSb/nInAs/AlAsSb quantum well (dielectric). The well width in the dielectric layers varies with each sample, but the total dielectric thickness is held constant at 80nm. The nInAs well is lightly doped such that the permittivity is near equivalent to that of the AlAsSb

barrier at 7μm. The samples are studied using infrared reflection and transmission spectroscopy. In the samples with lightly doped InAs between AlAsSb barriers, we see spectral features between λ = 5-7μm that emerge at high angles of incidence, potentially indicative of nonlocal response. These features do not appear in purely local simulations [10], which only show a feature associated with the epsilon-near-zero crossing of the degenerately doped layer.

The authors gratefully acknowledge support from the National Science Foundation DMREF program (Award No. 2119302).

[1] Lynch, David W. Handbook of Optical Constants of Solids. Academic Press, 1997. 189-212.
[2] Kobe, Donald H. American Journal of Physics 50.2 (1982): 128-133.
[3] Elser, Justin, et al. Applied physics letters 90.19 (2007).
[4] Poddubny, Alexander, et al. "Hyperbolic metamaterials." Nature photonics 7.12 (2013): 948-957.
[5] Fuchs, Ronald, and K. L. Kliewer. Physical Review 185.3 (1969): 905.
[6] S. I. Pekar, Sov. Phys. JETP 6, 785 (1958).
[7] V. M. Agranovich and V. L. Ginzburg, Springer Series in Solid-State Sciences Vol. 42 (Springer-Verlag, Berlin, 1984).
[8] Raza, Søren, et al. Physical Review B 84.12 (2011): 121412.
[9] Toscano, Giuseppe, et al. Optics express 20.4 (2012): 4176-4188.
[10] From V. A. Podolskiy's research group, see http://viktor-podolskiy-research.wiki.uml.edu/RCWA.

02:00 PM

Shadow Mask Molecular Beam Epitaxy (Student)

Ms. Shagorika Mukherjee[1], Mr. Sai Rahul Sitaram[1], Prof. Xi Wang[1], Prof. Stephanie Law[2]
[1]University of Delaware, [2]Pennsylvania State University

Shadow mask molecular beam epitaxy (SMMBE) is a type of selective area epitaxy (SAE) in which vacuum-deposited films can be patterned via a mechanical mask without the need for etching. Provided the mask is not a source of contamination itself and is adjacent to the substrate, epitaxial layers may be sequentially deposited on the substrate through holes in the mask. One unique feature of SMMBE is its shadowing effect that appears near the mask edges, causing the elemental fluxes to vary as a function of position. This gives rise to a gradient of film thickness and/or composition near the edges of the mask. By varying the mask thickness and/or the angle of the mask edges, this gradient can be controlled. In this work, we exhibit the potential of SMMBE to construct in-plane gradient permittivity materials (GPMs) by leveraging its shadowing effect.

The permittivity varies in a GPM as a function of position, making GPMs useful for a variety of applications. Our goal is to fabricate in-plane GPMs in which the permittivity varies horizontally in the plane of the material. On an in-plane GPM, different wavelengths of light can be confined at different horizontal locations. Such a material could be used to create an ultracompact on-chip spectrometer. We are interested in working in the infrared regime, so our GPMs are made of heavily silicon-doped InAs, which is known to be a good infrared plasmonic material. By varying the silicon doping density in the plane, we can control the Si:InAs permittivity in the lateral direction. We synthesize such a material using SMMBE with reusable silicon shadow masks. We start with shadow masks that are each 200 μm thick and are 1 cm x 1 cm in size. Each mask has an aperture at its center. The aperture has slanted inner walls, which makes its dimension 0.5 cm x 0.5 cm at the top and 0.528 cm x 0.528 cm at the substrate side. To date, we have studied the influence of several growth parameters in controlling the in-plane permittivity in the GPMs. In comparison to a non-SMMBE growth recipe, we have found that increased quantities of Bi surfactant (2.5x higher) and As (1.5x higher) in the growth recipe of the GPM can significantly minimize poor growth regions around the edges of GPM where the permittivity gradients exist. Nano-FTIR spectrum obtained by scattering-type scanning near-field optical microscopy (s-SNOM) using a mid-IR nano-FTIR module illustrates that the GPMs we have synthesized result in localization and enhancement of different light wavelengths at different locations. The GPM confines infrared light corresponding to wavenumbers ~650 cm-1 to 900 cm-1 over an in-plane distance of ~12 μm, setting the stage for the creation of a spectrometer on a chip.

Next, we were interested in understanding the impact of varying the mask thickness on the GPMs. To do so, we grew samples using masks with thicknesses of 200 μm and 500 μm. We grew three sets of GPMs using three different growth temperatures of 450 °C, 475 °C and 500 °C. Each set comprises of two GPMs, one using a 200 μm thick mask while the other using a 500 μm thick mask. The 500 μm masks have similar dimensions as the 200 μm masks, except the slanted inner walls of the aperture have a measurement of 0.571 cm x 0.571 cm at the substrate side. We found that a growth temperature of 500 °C works well for both in-plane GPMs fabricated using 200 μm and 500 μm masks, significantly minimizing poor growth regions around the edges where the permittivity gradients are and also in the mesa region, delivering shiny samples. The thick mask also provides a longer shadow in comparison to the thin mask, leading to a larger gradient in permittivity over a longer in-plane distance in comparison to the thin mask which provides less shadow. This results in the GPM synthesized by the thick mask to confine light wavelengths corresponding to wavenumbers ~650 cm-1 to 1400 cm-1 over an in-plane distance of ~26 μm, leading to a bigger surface area for the construction of an ultracompact spectrometer. In the future, careful mask design can be used to obtain in-plane GPMs with designer permittivity gradients.

1:00 PM
Graphene and Graphene Heterostructure Synthesis and Devices
Session Chairs: Kevin Daniels (University of Maryland), Susan Fullerton (University of Pittsburgh)
ESJ 2204

01:00 PM
Mechanics of Ultra-High Sensitivity Epitaxial Graphene ELISA Sensors (Student)
Mr. Michael Pedowitz[1], Dr. Nichole Pedowitz[2], Mr. Daniel Lewis[1], Dr. Daniel Pennachio[3], Dr. Jenifer Hajzus[3], Prof. Soaram Kim[4], Dr. Matthew Bogyo[2], Dr. Rachael Myers-Ward[3], Prof. Kevin Daniels[1]
[1]University of Maryland, College Park, [2]Stanford University, [3]Naval Research Lab, [4]Department of Electrical and Computer Engineering, Texas A&M University, College Station, TX 77843, USA

Graphene biological sensors have seen significant use in recent years, taking advantage of the excellent electrical properties of graphene to provide electrical transduction of biological binding events in enzyme-linked immunosorbent assays (ELISAs). This allows for a simpler analysis of these assays than traditional colorimetric or fluorometric approaches, as well as improved resolution at low concentrations 1,2. However, these devices rely on solution-gated FETs which present challenges to deployment and relatively slow response times limiting their use at the site of care. As a result, a resitometric biological sensor is more desirable for fast and accurate detection at the point of care if it can meet the LOD of this solution-gated FETs of 1 fgmL-1.
We previously reported a resistometric ELISA sensor-based antibody (AB) - poly-l-lysine (PLL) - epitaxial graphene – silicon carbide heterostructures, with an LOD of 1 agmL-1, indicating the ability to detect less than 100 binding events3. The sensors exhibited 2 distinct regimes of detection, above 1 pg mL-1 detection was consistent with traditional charge transfer between the AB and the epitaxial graphene bilayer via the PLL crosslinker, however, the region below 1fg mL-1 did not have a clear mechanistic description but was highly repeatable. In this work, we report on the mechanism for this low-concentration detection, as well as the extension of this epitaxial graphene ELISA sensor to alternate biological systems with lower binding affinities. The mechanism for this ultra-low detection relies on the inherent properties of the QEG-SiC system. Intercalated Epitaxial Graphene is hole-doped due to polar Si-H bonds under the interlayer, which trap electrons at the interface4. Additionally, epitaxial graphene is under compressive strain due to the interplay between the lattice constant mismatch of graphene and SiC, as well as the differing thermal expansion coefficients of the materials5. When PLL is coated on the graphene surface it binds via cation – π between protonated amines in the PLL and the π network. This also induces a tensile strain on the lattice as well as a polar field in opposition to the SiC field. This strain and doping effect is then further modulated by the addition of the antibody6. Inhomogeneities caused by binding events, which deprotonate amine groups in the PLL, then generate inhomogeneous strain across the graphene sheet which induces the conductivity changes detected. To verify this hypothesis, we utilized Raman spectroscopy which can separate the strain and doping effect on graphene via mapping the G vs 2D peak position7. From this, we found that the coating of PLL contributes a mixed doping and strain response, while antibody coating and reaction, even at low antigen concentrations, produce primarily strain responses consistent with predictions. In addition, we tested alternative non-polar intercalations (Mg and Ca) as well as unintercalated graphene, which should not exhibit the same strain and doping interplay. These samples did not have the low concentration response of QBLEG supporting our mechanistic description. We also tested the sensor with alternative biomarkers with significantly lower binding affinities such as proteases (TEV and CATL). From this, we observed strong binding-debinding changes in the conductivity to selective proteases (TEV) and a similar response to AB-AG binding with non-selective proteases, indicating that the mechanics hold and may be enhanced by lower binding event density. The potential of this ultra-low detection via simple resistometric sensors, considering its ability to transduce multiple classes of biological agents, is significant for improving health around the world. This mechanistic description may help to better guide the development of this heterostructure and make it available for point-of-care diagnosis and triage of biological agents.
References: [1]G. Manasa et al. Biosensors & Bioelectronics 11, 2022 [2]J. Gao et al. Analy. Chem. 94(3), 2022 [3] S. Kim et al. Biosensors & Bioelectronics 197 2022 [4] K M. Daniels et al. 4(2) 2017 [5] N. Ferralis et al. Phys. Rev. Lett. 101 (2008) [6] Chen et al. Chem. Comm. 59(35) 2023[7] J. E. Lee et al. Nat. Comm. 3(1) 2012

01:15 PM
Synthesis and Device Applications of Monolayer InO2 at the EG/n-SiC Interface (Student)
Mr. Furkan Turker[1], Mr. Bohan Xu[1], Dr. Chengye Dong[1], Mr. Zachary Trdinich[2], Mr. Eric Lawson[1], Mr. Michael Labella III[1], Prof. Vincent Crespi[1], Prof. Joshua Robinson[1]
[1]Pennsylvania State University, [2]Northwestern University

Novel confinement techniques facilitate the formation of non-layered 2D oxides and nitrides with a large bandgap, e.g. GaN and Ga2O3, with thickness-dependent optoelectronic properties [1, 2]. However, a gap lies in the experimental demonstration of 2D InOx with its true atomic structure, stoichiometry, and device applications. Here, we demonstrate, for the first time, the formation of highly crystalline monolayer InO2 (stoichiometry is different than bulk In2O3 due to confinement), at the quasi-free-standing epitaxial graphene (QFEG)/SiC (0001) interface via intercalation of metallic In and subsequent high-temperature oxidation. The stoichiometry of InO2 is measured as ~1:1.8 (In:O at%) via Auger spectroscopy and verified via Density Functional Theory (DFT). Scanning transmission electron microscopy (STEM) analysis shows that monolayer InO2 is epitaxial to the underlying SiC (0001) and isostructural to the bottom layer of α-In2Se3 with modified ferroelectric zinc blende (FE-ZB‘) structure. Theoretical analysis via DFT verified the thickness-dependent band gap of InO2, which increases from ~2.6 eV (bulk) to ~3.5 eV (monolayer). Ultimately, we fabricated a metal-oxide-semiconductor

(MOS) Schottky diode with EG/InO2/n-SiC stack via e-beam lithography, where EG and n-SiC serve as top and bottom electrodes, respectively, and InO2 acts as a tunnel barrier. Following the InO2 intercalation, The EG/n-SiC (0001) junction transforms from ohmic to tunnel junction with a threshold voltage of 0.8 eV, demonstrating that monolayer InO2 effectively acts as an electronic barrier. Importantly, our diode can operate with very high on-current (>107 A/cm2) and rectification ratio (1.1 x 104 at 1 V) at room temperature. Finally, by fitting the forward and reverse bias current-voltage curves in thermionic emission and Fowler-Nordheim Tunneling models, respectively, several key parameters were extracted, such as barrier height from n-SiC to InO2 and effective mass and dielectric constant of 2D InO2. We present one of the earliest demonstrations of vertical MOS Schottky diodes utilizing the EG/n-SiC (0001) interface, which is promising for high-speed 2D/3D electronics, such as hot electron transistors and bipolar junction transistors.

01:30 PM
High-Density and Responsivity NIP Axial-Core Shell GaAsSb Nanowire Photodetectors on Monolayer Graphene for Near-Infrared Applications (Student)
Mr. Hirandeep Reddy KUCHOOR[1], Ms. YUGWINI DESHMUKH[1], Ms. Rashmita Baruah[1], Mr. Hakeem Menefee[1], Mr. Joshua White[1], Dr. Jia Li[1], Dr. Shanthi iyer[1]
[1]North Carolina Agricultural and Technical State University

In this work, we present the molecular beam epitaxy (MBE) growth of high-density, self-assisted n-i-p core-shell (C-S) GaAs1-xSbx nanowires (NWs) on surface-functionalized monolayer graphene. We explored the effects oxygen plasma treatment duration, and critical growth parameters such as substrate temperatures and V/III ratio, on the vertical yield of core GaAs1-xSbx NWs. Employing the optimized parameters, we developed both traditional (TCS) and hybrid n-i-p C-S (HCS) architectures. The HCS architecture has a novel design with axial n-core Sb gradient, which includes an intrinsic GaAs1-xSbx segment over the n-core to enhance absorption. The optical properties of the HCS design were examined using low-temperature photoluminescence (PL) with 4K-PL emissions. Comparative electrical I-V analysis of devices from both architectures showed the HCS design's superiority, with higher responsivity (>103 A/W) and detectivity (>1014 Jones), and an extended spectral response beyond 1.5 µm on graphene, making it ideal for short-wave infrared applications. Further, temperature-dependent C-V and low-frequency noise measurements showed the HCS photodetector's remarkable thermal stability, characterized by constant positive capacitance and a low cut-off frequency under varying temperatures. These results underscore the significant potential of graphene substrates in photodetector applications and pave the way for future flexible devices.
Acknowledgement: This research work was funded through the US Army Grant Number W911NF-22-1-0114.

01:45 PM
Investigation of Dry Transfer of Epitaxial Graphene from SiC(0001)
Dr. Jenifer Hajzus[1], Dr. Daniel Pennachio[1], Dr. Shawn Mack[1], Dr. Rachael Myers-Ward[1]
[1]US Naval Research Laboratory

Transfer of high-quality graphene from its growth substrate to substrates of technological interest can be necessary to enable its use in certain applications, however it remains challenging to achieve large-area transfer of graphene that is clean and intact. This work utilizes a dry transfer technique involving an adhesive metal stressor to exfoliate epitaxial graphene from SiC [1]. For this method, the strain energy in the metal layer must be high enough to allow for uniform exfoliation, but low enough such that self-exfoliation of graphene does not occur. We investigate the dry transfer of monolayer epitaxial graphene (MEG) and hydrogen-intercalated, quasi-freestanding bilayer graphene (QFBEG) grown by sublimation of Si from 6H-SiC(0001) in a CVD reactor in Ar ambient. A magnetron sputtered Ni stressor layer is used to exfoliate epitaxial graphene and transfer to GaAs, glass, and SiO2/Si substrates. The Ar pressure during sputtering is found to impact the stress, film density, and roughness of the Ni film, as determined from wafer curvature and X-ray reflectivity (XRR) measurements. By using appropriate sputtering conditions, the Ni/graphene film exfoliates from the entire area of the SiC substrate with use of thermal release tape. Atomic force microscopy (AFM), scanning electron microscopy (SEM), Raman spectroscopy, x-ray photoelectron spectroscopy (XPS), and Nomarski microscopy are used to characterize the graphene. The Ni 2p peak was not detected in XPS of the transferred graphene after removal of the Ni film by etching in acid. Additionally, XPS revealed minimal oxide present at the graphene-GaAs interface, consistent with previous reports for this dry transfer method [2]. Raman spectroscopy mapping indicated that predominately monolayer graphene is transferred from MEG, while predominately bilayer graphene is transferred from QFBEG. Raman spectroscopy of the SiC substrate after MEG exfoliation shows the 6√3 buffer layer, which forms during growth of epitaxial graphene on SiC(0001), remains on the SiC substrate. Consequently, if there are regions of exposed 6√3 buffer layer in the as-grown MEG on SiC, AFM shows that there are corresponding gaps in the transferred graphene film where the areas of exposed buffer layer do not transfer. The 6√3 buffer layer is not present in QFBEG due to the hydrogen-intercalation process which severs the covalent bonds between the 6√3 buffer layer and SiC and converts the buffer layer to an additional graphene layer. It is found that the same Ni sputtering conditions that led to uniform exfoliation and transfer of MEG result in micron-scale tears in the Ni/QFBEG film. By lowering the strain energy in the sputtered Ni film, these tears can be reduced or eliminated.
[1] Kim, J., Park, H., Hannon, J.B., et al., Science, 2013, 342, (6160), 833–836.
[2] Kim, H.; Lu, K.; Liu, Y., et al., ACS Nano 2021, 15, (6), 10587–10596.

02:00 PM
Ionic Sieve Based - Redox Gas Sensing via Layered Manganese Dioxide Epitaxial Graphene Heterostructures (Student)
Mr. Michael Pedowitz[1], Mr. Daniel Lewis[1], Ms. Jennifer DeMell[2], Dr. Daniel Pennachio[3], Dr. Jenifer Hajzus[3], Dr. Rachael Myers-Ward[3], Prof. Kevin Daniels[1]
[1]University of Maryland, College Park, [2]Laboratory for Physical Sciences, [3]Naval Research Lab

Mixed valence manganese oxides (MnOx) have attracted

significant interest in recent years due to the easily reversible redox reactions between manganese oxidation states (Mn+2, Mn+3, and Mn+4)1, which has enabled applications in catalysis2, energy storage3, and gas sensing4. Manganese dioxide (MnO2), in particular, has demonstrated highly tunable properties, due to its wide variety of synthesizable structural polymorphs ((α, β) tunnel5, (γ) spinel5, and (δ) layered5) which allow for control over its available surface area and the reactive properties. Among these structural polymorphs, the α and δ phases exhibit strongly mixed-valence character, with Mn+3 defects found throughout the crystal structure5, which is desirable due to it being a highly active site6. Water-stabilized hexagonal δ-MnO2 (HMnO2) contains many Mn+3 ions as the interlayer contains Mn+2/+3 ions to neutralize the layer charge from Mn+3 lattice defects7. However, the direct synthesis of HMnO2 has not been reported extensively in the literature, as most synthesis routes rely on permanganate salts1, which leads to the synthesis of ion intercalated δ-MnO2 and a reduction in Mn+3 defects in the lattice9.

We have previously reported the synthesis of high Mn+3 content HMnO2 via electrodeposition on epitaxial graphene/silicon carbide (EG/SiC) substrates4. This as-deposited material grew via island-based nucleation and could consistently be grown with a 50nm thickness and 2.5nm roughness, as measured by atomic force microscopy (AFM). This HMnO2 was also highly conformal to patterned graphene dimensions which allows for the creation of micro-ribbon devices4 which can be utilized for ion storage and gas sensing4. In this work, we extend upon this by taking redox gas sensing measurements from the patterned heterostructure. As well as transforming also as-grown micro ribbons, varying in size from 100 to 10 μm, via intercalating with alkali and alkaline to form alternate birnessites, and measured their effect on the gas sensing capabilities. The electrodeposition was carried out by a three-pulse deposition in a three-electrode electrochemical cell, as described previously. The resulting δ-MnO2 thin films were then characterized through Raman spectroscopy, scanning electron microscopy (SEM), and atomic force microscopy. Raman spectroscopy confirmed the formation of δ-MnO2 as the peaks were consistent with the literature4,8. While SEM and AFM confirmed the previously reported surface morphology was maintained4. We then intercalated the patterned films with alkali metals via cyclic voltammetry in a similar three-electrode cell to the deposition, using a 2 M metal nitrate solution on the patterned HMnO2. Optical analysis of the film post patterned intercalation revealed two regions, a brown and blue region. Raman spectroscopy of these two regions indicated that both were Na-type birnessite. However, differing peak intensities indicate the crystallinity of the two regions is different. This demonstrates that we have successfully grown and transformed the H-type birnessite to Na-type birnessite with 100% efficiency on EG/SiC, allowing us to test its gas sensing properties, as well as extend the intercalation process to alternative alkali and alkaline metals. The HMnO2 films were also processed into gas sensors by wire bonding predeposited Al contacts into 14-pin dual inline packages and tested against NO2 and NH3. The resulting gas sensors exhibited a highly sensitive low noise response, with an SNR >40dB for both gases. Of particular interest is the 2-part response in the NH3 in high humidity environments, believed to be related to NH3+ - H2O substitution in the interlayer, as well as the suppression of NO2- intercalation in dry environments. These two effects indicate the presence of an ionic sieving effect in the gas-sensing measurements. The potential to modulate this ionic sieve with alkali and alkaline metal intercalants while maintaining the high SNR enabled by the QEG-MnO2 heterostructure presents the opportunity to produce tunable gas sensors with variable responses based on processing from the same material platform, an important step forward in this use of this heterostructure.

References: [1]L. Spinelle et al. Sensors 17(7), 2017 [2] F. Cheng et al. Chem. Mater 22(3), 2010 [3] Y.J. Huang et al. Electrochim Acta 99, 2013 [4] M. Pedowitz et al. Mat. Today Adv. 21, 2024 [5] Z. Chang et al. Proc Natl Acad Sci USA 115(23), 2018 [6] Julien et al. Spectrochim Acta A 60, 2004 [7] Drits et al. Am Mineralogist 82, 1997 [8] Julien et al. Solid State Ionics 159, 2003

1:00 PM
Growth and Characterization of Diamond and WBG-Nitride Materials
Session Chairs: Wojiech Jadwisienczak (Ohio University), Patrick Shea (Northrop Grumman Corporation)
ESJ 1224

01:00 PM
Investigation of Mechanical and Electrical Properties of Polycrystalline Diamond Membranes and Devices (Student)
Ms. Chenyu Wang[1], Mr. Dmitry Shinyavskiy[1], Dr. Matthias Muehle[2], Prof. Jung-Hun Seo[1]
[1]University at Buffalo, SUNY, [2]Fraunhofer USA

Single-crystalline diamond (SCD) has been an attractive wide bandgap semiconductor due to its superior mechanical and electrical properties, such as a wide bandgap of 5.54 eV, maximum thermal conductivity of 2200 W/mK, and carrier mobility of 2200 cm2/vs for holes and 1800 cm2/vs for electrons. However, the major drawback hindering the commercialization of diamond is its small substrate size (1 inch or less) with a slow growth rate. Therefore, despite several clear advantages, diamond has not become a mainstream material in semiconductor applications.On the other hand, polycrystalline diamond (PCD) shows about 30% to 50% lower transport properties compared to SCD due to the presence of grains and grain-size-dependent material properties. Despite the excellent scalability (>20 inches) of PCD with decent material properties, PCD has not been considered as a semiconductor for electronic applications, primarily due to (i) incompatibility of the growth process and (ii) difficulties in fabrication and heterogeneous integration processes. The PCD membrane, a micron-thick and free-standing form of PCD thin-film, can address these

technological hurdles, enabling us to utilize PCD membranes for various electronic applications. In this presentation, we will particularly focus on the synthesis process and mechanical properties of the PCD membrane, and then the electrical properties of the PCD membrane-based Schottky diode will be discussed.

Firstly, as shown in Figure (a), to investigate the mechanical properties of the PCD membrane, various PCD membrane cantilevers were fabricated based on the bulk PCD grown on a Si substrate using microwave plasma-enhanced chemical vapor deposition (MPECVD) technique. After the PCD membranes were patterned in a cantilever shape, they were transfer-printed onto the edge of the Si substrate with SU-8 adhesive. As PCD membranes have different surface morphologies between the top and bottom sides (Figure (b)), atomic force microscopy was used to measure the mechanical stiffness of the top and bottom sides of PCD membranes, which was then converted into Young's modulus. As shown in Figure (c), the measured Young's modulus values are 970 GPa and 1030 GPa when PCD membranes were measured from the top and the bottom side, respectively, which have different grain sizes. Raman spectroscopy was carried out to reveal the chemical composition of both the top and bottom sides of the PCD membranes, resulting in different degrees of sp2 and sp3 ratios on each side. Therefore, a slightly smaller Young's modulus from the bottom side of the PCD membranes is attributed to the presence of defects and sp2 contents that are incorporated mainly in the much denser grain boundaries. Secondly, the electrical properties were investigated with PCD membrane-based Schottky diodes as shown in Figure (d). From a transmission line measurement, ~1018 cm-3 of boron concentration with 18 ohm/sq of sheet resistance were measured. In PCD membrane Schottky diodes, Molybdenum electrodes were used to form a Schottky contact, and Ti/Au was used for an ohmic contact on free-standing PCD membranes. According to the I-V curves (Figure (d)), the device exhibits over 104 times on/off ratio at -/+2V, with an on-resistance of 0.5 Ohm-cm2 and a breakdown electric field of 0.2 MV/cm.
In conclusion, a free-standing form of PCD membranes was successfully created, and PCD membranes allow us to access both the top and the bottom surfaces for their mechanical and electrical properties investigation.

01:15 PM
X-ray Topography and Scattering of Single Crystal (001) Diamond Substrates for Wafer Bonding Applications
Dr. Michael Liao[1], Dr. Kenny Huynh[1], Mr. Kaicheng Pan[1], Prof. Mark Goorsky[1]
[1]University of California, Los Angeles

Commercial (001) diamond substrates were imaged using X-ray topography and a lattice-curvature deconvolution method was developed in order to clearly assess the localized tilt component due to defects. There are many literature reports cataloguing defects such as dislocations [1] and stacking faults [2] in diamond using X-ray topography, but far fewer of these studies perform quantitative lattice distortion analysis of X-ray topography images. One study [3] generated various lattice distortion maps including strain, curvature, and tilt maps for diamond substrates using X-ray topography. However, these maps were only generated for samples with low lattice curvature (30-70 m radius of curvature). Substrates with high lattice curvature or regions of substrates with high localized curvature (< 10 m) were ignored. High lattice curvature can obscure the localized lattice tilt component due to defects.

In this work, we present a lattice-curvature deconvolution method for X-ray topography images in order to enable quantitative analysis of defects regardless of lattice curvature. The method here is demonstrated on a relatively high lattice curvature (001) diamond substrate with a radius of curvature of ~5 m. Images were generated using different families of {113} and {606} reflections in glancing incident geometry and revealed an array pattern of nucleation sites during substrate growth. First, strain and tilt components from X-ray topography images were deconvoluted to produce strain and lattice tilt maps. We then further deconvolute the lattice tilt map into its (1) lattice curvature and (2) localized tilt components. By fitting a curvature plane, we obtain a deconvoluted localized tilt map due to defects only and can analyze the full wafer area. For the high curvature substrate, we observe the strain and localized tilt components spanned ±140 ppm and ±60”, respectively, which are due to nucleation sites during substrate growth. Successful wafer bonding of these single crystal diamond substrates to (001) Si is also demonstrated that are prepared with various interfaces including amorphous (Si and/or C) or metallic (Ti/Au) interfaces. The structural and thermal transport characteristics across these diamond-Si bonded interfaces will be presented for heat dissipation applications.
References
[1] S. Shikata, Functional Diamond, 2(1), 175 (2022).
[2] P.M. Martineau, et al., J. Phys.: Condens. Matter, 21, 364205 (2009).
[3] S. Stoupin, et al., Crystals, 9(396), 1 (2019).

01:30 PM
Thermal Performance and Interfacial Mapping of a Compression Bonded GaN/diamond Interface for Vertical Power Devices
Dr. William Delmas[1], Dr. Amun Jarzembski[1], Dr. Matthew Bahr[1], Mr. Anthony McDonald[1], Dr. Wyatt Hodges[1], Dr. Ping Lu[1], Mr. Logan Antiporda[1], Dr. Elbara Ziade[1], Dr. Zachary Piontkowski[1], Dr. Luke Yates[1]
[1]Sandia National Laboratories

As temperature increases inside a vertical GaN device, electron mobility decreases leading to degraded device performance. Thus, effective thermal management of vertical GaN devices has the potential to dramatically improve performance even as heat is generated during operation. Integration of high thermally conductive substrates as a backside heatsink has already been demonstrated in lateral GaN devices to great effect. (1) However, direct bonding of a high thermally conductive material, like diamond, in a vertical architecture has been lacking due to the necessity of maintaining the backside drain contact and concerns regarding the thermo-mechanical performance of the interface itself. Herein, we demonstrate bonding bulk GaN to diamond via compression bonding using an intermetallic layer to facilitate adhesion and act as a backside drain contact. This enables a vertical architecture simultaneous with diamond heat sink integration, providing a thermal management solution in vertical-type GaN devices. The GaN/metal/diamond interface is fully characterized with Confocal-Scanning Acoustic Microscopy, Transmission Electron Microscopy, Confocal Raman Microscopy, and Frequency Domain Thermoreflectance (FDTR). Small voids and delaminations at the interface are found and potential causes and solutions to their formation are discussed. Overall, this bonding method results in strong thermal

performance with a thermal boundary conductance of over 100 MW/m2K as measured by FDTR areal mapping and low bond-induced local stresses of < 70 MPa as visualized by Raman microscopy. Heat dissipation of the GaN/diamond stack is compared directly to similarly bonded GaN/SiC and the industry standard GaN/direct-bonded-copper stacks and shown to outperform both. This new bonding method and device schema shows promise to revolutionize heat management in high power vertical electronics.
Acknowledgements: Sandia National Laboratories is a multi-mission laboratory managed and operated by the National Technology & Engineering Solutions of Sandia, LLC, a wholly owned subsidiary of Honeywell International Inc., for the U.S. Department of Energy's National Nuclear Security Administration under contract No. DE-NA0003525. SAND2024-00528A

References:
Hong K-B, Peng C-Y, Lin W-C, Chen K-L, Chen S-C, Kuo H-C, Chang EY, Lin C-H. Thermal Analysis of Flip-Chip Bonding Designs for GaN Power HEMTs with an On-Chip Heat-Spreading Layer. Micromachines. 2023; 14(3):519. https://doi.org/10.3390/mi14030519

01:45 PM
Codesigned III-Nitride Devices: Thermal Boundary Resistance in AlN Heat Spreaders on Sapphire, Bulk AlN, and Copper (Student)
Mr. Abdullah Al Mamun Mazumder[1], Dr. Md Didarul Alam[2], Mr. Abdullah Mamun[1], Ms. Mafruda Rahman[1], Dr. Kamal Hussain[3], Dr. Richard Floyd[4], Dr. Grigory Simin[1], Dr. Asif Khan[1], Dr. Mvs Chandrashekhar[1]
[1]University of South Carolina, Columbia, USA, [2]Intel Corporation Hillsboro, OR, [3]Texas Instruments, Inc, U.S.A., [4]Sandia National Laboratory, USA

UWBG (Ultra-Wide Bandgap) semiconductors have emerged as promising technologies to succeed Si, SiC, and GaN power semiconductors due to their large critical breakdown electric field (EC)1,2. UWBG devices are projected to have ~100x better power densities than WBG SiC/GaN devices but may be limited by substrate or package thermal properties 3,4. A new paradigm known as "co-design" has emerged, which involves taking electrical and thermal design restrictions into account simultaneously 5. Pulsed I-V testing is suitable for preventing device self-heating or limiting charge trapping effects 6. In this paper, we demonstrate a method to measure thermal boundary resistance (TBR) at interfaces using a thermal method analogous to electrical transmission line model (TLM) methods.
We use AlGaN channel HEMTs grown on both single-crystal AlN and sapphire and GaN channel HEMTs grown on 2–16μm thick AlN heat spreaders on sapphire to extract TBR. We effectively separate electrical and thermal transmission by restricting the resistive heat source near the structure's surface, and heat transport is mostly vertical, with heat spreading laterally below the source. In a hydrogen environment, metalorganic chemical vapor deposition (MOCVD) was used to grow all epitaxial layers. The AlN heat-spreaders were grown on sapphire, utilizing modulation growth at ~2.5 μm/hr. The typical 2DEG sheet resistance for GaN channels was 300 ohm/sq 4, while that for AlGaN channels was ~2k ohm/sq 7,8. TLM (2-20μm spacing) and HEMT structures were then fabricated by photolithography. For one set of GaN channel HEMTs on 16μm thick AlN heat spreaders, laser liftoff was used to remove the sapphire substrate and solder directly to copper (k ~ 400W/mK) to show a situation similar to bulk AlN.
DC Thermal titration of thermochromic inks for dAlN = 12μm shows ~80 K-mm/W. The high intrinsic thermal conductivity of the ~12 μm AlN layer allows better spreading of heat, leading to lower Rth on sapphire. Thinner AlN layers, however, offer poorer heat removal performance; for example, layers below 6 μm thickness exhibited double that relative to thicker films. Combining these results and fitting to heat spreading theory through the transmission line relation of LT = sqrt(TBR*KAlN*dAlN) showed a true DC TBR value 2200K-m2/GW for sapphire/AlN ~10-100x higher than that measured by pulsed techniques by others. Similar analysis using bulk AlN substrates and Cu as a direct heat sink to GaN channel through solder gave a 5x improvement in TBR to 500K-m2/GW, although still higher than those through pulsed measurements.
To reconcile these differences, we perform pulsed I-V measurements to extract thermal time constants from which thermal boundary heat capacity may be estimated. Joule heating from the electrical load leads to a decrease in channel mobility and a decrease in current. In our measurements, typical time constants for heat spreading through the active layers were ~0.2μs, ~8-20μs through the buffer epitaxial layers, and >100μs through the final heat sink, die attach or other final section. In other words, any pulse faster than these characteristic time scales will lead to an underestimation of TBR. While pulse-width modulation (PWM) electronics are operated in pulsed mode, the duty cycles are typically 0.2–0.8, so that full cooling back to room temperature is not realistic in a single cycle. Small amounts of heat accumulating in each cycle lead to a slow transient of heating to a steady state over time, requiring accurate knowledge of the true resistive TBR as in this paper to predict codesign performance in real circuits.
References
Bindra, IEEE Power Electronics Magazine, 2015, 2, 42–47.
T. Razzak, et al., Electron Lett, 2018, 54, 1351–1353.
L. Yates, et al., ACS Appl Mater Interfaces, 2018, 10, 24302–24309.
M. D. Alam, et al., Appl Phys Lett, 2021, 119, 132106.
S. Choi, et al., Appl Phys Lett, 2021, 119, 170501.
K. S. Yuk, et al., IEEE Trans Microw Theory Tech, 2009, 57, 3322–3332.
A. Mamun, et al., ECS Meeting Abstracts, 2021, MA2021-01, 1075.
A. Mamun, et al., Applied Physics Express, 2023, 16, 061001.

02:00 PM
MPCVD Growth of Polycrystalline Diamond on (010) β-Ga2O3 for Thermal Management (Student)
Mr. Saleh Ahmed Khan[1], Mr. Stephen Margiotta[2], Prof. A F M Anhar Uddin Bhuiyan[3]
[1]Department of Electrical and Computer Engineering, University of Massachusetts Lowell, MA 01854, USA, [2]Department of Electrical and Computer Engineering, University of Massachusetts Lowell, MA 01854, USA, and Lincoln Laboratory, Massachusetts Institute of Technology, Lexington, MA 02421, USA. [3]University of Massachusetts Lowell

β-Ga2O3 stands out as a promising candidate in high-power electronic applications due to its ultra-wide bandgap (~ 4.8 eV), high breakdown field (~ 8 MV/cm), along with the availability of large single-crystal native substrates. However, the lower thermal conductivity (11-27 Wm-1K-1) of β-Ga2O3 necessitates the development of highly efficient thermal management solutions, especially for high-power density operations. Previous research has explored different thermal management strategies, including employing single-crystal diamond as a heat-spreading layer in β-Ga2O3 devices, but the use of large-area single-crystal diamond wafers is mostly restricted by cost and availability constraints. Alternatively, integrating polycrystalline diamond film on β-Ga2O3 wafers offers a viable and cost-efficient solution for thermal management [1,2], attributed to its impressive thermal conductivity of > 2000 Wm-1K-1.

In this study, we systematically investigated a three-step growth mechanism of polycrystalline diamond film on (010) β-Ga2O3 wafers using microwave plasma-assisted chemical vapor deposition (MPCVD), demonstrating high-quality diamond films characterized by large grain sizes, a high growth rate, and purity. Initially, a 50 nm thick SiO2 or SiNx layer was deposited on bare β-Ga2O3 substrates to protect the surface from high temperature and H2 plasma damage during MPCVD growth. Next, we employed a polymer-assisted seeding technique [2] utilizing a diamond nanoparticle solution to create diamond nucleation sites. Finally, MPCVD growth was performed at a plasma power of 1000 W, a temperature of 800˚C, a chamber pressure of 50 Torr, and a CH4/H2 ratio of 1%, with growth durations of 10, 30, and 60 minutes. Figure 1 shows the room temperature background subtracted Raman spectra for three different diamond films grown on β-Ga2O3 substrates coated with 50 nm SiO2 with different growth durations, indicating the appearance of sharp diamond peaks at around ~1332 cm-1. While other non-diamond peaks such as G-band peaks and polyacetylene are also observed in the spectra, high phase purity is still found to be maintained for all three diamond films with a high phase purity of > 96% for all three samples [3]. As the growth duration increases, a consistent shift of the Raman peak position for the diamond peak is observed, suggesting that the strain state of the diamond epilayer is influenced by the thicknesses of the film. The surface FESEM and AFM images of corresponding diamond films as shown in Figures 2 (a-f) reveal the changes in surface morphologies, grain size, and RMS roughness as the growth durations vary. The average grain size progressively increases from ~37 nm to ~126 nm as the growth duration increases from 10 minutes to 1 hour. The AFM images show increased surface RMS roughness from 9.24 nm to 19.1 nm with the increase of the growth time, aligning with the observations from SEM imaging. From a 60-minute growth duration, a diamond film thickness of approximately 315 nm was observed from SEM cross sectional imaging (inset, Fig. 2c), indicating a significantly fast growth rate of 5.25 nm/min. To understand the effects of different underlying adhesion layers on the quality of diamond film, we also conducted a comparative study of polycrystalline diamond growth on β-Ga2O3 using both 50 nm thick SiNx and SiO2 interlayers. The Raman spectra presented in Figure 3 shows a sharper and narrower diamond peak for the film grown on the SiO2 layer compared to the SiNx layer. Furthermore, SEM images in the inset demonstrate larger diamond grain sizes when grown on the SiO2 interlayer, indicating that SiO2 could possibly offer advantages as an interlayer for high quality diamond growth on β-Ga2O3 under the given growth conditions. Further characterizations utilizing atomic resolution transmission electron microscopy and X-ray photoelectron spectroscopy are underway to enhance the understanding of structural and interfacial quality and the impurity incorporation in the diamond film.

In summary, this work on the systematic investigation into MPCVD growth of high quality polycrystalline diamond films on β-Ga2O3 substrates offers a promising pathway toward realizing cost-effective, scalable, and efficient thermal management solutions for β-Ga2O3 based high power devices.

References: [1] Masten et. al., Appl. Phys. Lett. 124, 153502 (2024); [2] Malakoutian et. al., Appl. Phys. Express, 14, 055502 (2021); [3] Malakoutian et. al., Crystals 9, 498 (2019).

1:00 PM
Electrochemical Energy Storage
Session Chairs: Edward Yu (The University of Texas at Austin), Jung-Hyun Kim (Ohio State University)
ESJ 1202

01:00 PM
In-Operando Monitoring of V2O5 Interfacial Defects at Solid State Battery Interfaces (Student)
Mr. Daniel Halbing[1], Ms. Victoria Ferrari[2], Dr. David Stewart[2], Dr. Gary Rubloff[2], Prof. Leonard Brillson[1]
[1]The Ohio State University, [2]University of Maryland, College Park

As high-power electronics become more prevalent in daily life, battery research has largely been focused on increasing cycling longevity and power storage capacity. These battery research interests have become further amplified with the recent emergence of the all solid state battery (ASSB), as they have been found to be safer than liquid batteries and have also been found to have the potential for a much higher energy density compared to their liquid predecessors. However, in the development of ASSB's, there has been significant problems with battery breakdown due to defects, especially at the interface between electrodes and electrolytes. In this study, non-destructive depth-resolved cathodoluminescence spectroscopy (DRCLS) was used to analyze the interface between two materials (LiPON as the electrolyte and V2O5 as the electrode) that are of particularly high interest in ASSB research. Figure 1 shows the process of DRCLS, in which an incident electron beam causes impact ionization resulting in light emission due to recombination of electron hole pairs that is characteristic of the material's band structure. DRCLS allows us to monitor interfacial and lattice defects as a function of battery cycling. The nature of the V2O5/LiPON interface was investigated by incorporating varying percentages of chromium doping at the interface across several samples. Chromium has characteristic R1 (~1.78 eV) and R2 (~1.81 eV) emissions that were used as interfacial markers [1]. These peaks are

susceptible to shifting, depending on lattice environment. Figure 2a shows a broad Cr peak at ~1.6 eV beginning to appear at Eb = 1.4 keV, and then increase in intensity at 1.5 keV (figure 2b) and 1.6 keV (figure 2c). This peak indicates an increasing intensity of Cr emission as we probe deeper. Figure 3a shows interfacial chromium was detected at Eb = 1.7 keV as we receive the strongest Cr signal at this beam energy, and clearly shows two sets of Cr R1/R2 intramolecular transitions, specifically with one set of split peaks at 1.45 eV and 1.53 eV as well as another set at 1.66 eV and 1.81 eV. These two sets of R1/R2 Cr peaks can be used to obtain LiPON/V2O5 heterojunction band offsets. When we probe further past the interface at Eb =1.8 keV, figure 3b also shows the emergence of a broad 1.55 eV feature. This defect increases in intensity to a maximum at ~20 nm below the interface, and then decreases again, as shown in the depth profile in figure 4. This indicates an interfacial defect that can be associated with oxygen vacancies (VO), which are commonly attributed to lithium diffusion into V2O5 leading to Li bonding with vanadium. Multiple DFT calculations have predicted gap state energies [2] and photoemission has reported a VO-related state in this 1.5 eV region [3]. The LiPON/V2O5 heterojunction band offset and relative oxygen vacancy densities are pictured in figure 5. Since the VO vacancy defects decrease as we go further into the bulk, this indicates an interfacial defect which could increase as a function of increased lithiation.
The results show that DRCLS can be used for non-destructive, in-operando monitoring of physical properties at buried interfaces often attributed to battery oxide degradation, such as V2O5 phase changes, interface dipole formation, and defect formation as a function of battery cycles. Additionally, oxygen vacancies were found to form just under the interface inside the V2O5, indicating Li segregation into V2O5 lattice and band bending. Lastly, the appearance of two sets of R1/R2 Cr peaks can be used to obtain LiPON/V2O5 heterojunction band offsets which could be pivotal for understanding the long-term cycle stability of these important interfaces.
[1] Remple et al., J. Vac. Sci. Technol. A 41, 022702 (2023) https://doi.org/10.1116/6.0002340
[2] Qi-Hu Wu, A. Thissen, W. Jaegermann, and Meilin Liu, “Photoelectron spectroscopy study of oxygen vacancy on vanadium oxides surface,” Appl. Surf. Sci. 236, 473-478 (2004). https://doi.org/10.1016/j.apsusc.2004.05.112
[3] David O. Scanlon, Aron Walsh, Benjamin J. Morgan, and Graeme Watson, “An ab initio Study of Reduction of V2O5 through the Formation of Oxygen Vacancies and Li Intercalation,” J. Phys. Chem. C 112, 9903-9911 (2008). https://doi.org/10.1021/jp711334f
[4] Levy, Z. et al. Lithium Spatial Distribution and Split-Off Electronic Bands at Nanoscale V2O5/LiPON Interfaces. ACS Appl. Energy Mater. acsaem.2c03683 (2023) doi:10.1021/acsaem.2c03683.

01:15 PM
A nanoindentation platform for in-operando measurement of stress-electrochemical coupling in thin-film solid-state batteries (Student)
Ms. Bhuvsmita Bhargava[1], Dr. Yueming Song[1], Mr. Stefan Theodoru[1], Mr. Lane Crofton[1], Dr. David Stewart[1], Prof. Alexander Kozen[2], Dr. Gary Rubloff[1], Dr. Paul Albertus[1]
[1]University of Maryland, College Park, [2]University of Vermont

Controlled stress is critical to both fabrication and operation of solid-state batteries to ensure pristine, low-impedance interfaces. In addition to the applied stack pressure which can vary up to 100s MPa, internal and localized stresses up to a few ~1 GPa can be generated from volume changes during charge and discharge. The effects of these stresses on overall cell performance and degradation due to altered thermodynamics, interfacial kinetics, and bulk transport of the active species have been studied in several prior works1,2. The extent of these stress-electrochemistry couplings depends on the materials and geometry of interfaces that affects the local stress distribution.
To better control some of these stress-potential, stress-kinetics, and stress-transport coupling phenomena, we use a nanoindenter platform to apply controlled uniaxial compressive forces to thin-film electrochemical devices and batteries3. Interfaces in a thin-film sample can be uniform and planar over large areas, enabling us to study the effect of stress on the interfacial electrochemistry more directly and with greater quantitative accuracy and control. Thin-film devices also have low surface roughness on the order of <10 nm, which is crucial for homogenous stress distribution avoiding stress hotspots. In this work we present our observations and analysis on the direct electrochemical-mechanical coupling in sputter deposited thin-film TiO2 (120 nm) as the working electrode with LiPON (300 nm) as the single-ion Li+ conductor solid electrolyte in a stacked arrangement (shown in figure). The TiO2 electrode in this study is prelithiated from LiPON sputter deposition with a lithiation state of Li0.6TiO2. Preliminary results show that uniaxial compressive loads on the order of 1 MPa affect the potentials measured through the galvanostatic charge cycle of the cell and vary with the lithium content of the TiO2. In addition, we will also present our preliminary results on the effect of applied stress on thin-film sputter deposited V2O5 electrodes on a Li2O-Al2O3-SiO2-TiO2-P2O5 (LATP) electrolyte cycled against Li metal with a PEO-LiTFSi interlayer. The electrodes in this setup are deposited in a planar configuration on LATP to ensure the two electrode interfaces are mechanically decoupled.
References:
1. Carmona, E. A., Wang, M. J., Song, Y., Sakamoto, J. & Albertus, P. The Effect of Mechanical State on the Equilibrium Potential of Alkali Metal/Ceramic Single-Ion Conductor Systems. Advanced Energy Materials 11, 2101355 (2021).
2. Koerver, R. et al. Chemo-mechanical expansion of lithium electrode materials – on the route to mechanically optimized all-solid-state batteries. Energy Environ. Sci. 11, 2142–2158 (2018).
3. Song, Y. et al. Electrochemical-mechanical coupling measurements. Joule S2542435123001137 (2023) doi:10.1016/j.joule.2023.03.001.

01:30 PM
Tuning the composition and structure of high mobility NASICON-like thin films through atomic layer deposition (Student)
Mrs. Daniela Fontecha[1], Prof. Alexander Kozen[2], Dr. David Stewart[1], Dr. Gary Rubloff[1], Dr. Keith Gregorczyk[1]

[1]University of Maryland, College Park, [2]University of Vermont

The ionic conductivity of thin film solid state electrolytes (SSEs) fabricated by atomic layer deposition (ALD) has been limited by material development challenges, phase purity concerns when dealing with tertiary and quaternary systems, and challenges related to crystallinity. These complexities require careful consideration of the material system, precursor selection, process parameters, and post-annealing conditions to realize ideal ALD thin-film SSE materials with ionic conductivities >10-6 S/cm. Bulk oxide SSEs, such as Li1+xTi2-xAlx(PO4)3 (LATP) have a NASICON-like crystal structure, show high ionic conductivity when crystalline (10-3 S/cm), demonstrate air & water stability, and a high voltage stability window. ALD synthesis of LATP can be broken down into well-known constituent processes (e.g., Li3PO4, Al2O3, TiP2O7) which can be combined with respect to stoichiometric ratios.
LATP can be considered Al-doped LiTi2(PO4)3 (LTP), in which Al+3 ions partially replace Ti+4 ions in the NASICON-like structure. This facilitates fast Li+ ion conduction through the 3D network. With that in mind, an ALD process for LTP was first developed by alternating between Li2O and TiP2O7 sub-processes. The Li2O sub-process uses lithium tert-butoxide (LiOtBu) as the lithium source and water to complete the surface reaction. The TiP2O7 sub-process uses titanium (IV) isopropoxide (TTIP) as the titanium source, trimethyl phosphate (TMP) as the phosphorous source, and water. The growth rate of LTP was measured to be 0.4 Å/cycle at 300 oC. By adjusting the ratio between Li2O and TiP2O7 cycles, the Li concentration in LTP can be tuned between 8.4-34.3 at % Li.
A NASICON-like crystalline structure is achieved by post-annealing the LTP films between 650 oC – 850 oC. The ideal annealing temperature was found to be a function of Li-ion concentration. The resulting measured ionic conductivity of partially crystalline LTP thin films is 3.6x10-5 S/cm at 100 oC. In this talk, we will discuss the complex issues related to process parameters, stochiometric tunability, and the resulting ionic conductivity when exploring ternary and quaternary LTP/LATP metal phosphates phase space.

01:45 PM
Deposition of LiPON solid-electrolyte onto V2O5 leads to intense lithiation
Dr. David Stewart[1], Dr. Zoey Warecki[2], Ms. Victoria Ferrari[1], Dr. Gary Rubloff[1], Dr. Alec Talin[3]
[1]University of Maryland, College Park, [2]Naval Research Lab, [3]Sandia National Laboratories

During the reactive sputtering of lithium phosphorus-oxynitride (LiPON) thin films onto vanadium pentoxide (V2O5), a large flux of lithium diffuses into the underlayer, producing lithium vanadium oxide (LVO) cathodes that are ready for operation in ionic devices without the need for a subsequent lithiation step. In our experiments, the amount of Li inserted during deposition of 1 micron of LiPON amounts to more than 290 mAh/g-V2O5 (with a 200 nm V2O5 film). This Li can be reversibly cycled over 1500 times in pseudo-symmetric thin film solid-state batteries (e.g. V2O5/LiPON/LVO) with over 80% capacity retention. Li transfer reactions similar to this have been observed with other cathodes (e.g. LiCoO2), but often in the reverse direction,[1,2] and not to this degree,[3] although in our work we have observed high levels of lithiation in TiO2 as well. This degree of “autolithiation” provides an avenue for simplifying the fabrication of devices reliant on the storage of ions, such as thin film batteries and neuromorphic transistors.
To better understand the underlying mechanism, we have analyzed the early stages of LiPON deposition on V2O5. Clearly free Li ions may impinge on the LiPON/V2O5 surface during early stages of LiPON growth. Autolithiation seems to begin within the first 10 nm of LiPON growth, based on shifts in the oxidation state of the V measured by XPS, without modifying the chemistry of the growing LiPON. By 20 nm, the LiPON layer completely encases the V2O5 and is electronically insulating, yet further lithium insertion still occurs by inward diffusion, measured by sputter depth profiles through the bulk of the V2O5 film. We conclude that the autolithiation is not the product of breakdown or interphase formation, but is more likely driven by electrochemical gradients between the growth surface of LiPON and the V2O5 and supported by the relatively high ionic conductivity of these materials. It remains an interesting avenue of research just how mobile Li is during thin film processing, with the potential for lateral gradients to move the ions in other directions across devices.
1. Gittleson, F. S. & El Gabaly, F. Non-Faradaic Li + Migration and Chemical Coordination across Solid-State Battery Interfaces. Nano Lett. 17, 6974–6982 (2017).
2. Ohnishi, T. & Takada, K. Sputter-Deposited Amorphous Li 3 PO 4 Solid Electrolyte Films. ACS Omega 7, 21199–21206 (2022).
3. Leung, K. et al. Kinetics-Controlled Degradation Reactions at Crystalline LiPON/Li x CoO 2 and Crystalline LiPON/Li-Metal Interfaces. ChemSusChem 11, 1956–1969 (2018).

02:00 PM
Models for Solid-Electrolyte Fracture during Li-Metal Plating require Consistent Electrochemical-Mechanical Couplings
Dr. Taeho Jung[1], Dr. Eric Carmona[1], Dr. Yueming Song[1], Dr. Paul Albertus[1]
[1]University of Maryland, College Park

Lithium is known to penetrate through the solid electrolyte during the charging of the all-solid-state lithium-metal battery. This eventually causes a short circuit over multiple charge-discharge cycles and is one of the main failure mechanisms of the device [1]. Lithium being a soft ductile metal, cracks in the more rigid solid electrolyte must appear before its propagation during plating [2, 3]. Therefore, it is important to understand the solid-electrolyte fracture for the prediction of the system behaviors, as well as the optimization of the interfacial design. Mathematical modeling is a key tool for the fundamental understanding of the undergoing physical processes.
Due to the all-solid nature of the device, lithium/electrolyte interfacial interactions result in a stress build-up, which influences the thermodynamic states of the constituent materials, especially that of lithium [4]. This in turn affects the reaction kinetics and thus modifications to the interfacial kinetic expression are necessary. As such, a modified version of the Butler–Volmer equation as stipulated by Ganser et al. [5] is employed in our model. Furthermore, the incorporation of an appropriate lithium mechanical

constitutive behavior is equally important for an accurate depiction of the system behaviors. We believe the intimate communication between the electrochemical and mechanical principles is critical in describing the device behaviors accurately.
Unfortunately, existing solid-electrolyte fracture models in the literature are not satisfactory; they often treat none or a limited amount of the electrochemical–mechanical couplings. Consequently, we aim to build a model that brings together (1) rigorous electrochemical–mechanical couplings and (2) appropriate lithium properties at the battery-application length scale to study the crack initiation. We simulate an isolated Gaussian-curved lithium peak in perfect contact with the lithium-lanthanum-zirconium-oxide (LLZO) solid electrolyte. LLZO is treated as an elastic solid, while lithium is modeled as a fluid. A range of fluid models is explored to find the most appropriate (pseudo-)viscosity of lithium. Current flow in the LLZO is treated with Ohm's law and the model is solved for a steady-state application of current. Preliminary results show that electrochemical–mechanical couplings strongly influence the model outputs. The stress distribution is intertwined with the interfacial current distribution and lithium viscosity, which dictates the fracture initiation, as shown in Figure 1. The model is also sensitive to the asperity geometry but to a lesser extent. Model-parameter values that produce an experimentally observed fracture current density of around 1 mA/cm2 will be presented.

References

[1] Kazyak, E. et al. (2020). Li Penetration in Ceramic Solid Electrolytes: Operando Microscopy Analysis of Morphology, Propagation, and Reversibility. Matter, 2(4), p. 1025–1048.
[2] Ning, Z. et al. (2021). Visualizing plating-induced cracking in lithium-anode solid electrolyte cells. Nature Materials, 20(8), p. 1121–1129.
[3] Ning, Z. et al. (2023). Dendrite initiation and propagation in lithium metal solid-state batteries. Nature, 618(7964), p. 287–293.
[4] Carmona, E. A. et al. (2021). The Effect of Mechanical State on the Equilibrium Potential of Alkali Metal/Ceramic Single-Ion Conductor Systems. Advanced Energy Materials, 11(29), p. 2101355.
[5] Ganser, M. et al. (2019). An Extended Formulation of Butler-Volmer Electrochemical Reaction Kinetics Including the Influence of Mechanics. Journal of The Electrochemical Society, 166(4), p. H167.

2:15 PM
Coffee Break
ESJ Building

2:45 PM
Nitride Electronic Devices
Session Chairs: Chirag Gupta (University of Wisconsin), Mona Ebrish (Vanderbilt University)
ESJ 0202

02:45 PM
Probing the role of AlGaN's surface oxide in contacts to Al-rich AlGaN heterostructures (Student)
Mr. Matthew Alessi[1], Dr. Dolar Khachariya[2], Dr. Pramod Reddy[3], Mr. Md Azizul Hasan[1], Mr. Cris Quinones[1], Mr. Chao-I Liu[1], Dr. Will Mecouch[2], Dr. Seiji Mita[3], Prof. Erhard Kohn[1], Prof. Zlatko Sitar[1], Prof. Ramón Collazo[1], Prof. Spyrid
[1]North Carolina State University, [2]Adroit Materials Inc., [3]Adroit Materials

Al-rich AlGaN-channel heterostructures grown on single-crystal AlN substrates have exhibited record high critical electric-field strength [1]. However, to achieve record Baliga figures of merit (BFOM), the specific on-resistance (Rsp,on) of such devices needs to be minimized. Metal/semiconductor contact resistance is identified as one of the major hurdles for reducing Rsp,on in Al-rich AlGaN. An extremely stable native oxide is thought to act as a diffusion barrier for multi-layer metal stacks when undergoing annealing processes [2]. Removal of native oxides from Al-rich AlGaN films proves to be quite difficult, as the surface re-oxidizes very quickly once exposed to ambient environmental conditions. In this report, we explore a processing method in which the native oxide of an Al-rich AlGaN heterostructure is sputtered away using a low energy Ar+ ion source, followed by contact deposition within the same vacuum chamber. Morphology of the sputtered contacts, and subsequent electrical characterization analyses are discussed as a function of metallization stack and annealing conditions.

Al0.85Ga0.15N(20nm)/Al0.6Ga0.4N(300nm) heterostructure were grown by MOCVD on a bulk single-crystal AlN wafer. The top 150nm of the Al0.6Ga0.4N channel was doped with Si (5E17/cm3) to assist with contact formation on quasi-vertical devices. A custom E-beam evaporation chamber was utilized in this study, which contains an ion sputtering gun within the main chamber. To ascertain the influence of Ar+ ion sputter yield, ion energy was adjusted through a range of anode biases (75V:300V); a constant power of 400W was maintained on the ion source, while also maintaining a constant sputter duration of 5 minutes. All samples were chemically pre-cleaned in a solution of H2SO4:H2O2 (3:1) and HCl for 30 min and 5 min, respectively. Samples were then lithographically patterned in a linear array of stripes. A TMAH solution was used as the developer. All samples were descummed with O2 plasma following development. Considering that the native oxide on AlGaN is between 0.3:2nm [2], an optimal Ar+ sputtering condition was obtained with a bias of 100V. Confirmed via AFM, this condition yields an etch depth of 2nm and RMS surface roughness of 0.4nm, where the non-sputtered surface RMS roughness is 0.35nm. To assess the influence of Ar+ sputtering on the electronic properties of the heterostructure, quasi-vertical rectifier test structures were fabricated. Effects of sputtering were studied in the context of two binary experimental splits, where non-/Ar+ sputtering and anode ohmic/Schottky metallization were adjusted. Only the anode was sputtered. A Cl-based dry etch was used to recess an opening of the impurity doped Al0.6Ga0.4N layer for the cathode. Ohmic contacts in this study consisted of a multi-

layer metal stack, including Cr/Ti/Al/Ti/Au. Schottky contacts consisted of Ni/Au. Schottky contacts were left unannealed, whereas the ohmic contacts were annealed at 950oC, for 30 sec under flowing N2.
Optical microscopy analysis reveals the presence of a patchy alloy, which has formed only on the Ar+ sputtered region of annealed ohmic contacts. The alloy appears homogeneous in all other regions, including regions where Cl-based dry etching was performed. It is hypothesized that the AlGaN surface is non-stoichiometric following sputtering, due to preferential sputtering of nitrogen [3]. Sputter induced non-stoichiometry of the surface, combined with the removal of the native oxide is further hypothesized to be the root cause of morphological differences between the ohmic experimental splits.
C-V profiling of the Schottky contacts indicates that Ar+ sputtering shifts the anode pinch-off voltage from -3V to +1V; suggesting that there is significant depletion of the 2-DEG under the sputtered anode. Furthermore, there is significant frequency dispersion in the C-V analysis of the sputtered Schottky contacts, whereas non-sputtered contacts exhibit little to no frequency dispersion; these results suggest that (sub)surface defects have been introduced in the Ar+ sputtered contacts [4]. I-V analysis indicates that the Ar+ sputtered Schottky contacts exhibit an order of magnitude lower reverse bias current density compared to their non-sputtered experimental split. However, the ohmic experimental split does not exhibit any significant difference between either C-V or I-V characteristics. This suggests that a significant amount of sputter induced damage was recovered during the contact annealing process.
In conclusion, we have developed a process which allows for one to Ar+ sputter Al0.85Ga0.15N films with nanometer level precision while maintaining sub-nm RMS surface roughness. Moreover, Ar+ sputtering of AlGaN films and subsequent deposition of contact layers, without exposure to ambient environment, appears to induce a more pronounced alloying reaction at the semiconductor interface. Future STEM analysis is being pursued to inspect the sputtered interface's structure. With fine tuning of thermo-chemical reactions, this process may serve as path forward to enhance the alloying of multi-layer metal stacks on Al-rich AlGaN heterostructures and hence reduce their Rsp,on.

03:00 PM
The Deposition Temperature Impact in Sputtered Magnesium Oxide on n-Type Gallium Nitride for Metal-Oxide-Semiconductor Capacitors Applications (Student)
Mr. Liron Shvilberg[1], Mr. HAOTIAN XUE[2], Dr. Jonathan Wierer[2], Prof. Nikhil Shukla[1], Prof. Jon Ihlefeld[1]
[1]University of Virginia, [2]North Carolina State University

The demand for reliable, high-power, high-frequency devices operating at high temperatures expands to a broad range of applications, including power electronics for energy storage. One of the leading materials for such applications is gallium nitride (GaN), with a 3.4 eV bandgap and mature manufacturing know-how. However, matching a robust gate oxide to GaN remains a challenge. GaN has a wurtzite structure (hexagonal), while magnesium oxide (MgO) has a rocksalt structure (cubic). Previous studies showed that growing the (111) plane of the cubic structure will introduce ~7% misfit in lattice parameter with the (0001) plane of the hexagonal structure1,2. From high-resolution transmission electron microscope (HRTEM) micrographs in literature, an abrupt interface between the GaN and the MgO is seen when growing at relatively low deposition temperatures via molecular beam epitaxy1–6, pulsed laser deposition7, or atomic layer deposition8–10. Yet, in a previous study11, where a sputtering process was implemented at 700 °C, a relatively higher deposition temperature, a clear interfacial phase can be seen when exploring the interface using high angle annular dark field imaging in an HRTEM. Attempts to lower the deposition temperature were partially successful; epitaxial MgO films were achieved at temperatures as low as 550 °C, but less stable electrical performance was observed as the deposition temperature decreased. The less stable electrical performance of films grown at lower temperatures is speculated to be related to defects introduced during the films' growth process. This presentation will discuss a correlation between the structure, the processing conditions, and the achieved electrical properties of sputtered MgO thin films on n-type GaN for metal oxide semiconductor capacitors (MOSCaps) applications.

03:15 PM
Optimization of the BFoM: New Insights on the Power Performance of Wide- and Ultrawide-Bandgap Semiconductors
Dr. Franklin Nouketcha[1], Dr. Aivars Lelis[1], Dr. Ronald Green[1], Prof. Neil Goldsman[2]
[1]DEVCOM Army Research Laboratory, [2]University of Maryland, College Park

The Baliga figure-of-merit (BFoM) provides the standard characterization of the fundamental trade-off between the breakdown voltage, VBR, and the specific on-state resistance, RON, SP, in vertical, unipolar power devices, such that 4VBR2/RON, SP = μεξC3, wherein μ is the mobility of the material, ε is the dielectric constant, and ξC is the critical field [1]. However, this relationship is derived assuming a triangular field profile at breakdown, which optimizes the breakdown voltage for a given thickness and doping but does not optimize the trade-off between VBR and RON, SP. In addition, this expression is often misevaluated as a result of its different parameters being treated as constant material properties when in fact both mobility (dependent on doping and electric field) and critical field (dependent on doping and width of the drift layer [2], and not known a priori) vary with breakdown voltage.
This work proposes a more fundamental approach to evaluating the trade-off between VBR and RON, SP by considering the ratio 4VBR2/RON, SP (which is labeled the trade-off ratio), for a wide range of both doping concentrations and drift-layer widths. We analyzed SiC p-i-n diodes and calculated the breakdown voltage by setting the ionization integral, int(α(x)eint(β(u)-α(u), 0, x, u),0, W, x), equal to 1, wherein α and β are the impact ionization coefficients for electrons and holes, respectively. RON,SP was calculated as W/qμn, wherein W is the width of the drift layer, q is the electron charge, and n is the concentration of free carriers. This method of evaluating the trade-off ratio applies to devices independently of the shape of the internal electric-field profile during avalanche breakdown and allows the inclusion of important physics, such as the incomplete ionization of dopants [3]. The trade-off ratio calculated for 4H-SiC is shown as a function of device drift-layer width for several doping concentrations. It is seen that the peak of the trade-off ratio is doping-dependent, suggesting that the

power performance of semiconductors highly depends on the intended voltage of operation. It is shown that optimizing the breakdown voltage with a triangular field profile does not optimize the trade-off ratio. Instead, the optimized trade-off is obtained by a careful variation of thickness for a given doping, leading to a trapezoidal field profile. But to accurately apply this more precise approach to a given material, it is necessary to accurately calculate the impact ionization coefficients — which are a function of both electric field and temperature -— to determine the actual breakdown voltage; and to evaluate the specific on-resistance by accurately accounting for both the material mobility and dopant ionization.

03:30 PM

Enhancement Mode AlInN/GaN High Electron Mobility Transistors via Thermally Oxidized AlxIn1-xN Gates

Mr. Elia Palmese[1], Mr. HAOTIAN XUE[1], Prof. Spyridon Pavlidis[1], Dr. Jonathan Wierer[1]
[1]North Carolina State University

III-nitride high-mobility electron transistors (HEMTs) are useful for high-frequency [1] and high-power transistor applications [2, 3]. III-nitride HEMTs and MIS-HEMTs are typically normally on (depletion mode) because the 2-dimensional electron gas is formed under equilibrium. Techniques used to create enhancement mode devices include fluorine treatments, etching a recess under the gate, and selective regrowth of p-GaN to form a p-n junction under the gate [4,5]. A enhancement mode AlInN/GaN MIS-HEMT with completely thermally oxidized barrier layers under the gate is presented here [6]. This is an alternative and potentially easier device to process than other techniques.
A standard AlInN/GaN HEMT structure is used and consists of a 700 nm thick unintentionally doped GaN layer, a ~1 nm AlN layer, and a 10 nm unintentionally doped AlxIn1-xN (x=0.82) barrier, all grown on a GaN-on-Si substrate. Device processing begins with etching a mesa and depositing a 100 nm thick SiNx masking layer via PECVD. The SiNx is removed in the 5 mm wide gate region to thermally oxidize selectively in the open areas with O2. The gates are oxidized at a low temperature, then ramped to 850°C, and oxidized for 1 hour. Next, the SiNx mask is removed, and Ti/Al/Ni/Au ohmic contacts are deposited and annealed. A 20 nm thick ALD Al2O3 layer is deposited for passivation and to reduce gate leakage. Finally, vias are made to the contacts and gate, and metal pads are deposited. This process produces thermally oxidized OX-MIS-HEMTs. Processed on the sample simultaneously are normally-on or D-mode-HEMTs (Schottky gate) and ALD-MIS-HEMTs (ALD Al2O3 between the gate metal and AlInN).
STEM and EDS are performed on oxidized gate regions of the OX-MIS-HEMTs. Large gate areas are defect-free, where complete oxidation of the AlInN and AlN layer occurs. The interface between the GaN and oxide is smooth, and the thermal Al2O3 is indistinguishable from the deposited ALD Al2O3. EDS mapping cannot detect In in the oxide, indicating that most of the In is being removed during the oxidation and cleaning processes. However, the gate oxide does have rough regions caused by threading dislocations and edge cracking. Threading dislocation, over-oxidation, and stresses in the SiNx could contribute to roughness and cracking and require fine-tuning.
The current versus voltage (IV) measurements of different HEMTs are compared to characterize the device performance. Three transfer characteristics (Id vs. Vgs,) conditions are taken: an initial baseline measurement, a measurement after stressing the device, and a measurement 10 minutes after stressing the devices. The transfer characteristic of the OX-MIS-HEMT at 0 V shows low currents, indicating that the thermally oxidized gate removes the 2-dimensional gas and creates an enhancement mode HEMT. They exhibit low leakage currents in the off-state but are resistive, resulting in on-state currents 3 orders of magnitude lower when compared to the other HEMTs. On/Off ratios are ~107, which is greater than the D-mode-HEMT, ~105, and less than the ALD-MIS-HEMT ~109. The devices' subthreshold swing is large, with turn-on occurring over many volts. After stressing, the OX-MIS-HEMT has a threshold voltage shift to ~4 V. The observed shifts in the IV characteristics at different stress conditions indicate the presence of fixed and mobile charges at the oxide/GaN interface. The output characteristic, Id versus drain-source voltage (Vds), is measured for an unannealed OX-MIS-HEMT with Vgs from -2.5 V to 12.5 V with voltage steps of 2.5 V. Appreciable currents do not occur until ~5 V bias is applied, demonstrating enhancement mode operation.
An annealing study is conducted on the OX-MIS-HEMTs at 400°C and 500°C for 10 min in N2 to help improve the oxide interface. The threshold voltage increases to ~5 V after annealing at 400°C and to ~8 V after the 500°C anneal. This preserves enhancement mode behavior and improves the subthreshold swing by 2 times. The better performance indicates that annealing improves the oxide-semiconductor interface. A drawback to annealing is a further reduction in the on-state current.
There are certainly improvements that can be made in the device processing that will result in better performance. The non-ideal subthreshold swings, low on-state current, and shifts in threshold voltages are most likely a result of stresses in the SiNx masking layer and the extent of the thermal oxide. Other improvements include targeting the oxidation time to prevent over-oxidation and exploring smaller gate lengths. This should help reduce the number of interface traps and improve performance.
References
[1] M. A. Khan et al., Applied Physics Letters, vol. 58, no. 21, pp. 2408-2410, 1991, doi: 10.1063/1.104886.
[2] O. Ambacher et al., Journal of Applied Physics, vol. 87, no. 1, pp. 334-344, 2000, doi: 10.1063/1.371866.
[3] T. Oka et al., IEEE EDL, vol. 29, no. 7, pp. 668-670, 2008, doi:10.1109/led.2008.2000607
[4] Y. Cai et al., IEEE Trans. Elec. Devices, vol. 53, no. 9, pp. 2207-2215, 2006, doi: 10.1109/ted.2006.881054.
[5] W. B. Lanford et al., Electronics Letters, vol. 41, no. 7, 2005, doi: 10.1049/el:20050161.
[6] E. Palmese et al., IEEE Trans. Elec. Devices, 2023, doi: 10.1109/TED.2023.3343313.

03:45 PM

Ti-Based Contact Optimization for Demonstration of AlN MOSFET

Mr. Dhanu Chettri[1], Mr. Ganesh Mainali[1], Dr. Haicheng Cao[1], Mr. Juan Huerta Salcedo[1], Mr. Glen Isaac Maciel Garcia[1], Mr. Mingtao Nong[1], Mr. Mritunjay Kumar[1], Dr. Xiao Tang[1], Prof. Chehao Liao[2], Prof. Xiaohang Li[1]
[1]King Abdullah University of Science and Technology,

[2]National Yunlin University of Science and Technology

The demand for high-power and extreme environment electronics has witnessed a significant surge in recent years, driving research efforts toward the exploration of ultra-wideband gap (UWBG) semiconductors. Yet, surpassing Ga2O3 in terms of material properties, Aluminum Nitride (AlN) presents itself as an exceedingly compelling candidate. AlN boasts a superior bandgap of 6.2 eV and remarkable thermal conductivity, reaching 320 W/m·K, highlighting its potential for high-performance electronics [1], [2]. Despite its advantages, achieving efficient ohmic contacts with AlN remains a significant challenge, underscoring the need for contact optimization for AlN electronics. This study therefore delves into the effects of annealing temperature on Ti-based AlN contacts, culminating in the fabrication of AlN MOSFETs (metal-oxide-semiconductor field-effect transistors) employing these optimized contacts.
The epitaxial growth of n-type AlN with Si concentration of 4.5×1018 cm-3 was carried out using metal-organic chemical vapor deposition (MOCVD) on a 700 nm u-AlN buffer, which was grown on a top of a cleaned AlN/sapphire substrate. A metal stack comprising layers of Ti, Al, Ti, and Au with thicknesses of 20 nm, 100 nm, 70 nm, and 150 nm, respectively, was sputter-deposited onto the AlN to form a CTLM (circular transmission line model) pattern. The CTLM's design consists of a circular geometry with an inner radius of 300 µm, and contact spacings ranging from 3 µm to 50 µm. These contacts were then annealed in N2 ambient from temperature 750 ºC to 950 ºC with a 50 ºC step for 30 s each. The spacing of the contacts is measured using scanning electron microscopy (SEM) which is then used in the electrical analysis of the CTLM samples. Finally, using the optimized contact, recessed AlN MOSFET is fabricated. This device features a channel with a width-to-length (W/L) ratio of 400 µm to 30 µm and incorporates a 20 µm gate length.
Fig. 1 presents SEM images of the metal contacts pre- and post-annealing at varying temperatures, illustrating morphological changes. Correspondingly, Fig. 2 shows atomic force microscopy (AFM) images of the annealed and non-annealed samples. Notably, with rising annealing temperatures, there is a discernible increase in surface roughness, as quantified by the root mean square (RMS) roughness in Fig. 3 (a). Fig. 3(b) demonstrates that increasing the annealing temperature leads to a notable decrease in both specific contact resistance and overall contact resistance, indicating enhanced electrical performance for samples annealed at higher temperatures. The specific contact resistance as low as 5.3×10-2 Ω.cm2 is obtained for the sample annealed at 950 ºC. Fig. 3 (c) showcases the schematic of the fabricated AlN MOSFET along with the high-angle annular dark-field (HAADF) imaging of the device cross-section, revealing the Al2O3/n-AlN interface.
Figures 3(d) and (e) delineate the transfer characteristics, including the drain and gate currents, while Figure 3(f) displays the output characteristics. Notably, the transfer characteristics reveal an increase in off-current alongside the drain current, attributable to the semi-insulating layer beneath the n-AlN film. Furthermore, it is evident from the output characteristics, that there is room to improve the metal contact this is similar to the report [2]. The fabricated AlN MOSFETs have a threshold voltage of -10.91 V, which establishes their potential for reliable switching operations. However, the on-to-off current ratio (Ion/Ioff) is currently below expectations, standing at 2.06×102. Additionally, the subthreshold swing (SS) is measured to be 7.92 V/dec, indicating room for optimization in terms of gate control over the channel current. Field effect mobility in our devices is determined to be 2.95 cm2/Vs, demonstrating reasonable charge carrier transport characteristics. Thus, in this study, we explored the effects of annealing temperature on Ti-based metal contacts for AlN and proceeded to fabricate AlN MOSFETs under these optimized conditions. Although our initial results show room for improvement in key parameters such as Ion/Ioff and SS, these findings lay the groundwork for future research and optimization of AlN MOSFETs.
References
[1] Okumura, Hironori et al., Jpn. J. Appl. Phys., 57, 04FR11 (2018).
[2] Böcker J et al., Electron. Lett vol 56, p 838-840 (2020).

2:45 PM
Multifunctional Oxides: Characterization and Processing
Session Chairs: Lauren Garten (Georgia Institute of Technology), Patrick Lenahan (Penn State University)
ESJ 0224

02:45 PM
Developing X-ray Diffraction Methods for Multilayer Thin-Film 128° Y-cut LiNbO3 on Sapphire (Student)
Ms. Lezli Matto[1], Dr. Michael Liao[1], Prof. Mark Goorsky[1]
[1]University of California, Los Angeles

X-ray diffraction methods are developed to isolate and structurally characterize each layer in multilayer periodically poled thin film LiNbO3 on sapphire structures. Recently thin film LiNbO3 has received increasing attention for surface acoustic wave devices due to its high electromechanical coupling coefficient1 and quality factor2 at high (50+ GHz) frequencies. Moreover, the use of multilayer thin film LiNbO3 has been demonstrated to achieve higher device performance.2-4 There is a lack of fundamental understanding of how structural characteristics of the films impact device performance. Therefore, the ability to characterize each of the films in a multilayer structure is the first step towards optimizing and achieving next-generation surface acoustic wave devices.
In this work, commercially available 3-layer thin film 128° Y-cut LiNbO3 on sapphire fabricated via wafer bonding and grinding/chemical mechanical polishing are structurally characterized with triple-axis X-ray diffraction. Each adjacent thin layer of LiNbO3 is twisted in-plane 180° with respect to each other to provide a periodically poled piezoelectric film (P3F). Due to the symmetry of the 128° Y-cut LiNbO3 orientation, which is the (0114) surface plane, the in-plane [2110] zone axis has 1-fold symmetry which makes it crystallographically distinguishable between each adjacent LiNbO3 layers. Three peaks from a triple layer P3F structure were deconvoluted from (0114) symmetric rocking curves. Peaks were separated along the rocking curve scanning axis which results from the slight tilt misorientation between each

layer (~60” to ~560”). The peak widths for each layer were also measured, with peaks as narrow as 45”. Peak broadening is due to lattice mosaicity likely caused by polishing damage, and the wide range in widths is indicative of nonuniform quality among the layers. Because of the tilt misorientation, ω:2θ scans can be measured to determine layer thicknesses, which were found to be ~80 nm, ~100 nm, and 110 nm.
Further layer isolation can be strategically achieved by measuring reciprocal space maps of asymmetric reflections and extracting Qz line profiles from a reflection that belongs to the [2110] zone axis such as the (011.10) reflection. Note that Qz is parallel to the surface normal direction and is able to probe thickness information from thin films. Thickness fringes were observed in the asymmetric (011.10) reciprocal space map which corresponds to the 100 nm thick layer and agrees with the thickness measured along the symmetric (0114) ω:2θ scan for the same layer. Finally, through the means of X-ray diffraction the 3 layers were isolated and measured, and information such as tilt, in plane twist, and thickness values were nondestructively obtained. These measurements provide a better understanding of the structural characteristics of the multilayer stack and open the possibility for future device optimization.
The authors would like to acknowledge the support from DARPA through the Compact Front-end Filters at the EIEment-level (COFFEE) program.

03:00 PM
Nanomembrane Transfer based integration of High-k Crystalline SrTiO3 Thin Film with GaN (Student)
Mr. Md Tahmidul Alam[1], Dr. Kyoungjun Lee[1], Ms. Guangying Wang[1], Prof. Chang-Beom Eom[1], Prof. Chirag Gupta[1]
[1]University of Wisconsin-Madison

High-k thin films are becoming an increasingly attractive topic for transistor research because of two worthwhile applications-: high-k gate dielectrics facilitate device scaling [1] and high-k field dielectrics can enhance breakdown voltage [2]. Since wide-bandgap (e.g. GaN) transistors are popular in power electronics due to their ability to withstand high blocking voltage, integration of high-k dielectric with them has become a necessity [3]. There were attempts to integrate HfO2 (k = ~25) and BaTiO3 (BTO) (k = ~280) with GaN [4],[5]. However, direct growth of these dielectrics (k>25) on GaN results in polycrystalline films. Polycrystallinity lowers the dielectric constant, may result in defects, traps and reduce reliability. In this study, we have explored integration of crystalline SrTiO3 (STO) (k>110) on GaN by nanomembrane transfer process and analyzed its electrical properties.
The STO membrane (50nm and 200nm) was grown on 10nm SCAO (water soluble sacrificial layer)/ bulk STO by pulsed laser deposition at 750°C. Thereafter, Pt electrodes were deposited on the membrane. Following that the membrane was transferred on GaN after removing the sacrificial layer by DI water dip. After that, ohmic contacts were made to probe the n+ GaN layer. Then, the membrane was annealed in the atmosphere (250°C for 1 hour). The STO membrane-on-GaN (Fig. 1) was electrically characterized before and after annealing. An XRD measurement was performed to confirm its crystallinity (Fig.2).
Leakage current through the STO membrane was negligible up to -13V and -7V for the 200nm and 50nm membrane respectively (Fig. 3). It might have been caused by the lower crystallinity of the thinner membrane. Moreover, after annealing leakage current increased slightly. It might be possible that after annealing some vertical filament paths were created that increased the leakage. The capacitance-voltage characteristics (Fig. 5) show that capacitance is perfectly proportional to the electrode area. This indicates good dielectric quality of the STO membrane. Dielectric constant estimation from parallel plate capacitance formula (ignoring GaN depletion) predicts a dielectric constant (k) of at least 95 for the 200nm STO membrane. There was negligible frequency dispersion from 10kHz to 500kHz (Fig.4)- this also indicates high-quality of the STO membrane.
To obtain the dielectric constant (k) more accurately the depletion thickness in GaN was swept and k was extracted by two different methods. First, the depletion capacitance of GaN was considered in series with the STO capacitance. Second, the built in potential (found by 1/C2 vs V plot, Fig. 6) was equated to the area under the electric field in the depletion region. The intersection point of these two curves was assumed to give the true value of k (Fig. 7). The value of k was between 115-186 (105-160 before annealing) in different measurements for the 200nm membrane. For the 50nm membrane k ranged between 50-55 (31-38 before annealing). The lower k in thinner films or before annealing was possibly due to lower crystallinity or the presence of an additional interface capacitance [6]. As a conclusion, negligible leakage current up to several volts and promising dielectric constant of the crystalline STO membrane integrated on GaN makes it attractive choice for field or gate dielectric in transistors.
Acknowledgment: The work was supported by NSF through MRSEC and ASCENT program.
[1] Frank MM et al. Microelectronic Engineering, 2009 [2] Hanawa H et al. physica status solidi (a). 2014 [3] Cai Y et al. Effect of high-k passivation
layer on high voltage properties of GaN metal-insulator-semiconductor devices, 2020 [4] Cheng WC et al. Journal of Vacuum Science &
Technology B. 2022. [5] Rahman MW et al. Applied Physics Letters. 2021 [6] Boesch DS et al. Applied physics express. 2008.

03:15 PM
Characterization of ALD HfSiOx gate dielectric on β-Ga2O3 (001) (Student)
Mr. Xin Zhai[1], Mr. Zhuoqun Wen[1], Mr. Oguz Odabasi[2], Mr. Eyosyas Achamyeleh[3], Dr. Kai Sun[1], Prof. Elaheh Ahmadi[2]
[1]University of Michigan, [2]University of California, Los Angeles, [3]union college

β-Ga2O3 has garnered significant attention in the field of power electronics because of its exceptional properties. To achieve the full potential of β-Ga2O3 based power devices, a robust dielectric with high dielectric constant, large conduction band offset, high breakdown field and high crystallization temperature is crucial. Previous research has indicated that HfSiOx exhibits a dielectric constant within the range of 3.9 to 27 [1], a conduction band discontinuity of up to 2.38 eV [2] and a substantial breakdown field of up to 8

MV/cm with rapid thermal annealing between 800 ◦C to 900 ◦C [3]. In this talk, we will present an overview of the interface and bulk properties of ~ 20 nm hafnium-silicon-oxide (HfSiOx) dielectric deposited by atomic layer deposition (ALD) on (001) β-Ga2O3 by employing deep ultraviolet photo-assisted capacitance–voltage (C-V) and current–voltage (I–V) measurements. The ALD HfSiOx dielectric constant, bulk, and HfSiOx/Ga2O3 interface quality, and breakdown field were determined and the impacts of post-deposition annealing (PDA) on these parameters was studied. The HfSiOx dielectric, with a HfO2:SiO2 ratio of ~ 1:1, was deposited by ALD at 250 ◦C. The HfO2:SiO2 ratio was controlled by depositing 2 cycles of HfO2 and 3 cycles of SiO2 alternately with deposition rate 1 A/cycle for HfO2 and 0.7 A/cycle for SiO2. PDA reduced near-interface traps resulting in a smaller hysteresis without changing dielectric constant. An average trap density of 2.72 × 1012 cm−2 eV−1 and 1.06 ×1012 cm−2 eV−1 were measured on samples with PDA at 400 ◦C and 900 ◦C, respectively. A relatively low hysteresis of ~ 0.5 V and 5 V were achieved at minimum stress field of 1.8 MV/cm and at maximum stress field of 4.8 MV/cm, respectively, on sample annealed at 900 ◦C, indicating a significant reduction of electron trap density in both the bulk HfSiOx and the HfSiOx/Ga2O3 interface. Breakdown field as high as 8.7 MV/cm were achieved on devices by PDA at 900 ◦C. In addition, a high dielectric constant of 9.28 was extracted using C-V measurement.

03:30 PM
Rietveld refinement, Dielectric and Electrical response of DyFeO3 nanoparticles
Dr. Abhinav Yadav[1], Dr. SUSHRISANGITA SAHOO[1], Mr. Rifat Mahbub[2], Prof. Jeff Shield[3], Prof. Vijaya Rangari[1]
[1]Department of Material Science and Engineering, Tuskegee University, AL, 36088, USA, [2]Department of Mechanical & Materials Engineering, University of Nebraska-Lincoln, 68588,USA, [3]Department of Mechanical & Materials Engineering, University of Nebraska-Lincoln, 68588, USA

This work is mainly aimed on the synthesis of nanoparticles, temperature dependent structural and electrical characteristics of Dysprosium Orthoferrite (DyFeO3) nanoparticles. The DyFeO3 nanoparticles successfully synthesized using the nano agitator bead milling. The structural and microstructural information are performed by using the XRD, FE-SEM and TEM. The XRD of uncalcined DyFeO3 nanoparticles has been done at room temperature to 900 oC to understand about the change in crystallinty nature of material with temperature. The DyFeO3 powder calcined at 850 oC for 4 h in a muffle furnace. The Rietveld refinement of XRD data confirms the single phase formation of material with orthorhombic crystal symmetry and P n m a space group. The value of $\chi 2$ is 1.17, which justifies the experimental XRD data well matched with theoretical data [1]. The crystallite size of nanoparticles is calculated using the Willamson-Hall plot and Debye Scherrer's equation and their values are 60.8 nm (strain is 0.0028) and 31.6 nm. In addition, the average particle size of DyFeO3 is calculated through TEM and FE-SEM using the image J software and the obtained values are 49.5 and 58.2 nm, respectively. For better understanding about the crystal planes, we calculated the d-spacing in TEM pattern and their corresponding Miller indices or hkl planes are (111) and (002). The temperature dependent electrical behavior of material carried out using LCR meter over a wide frequency range (1 KHz to 1 MHz) at room temperature to 500 oC. The dielectric constant variation with frequency shows the maximum value in low frequency region which attributes the all four polarization mechanism contribute in dielectric behavior, while at higher frequency dielectric values are small due to absence of space charge induced polarization [2]. Furthermore, we have done the conductivity analysis of material and it is followed by Jonscher's power law. The Nyquist plot of the complex impedance gives the information regarding the grain and grain boundary relaxation of the material. The semicircular arc is best fitted with a series combination of two parallel R-C electrical module. For better understanding of the relaxation mechanism, the activation energies corresponding to the grain and grain boundaries are calculated using Arrhenius relation and found to be 0.25 eV and 0.2 eV respectively [3].
Acknowledgement:
Authors would like to acknowledge the financial support from NSF PREM #1827690 and NSF MRI grants: 2117242.

03:45 PM
Evolution of Insulator-Metal Transition and Magnetoresistance with Thickness in Oxygen deficient Strontium Titanate Thin Films
Dr. R. Shipra[1], Mr. Marcus Rose[1], Mr. Ryan Paxson[2], Dr. Shiva Pokhrel[3], Dr. Vera Smolyaninova[1], Dr. Michael Osofsky[3], Dr. Rajeswari Kolagani[3]
[1]Towson university, [2]University of Maryland, College Park, [3]Towson University

Oxygen vacancies (VO) induce metallicity in otherwise insulating stoichiometric Strontium Titanate (SrTiO3) with a bandgap of 3.27 eV. The direct gap becomes indirect, by the introduction of vacancy related donor defect levels, which lies ~1.0 eV below the edge of the conduction band. The Oxygen vacancies thus imparting free electrons, responsible for metallicity, get accommodated into the structure by the conversion of Ti4+to Ti3+ through the following conversion:
Sr^(2+) Ti_1^(4+) O_3^(2-)→Sr^(2+) Ti_(1-2y)^(4+) Ti_2y^(3+) O_(3-y)^(2-)
These VOs however are usually accompanied by cationic vacancies (VSr or VTi) and some previous systematic studies suggest effect of VTi in inducing magnetism observed in the thin films. Structurally, VOs have shown to increase the in-plane and out-of-plane lattice constants of SrTiO3-d. To control the structure, we employ epitaxial bi-axial stress induced by substrate lattice mismatch, which will allow control of the in-plane lattice parameter, while the out-of-plane lattice parameter adjusts to accommodate the strain. We will demonstrate the effects of compressive strain on the electrical conductivity and magneto-transport properties of SrTiO3-d thin films grown on LaAlO3 substrate, with varying film thickness. The compressive strain (-2.9%) suppresses metallicity up to a thickness of 69 nm, making the oxygen-deficient films insulating at room temperature and below. Films with thickness between 75 nm and 300 nm are metallic at room temperature and show an upturn in resistivity at lower temperatures, resembling a "metal-insulator transition" as shown in figure 1(a). With increasing thickness, metallicity extends to lower temperatures and the metal-insulator transition temperature shows a monotonic

thickness dependence up to 240 nm. Intriguingly, these films also show low temperature magnetoresistance, the nature of which evolves with increasing thickness as seen in figure 1(b). We will present systematic analysis of the thickness dependence of electrical transport data indicating that the low temperature state represents a diffusive metal rather than a true insulator. We will also discuss temperature and field dependence of the magnetoresistance, suggesting possible origins.

Acknowledgments: R. Shipra acknowledges support from the M. Hildred Blewett Fellowship from the American Physical Society. This work was also supported by the NSF Grant DMR 1709781 and graduate student summer research stipends from the Office of Graduate Studies and the Fisher College of Science and Mathematics at Towson University.

2:45 PM
Epitaxy of Dissimilar Materials
Session Chairs: Sadhvikas Addamane (Sandia National Laboratories), Seth Bank (The University of Texas at Austin)
ESJ 2206

02:45 PM
Defect Filtering at the Interface of III-V on Silicon though Templated Liquid Phase Growth (Student)
Mr. Hyun Uk Chae[1], Mr. Zezhi Wu[1], Mr. Juan Sanchez Vazquez[1], Prof. Rehan Kapadia[1]
[1]University of Southern California

Integrating high-quality III-V crystalline semiconductor materials onto silicon has been a longstanding challenge in the material and device community. Despite the unique electrical and optical properties of III-V materials, their adoption in silicon-based electronics and photonics has been hindered by the cost and complexity of integration, as well as challenges in controlling material quality during integration. Various techniques, such as epitaxial transfer and direct growth, have been explored to overcome these challenges. Epitaxial transfer methods, such as epitaxial lift-off (ELO) and wafer bonding, are promising integration approaches but face limitations in scalability. Direct growth of III-V on Si is an alternative way while it faces material quality issues. Defects in the III-V/Si interface can be filtered out by various growth techniques using graded buffers, quantum dots (QDs), strain layers (SLs), epitaxial lateral overgrowth (ELOG), and template-assisted selective epitaxy (TASE), while each of these has its own drawbacks. Here, we introduce an effective defect-filtering mechanism through templated liquid phase (TLP) growth. This approach enables the growth and manufacturing of high-quality crystalline III-V on silicon without complex growth steps. Both plane and cross-section view transmission electron microscope (TEM) images show the defect filtering through TLP growth on seed III-V layer on silicon, which can open a revenue towards the high-quality III-V integration on Si.

03:00 PM
A Platform Method to Growth Epitaxial III-V on LiNbO3 (Student)
Mr. Zezhi Wu[1], Mr. Hyun Uk Chae[1], Prof. Rehan Kapadia[1]
[1]University of Southern California

Thanks to its wide transparency window, high second-order nonlinear susceptibility, and strong piezoelectric effect, lithium niobate (LiNbO3) has emerged as a key material in developing surface acoustic wave devices, lasers, optical waveguides, and high frequency optical switches. Large quantities of optoelectronic systems like on-chip optical computing system and acoustic wave resonator can be built on LiNbO3. As an important part of these systems, it requires a layer of high quality III-V materials integrated as photon detectors and generators. Even though wafer bonding has been a mature and widely used method to have the heteroepitaxial III-V layer on LiNbO3 substrate, its performance is always limited by material constraints and compatibility issues. In this work, we present a platform method for the directly growth of patterned epitaxial III-V layers on LiNbO3 substrate. Utilizing the low-temperature templated liquid-phase (LT-TLP) growth method, we achieve uniform growth of III-V materials, such as InP and InAs, without the constraints of lattice matching. Our experimental results demonstrate the successful growth of an InAs layer with high electron mobility (2500) at room temperature and an InP layer with uniform photoluminescence on LiNbO3. Additionally, we also show the ability to tune the optical properties by doping the III-V layer during the growth process. This approach holds promising prospects for various applications, including the fabrication of lasers, photodetectors, acoustic wave amplifiers, and beyond.

03:15 PM
Electron Microscopy based Characterization of GaSb Growth on Silicon for Fabrication of Quantum Dots (Student)
Mx. Mega Frost[1], Ms. Subhashree Seth[1], Mr. Fatih Furkan Ince[1], Ms. Nazifa Tasnim Arony[2], Ms. Erika Sommer[1], Dr. Darryl Shima[1], Prof. Thomas J. Rotter[1], Dr. Marek Osinski[3], Dr. Matthew Doty[2], Dr. Joshua Zide[2], Prof. Ganesh Balakrishnan[
[1]Center for High Technology Materials, University of New Mexico, Albuquerque, New Mexico, [2]University of Delaware, [3]Center for High Technology MaUniversity of New Mexico, Albuquerque, NM-87106

GaSb-based quantum dots (QDs) provide emission in the NIR wavelength range of 1.1-1.6
μm, making them an alternative to the usual InAs QDs. Furthermore, the GaSb QDs can be grown fully strained by the traditional Stranski-Krastanov growth mode or fully relaxed by the interfacial misfit dislocation array (IMF) growth mode. To date, a variety of publications on the growth of GaSb QDs have been published resulting in devices such as lasers, detectors, memory devices, and photovoltaics. Integrating the growth of these dots on Silicon substrates would bring new applications in Silicon photonics and quantum computing. In this presentation we explore the growth of GaSb QDs grown directly on Silicon (100) substrates.

The growth of these samples is done using solid source molecular beam epitaxy (MBE). The samples are grown on Silicon (100), which is prepared for epitaxy by removing the native oxide with a 49% HF etch solution. The HF dip results in a hydrogen-passivated Silicon surface which is verified through observation of its reflection high energy electron diffraction (RHEED) pattern. Four samples of GaSb islands are grown directly on the Silicon surface with different thicknesses – 3 MLs, 5 MLs, 10 MLs, and 50 MLs – and characterized using electron microscopy techniques. A plan-view investigation of the surface is done through scanning electron microscopy (SEM) imaging and the crystallographic structure is interrogated through cross-sectional transmission electron microscopy (XTEM). In this presentation the growth of GaSb on Silicon is compared to AlSb on Silicon, which is well documented in the literature [1].
All four samples display an island growth mode, with no coalescence of the GaSb layer even at 50 MLs. Comparatively, AlSb will planarize on Silicon by the time 50 MLs is reached. Two distinct types of islands can be observed in the GaSb samples; smaller islands that are grown through the nucleation of Gallium and Antimony on the Silicon surface and noticeably larger islands which are catalyzed through the Vapour-Liquid-Solid (VLS) growth mode which arises from the formation of Gallium droplets on the substrate surface that act as traps for atoms and facilitates their growth. The VLS-catalyzed islands have a much faster growth rate, allowing them to increase in size much more rapidly compared to the directly nucleated GaSb islands. The presence of these two growth modes is clearly demonstrated upon inspection of the thicker 10 ML and 50 ML samples, where the VLS islands can be seen with an attached metal droplet. Additionally, the islands are highly faceted with equilibrium crystalline shapes. An XTEM analysis shows that the large islands are a high quality, fully relaxed crystal with no threading dislocations observed. In addition to the electron microscopy imaging, x-ray diffraction (XRD) and cryogenic photoluminescence (cryo-PL) analysis will be provided. We will also describe a growth method that we have developed which combines the self-catalyzed VLS growth mode and selective-area epitaxy to achieve better control of island size.
[1] Balakrishnan G, Huang S, Dawson LR, Xin Y-C, Conlin P, Huffaker DL (2005) Growth mechanisms of highly mismatched AlSb on a Si substrate. Applied physics letters, 86(3) https://pubs.aip.org/aip/apl/article-abstract/86/3/034105/509400

03:30 PM
Room temperature 3 – 8 µm photoluminescence in heteroepitaxial Pb1-xSnxSe on GaAs (Student)
Mr. Jarod Meyer[1], Prof. Leland Nordin[2], Dr. Rigo Carrasco[3], Dr. Preston Webster[3], Prof. Kunal Mukherjee[2]
[1]Department of Materials Science and Engineering, Stanford University, Stanford, CA 94305, USA, [2]Stanford University, [3]Air Force Research Laboratory, Space Vehicles Directorate, Kirtland Air Force Base, NM 87117

Light emitting diodes (LEDs) in the 3 – 12 µm range of the Mid-Infrared (MIR) operating at room temperature are key to low-cost optical gas sensing applications.1 Yet, traditional III-V based MIR emitters are hampered by low internal quantum efficiencies, stemming from high nonradiative Auger recombination rates that worsen with decreasing bandgap.2 Recently, we have found that thin films of the IV-VI semiconductor PbSe emit quite bright 4 µm photoluminescence (PL) at room temperature, despite the extreme 8% lattice-mismatch between the PbSe film and GaAs substrate.3 We attribute this bright luminescence to the low Auger recombination coefficient of PbSe, coupled with a high tolerance to crystal defects.4 Alloying PbSe with Sn to form Pb1-xSnxSe tunes the bandgap of PbSe across the entire MIR.5 Understanding optoelectronic properties of Pb1-xSnxSe is a critical step towards developing IV-VI-based MIR LEDs.
In this work, 40 – 250 nm Pb1-xSnxSe thin films are grown on GaAs (001) by molecular beam epitaxy at 300 °C, following a 400 °C PbSe flux surface treatment and a 345 °C nucleation layer. A subset of films are capped in-situ with amorphous GeSe after cooling below 160 °C.
We find the PL intensity of bare Pb1-xSnxSe films is severely quenched with respect to PbSe even for <1% alloying of Sn. Surface passivation of Pb1-xSnxSe with amorphous GeSe, and an optimized 50 nm thick PbSe buffer layer, greatly improves PL of Pb0.95Sn0.05Se by over an order of magnitude, and clear room temperature PL out to a wavelength of 8.4 µm for a Pb0.72Sn0.28Se layer is observed. Tensile strain from thermal expansion mismatch to GaAs, and lattice mismatch to the PbSe buffer blueshifts the PL wavelength, increasing the amount of Sn required to reach longer wavelengths. Time resolved PL measurements reveal minority carrier lifetimes on the order of 365 ns for a PbSe film at 280 K. PbSe and Pb0.95Sn0.05Se capped with GeSe, however, show injection dependent decays, with minority carrier lifetimes increasing from tens of ns to hundreds of ns with increasing injection, hinting at trap saturation effects.6 Intriguingly, the decay times of all samples are anomalously long when compared with both measured hall background carrier concentrations in the mid 1018 cm-3, and analysis of steady-state, power-dependent PL.
In summary, PL of Pb1-xSnxSe at room temperature is greatly improved via surface passivation and an optimized PbSe buffer layer, and room temperature PL emission from 3 – 8 µm is demonstrated. Initial optical characterization of these Pb1-xSnxSe films suggests complex luminescence and carrier recombination behavior, the understanding of which will be important for the development of MIR LEDs.
1 D Jung, S Bank, M L Lee, and D Wasserman, J. Opt., 19(12), 123001 (2017).
2 J.R Meyer et al… I. Vurgaftman, IEEE J. Quantum Electron. 57(5), 1 – 10 (2021).
3 J. Meyer et al… K. Mukherjee, APL Mater. 9(11), 111112 (2021).
4 G. Springholz, and G. Bauer, in Wiley Encyclopedia of Electrical and Electronics Engineering (John Wiley & Sons, 2014), pp 1 – 16.
5 H. Preier, Appl. Phys. 20(3), 189 – 206 (1979).
6 R.K Ahrenkiel, B.M. Keyes, and D.J. Dunlavy, J. Appl. Phys. 70(1), 225 – 231 (1991).

03:45 PM
Altermagnetic α-MnTe Films Grown by Molecular Beam Epitaxy on Al2O3 (0001) Substrates
Dr. Nicholas Combs[1], Dr. Cory Cress[1], Dr. Anton Ievlev[2], Dr. Olaf van 't Erve[1], Dr. Steven Bennett[1], Dr.

Connie Li[1]
[1]U.S. Naval Research Laboratory, [2]Oak Ridge National Laboratory

Altermagnetism is a newly-identified spin-symmetry classification of collinear magnets which is distinct from ferromagnetism and antiferromagnetism [1]. Altermagnets are a compensated magnetic phase with vanishing net magnetization – similar to antiferromagnets, but also exhibit non-relativistic lifting of Kramers spin degeneracy and spin-polarized bands – similar to ferromagnets, which can be utilized in the development of next-generation spin-based technologies such as spintronics. As such, the development of high-quality thin film materials is crucial for the advancement of both fundamental understanding as well as practical device applications of altermagnets.
MnTe with the hexagonal NiAs-type structure (α-MnTe) is predicted to be an altermagnet with a relatively large spin-splitting of ~1 eV and a relatively high critical temperature of 310 K [1,2]. Here, we present the growth of α-MnTe by molecular beam epitaxy on a robust, transparent, and widely-available substrate, Al2O3 (0001). While α-MnTe films grown directly on Al2O3 (0001) will crack due to tensile strain [Fig. 1(a)], we find that growth on novel buffer layers such as Bi2Se3 significantly improves growth morphology, as evident from a streaky RHEED pattern during growth and smooth surfaces revealed by atomic force microscopy [Fig. 1(b)]. SIMS measurements confirm that films grown directly on Al2O3 (0001) have cracks which extend down to the substrate surface, while those grown with a buffer layer are continuous. X-ray diffraction confirms the growth of single-phase, c-axis oriented films (Fig. 2). The impact of buffer layers other than Bi2Se3 on the MnTe morphology and phase will also be discussed. Magnetic characterization by SQUID magnetometry and electronic transport will also be presented.
[1] Šmejkal, L., et al. Phys. Rev. X 12, 031042 (2022).
[2] Mazin, I. I. Phys. Rev. B 107, L100418 (2023).

2:45 PM
Graphene and Graphene Heterostructure Synthesis and Devices
Session Chairs: Kevin Daniels (University of Maryland), Susan Fullerton (University of Pittsburgh)
ESJ 2204

02:45 PM
Mobility Enhancement in a 2D Electron Gas formed by a Topological Crystalline Insulator/Graphene Heterostructure
Dr. Gregory Stephen[1], Dr. Ivan Naumov[2], Dr. Nicholas Blumenschein[1], Mr. Leo Sun[3], Ms. Jennifer DeMell[1], Dr. Sharmila Shirodkar[2], Prof. Pratibha Dev[2], Dr. Patrick Taylor[4], Dr. Jeremy Robinson[5], Dr. Aubrey Hanbicki[1], Dr. Adam Friedman[1]
[1]Laboratory for Physical Sciences, [2]Howard University, [3]University of Maryland, College Park, [4]Army Research Laboratory, [5]Naval Research Lab

While heterostructures are ubiquitous tools enabling new physics and device functionalities, the palette of available materials has never been richer. Combinations of two emerging material classes, two-dimensional materials and topological materials, are particularly promising because of the wide range of possible permutations that are easily accessible. Individually, both graphene and Pb0.24Sn0.76Te (PST) are widely investigated for spintronic applications because graphene's high carrier mobility and PST's topologically protected surface states are attractive platforms for spin transport. Here, we combine monolayer graphene with PST and demonstrate a hybrid system with properties enhanced relative to the constituent parts. Using magnetotransport measurements, we find carrier mobilities up to 20,000 cm2/Vs and a magnetoresistance approaching 100%, greater than either material prior to stacking. The results can be explained using the polar catastrophe model, whereby a high mobility interface state results from a reconfiguration of charge due to a polar/non-polar interface interaction. As the 2DEG does result from the topological nature of the film, it should exist regardless of the Pb/Sn ratio in the film. Our results suggest that proximity induced interface states with hybrid properties can be added to the still growing list of behaviors in these novel materials.

03:00 PM
Emission Current Enhancement from Quasi-Freestanding Epitaxial Graphene Microstructure Electron Emitters Through Surface Layered Silicon Dioxide (Student)
Mr. Daniel Lewis[1], Mr. Jason Swart[2], Mr. Michael Pedowitz[1], Ms. Jennifer DeMell[3], Mr. Brendan Jordan[1], Dr. Rachael Myers-Ward[4], Dr. Daniel Pennachio[4], Dr. Jenifer Hajzus[4], Prof. Kevin Daniels[1]
[1]University of Maryland, College Park, [2]Arizona State University, [3]Laboratory for Physical Sciences, [4]Naval Research Lab

Enhanced electron emission from oxide-encapsulated quasi-freestanding bilayer epitaxial graphene (QFEG) devices is reported, demonstrating emission currents up to 9.4 μA and successful emission through oxide thicknesses of up to 1.25 μm. The low operating temperature (215 oC) and applied electric fields under which the devices operate indicate electron emission is due to phonon-assisted electron emission (PAEE), wherein forward-scattering hot phonons impart the necessary energy for the electrons to escape the graphene as an emission current. A suite of device structures and behaviors are cataloged, and various emission behaviors are demonstrated through encapsulating oxide layers. Emission current enhancement due to electron multiplication in the oxide layers is observed across multiple devices and oxide thicknesses.

03:15 PM
Microwave photoexcited transport studies of graphene
Prof. Ramesh Mani[1]
[1]Georgia State University

Graphene is an appealing material for spin-based quantum computing and spintronics due to the predicted long spin lifetimes resulting from the weak spin-orbit interaction and the scarcity of electron-spin dephasing spin-active-nuclei in

natural carbon. However, spin studies of graphene have been constrained because traditional techniques lack the sensitivity to detect the small number of spins in a one- or few atomic layer thick graphene nanostructure. Here, we examine the resistive electrical detection of spin resonance in graphene. Our microwave photo-excited transport study of graphene reveals, surprisingly, a strong microwave response and dual microwave-induced resonances. The results demonstrate resistive detection of spin resonance, identify a remarkable “orbital-cooling-mechanism” in resistive resonance detection, provide a measurement of the g-factor and spin relaxation time, and exhibit a finite splitting in the observed dual resonance transitions even in the limit of a vanishing magnetic field. The last feature has been suggested as a possible manifestation of the quantum spin Hall effect, predicted by Kane and Mele for the graphene system including a weak spin-orbit interaction. Lithographically realized, electrically contacted graphene devices were cooled to liquid helium temperatures inside a superconducting solenoid, and irradiated with microwaves transmitted via waveguides and coaxial cables over the frequency range of 10 ≤ f ≤ 50 GHz at a source-power 0.1 ≤ P ≤ 10 mW. Measurements are reported for p- and n-type samples. Typically, the observed resonances followed two lines in a excitation frequency vs. magnetic field plot: one set of resonances fit a a first line that satisfied the equation F = 27.2 B, as the second set of resonances fit a second line that satisfied F = 10.8 + 26.9 B. Here, F is in units of GHz and B is in units of Tesla. The observed slopes here suggest a g-factor g = 1.94 and g = 1.92 for the two branches, respectively, and a zero field splitting Δ = 44 μeV for the observed offset of 10.8GHz between the two spin resonance branches. The two observed resonance branches are thought to correspond to spin resonance at the edge- and within the bulk- of graphene, as the observed zero-field spin splitting is thought to be a direct measure of spin-orbit induced bulk splitting in graphene. In this presentation, we highlight these and other features in observed in our microwave excited transport study of graphene.

03:30 PM
Linear Stark shift of two-dimensional Ga via AC electric double layer gating (Student)
Mr. Nader Sawtarie[1], Dr. Jonathon Schrecengost[2], Mr. Krishnan Ananthanarayanan[2], Mr. Nithil Manimaran[3], Prof. Ke Xu[3], Prof. Joshua Robinson[2], Prof. Noel Giebink[4], Prof. Susan Fullerton[1]
[1]University of Pittsburgh, [2]Pennsylvania State University, [3]Rochester Institute of Technology, [4]University of Michigan

2D polar metals (PMets) synthesized via confinement heteroepitaxy (CHet) consist of 1-3 atomic layers of metal intercalated between a SiC substrate and graphene that are theorized to have an out-of-plane permanent electric dipole moment resulting from the non-centrosymmetric bonding with SiC substrate and graphene capping layer. 2D PMets, such as bilayer Ga, exhibit unique optical absorption attributed to a quantum-confined interband transition (~1.9 eV). In this work, 2D Ga field-effect transistors (FETs) were gated using electric-double-layer (EDL) side gating with polyethylene oxide (PEO):CsClO4. The EDL gating technique induces large (i.e., ~V/nm) electric fields, and in this case, AC EDL gating (2 Hz) is successfully demonstrated to enable the use of a lock-in amplifier to measure small changes in microreflectivity. AC EDL gating required an asymmetric pulse strategy to balance anionic and cationic EDL formation over long enough time scales (i.e., minutes) to complete a microreflectivity measurement over the visible range in the electromagnetic spectrum. COMSOL modeling confirms an RMS field strength of ~1.4 V/nm, which agrees with the ~5% RMS channel current modulation that is detected. These high fields induce a measurable electroreflectivity (ΔR/R ~ 8 x 10-4) resulting from a ~1.5 meV Stark shift. The Stark shift was determined to be linear based on the disappearing signal in the 2nd harmonic, and linear dependence of ΔR/R versus applied peak-to-peak side gate bias, which was shown with COMSOL modeling to vary linearly with ERMS. The linear Stark shift resembles the first derivative lineshape of the reflectivity, corresponding to 0.05 Debye changes in the permanent dipole moment between the ground and excited state of 2D Ga. These results provide the first direct experimental evidence of the theoretically predicted permanent dipole moment in PMets, as well as demonstrate a powerful new technique to safely deploy large time varying electric fields to 2D materials in the form of AC EDL-gating. This research was supported by NSF DMR-2011839 through the Penn State MRSEC - Center for Nanoscale Science.

2:45 PM
Growth and Characteristics of Diamond and WBG-Nitride Materials
Session Chairs: Wojciech Hadwisienczak (Ohio University), Patrick Shea (Northrop Grumman Corporation)
ESJ 1224

02:45 PM
High-Temperature AlN Schottky Barrier Diodes on Single-Crystal AlN Substrates (Student)
Mr. Dinusha Herath Mydiyanselage[1], Mr. Dawei Wang[1], Mr. Bingcheng Da[1], Mr. Ziyi He[1], Dr. Houqiang Fu[1]
[1]Arizona State University

Aluminum Nitride (AlN) is an ultrawide bandgap (UWBG) semiconductor material featuring a bandgap of 6.1 eV and a robust critical field of 12–15 MV/cm. In terms of Baliga's Figure of Merit (BFOM), AlN demonstrates the potential to outperform other wide bandgap semiconductors such as GaN, SiC, and Ga2O3. Despite this potential, AlN-based devices are still in the early stages of development, facing several challenges. These challenges include the necessity for high-quality epitaxial growth and the establishment of proper Ohmic and Schottky contacts. Additionally, AlN epilayers become resistive due to dopant compensation, resulting in relatively low effective carrier concentration and poor device performance at room temperature (RT) compared to other UWBG semiconductors. However, at high temperatures, they perform comparably to other UWBG materials. This work systematically investigates Ohmic contacts and Schottky barrier diodes (SBDs) behavior at high temperatures. The AlN epilayers were grown on bulk AlN substrates using metal-organic chemical vapor

deposition (MOCVD) with trimethylaluminum (TMAl) and ammonia (NH3) as the Al and N sources, and SiH4 as the n-type dopant Si. The AlN epilayers comprise a 1-µm-thick resistive UID AlN underlayer, a 200 nm Si-doped n-AlN layer, and a 2 nm UID GaN capping layer to prevent the oxidation of underlying AlN epilayers. Subsequently, lateral SBDs were fabricated through conventional photolithography, with varying distances between the anode and cathode (d = 5, 10, 25, 50 µm). The device configuration includes Ti/Al/Ni/Au as Ohmic contacts and Pt/Au for the Schottky contact, with the Ohmic contacts annealed at 950 °C for 30 s in an N2 atmosphere. Simultaneously, 100×200 µm Transmission Line Method (TLM) pads were fabricated to extract contact and material properties. Testing was conducted using a Keithley 4200 Semiconductor parameter analyzer equipped with a controllable thermal chuck, and high voltage measurements were performed using a Keysight B1505A Power device analyzer. Devices were tested from RT up to 350 °C. The TLM pads exhibited nonlinear I–V behavior at RT, transitioning to linear behavior at 350 °C. This transition is attributed to the increased excitation of electrons at elevated temperatures, leading to improved Ohmic contacts. The contact resistance improved from 287 to 1.1 kΩ, while the contact resistivity improved from 0.4 to 1.53×10–3 Ωcm2 as the temperature increased. The sheet resistance of the AlN film changed from 82 to 0.33 MΩ/sq, and the resistivity changed from 1643 to 6.58 Ωcm with increasing temperature. The SBDs exhibited rectification ratios ranging from 106 to 107 as the distance changed from 50 to 5 µm. Temperature-dependent measurements indicated an increasing ON/OFF ratio from 107 to 109 as the temperature varied from RT to 350 °C. Similarly, reverse leakage current testing at – 40 V showed an increase from 10–12 to 10–10 A. Breakdown testing indicated breakdown voltages of 0.62, 1.2, 2.6, and < 3 kV for devices with d = 5, 10, 25, and 50 µm, respectively. These results highlight AlN as a promising platform for high-temperature electronics and provide a valuable reference for the development of AlN-based high-temperature electronics.

03:00 PM

Growth of Cubic Boron Nitride by Plasma Assisted Chemical Vapor Deposition on Silicon and Diamond Substrate (Student)

Mr. Md. Jahangir Alam[1], Dr. Michael Spencer[1], Dr. Mvs Chandrashekhar[2], Dr. Chris Thomas[1], Dr. Birol Ozturk[1], Dr. Peker Milas[1], Mr. Kishak Cinfwat[1], Mr. Sheikh Mahtab[3], Dr. R. Shipra[4], Dr. Rajeswari Kolagani[5]
[1]Morgan State University, [2]University of South Carolina, Columbia, USA, [3]Department of Electrical and Computer Engineering Morgan State University, U.S.A, [4]Towson university, [5]Towson University

Cubic Boron Nitride (cBN) is an ultra-wide bandgap semiconductor that has many excellent material properties, including an indirect bandgap that allows N and P type doping, high-predicted breakdown field high predicted electron saturated high thermal conductivity and material hardness second only to diamond. The indirect bandgap together with a high breakdown field give the material a high Baliga Figure of Merit making it attractive for next generation power conversion devices while the high saturation velocity coupled with the high thermal conductivity give the material a high Johnson Figure of Merit indicating its potential for applications in high power high frequency devices.
In this work we report on the growth of cubic boron nitride using a custom designed Plasma Enhanced Chemical Vapor Deposition (PECVD) reactor Fig.1. The Electron Cyclotron Resonance (ECR) plasma was formed using a permanent magnet. The growth chemistry consisted of Boron Trifluoride (BF3), Nitrogen (N2), Hydrogen (H2) together with inert gases of Helium (He) and Argon (Ar) (to sustain the plasma). The growth was performed at growth pressures of 1-10mTorr and growth temperatures of 700-9000C. Si and diamond substrates were typically loaded together during an individual run Fig.2. Using gas flow rates of .25 sscm (BF3), 12.4 sscm (N2) 1 sscm (H2) 34 sscm (He) 2.5 sscm (Ar) growth of Boron Nitride was obtained on Silicon and Diamond substrates. Using optical interreference techniques the thickness of the BN films was measured as .1-.3um indicating a growth rate of 50nm to 100nm/hr. depending on the amount of BF3 flow. Fig.3 shows an image of the yellow diamond substrate before growth and after growth (Fig.4). The sample after growth showed differences in color between the edges and the center while the sample before growth showed a uniform yellow color (due to nitrogen incorporation). FTIR measurements were made on samples grown on Si and diamond substrates. Fig.5 shows the result on a silicon substrate a broad peak which is the signature of cBN. Results of FTIR measurements on diamond substrates were inconclusive due to the interreference of the diamond substrate signature in the region of interest (because of the nitrogen signature). Fig.6 shows the first XRD studies of our material. The initial results show an addition peak close to the main diamond signature that is not present on diamond substrates prior to growth. Energy Dispersive X-Ray analysis (EDX) was performed in an electron microscope on the grown substrates and on small platelets used in cutting applications. EDX in Fig.7 shows B/N ratio consistent with the presence of boron nitride on the commercial sample as well as the diamond and silicon substrates confirming that BN was grown over the entire surface. The surface morphology as measured in both the optical and electron microscopes was smooth. The AFM images in Fig.8 depict the surfaces of specimens grown on both diamond and silicon substrates. The surface roughness is measured at 7.5nm for cBN on diamond and 6.1nm on silicon, respectively. Additional measurements and growth of cBN on clear diamond substrates (reduced nitrogen content) will be presented.

03:15 PM

Assessing the quality of h-BN single crystals by metal-flux method for developing phosphors for deep-UV AC-driven powder electroluminescent devices (Student)

Mr. Weiqiang Yuan[1], Dr. Wojciech Jadwisienczak[1]
[1]Ohio University

Hexagonal Boron Nitride (h-BN) has a wide bandgap (~5.8 eV) and is considered a promising material for deep-UV (DUV) light generation [1]. Our previous studies showed that h-BN and its 2D nanosheets have the potential to become an effective phosphor material for DUV AC-driven powder electroluminescent devices (ACPEL) [2]. This study extends our previous findings and emphasizes the assessment of selected commercial h-BN powders for the synthesis of single h-BN crystals using the metal flux method. In this

context, we synthesized h-BN crystals via the Ni-Cr metal flux method under atmospheric pressure [3][4]. The ratio between the chromium (Cr) and nickel (Ni) is 0.53:0.47 which is near the eutectic point. The mixture of Cr and Ni powders was placed above pre-baked excessive commercial h-BN powder in a hot-pressed BN crucible. The whole assembly was loaded into the MTI GSL1700X high-temperature furnace.
The furnace was heated up to 1600 °C, then kept at this temperature for 24 hours with flowing ultra-high purity nitrogen (UHP) to allow h-BN to dissolve in the Ni-Cr metal flux. Subsequently, the system was cooled to 1200 °C with a cooling rate of 4°C/hour. A film of h-BN grains precipitated on the surface of the Ni-Cr metal alloy chunk. The h-BN crystals were mechanically exfoliated from the metal surface using thermal release tape. The exfoliated h-BN crystallites are colorless, optically transparent, and demonstrate very good optical transmittance. The average lateral diameter of the h-BN crystallite size is around 1mm and has a triangular shape. Moreover, we prepared the commercial h-BN powder pellets and annealed them at 1600 °C with flowing UHP for 5 hours as reference materials.
Both materials (h-BN crystals and reference h-BN powder pellets) were characterized using Raman, FTIR, thermogravimetric analysis (TGA), and temperature-dependent cathodoluminescence (CL). We focused on a comparative analysis of the raw-untreated h-BN powders, annealed h-BN pellets, and h-BN single crystals for achieving a high-quality phosphor for developing ACPEL devices. The outcomes of FTIR and TGA show that both powder and single-crystal samples contain carbon and oxygen impurities. The Raman shifts reveal a substantial enhancement of the h-BN crystals morphology as evidenced by a notable reduction in full-width at half-maximum (FWHM) from 10.51 cm^{-1} to 9 cm^{-1} for the 1365 cm^{-1} peak position as compared to the raw commercial powders. CL spectra of the heat-treated h-BN pellets exhibit a wide band luminescence spanning from 250 nm to 650 nm, devoid of any near band-edge emission down to 15 K. Conversely, the h-BN single crystals exhibit a dominant excitonic emission band centered at 228 nm accompanied by a defect/impurity band spanning ~245 nm to 400 nm. The temperature-dependent CL demonstrated that the defect emission band intensity was reduced by 90% when the sample temperature dropped from 300 K to 15 K. Finally, the similarity between the CL and electroluminescence excitation mechanisms let us use the CL as a gauge for developing a feedback loop between h-BN single-crystal metal-flux synthesis parameters and h-BN crystal-quality control essential for optimizing h-BN phosphor development for constructing deep-UV emitting ACTEL devices.
References: [1] K. Watanabe et al. Direct-bandgap properties and evidence for ultraviolet lasing of hexagonal boron nitride single crystal, Nature Mater, 3/6, 404–409, (2004). [2] W. Yuan et al., Design of Novel Deep Ultra-Violet ac-Driven Electroluminescence Devices Based on Boron Nitride nano-Materials, MRS Advances, 5/8–9, 421–430, (2020). [3] T. B. Hoffman et al., Optimization of Ni–Cr flux growth for hexagonal boron nitride single crystals, J. Crys. Grow., 393, 114–118, (2014). [4] Y. Kubota et al., Hexagonal Boron Nitride Single Crystal Growth at Atmospheric Pressure Using Ni−Cr Solvent, Chem. Mater., 20/5, 1661–1663, (2008).

03:30 PM
Charge distribution and transport coefficients of mobile holes in gated diamond heterostructures.
Dr. Sergey Rudin[1], Dr. Greg Rupper[1], Dr. Mahesh Neupane[1], Dr. Glen Birdwell[1], Dr. Tony Ivanov[1]
[1]U. S. Army Research Laboratory

The physical characteristics of diamond, such as high thermal conductivity of 23 W/cmK and high breakdown field of 13 MV/cm suggest that diamond is a promising semiconductor material for high power operation. A high carrier concentration of up to 1014 cm-2 in two-dimensional hole gas formed at a hydrogenated diamond surface by the mechanism of transfer doping is achievable [1], and high-performance diamond transistors based on the hydrogenated diamond channel were demonstrated in the past [2]. Additionally, an optical phonon energy in diamond results in suppression of optical phonon scattering and, consequently, in a very large momentum relaxation time limited by optical phonon scattering, opening a possibility of high-quality plasma resonance [3]. The goal of this work is to explore the transport properties of diamond based quasi-two-dimensional conduction channels formed at the hydrogenated diamond surfaces and at the interfaces of diamond/gate dielectric heterostructures, to enable modeling and characterization of diamond transistors. In thermal equilibrium for given distribution of acceptors and the gate voltage the distribution of mobile carriers (holes) is found by solving coupled Poisson and Schrodinger equations. The band parameters and valence band alignments used in our work were found from performing DFT calculations. The 2D density of mobile holes was calculated as a function of the gate voltage with the given acceptor density. For an example, the mobile hole density as a function of the gate voltage, and the threshold gate voltage as a function of the gate dielectric thickness are shown in Fig. 1 for the Al2O3/diamond heterostructure with the acceptor surface density of 8*1013 1/cm2. The mobile charge distribution n(z) where z is the distance from the diamond/dielectric interface is shown in Fig. 2 for two values of gate voltage and various dielectric thicknesses. At higher negative gate voltages the holes tunnel into dielectric thus degrading the conduction channel and promoting the gate leakage current.
In higher mobility channels subject to moderate electric fields a hydrodynamic model allows a convenient scheme for analysis of charge transport under both constant and high frequency electric fields. To apply hydrodynamic model, we evaluated relevant carrier relaxation times and obtained the temperature and density dependent transport parameters, such as carrier mobility, 2D Fermi gas viscosity, and thermal conductivity. The results for carrier mobility are illustrated in Fig. 3. The effect of Coulomb scattering of mobile holes by fixed negative charges on hole mobility μ was evaluated using dielectric FET model of gate dielectric/p-diamond interface. We find weak dependence on channel-to-gate distance d, but strong dependence on channel-to-fixed charges distance di. We also evaluated the effect of the carrier scattering by the polar dielectric phonons at the diamond/dielectric interface on mobility. In high carrier density channels, we find that the scattering by the interface phonons is weak due primarily to the Pauli blocking in the final states available for the scattered mobile charge carriers. At the carrier density of 1014 1/cm2 the Fermi en0rgy is 443 meV, and the mobile carriers at room temperature are to be treated as a strongly degenerate Fermi gas. We have also

obtained an analytical approximation for the viscosity and heat conductivity that can be conveniently used in the numerical solutions of hydrodynamic model equations to study the current and voltage response of the gated diamond channel to the high frequency electric field. In the modeling of transport in the strongly non-equilibrium case by MC simulation the relevant scattering processes and band structure effects were included.

[1] D. Ruzmetov, J. Weil et al. “RF Performance of Diamond Transistors”, Proceedings of Government Microcircuit Applications and Critical Technology Conference GOMAC 2023

[2] T. G. Ivanov, J. Weil, P. B. Shah, A. G. Birdwell, K. Kingkeo, and E. A. Viveiros, “Diamond RF transistor technology with ft=41 GHz and fmax= 44 GHz,” IEEE MTT-S Int. Microw. Symp. Dig., Philadelphia, PA, USA, Jun. 2018, pp. 1461–1463.

[3] M. Shur, S. Rudin, G. Rupper, and T. Ivanov, "p-Diamond as a candidate for plasmonic terahertz and far-infrared applications," Applied Physics Letters, vol. 113, no. 25, p. 253502, 2018. DOI: 10.1063/1.5053091

03:45 PM

Epitaxial AlN film with improved quality on Si (111) substrates realized by boron pretreatment via MOCVD

Mr. Mingtao Nong[1], Prof. Chehao Liao[1], Dr. Xiao Tang[1], Dr. Haicheng Cao[1], Mr. Tingang Liu[2], Mrs. Patsy Miranda Cortez[2], Mr. Dhanu Chettri[1], Mr. Glen Isaac Maciel Garcia[1], Prof. Xiaohang Li[1]

[1]King Abdullah University of Science and Technology, [2]Advanced Semiconductor Laboratory, Electrical and Computer Engineering program, CEMSE Division, King Abdullah University of Science and Technology, Thuwal 23955-6900, Saudi Arabia.

Nowadays, Aluminum Nitride (AlN), distinguished by its direct-gap semiconductor nature and a wide bandgap (Eg = 6.2 eV), holds significant promise for advancing technologies such as ultraviolet (UV) light-emitting diodes, photodetectors, acoustoelectric devices, high electron-mobility transistors, and various piezoelectric applications.1 Due to the high cost of the native substrate, AlN is commonly grown on foreign substrates, including sapphire, SiC, and silicon (Si), etc. Compared with sapphire and SiC, Si can be a promising alternative for AlN growth owing to its cost-effectiveness, high thermal conductivity, widespread availability, large-scale production feasibility, and potential for integration with other electronics.2 However, the large lattice mismatch of 19% and the coefficient of thermal expansion (CTE) of ~43% between AlN and Si leading to an extremely high density of misfit dislocations (>1010 cm−2) near the AlN/Si interface and cracks of AlN during cooling.3

The study investigated the growth AlN thin films on Si (111) by metal-organic chemical vapor deposition (MOCVD). Through the introduction of triethylboron (TEB) during trimethylaluminum (TMAl) pretreatment4, high-quality nearly crack-free AlN films were acquired, with a thickness of 500 nm. The study compared the growth of AlN films without TEB (sample A) to that with added TEB (sample B) during TMAl pretreatment. The Laytec reflection curves depicted in Figure 1(a) indicate that sample B undergoes a morphological transition from 3D growth to 2D growth during AlN deposition. Notably, Figure 1(b) shows that the curvature of sample B decreases significantly by 20 km-1 during the growth process, indicating a substantial reduction in surface tensile stress. Optical microscopy images in Figure 2 highlight a clear contrast between the two samples; Sample B presents a crack-free surface, while Sample A is marred with cracks. Atomic force microscopy (AFM) images in Figure 3, reveals larger grains on the surface of sample B after TEB introduction, promoting a 3D growth pattern of the subsequent AlN buffer layer. This is beneficial for stress relief and defect reduction during the subsequent AlN growth process, effectively reducing cracks and enhancing crystal quality. X-ray diffraction (XRD) analysis supports this observation. In Figure 4(a) and (b), the full width at half maximum (FWHM) values of (002) and (102) are recorded at 0.22° and 0.36°, respectively, representing the lowest values observed for AlN films grown on planar Si (111) by MOCVD. Furthermore, Figure 4(c) shows that the Raman's E2(high) peak of sample B exhibits a smaller blue shift and narrower FWHM, confirming that adding TEB in TMAl pretreatment effectively mitigates the tensile stress and enhances crystal quality of AlN.

In conclusion, the integration of TEB in the pretreatment during the MOCVD growth of AlN thin films on Si (111) substrates had proven to be a transformative step. The analysis of AFM images, Laytec reflection curves, Raman spectra, and XRD rocking curve FWHM values collectively highlighted the positive impact of TEB on the growth dynamics and structural properties of AlN films. This study not only advanced the understanding of AlN deposition processes but also paved the way for the practical realization of high-quality AlN films with significant implications for advanced electronic and optoelectronic applications.

1. Strite, S.; Morkoç, H., GaN, AlN, and InN: A review. Journal of Vacuum Science & Technology B: Microelectronics and Nanometer Structures Processing, Measurement, and Phenomena 1992, 10 (4), 1237-1266.

2. Feng, Y.; Wei, H.; Yang, S.; Chen, Z.; Wang, L.; Kong, S.; Zhao, G.; Liu, X., Competitive growth mechanisms of AlN on Si (111) by MOVPE. Sci Rep 2014, 4, 6416.

3. Robin, Y.; Ding, K.; Demir, I.; McClintock, R.; Elagoz, S.; Razeghi, M., High brightness ultraviolet light-emitting diodes grown on patterned silicon substrate. Materials Science in Semiconductor Processing 2019, 90, 87-91.

4. Bao, Q.; Luo, J.; Zhao, C., Mechanism of TMAl pre-seeding in AlN epitaxy on Si (111) substrate. Vacuum 2014, 101, 184-188.

2:45 PM
Advances in Thermal Co-Design and Solutions for Wide Bandgap Semiconductors
Session Chair: Samuel Graham (University of Maryland)
ESJ 1202

02:45 PM
Gallium Oxide Epitaxy and Devices For Enhanced Electro-thermal performance
Prof. Sriram Krishnamoorthy[1], Prof. Sukwon Choi[2]
[1]University of California, Santa Barbara, [2]Pennsylvania State University

Leading research institutions and U.S. government laboratories are actively pursuing the development of ultra-wide bandgap (UWBG) semiconductor devices to enable next-generation electric power conversion systems. Devices based on β-phase gallium oxide (Ga_2O_3) offer the potential to achieve higher power switching performance and efficiency than today's wide bandgap (WBG) electronics based on GaN and SiC. Ultimately, UWBG devices promise to improve system-level size, weight, and power (SWaP), and efficiency. However, one of the most critical challenge to the performance of UWBG device technologies is to overcome adverse thermal effects that impact the device performance and reliability.

In this presentation we will discuss an use case of electro-thermal design and realization of beta-Gallium Oxide field-effect transistors on Gallium Oxide/ Silicon Carbide composite substrates. β-phase gallium oxide (Ga_2O_3) is an emerging ultrawide bandgap (UWBG) semiconductor (EG ~ 4.8 eV), which promises generational improvements in the performance and manufacturing cost over today's commercial wide bandgap power electronics based on GaN and SiC. However, overheating has been identified as a major bottleneck to the performance and commercialization of Ga_2O_3 device technologies. In this work, a novel Ga_2O_3/4H-SiC composite wafer with high heat transfer performance and an epi-ready surface finish has been developed using a fusion-bonding method. By taking advantage of low-temperature metalorganic vapor phase epitaxy, a Ga_2O_3 epitaxial layer was successfully grown on the composite wafer while maintaining the structural integrity of the composite wafer without causing interface damage. An atomically smooth homoepitaxial film with a room-temperature Hall mobility of ~94 cm2/Vs and a volume charge of ~3 × 1017 cm–3 was achieved at a growth temperature of 600 °C. Phonon transport across the Ga_2O_3/4H-SiC interface has been studied using frequency-domain thermoreflectance and a differential steady-state thermoreflectance approach. Scanning transmission electron microscopy analysis suggests that phonon transport across the Ga_2O_3/4H-SiC interface is dominated by the thickness of the SiN_x bonding layer and an unintentionally formed SiO_x interlayer. Extrinsic effects that impact the thermal conductivity of the 6.5 μm thick Ga_2O_3 layer were studied via time-domain thermoreflectance. Thermal simulation was performed to estimate the improvement of the thermal performance of a hypothetical single-finger Ga_2O_3 metal–semiconductor field-effect transistor fabricated on the composite substrate. This novel power transistor topology resulted in a ~4.3× reduction in the junction-to-package device thermal resistance. Furthermore, an even more pronounced cooling effect is demonstrated when the composite wafer is implemented into the device design of practical multifinger devices.
We fabricated a Ga_2O_3/4H–SiC composite wafer using a fusion-bonding method. A low-temperature (≤600 °C) epitaxy and device processing scheme was developed to fabricate MOSFETs on the composite wafer. The low-temperature-grown epitaxial Ga_2O_3 devices deliver high thermal performance (56% reduction in channel temperature) and a power figure of merit of (~300 MW/cm2), which is the highest among heterogeneously integrated Ga_2O_3 devices reported to date. Simulations calibrated based on thermal characterization results of the Ga_2O_3-on-SiC MOSFET reveal that a Ga_2O_3/diamond composite wafer with a reduced Ga_2O_3 thickness (~1 μm) and a thinner bonding interlayer (<10 nm) can reduce the device thermal impedance to a level lower than that of today's GaN-on-SiC power switches. These innovations in device-level thermal management give promise to the full exploitation of the promising benefits of the UWBG material, which will lead to significant improvements in the power density and efficiency of power electronics .
We acknowledge funding from NSF Future of Semiconductors (Award 2234479) planning grant. We acknowledge collaboration with Kyma Tech and Modern Microsystems.

03:00 PM
Considerations and Strategies for Gallium Oxide Power Module Packaging
Dr. Christina DiMarino[1], Mr. Benjamin Lyon[2], Mr. Lester Lopez[1], Mr. Boyan Wang[1], Dr. Yuhao Zhang[1]
[1]Virginia Tech, [2]NIST

In the recent years, gallium oxide (Ga_2O_3), has emerged as a viable next-generation device candidate for high-density, high-voltage power electronics with capabilities beyond existing technologies due to its large bandgap, controllable doping, and the availability of large-diameter, relatively-inexpensive substrates. The fundamental limit for high-temperature operation of semiconductors is the concentration of intrinsic carriers, which increases with temperature. Thanks to the ultra-wide-bandgap of Ga_2O_3 (4.8 eV, compared to 1.1 eV for Si, 3.2 eV for SiC, and 3.4 eV for GaN), it achieves over 10-times lower intrinsic carrier concentration than Si. Compared to Si, SiC, and GaN devices, unipolar Ga_2O_3 devices also have superior theoretical limit for the trade-off between on-resistance and breakdown voltage, enabling a higher power conversion efficiency and power density.
While Ga_2O_3 shows promise in these respects, due to its low thermal conductivity (over 10 times lower than that of SiC), conventional packaging and cooling strategies result in greater hot spot effects with higher peak junction temperatures and greater temperature differences across the chip, which could reduce the reliability of the packaged device. However, preliminary studies show that junction-side cooling can offset these effects and result in comparable thermal performance to SiC devices. This suggests that the

packaging approach can aid in alleviating the low-thermal-conductivity concerns of Ga2O3 devices.
Though, to better understand the role of the package on the device performance, new modeling approaches that link the device electro-thermal characteristics with those of the package are needed. The traditional package-level FEA simulation usually assumes a uniform power density and junction temperature in the devices, while neglecting the temperature variations in the sub-micron device structures; this variation can be up to tens of kelvin under high-power device operations. Conversely, the typical physics-based TCAD simulation accurately models the electrothermal behaviors within the device, but simplifies the packaging into a nominal boundary thermal resistance or heat extraction coefficient, neglecting larger packaging elements in the heat flow path (e.g., substrate and baseplate). To better understand the interactions between the device layout and package structures and how their designs affect each other, a proposed co-design modeling strategy was employed. Using this analysis, a half-bridge package was designed with junction-side-cooling for the Ga2O3 diodes and bottom-side-cooling for the SiC transistors. For the junction-side-cooling of the Ga2O3 diodes, a spacer is needed between the anode and the substrate due to the high electric field. The proposed modeling framework was used to analyze the electric field and thermal tradeoffs associated with spacer height, and an optimal post height of 1 mm was selected. Thus far, a half-bridge module prototype has been fabricated with dummy large-area Ga2O3 diodes to verify the packaging processes. Next, half-bridge prototypes with functional large-area Ga2O3 diodes will be fabricated and undergo electrical and thermal characterization. This presentation will review the critical device-package electro-thermal interactions, as well as packaging technologies and approaches that are needed to enable Ga2O3 power modules.

03:15 PM
Enhancing Thermal Transport at Interfaces in Wide Bandgap Electronics
Dr. Henry Aller[1], Dr. Thomas Pfeiffer[2], Prof. Sukwon Choi[3], Prof. Patrick Hopkins[2], [Prof. Samuel Graham][1]
[1]University of Maryland, College Park, [2]University of Virginia, [3]Pennsylvania State University

Wide bandgap semiconductors made from GaN, AlGaN alloys, and Ga2O3 have promise for future rf electronics and power switches. One of the key issues that arises in developing future electronics from these materials is the desire for high power operation which will place more demands on managing the heat dissipation from these devices. This is especially true when using ternary nitride alloys and Ga2O3 since they possess an intrinsically low thermal conductivity. This requires careful design of the device architecture and layout in order to yield effective heat dissipation pathways for wide bandgap semiconductor systems.
In this talk, we will present results on the integration of high thermal conductivity materials with wide bandgap semiconductors as a viable pathway to improve heat dissipation. We will discuss the important role that interfaces play in enabling the integration of materials such CVD diamond, AlN, and SiC while supporting enhanced heat dissipation. We will present results on the use of interlayers to reduce the thermal boundary conductance between diamond and nitride semiconductors. We will demonstrate the important role that surface activated bonding plays in materials integration, providing both improved thermal interfaces between GaN and diamond while lowering stress gradients in the active layers. Finally, we will discuss the improvements in measurement techniques that allow for the characterization of these complex interfaces being developed for advanced nitride and oxide rf and power electronics. The use of a combination of time domain thermoreflectance and steady state thermoreflectance provides a new way of lowering the uncertainty of measuring buried diamond-GaN interfaces.

4:30 PM
Student Finalists Oral Presentation Award – Part A
Session Chair: Parsian Mohseni (Rochester Institute of Technology)
ESJ 0202

04:30 PM
GaAsSb/Si heterojunction photodiodes fabricated with epitaxial layer transfer (Student)
Ms. Manisha Muduli[1], Mr. Yongkang Xia[1], Ms. Sophie Mills[1], Dr. Seunghyun Lee[1], Prof. Shamsul Arafin[1], Prof. Sanjay Krishna[1]
[1]The Ohio State University

Silicon has been widely used in optical communications for data transfer and light detection beyond 1100 nm. However, at the telecommunication and optical communication wavelength (1300 - 1550 nm), III-V materials such as InAs, InGaAs, GaAsSb, etc. surpass the capabilities of Si. Several methods to integrate III-V materials have been studied, including wafer bonding, epitaxial growth, epitaxial layer transfer, and micro-transfer printing. Wafer bonding can impart defects such as voids and cracks in the hetero-structure interface, whereas epitaxial growth of III-V materials on Si can be challenging. Unlike the other techniques, epitaxial layer transfer does not cause interfacial defects in the III-V/Si hetero-structure. In this study, we focus on epitaxial layer transfer of GaAsSb membranes using AlAsSb sacrificial layers to make GaAsSb/Si photodiodes. GaAsSb absorbs in the telecom wavelength of 1550 nm and has a small conduction band offset with Si (<0.1 eV), which favors electron transport between GaAsSb and Si and eliminates the need for a grading layer. These properties make GaAsSb an excellent material for integrating with Si to develop high-speed avalanche photodiodes and receivers with low noise. In this study, we develop the technique to integrate GaAsSb with Si through epitaxial layer transfer. GaAsSb is grown on an InP using molecular beam epitaxy. Mesa structures of the GaAsSb membrane are then epitaxially lifted-off through substrate etching of InP and selectively etching the sacrificial layer of AlAsSb. Further, the GaAsSb mesa membrane is transfer-printed onto a Si

substrate using a poly(dimethylsiloxane) (PDMS) stamp to make the GaAsSb/Si PIN diodes. The quality of the membrane post-transfer was studied through atomic force microscopy. The electronic properties of the PIN diodes were studied with current-voltage and capacitance-voltage measurements. Further, the GaAsSb-Si interface is characterized through simulations and experimentation to quantify the conduction band offset and the sheet charge density at the interface.

04:45 PM
Molecular Beam Epitaxy Selective Area Regrowth of High Aspect Ratio Microstructures for Mid-Infrared Optoelectronics (Student)
Ms. Ashlee Garcia[1], Mr. Byron Aguilar[2], Mr. William Doyle[1], Mr. Yiteng Wang[3], Dr. Daniel Ironside[1], Dr. Alec Skipper[1], Ms. Morgan Bergthold[4], Dr. Minjoo Lee[5], Prof. Daniel Wasserman[4], Prof. Seth Bank[6]
[1]Chandra ECE Department, The University of Texas at Austin, [2]The University of Texas at Austin, [3]University of Illinois, [4]Department of Electrical and Computer Engineering, University of Texas at Austin, Austin, TX 78758, [5]University of Illinois Urbana-Champaign,[6] University of Texas at Austin

A molecular beam epitaxy (MBE) approach to selective area epitaxy (SAE) of III-V semiconductors enables the seamless integration of metals, dielectrics, and high-quality crystalline semiconductors. This technique has the potential to advance novel optoelectronic structures, such as high-contrast photonics, site-controlled quantum emitters, stacked pixel detectors, and photonic integrated circuits. While SAE by metal organic chemical vapor deposition has been widely successful due to its high material deposition selectivity, an SAE MBE method could enable further advances through its high layer precision and access to non-equilibrium growth conditions1,2.
However, MBE SAE has been historically difficult to achieve under conventional growth conditions as a result of its poor III-V deposition selectivity. This leads to an aggregation of adatoms on the amorphous surface which results in the formation of polycrystalline material on the mask surface.2-7 Despite many efforts to expand selectivity by modulating the group-III and -V fluxes2,4,5, modeling growth mechanisms3,6, or utilizing hydrogen-assisted MBE7, the accessible growth window remains quite narrow necessitating high growth temperatures and low growth rates. Successful selective growth techniques rely on minimizing the interaction of the adatoms with the surface of the amorphous structure by enhancing desorption off the mask surface and/or diffusion to the crystal growth window.2-7 For this reason, surface roughness and defects can even further restrict the MBE selective growth regime by lowering the barrier for polycrystal nucleation.8 This presents a particularly challenging barrier for applications requiring microns-tall high-aspect-ratio dielectric structures, such as mid- and long-wave infrared high-contrast photonics9-11 and aspect ratio trapping of threading dislocations for metamorphic growth12, due to the innately rough surfaces produced by plasma-enhanced chemical vapor deposition (PECVD) of thick films.13
To enable fully selective growth of such structures, a MBE-compatible surface restoration technique is required. Hydrogen silsesquioxane (HSQ) is an inorganic flowable oxide that has been utilized to create high quality planar SiO_2 interfaces which are vacuum compatible and stable at high temperatures once cured.14,15 Here we demonstrate HSQ as an effective solution to aid MBE regrowth selectivity for the design of novel device and optical structures by mitigating the surface roughness of micron-scale dielectric features. Integrating the HSQ surface planarization with a 100 nm layer of HSQ in the fabrication of 2 μm tall features demonstrated a significant decrease in film roughness from a root-mean-square roughness of 3.95 nm to 0.98 nm. GaAs selective regrowth of 2 μm tall SiO_2 features fabricated with this approach was performed; a significant improvement in selectivity was observed as compared to the un-planarized features with no polycrystalline material formation on SiO_2 bars <10 μm wide alongside a commensurate 30 increase in achievable feature aspect ratio (1:3 10:1). Experiments are currently underway to extend this approach to regrowth of InAs to access wavelengths in the mid-wave infrared regime and demonstrate the complete encapsulation of high aspect ratio dielectric microstructures via the all-MBE regrowth technique. This work was supported by the National Aeronautics and Space Administration (NASA) through the Quantum Pathways Institute (Award 80NSSC22K0287), the National Science Foundation (ECCS-1926187), and Lockheed Martin.
[1] D.J. Ironside et al., J. Cryst. Growth (2019). [2] F.E. Allegretti et al., J. Cryst. Growth (1995). [3] S.C. Lee et al. J. of Appl. Phys. (2002). [4] Y. Horikoshi. J. Cryst. Growth (1999). [5] S. Yokoyama et al. J. Cryst. Growth (1989). [6] Aseev et al. Nano Lett. 2019. [7] T. Sugaya et al. Jpn. J. Appl. Phys. (1992). [8] M. Ohring, The Material Science of Thin Films, Academic Press (1992). [9] Jun Wang et al. 2017 Laser Phys. Lett. 14 125801. [10] C. J. Chang-Hasnain et al. Adv. Opt. Photon., Sep 2012. [11] S. S. Wang et al. Appl. Opt., May 1993. [12] J.Z. Li et al. Appl. Phys. Lett. 91 (2) (2007). [13] M. R. Amirzada et al. Appl Nanosci (2016). [14] F. Salmassi et al, Appl. Opt. (2006). [15] C.-C. Yang et al., J. Mater. Chem. (2002).

05:00 PM
Shadow Mask Molecular Beam Epitaxy (Student)
Ms. Shagorika Mukherjee[1], Mr. Sai Rahul Sitaram[1], Prof. Xi Wang[1], Prof. Stephanie Law[2]
[1]University of Delaware, [2]Pennsylvania State University

Shadow mask molecular beam epitaxy (SMMBE) is a type of selective area epitaxy (SAE) in which vacuum-deposited films can be patterned via a mechanical mask without the need for etching. Provided the mask is not a source of contamination itself and is adjacent to the substrate, epitaxial layers may be sequentially deposited on the substrate through holes in the mask. One unique feature of SMMBE is its shadowing effect that appears near the mask edges, causing the elemental fluxes to vary as a function of position. This gives rise to a gradient of film thickness and/or composition near the edges of the mask. By varying the mask thickness and/or the angle of the mask edges, this gradient can be controlled. In this work, we exhibit the potential of SMMBE to construct in-plane gradient permittivity materials (GPMs) by leveraging its shadowing effect.
The permittivity varies in a GPM as a function of position, making GPMs useful for a variety of applications. Our goal is to fabricate in-plane GPMs in which the permittivity varies

horizontally in the plane of the material. On an in-plane GPM, different wavelengths of light can be confined at different horizontal locations. Such a material could be used to create an ultracompact on-chip spectrometer. We are interested in working in the infrared regime, so our GPMs are made of heavily silicon-doped InAs, which is known to be a good infrared plasmonic material. By varying the silicon doping density in the plane, we can control the Si:InAs permittivity in the lateral direction. We synthesize such a material using SMMBE with reusable silicon shadow masks. We start with shadow masks that are each 200 µm thick and are 1 cm x 1 cm in size. Each mask has an aperture at its center. The aperture has slanted inner walls, which makes its dimension 0.5 cm x 0.5 cm at the top and 0.528 cm x 0.528 cm at the substrate side. To date, we have studied the influence of several growth parameters in controlling the in-plane permittivity in the GPMs. In comparison to a non-SMMBE growth recipe, we have found that increased quantities of Bi surfactant (2.5x higher) and As (1.5x higher) in the growth recipe of the GPM can significantly minimize poor growth regions around the edges of GPM where the permittivity gradients exist. Nano-FTIR spectrum obtained by scattering-type scanning near-field optical microscopy (s-SNOM) using a mid-IR nano-FTIR module illustrates that the GPMs we have synthesized result in localization and enhancement of different light wavelengths at different locations. The GPM confines infrared light corresponding to wavenumbers ~650 cm-1 to 900 cm-1 over an in-plane distance of ~12 µm, setting the stage for the creation of a spectrometer on a chip.

Next, we were interested in understanding the impact of varying the mask thickness on the GPMs. To do so, we grew samples using masks with thicknesses of 200 µm and 500 µm. We grew three sets of GPMs using three different growth temperatures of 450 °C, 475 °C and 500 °C. Each set comprises of two GPMs, one using a 200 µm thick mask while the other using a 500 µm thick mask. The 500 µm masks have similar dimensions as the 200 µm masks, except the slanted inner walls of the aperture have a measurement of 0.571 cm x 0.571 cm at the substrate side. We found that a growth temperature of 500 °C works well for both in-plane GPMs fabricated using 200 µm and 500 µm masks, significantly minimizing poor growth regions around the edges where the permittivity gradients are and also in the mesa region, delivering shiny samples. The thick mask also provides a longer shadow in comparison to the thin mask, leading to a larger gradient in permittivity over a longer in-plane distance in comparison to the thin mask which provides less shadow. This results in the GPM synthesized by the thick mask to confine light wavelengths corresponding to wavenumbers ~650 cm-1 to 1400 cm-1 over an in-plane distance of ~26 µm, leading to a bigger surface area for the construction of an ultracompact spectrometer. In the future, careful mask design can be used to obtain in-plane GPMs with designer permittivity gradients.

05:15 PM

Bismuth Incorporation into InSb Towards Long-Wave Infrared Photodetectors (Student)

Ms. Corey White[1], Ms. Morgan Bergthold[1], Ms. Amberly Ricks[1], Mr. Felix Estevez Hilario[1], Prof. Daniel Wasserman[1], Prof. Seth Bank[2]
[1]Department of Electrical and Computer Engineering, University of Texas at Austin, Austin, TX 78758, [2]University of Texas at Austin

Sensitive photodetectors operating across the long-wave infrared (LWIR, 8-14 µm) are critical to a number of applications including chemical sensing, astronomical imaging, and thermography. As the incorporation of small concentrations of bismuth into InSb produces dramatic bandgap reductions,1,2 there is a unique opportunity to span the entirety of the LWIR with a bulk III-V alloy that can be grown directly on commercially available III-V substrates, thus circumventing the fabrication, growth, and toxicity challenges plaguing the current state-of-the-art narrow bandgap material system, HgCdTe. InSb1-xBix is a particularly well-suited III-V-Bi alloy for high-performance optoelectronic devices due to (1) the minimal bismuth incorporation necessary to reach the LWIR and (2) the relatively similar ideal growth conditions for InSb and III-Bi materials. To date, InSb-based dilute-bismide alloys exhibit the longest wavelength emission and detection from a lattice-matched III-V alloy3 highlighting the potential of this novel approach for efficient long-wave infrared detection. Recently, we have optimized the growth of InSb1-xBix by molecular beam epitaxy enabling highly substitutional bismuth incorporation and photoluminescence at extended wavelengths beyond that of bulk InSb.4 Building on this foundation, we present room temperature photoluminescence out to 8 µm from InSb1-xBix indicating high optical quality at LWIR wavelengths as well as the first InSb1-xBix nBn photodetector with an extended cutoff wavelength beyond that of InSb. Furthermore, we will show how arsenic incorporation can be leveraged to lattice-match to InSb substrates enabling thick absorbers for strong absorption and carrier collection.

InSb-1-xBix and InAsySb1-x-yBix alloys were grown by solid-source molecular beam epitaxy on InSb substrates under growth conditions targeting a kinetically-limited growth regime similar to that employed for the growth of high-quality GaAs1-xBix.5 A low substrate temperature of ~280˚C and an Sb/III flux ratio of ~0.975× were combined with a relatively fast indium growth rate to kinetically limit bismuth surface segregation during growth. X-ray diffraction, atomic force microscopy, and photoluminescence measurements were performed to quantify the structural and optical properties of the InSb1-xBix films. Room temperature photoluminescence from a 1 µm thick InSb0.98Bi0.02 film exhibited peak emission at 8 µm highlighting both the high optical quality of the InSb1-xBix alloys and how little bismuth incorporation is required to access technologically-important wavelengths in the LWIR.

To demonstrate a prototype InSb1-xBix photodetector, an nBn detector was grown employing a 400 nm thick InSb0.99Bi0.01 absorber and a 50 nm thick Al0.15In0.85Sb barrier. Comparing this detector with an otherwise identical device containing no bismuth, we observed a significant extension in cutoff wavelength at 79 K from 5.5 µm for InSb to 6.6 µm for InSb0.99Bi0.01. From this, we estimate that less than 5% bismuth incorporation is necessary to reach a 14 µm cutoff wavelength, which would enable InSb1-xBix to span the entire LWIR at ~77 K. The InSb and InSb0.99Bi0.01 detectors, which were grown under very similar growth conditions, exhibited similar peak intensities in their spectral responses suggesting that the presence of bismuth within the alloy does not inherently degrade the optical quality of InSb1-xBix materials, which is very

promising for future detectors operating at longer wavelengths.
By also incorporating small quantities of arsenic, the quaternary alloy InAsySb1-x-yBix can be grown lattice-matched to InSb substrates. Furthermore, arsenic incorporation is expected to further assist in decreasing the alloy bandgap energy due to the band bowing between InAs and InSb.6 By incorporating arsenic and bismuth in ~1:3 proportions, we grew an InAsSbBi film lattice-matched to InSb with 1.3% bismuth and 0.4% arsenic incorporation as quantified by X-ray diffraction and Rutherford backscattering spectrometry measurements. From this film, we observed photoluminescence at room temperature at extended wavelengths beyond that of InSb confirming the compatibility of this alloy for high-quality LWIR detectors. Building on this, growth and characterization of optimized detectors with thicker InAsySb1-x-yBix absorbers containing greater bismuth and arsenic concentrations are underway and results will be presented at the conference.
This work was supported by the National Science Foundation (Award No. ECCS-1933836) and an NSF Graduate Fellowship. The work was performed in part at the University of Texas Microelectronics Research Center, a member of the NNCI.

4:30 PM
Student Finalists Oral Presentation Award – Part B
Session Chair: Nadeemulal Mahadik (Naval Research Lab)
ESJ 0224

04:30 PM
Expanded stability of layered SnSe-PbSe alloys and evidence of displacive phase transformation from rocksalt in heteroepitaxial thin films
Ms. Pooja Reddy[1], Prof. Leland Nordin[1], Ms. Lillian Hughes[2], Ms. Anna-Katharina Preidl[1], Prof. Kunal Mukherjee[1]
[1]Stanford University, [2]University of California, Santa Barbara

The IV-VI semiconductor family of PbSe-SnSe alloys spans narrow direct bandgap materials in the Pb-rich cubic rocksalt phase, and indirect bandgap semiconductors in the Sn-rich layered orthorhombic phase. This alloy system hosts a wide array of properties key to next-generation thermoelectrics, infrared optics, ferroelectrics, and most recently for quantum information sciences. Moreover, several research groups have shown a large contrast in electronic and optical properties for phase-change devices across the orthorhombic to rocksalt structural transition that can be driven by temperature and direct application of intense light-fields [1,2]. The development of growth techniques to fabricate high quality thin films of not only SnSe but also Pb1-xSnxSe offers new compositional routes to tune these properties.
We epitaxially integrate thin films of PbSnSe on GaAs by molecular beam epitaxy (MBE), using a Riber Compact 21 system with compound PbSe and SnSe cells. (001)-oriented semi-insulating GaAs substrates are prepared by desorbing the surface oxide under a Se overpressure, followed by a PbSe dose and buffer layer, which results in smooth, out-of-plane single oriented PbSnSe films. The Pb1-xSnxSe alloy composition is varied by changing relative fluxes of the PbSe and SnSe compound cells.
Our MBE grown PbSnSe films show a significantly reduced two-phase region by stabilizing the Pnma layered structure out to Pb0.44Sn0.55Se, beyond the bulk-limit of Pb0.25Sn0.75Se. Pushing composition even more Pb-rich, we directly access metastable two-phase films of layered and rocksalt grains that are nearly identical in composition around Pb0.5Sn0.5Se and entirely circumvent the miscibility gap present in the bulk phase space. We present microstructural evidence for an incomplete displacive transformation from rocksalt to layered structure in these films that we speculate occurs shortly after synthesis as the sample cools down to room temperature. There seem to be well-defined orientation relationships between the phases forming in the process and unconventional strain relief mechanisms involved in the crystal structure transformation revealed by transmission electron microscopy. We will discuss STEM-EDS measurements to explore the possibility of local diffusion at grain boundaries and confirm the lack of compositional contrast between phases.
In-situ temperature dependent x-ray diffraction measurement of as-grown rocksalt PbSnSe films result in a phase transition to the layered phase on cooling, which reproduces key attributes expected of a displacive transition, thus validating our hypothesis. We are able to quantify phase fraction as a function of temperature and see the beginning of a hysteretic behavior in the phase change, where we expect further heating of the sample to revert the transformed sample back to single-phase cubic. Room temperature Hall and UV-Vis spectroscopy show clear property dependence on phase of as grown PbSnSe samples. As expected, cryogenic hall measurements capture this electronic property change with the temperature induced phase change. We see unusually high carrier concentration for the resulting layered phase. This may be a result of the sample retaining Sn vacancies typical to the cubic phase. We plan to verify the hysteretic nature of the phase transition and related properties via heating experiments.

04:45 PM
Lathe-based Aerosol Jet Printing: A New Additive Manufacturing Method for Fabricating Conformal Electronics on 3D Curvilinear Substrates (Student)
Mr. Hansel Hobbie[1], Mr. James Doherty[2], Ms. Brittany Smith[2], Dr. Paolo Maccarini[1], Dr. Aaron Franklin[2]
[1]Department of Electrical & Computer Engineering, Duke University, [2]Duke University

Of the methods available for the additive manufacturing (AM) of electronic materials1,2, aerosol-jet (AJ) printing has proven to be a versatile option for achieving high-resolution, rapid fabrication of multi-material componentry3. AJ printing is capable of producing micron-scale structures and electronics by direct-write deposition of aerosolized inks. Thanks to the jetting nature and large standoff distance of the material deposition, AJ printing has shown particular utility in the areas of flexible and conformal printed electronics4,5. However, the conventional planar AJ printing format becomes limited for substrate geometries that are 3D

and possess non-linear curvature. To overcome these limitations, we engineered a mechanism that upgrades the planar AJ printing process to lathe AJ printing – a custom method that utilizes cylindrical-coordinate orientation to print onto 3D objects of rotation (Fig. 1).
Lathe AJ printing functions by converting the linear motion of the planar printer platen into rotation about a sliding axis, onto which a substrate can easily be mounted and fixed in position underneath the print nozzle. This enables printing with full conformity around the circumference of any rotatable object or film, thus providing a new approach to AJ printing that expands upon current capabilities. The difference between planar and lathe AJ printing approaches becomes apparent when attempting to print a conformal trace onto a cylinder where the inability to change the angle of print incidence in correlation with the curvature of the substrate causes planar printing to fail, whereas lathe printing succeeds (Fig. 2). Deposition of electronics thin films onto increasingly complex rotational objects is shown in Fig. 3, including flat substrates wrapped about a cylinder, concavities, cones, and even directly onto 3D parts. The only limitations of the system are that a substrate must be able to rotate about a given axis and be between 1 and 40 mm in outer diameter for the rotating substrate. To verify that the lathe mechanism could provide the same precision as the planar AJ printing approach, the resolution in the circumferential- (theta-) and axial-directions was tested by measuring the distances between printed microstrips and comparing them to the expected target values (Fig. 4). The almost negligible error between the target and measured pitch values all the way down to 20 µm in either print direction proves the consistent accuracy of the lathe system to planar AJ printing. After successfully prototyping the lathe mechanism, we applied the fabrication method to the unique task of installing electronic sensing capabilities directly on the surface of an esophageal catheter balloon (Fig. 5). Catheter-based electronics present an interesting AM application space but have barely been demonstrated because of the difficulty in fabricating complex designs in a practical way. The ease of fabrication with lathe AJ printing enables simple functionalization of catheters with the broad catalog of electronic materials that AJ printing is capable of depositing. Lastly, to emphasize the robustness of the lathe AJ printing technique, we fabricated electronic devices of conductive traces, capacitors, and multilayer thin-film transistors (TFTs). For the TFTs, three carbon-based materials were used – graphene, cellulose nanocrystals (CNC), and carbon nanotubes (CNTs)6. Together, these materials form fully printed CNT-TFTs, which make a completely eco-friendly, recyclable transistor when fabricated on paper (Fig. 6).
Ultimately, the work that we are presenting ranges from a full description of the lathe AJ printing mechanism and method to a complete characterization of the system's mechanical performance. Lathe AJ printing has clear implications for expanding the scope of application for AM of electronic materials as we demonstrate for fully printed electronics and catheter-based electronic sensing. Additionally, because of the versatility and scalability of the presented solution, there is potential for unlocking even more application spaces using lathe AJ printing.

05:00 PM
Heteroepitaxial Integration of Embedded Visible InP Quantum Dot Lasers on SiN/Si Photonic Integrated Circuits (Student)
Mr. Yiteng Wang[1], Dr. Christopher Heidelberger[2], Dr. Jason Plant[2], Dr. Cheryl Sorace-Agaskar[2], Dr. Dave Kharas[2], Dr. Pankul Dhingra[1], Dr. Paul Juodawlkis[2], Dr. Minjoo Lee[1]
[1]University of Illinois Urbana-Champaign, [2]MIT Lincoln Laboratory

Heterogeneous integration of visible lasers with low-loss SiN waveguides is attractive for on-chip photonic applications such as quantum computing, biosensing and displays.1-3 Direct epitaxial growth of III-V devices on complementary metal–oxide–semiconductor (CMOS)-compatible SiN/Si photonic integrated circuits (PICs) leverages the maturity of Si manufacturing with the potential for high-density integration of optical gain. Quantum dots (QDs) are a promising gain medium for semiconductor lasers on Si substrates due to their great dislocation tolerance, thermal stability, and optical feedback immunity.4-5 Recently, several groups have demonstrated near- to mid-infrared III-V lasers on patterned Si PICs by direct epitaxial growth.6-8 We earlier proposed a scheme for butt-coupling III-V gain, detection, and modulation with SiN passives with the III-V devices grown in pockets.9 In this work, we demonstrate the first visible-spectrum InP QD lasers directly grown on SiN/Si PICs with room-temperature (RT), continuous-wave (CW) operation at low threshold current density and mW-level power output.
The PIC structure consists of SiN waveguides and SiO_2 clads with a total thickness of 6 µm, fabricated at Lincoln Laboratory on 200 mm Ge-on-Si (001) with a 6° offcut and a threading dislocation density of ~2-3×107 cm-2. After cutting into coupons, metal-organic chemical vapor deposition (MOCVD) was used for selective growth of a 3.2 µm n-GaAs buffer in dry-etched pockets that expose the surface of the Ge layer. The coupons are then transferred to UIUC for non-selective molecular beam epitaxy (MBE) growth of InP QD lasers. Post-growth rapid thermal annealing (RTA) was performed at 850 °C for 4 minutes to improve the optical quality of the active region without damaging the Ge layer (Tmelt, Ge = 937 °C). The polycrystalline layer on top of the SiO_2 was removed by a combination of dry and wet etching before Fabry-Perot edge-emitting laser fabrication. Next, narrow ridges (2.6 – 9.6 µm wide, ~ 3 µm tall) were defined by Cl-based ICP-RIE etching, with their sidewalls passivated by PECVD-deposited SiO_2. Lastly, contact metals were deposited, and the sample was manually cleaved into 4 mm long Fabry-Perot lasers for device testing.
Micro-photoluminescence (micro-PL) shows the QD emission at ~740 nm after RTA, and Nomarski images confirm there is no cracking or other RTA-induced damage. The RT CW light-current (L-I) measurements show threshold current densities of 580 and 750 A/cm2 for 2.6 and 4.6 µm-wide ridge lasers, respectively; the 2.6-µm ridge laser reaches 10 mW output from a single facet. Overall, the performance of the embedded narrow-ridge lasers is comparable to our previous broad-area lasers on unpatterned GaAs/GaP/Si (threshold of 670 A/cm2 with > 10 mW output power)10. T-dependent L-I testing shows CW lasing up to 50 °C with characteristic temperature T0 = 51 K. With the demonstration of visible lasers grown within SiN PICs, future work will focus on efficient butt-coupling of the

laser light into SiN waveguides to enable on-chip visible light applications.
[1] J. Wang et al. Nat. Photonics 2020, 14 (5), 273–284.
[2] K. De Vos et al. Opt. Express 2007, 15 (12), 7610.
[3] H. Hamada et al. Fiber and Integr. Opt. 2015, 34 (5–6), 259–281.
[4] P. Dhingra et al. Appl. Phys. Lett. 2020, 117 (18), 181102.
[5] H. Huang et al. APL Photonics 2020, 5 (1), 016103.
[6] C. Shang et al. Light Sci. Appl. 2022, 11 (1), 299.
[7] W. Wei et al. Light Sci. Appl. 2023, 12 (1), 84.
[8] A. Remis et al. Light Sci. Appl. 2023, 12 (1), 150.
[9] C. Heidelberger et al. 2021 IEEE Photonics Conference (IPC), 2021, pp 1–2.
[10] P. Dhingra et al. Optica 2021, 8 (11), 1495.

05:15 PM
Exploring Form and Functionalization in Crystalline Nanocellulose Inks for Environmentally Sustainable Printed Electronics (Student)
Ms. Brittany Smith[1], Mr. Nicolas Chen[1], Mr. James Doherty[1], Dr. Aaron Franklin[1]
[1]Duke University

Printed flexible electronics show promise for providing a sustainable solution to the increasingly negative impact of electronics manufacturing and waste1. However, current print processes and inks tend to rely on hazardous solvents, extensive post-processing at high temperatures, and/or materials that are not recyclable or biodegradable. Recent work on water-based inks from nanomaterials shows that these challenges can be overcome (i.e., no hazardous chemicals, relatively low temperature processing, and all recyclable or biodegradable materials), but the resultant devices still require improvement in performance and reproducibility2,3. In this work, we investigated two new water-based inks for use in printed carbon nanotube (CNT) thin-film transistors (TFTs): nanocellulose, a biodegradable ionic dielectric, and nanoparticle gold, a recyclable conductor. We developed inks and aerosol jet printing processes for crystalline nanocellulose (CNC) and cellulose nanofibrils (CNF) with various surface modifications, including sulfate, carboxylmethylate (CM), and 2-2-6-6 tetramethylpiperidine 1-oxyl mediated oxidation (TEMPO), to gain insights into the working mechanisms of nanocellulose as an ionic dielectric. Our results reveal that the general ionic nature of the printed films is invariant with the nanostructure form or surface group through capacitor measurements, showing CNF-TEMPO yields the highest capacitance of the six types studied (Fig. 1A-C). Further, we investigated the influence of the sulfonic surface group content on capacitor performance, revealing that the sulfonation content has minimal impact on the dielectric performance. Each nanocellulose type was demonstrated as the gate dielectric for fully printed top-gated CNT-TFTs with low operating voltages (Fig. 1D-E). The average subthreshold swing (SS) of each nanocellulose type falls within 200 – 300 mV/dec, with CNC-DS (de-sulfated) devices having the lowest average SS of all the types at 224 mV/dec (Fig. 1F). For all nanocellulose types, the average off-current was below 0.05 μA/mm, the average on-current above 1 μA/mm, and the average on/off-current ratio was above 100 with CNC-DS, CNC-Reg, and CNF-CM showing the best performance (Fig. 1G). Since nanocellulose breaks down under high temperatures, the top-gate contact must be conductive with minimal post-processing to form fully printed CNT-TFTs. Therefore, as an alternative to using graphene, a novel gold ink formulation was used as the contacts for CNT-TFTs since it is a well-known recyclable material with a high market demand4. This new ink exhibited a resistance of ~5 Ω after a 1-hour sinter at 250 °C and improved the on-current and transconductance of the CNT-TFTs when compared to the graphene electrode devices (Fig. 1H-K). The impressive device performance of these printed CNT-TFTs shows promise for the use of water-based inks in environmentally sustainable printing of electronics.
1. Chandrasekaran, S., Jayakumar, A. & Velu, R. Nanomaterials vol. 12 4251 (2022).
2. Lu, S., Smith, B. N., Meikle, H., Therien, M. J. & Franklin, A. D. Nano Lett. 23, 2100–2106 (2023).
3. Williams, N. X., Bullard, G., Brooke, N., Therien, M. J. & Franklin, A. D. Nat. Electron. 4, 261–268 (2021).
4. Valayil Varghese, T. et al. ACS Mater. Au 4, 65-73 (2023).

6:00 PM
Welcome Reception and Poster Session
ESJ Building, Ground Floor

MXene-contacted Carbon Nanotube Thin-film Transistors Using Aerosol Jet Printing (Student)
Ms. Baiyu Zhang[1], Dr. Aaron Franklin[2], Mr. Hansel Hobbie[1], Dr. Yizhang Wu[3], Dr. Wubin Bai[3]
[1]Department of Electrical & Computer Engineering, Duke University, [2]Duke University, [3]Department of Applied Physical Sciences, The University of North Carolina at Chapel Hill

Low-cost additive manufacturing has garnered considerable research attention for electronic device applications due to its versatility and rapid turnaround time. Specifically, aerosol jet printing (AJP) is a low-cost fabrication technique with many demonstrated uses, including for printing ink suspensions of low-dimensional nanomaterials. Printing electronics using nanomaterials shows great promise for applications in biosensing, IoT devices, and flexible/wearable electronics [1]. However, the printing of nanomaterial-based devices, such as thin-film transistors (TFTs), still faces multiple challenges, including the difficulty of forming uniform, low-resistance contact interfaces and the need for processing printed devices without reliance on high-temperature sintering. In the emerging MXenes family of nanomaterials, Ti3C2Tx is the most extensively studied given its remarkable electrical and mechanical properties. However, the fabrication of MXene thin films using AJP, as well as their potential application as contact electrodes for aerosol-jet printed TFTs, remains largely unexplored [2, 3]. Ti3C2Tx is an ideal candidate as an electrode material due to its high mechanical strength and metallic conductivity. Moreover, thanks to its nature as a two-dimensional material, Ti3C2Tx holds promise in mitigating Fermi-level pinning

caused by conventional metal electrodes, thereby reducing contact resistance [4].
In this work, we demonstrate the successful fabrication of MXene-contacted carbon-nanotube (CNT) TFTs using AJP and a water-based Ti3C2Tx ink. The impact of printing parameters on the resultant film morphology, thickness, and resistivity was explored. Printed thin films of Ti3C2Tx with a varying number of printing passes are shown in Fig. 1a. Scanning electron microscopy (SEM) images taken at

different magnifications reveal the surface morphology of the films, which exhibit a flake-like structure at the microscale. Profilometry measurements of surface roughness for films printed using 1, 2, and 3 passes are shown in Fig. 2. To better understand the impact of printing conditions on film conductivity, a series of experiments were performed to investigate changes in sheet resistance using different substrate materials, printing temperature, and post-printing treatment. As shown in Fig. 3a, the substrate material did influence the resultant thin-film sheet resistance, with glass yielding the highest and parylene the lowest resistance. This substrate-dependent variation is attributed to the hydrophobicity of substrate surfaces and the heat conduction of different substrates when the platen was heated during printing. As expected, the sheet resistance of Ti3C2Tx decreased with an increase in printing passes, as more passes created thicker and more continuous films. The impact of printing temperature (during printing) on sheet resistance was also studied by varying the platen temperature from 20°C to 60°C. Since aqueous ink was used, heating the platen enabled accelerated evaporation of the water in the deposited ink solution. The rapid evaporation resulted in the removal of water molecules intercalated between Ti3C2Tx flakes and a decrease in sheet resistance. Interestingly, when a sample was heated in an oven to sinter at 120°C for 30 minutes after printing, the trend originally observed for the impact of platen temperature on sheet resistance was reversed (see Fig. 3b). Although all samples exhibited a decrease in sheet resistance post-sintering, the sample originally printed on a hot platen showed a higher sheet resistance compared to the sample printed on a room-temperature platen. CNT-TFTs with a substrate-gated structure and Ti3C2Tx source and drain contacts were successfully fabricated by first printing Ti3C2Tx electrodes then the CNT thin-film channel (Fig. 4a, b). As seen in the subthreshold and output characteristics of Fig. 4c, the on-current reached 11.7 μA/mm and the on/off-current ratio reached nearly 4 orders of magnitude. This initial experiment demonstrated a 100% yield in the fabrication of CNT-TFTs with MXene contacts, indicating that Ti3C2Tx holds significant potential as a suitable ink material for fully printed device fabrication. The successful fabrication of a water-based MXene ink and the demonstration of the use of MXenes as a CNT-TFT electrode material opens up new avenues of exploration for printed electronics.
[1] S. Lu and A. D. Franklin, “Printed carbon nanotube thin-film transistors: progress on printable materials and the path to applications,” Nanoscale, vol. 12, no. 46, pp. 23371–23390, 2020, doi: 10.1039/D0NR06231F.
[2] H. Vadakke Neelamana, S. M. Rekha, and S. V. Bhat, “Ti3C2Tx MXene: A New Promising 2D Material for Optoelectronics,” Chem. Mater., vol. 35, no. 18, pp. 7386–7405, Sep. 2023, doi: 10.1021/acs.chemmater.3c01660.
[3] [1] M. Borghetti, M. Serpelloni, E. Sardini, D. Spurling, and V. Nicolosi, “Temperature influence on Ti3C2Tx lines printed by aerosol jet printing,” Sensors and Actuators A: Physical, vol. 332, p. 113185, Dec. 2021, doi: 10.1016/j.sna.2021.113185.
[4] Z. Wu, S. Liu, Z. Hao, and X. Liu, “MXene Contact Engineering for Printed Electronics,” Advanced Science, vol. 10, no. 19, p. 2207174, Jul. 2023, doi: 10.1002/advs.202207174.

TOWARDS P3HT INKJET PRINTABILITY OF SENSORS (Student)

Mr. Jesus Marquez[1], Ms. Abigail Linhart[2], Dr. Michael Kilbey[2], Dr. Robert Roberts[1]
[1]The University of Texas at El Paso, [2]The University of Tennessee, Knoxvile

Here we propose a method to inkjet print sensors using poly(3-hexylthiophene) (P3HT) and present data that demonstrates the printability potential of this material. P3HT is a semiconducting polymer that is usually used as a hole transport material in the fabrication of transistors and solar cells. There is a desire to transpose this technology to inkjet printing to ease the fabrication and testing of semiconducting polymer-based devices. However, there has been little success in the inkjet printing of P3HT due to the lack of key information such as viscosity and surface tension and the additional issues of using a strong solvent to dilute P3HT. In this work we propose a method to inkjet print P3HT sensors using a commercially available inkjet printer. This method is reinforced with properties obtained from measurements of viscosity and surface tension.
A long shelf life, safe material compatibility, and low gelation and aggregation are desired characteristics to achieve simpler and more efficient inkjet printing with conjugated polymers like P3HT. Unfortunately, prior work has not achieved a solution that satisfies the three points mentioned above. In [1], an inkjet printed P3HT layer using compliant o-Xylene as the solvent achieved a long shelf life or low gelation, but not both. In [2], several high boiling solvents were used to fabricate a transistor, but these were complicated by issues of shell life or gelation, too. The main issue that prevents P3HT printability is the requirement for a compliant set-up that can handle strong organic solvents.
A Brookfield DVE Viscometer was used to measure the viscosity of solutions comprising 50 mg of P3HT in 66 ml chlorobenzene at 18.5°C. The surface tension values were obtained at the same temperature and scaled in proportion to the certified values used in the industry. A MicroFab Technologies Jetlab 4 – Tabletop printer was used to test the printability of water, due to it having a similar viscosity and surface tension compared to the P3HT solution.
Surface tension (between 20 to 70 mN/m) and viscosity (below 20 mPa s) both fall between the required values to inkjet print the solution using a 30 μm micro dispenser. Profilometry measurements verify the presence of polymer at low P3HT concentrations, and the thickness can be tuned by increasing the P3HT concentration in solution. Finally, due to the similarities of the P3HT solution and water, a simple calibration based on inkjet printing of water is necessary to enable inkjet printing of P3HT solutions. These results suggest that the printability of P3HT is achievable with the proper replacement of non-compliant materials that would be in contact with chlorobenzene. This work unlocks

another way to print sensors or other organic electronic devices as an alternative to regular deposition techniques.
Word Count: 448 words
This work was sponsored by Honeywell FM&T. Honeywell Federal Manufacturing & Technologies, LLC operates the Kansas City National Security Campus for the United States Department of Energy / National Nuclear
Security Administration under Contract Number DE-NA0002839

Resolving Complex Surface Engineering Challenges by Taguchi Design of Optimization of Electroless Nickel Coating Parameters on Additively Manufactured Binder Jetted Composites* (Student)
Mr. Andrew Grizzle[1], Dr. Amy Elliott[2], Mr. Pablo Sanchez[1], Dr. Pawan Tyagi[3]
[1]University of the District of columbia, [2]Oak Ridge National Laboratory, [3]University of the district of Coulombia

Binder jetting is an economical and rapid additive manufacturing process that offers vast opportunities to combine a variety of materials, yielding interesting and valuable properties. However, binder-jetted parts, which can involve at least one hard and one soft material, can be more susceptible to corrosion and wear-like damages as compared to conventional single alloy components produced by laser sintering or other high-temperature processes. Electroless nickel plating is a well-known coating technique that provides high corrosion resistance and hardness and is suitable for resolving issues caused by multiple components of the parent material. This paper discusses the electroless nickel plating on Binder-Jetted Composites (BJC's) composed of 420 stainless Steel and bronze. We utilized the Taguchi Design of the Experiment method to understand the role of processing parameters that enable high-quality and smooth electroless nickel plating (Table 1). We statistically investigated the role of surface finishing methods, phosphorus content, temperature, and time for the production of smooth and substantial deposition. Optical microscopy was performed for qualitative and quantitative analysis of the surface finish and coating properties. We also performed SEM to investigate the microstructures of the different electroless coatings on BJCs (Fig. 1). Interestingly, all the combinations of parameters used in the electroless nickel plating produced different microstructures, as shown in Fig.1a-c. We found that surface preparation was a critical factor in determining the smoothness of the film. We also showed that the thickness of the nickel plating was mainly dependent on the Ni solution's phosphorus level and temperature. Our research provides fundamental insights for improving the usefulness of a wide variety of BJCs composed of drastically different components by employing application environment-specific coatings.

Machine Learning-Enabled Quantitative Analysis of Optically Obscure Scratches on Nickel-Plated Additively Manufactured (AM) Samples
Ms. Betelhiem Mengesha[1], Mr. Andrew Grizzle[1], Mr. Wondwosen Demisse[2], Dr. Kate Klein[2], Dr. Amy Elliott[3], Dr. Pawan Tyagi[4]
[1]University of the District of columbia, [2]University of the District of Columbia, [3]Oak Ridge National Laboratory, [4]University of the district of Coulombia

Additive manufacturing(AM) is increasingly becoming useful to create innovative shapes and designs and produce innovative materials. Binder jetted AM process can produce hard and soft phases of metals to yield creative material solutions for thermal management promising for the microelectronic systems. Additively manufactured metal components often have rough and uneven surfaces, necessitating post-processing and surface polishing. Hardness is a critical characteristic that affects overall component properties, including wear. This study employed K-means unsupervised machine learning to explore the relationship between the relative surface hardness and scratch width of electroless nickel plating on additively manufactured composite components. The Taguchi design of experiment (TDOE) L9 orthogonal array facilitated experimentation with various factors and levels[1]. Initially, a Keyence light microscope was used for 3D surface mapping and scratch width quantification. However, the microscope struggled with the reflections from the shiny Ni-plating and small scratches. To overcome this, a scanning electron microscope (SEM) generated grayscale images and 3D height maps of the scratched Ni-plating, thus enabling the precise characterization of scratch widths (Fig.1). Optical identification of the scratch regions and quantification were accomplished using Python code with a K-means machine-learning clustering algorithm. The TDOE yielded distinct Ni-plating hardness levels for the nine samples, while an increased scratch force showed a non-linear impact on scratch widths. The enhanced surface quality resulting from Ni coatings will have significant implications in various industrial applications, and it will play a pivotal role in future metal and alloy surface engineering.
Keywords: unsupervised machine learning; K-means clustering; additive manufacturing; nickel plating; hardness; scratch width
References
[1] B. N. Mengesha, A. C. Grizzle, W. Demisse, K. L. Klein, A. Elliott, and P. Tyagi, "Machine Learning-Enabled Quantitative Analysis of Optically Obscure Scratches on Nickel-Plated Additively Manufactured (AM) Samples," Materials, vol. 16, p. 6301, 2023.

Investigating the Role of Machine Learning and Deep Learning for Determining the Performance of Perovskite-Based Solar Cells (Student)
Mrs. Srabanti Datta[1], Mr. Gobinda Chandra Sarker[2], Mr. Anik Baul[3], Mr. Mahir Abrar[1], Dr. Deidra Hodges[1]
[1]Florida International University, [2]University of Dhaka, [3]Central Michigan University

Solar energy is a promising source of renewable energy, but its low efficiency, instability, and high manufacturing costs remain a big challenge. Recently, machine learning (ML) techniques have gained attention in the photovoltaic (PV) sector because of advances in computer power, tools, and data creation. In this research paper we have implemented both ML technique and Deep Learning (DL) technique. The main goal of our work is to find out, how DL techniques perform to predict the performance of perovskite solar cells (PSCs). Our result shows that DL methods can be used for this research field after preprocessing the dataset finely. Though, ML algorithm performed better than the DL technique, there is a very big opportunity of DL in this sector.

Graphical User Interface and Data Visualization for Monte Carlo-based simulation of Molecular Tunnel Junction Spintronics Devices

Mr. Christopher D'Angelo[1], Dr. Pawan Tyagi[2], Mr. Robert Juliano[1], Mr. Antwan Russell[3], Mr. Clarence Alexander[3], Mr. Andrew Grizzle[3]
[1]University of the District of Columbia, [2]University of the district of Coulombia, [3]University of the District of columbia

We are working on adding a Graphical User Interface (GUI) including data visualizations to our previous Monte Carlo-based Simulation software used for modeling Molecular Tunnel Junction Spintronics Devices (MSDs). The software currently allows for the simulation of MSDs with a wide range of materials and molecules through the use of 60+ parameters including device geometry, Heisenberg direct exchange coupling (J), biquadratic coupling (b), Dzyaloshinsky–Moriya skyrmion interaction (DMI), and more. This MSD software has produced many insights about the wide range of experimentally observed phenomena on magnetic tunnel junction-based molecular devices[1, 2]. However, this software is currently only usable via an unintuitive interface, making it a considerable investment of time and effort to train new users, and a less-than-optimal educational tool. To date, we obtained magnetic properties at each atomic site and shape after completing full simulation and by doing post-analysis using a secondary program (Fig.1). The equilibrium magnetic moment of each magnetic layer is governed by the nanoscale material present between them along with a large list of variables. We have completed preliminary work in GUI preparation and real-time simulation data analysis (Fig. 2). We are able to generate simulation models and also quickly study the spatial regions where change in a specific simulation parameter is likely. Our team is in the process of designing a GUI interface that will aim to reduce user errors, lower the learning curve for new users, allow the software's user base to include younger high school students, and professionals outside the expert group, and all without appreciably impacting runtime performance.

[1] P. Tyagi, H. Brown, A. Grizzle, C. D'Angelo, and B. R. Dahal, "Molecular coupling competing with defects within insulator of the magnetic tunnel junction-based molecular spintronics devices," Scientific Reports, vol. 11, pp. 1-13, 2021.
[2] P. Tyagi, C. Baker, and C. D'Angelo, "Paramagnetic Molecule Induced Strong Antiferromagnetic Exchange Coupling on a Magnetic Tunnel Junction Based Molecular Spintronics Device," Nanotechnology, vol. 26, p. 305602, 2015.
[3] Video of the development version of GUI: https://youtu.be/F2lcDAzB1yU?si=EtclW10ddHbD_BH3

Evaluation of Machine Learning Models for Monte Carlo Simulation study of Magnetic Tunnel Junction based Spintronic Devices (MTJMSDs). (Student)

Mr. Andrew Grizzle[1], Mr. Christopher D'Angelo[2], Dr. Pawan Tyagi[3]
[1]University of the District of columbia, [2]University of the District of Columbia, [3]University of the district of Coulombia

This study evaluates the performance of machine learning (ML) models in simulating Magnetic Tunnel Junction based Spintronic Devices (MTJMSDs) through Monte Carlo (MC) simulations. By analyzing the charge transport in paramagnetic single-molecular magnets within MTJ electrodes, the research identifies optimal material characteristics for advanced molecular electronics. Incorporating findings from study on the molecular spin state's influence on magnetic tunnel junctions [1] [2], the MC simulation informed the parametric study of MTJMSDs, focusing on molecular coupling and magnetic properties. The data was analyzed using linear regression, polynomial ridge regression, and random forest regression models, with the latter proving to be the most effective in predicting magnetic properties. This paper underscores the potential of ML models to enhance the accuracy and efficiency of MTJMSD simulations and offers a path toward optimizing spintronic devices.

Influence of Edge-Contact Formation Conditions on Monolayer MoS2 Transistors

Ms. Victoria Ravel[1], Dr. Hattan Abuzaid[1], Dr. Zhihui Cheng[1], Mr. James Doherty[1], Dr. Aaron Franklin[1]
[1]Department of Electrical & Computer Engineering, Duke University

Introduction:
The edge-contact configuration is a promising scheme for realizing maximum scalability of metal-semiconductor contacts in transistors from two-dimensional semiconductors [1], [2]. While most research efforts target channel length miniaturization, reducing contact footprint without compromising performance is just as critical for relevance in future technology nodes [3],[4]. While edge contacts are encouraging for contact-length scaling, there has been limited analysis of the impact of process conditions on the formation of the edge interface. The structure itself necessitates the creation of edge states in the 2D semiconductor, to which the contact metal is connected. Does atmospheric exposure of dangling bonds at the edge of the 2D material prior to metal deposition hamper optimal edge-contact formation? In this work, we present a much-needed analysis of the influence of different edge-contact formation approaches on Ni edge contacts to monolayer chemical-vapor-deposited (CVD) MoS-2 channels. Four different edge-defining strategies are studied: ex-situ reactive ion etch (RIE), ex-situ RIE with in-situ 60 eV Ar-+-ion clean, in-situ 600 eV Ar+ ion etch, and in-situ 600 eV Ar+/N2+ ion etch.
Device Fabrication:
The transistors in this study were fabricated using standard electron beam lithography (EBL) to pattern the contact region, RIE plasma and/or convergent ion beam to define and etch the MoS2 in the contact region (Fig. 1A), and electron-beam (e-beam) metal evaporation to deposit the metal contacts (Fig. 1B). The devices were imaged using a cross-section STEM to confirm the edge-contact interface and monolayer thickness of the MoS2 (Fig. 1C). Since the MoS2 covers the entire substrate, individual channel segments were patterned using polymethyl methacrylate (PMMA) 950k as an etch mask. The four types of edge-formation processes were fabricated sequentially as seen in Fig. 1D (first to last is left to right). The in-situ devices were physically etched with an Ar+ and/or N2---+ ion beam at 600eV to define the channel region and remained in the same tool (not exposed to the ambient environment) for the 20 nm Ni/20 nm Pd source/drain e-beam evaporation (Fig. 1E). After being chemically etched with CF4 at 100W under a pressure of 100mTorr in the RIE, the ex-situ devices were exposed to the ambient environment when being transferred

to the e-beam evaporator for the source/drain metal deposition (20 nm Ni/20 nm Pd) (Fig. 1F). An optical image of one complete device set is seen in Fig. 1G.
Results:
Each device set was fabricated on the same channel segment to conduct a direct comparison and minimize the variability within the channel. The subthreshold curves shown in Fig. 2A demonstrate a device set where all four edge-contact processes yielded functional devices. The results suggest the superiority of the in-situ processed Ni-MoS-2 device, which exhibited a higher ION even after adjusting for the threshold voltage (Vth) differences. Vth was extracted using a constant-current method at ID = 0.1 nA/mm for all devices. The ion-beam etched devices also exhibited an on/off-current ratio of >104. The transfer curves of the same device set demonstrate that the in-situ Ar+/N2+ device exhibits a nearly 10´ improvement in the ION compared to its ex-situ RIE counterpart (Fig. 2B). The subthreshold and transfer curves in Fig. 2C-D provide additional insight from a device set where only the two in-situ processed devices were functional. Nearly half of the fabricated device sets had a similar behavior, where the ex-situ RIE and ex-situ RIE + Ar-+ cleaned transistors did not function. The performance of the in-situ Ar+/N2+ devices were better than the in-situ Ar+ in most of the device sets. The in-situ Ar+/N2+ device shown in Fig. 2D had the highest ION throughout the chip at 1.4 mA/mm.
Conclusion:
Our work presents a study of the impact of different processing conditions on the yield and performance of edge-contacted Ni-MoS-2 transistors, revealing the advantage of in-situ processing between edge formation and metal deposition. These results indicate the importance of similar investigations involving other edge-contacted transition metal dichalcogenide transistors.
[1] Z. Cheng et al., Nano Lett., 19:5077 (2019). [2] W. Cao et al., Nature, 620:501 (2023). [3] W. Wu et al., IEEE Transactions on Electron Devices, 70:6680 (2023). [4] T. Schranghamer et al., Nano Lett., 23:3426 (2023).

Electrical and material characterization of ion beam-modified contact interfaces in WS2 field-effect transistors (Student)

Ms. Samantha Holmes[1], Mr. Alexander Mangus[1], Ms. Baiyu Zhang[1], Ms. Victoria Ravel[1], Dr. Aaron Franklin[2]
[1]Department of Electrical & Computer Engineering, Duke University, [2]Duke University

Introduction:
Recently, the use of 2D transition metal dichalcogenides (TMDs) has been explored to improve the performance and scalability of field-effect transistors (FETs) [1], [2]. However, high contact resistance at the metal-semiconductor interface and variability between devices remains a challenge for these 2D FETs [2], [3]. Prior work has shown that ion beam bombardment of molybdenum disulfide (MoS2) results in surface etching of the multilayer 2D semiconductor. By selectively exposing the source/drain contact regions of an MoS2 FET to such an ion beam immediately prior to metal contact deposition (in an in-situ process), the interface was modified to yield FETs exhibiting lower contact resistance and improved device performance compared to control (unmodified) devices [4]. This prompts a need to investigate the effect of ion beam modification at the metal-semiconductor contact interface for other TMD materials used in FETs. In this work, we investigate the impact of in-situ ion beam modification to the contact interface of tungsten disulfide (WS2) FETs. Preliminary data suggests that modification induces ambipolar characteristics, with p-branch current that surpasses that of the n-branch – an unexpected polarity shift for typically n-type WS2 FETs. Further work to determine if this change is due to alterations in the material properties of WS2 or of the contact interface itself was also completed.
Device Fabrication:
WS2 was mechanically exfoliated onto a doped-Si/90 nm SiO2 chip, followed by spin coating with poly-methyl methacrylate (PMMA) and patterning with electron-beam lithography (EBL). Unmodified devices were fabricated by direct deposition (and subsequent lift-off) of Ti/Pd (0.5 nm / 10 nm) contacts. Ion beam-modified devices are fabricated on the same flakes as unmodified devices by re-coating the chip in PMMA, patterning new contacts with EBL, and then exposing the chip to the ion beam immediately prior to contact metal deposition – hence, an in-situ modification process. The fabrication process is illustrated in Fig. 1. Devices of various channel lengths were fabricated in order to determine the contact resistance with the transfer length method. Channel width varies due to the abnormal flake sizes that result from mechanical exfoliation. Electrical characterization occurred in ambient conditions.
Preliminary Results and Characterization:
Initial testing of WS2 FETs (Lch = 400 nm) resulted in a maximum Ion/Ioff of 106 in modified devices with a drain-source voltage of 1 V. Preliminary results also show an increase and dominance in the p-branch of WS2 FETs after modification with the ion beam in comparison to unmodified control devices that display the anticipated n-type behavior (Fig. 2). This unanticipated polarity shift is likely a result of either residual W in the contact region causing a modification to the work function of the deposited contact metal or a modification of the interface that altered the Fermi-level alignment and/or pinning effects. To ascertain the changes to the material properties, Raman spectroscopy and atomic force microscopy are used to characterize the effect of ion beam modification on the mechanically exfoliated WS2 flakes. Compositional analysis was completed using x-ray photoelectron spectroscopy.
Conclusion:
This work investigates the effect of ion beam modification to the contact interface of multilayer WS2 FETs. Preliminary data suggests that modification results in an amplification of the p-branch to yield ambipolar characteristics in the devices. The source of this shift is explored via interface and material characterization.
[1] D. Jariwala et al., ACS Nano, 8 (2014). doi: 10.1021/nn500064s [2] M. Chhowalla et al., Nat Rev Mater, 1 (2016). doi: 10.1038/natrevmats.2016.52 [3] Y. Liu et al., Nature, 591 (2021). doi: 10.1038/s41586-021-03339-z [4] Z. Cheng et al., 2D Mater., 6 (2019). doi: 10.1088/2053-1583/ab1764

Fabrication and Characterization of Exfoliated h-BN/Graphene Devices on prepatterned contacts

Dr. Udagamage Wijewardena[1], Mr. Rameshwor Poudel[2], Dr. Annika Kriisa[2], Prof. Ramesh Mani[2]
[1]Georgia State University, and Georgia College & State University, [2]Georgia State University

Graphene is an exceptional two-dimensional crystal

structure composed of a single layer of carbon atoms arranged in a honeycomb lattice, which has garnered significant attention for its extraordinary properties and diverse potential applications[1-3]. This study focuses on the fabrication and characterization of multilayer devices combining exfoliated hexagonal boron nitride (h-BN) and graphene, employing mechanical exfoliation and dry transfer methods.
The challenge in producing high-quality graphene devices arises due to process-induced impurities and the susceptibility of graphene to the surrounding environment. Utilizing pristine graphite to exfoliate graphene using dry transfer techniques proves to be a method that significantly reduces process-induced impurities[4]. Additionally, covering the graphene device with an insulating material like h-BN prevents degradation of the graphene due to interaction with water, oxygen, and other impurities in the surroundings[5]. In this work, we summarize our efforts in the fabrication of graphene/h-BN devices onto prepatterned Au-contacts on Si-substrates, such as those illustrated in Figure 1, and provide detailed characterization using an optical microscopy and AFM imaging to determine the “thickness” and topography of samples. AFM images revealed that the multi-layer graphene sample depicted in Figure 1 has a thickness of around 6.5 nm. Furthermore, we present our transport measurements on the fabricated multilayer graphene devices on a silicon/silicon dioxide substrate, with a back gate electrode on the conducting silicon substrate. This allows us to study the evolution of resistance versus gate voltage, revealing the Charge Neutrality Point of the device[6]. The resistance-versus-voltage data also illustrated a broadened peak at the Charge Neutrality Point, indicative of multiple graphene layers. Transport properties were assessed using standard low-frequency lock-in techniques, and the data were examined comparing data from uncovered devices with h-BN capped ones to understand the impact of the h-BN cover on the device quality.
[1] K.S. Novoselov, A.K. Geim, S.V. Morozov, D. Jiang, M.I. Katsnelson, I.V. Grigorieva, S.V. Dubonos, A.A. Firsov, Two-dimensional gas of massless Dirac fermions in graphene, Nature, 438 (2005) 197-200.
[2] A.K. Geim, K.S. Novoselov, The rise of graphene, Nat Mater, 6 (2007) 183-191.
[3] R.G. Mani, A. Kriisa, R. Munasinghe, Radiation-induced magnetoresistance oscillations in monolayer and bilayer graphene, Scientific Reports, 9 (2019) 7278.
[4] M. Yi, Z. Shen, A review on mechanical exfoliation for the scalable production of graphene, Journal of Materials Chemistry A, 3 (2015) 11700-11715.
[5] N. Petrone, T. Chari, I. Meric, L. Wang, K.L. Shepard, J. Hone, Flexible Graphene Field-Effect Transistors Encapsulated in Hexagonal Boron Nitride, ACS Nano, 9 (2015) 8953-8959.
[6] U.K. Wijewardena, T. Nanayakkara, R. Samaraweera, S. Withanage, A. Kriisa, R.G. Mani, Effects of Long-Time Current Annealing to the Hysteresis in CVD Graphene on SiO2, MRS Advances, 4 (2019) 3319-3326.

Supercapacitive Properties of Pulsed Laser Deposited Ba(Fe0.7Ta0.3)O3–δ Thin Films Deposited on Ni Foil (Student)

Mr. Nolan Herbort[1], Dr. Ambadi Lakshmi-Narayana[1], Dr. Debabrata Das[1], Dr. Ramana Chintalapalle[1]
[1]The University of Texas at El Paso

The development and research into the area of semiconducting metal oxides (SMO) is continuously growing and adapting to the wide uses of SMOs in domestic and industrial applications. Being able to incorporate nano scale supercapacitors into modern devices would allow for greater power requirements to be fulfilled with a smaller storage solution. Recently Ba(Fe0.7Ta0.3)O3–δ (BFTO) has been studied as a sensor for Oxygen in high temperature applications. In this work, BFTO thin films have been deposited using pulsed laser deposition (PLD) on Ni substrates ranging from room temperature to 600 °C in a partial pressure of 50 mTorr of Oxygen. Microstructural characterization of BFTO at 600 °C revealed crystalline size of about 21nm, with uniform distribution of spherically shaped grains 40-100 nm in size. As electrodes for micro supercapacitors, BFTO thin films deposited at 600 °C displayed a specific capacitance of 400 mF cm−2 at a current density of 1 mA cm−2 and retained 94% capacitance over 3000 cycles with good structural stability. These findings may offer new uses for BFTO thin films in portable energy storage devices and a potential for next generation high performance energy storage applications.

Growth Optimization and Characterization of Sn-doped Gallium Oxide Thin Films by Pulsed Laser Deposition for κ-Ga2O3 Stabilzation

Mrs. Francelia Sanchez[1], Dr. Debabrata Das[1], Dr. Ramana Chintalapalle[1]
[1]The University of Texas at El Paso

There is great interest over the ultrawide-bandgap semiconductor gallium oxide (Ga2O3). The material has potential for high power electronic and optoelectronics because of its large theoretical breakdown field. Though β-Ga2O3 is the most studied phase because of its high thermal and chemical stability, there is growing interest in the metastable phases of Ga2O3. κ-Ga2O3 is the second most stable phase at atmospheric among the polymorphs of gallium oxide. κ-Ga2O3 and its alloy have potential applications in sophisticated devices, such as high-electron mobility transistors and quantum-well infrared photodetectors because of its high estimated spontaneous electrical polarization and its susceptibility to form a two-dimensional electron gas at the heterostructure interfaces. Further, κ-Ga2O3 has also demonstrated ferroelectric properties which makes the material suitable for piezoelectric and pyroelectric applications. However, phase stabilization and control of the electronic transport are the two major challenges of κ-Ga2O3. n-type doping of κ-Ga2O3 using Si or Sn demonstrate high resistivities and low electron mobilities that limit the current transport. In the pulsed laser deposition (PLD) of κ-Ga2O3, Sn is necessary as a metal catalyst to facilitate the synthesis of κ-Ga2O3. In this project, a low content of Sn has been incorporated to a Ga2O3 PLD target. The structural and optical properties of the thin films have been characterized. The device performance of a MSM photodetector have been measured.

Synthesis of 5,10,15,20-Tetrasulphonatophenyl Porphyrin Molecular Channels for Harnessing Magnetic Tunnel Junction based Molecular Spintronic Device for Fuel Cell Application

Dr. BUSHRA BARI[1], Prof. Uche Udeochu[1], Dr. Pawan Tyagi[2]
[1]University of the District of columbia, [2]University of the

district of Coulombia

Hydrogen fuel cells are promising for next generation power sources and already being used. However, this technology has major challenge that it relies on rare and costly platinum metal as the electrodes. To overcome the platinum related challenges in fuel cell worldwide research is going on to find the replacement material that has platinum like or better electro-catalytic properties. Porphyrin molecules are considered as catalyst but so far advantages of using molecule as catalyst are unable to compete with platinum. This paper presents a concept where porphyrin molecule will be utilized as a spin channel between the two nickel ferromagnetic electrodes separated by the ~2 nm insulator. The rational for this approach is our recent studies showing that molecular spin channels transform 1-10 nm thick ferromagnetic films into light absorbing materials via spin filtering mechanism [1, 2]. In this paper we explore electro-catalytic properties of molecules when connected along the exposed sides of ~1-5 μm diameter magnetic tunnel junction. As the first step we have begun the synthesis of suitable porphyrin molecules to be used for the investigation of electro-catalytic properties of the molecules. For that purpose, in the first part free base tetraphenylporphyrin (TPP) was synthesized by Adler-Longo method followed by treatment with H2SO4 to form tetrasulphonatophenyl porphyrin (TPPS4). TPPS4 was coordinated with various transition metals Co, Fe and Ni at porphyrin center to form metalloporphyrin complexes as a potential alternative to expensive platinum catalysts in fuel cells. Porphyrin complexes were analyzed by multiple spectroscopic techniques such as UV-VIS spectroscopy, NMR, FTIR and electro-catalytic measurements. UV-VIS spectra of TPP shows corresponding absorption peak around 420 nm (Fig.1) signifying the presence of porphyrin structure. In the next step we are advancing synthesis to add thiol groups to the porphyrin molecules to make them capable of forming covalent bonds with the ferromagnetic electrodes. This talk will also present our theoretical calculations that were performed by Monte Carlo simulation method to understand the molecule electron exchange tendency with hydrogen atom. We anticipate the use of these results in the designing of fuel cells.
References:
Pawan Tyagi and Christopher Riso, 2019 Nanotechnology 30 495401
Marzieh Savadkoohi, Daniel Gopman, Pius Suh, Carlos Rojas-Dotti, José Martínez-Lillo, Pawan Tyagi, ACS Appl. Electron. Mater. 2023, 5, 6, 3333–3339

Photovoltaic effect on silicon-alumina-ferromagnet tunnel junction providing insights about spin-dependent molecular spintronics solar cells
Mr. Pius Suh[1], Dr. Pawan Tyagi[2]
[1]University of the District of columbia, [2]University of the district of Coulombia

We have recently studied the spin photovoltaic effect on Ferromagnet(FM)/AlOx/FM tunnel junction-based molecular spintronics devices[1,2]. This study focuses on the observation of the photovoltaic (PV) effect on Si/AlOx/FM semiconductor-insulator-ferromagnetic metal (SIFM) structure(Fig.1). Utilization of ~10 nm NiFe film as the top FM layer was permeable for sufficient light radiation necessary for reaching the silicon substrate for the generation of electron-hole pairs upon photoexcitation. The effect of light intensity and magnetic field was studied on the SIFM's PV response. We also investigated the role of silicon doping and the AlOx tunnel barrier between Si and FM for exploring suitable band bending necessary for separating the electron-hole pairs. Increasing the dopant density in Si and a damaged AlOx tunnel barrier quenched the PV effect. FMIFM was also studied to gain deeper mechanistic insights into the spin-dependent photovoltaic effect observed on FM/AlOx/FM tunnel junction-based molecular spintronics devices. Bridging of magnetic molecules between the Si and FM electrodes of SIFM increased the overall device current by establishing additional parallel conduction channels along with the AlOx tunnel barrier. However, SIFM with molecular conduction channels did not produce a PV effect. This study reported the PV effect on well-designed SIFM and opened possibilities of exploring new systems. More importantly, this paper provided insights into the role of molecule-induced exchange coupling in transforming an ordinary cheap and widely available ferromagnet into a semiconductor-like material capable of showing PV.
[1] M. Savadkoohi, D. Gopman, P. Suh, C. Rojas-Dotti, J. Martínez-Lillo, and P. Tyagi, "Spin Solar Cell Phenomenon on a Single-Molecule Magnet (SMM) Impacted CoFeB-Based Magnetic Tunnel Junctions," ACS Applied Electronic Materials, 2023/05/31 2023.
[2] P. Tyagi and C. Riso, "Molecular spintronics devices exhibiting properties of a solar cell," Nanotechnology, vol. 30, p. 495401, 2019/09/19 2019.

Paramagnetic Molecules Lose Identity When Connected to Diverse Combinations of Metal Electrodes In MTJ Based Molecular Spintronics Devices (Student)
Dr. Eva Mutunga[1], Mr. Christopher D'Angelo[1], Mr. Andrew Grizzle[2], Dr. Pawan Tyagi[3]
[1]University of the District of Columbia, [2]University of the District of columbia, [3]University of the district of Coulombia

Does molecule strongly exchange coupled with metal electrodes retain its intrinsic properties? Answering this question by studying the magnetic molecules' interaction with different combinations of metal electrodes is vital to advancing molecular spintronics[1]. This paper describes experimental and theoretical understanding showing how paramagnetic single-molecule magnet (SMM) catalyzes long-range effects on metal electrodes and, in that process, loses their basic magnetic properties. For the first time, our Monte Carlo simulations, verified for consistency with regards to experimental studies (Fig.1), discuss the properties of the whole device and molecules connected to the combinations of ferromagnet-ferromagnet, ferromagnet-paramagnet, and ferromagnet-antiferromagnet metal electrodes. We studied the magnetic moment vs. magnetic field of SMM analog exchange coupled between two metal electrodes along the exposed side edge of cross junction-shaped magnetic tunnel junction (MTJ). We also studied SMM-metal electrode interfaces' magnetic moment vs. magnetic field response. Additionally, we have found that the MTJ dimension also impacted the SMM response. Combining SMM along the MTJ exposed sides offers a unique and high-yield method of connecting molecules to virtually endless types of magnetic and non-magnetic electrodes and observing unprecedented phenomena in the molecular spintronics field. This research provides insights for designing novel device structures.

References
[1] E. Mutunga, C. D'Angelo, and P. Tyagi, "Magnetic molecules lose identity when connected to different combinations of magnetic metal electrodes in MTJ-based molecular spintronics devices (MTJMSD)," Scientific Reports, vol. 13, p. 16201, 2023/09/27 2023.

Photoluminescence maps of defects in β-Ga2O3

Prof. Matt McCluskey[1]
[1]Klar Scientific, 1615 NE Eastgate Blvd., Unit G, Ste. 3E, Pullman, WA, USA 99163-5300; Dept. of Physics and Astronomy, Washington State University, Pullman, WA, USA 99164-2814

Photoluminescence (PL) spectra with high spatial resolution provide insight into semiconductor defects, inhomogeneous composition, and surface imperfections. The method serves as a valuable tool for failure analysis. Typical PL spectroscopy is not spatially resolved. Excitation photons impinge on a sample; emitted light is collected by a spectrometer. Spatial variations get averaged into one overall spectrum. This approach is adequate for a homogeneous sample but there are many instances where one requires a spectrum at each (x,y) point on the surface as well as the ability to visualize the data.
This poster presents PL mapping of several key semiconductor materials, with excitation wavelengths ranging from 266 to 975 nm. The sample is scanned in the x-y plane and emitted light is collected by an Ocean Optics spectrometer (detection ranges encompass 200 to 1700 nm). This system yields a map that covers an area as large as 100 × 100 mm. Analysis software performs rapid peak fitting on each spectrum and displays the data in a -color image. An autofocusing routine analyzes the laser spot and adjusts the objective height to keep the laser spot in-focus on the sample surface, ensuring diffraction-limited resolution. Monoclinic gallium oxide (β-Ga2O3) is an ultrawide bandgap semiconductor with potential applications in power electronics. Photoluminescence (PL) spectroscopy is an important method to characterize dopants and defects in this material. Common features in the PL spectrum include the intrinsic UV band, blue and green bands that involve donor-acceptor pairs, and red emission due to Cr3+ impurities. PL mapping with excitation wavelengths ranging from 266 to 532 nm reveals the spatial distribution of these features with micron resolution. In Czochralski-grown β-Ga2O3, the Cr3+ emission intensity shows striations that are attributed due to inhomogeneities during growth. In addition to defects in the bulk, PL microscopy has revealed several specific defects on the surface. Some of these localized centers are very bright UV emitters.
Homoepitaxial layers show defects that are observed via the shifts in the PL band, likely due to the strain field around a dislocation core. Damage due to high-intensity laser pulses results in significant changes in the intensity and energy of the UV band. In situ PL spectroscopy performed with a pulsed 266 nm laser shows characteristic emission peaks attributed to Ga atoms ablated from the surface.

Fabrication and Characterization of SnO2 Electron transport Layer (Student)

Mr. Gavin Robinson[1], Mr. Akhil Prio Chakma[2], Mr. Ervin Graddick[3], Mr. Twelede semere[3], Dr. Hongmei Dang[4], Mr. Adrion Celey[5]
[1]Graduate Student, [2]Graduate Research Assistant, [3]Undergraduate Research Assistant, [4]Associate Professor(Research Advisor), Electrical and computer Engineering dept, University of the District of Columbia., [5]Gradute Research Assistant

Perovskite solar cells (PSCs) have achieved power conversion efficiency beyond 25% [1-2], however, long-term stability is the most pressing issue impeding their applications [3]. To improve the performance and stability of PSCs, the electron transport layer (ETL) is extremely important. Recent efforts have been devoted to developing SnO2 as a stable and efficient electron transport layer (ETL) to overcome the essential limitations of TiO2 ETL. In this project, we developed four types of SnO2 precursor solutions to spin coat SnO2 films on ITO/glass substrate and characterized their materials properties by Scanning electron microscopy (SEM) with energy dispersive X-ray spectroscopy (EDX) and X-ray diffraction analysis (XRD). The SnCl4 precursor was difficult to manage and form SnO2 films and the formed films demonstrated discontinuous features. It is found that tin oxide with 15% H2O colloidal dispersion is the optimal precursor. The optimal precursor solutions were spin-coated with 3000rpm for 30 seconds one time and two times for comparison. The films were annealed at 150°C -190 °C. SEM demonstrated that SnO2 films formed by the optimal precursor were uniformly coated on the substrate and had continuous, dense, and closed-packed small grains at the nanoscale. The EDX showed that the atomic ratio of Sn/O is close to 1/2. Next, we plan to optimize the SnO2 spin coating process and passivate the SnO2 surface to form the SnO2 Schottky diodes to compare the devices' optical-electronics properties to obtain the optimal SnO2 films. Then we will combine SnO2 and perovskite layers to form Perovskite Solar Cells.
Reference:
[1] A. Agresti et al., "Titanium-carbide MXenes for work function and interface engineering in perovskite solar cells," Nature Materials, vol. 18, no. 11, pp. 1228-1234, 2019.
[2]C. Liu et al., "Tuning structural isomers of phenylenediammonium to afford efficient and stable perovskite solar cells and modules," Nature Communications, vol. 12, no. 1, pp. 1-9, 2021.
[3]Z. Liu et al., "A holistic approach to interface stabilization for efficient perovskite solar modules with over 2,000-hour operational stability," Nature Energy, vol. 5, no. 8, pp. 596-604, 2020.
[4]X. Ren et al., "Chlorine-modified SnO2 electron transport layer for high-efficiency perovskite solar cells," InfoMat, vol. 2, no. 2, pp. 401-408, 2020.
[5]C. C. Lin, T. N. Murakami, M. Chikamatsu, T. Bessho, M. Furue, and H. Segawa, "A Sodium Chloride Modification of SnO2 Electron Transport Layers to Enhance the Performance of Perovskite Solar Cells," ACS omega, vol. 6, no. 28, pp. 17880-17889, 2021.
[6] H. Min et al., "Perovskite solar cells with atomically coherent interlayers on SnO2 electrodes," Nature, vol. 598, no. 7881, pp. 444-450, 2021.

Carrier Recombination Dynamics in Intrinsic and Alloyed β-Ga2O3 Thin Films on Sapphire Substrate

Dr. Debabrata Das[1], Mrs. Francelia Sanchez[1], Dr. Paul Nalam[1], Dr. Ramana Chintalapalle[1]
[1]The University of Texas at El Paso

We conducted photoluminescence experiments on β-Ga2O3

and β-(GaxIn1-x)2O3 thin films made by pulsed laser deposition (PLD) onto sapphire substrates. These measurements involved studying the dependence of excitation and time on the photoluminescence properties. The luminescence spectra of all the samples exhibit transitions in the form of clearly defined peaks and shoulders, which remain constant throughout time. Both Ga2O3 and the β-(GaxIn1-x)2O3 films exhibit three transitions within certain wavelength ranges: 329-367nm, 475-490nm, and 545-596nm. Furthermore, Ga2O3 exhibits emissions at wavelengths of 404 and 693nm. Photoluminescence measurements were conducted to analyze both steady-state and time-resolved behavior, with a focus on the influence of excitation intensity. The integrated intensity versus excitation graphs of all transitions demonstrates a slope k within the range of 1 to 2. The peak location, linewidth, and recombination durations of all the transitions remain almost constant regardless of the excitation. These data indicate that the changes in these oxide semiconductors are associated with excitons.

Structural characterization and surface morphology of thick homoepitaxial growth on miscut (100) β-Ga2O3 substrates by MOCVD (Student)

Mr. Joshua Buontempo[1], Mr. Cameron Gorsak[1], Prof. Hari Nair[1]
[1]Cornell University

Monoclinic gallium oxide (β-Ga2O3) is a promising ultra-wide bandgap (~4.85 eV) semiconducting material with a high breakdown field of ~8MV/cm, controllable n-type doping, and availability of large-area melt-grown substrates [1, 2]. Prior work from multiple groups has demonstrated smooth homoepitaxial growth of β-Ga2O3 on (010)-orientated substrates. However, when growing thick > 500 nm epitaxial films, defects can become pronounced on the surface [3, 4]. Some of these defects originate from the underlying voids/defects at the surface of the (010) substrates [3]. By using (100) substrates grown via edge-defined film-fed growth (EFG) technique, the nanopipes lie in-plane and would likely not thread into the epitaxial film, potentially resulting in lower surface defect density.
Typically, the growth of β-Ga2O3 on on-axis (100) substrates is characterized by 2D island nucleation leading to the formation of twin lamellae, resulting in poor structural quality and degraded electron mobility [1, 5]. However, using (100)-orientated substrates that are deterministically miscut by >4˚, the growth mechanism shifts from islanding to step-flow growth, leading to a higher crystalline quality [6]. In this work, we will investigate the growth and surface morphology of thick (>4 µm) homoepitaxial layers on (100) β-Ga2O3 substrates with varying miscut angles toward [00-1] grown by metal organic chemical vapor deposition (MOCVD).
The (100)-orientated substrates were grown from the EFG technique and have miscut angles of approximately 2˚, 4˚, and 6˚ toward [00-1]. The thick (>4 µm) UID layer is grown on top of the nucleation layer using Trimethylgallium (TMGa) and pure O2 as the gallium and oxygen precursors, respectively. The films are characterized with optical microscopy, high resolution x-ray diffraction (XRD), and atomic force microscopy (AFM). Growth of high quality β-Ga2O3 films on (100) substrates will aid in the development of vertical power electronic devices [7].
References

[1] Wagner, G., Baldini, M., et al., Phys. Status Solidi A 211, 27 (2014)
[2] Janowitz, C., et al., New J. Phys. 13 085014 (2011)
[3] Cooke, J., Ranga, P., et al., J. Vac. Sci. Technol. A 41, 013406 (2023)
[4] Meng, L., et al., Cryst. Growth Des. 23, 7365-7373 (2023)
[5] Schewski, R., Baldin, M., et al., J. Appl. Phys. 120, 225308 (2016)
[6] Schewski, R., Lion, K. et al., APL Materials 7, 022515 (2019)
[7] Rehm, J., Chou, T., et al., Appl. Phys. Lett. 121, 240503 (2022)

Studying Single Molecule Magnet (SMM) induced coupling effect on Magnetic Tunnel Junction (MTJ) using Electron spin resonance (ESR) (Student)

Mr. Juan Estevez Hernandez[1], Ms. Betelhiem Mengesha[2], Mr. Arnold Feutmba[1], Dr. Pawan Tyagi[3]
[1]University of the District of Columbia, [2]University of the District of columbia, [3]University of the district of Coulombia

New types of metamaterials can be produced by enhancing the magnetic coupling between the two ferromagnetic layers of a magnetic tunnel junction (MTJ). One potential method to achieve strong coupling involves attaching molecules along the exposed side of the MTJ, acting as spin channels that connect the top and bottom ferromagnetic layers. This study focuses on examining the coupling effect of Single Molecule Magnetic (SMM) on MTJs with varying insulator thicknesses. The fabrication process of the MTJ involves coating a silicon wafer with photoresist through spin coating, creating patterns via photolithography, depositing thin films through sputtering, and finally removing the unwanted material through liftoff. After fabrication, the top and bottom electrodes are covalently connected on the exposed side edges using SMMs to establish a strong magnetic coupling. Through multiple experiments, it has been observed that strong coupling, facilitated by SMM channels, alters the magnetic properties of both ferromagnetic metals. Electron spin resonance (ESR) is a valuable technique utilized to characterize the magnetic properties, interactions, and dynamics of the individual layers within the structure of a magnetic tunnel junction (MTJ). In this study, an ESR investigation was conducted both before and after the treatment of the MTJ with the SMM to assess the impact of the molecules. The ESR results displayed a discernible shift in the acoustic and optical modes of the MTJ subsequent to the introduction of the SMM. This shift observed in the ESR spectra indicates that the SMM has a significant effect on the properties of the ferromagnetic electrodes within the MTJ. To understand the SMM impact, the ESR response of the heated MTJs was compared. It was found that the shift induced by the SMM on the MTJ was of a similar magnitude to the shift observed on a heated sample. Examining the influence of SMM coupling in magnetic tunnel junctions (MTJs) is of utmost importance, as MTJs based on molecular components open up novel possibilities for nanoscale electronics, quantum information processing, and advanced sensor technologies.
Keywords: Single Molecule Magnetic (SMM), Electron spin resonance (ESR), Magnetic Tunnel Junction, and coupling.
References:

[1] X. Fan, R. Cao, T. Moriyama, W. Wang, H. W. Zhang, and J. Q. Xiao, "Magnetic tunnel junction based microwave detector," App. Phys. Lett., vol. 95, p. 122501, 2009.

[2] A. Grizzle, C. D'Angelo, J. Martínez-Lillo, and P. Tyagi, "Spin state of a single-molecule magnet (SMM) creating long-range ordering on ferromagnetic layers of a magnetic tunnel junction – a Monte Carlo study," RSC Advances, vol. 11, pp. 32275-32285, 2021.

Correlation between Local chemistry, Bottleneck size, and Lithium conductivity in perovskite solid electrolytes

Dr. Junghwa Kim[1], Dr. Kiarash Gordiz[2], Mr. Daniele Vivona[3], Prof. Shao-Horn Yang[3], Prof. James LeBeau[1]
[1]Department of Materials Science and Engineering, Massachusetts Institute of Technology, [2]Research Laboratory of Electronics, Massachusetts Institute of Technology, [3]Department of Mechanical Engineering, Massachusetts Institute of Technology

Solid-state lithium batteries based on inorganic solid electrolytes have gained increasing attention, attributed to their enhanced safety and excellent energy density [1]. Various structural features, such as composition, structural order, or various defects, directly impact the overall ionic conductivity. [2] As an example, the degree of La/Li ordering and domain/grain boundary in lithium-lanthanum titanate Li3xLa2/3-xTiO3 (LLTO) significantly affect the ion conductivity [3,4]. Because oxygen (O) bottlenecks, which are formed between four neighboring TiO6 octahedra, serve as pathways for Li+-ion migration [5], studying local structural features that affect this bottleneck size becomes essential for obtaining descriptors for high ionic transport and designing structures with high performance.
In this presentation, we will show the local structural characteristics of LLTO and highlight the connection between local environments and Li+-ion mobility, using a combination of aberration-corrected scanning transmission electron microscopy (STEM), multislice ptychography, DFT/MD calculations. First, the simultaneously obtained annular dark field (ADF) and integrated differential phase contrast (iDPC) images reveal a reduction in bottleneck size with the increased La(/Li) occupancy. Second, multislice ptychography reconstructions enable the direct observation of O displacements coupled to the neighboring A-site occupancy. Third, investigation through DFT/MD, we will show that the Coulombic forces applied from neighboring cation chemistry towards the bottleneck determine O displacements and O bottleneck size, which is found to be correlated between bottleneck size and Li+-ion migration behavior. These results help establish a robust understanding of the linkage between local chemistry, structure, and ionic conductivity.

Improvement of CdTe Solar Cells Using Patterned Al2O3 Reflectors

Ms. Etee Roy[1], Mr. Ashraful Mamun[1], Prof. Heayoung Yoon[1]
[1]University of Utah

CdTe solar cells have emerged as a leading photovoltaic (PV) technology in the commercial market today due to their excellent optical absorption, operational reliability, and fast manufacturing processes. Recent advancements in front-contact optimization have yielded impressive results, with a short-circuit current (Jsc) of 31.7 mA/cm2 and a fill factor (FF) of 78.5 %, approaching their theoretical maximum values. However, the open-circuit voltage (Voc) remains within the range of 0.8 V to 0.9 V, significantly below the theoretical limit of approximately 1.2 V.
This study investigates innovative back-contact architectures utilizing patterned Al2O3 reflectors. We explore how the configuration of microholes on Al2O3 can enhance the collection of majority carriers through point contacts (metal/CdTe) while preserving surface passivation (Al2O3/CdTe). We apply the same geometry to as-grown and post-annealed CdS/CdTe solar cells to examine the interaction between back-contacts and the CdTe absorber materials. The post-annealed CdTe samples, derived from the as-grown sample set, undergo additional CdCl2-activation processes, effectively passivating various defects (e.g., point defects, dislocations, 2D structural defects), resulting in an improved quality of the CdTe absorber. Our analysis reveals that in as-grown CdTe devices, losses in fill factor (FF) and short-circuit current (Jsc) are primarily associated with the extent of Al2O3 coverage (Al2O3/CdTe). In contrast, post-annealed devices notably enhance these parameters when the microhole point-contact area exceeds 10 %. We employ cathodoluminescence analysis to confirm increased radiative recombination with Al2O3. Additionally, we analyze the Voc trend with the contact fraction (Au/CdTe) of the patterns. Our results suggest a delicate balance between the impact of Al2O3 reflectors on passivation and selectivity and the inherent properties of the CdTe absorber influencing lateral transport.

Thermal Conductivity of High Al Content AlGaN Multiple Quantum Well Heterostructures

Dr. LeighAnn Larkin[1], Dr. Mihee Ji[1], Dr. Gregory Garrett[1], Dr. Anand Sampath[1], Dr. Michael Wraback[1]
[1]Army Research Laboratory

High-Al content AlxGa1-xN heterostructures provide a platform for UV-light emitting diodes (LEDs) and laser diodes (LDs) well into the UV-C regime (200 – 280 nm). However, multiple quantum-well (MQW) structures commonly employed in LEDs and LDs exacerbate self-heating, owing to the multiple interfaces and boundaries which significantly scatter phonons, limiting thermal conduction through these materials [1, 2]. Addressing thermal management will become more critical as the output power of UV emitters increases. In this paper, we discuss the impact of AlGaN-based heterostructure design on thermal conduction.
The effective thermal conduction (κeff) of six AlGaN MQW structures grown by metalorganic chemical vapor deposition (MOCVD) on bulk AlN substrates was measured by Time-domain Thermoreflectance (TDTR). Samples A-C in Set 1 consisted of 11-period MQWs of 2 nm Al0.55Ga0.45N wells with 6 nm Al0.85Ga0.15N barriers (A), 3 nm AlN barriers (B), or 6 nm AlN barriers (C). Samples D-F in Set 2 had 8 periods of 0.6 nm Al0.61Ga0.39N wells (D), 8-periods of 1.35 nm Al0.61Ga0.39N wells (E), and 6-periods of 2 nm Al0.61Ga0.39N wells (F), all with 7 nm AlN barriers. When the number of periods is the same (Set 1), the κeff is most sensitive to the percentage of the structure composed of AlN, with κeff of Sample A (3 ± 0.5 W/mK) < B (4.5 ± 0.6 W/mK) < C (5.4 ± 0.6 W/mK). However, for structures with similar AlN barrier and well thickness, comparison with Set 2 implies that the number of periods has the most significant effect on κeff. Both sample E and F in Set 2 possess a value of κeff higher than all the samples in Set 1. The κeff of Sample F was 8 ± 1 W/mK, which is comparable to the thermal conductivity of thin (< 200 nm) high-Al content

AlGaN films [3]. By increasing the number of periods from six to eight (Sample E), κeff decreases to 6 ± 1 W/mK. However, a further reduction in κeff to 3.4 W/mK in sample D for the same number of periods but a smaller well width implies that the distance between some interfaces afforded by the smaller well width may also play a role.
A more detailed study in which well width, barrier width, number of periods, and barrier Al composition are independently varied while the well Al composition (~ 60 %) and the other parameters remain fixed will provide insight into the optimization of κeff for AlGaN heterostructures employed in UV-C emitters and other high Al content AlGaN devices.
References
[1] A. Balandin and K.L. Wang, Phys. Rev. B 58, 1544 (1998).
[2] A. Khitun, A. Balandin, J.L. Liu, and K.L. Wang, J. Appl. Phys. 88, 696-699 (2000).
[3] D.Q. Tan, R.D. Carrascon, M. Iwaya, B. Monemar, V. Darakchieva, and P.P. Paskov, Phys Rev Mat. 6 104602 (2022).

Benchmarking Diamond Surface Preparation via Inductively Coupled Plasma-Reactive Ion Etching (ICP-RIE) (Student)
Ms. Tia Gray[1], Dr. Xiang Zhang[1], Dr. Pulickel Ajayan[1]
[1]Rice University

Diamond, with its exceptional semiconducting properties, is a promising material for high-performance power electronics, optics, quantum, and biosensing technologies. This work systematically explores the optimization of polycrystalline diamond (PCD) surfaces through Inductively Coupled Plasma Reactive Ion Etching (ICP-RIE). Various parameters, including gaseous species, gas flow rates, and ICP-RIE powers, were tuned to understand their impact on surface morphology and chemical composition. Comprehensive chemical, spectroscopic and microscopic characterizations provide insights into the effects of different gaseous species on the surface properties. Notably, CF4+O2 plasma was identified as pivotal for achieving a smooth PCD surface with minimal etch pit formation. X-ray Photoelectron Spectroscopy (XPS) and depth-profile analysis revealed uniform surface fluorination with CF4+O2 treatment. Additionally, contact angle measurements demonstrated increased hydrophobicity post-fluorination. The study provides valuable insights for precise diamond surface engineering, crucial for the development of future diamond-based semiconductor technologies.

In-situ annealing induced phase transition of α, κ, γ-Ga2O3 in different atmospheric conditions (Student)
Mr. Po-Sen Tseng[1], Mr. Jingyu Tang[1], Prof. Rachel Kurchin[1], Prof. Robert Davis[1], Prof. Lisa Porter[1]
[1]Carnegie Mellon University

Gallium oxide (Ga2O3) is a promising material for high-voltage applications and power electronics due to its ultra-wide bandgap, high breakdown voltage, and excellent thermal stability. Ga2O3 occurs in five different crystalline phases – the stable phase (β) and the metastable phases (α, κ, γ, and δ). Each phase exhibits notable features, such as the highest bandgap (α phase), piezoelectric and/or ferroelectric properties (κ phase), ferromagnetism (γ phase). However, because the β phase is the most thermodynamically favorable, the metastable Ga2O3 phases will transform to β-Ga2O3 upon heat treatment, potentially limiting the application of these metastable phases. In this study α, κ, and γ-Ga2O3 epitaxial films ~ 1 μm thick were annealed in air (from 500 °C to 900 °C) and in vacuum (2–5 x 10-5 Torr, from 500 °C to 1500 °C) and characterized using in-situ X-ray diffraction (XRD) and ex-situ scanning electron microscopy (SEM). κ-Ga2O3 on (0001) Al2O3 and γ-Ga2O3 on (100) MgAl2O4 were grown using metalorganic chemical vapor deposition (MOCVD); α-Ga2O3 films on (0001) Al2O3 substrates were purchased from Kyma. Next, the morphology of as-grown and annealed samples was examined using SEM. As shown in Fig. 1, we observed that all three phases undergo transformation to the most stable phase, β, within the temperature range considered, but at different temperatures. Additionally, the SEM characterization in Fig. 2 reveals distinct morphological changes during each phase's transition process. These results imply differences in the mechanism of phase transition amongst the metastable phases, likely as a result of structural differences. Notably, in the vacuum atmosphere, all three phases not only demonstrate higher transition temperatures but also more severe deformation upon transition. Our results are qualitatively consistent with recent observations by Wen et al., showing the enhanced thermal stability of α-Ga2O3 in air compared to vacuum. They observed somewhat different transition temperatures, which could arise from differences in film orientation, deposition technique, film thickness, or chamber pressure. Therefore, the annealing experiments will also be conducted in the N2 atmosphere to validate these results further.

Solution-Processed SnO2 Thin Film Transistor with Low Operating Voltage Enabled by Li2SnO3/SnO2 Stacked Gate Dielectric (Student)
Dr. Vishwas Acharya[1], Mr. Himanshu Marothya[1], Prof. Sandip Mondal[1]
[1]Indian Institute of Technology, Bombay

In the present work, we demonstrated a SnO2-based thin film transistor using lithium stannate (Li2SnO3) as a gate dielectric.[1] Due to low carrier concentration and mobile lithium ions (Li+), this material exhibits considerable areal capacitance and low DC conductivity. We have prepared two different devices, one with Li2SnO3 as a dielectric layer and the other is a SnO2/Li2SnO3 bilayer stack as a dielectric layer and we observed the considerable improvement with the SnO2/Li2SnO3 bilayer stack. The measured areal capacitance for SnO2/Li2SnO3 bilayer thin films was 545 nF/cm2. The SnO2 and Li2SnO3 thin films in this TFT configuration are all classified as polycrystalline. With an on/off ratio of 500, the improved TFT demonstrate an electron mobility of 0.7 cm2 V−1 s−1 and only requires an external bias of 4 V. This work offers a convincing low-operational-voltage TFT solution that has the potential for a wide range of electronic device applications.
The precursor materials for the preparation of Li2SnO3 were tin chloride (SnCl2) and Lithium acetate dehydrate (C2H3LiO2·2H2O). First, SnCl2 and (C2H3LiO2·2H2O) were independently produced in a 300 mM solution in 2-methoxyethenol solvent.[1] For uniform mixing and transparency, the solutions were stirred for one hour. After combining the two solutions in a 1:2 ratio, they were blended for 15 minutes at room temperature. A separate SnCl2

solution of concentration 300 mM was prepared for semiconductor preparation in 2-methoxyethenol solvent.[2,3] All metal oxide TFTs were fabricated with a bottom-gated and top-contact geometry over 15 mm × 15 mm (p+–Si) substrate as gate electrodes. The device schematic is described in Figure 1. Figure 2 shows the Areal capacitance versus frequency data of Li2SnO3 (283 nF/cm2) and SnO2/Li2SnO3 (545 nF/cm2) with MIM structure. Figure 3(b) shows that the whole device stack is more than 90% transparent in the optical region and we have also calculated the band gap[Figure 3(c)] of Li2SnO3 and it was 3.9 eV. Figure 4 shows the surface roughness of both the devices and Figure 5 shows the output and transfer characteristics of both devices. The electric characteristics show that the device-1 have an on/off ratio of 52 and a mobility of 0.13 cm2 V− 1 s − 1 but the device -2 shows considerable improvement and has an on/off ratio of 500 and a mobility of 0.7 cm2 V− 1 s – 1.

Intercalation of Nanostructured Polyacrylonitrile Particles on Ti3C2 MXene Layers for Improved Supercapacitance

Dr. Bishnu Bastakoti[1], Ms. Shanna Marie Alonzo[1], Dr. Daniel Autrey[2], Dr. Bhoj Gautam[2], Ms. Vanessa Morris[2]
[1]North Carolina Agricultural and Technical State University, [2]Department of Chemistry, Physics, & Materials Science, Fayetteville State University, Fayetteville, NC 28301, USA

The insertion of ions into two-dimensional (2D) layered materials has been widely utilized in energy storage devices. MXene, a relatively new but fast-growing class of 2D metal carbides/nitrides have impressive conductivity, ability to accommodate cations, and tunability using diverse organic and inorganic molecules [1,2]. However, the tendency of MXene sheets to restack significantly impedes its performance [3,4]. Herein, we report the pre-intercalation of Ti3C2 MXene layers with polyacrylonitrile (PAN) through simple sonication (Figure 1). The use of nanostructured PAN particles, which were synthesized via radical polymerization in acetone [5], offered dual benefits: (1) it increased the interlayer spacing of Ti3C2 MXene, thereby enhancing ion transport channels during charge and discharge, and (2) the surface of PAN could adsorb cations due to the lone pair of electrons of the nitrogen atoms and thus, in itself, contributed to the capacitance. XRD results showed an increase in the c-lattice parameter from 23.0 Å for the pristine Ti3C2 to 37.1 Å when intercalated with PAN. Cyclic voltammetry (Figure 2) tests showed that the specific capacitance of the PAN-intercalated Ti3C2 doubled compared to the pristine MXene (85.5 F/g vs. 39.3 F/g at 100 mV/s in 1 M H2SO4).

Structural Profiling of SnO2 Aerogels for Electronic Applications (Student)

Prof. Carlo daCunha[1], Mr. John Hardy[1], Ms. Madison King[1], Prof. Stephanie Hurst[1]
[1]Northern Arizona University

Aerogels, known for their ultralight and highly porous nature with low thermal conductivity, present a unique class of materials. However, their electrical properties, especially in the case of SnO2 aerogels, remain relatively unexplored. In this study, we examine the synthesis and characterization of SnO2 aerogels, aiming to uncover and understand their electrical behavior for potential applications in neuromorphic computing.

Synthesis procedure: The SnO2 aerogel was synthesized using the epoxide method. In a typical synthesis, 0.65 g of tin tetrachloride pentahydrate (SnCl4·5H2O) was dissolved in a 1:2 co-solvent mixture of EtOH:H2O for 2 minutes under magnetic stirring. Upon complete dissolution of the tin precursor, 0.8 ml of propylene oxide (CH3CHCH2O) was gradually added to the solution. The resulting mixture was promptly poured into a silicone mold, initiating hydrogel formation within 40 seconds. The hydrogel underwent a week-long aging process before undergoing an ethanol solvent exchange. Subsequently, a critical point drying process using liquid CO2 was employed to transform the hydrogel into an aerogel.
To investigate potential annealing effects, the aerogel was divided into five sections. Four samples underwent annealing in a tube furnace at 100°C under atmospheric pressure, with one sample removed every 30 minutes for further characterization.
Characterization: Figures 1a-c present high-resolution transmission electron microscope (HRTEM) images revealing distinct SnO2 crystallite formations within the aerogel. The Tauc plots shown in Figure 2a-c were derived from ultraviolet-visible spectroscopy (UV-Vis) using Beer Lambert's formula. They showcase an increasing bandgap as a function of the annealing time. The Urbach energy was calculated, providing a quantitative measure of disorder in the aerogel's crystal lattice. Corresponding edge absorption graphs in Figure 3a-c demonstrate that as the aerogel undergoes annealing, the Urbach energy decreases, indicating a reduction in the density of defects in the crystallites.
To delve deeper into the crystal structure and the annealing procedure, electron diffraction results will be presented. Additionally, Fourier transform infrared spectroscopy (FTIR) will be employed to elucidate the chemical structure of the SnO2 aerogel. In parallel, electrical conduction testing will be conducted, offering indirect insights into parameters governing the gelation process.
Future steps: As the next phase of this research, we aim to investigate the growth behavior of the aerogel under the influence of electric fields. Following this, we plan to delve into a comprehensive analysis of both electronic and ionic conductivities. This exploration will provide valuable insights into the material's response to external stimuli and potential applications in neuromorphic devices.

Effect of metal doping on topographic, microstructure, optical and thermal properties of ZONP

Prof. Rahima Nasrin[1]
[1]University of Barisal

Nanomaterials have gained considerably more interest in the earlier era due to their outstanding optical, structural, and electrical behaviors [1]. Nowadays semiconductor nanoparticles (NPs) are a significant topic of research in nanoscience and nanotechnology [2, 3]. In this research, understanding the effect of metal doping on the characteristics of zinc oxide nanoparticles (ZONP), cobalt-doped zinc oxide nanoparticles (CDZONP) at various Co contents and pristine zinc oxide nanoparticles PZONP has been prepared via chemical bath deposition (CBD) method. Different characterization techniques have been performed to investigate the synthesized samples' surface topography, microstructure, optical and thermal properties. The scanning electron micrographs displayed a slightly olive-like structure

of PZONP which altered to flower-like structure after co-doping. Nearly all the NPs seem to be spherical in shape, nevertheless, a few lengthened particles are present in the prepared samples as observed by AFM images. The sample's microstructure represented hexagonal wurtzite structure as detected by the XRD pattern. The computed crystallite size of PZONP significantly varies with doping content. Optical analysis revealed that with the increase of Co-doping content, a little shift happened on the absorption edges. The uppermost Eg was found for PZONP. With the increase of Co-doping content up to 10 %, the value of Eg reduces to 2.54 eV. TGA analysis exhibited that the CDZONP sample is more thermally stable than the CDZONP. The DSC spectra of PZONP and CDZONP displayed two endothermic peaks at around 105 ℃, 211℃ and 80℃, 208 ℃ respectively.

K.Gherab,Y.Al-Douri,C.H.Voon,U.Hashim,M.Ameri,A.Bouhemadou, Results in Physics, 7, 1190-1197 (2017).
L.G. Valluzzi, M.G. Valluzzi, G. N. Darriba, M. Meyer, L.C. Damonte, J. Alloys and Compounds, 829, 154488 (2020).
R. Bekkaria, L. laânaba, D. Boyerb, R. Mahioub, B. Jaberc, Materials Science in Semiconductor Processing 71, 181–187 (2017).

Multi-level Switching of ZnS-Based RRAM (Student)

Mr. Sanghun Lee[1], Dr. Sobia Ali Khan[2], Dr. Jae-Hyung Jang[2]
[1]School of Electrical Engineering and Computer Science, GIST, Gwangju 61005 Korea, [2]KENTECH Institute of Energy Materials and Devices, KENTECH, Naju 58330, Korea

Resistive random-access memories (RRAM) are attracting attention as a next-generation non-volatile memory device because it has a simple structure, high endurance, low power consumption, fast switching speed, high scalability, and good CMOS compatibility [1]. In general, RRAM has a metal-insulator-metal structure, and oxide materials are often used as the insulator, such as HfO2, TiO2, and ZrO2 which have been reported [2-4]. Nowadays, among many characteristics of RRAM, multi-level switching is emerging as an important property. The reason is that it increases the storage density of the memory by allowing more than one bit of memory to be stored in one cell without reducing the size of the device [5]. Moreover, RRAM is used in the field of neuromorphic synapses, which has recently been actively studied, and multi-level switching is one of the important characteristics of this device. Multi-level switching can be achieved by controlling set voltage, set compliance current (Icc) and reset voltage [6].

In this study, we fabricated a RRAM device using Zinc sulfide (ZnS). ZnS is a material that widely used in the optical field such as LED, solar cells, and display panels. However, not much is reported in memory device field. So, we tried to fabriacte RRAM using ZnS as insulator and find out what characteristics it had. Zinc sulfide was deposited 30nm using magnetron sputtering. The top and bottom were deposited using E-beam for 150nm each. Measurements were made using Keithley 4200-SCS, and all measurements are conducted at room temperature, positive voltage at the top and common at the bottom.

Figure 1 shows typical multi-level switching I-V characteristics of ZnS-based RRAM at Icc=1m, 7mA, and 30mA. Multilevel switching was achieved by controlling Icc, it shows 3 step of multilevel switching. Figure 2 and 3 show endurance and retention characteristics. Endurance is measured for 50 cycles for each Icc, for set voltage at 3V, and reset voltage at -3. Retention test conducted for 1000s for each Icc, stress bias at 0.02V.

References

[1] Ielmini, Daniele. "Resistive switching memories based on metal oxides: mechanisms, reliability and scaling." Semiconductor Science and Technology 31.6 (2016): 063002.
[2] Fantini, Andrea, et al. "Intrinsic switching behavior in HfO2 RRAM by fast electrical measurements on novel 2R test structures." 2012 4th IEEE International Memory Workshop. IEEE, 2012.
[3] Regoutz, Anna, et al. "Role and optimization of the active oxide layer in TiO2-based RRAM." Advanced Functional Materials 26.4 (2016): 507-513.
[4] Wang, Sheng-Yu, et al. "Improved resistive switching properties of Ti/ZrO2/Pt memory devices for RRAM application." Microelectronic engineering 88.7 (2011): 1628-1632.
[5] Zahoor, Furqan, Tun Zainal Azni Zulkifli, and Farooq Ahmad Khanday. "Resistive random access memory (RRAM): an overview of materials, switching mechanism, performance, multilevel cell (MLC) storage, modeling, and applications." Nanoscale research letters 15 (2020): 1-26.
[6] Kim, Tae-Hyeon, et al. "Multilevel switching memristor by compliance current adjustment for off-chip training of neuromorphic system." Chaos, Solitons & Fractals 153 (2021): 111587.

Effect of Co-suppering NiO: V2O5 Thin Film for Hydrogen Sensing Application (Student)

Mr. Jing-Lian Li[1], Mr. Yuh Huang[2], Prof. Tien-Chai Lin[1], Prof. Wen-Chang Huang[1]
[1]Kun Shan University, [2]National Cheng Kung University

Metal oxide semiconductor (MOS) gas sensors are extensively studied because of their superior quality in terms of low cost, highly sensitive, fast response and compact size. Vanadium oxides, in particular, have attracted the attention of researchers for the development of gas sensors due to their multivalent state and exceptional electrical and optical properties.[1, 2]

High sensing response for hydrogen gas based on the nickel oxide doped with vanadium pentoxide thin film (NiO:V2O5) sensor is presented in the research. The NiO:V2O5 thin film was deposited by a co-sputtering system and with varied RF powers toward NiO target to study the Ni doping effect of the hydrogen sensor. The sensing response value is defined as S%=[(Ig-Ia)/Ia]´100%, where Ia is the current of the sensor in the air and Ig is the current in the presence of certain H2 concentration. Structural, morphological and hydrogen sensing behaviour were excused to observe the enhancement of sensibility of the thin film sensor. It is found that the NiO:V2O5 thin film with power of 30 W toward NiO target exhibits highest hydrogen sensing response. It shows a high response value of 2355.8% in the sensor and as compared to the undoped V2O5 thin film sensor with the sensing response of 131.6% at the hydrogen concentration of 1000 ppm at 300 °C. The sensor also shows a response time of 27 sec and a recovery time of 78 sec. The The improvement of sensing response of the NiO:V2O5 thin film is due to the modification of V2O5 surface morphology as shown in SEM and AFM analysis. The increase of surface

roughness promotes more reacted sites for chemisorbed oxygen and hydrogen on the surface of the sensor. And these effects would lead to the increase of the sensing ability. The NiO:V2O5/ZnO nanorod also superior sensing response as compared to the ZnO nanorod sensor.

Effect of Dzyaloshinskii -Moria interaction on Magnetic Tunnel Junction-Based Molecular Spintronics Devices (MTJMSDs)

Dr. Babu Sankhi[1], Ms. Danielle Thompson[2], Dr. Pawan Tyagi[3]
[1]University of the District of Coulombia, [2]University of the District of Columbia, [3]University of the district of Coulombia

The investigation into the profound implications of Dzyaloshinskii-Moria interaction (DMI) on Magnetic Tunnel Junction-based Molecular Spintronics Devices (MTJMSDs) represents a pivotal stride towards unraveling the intricacies of magnetic metamaterials. DMI, characterized by antisymmetric exchange interactions, plays a seminal role in the formation of magnetic spin textures—a foundational component of advanced magnetic data storage devices. This work employs a rigorous Monte Carlo Simulation (MCS) methodology to dissect the potential mechanisms underlying the impact of DMI on MTJMSDs, seeking to elucidate fundamental insights into the intricate interplay between DMI and magnetic electrodes. The focus is directed towards cross-junction shaped MTJMSDs, and the atomistic behaviors of these devices are scrutinized by simulating a diverse array of DMI values under specific symmetric Heisenberg exchange interaction conditions. Our study reveals that the discernible effects of DMI materialize at specific values, manifesting in oppositely aligned magnetic moments configured in band-like formations within the DMI-treated electrode. While a nominal impact is observed on the DMI-treated electrode, the electrode devoid of DMI exhibits pronounced susceptibility to molecular influence. Furthermore, we explore different ways molecules interact for varying MTJ electrode's thickness and widths. This helps us understand how DMI, molecules, and Heisenberg exchange interactions all work together in subtle ways. In essence, this work not only advances our understanding of the nuanced dynamics within MTJMSDs but also contributes essential knowledge for the potential design and optimization of magnetic metamaterials through judicious manipulation of DMI in molecular spintronics devices.

Resistive-Switching characteristics in ALPO (Student)

Mr. Nitupon Dihingia[1], Prof. Sandip Mondal[2]
[1]Ph. D Research Scholar, IIT Bombay, [2]Assistant Professor, IIT Bombay

Resistive-Random Access Memory (RRAM) is the most widely explored emerging memory technology due to its outstanding characteristics compared to conventional memory technology. We explored a novel solution-processed resistive switching material ALPO (Aluminium Oxide-Phosphate) for RRAM applications with a 2-terminal RRAM structure of ITO/ALPO/Al fabricated on Si-wafer. The devices exhibited compliance free resistive switching in low-voltage ranges of 2 V to -2.3 V with no forming step involved. The current ranges were also very low being <500 μA. With voltage pulses, the devices showed fast switching speed of 50 ns with 4.5 V and -5 V pulses for SET and RESET respectively. The endurance test conducted upto 104 cycles maintained a memory-window >10 with good retention of the states measured upto 106 s. The resistive switching demonstrated in ALPO-based RRAM devices has promising potential for use in non-volatile memory applications by virtue of its fast-switching, stable retention and good endurance.

Fabrication and Characterization of Flexible PVDF-TrFE/MnCoFe204 Nanocomposite Thin Film for Electrical Applications (Student)

Mr. Faruk Soso[1], Prof. Vijaya Rangari[2], Prof. Jeff Shield[3]
[1]Tuskegee University/University of Nebraska-Lincoln, [2]Tuskegee University, [3]Department of Mechanical & Materials Engineering, University of Nebraska-Lincoln, 68588, USA

Multiferroic composites which integrates magnetic and ferroelectric materials exhibit a higher operational temperature (above room temperature) and superior ME coupling parameter when compared to single-phase multiferroic materials. Room temperature control and the switching of magnetic properties via an electric field and electrical properties by a magnetic field has motivated research towards the goal of realizing ultralow power and multifunctional electronic devices. In this research we report the synthesis and characterization of flexible PVDF-TrFE/MnCoFe2O4nanocomposite thin film for electrical applications.
Manganese cobalt ferrite nanoparticles were synthesized via microwave assisted method and incorporated into ferroelectric polyvinylidene fluoride-trifluoro ethylene PVDF-TrFE co-polymer matrix at various percent weight of 1%,3%,5%,7%, and 10%. The nanocomposite thin film show the 0-2 type architecture, where 0 dimensional magnetic nanoparticles were incorporated into 2-dimentional ferroelectric polymer films. The flexible nanocomposite void free films were prepared via 3D printing technique. XRD verified the ferroelectric polar beta phase of PVDF-TrFE and the highly crystalline cubic spinel structure of the nanocomposite powder, which is in good agreement with the ICDD data. High Resolution Transmission electron microscope HRTEM and Selected Area Electron Diffraction SAED revealed the cubic crystal structure, phase, inter planar spacing (d=0.27nm) and average particle size (7nm) where spherical which is in good agreement with the XRD data. Field Emission Scanning Electron Microscopy FESEM was used to investigate the morphology and grain distribution of the nanocomposite on the polymer films. The nanocomposite film were slightly aggregated, this could be due to the calcination temperature at 350°C with the increase in the content of the nanoparticle in the PVDF-TrFE matrix. Differential scanning calorimetry DSC revealed the curie, melting, crystallization and para to ferroelectric nature of the polymer thin film. Thermal gravimetric analysis TGA was used to analyze the weight loss, reaction calcination temperature, and decomposition temperature. Notable improvement was observed in the thermal properties with the incorporation of the nanocomposite powder. The reactive temperature for calcination (350C°) was slightly above the decomposition temperature (320C°) to ensure rapid decomposition of the acetates to form the final product. Magnetic hysteresis measurements were performed on the nanoparticle films using a VSM analyzer in the field range of -1.0T to 1.0T to determine the magnetic properties of the

polymer nanocomposite film. Magnetic saturation of 30 emu/g at room temperature was observed on 3% nanocomposite film, while the pure bulk nanocomposite powder showed a max magnetic saturation of 45 emu/g. The ferroelectric behavior of the nanocomposite film showed significant improvement and maximum polarization (0.5 μC/cm2) with 3% nanocomposite film compare to other nanocomposite films.

Enhancing IGZO Thin Film Transistors: A Dual Treatment Approach (Student)

Mr. Guoduan Liu[1], Dr. Zefan Yao[1], Ms. Huiming Guo[1], Dr. Camilo Velez[1]
[1]University of California Irvine

We report a treatment for IGZO thin films that combines annealing in forming gas atmosphere and ultraviolet ozone (UVO) to modify electrical characteristics of IGZO-based TFTs in 3 orders of magnitude. Previous reports from our group [1] confirmed that the saturation current could be tuned by UVO treatment, but here we propose a modified treatment to further improve device performance. Better control of IGZO conductivity is necessary to reduce power consumption and better tune transistor performance. Indium Gallium Zinc Oxide (IGZO) has been gaining increasing attention as an amorphous wide bandgap semiconductor due to its excellent electrical, and optical transparency properties broadly applied in thin film transistors (TFTs), solar cells, sensors, flexible and transparent electronic devices [2], [3]. Compared to traditional single-crystal semiconductors such as Si, Ge, and Ga, IGZO offers compatibility with various substrate materials, easier manufacturing processes, a high breakdown voltage due to its amorphous nature, relative chemical stability, low-temperature processing, and a wide band gap [4], [5].
The IGZO TFTs were fabricated on P-type (100) oxide-silicon carrier wafers, featuring Cr/Au (10 nm /50 nm) metal contact layers, 50 nm IGZO channel layer, and 10 nm Al2O3 dielectric layer (Fig. 1a-1b). Proposed treatment includes 1h annealing at 350ºC in 4000 sccm forming gas followed by 3 min UVO treatment with light intensity 28-32 mW/cm2 and wavelengths of 184.5 nm / 253.7 nm (17% and 83% respectively). Metal-Oxide-Semiconductor (MOS) stack's cross-section was characterized using TEM and EDS (Fig. 2). The proposed method altered the IGZO's band gap from 3.62 eV to 3.74 eV, as evidenced by Tauc plots from spectrometer measurements [6] (Fig. 3). Semiconductor I-V curves demonstrated the impact of each step of the proposed method (Fig. 4), with a threshold voltage (VTH) of 1.73 V achieved through the process, which was calculated from transfer curves (Fig. 5a-b). and saturation currents of ~1.1 μA and ~1.3 nA before and after treatment were obtained (Fig. 5c-d). Photoelectron spectroscopy (XPS) characterization of the IGZO thin film, conducted before and after treatment, revealed the origin of these changes (Fig. 6). It was found that the semiconductor's conductivity is primarily regulated by the proportion of metal-oxygen (M-O) bonding, hydroxyl groups (-OH), and oxygen vacancies (Vo) within the material. This balance is altered by the introduction of oxygen groups during the UVO treatment and the recombination of species during the annealing process.
References:
[1] G. Liu, C. Velez. 65th Electronic Materials Conference. Santa Barbara, California. 2023.
[2] Y. Zhu, Y. He, S. Jiang, L. Zhu, C. Chen, and Q. Wan, Journal of Semic., vol. 42, no. 3.
[3] T. Chen et al., Adv Mater Technol, vol. 8, no. 1, Jan. 2023.
[4] E. Lueder, et. all. Liquid Crystal Displays: Addressing Schemes and Electro-Optical Effects. United Kingdom: Wiley, 2022.
[5] J. Shi, J. Zhang, L. Yang, M. Qu, D. C. Qi, and K. H. L. Zhang, Advanced Materials, vol. 33, no. 50. 2021.
[6] P. Makuła, M. Pacia, and W. Macyk, Journal of Physical Chemistry Letters, vol. 9, no. 23. American Chemical Society, pp. 6814–6817, 2018.

In situ growth of lead-free perovskite crystals on fine fibers for flexible fiber-based solar cell manufacturing

Ms. Julia Salas[1], Ms. Annacaren Gutierrez[1], Mr. Raul Garza[1], Mr. Diego Setien[1], Dr. M. Jasim Uddin[1], Dr. Karen Lozano[1], Dr. Victoria Padilla[1]
[1]University of Texas Rio Grande Valley

Perovskite solar cells (PSC) belong to the third generation of solar cells, showing a remarkable progress in power conversion efficiency, increasing from 3% in 2009 to 25% today according to the Department of Energy (DOE). Their easy fabrication process, low-cost materials, band gap tuning and ultra-lightweight space have made them reckoned as the future of photovoltaic cells. In this study we present the in-situ growth of perovskite crystals on polymeric fiber mats synthetized via the Forcespinning technology®, to improve the stability of lead-free perovskite crystals and get a higher efficiency. Methylammonium tin (MASnX3)(where X: I or Cl, or a percentage of each) were obtained in a polyvinylpyrrolidone (PVP) mat. Field emission scanning electron microscopy (SEM) and energy dispersive X-ray spectroscopy (EDX) were the characterization techniques used to analyze the fiber and crystal morphologies and their elemental composition. The size of the crystals varies from approximately 30 nm up to 800 nm depending on the annealing temperature and time, preparation time, room humidity and the elemental composition. Additionally, the PVP fibers obtained using dimethyl formamide (DMF) presented an average diameter ranging from approximately 500 nm to 1 μm, depending on the speed of rotation, weight concentration and room humidity. The crystalline structure of perovskite was evaluated using X-ray diffraction (XRD), revealing a distinct peak at a 2Θ angle of 14.6 degrees, which corresponds to the 2D perovskite structure. UV-Vis proved that the fiber mat could absorb visible light and infrared spectrum. TGA and DSC were also explored as characterization techniques, and a detailed study of the parameters that affect crystal growth via spin coating, helping to determine the optimal combination for fiber synthesis is also included. Later different materials were tested to define the efficiency and how the addition of polymers affects the stability of the solar cell over time.

Structural Improvement in epitaxial NbN films grown on vicinal c-plane Sapphire (Student)

Mr. Anand Ithepalli[1], Mr. Saumya Vashishtha[1], Ms. Qiao Liu[1], Dr. Matthew Barone[1], Prof. Darrell Schlom[1], Prof. Huili (Grace) Xing[1], Prof. Debdeep Jena[1]
[1]Cornell University

Niobium Nitride (NbN) has become a popular material platform for superconducting (SC) circuits due to its high superconducting transition temperature (Tc) and critical field.

It has applications in SC nanowires, single-photon detectors, and cryogenic computation. However, growing high quality δ-NbN films through plasma-assisted molecular beam epitaxy (MBE) has been difficult and there is room for significant structural improvement of these films.
During growth by plasma-assisted MBE, at low temperatures NbN adatoms tend to have low surface diffusivity thus leading to a higher defect density—reducing crystalline quality. But increasing substrate temperatures to increase diffusivity also leads to a phase change in NbN films [1]. Instead, we deposit on a vicinal, or atomically stepped substrate surface. Increasing the miscut angle decreases the terrace-width adatoms need to diffuse through to create lower energy configurations. Our samples were 40nm of NbN grown on c-plane Sapphire at 600ºC with various miscut angles towards the m-axis (0.5º, 2º, 4º, 10º). Three series of these samples were grown with on as-received, annealed, and nitrided sapphire with an additional series grown on as-received sapphire with constant 0.5º miscut as a control. Samples in each series were co-loaded in MBE using Indium mounting to prevent growth-to-growth variations.
We report improvement in structural properties of NbN when grown on higher miscut substrates. Atomic Force Microscopy scans of all films grown reveal a sub-nanometer root-mean-squared (RMS) roughness which subtly increases with the miscut in all series. X-ray diffraction scans verify that our films were grown according to vicinal modes reported in earlier studies. [2] A constant mismatch between the c-axis lattice constant of sapphire and interplanar spacing of (1 1 1)-NbN, together with increasing miscut, causes increasing misalignment between these planes—causing NbN (1 1 1) rocking curve peaks to shift. Most importantly, we report that the full-width half-maxima of rocking curve scans of the NbN decrease as miscut increases approaching 20 arcsecs for 10º miscut, which is close to the value for the substrate—indicating higher quality films. Furthermore, for NbN on annealed sapphire, we report a small increase in Tc from 12K for 0.5º miscut substrate to 12.5K for 10º miscut substrate. But overall, electrical transport measurements do not seem to improve with miscut conclusively. Structural improvement does not seem to be the dominant scattering mechanism, other factors seem to limit electrical properties of the films. We do however, demonstrate that increasing crystalline quality of epitaxial NbN films grown on vicinal sapphire is plausible.
[1] J. G. Wright et al., Phys. Rev. Materials 7, 074803 (2023)
[2] H. Nagai J. Appl. Phys. 45, 3789–3794 (1974)

Rolled-up metamaterials (RUMMS) for infrared imaging (Student)
Mr. Gokul Nanda Gopakumar[1], Prof. Stephanie Law[1]
[1]Pennsylvania State University

The subwavelength information about an object is carried by waves with large wavevectors. The diffraction limit is caused by the rapid evanescent decay of these large wavevector waves at the surface of a material. Hyperbolic materials allow light with large wave vectors to propagate within the material without decaying exponentially close to the surface. These materials have a negative real part of the permittivity tensor along at least one direction and a positive permittivity along at least one other direction, leading to an open isofrequency surface, in contrast to the closed isofrequency surface of normal materials. In a flat hyperbolic material, the sub-diffractional information will still exponentiallly decay once it leaves the hyperbolic medium. However, in a rolled-up hyperbolic material, the wavevector of the light decreases as it propagates radially, and the image is magnified, enabling propagation beyond the surface.
In this work, we present rolled up semiconductor-based infrared hyperbolic metamaterials. We fabricate these structures by using a strained bilayer that can be released from the substrate. The strained bilayer is grown using molecular beam epitaxy and comprises a compressively strained Ga1-xInxSb bottom layer and tensile strained GaAsySb1-y top layer. The bilayer is grown on an AlSb sacrificial layer, and a Si:InAs layer is grown on top of the bilayer. Fabrication of the RUMMs was done using standard lithographic techniques. A mesa is patterned on the wafer and wet etched partially through the strained bilayer. The photoresist is removed and applied again to create a window through which the structure is etched to the sacrificial AlSb layer. The photoresist is removed and a wet etch that selectively removes the sacrificial layer is used to gradually release the strained bilayer, causing it to roll up. By changing the alloy composition, the stress in the bilayers can be tuned to change the diameter of the rolled-up tube.
High resolution X-ray diffraction is used to demonstrate growth of the strained bilayer and determine the degree of strain. Scanning electron microscopy is used to image the rolled-up tubes and correlate their diameter to the bilayer strain. Finally, infrared spectroscopy will be used to measure the optical properties of the RUMMs. Overall, this is the first step in creating a fully semiconductor-based curved hyperbolic metamaterial that can be used in subdiffractional imaging in the IR.

Engineering ErAs:InGaAlBiAs Photoconductive Switches for THz Emission and Detection: Material Design, Growth, and Characterization (Student)
Mr. Wilder Acuna[1], Mr. Weipeng Wu[1], Mr. James Bork[1], Dr. Matthew Doty[1], Dr. Benjamin Jungfleisch[1], Dr. Lars Gundlach[1], Dr. Joshua Zide[1]
[1]University of Delaware

Terahertz (THz) technology has gained significant interest due to its many applications, such as medical imaging, communications, and non-destructive testing. We present our updated research on developing photoconductive switches (PCS) for the emission and detection of terahertz (THz) pulses, using ErAs:InGaAlBiAs as the active material grown by molecular beam epitaxy. We tested our PCS detectors on a THz time-domain spectroscopy setup as a proof concept for this semiconductor material (ErAs:InGaAlBiAs) [1]. ErAs:InGaAlBiAs offers enough flexibility to engineer a material compatible with 1550 nm as excitation wavelength. ErAs self assembles into nanoparticles during growth when incorporated above the solubility limit, reducing the free carrier lifetime to subpicosecond values. This diminution is highly desirable for photoconductive switch emitters and indispensable for detectors. Moreover, ErAs exhibits a robust pinning effect on the effective Fermi level within the material, directly influencing parameters such as free carrier concentration, material dark resistivity, and the signal-to-noise ratio of emitted/detected THz pulses.
Furthermore, integrating Al and Bi into the InGaAs base material facilitates precise band engineering, allowing tuning

bandgap and alignment while ensuring the growth of high-quality material with lattice matching to an InP (001) substrate. However, it is noteworthy that incorporating Bi necessitates relatively low-temperature growth conditions (~280°C), which can adversely affect material properties. Specifically, ErAs nanoparticles are smaller at low-temperature growth due to the constrained adatom mobility, and small nanoparticles pinned the Fermi level near the conduction band in this material, increasing the free electron concentration. Nevertheless, incorporating ErAs by interrupted growth enables the formation of larger nanoparticles.

A variety of characterization techniques are utilized to measure semiconductor crucial properties. Dark resistance is determined through both the Hall effect and Van der Pauw measurements. Carrier lifetime, a vital aspect, is evaluated using optical pump THz probe spectroscopy, providing insights into the dynamic behavior of carriers within the material. Optical bandgap measurements are conducted using spectrophotometry, enabling the determination of this fundamental property. Additionally, material quality is explored through high-resolution X-ray diffraction analysis, offering insights into the structural integrity of the material lattice.

This research was primarily supported by NSF through the University of Delaware Materials Research Science and Engineering Center, DMR-2011824.

[1] Acuna, W.; Wu, W.; Bork, J.; Doty, M. F.; Jungfleisch, M. B.; Gundlach, L.; Zide, J. M. O. Band Engineering of ErAs:InGaAlBiAs Nanocomposite Materials for Terahertz Photoconductive Switches Pumped at 1550 nm. Adv. Funct. Mater. (2024). 2401853. DOI:10.1002/adfm.202401853.

Modeling the Optical Properties of Reconfigurable Phase Change Materials on Nanostructured Silicon (Student)

Ms. Miranda Szwej[1], Dr. Parsian Mohseni[1]
[1]Rochester Institute of Technology

Germanium-antimony-telluride (GST) is a chalcogenide phase change material (PCM) with various applications in defense, computing, communication, and healthcare. Integrating GST with silicon nanostructures is especially beneficial in devices for which large heating energies are required to switch between crystalline and amorphous phases. However, GST faces challenges in optically induced phase cycling due to its heat dissipation properties and associated ablation and elemental migration failure mechanisms. Using nanostructured silicon as a scaffold for GST introduces an aspect of thermal engineering, which aims to balance heat accumulation and dissipation, while simultaneously allowing the manipulation of its optical response behavior.

Here, we explore the optical properties of GST thin films integrated with various configurations of nanostructured silicon using the rigorous coupled-wave analysis (RCWA) approach. Simulation parameters such as GST film thickness, GST position within an array of Si nanowires (NWs), and configuration of NWs in both periodic and aperiodic arrays were modified to investigate their influence on local light absorption within the PCM. Additional simulations were performed to study the effect of SiO_2 on the optical response behavior of GST when deposited either as a planarization layer between the NWs or as a protective layer on top of the GST film. The difference in absorption between fixed-diameter and random-diameter NWs in both periodic and aperiodic array configurations was also studied. Periodic array configurations with 90 nm fixed-diameter NWs showed the greatest potential for enhancement of localized absorption. Periodic NW configurations showed up to 15% greater absorption than aperiodic configurations. In all cases, it was found that limiting the fill fraction of Si NWs to roughly 30% enables more efficient absorption in the GST film. The addition of a 100 nm SiO_2 layer covering the GST film creates a refractive index gradient, aiding coupling and increasing absorption by up to 75% in crystalline GST and 52% in amorphous GST. Additionally, an SiO_2 layer serves to prevent GST ablation and is, therefore, beneficial to both the optical properties and the stability of the system. Depositing SiO_2 between the NWs and beneath the GST film does not have a significant impact on the optical behavior (less than 5% decrease in absorption in both crystalline and amorphous phases). The optimal GST-on-nanostructured-Si configuration for efficient light absorption and controlled phase change consists of a periodic, fixed-diameter Si NW array with a 35 nm GST film positioned symmetrically about the top surface of the Si NWs, and encapsulated by a 100 nm SiO_2 layer to mitigate ablation effects. In this system, enhanced absorption is localized at the center of the GST film in regions between the NWs. The integration of PCMs with nanostructured Si can enable “beyond binary” and reconfigurable free-space optical and optoelectronic devices.

Fabrication of PDMS-based Piezoelectric Nanogenerator Using Indium Doped Zinc Stannate towards Energy Harvesting and Sensory Applications (Student)

Dr. Md Wasikur Rahman[1], Mrs. Tamanna Zakia[1], Mr. S M Anyet Ullah Shohag[1], Dr. M. Jasim Uddin[1]
[1]University of Texas Rio Grande Valley

Piezoelectric materials present a promising avenue for energy harvesting and wireless sensory applications, offering a viable solution to the escalating global energy demand. Upon mechanical stress, these materials exhibit a unique ability to accumulate electric charges on their surfaces. By integrating them into circuits, these accumulated charges can be harnessed to generate electricity. Based on this hypothesis, piezoelectric nanogenerator (PENG) has been fabricated. Recent research has spotlighted ternary oxide semiconductors as suitable promoters. Zinc stannate ($ZnSnO_3$), in particular, has garnered attention due to its exceptional electrical conductivity. In this study, we reported hydrothermal synthesis method of hexagonal $ZnSnO_3$ nanorods and characterized by XRD, EDX and SEM. Besides, In doped $ZnSnO_3$-polydimethylsiloxane (PDMS) piezoelectric nanogenerator has been fabricated and explored the piezoelectric properties of undoped and In-doped $ZnSnO_3$-PDMS films at varying concentrations. Current findings reveal significant piezoelectric potential across different frequency ranges, culminating in an impressive 9 V open circuit voltage and a peak-to-peak current of 14.26 μA at 120 BPM (Beats per minute). Considering the data presented in the work, the device was mounted in shoe soles and tested as an energy harvester and wireless human motion sensor, which can generate electric charge as well as detect human movements and transmit the corresponding signals wirelessly [1-3].

Keywords: Piezoelectricity, hydrothermal method, zinc stannate, energy harvesting, sensory application.

DFT-Based Modeling of Epitaxial Silicon Growth from TCS-H2 systems (Student)

Mr. Seokmin Oh[1], Mr. Dongmin Yoon[2], Mr. Dae-hong Ko[1]
[1]Yonsei university, [2]Yonsei univeristy

High-performance semiconductor devices, such as CMOS image sensors (CIS) and solar cells, are manufactured using epitaxial wafers because of high purity, adjustable doping levels, and homogeneous wafer thickness [1-2]. In the process of growing Si epitaxial layers on polished wafers, trichlorosilane (TCS) is utilized with hydrogen due to the rapid growth rate of Si at high temperatures (≥1100℃) and atmospheric pressure [2-3]. These conditions facilitate the deposition of thin films on the micrometer scale. Therefore, understanding the growth mechanisms of the TCS-H2 system is essential. In this study, we investigated the surface reaction pathways in the TCS-H2 system. The Si-Cl-H three-component system contains significant amounts of molecules such as SiCl2, SiHCl3, and SiCl4 [4]. A model of epitaxial growth from the TCS-H2 system can be proposed by calculating the energies associated with surface reactions such as adsorption, decomposition, and desorption. Ab initio calculations were conducted using the Vienna Ab initio Simulation Package (VASP), which is well-suited for calculating crystal structures and surfaces. The GGA-PBE functional with the DFT-D3(BJ) dispersion correction was employed with an 8-layer Si slab model to represent the Si(001)-c(4x2) reconstructed surface. A (4x4) supercell was utilized to prevent interactions between repeated supercells. Transition states were initially calculated using the Nudged Elastic Band (NEB) method with four images, subsequently refined by the Climbing Image Nudged Elastic Band (CI-NEB) method. Our findings offer the pathway of silicon growth with the calculation of energy for each reaction step and transition state, providing insights into the epitaxial process.

Keywords: Si epitaxy, Silicon growth model, DFT
Acknowledgements
This work was supported by the Technology Innovation Programs (20010598 & 20022480) funded by the Ministry of Trade, Industry & Energy (MOTIE, Korea).

[1] Ryosuke Okuyama, et al. Hydrogen Termination Effect on SiO2/Si Interface State Density in CH3O-Molecular-Ion-Implanted Silicon Epitaxial Wafer for CMOS Image Sensors, ECS Journal of Solid State Science and Technology 13.1 (2024) 017005
[2] Clara Rittmann, et al., Toward Highly Efficient Low-Carbon Footprint Solar Cells: Impact of High-Temperature Processing on Epitaxially Grown p-Type Silicon Wafers, Solar RRL (2024) 2300882
[3] Kyuhyung Lee, et al., Generation mechanism of large-size invisible defects on Si epitaxial wafers, Journal of Crystal Growth 462 (2017) 12-17
[4] Vladimir S.Ban, et al., Chemical processes in vapor deposition of silicon: I. Deposition from and etching by, Journal of the Electrochemical Society 122.10 (1975) 1382

Morphology-Driven Magnetic Property Manipulation in Binary Particle Mixtures for Microscale Magnetic Control. (Student)

Mr. Khalil ur Rehman[1], Prof. Mario Hofmann[1], Prof. Ya-Ping Hsieh[2]
[1]National Taiwan University, [2]Academia Sinica

Magnetic microactuators and microrobots have the potential to revolutionize remote manipulation and swarm-based collaboration. Unfortunately, conventional approaches to controlling individual magnetic systems cannot be shrunk to the microscale due to fundamental challenges in the generation and modification of magnetic fields. We here demonstrate the manipulation of magnetic properties in binary particle mixtures through morphology control. A combination of ferromagnetic and non-magnetic particles demonstrates the emergence of ordering and magnetic anisotropy under conditions that induce mechanical jamming in the assembly. Combined theoretical and experimental investigation confirm the importance of arresting forces from neighboring particles as the origin of this behavior. Utilizing this insight, a novel actuator, termed “Magnet with Mechanical Tunability (MagMeT)” was developed that transduces mechanical deformation in magneto/elastomer particle mixtures into magnetic torque. Our results open up a route toward actively controlling magnetic microrobots for future remote operating applications.

Impact of Mg Incorporation in Semipolar Planes of N-polar and Ga-polar 3D Microstructures on Photocathode Internal Quantum Efficiency

Ms. Shadi Omranpour[1], Dr. Emma Rocco[1], Dr. Vincent Meyers[1], Mr. Benjamin McEwen[1], Mr. Alireza Lanjani[2], Dr. Lloyd Douglas Bell[3], Prof. F. Shahedipour-Sandvik[1]
[1]Department of Nanoscale Science and Engineering, University at Albany, [2]College of Nanotechnology, Science, and Engineering, University at Albany, [3]Jet Propulsion Laboratory, California Institute of Technology, Pasadena, USA

Photocathode detectors have practical utilization in astronomy and military for low signal photon detection and image intensifiers [1] [2]. The III-nitride material system is a noticeable candidate for photocathodes, with properties of wide and tunable bandgap energies and radiation hard [3] [4]. Previously, dopant incorporation studies of the p-type dopant incorporation, Mg, within GaN hillock structures indicated enhanced Mg incorporation efficiency on the semi-polar facets. This led to improved optical and electrical device performance. In addition, microstructures with stabilized semi-polar sidewalls in both Ga and N polarity were reported by a combination of V/III ratio and growth time optimization. N-polar and Ga-polar microstructures with semi-polar facets, achieved a maximum internal quantum efficiency (IQE) of 2.71% compared to polar planes. The higher QE is attributed to improved incorporation efficiency of Mg-dopants within the semi-polar facets [5]. Our previous work has demonstrated higher rates of MgGa and less Mg clustering in semi-polar facets than in c-plane films [5]. This suggests that the controlled growth of semi-polar GaN:Mg may enable enhanced p-type conductivity, and therefore IQE, of photocathode devices.
As previous studies have shown, conductivity of Ga-polar p-GaN films does not increase monotonically with [Mg] [6]. In this work we investigate the impact of varying Mg and Ga precursor molar flow ratio on photocathode IQE in response to increased semi-polar facet area relative to planar structures of both N and Ga polarity. We accomplish this by performing selective area growth (SAG) via metal-organic chemical vapor deposition (MOCVD) to create 3D p-GaN photocathode structures on (0001)- and ()-oriented GaN

templates. Their IQE is compared to planar films at comparable growth conditions using photoemission spectroscopy. SAG structures on Ga- and N-polar substrates exhibit maximum IQE of 3.6% and 7.8% respectively. However, the precursor molar flow ratio at which these maxima occur varies drastically with differing polarity This suggests that the optimal precursor flow ratio for p-conductivity in semipolar planes relative to (0001) and () differs. The variation of IQE is discussed in the context of polarity dependence of Mg incorporation. The optical and structural characteristics of the designed photocathode microstructures will be presented through analysis of micro-photoluminescence and transmission electron microscopy (TEM).

[1] M. P. Ulmer, Quantum Sensing and Nanophotonic Devices VI, 2009.
[2] Peter D. Townsend, Contemporary Phys, vol. 44, no. 1, 2010.
[3] E Muñoz, et al, J. Phys, vol. 13, 2001.
[4] Carlos Rivera, Jet al," The Open Electrical & Electronic Engineering Journal, vol. 4, 2010.
[5] Emma Rocco, State University of New York, Polytechnic Institute, 2023.
[6] H. Obloh, et al," Journal of Crystal Growth, 1998.

TECHNICAL PROGRAM

THURSDAY

JUNE 27, 2024

8:00 AM
Registration Opens
ESJ Building, Ground Floor

8:30 AM
III-N Device and Material Characterization
Session Chairs: Mona Ebrish (Vanderbilt University), Mihee Ji (Army Research Laboratory)
ESJ 0202

08:30 AM
Dependence of Minority Carrier Lifetime on Alpha Irradiation Fluence in n-type Free-Standing GaN
Dr. LeighAnn Larkin[1], Dr. Gregory Garrett[1], Dr. Mihee Ji[1], Dr. Marc Litz[1], Dr. J. Derek Demaree[1], Dr. Vijay S. Parameshwaran[1], Dr. Michael Wraback[1]
[1]Army Research Laboratory

Wide bandgap (WBG) semiconductors are desirable for α-voltaic power sources because of higher conversion efficiency associated with larger open circuit voltages and greater tolerance to radiation damage. While the strong bonding in WBG semiconductors enables intrinsic radiation hardness, the effects of irradiation are still evident on the performance of GaN-based electronic devices [1]. Declining device performance as a function of dosage is attributed to defects related to displacement damage, which leads to a reduction of mobility and carrier concentration as a function of irradiation, primarily at proton and neutron irradiation fluences > 1013cm-2 [1,2]. However, for power conversion devices such as α-voltaics, the primary factor limiting performance is the dependence of minority carrier lifetime and diffusion length on irradiation fluence, which are expected to be far more sensitive to radiation damage in general, and even more so from the massive α-particles, especially for low defect density, high performance devices on bulk substrates. In this work, we present direct measurements of the minority hole lifetime τ in 330-μm-thick free-standing (0001) GaN substrates (n > 8 × 1017 cm-3) as a function of 3.7 MeV α-irradiation fluence in the range from 108 – 1012 ions/cm2 for which the lifetime is most significantly affected.
Picosecond time-resolved (TR) cathodoluminescence (CL) studies of the near-band edge emission (~3.4 eV) were performed using time-correlated single photon counting and ultrafast electron pulses created by 400 nm fs pulse stimulated photoemission from an electron gun LaB6 cathode and accelerated to 30 keV. The low density (~ 1015 cm-3) and high penetration depth (up to 2 microns) of the electron-hole pairs created by these high energy electrons minimizes the importance of the initial decay associated with carrier diffusion and light reabsorption, with the longer, more dominant decay approximating the minority hole lifetime. At fluence F = 108 ions/cm2, the TRCL decay is indistinguishable from that of the unirradiated material with τ ~ 15 ns. The onset in reduction in τ is evident by F =109 ions/cm2, when τ decreases to 11 ns. A more precipitous drop in τ occurs between 1010 ions/cm2 (8.9 ns) and 5 X 1010 ions/cm2 (4.5 ns), similar in shape to that observed in very high quality silicon (unirradiated τo = 10 ms) under fission neutron irradiation [2]. The lifetime continues to drop significantly as the fluence is increased, and at 1012 ions/cm2 τ becomes 1.5 ns. Assuming a minority hole mobility of 10 cm2/Vs, the diffusion length L can also be calculated from τ as a function of irradiation fluence, decreasing from ~ 550 nm for the unirradiated material to ~ 200 nm for 1012 ions/cm2. While this correlates roughly with the calculated reduction in spacing between the α induced defects from ~ 700 nm to < 50 nm, the observation that L is less than the defect spacing for the unirradiated material and greater than that spacing for the highest F implies that other types of traps and recombination centers independent of the radiation damage also play a role. In addition, the drop in L with increasing F is directly correlated with a similar drop in charge collection efficiency in α-voltaic cells [3].
[1] S.J Pearton, ECS Journal of Solid State Science and Technology 5, 35-60 (2016).
[2] A.H. Johnston, IEEE Transactions on Nuclear Science 60, 2054-73 (2013).
[3] R. Gao et al., Communications Materials (2023) https://doi.org/10.1038/s43246-023-00360-9

08:45 AM
Temperature-dependent measurement of hole velocity vs. electric field in polarization-induced two-dimensional hole gases in GaN/AlN heterojunctions
Mr. Joseph Dill[1], Mr. Chuan Chang[1], Mr. Jonah Shoemaker[2], Dr. Zexuan Zhang[1], Dr. Jimy Encomendero[1], Dr. Kazuki Nomoto[1], Prof. Stephen Goodnick[2], Prof. Debdeep Jena[1], Prof. Huili (Grace) Xing[1]
[1]Cornell University, [2]Arizona State University

We present measurements and Monte Carlo simulations of the velocity vs. electric field (v-E) characteristic of a polarization-induced two-dimensional hole gas (2DHG) in gallium nitride (GaN) on metal-polar aluminum nitride (AlN) heterostructures at temperatures from 4 to 300K. The v-E characteristic of a semiconductor exhibits the carrier mobility in the low-field regime and the saturation velocity in the high-field regime, providing an essential benchmark for high-field transport theories.
Our sample is grown by molecular beam epitaxy on a single-crystal AlN substrate. A 12 nm coherently strained GaN layer is grown on AlN, producing a high-density 2DHG (verified by Hall-effect measurements) at the interface due to the polarization discontinuity. A 12 nm heavily Mg-doped InGaN cap layer is grown on the GaN to facilitate ohmic contact formation. This layer is removed from the channel region by reactive ion etching, leaving 7 nm of GaN.
A two-point current and voltage (IV) measurement of an etched constriction test structure is used. Measurements of this kind have been performed with many semiconductors, including silicon [1], silicon carbide [2], bulk GaN [3], and AlGaN/GaN HEMT heterostructures [4,5]. In recent years, our group has realized high-quality undoped GaN/AlN

heterostructures with a sizeable polarization-induced 2DHG at the interface [6]. Subsequent efforts to fabricate p-channel GaN finFETs [7] have motivated measurements of v-E to understand hole transport and the intrinsic limits of high-frequency p-GaN device performance.
The etched constriction has a ~1 um length, L, and width, W, determined from scanning electron microscope images. The sheet hole density, p-s, measured by Hall-effect rises quasi-linearly from 2.2×1013 to 4.8×1013 cm-3 between 4 and 300K. The exact mechanism behind this change in carrier concentration is not fully understood. The IV through the constriction is measured using a microsecond-width pulsed voltage to minimize heating effects. The measured voltages are corrected to account for the voltage drop between the source pads and the constriction edges. The electric field, E, in the constriction and the mean hole velocity, v, are extracted with the equations E = V/L and v = I/qWps (q is the electron charge).
We measure saturated hole velocities of 5.2×106 cm/s at 4K and 1.6×106 cm/s at 300K. These values are of comparable magnitude to previous measurements of saturated hole velocity in p-doped bulk GaN (6.6×106 cm/s at lower hole density) [8]. Our theoretical v-E curve at 300 K, extracted from a 2D full-band Monte Carlo transport simulation of the constriction device, over-predicts the measured velocity at 300 K but agrees with measurements at lower temperatures, implying an overestimate of the hole mobility. Because the measured hole density changes with temperature, these measurements do not elucidate whether the change in saturated velocity is due to the temperature or carrier density change.
1) C. Jacoboni et al., Solid State Electron. 20, 77 (1977).
2) I.A. Khan and J.A. Cooper, IEEE Trans. Electron Devices 47, 269 (2000).
3) J.M. Barker et al., Phys. Status Solidi 190, 263 (2002).
4) J.M. Barker et al., J. Vac. Sci. Technol. B Microelectron. Nanom. Struct. 22, 2045 (2004).
5) S.A. Vitusevich Semicond. Physics, Quantum Electron. Optoelectron. 9, 66 (2006).
6) R. Chaudhuri et al., Science 365, 1454 (2019).
7) S.J. Bader et al., IEEE Electron Device Lett. 39, 1848 (2018).
8) D. Ji et al., IEEE Electron Device Lett. 41, 23 (2020).

09:00 AM
Growth and Characterization of UV-A Light-Emitting Diodes (Student)
Ms. Alexandra Dolgashev[1], Dr. Theeradetch Detchprohm[1], Dr. Hunter Chan[2], Dr. Zhitao Kang[2], Prof. Russell Dupuis[1]
[1]Georgia Institute of Technology, School of Electrical and Computer Engineering, [2]Georgia Institute of Technology

Ultraviolet (UV) AlGaN LED's have been the focus of development due to their diverse applications in disinfection, communication, time-resolved fluorescence detection, and more. In this work, we seek to optimize 385nm-emitting UV LEDs by exploring the impact of the epitaxial structure design and device mesa size to improve the emission efficiency. The UV LED epitaxial structures were grown by metalorganic chemical vapor deposition (MOCVD) and studies were made of the performance of LEDs having different device sizes and different active region designs. The III-N LED p-n junction heterostructures designed for UV emission at ~385 nm were grown on (0001) sapphire substrates using standard high-purity metalorganic and hydride precursors. The LED heteroepitaxial structure consisted of: (1) a low-temperature GaN buffer layer, (2) an unintentionally doped GaN template layer, (3) an n-GaN:Si layer, (4) an undoped InGaN/AlGaN multiple quantum well (MQW) active region with five QWs, (5) a p-AlGaN:Mg electron blocking layer (EBL), (6) a p-GaN:Mg layer, and (7) a p+-GaN:Mg contact layer. The MQW active region consisted of five alternating InGaN quantum wells and AlGaN quantum-well barriers (QWBs) having various AlN mole fractions while the EBL was a layer of p-AlGaN:Mg. Epitaxial wafers were fabricated into individual LEDs with mesa diameters of 26, 36, 64 and 140 mm. Characterization of these (unpackaged) devices showed higher optical power density at a fixed current density with a decrease in the mesa size. In addition, the LED performance was optimized by studies made to increase the quantum efficiency of the active region. To compare carrier confinement based on the quantum-barrier height, test MQW-only and full MQW LED structures were grown with QWB layers having different AlGaN alloy compositions of Al0.09Ga0.91N and Al0.12Ga0.88N. The LED active-region-only samples employing different quantum-well barriers were evaluated using 300K photoluminescence and the performance of complete MQW LEDs were compared using fully processed large-area quick-diodes (QDs) and simple on-wafer scratched-diode (SD) LED test structures using electroluminescence (EL) at 300K. While the PL tests on the active-region-only MQW samples showed no significant change in the emission intensity with QWB alloy composition, SD EL tests on the complete MQW LED wafers revealed that the use of the higher-aluminum-composition QBs yielded higher UV optical power output vs. DC current drive.
Using the design of the improved LEDs with Al0.12Ga0.88N QWBs as a guide, further studies were made by the growth of full UV LEDs with different AlGaN EBL structures and EBL alloy compositions. LEDs with a graded-composition EBL (5nm p-Al0.20Ga0.80N and 15nm p-Al0.20->0.05GaN tapered compositions) and LEDs with a higher composition EBL (20nm of p-Al0.28Ga0.72N) were grown and compared with the original Al0.20Ga0.80N EBL composition LEDs using SD EL tests. Under these test conditions, the SD-LED with the graded-composition AlGaN EBL had the highest optical power output but also experienced a notable change in emission to a longer peak wavelength. We will present the device testing performance results for completely fabricated LED devices with these MQW heterostructures in more detail.

09:15 AM
Epitaxially Grown N-polar GaN Quantum Dots for Short Wave Ultraviolet (UV-C) Applications (Student)
Mr. Md Mehedi Hasan Tanim[1], Mr. Shubham Mondal[1], Dr. Yuanpeng Wu[1], Mr. Samuel Yang[1], Mr. Mingtao Hu[1], Dr. Ding Wang[1], Prof. Zetian Mi[1]
[1]University of Michigan, Ann Arbor

In this study, we have presented the first demonstration of N-polar GaN quantum dots (QDs) exhibiting extreme quantum confinement within an AlN matrix by utilizing plasma assisted molecular beam epitaxy. Notable benefits of the N-polar orientation include less electron overflow and increased

electrical efficiency, outperforming their metal-polar counterparts in these areas, for applications in mid and deep-ultraviolet (UV) optoelectronics [1]. These GaN QDs, because of strong quantum confinement, can emit photons at a strikingly short wavelength of 243 nm (ħω = 5.10 eV), significantly blueshifted from the bulk edge emission energy of GaN at 3.4 eV [2]. The growth process of N-polar GaN QDs initiates with the deposition of an AlN buffer layer on top of a c-face 4H-SiC substrate, followed by the growth of the GaN QD layer in N-rich condition. Subsequently, a thin low-temperature AlN layer is immediately deposited onto this QD layer. The ensuing annealing process, meticulously timed, serves the purpose of reducing the dimensions of the QDs and mitigating defects within the layer. Remarkably, this reduction in QD dimensions manifests as an augmentation in the photoluminescence (PL) quantum efficiency of the QDs. For PL measurements, we employed a laser with a 193 nm wavelength, conducting our experiments on QD samples with a single QD layer covered by a 27 nm thick AlN capping layer. A total of five distinct samples were prepared by varying the GaN QD layer growth time and the AlN barrier growth time prior to annealing. This strategic manipulation enabled precise tuning of the emission peak wavelength of the QDs across the mid and deep UV spectra. For each of these five samples, PL spectra of the QDs were meticulously recorded at room temperature under a spectrum of excitation power levels, ranging from 10 μW to 1 mW. As the excitation power was systematically increased from 10 μW to 1 mW, the emission peak exhibited a consistent and significant blueshift, attributed to the quantum confinement effect. For instance, in the case of the sample with a 30 s GaN QD growth time, the emission peak shifted from 256 nm to 243 nm with increasing excitation power, a notable manifestation of the profound quantum confinement effect. Subsequently, to quantify the radiative recombination efficiency of GaN QD, we prepared a sample with three GaN QD layers separated by 10 nm AlN barrier and measured temperature-dependent PL. This measurement revealed a significant blue shift in the emission peak to 233 nm at low temperature (20 K). Assuming the defect related non-radiative recombination at 20 K is zero, we have measured the internal quantum efficiency of the sample is 75.7%. This N-polar GaN quantum dot presents a compelling solution for applications in air/water purification, through deep ultraviolet (UV) optoelectronic devices like light-emitting diodes (LEDs) and lasers.

09:30 AM
Hole Transport and Doping in Polarization-Graded p-type AlGaN

Dr. Chandan Joishi[1], Mr. Andy Xie[2], Mr. Sheikh Ifatur Rahman[1], Prof. Siddharth Rajan[1]
[1]The Ohio State University, Columbus, OH 43210, [2]Qorvo, Inc., Richardson, TX 75081

High p-type conductivity III-Nitride layers could enable many devices such as AlGaN/GaN NPN heterojunction bipolar transistors, multi-active region LEDs, and lasers with excellent device performance. In this work, we report on the design and demonstration of low-resistive p-type base layers using polarization engineering. We find that polarization grading does help impart high hole concentration in thin p-AlGaN layers, but the associated drop in mobility due to alloy scattering is significant. We show abrupt polarization-engineered designs that can enable high hole sheet carrier density (1.2x1013 cm-2) and hole mobility (16 cm2/Vs) simultaneously, enabling sheet resistance as low as 33 kΩ/□, one of the lowest reported for an AlGaN/GaN two dimensional hole gas till date.
Motivation: Conventional approaches to develop thin p-type III-Nitride layers rely on carrier activation of acceptor dopants with high activation energy. An alternate approach to improve hole concentration is to exploit the polarization property of the material to form three-dimensional hole gas (3-DHG). For p-type graded III-Nitride alloys, however, the 3-DHG mobility is severely impacted by alloy scattering [1] which strongly depends on the alloy composition (x) and hole effective mass (m*). The alloy scattering limited mobility can be calculated using the equation [2]
μalloy = 2ehkBT*(1/(6π2m*Vo2Vcellx(1-x)p3D))*ln(1+exp(EF/kBT)
where Vo is the alloy scattering potential, Vcell is the unit cell volume, p3D is the hole concentration, EF is the Fermi energy, and other symbols have their usual meanings. This degradation in hole mobility negates the improvement in hole concentration achieved through grading across a wider alloy composition, with no concurrent enhancement in sheet resistance. As such, innovative device designs to mitigate the impact of alloy scattering by utilizing 2-DHGs from AlGaN/GaN heterointerfaces [3] and/or reverse-graded AlGaN layers with low Al-content emerge as pivotal aspects in advancing GaN device technology that utilize these thin p-type conductive layers.
Experimental: The p-type AlGaN layers with continuous and abrupt grading profiles were epitaxially grown in a metal-organic chemical vapor deposition system. Five sets of samples were grown to study hole transport and doping in these layers, (a) a 100 nm p-type GaN layer, (b) 50 nm p-Al0.3Ga0.7N graded to p-GaN, (c) 50 nm p-Al0.15Ga0.85N graded to p-GaN, (d) p-GaN graded to p-Al0.25Ga0.75N with an abrupt p-Al0.25Ga0.75N/p-Al0.15Ga0.85N interface followed by a linearly graded p-Al0.15Ga0.85N p-GaN layer, and (e) p-GaN graded to p-Al0.25Ga0.75N with an abrupt p-Al0.25Ga0.75N/p-GaN heterointerface. The corresponding schematics and band diagrams calculated using a self-consistent Schrodinger Poisson solver (BandEng) are shown in Fig. 1. To characterize the p-type AlGaN layer, ohmic contacts were fabricated using Pd/Ni/Au annealed at 500 0C for 5 mins in N2 ambient. Thereafter, the p-type layers were MESA isolated using BCl3/Cl2 based etch chemistry in an inductively coupled plasma reactive ion etch chamber (ICP-RIE) at a low power etch condition of ~5 W RIE and 40 W ICP.
Results: The p-GaN layer sample consistently displayed a high sheet resistance of 134 kΩ/□, measured using both Hall and transfer length measurements (TLM). Negligible isolation leakage (~μA/cm2) and ohmic p-contact behavior were obtained in all the device designs (Fig. 3(b)). In an effort to improve sheet resistance (RSH), the linearly graded AlGaN layer (GaN -> Al0.3Ga0.7N -> GaN) showed a reverse trend in RSH, measured to be 472 kΩ/□, with a hole mobility of ~1.5 cm2/Vs and hole concentration ~ 2x1018 cm-3, shown to be severely impacted by alloy scattering (Fig. 4(a)). Limiting the Al-composition to 15% mitigated the impact of alloy scattering to increase Hall mobility to 12.5 cm2/Vs, with a sheet charge density of 4.5x1012 cm-2, and extracted RSH of 111 kΩ/. To further improve the sheet resistance, the abrupt junction design proved vital with the p-Al0.25Ga0.75N/p-Al0.15Ga0.85N interface sample

displaying a lower RSH of 80 kΩ/□. The p-Al0.25Ga0.75N/p-GaN sample displayed further improvement in RSH down to 33 kΩ/□, with a sheet carrier density of 1.2x1013 cm-2 and mobility of 16 cm2/Vs. This sheet resistance features among the best reported for AlGaN/GaN 2-DHGs to date.
Conclusions: We designed and demonstrated thin p-type AlGaN layers using AlGaN/GaN heterointerfaces and/or low Al-content reverse-graded layers with high conductivity. The results are promising for the future development of devices such as III-Nitride HBTs which require highly conductive p-type layers for excellent performance.
We acknowledge funding from the Office of Naval Research under Grant No. N00014-22-1-2260 (Dr. Paul A. Maki).
References:
[1] J.Simon et al., Science, 327, 60-64, (2010) [2] C. Hamaguchi, vol. 9., Springer-Verlag, (2010). [3] A. Nakajima et al., APEX, 3, 121004 (2010)

8:30 AM
Oxide Semiconductor Thin Films and Devices
Session Chairs: Sarah Swisher (University of Minnesota), William Scheideler (Dartmouth College)
ESJ 0224

08:30 AM
Electrically Active Defects and Their Impact on Carrier Mobility and Density in Indium Tin Oxide (ITO) (Student)
Mr. Jade Cowsky[1], Prof. Leonard Brillson[1], Dr. Oliver Bierwagen[2]
[1]The Ohio State University, [2]Paul Drude Institute for Solid State Electronics

Indium Tin Oxide (ITO) is a widely used transparent conducting oxide (TCO) with a large band gap of 3.5 eV or higher with high conductivity. ITO is a semiconductor that is degenerately doped with Sn atoms that integrate into the In2O3 lattice as SnIn, producing carrier concentrations in excess of 1021 cm-3. Its applications include touchscreens, solar cell contacts, light-emitting diodes (LEDs), gas sensors, and heat-reflecting windows. We used depth-resolved cathodoluminescence spectroscopy (DRCLS) to probe the electronic and defect structure of a set of ITO films with systematically varied Sn doping density and study the effects of various treatments on degenerately-doped ITO films. Using DRCLS, we can identify the physical nature of defects and track their evolution throughout the bulk of a film by comparing observed luminescence energy with known energy levels within the ITO band gap and measuring how the luminescence peaks are affected by different treatments. Our DRCLS results identify luminescence from Oi (1.8-1.9 eV) as well as two Sn and Oi containing complexes, one tightly bound (2.9 eV, 2SnIn●Oi”3OO, also written Sn2O4) and a more loosely bound (2.4 eV, 2SnIn●Oi”) defect. The density of these defects is directly dependent on Sn doping density, with SnIn densities below 1020 cm-3 leading to the formation of (2SnIn●Oi”) complexes and additional dopants above 1020 cm-3 primarily promoting the formation of (Sn2O4) instead. Reducing/annealing treatments are shown to break up the loosely bound complexes and diffuse excess O out of the film, while the tightly bound complexes are unaffected. Conversely, exposure to remote oxygen plasma is shown to facilitate the formation of Sn-O complexes by supplying excess O to bond with existing Sn dopants. CL data shows a strong correlation between Oi density and electron mobility, suggesting that Oi may impede mobility less than the complexes it forms with Sn.
Figure 1 shows a set of curves relating oxygen partial pressure during growth, Sn doping density, carrier concentration, and electron mobility in ITO films. Defect formation in the film is affected by oxygen partial pressure and Sn doping density, which reverses gains in carrier concentration from increased doping[1]. Figure 2 shows a typical ITO CL emission spectrum and deconvolutions of a very heavily Sn-doped (N ≈ 3*1020 cm-3) In2O3 film, with band gap features at 3.6 and 4.0 eV and sub-EG luminescence peaks ranging from 1.8 to 3.3 eV. The 1.8-1.9 eV feature is associated with Oi defects, while the 2.4 and 2.9 eV features come from complexes of Oi and Sn above. Figure 3 shows the evolution of 1.8 and 2.9 eV luminescence as a function of Sn-doping, including a pronounced transition around 1020 cm-3, indicating onset of (Sn2O4) complex formation as Oi complex with SnIn. Figure 4 shows a depth profile of the 2.4 eV (2SnIn●Oi”) complex before and after remote oxygen plasma. The O-rich environment of the ROP causes additional Oi-containing complexes to form near the free surface. Figure 5 shows depth profiles of Oi and (2SnIn●Oi”) in as-grown films and after deposition of a 10 nm In layer and a subsequent anneal in reducing environment. The anneal and indiffusion of In atoms breaks up the loosely-bound complexes near the surface and removes excess Oi from the sample surface. Figure 6 relates Oi defect density to electron mobility, showing a strong correlation between increasing Oi density and higher mobility.
1: G. Frank and H. Köstlin, “Electrical properties and defect model of tin-doped indium oxide layers,” Applied Physics A Solids and Surfaces, vol. 27, no. 4, pp. 197–206, Apr. 1982, doi: https://doi.org/10.1007/bf00619080.

08:45 AM
Enhanced Charge Transport and Transistor Performance of α-IGZO Oxide Semiconductor via High-k/Low-k Bilayer Gate Dielectrics (Student)
Ms. Reem Alshanbari[1], Dr. Imai Takahito[2], Mr. Oliver Durnan[1], Prof. Shin-ichi YAMAMOTO[1], Prof. Ioannis Kymissis[1]
[1]Columbia University, [2]Ryukoku University

The next generation of high-resolution displays, memory chips, and 3D brain-mimicking integrated circuits depends on high-mobility transistors. Indium gallium zinc oxide (α-IGZO) is one of the most promising amorphous oxide semiconductors because it has a high on/off ratio due to a large band gap (>3.1 eV), low leakage current (~10-18 A/μm), and high field effect mobility (>10 cm2/Vs). In the theory of metal-oxide-semiconductor field-effect transistors (MOSFETs), it is necessary to increase the capacitance of the gate insulator (Ci) to boost the drain current (ID), where ID ∝ Ci. However, α-IGZO transistors operate as accumulation field-effect transistors (FETs) instead of the

usual inversion mode of silicon MOSFETs. Therefore, the field-effect mobility (μFE) in disordered structure materials depends on the channel's accumulated charge carriers. In addition, α-IGZO is sensitive to oxygen and hydrogen defects, especially oxygen defects, which include oxygen vacancies and hydroxides, which play a crucial role in the transport of charge carriers by impacting μFE and threshold voltage. The industry needs novel dielectric materials with a sufficient dielectric constant, a large band gap, good interfacial characteristics, and a reasonable conduction and valence band offset with Si. Thus, the alloy of different gate dielectrics and studying how this impacts transistor performance is crucial for enhancing carrier mobility and electrostatic control, which play a significant role in high-speed operation and low power consumption in FETs. Here, we look into how the device's properties affect the μFE by looking into how interface engineering affects the transport properties and electrical performance of α-IGZO transistors. In this research, we integrate a material with a large band gap (Eg) and a material with a high permittivity as a gate insulator, which could raise the Eg and make the material more disordered. Our results showed that the linear μFE of α-IGZO FETs with Al2O3/SiO2 gate dielectrics was 16 cm2/Vs and increased to 50 cm2/Vs with optimized HfO2/SiO2 gate dielectrics. The α-IGZO FETs with HfO2/SiO2dielectrics showed superior electrical performance, high-field effect mobility, and an on-current (Ion) of 2 μA. The off-current (Ioff) value was 14 pA under a drain-to-source bias of 0.1 V without any dielectric leakage. In addition, it decreased the hysteresis level and interface trap charge density (Dit). We hypothesize that the theory behind boosting the mobility of α-IGZO FETs with HfO2/SiO2 gate dielectrics is because of the increase in carrier concentration that fills localized states and allows band-like transport and reduced trap density at the interface between semiconductor and gate dielectric. Our findings show that with HfO2/SiO2, the α-IGZO channel has higher conductivity, which shows a higher output current with a higher capacitance density of the gate insulator, and the carrier concentration in the channel increases. The process of hydrogen diffusion into the channel leads to an increase in both carrier concentration and channel conductivity. In contrast, there was a degradation in the electrical performance of α-IGZO FETs with Al2O3/SiO2 gate dielectrics. As a result of the oxygen diffusion, more oxygen atoms diffuse from Al2O3 to the α-IGZO layer. Mainly, defect relaxation and suppression of free carriers result from material diffusion from the gate insulator to the channel. This study contributes insight into developing high-performance α-IGZO transistors through interface engineering.

09:00 AM
Metastability Of Indium-Tungsten-Oxide Thin-Film Transistors And Associated Operational Dependence On Oxygen Partial Pressure (Student)
Mr. Eli Powell[1], Ms. Meghana Nagesha[1], Dr. Karl Hirschman[1], Dr. Robert Manley[2], Dr. Bin Zhu[2]
[1]Rochester Institute of Technology, [2]Corning Incorporated

The demand for larger displays with higher resolution and refresh rates pushes the demand for thin film transistors (TFTs) with higher performance. The success of the amorphous oxide semiconductor (AOS) IGZO has driven efforts towards alternative AOS materials to produce TFTs with higher electron mobility. The focus of this study is on Indium-Tungsten-Oxide (IWO), which has shown promise in literature [1-3] as a high-mobility AOS candidate. Experimental factors include the partial pressure of oxygen in the sputter ambient, and the anneal condition used to passivate defects states which shift and distort electrical characteristics.
Unpassivated TFTs were fabricated in a staggered bottom-gate configuration with a 100 nm SiO2 gate dielectric. A 30 nm IWO channel material was sputter deposited with oxygen partial pressure (PO2) ranging from 2.5 – 10%. Annealing was conducted at temperatures ranging from 100ºC to 300ºC, with varying durations and ambient conditions. From electrical testing, a pronounced interaction between PO2 and passivation anneal conditions on the transfer characteristics was identified. Devices annealed at 100ºC in air ambient demonstrated characteristics which appear linked to the initial PO2 in the IWO film. With increasing PO2- device characteristics right-shift, exhibiting progressively more enhancement mode behavior, as shown in Figure 1a. This behavior implies a significant reduction in donor-like defects and a pronounced dependence on the initial PO2 of the devices. Devices annealed at 200ºC in air ambient demonstrated a significant left shift in transfer characteristics and depletion mode operation, similar to those of the un-annealed devices, possibly indicating a reconfigured defect state. Donor state passivation is successfully re-established following anneal at 275ºC however, the interaction between PO2 and anneal temperature appears less pronounced than at 100ºC, as shown in Figure 1b. Using Silvaco TCAD a hypothetical model is developed using the creation and adjustment of defect states at the back channel due to the lack of a passivation material.

09:15 AM
Kinetically Controlled Liquid Metal Printed Ternary 2D Semiconducting Oxides
Prof. William Scheideler[1], Mr. Simon Agnew[1], Mr. Samuel Ong[1]
[1]Dartmouth

Two-dimensional (2D) van der Waals metal oxide semiconductors and conductors offer a family of high-performance electronic materials distinguished by their ultrahigh transparency, flexibility, and efficient electronic transport (μeff > 30 cm2/Vs). The unique advantage of this class of ceramic materials is that they may be deposited at low process temperatures (< 150 ºC) via surface oxidation of liquid metals and their alloys. Here we report kinetically controlled continuous liquid metal printing for scalable fabrication of high-performance ternary metal oxide semiconductors and conductors. Through automated methods, we demonstrate precise kinetic control of continuous Cabrera Mott oxidation for printing high performance 2D oxide semiconductors from the interfacial oxide of liquid metals. This control of the oxidation kinetics is applied to modulate electronic properties as well as crystallinity and oxygen stoichiometry of 2D oxides, with low oxidation speeds leading to thicker (> 4 nm) and more degenerate films while high speed printing leads to thinner semiconducting channels (~ 2 nm).
These studies also identify the influence of liquid metal alloy dopants including Ga, Zn, and Sb on oxidation kinetics and

electrical properties of 2D In2O3. Understanding the stoichiometry of liquid metal dopants allows deeper control of the high electron concentration of low-temperature printed In2O3 channels (n0 > 1019 cm-3). For example, liquid metal printed InGaOx transistors printed from trace Ga-doped In precursor alloys with steep switching and improved bias-stress stability compared with pure In2O3. By comparison, Sb-doped In2O3 increases channel conductivity and the field effect mobility (< 180 ºC) while leading to lower device variability. Finally, using XPS, AFM, and XRD, we consider the influence of Ga and Sb doping on the 2D oxide composition, film morphology, and crystallinity, observing the limits of doping for printing the crystalline vs amorphous phase.

09:30 AM
Oxide Transistors on Gallium Nitride as a Platform for Monolithic MicroLED Displays (Student)
Mr. Oliver Durnan[1], Mr. Vikrant Kumar[1], Ms. Reem Alshanbari[1], Ms. Megan Noga[1], Prof. Ioannis Kymissis[1]
[1]Columbia University

We present a method of fabricating indium gallium zinc oxide (IGZO) thin-film transistors on gallium nitride to yield a monolithically integrated, active-matrix microLED display. The microLEDs use a ringed mesa structure to obviate the need for planarization. Beyond the fabrication process, we evaluate the behavior of individual microLEDs, transistors, as well as the integrated system. The outcome is a microdisplay with a resolution of 32x32 pixels, at a density of 78.4 pixels per inch, with a luminance greater than 1500 nits. This device showcases a step towards the development of the high resolution, high luminance, transparent displays necessary for future augmented reality applications.

8:30 AM
Narrow Gap and Highly Mismatch Alloys
Session Chairs: Aaron Muhowski (Sandia National Labs), Sadhvikas Addamane (Sandia National Laboratories)
ESJ 2208

08:30 AM
Bismuth Incorporation into InSb Towards Long-Wave Infrared Photodetectors (Student)
Ms. Corey White[1], Ms. Morgan Bergthold[1], Ms. Amberly Ricks[1], Mr. Felix Estevez Hilario[1], Prof. Daniel Wasserman[1], Prof. Seth Bank[2]
[1]Department of Electrical and Computer Engineering, University of Texas at Austin, Austin, TX 78758, [2]University of Texas at Austin

Sensitive photodetectors operating across the long-wave infrared (LWIR, 8-14 μm) are critical to a number of applications including chemical sensing, astronomical imaging, and thermography. As the incorporation of small concentrations of bismuth into InSb produces dramatic bandgap reductions,1,2 there is a unique opportunity to span the entirety of the LWIR with a bulk III-V alloy that can be grown directly on commercially available III-V substrates, thus circumventing the fabrication, growth, and toxicity challenges plaguing the current state-of-the-art narrow bandgap material system, HgCdTe. InSb1-xBix is a particularly well-suited III-V-Bi alloy for high-performance optoelectronic devices due to (1) the minimal bismuth incorporation necessary to reach the LWIR and (2) the relatively similar ideal growth conditions for InSb and III-Bi materials. To date, InSb-based dilute-bismide alloys exhibit the longest wavelength emission and detection from a lattice-matched III-V alloy3 highlighting the potential of this novel approach for efficient long-wave infrared detection. Recently, we have optimized the growth of InSb1-xBix by molecular beam epitaxy enabling highly substitutional bismuth incorporation and photoluminescence at extended wavelengths beyond that of bulk InSb.4 Building on this foundation, we present room temperature photoluminescence out to 8 μm from InSb1-xBix indicating high optical quality at LWIR wavelengths as well as the first InSb1-xBix nBn photodetector with an extended cutoff wavelength beyond that of InSb. Furthermore, we will show how arsenic incorporation can be leveraged to lattice-match to InSb substrates enabling thick absorbers for strong absorption and carrier collection.
InSb-1-xBix and InAsySb1-x-yBix alloys were grown by solid-source molecular beam epitaxy on InSb substrates under growth conditions targeting a kinetically-limited growth regime similar to that employed for the growth of high-quality GaAs1-xBix.5 A low substrate temperature of ~280˚C and an Sb/III flux ratio of ~0.975× were combined with a relatively fast indium growth rate to kinetically limit bismuth surface segregation during growth. X-ray diffraction, atomic force microscopy, and photoluminescence measurements were performed to quantify the structural and optical properties of the InSb1-xBix films. Room temperature photoluminescence from a 1 μm thick InSb0.98Bi0.02 film exhibited peak emission at 8 μm highlighting both the high optical quality of the InSb1-xBix alloys and how little bismuth incorporation is required to access technologically-important wavelengths in the LWIR.
To demonstrate a prototype InSb1-xBix photodetector, an nBn detector was grown employing a 400 nm thick InSb0.99Bi0.01 absorber and a 50 nm thick Al0.15In0.85Sb barrier. Comparing this detector with an otherwise identical device containing no bismuth, we observed a significant extension in cutoff wavelength at 79 K from 5.5 μm for InSb to 6.6 μm for InSb0.99Bi0.01. From this, we estimate that less than 5% bismuth incorporation is necessary to reach a 14 μm cutoff wavelength, which would enable InSb1-xBix to span the entire LWIR at ~77 K. The InSb and InSb0.99Bi0.01 detectors, which were grown under very similar growth conditions, exhibited similar peak intensities in their spectral responses suggesting that the presence of bismuth within the alloy does not inherently degrade the optical quality of InSb1-xBix materials, which is very promising for future detectors operating at longer wavelengths.
By also incorporating small quantities of arsenic, the quaternary alloy InAsySb1-x-yBix can be grown lattice-matched to InSb substrates. Furthermore, arsenic incorporation is expected to further assist in decreasing the

alloy bandgap energy due to the band bowing between InAs and InSb.6 By incorporating arsenic and bismuth in ~1:3 proportions, we grew an InAsSbBi film lattice-matched to InSb with 1.3% bismuth and 0.4% arsenic incorporation as quantified by X-ray diffraction and Rutherford backscattering spectrometry measurements. From this film, we observed photoluminescence at room temperature at extended wavelengths beyond that of InSb confirming the compatibility of this alloy for high-quality LWIR detectors. Building on this, growth and characterization of optimized detectors with thicker InAsySb1-x-yBix absorbers containing greater bismuth and arsenic concentrations are underway and results will be presented at the conference.
This work was supported by the National Science Foundation (Award No. ECCS-1933836) and an NSF Graduate Fellowship. The work was performed in part at the University of Texas Microelectronics Research Center, a member of the NNCI.
References:
1A. M. Jean-Louis, B. Ayrault, and J. Vargas, Phys. Status Solidi 34 (1969). 2M. K. Rajpalke et al., Appl. Phys, Lett. 105 (2014). 3R. C. White et al., 64th Electronic Materials Conf. (2022). 4R. C. White et al., Appl. Phys. Lett. 121 (2022). 5A. J. Ptak et al., J. Cryst. Growth 338 (2012). 6S. P. Svensson et al., Phys. Rev. Bi 86 (2012).

08:45 AM
Analysis of Highly Mismatched Sb-based Alloys grown on InAs Substrates (Student)
Mr. Fatih Furkan Ince[1], Prof. Thomas J. Rotter[1], Dr. Darryl Shima[1], Mx. Mega Frost[1], Ms. Subhashree Seth[1], Prof. Ganesh Balakrishnan[1]
[1]Center for High Technology Materials, University of New Mexico, Albuquerque, New Mexico

Mid-wave infrared (MWIR) detectors are essential for various applications such as medical devices, remote sensing, and spectroscopy[1]. In the MWIR detection, antimonide-based narrow bandgap semiconductors are ideal due to their stronger bonding compared to II-VI's and better spatial uniformity, scalability and lower cost[2]. InSb infrared focal plane arrays are extensively utilized due to their cut off wavelength of 5.3μm and the operation wavelength can be extended to long-wave infrared (LWIR) spectrums using type-II superlattices such as InAs/InAsSb or bulk InAsSb grown metamorphic buffers[3]. However, the absence of suitable binary substrates between 6.09 Å and 6.47 Å has led to the exploration of metamorphic buffers using InGaSb and AlInSb ternary alloys. In the literature, antimonide based step graded and linearly-graded buffers are widely studied. Metamorphic buffers often require thicknesses over 4μm to achieve the desired lattice constant which involves challenges in repeatability and cost-efficiency for III-V based MWIR detectors.
To create cost-effective and easily manufacturable III-V based MWIR detectors, interfacial misfit dislocation (IMF) arrays can be used to achieve fully relaxed buffers for a lattice constant of interest for antimonide alloys. A key example in this area is the growth of GaSb on GaAs substrates. The research shows that nearly 100% relaxation of GaSb buffers are achieved due to the IMF dislocations at the GaSb/GaAs interface. Analysis of transmission electron microscopy (TEM) images has shown that the formation of periodic Lomer type dislocations is essential in reducing strain caused by lattice mismatches on GaAs (001) substrates. It has been found that the Lomer dislocations are more effective than the 60o ones since their Burgers vector is completely aligned with the (001) interface plane[4]. This alignment is crucial for effectively relieving strain and achieving better quality epilayers with lower threading dislocation density.
In this research and presentation, we investigate the impact of mismatch strain on the relaxation mechanism of antimonide alloys grown on commercially available substrates such as InAs and InP. The dominant strain relief mechanism is analyzed using HR-TEM to gain a comprehensive understanding of the formation of misfits in these alloys. X-ray diffraction (XRD) and reciprocal space mapping of these epilayers indicate a change in relaxation with the effective misfit dislocation type linked to the mismatch between the epilayer and the substrate. Finally, we will compare the quality of these buffers to the latest findings, to create a broader understanding of ternary alloys grown on binary substrates using this method.
[1] W. L. Sarney, S. P. Svensson, Y. Xu, D. Donetsky, and G. Belenky, "Bulk InAsSb with 0.1 eV bandgap on GaAs," J. Appl. Phys., vol. 122, no. 2, p. 025705, Jul. 2017.
[2] A. Rogalski, "Next decade in infrared detectors," in Electro-Optical and Infrared Systems: Technology and Applications XIV, Warsaw, Poland, 2017.
[3] A. A. Klimov et al., "Long-wave infrared InAs0.6Sb0.4 photodiodes grown onto n-InAs substrates," J. Phys. Conf. Ser., vol. 1851, no. 1, p. 012019, Mar. 2021.
[4] A. Gangopadhyay, A. Maros, N. Faleev, and D. J. Smith, "Strain relaxation in low-mismatched GaAs/GaAs1-xSbx/GaAs heterostructures," Acta Mater., vol. 162, pp. 103–115, Jan. 2019.

09:00 AM
Bismuth Incorporation in AlInSb for an Improved Barrier Layer Material (Student)
Ms. Amberly Ricks[1], Ms. Corey White[2], Ms. Qian Meng[3], Dr. Hussein Hijazi[4], Prof. Mark Wistey[5], Prof. Seth Bank[6]
[1]Department of Electrical and Computer Engineering, University of Texas at Austin, Austin, TX 78758, [2]The University of Texas at Austin, [3]Microelectronics Research Center and ECE Dept., The University of Texas at Austin, [4]Rutgers University, [5]Texas State University, [6] University of Texas at Austin

InSb-based photodetectors have been widely explored as an alternative material system to HgCdTe-based devices for mid-wave infrared operation.1,2 While InSb alone does not operate in the long-wave infrared (LWIR), incorporating small amounts of Bi into III-V materials offers the ability to decrease the bandgap energy, enabling extended infrared response.3 In particular, InSbBi has already demonstrated photoluminescence out to 7.6 μm at 230K, illustrating its potential for LWIR optoelectronic devices.4 Because materials with very narrow bandgaps are required for extended infrared operation, parasitic dark currents are likely to arise to the detriment of device performance.2 While nBn structures have been shown to suppress many sources of dark current, the use of AlInSb barriers in InSb-based nBn detectors introduces a tradeoff between a desirably large conduction band offset and an undesirably large valence band offset and high barrier layer strain that is difficult to

manage.5 This tradeoff will be exacerbated for InSbBi absorbers as experimental evidence suggests that the bandgap energy of InSb is expected to decrease by 29 meV/% Bi incorporated.4 Additionally, the majority of this bandgap change is expected to manifest in the valence band.6 Thus, a flexible method to mitigate these challenges in InSb-based nBn detectors is to incorporate small amounts of Bi into the AlInSb barrier to independently decrease the valence band offset, while maintaining a sufficiently high conduction band offset and restoring lattice matching.
To optimize the quaternary for use as a barrier layer with an InSbBi active region, density functional theory (DFT) and nextnanomat simulations were performed. The DFT simulations were run with hybrid functionals (HSE06) using a 54-atom supercell with 1 Al and 1 Bi atom (corresponding to 3.7% Al and Bi). These simulations predict that the direct bandgap energy of Al0.037In0.963Sb0.963Bi0.037 is reduced by ~20 meV from that of InSb, and that the quaternary behaves similarly to other III-Vs, with a comparable dispersion to that of InSbBi. Using these projections, nBn devices were designed using nextnanomat to find a range of Al and Bi concentrations that would maximize the conduction band offset while simultaneously minimizing the valence band offset. For a conduction band offset minimum of 0.3 eV with respect to an InSb0.98Bi0.02 absorber, approximately 25% Al and 3% Bi incorporated would be required in the barrier layer; this results in a valence band offset of only 0.088 eV.
AlInSbBi films were grown by solid-source molecular beam epitaxy on n-type InSb substrates. To promote Bi incorporation, similar growth parameters used to grow high quality InSbBi and GaAsBi were used:4,7 the substrate temperature was maintained at 300ºC and a low V/III flux ratio of 0.975x was employed. The growth rate was chosen to be ~1 μm/hr. At low Al concentrations, Bi incorporation is limited to ~0.4% and the excess Bi precipitates out into droplets on the surface, a phenomenon similarly found in Bi-containing alloys.7,8 However, we found that greater concentrations of Bi can be incorporated as the Al concentration is increased; this may be due to the shorter AlBi bond being more energetically favorable in the InSb zincblende host matrix than the longer InBi bond.9 AlInSbBi films targeting 25-35% Al and 3-4% Bi were grown, and ω-2θ measurements show film peaks that shift toward the InSb substrate peak compared to their AlInSb control films, suggesting Bi incorporation. Atomic force microscopy scans performed on the AlInSbBi films reveal Bi droplets, indicating an upper limit of Bi incorporation was reached at these growth conditions. Future growths will aim to optimize the growth regime, and Rutherford Backscattering measurements are in progress to quantify the Bi concentrations in the films. Growth of quantum well structures is underway to quantitatively measure the band offsets in these materials by photoreflectance measurements, the results of which will improve our nBn simulations and help us to better understand the efficacy of Bi in an AlInSb barrier layer for LWIR devices. This work was supported by the National Science Foundation (Award Nos. ECCS-1933836).
1S. P. Svensson et al., Appl. Opt., 56, 2017. 2P. Martyniuk, M. Kopytko, and A. Rogalski, Opto-Electron. Rev., 22, 2014. 3S. Francoeur et al., Appl. Phys. Lett., 82, 2003. 4R. C. White et al., Appl. Phys. Lett., 121, 2022. 5A. Evirgen et al., Elec. Lett. 50, 2014. 6M. P. Polak et al., Semicond. Sci. Technol. 30, 2015. 7A. J. Ptak et al., J. Cryst. Growth, 338, 2012. 8M. K. Rajpalke et al., Appl. Phys. Lett. 105, 2014. 9J. Zhang et al., J. Appl. Phys. 126, 2019.

09:15 AM
Negative Differential Resistance in Ultra-Thin Mid-Wave Infrared Detectors (Student)
Mrs. Yadviga Tischenko[1], Mr. Noah Mansfield[2], Ms. Morgan Bergthold[2], Ms. Sreeja Purkait[3], Dr. Aaron Muhowski[4], Prof. Viktor Podolskiy[3], Prof. Daniel Wasserman[2]
[1]Department of Electrical and Computer Engineering, University of Texas Austin, TX 78758, USA, [2]Department of Electrical and Computer Engineering, University of Texas at Austin, Austin, TX 78758, [3]Department of Physics, University of Massachusetts,Lowell, MA 01854, [4] Sandia National Las, Albuquerque, NM 87185, USA

The long-time detector of choice in the mid-IR (mid-IR, λ = 2 − 30 μm) is the HgCdTe (MCT) detector, which offers low noise, high responsivity, and wavelength flexibility. However, MCT suffers from non-uniform growth, a limited fabrication and processing infrastructure, and increasing concern about the environmental effects of its toxic constituent materials. There is thus a continued interest in the demonstration of mid-IR detectors leveraging III-V semiconductor materials, which offer more uniform growth and a mature fabrication infrastructure. Among the III-V's, type-II superlattice (T2SLs) are of particular interest, as they offer significant wavelength flexibility and the potential for reduced Auger recombination. When integrated into bariode devices (such as the nBn or CBIRD architectures [1,2]), a dramatic reduction in Shockley–Read–Hall (SRH) recombination can be achieved as well, making T2SL-based bariode photodetectors an appealing alternative to the MCT.
T2SLs, because of the spatial separation of electrons and holes in the superlattice minibands, have reduced absorption compared to bulk ternary III-Vs. However, this deficiency can be overcome when the detector is integrated with photonic structures designed to strongly confine incident light to the detector absorber. [3,4,5] Such designs allow for a dramatic reduction in the absorber thickness, while maintaining strong responsivity, and perhaps most importantly, show a reduction of dark current to below the Rule 07, the long-time heuristic for state-of-the-art detectors. [6] However, in recent years, Law 19 has supplanted the Rule 07 as the heuristic for HgCdTe detector performance. [7] Law 19 provides the theoretical lower bound (background radiative limit) on dark current in MCT detectors, and has been experimentally demonstrated in MCT detectors with depleted absorber regions. Depleting the absorber of a mid-IR detector effectively removes the Auger component of dark current, which is the recombination/generation process that dominates, and limits detector performance, at high temperature. Implementing these design changes, MCT detectors have leapt forward in the metric most commonly used to compare IR detectors across materials and device architectures: specific detectivity (D*). D* is effectively an area-normalized ratio of responsivity (external quantum efficiency) to detector noise, which is proportional to the square root of dark current (for diffusion-limited detector operation).
In order for III-V mid-IR detectors to compete with MCT detectors, particularly at elevated temperatures, mechanisms for quenching Auger processes must be demonstrated. The thick absorbers required for typical mid-

IR III-V detectors are not easily depleted, due to the relatively high background carrier concentrations of the narrow bandgap III-V absorbers, and the onset of tunnelling and SRH currents at large applied biases. However, for the ultra-thin detector architectures, there does exist an opportunity to demonstrate absorption layer depletion. In this presentation we demonstrate, experimentally, negative differential resistance (NDR) in ultra-thin mid-wave infrared (MWIR, 3 − 5 μm) nBn detectors. We investigate the temperature and doping dependence of the NDR, and correlate the observed NDR to the detector band structure and the temperature-dependence of different dark current mechanisms. We show that NDR emerges only for higher temperature operation, and is not observed at lower, cryogenic, temperatures, which suggests that the observed NDR may signify Auger quenching and absorber layer depletion. The NDR effect is also more prominent in detectors with lower, or unintentionally, doped absorber layers. The demonstration of NDR, and possibly absorber layer depletion, in ultra-thin MWIR detectors, offers a potential path towards extreme reduction of mid-IR detector dark current and high temperature performance competitive with MCT detectors.

The authors acknowledge funding from the NASA ACT program (22-ACT22-0041). Sandia National Labs is managed and operated by NTESS under DOE NNSA contract DE-NA0003525.

[1] Appl. Phys. Lett., 89, 151109, (2006) [2] Appl. Phys. Lett., 95, 023508, (2009). [3] Appl. Phys. Lett., 106, 261109, (2015). [4] Appl. Phys. Lett., 109, 251103, (2016). [5] Opt. Exp., 27, pp. 23970–23980, (2019) [6] IEEE Photonics Tech. Lett., 34, pp. 615-618, (2022) [7] Proc. SPIE 11407, Infrared Technology and Applications XLVI, 114070X, (2020)

09:30 AM

Heteroepitaxial IV-VI semiconductor mid-infrared light-emitting diodes and detectors

Prof. Leland Nordin[1], Mr. Jarod Meyer[2], Prof. Kunal Mukherjee[3]
[1]CREOL, University of Central Florida, [2]Department of Materials Science and Engineering, Stanford University, Stanford, CA 94305, USA, [3]Stanford University

The mid-infrared (MIR) spectral range is key for a broad range of applications, including chemical sensing, medical diagnosis, and defense. These applications require compact, high-power, solid-state, room-temperature (RT) light sources. However, type-I quantum well MIR emitters, which rely on III-V semiconductors, encounter challenges in achieving efficient performance due to fast Auger recombination rates and small band offsets in narrow-bandgap III-V materials [1]. To tackle these issues, researchers have utilized type-II or intersubband III-V heterostructures, such as quantum cascade lasers, interband cascade lasers, and type-II superlattice light emitting diodes. Despite their commercial availability, these devices face significant growth complexity, poor subthreshold performance, and/or low efficiency at RT. These limitations underscore the need for MIR devices with simple growth, RT operation, and, perhaps most importantly, the ability to seamlessly integrate into established III-V or CMOS processes.

In this work, we demonstrate RT MIR electrically driven light emission and detection from PbSe/III-V devices. The devices were grown on a pGaAs (001) substrate using a molecular beam epitaxy (MBE) system. The growth began by desorbing the GaAs substrate's native oxide under a Se flux [2]. Following oxide desorption, a PbSe dose procedure was performed, and a PbSe nucleation layer was grown [3]. After the PbSe nucleation layer, the growth temperature was lowered to ~170 °C, and 293 nm of PbSe was grown. Finally, a 15 nm n-doped Sb:PbSe top contact was grown.

After growth, we fabricated single devices using optical lithography, Ar-based dry etching for mesa delineation, and electron beam evaporation of Au/Cr metal for both top and bottom contacts. Fig. 1(a) illustrates the current-voltage (I-V) measurements of the fabricated devices. The I-V behavior of the devices displays rectifying behavior characteristic of semiconductor diodes. The series resistance, show in Fig. 1(b), of the diodes is 1.6 Ω and suggests good device contacts. The resistance area (R0A) product of these diodes is 1.84 Ω cm2, which is larger than the theoretical and experimental RT R0A for photovoltaic PbSe detectors [4, 5]. This discrepancy could be attributed to the heteroepitaxial junction, or the relatively thin PbSe layer.

We measured the electroluminescence (EL) of the heteroepitaxial diodes using a micro-luminescence setup and a FTIR spectrometer operating in step scan mode. Fig. 2(a) displays the measured EL signal as a function of drive current. The peak EL of the devices occurs at ~4 μm, falling within the technologically important 3 – 5 μm spectral range. Typical of LED devices, we do observe some saturation to the EL magnitude at high injection current.

In addition to their light emission capabilities, photovoltaic diodes should be able to detect light under zero bias conditions. To assess this, we utilized the same FTIR spectrometer to measure the instrument-corrected photoresponse of the heteroepitaxial diodes, as depicted in Fig. 2(b). These diodes do indeed exhibit light detection at zero bias, indicating a small offset between the PbSe film and the GaAs substrate. Additionally, the 50% maximum photoresponse occurs at approximately 4 μm, aligning well with the peak EL.

We synthesized and fabricated PbSe/GaAs n-i-P diodes and characterized their (opto)electronic properties. At RT, these devices emit mid-infrared light under forward bias, and detect mid-infrared light at zero bias. The electroluminescence peaks at ~4 μm, and the photoresponse cutoff (50% maximum response) also occurs near 4 μm. Most importantly, the realization of RT active heteroepitaxial devices represent a significant advancement in IV-VI optoelectronics and dissimilar semiconductor devices. This heteroepitaxial system offers numerous promising avenues for developing innovative dissimilar semiconductor devices that harness the best properties of the both the III-V semiconductor substrate and the IV-VI semiconductor film.

[1] D. Jung, et al. … D. Wasserman, J. Opt. 19, 123001 (2017).
[2] S. Vishwanath, et al. … H.G. Xing, JMR 31, 900 (2016).
[3] B.Haidet, E.T. Hughes, K. Mukherjee, Phys. Rev. Mater. 4, 033402, (2020).
[4] J. Xu and M. Tacke, Infrared Phys. 33, 151 (1992)
[5] A. Rogalski and J. Rutkowski, Infrared Phys. 21, 191 (1981).

8:30 AM
Materials for Quantum Applications
Session Chairs: Michael Hamilton (Auburn University), Stephanie Law (Pennsylvania State University)
ESJ 2204

08:30 AM
MBE grown site-templated quantum dot platforms with spectral control for quantum devices (Student)
Ms. Nazifa Tasnim Arony[1], Dr. Lauren McCabe[2], Ms. Lottie Murray[1], Dr. Joshya Rajagopal[1], Mr. Prashant Ramesh[1], Mr. Lan Mai[1], Mr. Townsend Long[1], Dr. Matthew Doty[1], Dr. Joshua Zide[1]
[1]University of Delaware, [2]University of Delaware- Now at Yale University

Epitaxially grown semiconductor quantum dots (QDs) have been well studied in the past few decades and have shown great promise as single photon emitters, and as a basis for potential qubits. These features of QDs grown on a semiconductor matrix make it a desirable platform/building block for quantum devices which has a wide-range of applications in quantum information, quantum sensing and quantum computing. For a complete epitaxially grown quantum device, spatial, spectral, and structural homogeneity, and scalability are the key requirements. Recent work from our group has shown a method for site controlled QD growth where InAs/GaAs quantum dots are grown on nano-fabricated substrates with site-templated arrays of nano-pits1. However, achieving spectral homogeneity and thus, scalability is still a big challenge due to the impurities introduced in the regrowth surface from the nanofabrication process. This work addresses these challenges and explores three different objectives, first one being the domain of quantum dot columns (QDCs) as a buffer layer for the top QD-arrays of interest while burying defects underneath the QDCs. Additionally, initial experiments on spectral control of InAs/GaAs QDs by an in-situ method called ‘cap and flush’ are discussed and finally, the concept of quantum dot molecules QDMs is introduced for optical tunability and site-templated scalable device platform.
[1] J. Vac. Sci. Technol. B 38, 022803 (2020)

08:45 AM
Selective Area Regrowth for Chipscale Trapped Atom/Ion Quantum Systems (Student)
Ms. MaryClare Cassidy[1], Mr. John Duncan[1], Ms. Ashlee Garcia[1], Mr. William Doyle[1], Prof. Daniel Wasserman[2], Prof. Seth Bank[3]
[1]Chandra ECE Department, The University of Texas at Austin, [2]Department of Electrical and Computer Engineering, University of Texas at Austin, Austin, TX 78758, [3]University of Texas at Austin

Trapped atom/ion systems are integral to a growing number of photonics-based approaches to quantum metrology, computing, and communications systems. However, the need to address scalability and connectivity challenges to realize the full potential of such systems has created a significant driving force to integrate atom/ion traps with chipscale photonics platforms. Unfortunately, the large optical power requirements of traditional trapping and manipulation approaches, such as for shaken lattice interferometry,1 create significant reliability challenges, particularly for chipscale sources. Additionally, chipscale atom/ion chambers tend to employ relatively low vacuum levels, limiting integration times, hence sensitivities in the case of quantum metrology. Here, we explore a novel bottom-up approach to epitaxially integrate trapped atom/ion chambers using selective area regrowth to mitigate these challenges.
We have previously demonstrated the first III-V planar encapsulation of buried dielectric structures with selective area molecular beam epitaxy by combining period supply epitaxy (PSE) with planar coalescence.2 Additionally, we have achieved selective regrowth of SiO_2 microstructures up to 2 μm tall and with aspect ratios up to 10:1.3,4 These advances can be combined to epitaxially integrate vacuum cavities onto III-V substrates. Here, we explore the design and growth of such structures to provide optical field concentration through the slot waveguide effect,4 in turn reducing the optical powers required for trapping and manipulation of atoms/ions within the vacuum waveguides. Structures were designed using finite difference time-domain (FDTD) simulations solving Maxwell’s equations via discrete spatial and temporal meshes coupled with finite differences for derivative computation. This computational approach affords a high degree of accuracy in broadband analysis and avoids the need for specific geometries and the direction of light propagation, making it particularly suitable for the optimization of slot waveguides.
Preliminary cavities were designed using a GaAs substrate and patterned SiO_2 to guide the epitaxial regrowth of GaAs. PSE regrowth of GaAs on SiO_2 gratings along the [1-10] direction results in growth of vertical columns that can be coalesced in a manner similar to the well-established pendeo-epitaxy method to form the slot waveguide. Various simulations were conducted that explored the slot height, width, and source modes assuming 1550 nm wavelength. Evaluation criteria included the optical confinement factor, intensity enhancement, and propagation loss. While the mode volume could be reduced by >8000x compared to the bulk optics manipulation reported in Ref. 1, further optimization is required to mitigate propagation loss. This work is ongoing, as are experimental studies, and results will be reported at the conference.
This work was supported by the National Aeronautics and Space Administration (NASA) through the Quantum Pathways Institute (Award 80NSSC22K0287).
1 C.A. Weidner et al., Phys. Rev. Lett. 120 (27 June 2018).
2 D.J. Ironside et al., Crystal Growth and Design, vol 19 (April 2019).
3 A.M. Garcia et al., 65th Electronic Materials Conf. (EMC) (June 2023).
4V. R. Almeida et al., Optics Letters vol 29 issue 11 (2004).
5 D.J. Ironside, “Embedded Dielectric Microstructures in MBE: High-quality Planar Coalescence toward Enhanced Optoelectronic Materials”, Doctoral Defense, University of Texas-Austin (2018).

09:00 AM
Quantum Sensing with Defects in Diamond and Wide Bandgap Semiconductors (Student)
Mr. Sheikh Mahtab[1], Dr. Peker Milas[1], Mr. Tomas Sujeta[1], Mr. Tanmay Talukder[1], Mr. Rapsan Anonto[1], Mr. Joseph Chavez[1], Ms. Jocelyn Pellegrino[1], Dr. Michael Spencer[1], Dr. Birol Ozturk[1]
[1]Morgan State University

Quantum sensing is a paradigm shift, relying on the intrinsic sensitivities of quantum state to their surrounding environment to detect extremely small changes in temperature, magnetic, and electric fields. Quantum sensing, among the diverse range of emerging quantum science applications such as computing and communication, is gaining increasing recognition as a viable technology, with commercially available products already making their mark in the market. Nitrogen vacancy (NV) color center defects in diamond have drawn considerable attention as a solid-state quantum sensing platform that, unlike many other systems, can operate under ambient conditions. NV defect-based diamond sensors, as qubit platforms, are highly susceptible to various sources of noise from experimental setup hardware and external factors, such as fluctuations in excitation lasers, unwanted sample heating caused by laser excitation and microwave drives, and impurities in the sample. To mitigate the effects of these experimental artifacts, we employed hardware improvements and better data processing techniques in our measurements. We utilized machine learning (ML) algorithms which not only increased the fidelity of our data but also dramatically increased the sensitivity in our measurements [1]. Efficient delivery of microwave radiation to the samples is a critical aspect of solid-state defect-based quantum sensing experiments. We have developed methods for the fabrication of high efficiency microstrip and coplanar RF antennas for quantum sensing applications. Antennas displayed over 37dB return loss at 2.87 GHz, the zero-field splitting frequency (ZFS) of negatively charged NV defects in diamond (Figure 1). These antennas removed the need for the use of an RF amplifier in optically detected magnetic resonance (ODMR) based quantum sensing of magnetic fields due to their high efficiencies as shown in Figure 2 [1]. Moreover, we have demonstrated the feasibility of ODMR experiments and external magnetic field quantum sensing with nanodiamonds in live mouse brain cell solutions for their possible use in action potential recording in future experiments. Nanodiamonds were also deposited on tungsten microprobe and glass micropipette tips and tested in external magnetic field sensing experiments, enabling their use in scanning probe microscopy experiments. Furthermore, we have observed RC series ZPL emission at room temperature for the first time from electron beam irradiated cubic boron nitride crystals as depicted in Figure 3 [2]. In addition, we have tested defects in 3C and 4H SiC in quantum sensing experiments. Room temperature ODMR experiments with silicon vacancy (V1) defects were 30% successful (Figure 4). Zero phonon line (ZPL) emission from V2 defects were observed. Recent results from ODMR experiments in 3C and 4H SiC will also be presented.

09:15 AM
Annealing Modulated Structural and Electrical Properties of Crystalline NbN Superconductor on GaN substrate by Sputter Deposition (Student)
Mr. Stephen Margiotta[1], Mr. Saleh Ahmed Khan[2], Prof. A F M Anhar Uddin Bhuiyan[2]
[1]Department of Electrical and Computer Engineering, University of Massachusetts Lowell, MA 01854, USA, and Lincoln Laboratory, Massachusetts Institute of Technology, Lexington, MA 02421, USA, [2]Department of Electrical and Computer Engineering, University of Massachusetts Lowell, MA 01854, USA

NbN superconductors have emerged as a crucial material in the field of quantum computing due to their relatively higher superconducting transition temperature (Tc), making it a promising material for diverse applications such as superconductor quantum computers, single photon detectors, and hot electron bolometers. Since the properties of NbN are intricately linked to its crystal structure, quality, and nitrogen content, precise control of the structural and electrical characteristics of NbN films is vital for realizing NbN-based quantum devices. The small lattice mismatches between NbN and group-III nitride semiconductors indicate the potential of depositing crystalline NbN superconductor on nitride semiconductors. Previous success with AlGaN/GaN HEMTs on NbN films operating under Tc with negative differential resistance suggests that integrating nitride semiconductors and superconductors can be utilized for Josephson junctions [1]. To achieve all-nitride NbN/GaN/NbN Josephson junctions, a comprehensive understanding on the growth and structural quality of NbN/GaN heterointerfaces is essential. The recent demonstration of MBE epitaxial growth of NbN film on GaN revealed a superconducting critical temperature exceeding 10 K [2]. In this work, we investigated the deposition of high-quality crystalline NbN film on GaN/sapphire templates using sputter deposition technique followed by a rapid thermal annealing. The deposition was performed at 20°C using a 99.95% purity Nb target. Post deposition annealing at 950 °C was performed under Ar atmosphere for 15sec to 30mins durations.
The crystalline structure, quality, surface morphologies, film resistance and superconducting transition temperatures of the 100 nm thick NbN films are evaluated by comprehensive characterizations. High resolution XRD measurements reveals a phase transformation of NbN films from hexagonal (100) NbN to cubic (111) δ-NbN on wurtzite GaN substrates after high temperature annealing, as observed from XRD ω-2θ scans. Omega rocking curve FWHM measurements on (111) NbN reveals that post deposition annealing leads to narrower rocking curves, indicative of improved crystallinity as compared to the non-annealed sample. XRD asymmetrical RSM mapping of 100 nm thick NbN film indicates the deposition of fully relaxed epitaxial layer on GaN after annealing. The lattice orientation of the NbN film relative to the GaN substrate is also analyzed by performing XRD φ-scanning around asymmetrical (105) GaN and (311) NbN planes, indicates a sixfold symmetry of the NbN due to the presence of a rotational domain, which is consistent with MBE grown NbN film on GaN substrate [2]. While the films exhibit smooth surface morphologies, the surface RMS roughness is found to decrease after 1 min annealing as compared to the as-deposited film, however, longer time (30 mins) annealing results in granular surface morphologies with higher RMS roughness. The measurements of the

resistance vs temperature show a decrease of the transition temperature from 12.82 K (as-deposited) to 8.69 K as well as an increase of the film resistance after 30 mins annealing at 950 °C, which could potentially be related to the phase transition, surface roughening, incorporation of impurities and alteration in nitrogen content within the NbN films after high temperature annealing. Further characterizations using atomic resolution transmission electron microscopy and X-ray photoelectron spectroscopy will be performed to investigate the influence of annealing temperature on structural modifications and impurity incorporation in NbN films deposited on GaN substrates.
This study on integrating superconducting NbN with GaN semiconductors while comprehending the growth and structural aspects of the NbN layer and interface will provide a pathway to develop innovative and improved III-nitride semiconductor-based electronic devices.

09:30 AM
Electron Spin Resonance of Defects in the Nb/a-Si/Nb Materials System
Dr. Stephen Moxim[1], Dr. Peter Hopkins[1], Dr. David Olaya[1], Dr. John Biesecker[1], Dr. Jason Ryan[1]
[1]National Institute of Standards and Technology

Electron spin resonance (ESR) and related techniques have proven to be valuable for understanding atomic-scale, paramagnetic defects in semiconductor/insulator-based materials and devices [1]. The majority of prior work in this field focuses on defect chemistry in classical semiconductor devices (transistors, diodes, capacitors, etc); however, literature concerning defects relevant to other semiconductor-based devices is scarce. One obvious extension of this field is to superconducting Josephson junction structures, which are fabricated with junction barriers made of the same/similar semiconductor and insulator materials as the devices mentioned above. In this work, we present room-temperature ESR results on a-Si and Nb/a-Si/Nb thin films in order to study the defects within the bulk a-Si as well as the influence of Nb/a-Si interfaces on the defect chemistry.

Fig. 1 shows the ESR response from as-grown a-Si (20 nm) and Nb/a-Si/Nb (15 nm/20 nm/15 nm) films. The strong central feature present in both ESR traces (g = 2.0058 ± 0.0003) is due to Si dangling bonds in the bulk a-Si. Additional, broad features are seen in the Nb/a-Si/Nb films, which we tentatively attribute to a Nb-related defect. The broadness and complexity of these features could be explained by hyperfine interactions from Nb nuclei (spin 9/2), and additional electron spin-spin interactions from unpaired d-orbital electrons within the Nb atoms. Within our measurement capabilities, both responses are isotropic. Fig. 2 shows the relative intensities of the central, Si dangling bond response after a variety of annealing times/temperatures (in an argon environment). For the plain a-Si film, the amplitude is reduced significantly under all annealing conditions tested; however, it remains constant (within experimental error) in the case of the Nb/a-Si/Nb film. While we cannot be quantitative about the broad response in the Nb/a-Si/Nb films, it's amplitude is qualitatively reduced by annealing, as shown in Fig. 3.
Electrically detected magnetic resonance (EDMR) measurements via spin-dependent tunneling [2] are possible in the plain a-Si film by mounting a small sample on a PCB board and contacting the a-Si layer with a wirebond. An applied voltage induces a trap-assisted tunneling current through the film, which can be monitored for resonance-induced changes. The results of such an experiment are shown in Fig. 4. The Si dangling bond response is present in the EDMR trace; this indicates that the defects are not only paramagnetic, but also electrically active, and can act as tunneling centers. Our results demonstrate that silicon dangling bonds, as well as another defect which we tentatively describe as Nb-related, could be relevant to performance issues in superconducting Josephson junctions based on the Nb/a-Si/Nb system.
[1] Lenahan, Patrick M., and J. F. Conley Jr., Journal of Vacuum Science & Technology B: Microelectronics and Nanometer Structures Processing, Measurement, and Phenomena 16.4 (1998): 2134-2153.
[2] Anders, M. A., et al. Journal of Applied Physics 124.21 (2018)

8:30 AM
Doping and Impurities
Session Chairs: Minjoo Lee (University of Illinois Urbana-Champaign), Rachel Goldman (University of Michigan)
ESJ 1224

08:30 AM
Optical Properties of β-Ga2O3 Due to Impurities and Electron Irradiation (Student)
Ms. Cassandra Remple[1], Dr. Jesse Huso[2], Mr. Benjamin L. Dutton[3], Dr. Marc H. Weber[4], Prof. John S. McCloy[3], Prof. Matt McCluskey[5]
[1]Materials Science & Engineering Program, Washington State University, Pullman, WA, USA 99164-2711, [2]Klar Scientific, 1615 NE Eastgate Blvd., Unit G, Ste. 3E, Pullman, WA, USA 99163-5300, [3]Materials Science & Engineering Program, Washington State University, Pullman, WA, USA 99164-2711; Institute of Materials Research, Washington State University, Pullman WA, USA 99164-27113, [4]Institute of Materials Research, Washington State University, Pullman WA, USA 99164-27113, [5]2 Klar Scientific, 1615 NE Eastgate Blvd., Unit G, Ste. 3E, Pullman, WA, USA 99163-5300; Dept. of Physics and Astronomy, Washington State University, Pullman, WA, USA 99164-2814

Monoclinic gallium oxide (β-Ga2O3) is an ultrawide bandgap semiconductor with potential applications in high-power devices. To better understand defects in this material, the optical properties of β-Ga2O3 samples were altered via high-energy electron irradiation. β-Ga2O3:Hf irradiated with 2.5 MeV electrons experienced a color change from blue to yellow and a large drop in conductivity due to the creation of gallium vacancies, which compensate donors. This irradiation resulted in the absence of free carrier absorption and the presence of Cr3+ photoluminescence (PL). PL mapping revealed optically active ZnO precipitates that formed during the growth of β-Ga2O3:Zn. These precipitates had a 384 nm (3.23 eV) band-edge emission in the core; in the outer shell of the precipitate, the band-edge PL was blue-shifted to 377 nm (3.29 eV), and a broad defect band was

observed. After 0.5 MeV electron irradiation, the defect band broadened and increased in intensity. The blue PL band (435 nm) of β-Ga2O3 was enhanced for both Hf- and Zn-doped samples irradiated with 0.5 MeV. This enhancement is attributed to an increase in oxygen vacancies. PL and Raman mapping of Mn-doped β-Ga2O3 with excitation wavelengths of 375 and 405 nm reveals the spatial distribution of these features with submicron resolution. The Cr3+ emission intensity shows striations that are attributed to inhomogeneities during growth. Ir4+ can also be imaged and shows similar striations through resonant Raman scattering.

08:45 AM
Electrical and Optical Characteristics of Si- and Ge-implanted AlN annealed at 1500 ºC (Student)
Mr. Chao-I Liu[1], Dr. Shashwat Rathkanthiwar[1], Mr. Masahiro Kamiyama[1], Ms. Auditee Majumder Momo[1], Mr. Cris Quinones[1], Dr. Seiji Mita[2], Dr. Pramod Reddy[2], Dr. Ronny Kirste[2], Prof. Ramón Collazo[1], Prof. Zlatko Sitar[1]
[1]North Carolina State University, [2]Adroit Materials

The UWBG semiconductor, AlN, has tremendous promise for deep-UV optoelectronics and high-power, high-frequency electronics thanks to its ultrawide bandgap (6.1 eV), high critical electric field (16 MV/cm), reasonably high electron mobility (400 cm2/Vs) and high thermal conductivity (2.85 W/cmK). The main challenge related to AlN is controllable n-type and p-type doping, an essential building block for device applications. While Si and Ge have been established as donors in AlxGa1-xN, they have been found to undergo a shallow to deep transition at x=0.8 and x=0.5, respectively. This leads to an abrupt increase in the ionization energy of the donors and is associated with a drastic drop in the carrier concentration and conductivity at room temperature by several orders of magnitude. Previously, we demonstrated in Si and Ge ion implanted AlN that a low thermal annealing budget kinetically stabilizes the shallow donor state leading to low activation energies, around 80 meV, and high conductivity.1,2 In this work, we investigate the impact of high thermal annealing budget conditions on the electrical and optical properties of Si- and Ge-implanted AlN. Homoepitaxial AlN films were grown using low pressure metalorganic chemical vapor deposition. Si and Ge ion implantation was performed at room temperature. Implantation doses of 1.0×1014 and 8.5×1013 cm-2 were investigated for Si and Ge, respectively. Post-implantation annealing for damage recovery was performed at 1500 ºC for 2 hours under a N2 ambient. Both Ge- and Si-doped AlN films showed smooth surface morphology with bilayer step structure with RMS roughness <1 nm, as observed by atomic force microscopy before and after implantation and annealing. Complete damage recovery after post-implantation annealing was confirmed by high-resolution x-ray diffraction measurements. Electron concentration and mobility were characterized by temperature dependent Hall measurements in a temperature range of 120-750 ºC. A charge-balance model based on Fermi-Dirac statistics was implemented to extract donor concentration (ND), compensating acceptor concentration (NA), and the donor ionization energy. The activation ratio (ND/[doping]) was extracted to be >99% for Ge and ~40% for Si. The ionization energy was extracted to be 1 eV for Ge and 0.3 eV for Si. Prominent defect peaks related to VAl and CN were observed in room-temperature photoluminescence (PL) spectra for the as-implanted samples. Compared to the as-implanted samples, the annealed samples showed a decrease in the relative intensities of the VAl indicating damage recovery. However, an increase in the intensity of the broad VAl-donor complex related peak was observed suggesting self-compensation. The intensity of this peak was found to be the highest for the case of Si implantation which agrees to the observation of low activation ratio from the electrical measurements. Lastly, Gaussian deconvolution was performed to distinguish the peak positions of VAl-donor complex peaks. The main self-compensators were revealed to be the electrically neutral VAl-3GeAl and VAl-3SiAl and acceptor type VAl-2GeAl and VAl-2SiAl complexes.
1. Bagheri, P. et al. High conductivity in Ge-doped AlN achieved by a non-equilibrium process. Appl. Phys. Lett. 122, (2023).
2. Breckenridge, M. H. et al. High n-type conductivity and carrier concentration in Si-implanted homoepitaxial AlN. Appl. Phys. Lett. 118, (2021).

09:00 AM
Band gap luminescence of Si and Ge doped homoepitaxial AlN (Student)
Ms. Auditee Majumder Momo[1], Dr. Ronny Kirste[2], Mr. James Loveless[1], Mr. Chao-I Liu[1], Dr. Seiji Mita[2], Dr. Shashwat Rathkanthiwar[1], Prof. Ramón Collazo[1], Prof. Zlatko Sitar[1]
[1]North Carolina State University, [2]Adroit Materials

AlN and its ternary compound AlGaN are envisioned for next generation UVC optoelectronics and power electronics. Challenges in making these devices on foreign substrates such as sapphire include low thermal conductivity, low lattice mismatch, difficulties in doping, high extended and point defect concentration. Homoepitaxial growth on high quality AlN substrates allows to overcome defects induced by lattice and thermal expansion coefficient mismatch. However, incorporation of point defects in these materials, and their role in optical and electric properties need to be explored. Photoluminescence (PL) spectroscopy is a powerful tool for mapping of point defects that provides a complementary analysis for electrical characterization of AlN and AlGaN with different doping profiles. As an example, higher n-type conductivity and electron concentration has been reported in AlN doped through implantation with Ge than those doped in a similar way with Si.1 Room temperature PL confirmed that deep level dopant-vacancy complexes in Si doped AlN are responsible for the difference in the electrical properties.1 Self-compensation through shallow to deep donor transition has been seen for both Ge and Si doped AlN.1 A low temperature PL study has given insight on the shallow behavior (~63.5±1.5 meV ionization energy) of Si dopant from the donor bound exciton peak (6.013 eV) and satellite peak (5.965 eV) related to it.2 In this work, we investigate the band edge luminescence of a series of doped and implanted homoepitaxial AlN with Si and Ge while identifying the emission peaks associated with these defects. Based on their corresponding donor bound exciton luminescence, their shallow and deep donor behavior can be classified, supporting the hypothesis of deep/ metastable shallow donor states.
Homoepitaxially grown, undoped, Si, and Ge doped AlN samples were grown by metal organic chemical vapor deposition (MOCVD). Ge and Si doping concentration in

these samples were confirmed using SIMS at levels from 1017 to 1019 cm-3 . In addition, AlN samples implanted with Ge and Si and concentration ranging from 1018 to 1019 cm-3 we investigated. All implanted samples were annealed at 1500 0C for 2 hrs under N2 environment to mitigate implantation damage. PL measurements were carried out using a pulsed ArF excimer laser (λ = 193 nm). For low temperature PL studies, a closed-cycle Helium cryostat, Princeton Instruments Acton SP2750 0.75 m high-resolution monochromator with 3600 grooves/mm grating, and a PIXIS: 2KBUV cooled charge-coupled device camera have been used. Near band edge emission peaks were observed, classified and compared between Ge and Si doped and implanted samples. Temperature dependent behavior was used to distinguish between bound and free excitons in AlN. In both Ge and Si doped samples, the donor bound exciton (D0X) peak is found at 6.013 eV. This indicates a similar binding energy for Ge and Si. In addition, other peaks were identified as ground and excited states of free excitons (XAn=1 , XAn=2), satellite peaks of donor bound exciton (TES), and longitudinal optical (LO) phonons of free exciton. Interestingly, oxygen impurities which are known to have a bound exciton at 6.006 eV were not observed. This might be related to the clean growth of the homoepitaxial AlN layers. In summary, a study of the near band edge and defect luminescence of doped and undoped AlN is presented. The 6.013 eV emission peak from Si and Ge bound exciton and the associated satellite peaks respectively at 5.965 eV and 5.951 eV in the NBE indicates the shallow donor behavior, supporting the hypothesis of the existence of a metastable donor shallow state, that can be accessed to provide for higher carrier concentrations in AlN.
1. Bagheri, P. et al. High conductivity in Ge-doped AlN achieved by a non-equilibrium process. Appl. Phys. Lett. 122, (2023).
2. Neuschl, B.et al. Direct determination of the silicon donor ionization energy in homoepitaxial AlN from photoluminescence two-electron transitions. Appl. Phys. Lett. 103, (2013).

09:15 AM
Deterministic generation of optical defects in van der Waals materials (Student)
Mr. Aqiq Ishraq[1], Mr. Collin Maurtua[1], Mr. Shahidul Asif[1], Mr. Muhammad Hassan Shaikh[1], Dr. Chitraleema Chakraborty[1]
[1]University of Delaware

High-quality, on-demand quantum emitters (QE) are essential for integrated on-chip quantum sensing applications. Until recently, QEs were mostly confined in the bulk of solid-state materials, for example, color centers in diamond and silicon carbide. Two-dimensional (2D) materials such as transition metal dichalcogenides (TMD) [1,2] and hexagonal boron nitrides (hBN) [3] have become promising new bases for generating on–demand QEs. Unlike bulk solids, 2D materials have extremely high flexibility, allowing the device to conform to the shape of any subject - be it a human brain or a spintronics material platform- thereby improving the resolution. We envision that by utilizing the unique optical and spin properties of these 2D emitters, it will be possible to develop the next generation of 2D quantum sensing platforms. Quantum sensing allows us to understand how we interact with the world by detecting small changes in electric or magnetic fields and other physical quantities with superior accuracy over classical sensing techniques. This makes optical quantum sensors highly interesting for biomedical applications like magnetic encephalography as well as detecting topological spin textures like skyrmions in magnetic materials for quantum spintronics. In this work, we explore different techniques such as ion bombardment and high-temperature annealing to deterministically generate optical defects in hBN and TMD materials as a basis for surface QEs. We utilize a commercial plasma-focused ion beam device to selectively expose the surface of a few tens of nm thick hBN with variable fluence to generate site-controlled optical defects with ~ 850 nm peak emission with high formation yield. The fluence or dosage of the irradiation is controlled by the number of scans. We note that higher fluences result in brighter emissions due to larger defect densities. In addition to hBN, we carry out high-temperature annealing under a hydrogen environment of monolayer Molybdenum disulfide (MoS2) to introduce large defect density on the surface of the material. The presence of defect states in TMDs like MoS2 has been shown to play an important role together with localized strain in forming bound excitons which can serve as quantum emitters [4]. In our initial results, we observe that annealing under certain environments causes a red shift in the average peak energy of the excitons as well as a reduction in peak intensity. This preliminary data points to the formation of a large number of surface defects which can potentially trap and confine excitons in the defect states. We employ optical characterization techniques such as photoluminescence (PL) spectroscopy and optically detected magnetic resonance to study the optical and spin properties of these defects to gain a deeper insight into the relationship between the quantum properties of these emitters and the defect engineering process.

09:30 AM
Adatom Surface Diffusion and Phase Separation in III-V Semiconductor Alloys
Dr. Mark Twigg[1], Dr. Stephanie Tomasulo[2], Dr. Margaret Stevens[3], Dr. Nadeemulah Mahadik[4], Dr. Nicole Schmieder[5], Dr. Michael Yakes[6]
[1]US Naval Research Laboratory, [2]U.S Naval Research Laboratory, [3]U.S. Naval Research Laboratory, [4]Naval Research Lab, [5]U.S. Patent and Trademark Office, [6]Air Force Research Office of Scientific Research

Cross-sectional transmission electron microscopy (XTEM) has been used to analyze phase separation in the III-V semiconductor alloy InGaAs grown by molecular beam epitaxy (MBE) on (001) InP substrates with a 2° offcut, as well as InGaP grown upon on-axis (001) GaAs. Both films were deposited using a time of 20 seconds for each substrate rotation, with deposition rate of 0.278 nm/s. Phase separation resulting in lateral composition modulation (LCM) along the [110] direction was analyzed via XTEM for InGaAs grown at the temperatures 400, 450, and 500°C (Fig.1). An Arrhenius analysis of InGaAs XTEM LCM measurements, based on the phase separation models of Malyshkin and Shchukin [1], yields the activation energy of 0.54+/-0.05 eV associated with cation adatom surface diffusion, which compares favorably with the activation energy of 0.55+/-0.02 eV determined by in-situ MBE In droplet epitaxy surface diffusion measurements [2]. XTEM analysis of vertical composition modulation (VCM) for InGaP grown on an on-

axis (001) GaAs substrate reveals a wavelength of 5.5 nm, which matches the product of the rotation time and the deposition rate. However, for InGaAs grown on an off-axis InP (100), the VCM wavelengths observed by XTEM deviates significantly from the expected 5.5 nm and instead ranges from 7-9 nm, due to the step-bunching promoted by deposition on the off-axis InP substrate (Fig.2). Both the effects of LCM and VCM phase separation in InGaAs can be understood in terms of the greater surface diffusivity of In adatoms relative to Ga adatoms as revealed by droplet epitaxy measurements. Trends in surface diffusion in ternary alloys are also applied to quaternary alloys for photovoltaics, leading to a more accurate critical temperature and better assessment of optimal growth conditions.

[1] V. G. Malyshkin and V. A. Shchukin, Semicond. 27 (1993) 1062.
[2] M. E. Twigg, S. Tomasulo, M. A. Stevens, N. A. Mahadik, N. A. Kotulak, and M. K. Yakes, Thin Solid Films 793 (2024) 140255.

8:30 AM
Wearable Electronics and Biosensors
Session Chairs: Jae-Hyun Ryou (University of Houston), Shayla Sawyer (Rensselaer Polytechnic Institute)
ESJ 1202

08:30 AM
Eutectic Gallium-Indium (EGaIn) Electrodes for Wearable Electroencephalography (EEG)
Mr. Scott Phillips[1], Dr. Jung-Bin Ahn[2], Prof. Soaram Kim[2]
[1]Department of Biomedical Engineering, Texas A&M University, [2]Department of Electrical and Computer Engineering, Texas A&M University, College Station, TX 77843, USA

Non-invasive, wearable biosensors analyze physiologically relevant biomarkers directly from human skin, enabling long-term, real-time monitoring of an individual's health status.1 Deformable biosensors stretch with the surface of the skin as the patient performs realistic activity, allowing us to gather high-quality, real-world data. Human electrocortical activity can be monitored using EEG, but signal quality is impeded by topography mismatches between the uneven scalp and rigid electrodes.2 Mechanical pressure is applied on EEG electrodes to enhance skin-electrode contact but leads to subject discomfort after extended periods of time.3 Conductive gel amplifies biopotentials and fills air gaps between the scalp and electrodes, but application time significantly prolongs study preparation time and as the gel dries, signal quality decreases.2 Developing a soft, flexible EEG electrode that conforms to rough scalp geometry, eliminates the need for conductive gel, and maintains high signal-to-noise ratio will allow us to non-invasively record long-term neural activity, improving our ability to monitor and diagnose neurological disorders.
Soft substrates such as flexible silicone rubbers are commonly used to fabricate deformable biosensors due to their tunable stretchability, ease of fabrication, and non-toxicity with human skin.4 Liquid metal, specifically eutectic gallium-indium (EGaIn), is a popular sensing element for wearable strain and pressure sensors due to its liquid state at room temperature, electrical conductivity, and non-toxicity to the human body.5 Microchannels etched within the polymer substrate are filled with EGaIn and deform as the sensor moves, changing EGaIn electrical properties, which are then used to quantify strain and pressure changes. Wearable EGaIn-based flexible strain and pressure sensors have been used extensively for joint angle monitoring and gait analysis.6,7 Flexible EGaIn electrodes for invasive electrocorticography have been developed and tested on mice, but wearable EGaIn-based EEG electrodes have not been studied extensively.8,9
We built a flexible EEG electrode using EGaIn encased in Dragon Skin silicone rubber. This electrode includes two layers of Dragon Skin 15, along with an embedded microchannel and electrode recording surface (Fig. 1). Dragon Skin 15A and 15B were mixed in a 1:1 volume ratio, degassed, and poured into the electrode mold. The mold was then placed on a 40° C hot plate to cure for 7 hours. After degassing, some liquid Dragon Skin was spin-coated to form a thin layer film. Once the electrode shell was fully cured, it was placed on the liquid thin film and the same curing process was repeated to wet-bond the two separate layers. EGaIn was then injected into the microchannel using a pair of syringes (Fig. 2).
An electrode testing schematic is shown in Figure 3. Bipolar, bare-ended antennae are embedded within a layer of ballistics gelatin and broadcast a sinusoidal signal from within the known neural frequency bandwidth. A Texas Instruments analog-to-digital converter collects the signals recorded from the electrodes and sends data to a computer for offline analysis. We anticipate that recording simulated neural signals using flexible EGaIn EEG electrodes instead of rigid conventional electrodes will increase signal-to-noise ratio due to better geometry matches between the electrode-gelatin interface. After validating single flexible EEG electrode detection of single frequency simulated EEG signals, we will develop and test a sixteen-electrode array using an electrical head phantom device in Nordin et. al (Figure 4a).10 This head phantom device accurately models human brain activity and material properties of the human head. Electrical signal broadcast sources and scalp surface roughness can be modified to simulate increasingly realistic neuromuscular activity, providing a robust testbed for evaluating EGaIn and conventional rigid electrode performance in capturing simulated neural signals. Figure 4b shows a power spectral distribution of simulated EEG signals collected by two conventional rigid electrodes instrumented on a phantom head broadcasting simulated neural signals at 5, 11, 23, and 37 Hz. Power spectral distribution results from the phantom head will confirm greater neural signal power peaks from flexible EEG electrodes due to better scalp curvature and topography matches.

08:45 AM
Skin-Attachable Piezoelectric III-N Thin-Film Sensors for Continuous Monitoring of Cortisol and Glucose Levels from Sweat
Dr. Nam-In Kim[1], Ms. Jiyun Lee[2], Mr. Asad Ali[1], Prof.

Jae-Hyun Ryou[1]
[1]University of Houston, [2]Gyeongsang National University

The general health of people is greatly impacted by external and internal chronic conditions of the human body such as stress levels and diabetes. Stress prompts the adrenal gland to release cortisol and adrenaline into the bloodstream, expelled through fluids like sweat and tears. Chronic stress harms overall homeostasis, impacting the immune, renal, skeletal, cardiovascular, and endocrine systems, potentially causing chronic illnesses. Diabetes is a type of metabolic disease, such as insufficient secretion of insulin or lack of normal function, characterized by high blood sugar levels, causing various symptoms and signs due to high blood sugar and discharging glucose out of the body. Thus, monitoring of chemical levels in body fluids is crucial for maintaining healthy conditions.

Recent advancements involve the integration of antibody embedding technology with organic electrochemical transistors and field-effect transistor-based sensors for sensing applications. However, both designs face challenges, such as vulnerability to interference from ions in body fluids. Furthermore, applying voltage to electrodes may accelerate the absorption of off-target analytes, potentially causing sensor malfunction. Piezoelectric-based quartz crystal microbalance (QCM) sensors are employed to form the sensing layer due to their specific resonant frequency ranges. The target substance's (cortisol and glucose) mass and antigen-antibody interactions alter the initial resonant frequency oppositely, as per Sauerbrey's equation. Rapid antigen-antibody interactions contribute to the exceptional response times of QCM-type piezoelectric sensors (within minutes). A higher initial frequency enhances sensitivity, enabling the detection of low chemical concentrations. The sensor's selectivity is highly reliable, as the bonding energy between the analyte and antibody is the driving force, ensuring minimal reaction with other substances or hormones.

In this study, a III-N thin film-based QCM-type sensor, with relatively high resonant frequency (~ 6.9 GHz) for the detection of cortisol and glucose under diverse conditions was designed and shown. The layer transfer process was used to create III-N thin-film sensors. The quality of the thin film and the functionalized surface was investigated by X-ray diffraction and Fourier-transform infrared spectroscopy analysis, respectively. The sensor was exposed to the controlled conditions, and the concentration affected the resonance frequency. The selectivity of our sensor was then confirmed using diluted versions of several hormones. To make a comparison, synthetic bodily fluid and authentic sweat were collected from volunteers engaged in running and sauna sessions to assess cortisol levels and individuals with type 1 diabetes mellitus.

09:00 AM
Development of real-time wireless gait analysis system with wearable sensor
Dr. Jung Ahn[1], Dr. Byungseok Yoo[2], Ms. Chia-Ying Kuo[1], Prof. Soaram Kim[1]
[1]Department of Electrical and Computer Engineering, Texas A&M University, College Station, TX 77843, USA, [2]University of Maryland, College Park

The demand for precise pressure sensing in industries such as automotive, aerospace, healthcare, and robotics has driven advancements in pressure sensor technology [1,2]. Research has focused on various materials and methods to create a high-performance pressure sensor. However, limitations still exist, such as small quantification ranges to tens of kPa or a costly fabrication procedure. To address these limitations, there is a need to suggest a cost-effective and practical solution to ensure sensing performance and mechanical durability. Liquid-state electronics like eutectic gallium indium (EGaIn), with low viscosity at room temperature and high electrical conductivity, have advantages as sensing material capable of detecting pressure across a wide range up to a few MPa [3,4]. To fully exploit these advantages with high efficiency, it is essential to choose a suitable substrate that balances mechanical durability with susceptible deformability under pressure. Among the deformable elastomers, EcoFlex stands out for its extra flexibility, mechanical stability, and chemical inertness.

In this work, we propose a multi-functional pressure sensor by EGaIn encapsulated in an EcoFlex-based microchannel with a novel architecture. The microchannel in the EcoFlex substrate was obtained by simply employing a 3D-printed plastic mold printed. As depicted in Figure 1, the fabricated sensor showed no leakage or breakage of EGaIn under moderate stretching of 250% strain, indicating the EGaIn was safely filled in the microchannel and able to act as a stretchable conductor. The sensor configuration is displayed at the bottom of Figure 1. The proposed sensor is a single device having two sensing channels with five different sections. Based on this unique design, the channels' resistance changes enable distinguishing the applied pressure location. When the gradual pressure up to 1 MPa was loaded/unloaded to each section (Figure 2 (a)), the response was significantly different according to the section in the channels (Figure 2 (b)). In channel 1, the maximum resistance values increased from section 1 to section 5, while channel 2 showed a decreasing trend in maximum resistance values with a higher section number. The cyclic test was conducted by applying different pressures to section 5, and the resistance variance of channel 1 and channel 2 was shown in Figures 2 (c) & (d). The resistance changes, and the applied pressure exhibited a parabolic relation and overlapped consistently across different pressures, indicating the reliability of the sensor to have a wide pressure range, leveraging the benefits of EGaIn and EcoFlex.

The potential of the sensor as a gait monitoring sensor was assessed by attaching the sensor to the subject's metatarsus, where section 1 was affixed to the thumb and section 5 was attached beneath the little toe (Figure 3). The test was conducted with correct and incorrect casual walking and casual jogging postures. The sensor results demonstrated distinguishable patterns along with the individual postures. The magnified graphs of each posture are displayed on the right side of Figure 3 for a better comparison of the patterns. Under the correct casual walking posture, R2 (red line, the response of channel 2) initially showed higher values than R1 (black line, the response of channel 1), indicating more pressure was applied to the little toe of the subject. With time, R1 exceeded R2 while R2 exhibited a double peak simultaneously, indicating the center

of gravity was transitioned from the little toe to the thumb. On the other hand, with the incorrect walking posture, the R2 value was consistently higher than R1, confirming that the center of gravity remained on the little toe with a walking cycle. When the subject conducted casual jogging, R1 and R2 registered comparable values with the testing time, which is interpreted as an even pressure distribution across the forefoot. The specific patterns of the sensor outcomes associated with the walking postures provide applicability of the sensor for distinguishing the gait posture of the subject. The sensor was further developed to collect the data to a personal computer via an WiFi connection. This improved the comfort and practicality of the sensor while walking, thereby enabling the sensor to be utilized as a wireless gait monitoring sensor for diagnosing the walking habits of individuals with Parkinson's disease in their rehabilitation treatments.

09:15 AM
Piezoelectric Flexible Pressure Sensor Array with Single-Crystalline III-N Thin Film for Practical Rehabilitation by Detection of Muscle Motions
Dr. Nam-In Kim[1], Ms. Jiyun Lee[2], Dr. Gang Seo[1], Mrs. Hey Min Lee[3], Mr. Asad Ali[1], Prof. Jinsook Roh[1], Prof. Jae-Hyun Ryou[1]
[1]University of Houston, [2]Gyeongsang National University, [3]MD Anderson Cancer Center

Rehabilitation after a stroke is a variety of therapeutic programs that are important to help patients regain the skills and independence they need to live daily life. Depending on the part of the brain affected by the stroke, rehabilitation can help with movement, speech, strength, and daily living skills. In the case of movement, in particular, a person who has suffered a stroke can make significant improvements that would otherwise be quite unnatural, such as hemiplegia. To date, there are several approaches to help stroke patients recover. For example, physical activity can include motor skills exercises, mobility training, constraint-guided therapy, and range-of-motion therapy. Technology-assisted physical activities may include functional electrical stimulation, robotic technology, wireless technology, and virtual reality. However, most rehabilitation therapies focus on performing repetitive movements, which causes patients to feel bored throughout rehabilitation, which is a major cause of loss of interest and concentration. In addition, the repetition of these simple movements is dependent on the patient's willingness, although quantitative goals are achieved by measuring the number of times or times. Successful stroke rehabilitation depends on many factors, not only physical movement but also emotional factors such as mood and the ability to sustain rehabilitation activities outside of therapy. Therefore, recent rehabilitation research uses motivational methods. For example, by using simulations or games to make it easier and longer for patients to concentrate.

Methodologically, electrophysiological activities such as electromyography (EMG) and electroencephalography (EEG) are commonly used. Recently, there has been a lot of research investigating muscle movement, with the promise of replacing EMG and EEG. As a muscle movement sensor, piezoelectric devices that can generate voltage directly in response to movement are promising, and among them, III-N-based single-crystal materials are attracting attention for their high performance, accuracy, and good biostability.
In this study, a III-N thin film-based single crystal piezoelectric pressure sensor fabricated by layer transfer method is utilized to detect muscle movement. X-ray diffraction analysis reveals that they have a single crystal structure and are free of secondary phases or defects. We test single sensors at different bending pressures in a lab-built test station. We then organize the sensors into an arrangeable system and attach them to different points on the fingers and forearm that are associated with muscle movement according to the nerves involved. We design and execute a simple game (rock-paper-scissors) with a combination of sensors attached to the forearm. We expect that our research will greatly help the rehabilitation process of stroke patients in the future.

09:30 AM
pH dependence of SARS-CoV-2 Detection using Graphene FET Array Biosensor
Ms. Kaori Yamamoto[1], Ms. Natsuki Sato[1], Mr. Kiyoji Sakano[1], Mr. Takao Ono[1], Mr. Hidekazu Tanaka[1], Mr. Shota Ushiba[2], Mr. Naruto Miyakawa[2], Mr. Shinsuke Tani[2], Mr. Masahiko Kimura[2], Mr. Kazuhiko Matsumoto[1]
[1]Osaka Univ., [2]Murata Manufacturing Co., Ltd.

1. Introduction
The dependence of pH on the detection of the virus using the integrated graphene FET array was investigated. Two kinds of buffer solutions with difference pH were used such as PBS and acetate buffer. PH of 0.01×PBS is about 7.4, and that of acetate buffer is about 4. It is said that pI of SARS-CoV-2 is from 5.2 to 6.1. Depend on the pH, the shift of the Dirac point changed from positive to negative direction owing the difference of the induced charge of the virus. For the high sensitive detection of virus, it is important to select the buffer solution and its pH.
2. Experimental Process
The fabricated graphene FET has a inter digital source and drain structure with the channel length and width of 10 μm and 400 μm, respectively. 32 graphene FET’s are integrated on the SiO2 substrate. The microfluidic channel was installed onto the G-FET array in order to flow acetate buffer and/or PBS from the inlet hole, pass over the FETs, and drain out from the outlet hole. Buffer solution was introduced from the reservoir and the amount, the duration time, and the speed of the buffer solution is controlled by the computer controlled-micropump. Using the microfluidic channel, the exchange of the buffer solution and washing of the physisorbed virus becomes possible for the precise detection of viruses.
The half of the graphene FET’s in the integrated graphene FET array are modified by antibody of SARS-CoV-2 through PBASE, and the other half FET’s by antibody of H10N8 influenza virus and used as reference FET. In order to get the higher sensitivity, poly-L-lysine (PLL) with positive charge was introduced which can cancel out the negative charges of the graphene surface and modulate the surface potential of graphene FET to enhance the sensitivity.
When the virus (SARS-CoV-2) was introduced to the graphene FET, the high concentration of 150 mM PBS (1×PBS) was used for the virus to sufficiently connect to the antibody. In order to detect the charge of the virus, 100 times

thinner buffer solution of 1 mM was used to extend the Debye length more than 10 times.
Furthermore, in order to investigate the effects of the pH to the virus detection, two kinds of buffer solutions are used, i.e., 1) 1 mM phosphate-buffered saline (PBS) with pH of ~7.4 and 2) 1 mM acetate buffer with pH of 4.0. PH of the virus is considered to be about 5.2 to 6.1., therefore, the virus is expected to be charged plus or minus depend on the pH of the buffer solution. Depend on the plus or minus charge of the virus, it is expected that Dirac point of the graphene FET shifts also minus or plus direction, respectively.
3. Results & Discussions
The time dependence of the Dirac point (DP) of G-FET was measured before and after the introduction of the SARS-CoV-2 using the two kinds of buffers such as 1 mM acetate buffer and 1mM phosphate-buffered saline (PBS). 2 times of 1×PBS (150 mM) was introduced into the system without virus to confirm the no influence by the exchange of the high concentration of PBS.
Dirac point shift was calculated by subtracting the Dirac point of G-FET modified with influenza virus Ab from that of SARS-CoV-2 Ab to remove the effect of the physical adsorption of the virus and the drift.
In 1 mM PBS solution with pH of 7.4, Dirac point shift was 10 mV in the positive direction after the introduction of the SARS-CoV-2 with 1×107 FFU/mL in the time dependence of the Dirac point of the graphene FET. On the other hand, in using the acetate buffer with pH of 4, Dirac point shift was 17 mV in the negative direction.
The transfer characteristic of G-FET before and after the introduction of SARS-CoV-2 was extracted. In PBS, the transfer characteristic shifted in the positive direction. On the other hand, the transfer characteristic shifted in the negative direction in acetate buffer.
These results indicate SARS-CoV-2 has positive charge in acetate buffer because acetate buffer is acidic buffer. On the other hand, SARS-CoV-2 has some negative charge in PBS. Thus, pI of SARS-CoV-2 is considered to be between 4.0 and 7.4.
3. Conclusions
Using the different pH buffer solution for the detection of SARS-CoV-2, the charge of the virus changes plus and minus depend on the pH value. Following these results, it is found that the pI of SARS-CoV-2 is considered to be between 4.0 and 7.4. These results may contribute to the further high sensitive detection of virus using graphene FET.

8:30 AM
Epitaxial Materials
Session Chairs: Mark Wistey (Texas State University), Nadeemulal Mahadik (Naval Research Lab)
ESJ 1215

08:30 AM
Developing Piezoelectric Barium Nickelate for Catalysis
Mr. Ian Graham[1], Mr. Marshall Frye[1], Dr. Lauren Garten[1]
[1]Georgia Institute of Technology

The oxygen evolution reaction (OER) is the rate limiting step in the splitting of water for fuel; further increases in OER activity are critically needed in order to efficiently create fuel from water for applications such as fuel cells and metal-air batteries.1,2 The potential generated in a piezoelectric material under stress has long been proposed as a route to increase OER and similar catalytic activity, but a lack of suitable materials has slowed progress in piezocatalysis. Barium nickelate is an ideal piezocatalytic candidate because of its strong catalytic response, variable oxidation state, and large predicted piezoelectric coefficient. Barium nickelate ($BaNiO_3$) has already been shown to increase the activity of the oxygen evolution reaction (OER) by an order of magnitude with respect to currently materials like iridium oxide (IrO_2).1 Additionally, while the ground state of $BaNiO_3$ is centrosymmetric (which cannot be piezoelectric), there is a piezoelectric phase (P63mc) of $BaNiO_3$ that is predicted to be close in energy to the ground state and thus likely accessible.3
In this work, we describe the stabilization of the piezoelectric P63mc phase of $BaNiO_3$ and the investigation into using this piezoelectricity as a route to enhance catalysis. Strain engineering during pulsed laser deposition (PLD) and post annealing in oxygen preferentially stabilize the P63mc phase of $BaNiO_3$. $BaNiO_{3-x}$ thin films were deposited on (0001) Al_2O_3 and (111) Nb:$SrTiO_3$ from a $BaNiO_{2.36}$ target. In order to identify the processing window for the piezoelectric phase, films were deposited at temperatures ranging from 400-600 °C, laser fluences of 2.0-3.5 J/cm2, and oxygen partial pressures of 0.009-0.16 mbar. Because nickel must be in a 4+ state in fully oxidized $BaNiO_3$, post annealing in an oxygen atmosphere was critical in stabilizing the high oxidation state of nickel in the $BaNiO_3$ films. X-ray diffraction showed that the P63mc phase was stabilized with a (110) orientation on (0001) Al_2O_3 substrates. Co-planar top electrodes were then deposited on these films for impedance spectroscopy, and dielectric measurements. Impedance spectroscopy results indicate that the oxidation state of nickel plays a large role in the overall electronic and ionic conductivity in barium nickelate. Finally, the piezoelectric response of the $BaNiO_3$ films with the highest oxidation state was measured using an e31,f wafer flexure method.
References
1. Lee, J. G. et al. A New Family of Perovskite Catalysts for Oxygen-Evolution Reaction in Alkaline Media: BaNiO 3 and BaNi 0.83 O 2.5. J. Am. Chem. Soc. 138, 3541–3547 (2016).
2. Plevová, M., Hnát, J. & Bouzek, K. Electrocatalysts for the oxygen evolution reaction in alkaline and neutral media. A comparative review. J. Power Sources 507, 230072 (2021).
3. Jain, A. et al. Commentary: The Materials Project: A materials genome approach to accelerating materials innovation. APL Mater. 1, 011002 (2013).

08:45 AM
Correlation Between Optical Spectra and Dislocation Content in ZnS Epilayers
Mr. Alexander Blackston[1], Ms. Alexandra Fonseca Montenegro[1], Ms. Marzieh Baan[1], Ms. Sevim Polat Genlik[1], Mr. Evan Freeland[1], Mr. Md Adnan[1], Prof. Tyler Grassman[1], Prof. Maryam Ghazisaeidi[1], Dr. Roberto Myers[1]
[1]The Ohio State University

Dislocations are known to greatly impact the recombination and transport properties of semiconductor devices. However, until recently it has not been possible to reliably calculate the band structure of dislocations. In diamond, such calculations were recently used to predict the emergence of one-dimensional quantum wire channels and direct band gap photoluminescence from core states of dislocations [1]. ZnS displays electro-optically active dislocations, observed through photo-plastic phenomena [2, 3]. Motivated by these recent reports, we aim to study the optical and electronic properties of networks of misfit dislocations in epilayers of ZnS grown on GaP. Zincblende ZnS thin films with thicknesses of 15 nm, 20 nm, 25 nm, and 50 nm are grown using molecular beam epitaxy (MBE) on GaP substrates, and the misfit dislocations are imaged using electron channeling contrast imaging (ECCI) [4]. From this data, the properties of the dislocation networks are quantified. Spectroscopic ellipsometry is used to extract the absorption spectra, which are fit to obtain Urbach energies. Low temperature photoluminescence (PL) spectra show a quadruplet of narrow emission peaks near the band edge (~3.70 eV), as well as two broad peaks at 2.79 eV and 3.10 eV, which were previously reported in literature as associated with defects [5, 6]. The Urbach energy was founded to be correlated with the relative intensity of both defect PL peaks. The intensity of the 2.79 eV PL peak increases as a function of misfit dislocation density (length per area) relative to the band edge PL. Density functional theory (DFT) calculations of the band structure of ZnS predict a 2.82 eV transition from the one-dimensional conduction band core states of a Zn-core edge dislocation and the valence band of ZnS implying that the 2.79 eV PL peak is associated with misfit dislocations.

09:00 AM
Statistical analysis of dislocation nucleation and growth on epitaxial ZnS (Student)
Ms. Alexandra Fonseca Montenegro[1], Dr. Roberto Myers[1], Prof. Tyler Grassman[1], Ms. Marzieh Baan[1]
[1]The Ohio State University

We provide in-depth characterization of ZnS grown on GaP (001) by molecular beam epitaxy (MBE) using traditional epitaxial techniques including reflection high energy electron diffraction (RHEED), high-resolution x-ray diffraction (HRXRD) and scanning transmission electron microscopy (STEM). During growth of thin films, the strain energy from lattice mismatch produces misfit dislocations at the interface once relaxation occurs. The dislocation network in this system is investigated through electron channeling contrast imaging (ECCI) and processing of the micrographs allows to quantitatively compare dislocation density with increasing film thickness. Additionally, dipole features suspected to be dislocation nucleation surface loops are also quantified. Strain relaxation calculated from defect density results in comparable values to those determined by HRXRD. Furthermore, by analyzing surface morphology, surface roughness and feature area can be correlated to defect density, establishing the transition from 2-dimensional to 3-dimensional growth. Misfit dislocation length across all samples follow a log-normal distribution for both line directions. The mean and standard deviation parameters extracted from the fit are compared and anisotropy is observed for misfit dislocation length. Glide velocity calculated from the cumulative function distribution as a function of critical thickness (tcrit) establishes tcrit in the range of 15 to 19 nm. The peak glide velocities, studied in the longest dislocations, ranges between 90 to 140 nm/s for the [-110] line direction. Whereas, in the [110] line direction the peak glide velocity is only between 50 to 80 nm/s. Finally, through assessment of the glide velocity and strain energy density at the interface, the mechanism causing a decrease in glide can be identified as the traversing of misfit dislocation in perpendicular line directions.
Acknowledgment:
Funding for this research was by the AFOSR (Grant FA9550-21-1-0278, Program Manager Dr. Ali Sayir).

09:15 AM
Expanded stability of layered SnSe-PbSe alloys and evidence of displacive phase transformation from rocksalt in heteroepitaxial thin films
Ms. Pooja Reddy[1], Prof. Leland Nordin[1], Ms. Lillian Hughes[2], Ms. Anna-Katharina Preidl[1], Prof. Kunal Mukherjee[1]
[1]Stanford University, [2]University of California, Santa Barbara

The IV-VI semiconductor family of PbSe-SnSe alloys spans narrow direct bandgap materials in the Pb-rich cubic rocksalt phase, and indirect bandgap semiconductors in the Sn-rich layered orthorhombic phase. This alloy system hosts a wide array of properties key to next-generation thermoelectrics, infrared optics, ferroelectrics, and most recently for quantum information sciences. Moreover, several research groups have shown a large contrast in electronic and optical properties for phase-change devices across the orthorhombic to rocksalt structural transition that can be driven by temperature and direct application of intense light-fields [1,2]. The development of growth techniques to fabricate high quality thin films of not only SnSe but also Pb1-xSnxSe offers new compositional routes to tune these properties.
We epitaxially integrate thin films of PbSnSe on GaAs by molecular beam epitaxy (MBE), using a Riber Compact 21 system with compound PbSe and SnSe cells. (001)-oriented semi-insulating GaAs substrates are prepared by desorbing the surface oxide under a Se overpressure, followed by a PbSe dose and buffer layer, which results in smooth, out-of-plane single oriented PbSnSe films. The Pb1-xSnxSe alloy composition is varied by changing relative fluxes of the PbSe and SnSe compound cells.
Our MBE grown PbSnSe films show a significantly reduced two-phase region by stabilizing the Pnma layered structure out to Pb0.44Sn0.55Se, beyond the bulk-limit of Pb0.25Sn0.75Se. Pushing composition even more Pb-rich, we directly access metastable two-phase films of layered and rocksalt grains that are nearly identical in composition around Pb0.5Sn0.5Se and entirely circumvent the miscibility gap present in the bulk phase space. We present microstructural evidence for an incomplete displacive transformation from rocksalt to layered structure in these films that we speculate occurs shortly after synthesis as the sample cools down to room temperature. There seem to be well-defined orientation relationships between the phases forming in the process and unconventional strain relief mechanisms involved in the crystal structure transformation revealed by transmission electron microscopy. We will

discuss STEM-EDS measurements to explore the possibility of local diffusion at grain boundaries and confirm the lack of compositional contrast between phases.
In-situ temperature dependent x-ray diffraction measurement of as-grown rocksalt PbSnSe films result in a phase transition to the layered phase on cooling, which reproduces key attributes expected of a displacive transition, thus validating our hypothesis. We are able to quantify phase fraction as a function of temperature and see the beginning of a hysteretic behavior in the phase change, where we expect further heating of the sample to revert the transformed sample back to single-phase cubic. Room temperature Hall and UV-Vis spectroscopy show clear property dependence on phase of as grown PbSnSe samples. As expected, cryogenic hall measurements capture this electronic property change with the temperature induced phase change. We see unusually high carrier concentration for the resulting layered phase. This may be a result of the sample retaining Sn vacancies typical to the cubic phase. We plan to verify the hysteretic nature of the phase transition and related properties via heating experiments.

09:30 AM
Growth and Characterization of Ternary-Containing AlInAsSb Digital Alloys (Student)
Ms. Ellie Wang[1], Ms. Hannaneh Karimi[2], Dr. Moaz Waqar[3], Prof. Xiaoqing Pan[3], Prof. Joe Campbell[2], Prof. Seth Bank[1]
[1]University of Texas at Austin, [2]University of Virginia, [3]University of California Irvine

AlxIn1-xAsySb1-y (referred to as AlInAsSb) grown as a digital alloy has been shown to have characteristics useful for avalanche photodetectors (APDs) operating at near- to mid-IR wavelengths. In addition to a broadly tunable bandgap over a wide compositional range, the material system has favorable band offsets, with most of the bandgap change occurring in the conduction band, and it exhibits low excess noise due to impact ionization coefficient ratios as low as k = 0.01 [1]. The digital alloy method of growing thin binary layers to form extremely short-period superlattices not only helps to overcome phase separation that challenges the growth of the random alloy, but it also provides finer control over compositional gradings in the growth of complex heterostructures [2]. This has allowed for advanced devices on GaSb, such as separate absorption, charge, multiplier (SACM) APDs [3]. Translating these photodetectors to InP substrates would be advantageous due to the availability of semi-insulating InP and its existing mature manufacturing infrastructure; indeed, a SACM device on InP using digitally-grown AlInAsSb for the multiplier region was recently demonstrated with excess noise comparable to Si APDs [4]. However, methods to improve other metrics such as dark current and gain should be explored. This is more challenging on InP substrates than on GaSb because of the larger lattice mismatch between InP and the constituent binaries conventionally used in AlInAsSb digital alloy growth. This often results in phase separation, which is readily apparent in scanning transmission electron microscopy studies. To this end, we demonstrate that alternate phase formation can be suppressed in digital alloys built from ternary constituents, which could improve material quality by reducing the amount of strain in the structure, while maintaining its low noise characteristics [5].
Here, we report the growth and characterization of AlInAsSb on InP as a digital alloy consisting of both ternary and binary components. A period thickness of 10 monolayers (2.93 nm) and an aluminum composition of 70% were used in preliminary samples, and the thicknesses of the constituent layers were varied to strain balance to the InP lattice constant. PIN diodes with two different structures were grown via molecular beam epitaxy on semi-insulating InP substrates with Te- and Be-doped contact regions. High resolution X-ray diffraction ω-2θ scans indicated excellent structural quality, as well as strain balancing to the InP substrates. 100 um diameter devices were fabricated, and current-voltage characteristics under dark and illuminated conditions were collected at room temperature. Both devices exhibited high gains >100 before breakdown. Further investigation of structural quality and excess noise characteristics, as well as the growth of these devices on InP/Si templates, are in progress and results will be presented at the conference. This work was supported by Multidisciplinary University Research Initiative from the Air Force Office of Scientific Research (AFOSR MURI Award No. FA9550-22-1-0307), the Army Research Office (W911NF22P0067), and Northrop Grumman.
References:
[1] S. R. Bank, et al. JSTQE (2018). [2] A. J. Muhowski, et al. JVST (2021). [3] Ren, et al. JLT (2017) [4] Martyniuk, et al. App Phys Rev (2014). [4] B. Guo, et al. APL. (2023). [5] Y. Yuan, et al. JLT (2019).

9:45 AM
Coffee Break
ESJ Building

10:15 AM
III-N Device and Material Characterization
Session Chairs: Mona Ebrish (Vanderbilt University), Mihee Ji (Army Research Laboratory)
ESJ 0202

10:15 AM
Low Leakage GaN p-i-n Homojunction Avalanche Photodiodes via Shallow-Bevel-Mesa Edge Termination (Student)
Ms. Zhiyu Xu[1], Dr. Theeradetch Detchprohm[1], Prof. Shyh-Chiang Shen[1], Prof. Nepomuk Otte[2], Prof. Russell Dupuis[1]
[1]Georgia Institute of Technology, School of Electrical and Computer Engineering, [2]Georgia Institute of Technology, School of Physics

With the advantages of bandgap engineering flexibility and direct bandgaps, III-nitride materials are promising candidates for ultraviolet (UV) light detection. Compared to

current UV detection solutions based on vacuum-tube photomultiplier tubes (PMs), III-nitride avalanche photodiodes (APDs) are more rugged, can have higher sensitivity, lower dark currents, and the capability of high-temperature operation under relatively low input voltages. Homojunction GaN APDs grown on native GaN substrates can achieve low threading dislocations and robust avalanche breakdown. However, to reduce leakage currents and improve device performance and reliability, field crowding at the junction interface near device edge needs to be mitigated by effective edge termination approaches such as shallow bevel mesas1, 2.
In this work, low-leakage homojunction GaN p-i-n (PIN) APDs with shallow-bevel-mesa edge termination of ~1-2° were demonstrated. The metalorganic chemical vapor deposition (MOCVD)-grown device structure consisted of a 1μm n-GaN:Si ([n] = 7×1018 cm-3), a 350 nm GaN:uid drift layer, a 300 nm p-GaN:Mg ([p] ~ 1×1018 cm-3), and a 20 nm p+-GaN:Mg ([Mg] = 1×1020 cm-3) on the Ga-face of an ammonothermal (0001) n-type bulk GaN substrate. Photoresist masks were used for shallow-bevel etching by multi-step lithography followed by thermal reflow of the photoresist pattern above 200°C. The bevel-edged mesa was then formed separately by Cl2/BCl3 based inductively coupled plasma (ICP) etching. To compensate for the absorption loss in the thick p-GaN:Mg layer, a 150 nm recessed window region was formed by ICP etching in the center of the device to partially remove a portion of the p-GaN layer. The p-contact of Ni/Ag/Pt was formed by electron-beam (e-beam) evaporation followed by annealing in compressed air, and the backside n-contact was formed by e-beam evaporation of Ti/Al/Ti/Au. The sample was passivated with spin-on glass (SOG). No anti-reflection coatings were applied.

The J-V characteristics at 300K of a 90-μm-diameter GaN PIN APD with shallow-bevel-mesa edge termination and an etched recessed window under dark and UV-illuminated conditions were measured.3 The leakage current density in the dark condition is less than 10-9 A/cm2 up to a reverse bias of -70 V. The breakdown voltage (BV) is -106.9 V, and the leakage current density at the onset of reverse breakdown is 3.4 × 10-5 A/cm2. The APDs are stable under repeated reverse-bias testing. Under UV illumination at λ = 360 nm, the avalanche gain increases up to 4.7 × 106 limited by a current compliance of 1 mA. The spectral response of a fabricated GaN UV APD with a mesa diameter of 90 μm and 150 nm recess window was measured. At zero bias, the peak absorption was at λ = 350 nm with a photo-responsivity of 121 mA/W. At reverse bias of -110 V, the responsivity was increased across the UV wavelengths with a peak responsivity of 772 mA/W and peak absorption shifted to λ = 360 nm. The avalanche capability of the fabricated APD is confirmed by temperature-dependent BV with derived positive temperature coefficient of 0.02V/K. Further details of the device design, processing, and operation will be presented.
1. T. Shoji, et al., Applied Physics Express, 14 (11), 114001 (2021).
2. T. Maeda, et al., IEEE Electron Device Letters, 40 (6), 941-944 (2019).
3. Z. Xu, et al., IEEE Electron Device Letters, in review (2024).

10:30 AM
A Linear Spectroscopy Method to Investigate Plasma Damage in GaN Films Grown on CTE Matched Substrates (Student)
Mr. Owen Meilander[1], Mr. Swarnim Neema[1], Ms. Haley Dishman[1], Prof. Mona Ebrish[1]
[1]Vanderbilt University

As the commercialization of gallium nitride semiconductor devices continues, consistent, high-quality substrates are needed for high yield production. While freestanding or homoepitaxially grown GaN is preferred from a material quality's perspective, the high cost and the small size make them a less attractive option for commercial applications. Instead, engineered substrates have become an appealing choice. In this work, we evaluate the quality of an AlGaN/GaN structure grown on an engineered substrate produced by Qromis and compare it against commercially available GaN on sapphire using Raman spectroscopy. We assess the consistency of the material properties across the samples by examining the E2H and A1(LO) peaks of GaN. By specifically analyzing the E2H peak shift, we determined that the GaN in the engineered heterostructure has a lower biaxial stress as compared to GaN on sapphire. Furthermore, we evaluated the effect of a Cl2/Ar inductively coupled plasma (ICP) reactive ion etch (RIE) on the stress in the GaN layer. After an eighty second etch, the stress increased from 0.395 GPa to above 0.710 GPa. This increase of stress is undesirable as it can result in device leakage and unreliability. Therefore, several wet treatments were examined to revert the stress to its initial value. Treatments of an hour in KOH and two minutes in TMAH were compared. In either case, the stress was decreased by about the same amount. The wet treatments reduced the roughness on the sidewalls from the ICP-RIE etch. The quality of this treatment, however, is heavily dependent on the crystallographic direction of GaN. With both treatments, spikes seen are characteristic of a sidewall in the <1-100> direction, but smooth walls are observed in the <11-20> direction. While both treatments yield the same stress reduction and sidewall smoothness, the electrical data indicates an advantage to the TMAH treatment over the KOH one. GaN HEMTs were completed after treatment by depositing a Pd/Pt/Au gate and a Ti/Al/Ni/Au source and drain. The ID-VGS characteristics show that the TMAH treatment results in a higher Ion and consequently higher Ion/Ioff ratio as compared to the KOH and the control samples. Therefore, further work is needed to explain the origin of this electrical difference.

10:45 AM
Oxide interface characterization of n/p-GaN for power electronics
Dr. Yasuo Koide[1], Dr. Yoshihiro Irokawa[1], Dr. Toshihide Nabatame[1], Dr. Kazutaka Mitsuishi[1]
[1]National Institute for Materials Science (NIMS)

There has been a growing research effort to develop vertical power MOSFETs which use the MOS inversion electron layer in the epitaxial and/or implanted p-GaN layers. One of key issues to develop the vertical power MOSFET is to control the reliable threshold voltage (VTH) free from the variation. The insulating SiO2, Al2O3, SiNx, and AlSiOx films have been reported as gate materials for GaN MOSFETs.

Plasma chemical-vapor-deposition (PCVD) and atomic-layer-deposition (ALD) methods have been tried to fabricate insulating films, and in combination with post-annealing the good interfacial property with low interfacial density was obtained at the n-GaN MOS interface. On the other hand, for p-GaN MOS capacitor, the hysteresis capacitance-voltage (C-V) curve and frequency dispersions were reported to be observed, which suggested the existence of high-density trap states close to the MOS interface. In this presentation, we will show the electrical and microstructural properties in the GaN MOS interface by comparison between n and p-GaN epilayers and also the significant VTH variation property of p-GaN MOSFET. In addition, we will discuss the mechanism for understanding the VTH variation.

11:00 AM
Ohmic Contact Improvement of AlN/Al0.8Ga0.2N Heterostructure by Atomic Layer Etching (ALE) (Student)
Mr. Tingang Liu[1], Dr. Haicheng Cao[2], Mr. Mingtao Nong[2], Mr. Zhiyuan Liu[2], Prof. Xiaohang Li[2]
[1]Advanced Semiconductor Laboratory, Electrical and Computer Engineering program, CEMSE Division, King Abdullah University of Science and Technology, Thuwal 23955-6900, Saudi Arabia., [2]King Abdullah University of Science and Technology

AlGaN/GaN heterostructures are extensively used in applications such as radio frequency (RF) and power devices. For higher power applications, there is a growing trend to shift from conventional AlGaN/GaN to AlN/AlGaN structures, due to the higher electric breakdown field of AlGaN compared to GaN as the channel layer. However, a significant challenge with AlN/AlGaN heterostructures is the formation of effective ohmic contacts, impeded by difficult electron tunneling through the AlN cap layer between the contact and the AlGaN layer. The typical approach involves etching down this cap layer to bring the contacts closer to the AlGaN channel layer, thereby improving electron tunneling. However, the common reactive ion etching (RIE) method can cause significant plasma-induced damage, negatively impacting contact quality. Atomic Layer Etching (ALE) offers a solution, being a self-limiting process that removes layers atomically with minimal damage, thereby enhancing the surface quality for contacts. This study employs ALE to etch recessed ohmic contacts in AlN/Al0.8Ga0.2N heterostructures, achieving a reduced contact resistivity of 4.59×10-3 Ω·cm2. This demonstrates ALE's effectiveness in advancing ohmic contact, potentially for HEMT applications.

In this study, an AlN (26 nm)/Al0.8Ga0.2N (200 nm)/AlN (600 nm) heterostructure, as shown in Fig.1, was synthesized using Metal-Organic Chemical Vapor Deposition (MOCVD) on a 1 μm AlN commercial template. The 80% aluminum composition in the AlGaN layer was confirmed by UV-Vis and X-ray diffraction analysis. The Full Width at Half Maximum (FWHM) values for the (002) and (102) rocking curves of the AlGaN layer were determined to be 179 and 256 arcsec, respectively as shown in Fig.2. Root Mean Square (RMS) shown in Fig.3 of the roughness of the surface is 493 pm measured by Atomic Force Microscope (AFM). The AlN/Al0.8Ga0.2N heterostructure has a sheet concentration of 3.994×1013 /cm2, measured via the Hall effect, and sheet resistance of 2.061×103 Ω/square extracted from CTLM. To investigate the ALE effect, Ti/Al/Ti metal stack (20 nm/120 nm/80 nm) was deposited on the heterostructure etched by RIE (25 nm), etched by RIE (18 nm) and ALE (7 nm), and without etching, and are named as S1, S2, and S3, respectively. The samples S1, S2, and S3 show onset voltage of 2V, 0.5V, and 5V, respectively; and contact resistivity of 1.96×10-2, 4.59×10-3, and 3.02×10-2 Ω·cm2, respectively. The results reveal a positive effect of ALE by inducing a significant decrease in current and contact resistivity as the I-V characteristics shown in Fig.4. This contact resistivity is comparable with published works listed in Fig.5.

11:15 AM
Decoupling semiconductor thermal and electrical properties for improved thermoelectric performance
Dr. Kris Bertness[1], Dr. Bryan Spann[1], Dr. Joel Weber[1], Dr. Matt Brubaker[1], Mr. Todd Harvey[1], Dr. Lina Yang[2], Dr. Hossein Honarvar[3], Dr. Chia-Nien Tsai[3], Dr. Andrew Treglia[3], Prof. Minhyea Lee[3], Prof. Mahmoud Hussein[3]
[1]National Institute of Standards and Technology, [2]Beijing Institute of Technology, [3]University of Colorado Boulder

We demonstrate experimentally a new method of improving thermoelectric materials properties by using coupled phonon resonances. Specifically, we show that the thermal conductivity of a thin silicon membrane can be reduced by 21 % with the addition of GaN nanopillars on its surface, relative to a bare membrane of the same thickness.[1] The phonon modes in the GaN nanopillars couple to phonon modes in the silicon membrane, creating a nanophononic metamaterial (NPM). This NPM has a new phonon band structure in which thermal transport in the membrane is reduced both by reduction of the phonon group velocity over a broad range of frequencies and by localization of the resonant modes in the nanopillars, as demonstrated by theoretical investigations. [2,3] The specimens were fabricated by growing randomly nucleated GaN nanopillars using molecular beam epitaxy on silicon-on-insulator (SOI) substrates. The height of the nanopillars was varied by using different growth times. The Si handle and buried oxide layers were then removed via backside etching to create suspended 200 nm thick membranes with a square shape approximately 750 μm on a side. The thermal conductivity of the film was measured using Raman thermometry while the film was heated with a UV laser from the bottom side at several different power levels.

Unlike many other methods of reducing thermal conductivity κ of materials, the NPM mechanism does not rely on scattering centers, surface roughness, or other modifications that can significantly slow charge carrier transport. Test samples from the same growth runs showed that neither membrane electrical conductivity σ nor Seebeck coefficient S were significantly affected by the presence of the GaN nanopillars. The thermoelectric material figure of merit, ZT = T S2 σ/κ , thus increases due to the reduction of κ without decreases in S or σ. The interpretation of the electrical data in the first data set was complicated by the diffusion of Ga into the silicon membrane, causing changes in membrane electrical conductivity as a function of growth time. A second set, grown with a thin AlN buffer layer, reduced Ga diffusion

and produced a data set with electrical conductivity and Seebeck coefficient that were approximately independent of growth time.

The NPM effect was first identified by lattice dynamics calculations and in molecular dynamic simulations, [2,3] which predicted that the effect would grow stronger as the nanopillars increase in volume. The experimental data support this prediction, with longer growth times producing longer nanopillars that correlate with a greater reduction in thermal conductivity, up until the nanopillars begin to coalesce together. The non-ideal growth habit of randomly nucleated nanopillars limits the NPM effect, which in theory could cause thermal conductivity reduction of two orders of magnitude. We will also briefly discuss structures that eliminate coalescing and take better advantage of this unique phonon mechanism.

[1] B. T. Spann, J.C. Weber, M. D. Brubaker, T. E. Harvey, L. Yang, H. Honarvar, C-N Tsai, A. C. Treglia, M. Lee, and M. I. Hussein, Adv. Mater. 35, 2209779 (2023).
[2] B. L. Davis, M. I. Hussein, Phys. Rev. Lett. 112, 055505 (2014).
[3] H. Honarvar, M. I. Hussein, Phys. Rev. B 97, 195413 (2018).

10:15 AM
Oxide Semiconductor Thin Films and Devices
Session Chairs: Sarah Swisher (University of Minnesota), William Scheideler (Dartmouth College)
ESJ 0224

10:15 AM
Crystal orientation-dependent electronic properties of β-Ga2O3 surfaces
Dr. Andrew Winchester[1], Mr. Dinusha Mudiyanselage[2], Dr. Houqiang Fu[2], Dr. Sujitra Pookpanratana[1]
[1]NIST, [2]Arizona State University

β-Ga2O3 is a promising next-generation wide bandgap material for high voltage device applications. One significant advantage over other wide bandgap semiconductors is the ability to grow bulk β-Ga2O3 wafers directly from the melt. This has enabled rapid development of low defect density substrates with several different possible crystal facets for epitaxial growth of vertical device architectures1,2. Due to the different atomic termination of these facets, they possess different surface energies, resulting in different etching rates and contact formation3, as well as Schottky diode behavior.4 However, there have been few systematic experimental studies on the surface electronic properties of different β-Ga2O3 facets, including the (001) facet which can also achieve large substrate sizes. Furthermore, there are reports on β-Ga2O3 Schottky diodes on various substrate orientations showing evidence for non-uniform barrier heights4,5. Therefore, there is a significant degree of electronic variation present in β-Ga2O3 that strongly affects contact formation, and it is not yet clear how these variations depend on substrate orientation.
Here, we use photoemission-based microscopy and spectroscopy and atomic force microscopy (AFM) to evaluate the surface electronic properties of β-Ga2O3 substrates with (010), (001), and (-201) orientations. We observe nanoscale electronic variation on all three facets that corresponds to local regions of different doping and gap state density. Electronic differences are observed at nanoscale particles on all three faces; however, the (010) orientation shows an order of magnitude higher particle density than the (-201) orientation. In contrast, larger electronic features not due to topography are observed on the (001) orientation and may cause different local conduction behavior. In addition, we find that the work function and ionization potential of the (010) surface are substantially lower than the other two orientations using photoemission spectroscopy, which is consistent with reported differences in Schottky barrier heights4. We find that the electronic properties of different β-Ga2O3 orientations can vary at both nanoscale and bulk levels, which leads to local and macroscopic differences that will influence diode operation.

References

1. Ahmadi, E. & Oshima, Y. J. Appl. Phys. 126, 160901 (2019).
2. Roy, S. et al. IEEE Electron Device Lett. 42, 1140–1143 (2021).
3. Jang, S. et al. J. Alloys Compd. 731, 118–125 (2018).
4. Fu, H. et al. IEEE Trans. Electron Devices 65, 3507–3513 (2018).
5. Sheoran, H., Kaushik, J. K. & Singh, R. Mater. Sci. Semicond. Process. 165, 107606 (2023).

10:30 AM
Application of Ion Energy Spectroscopy to Study the Plasma Kinetics during the Pulsed Laser Deposition of Strontium Titanate Thin Films
Mr. Marcus Rose[1], Dr. R. Shipra[2], Mr. Ryan Paxson[3], Ms. Madison Previti[1], Mr. Luke Thress[1], Dr. Jeonggoo Kim[4], Dr. Rajeswari Kolagani[1]
[1]Towson University, [2]Towson university, [3]University of Maryland, College Park, [4]Neocera LLC

Properties of multi-component oxide thin films grown by the Pulsed Laser Deposition (PLD) are known to be very sensitive to even small variations of the intercoupled process parameters such as laser fluence and spot size, target-substrate distance, deposition rate, growth oxygen pressure etc. Such sensitivity poses a challenge for optimizing growth parameters to reproducibly obtain subtle variations in film properties. This challenge can be addressed by utilizing the fact that the influence of these process parameters is mainly through their influence on plasma kinetics, represented by the energy distribution of the different ionic species in the plasma. The Ion Energy Spectrum thus emerges as the most important single parameter that controls properties of films formed on the surface of a substrate under the action of laser-produced plasma flux. The Ion Energy Spectrometer (IES) allows PLD users to map the energy distribution of ions during film growth under a given set of parameter combinations. IES probes the ion energy spectrum as it is at the actual substrate location, at actual process gas pressure, and quantifies the effects of any change a user makes in parameters of the multi-variables space of PLD process, in real-time. Our preliminary experiments involving the deposition of oxygen deficient Strontium Titanate thin films

show that there is a clear correlation between the ion energy spectrum and film characteristics, in terms of both structural and electronic properties. Even with variation of the deposition parameters, so long as one can confirm the ion energy spectrum is replicable, the PLD process facilitates replicable growth of high quality single and multi-component films. IES has an operational limit that requires oxygen pressure to be below 200mTorr. Studies of correlation between oxygen pressure and ion energy may allow us to extrapolate to higher oxygen pressures in future experiments.

This work was partially supported by the NSF Grant DMR 1709781. Marcus Rose acknowledges summer research support from the Office of Graduate Studies, and the Fisher College of Science and Mathematics, Towson University. R. Shipra acknowledges support from the M. Hildred Blewett Fellowship from the American Physical Society.

10:45 AM

Impact of Gate Roughness on the Field Effect Mobility of IGZO TFTs

Dr. Andre Zeumault[1], Mr. Jose Mendez[1], Mr. John Brewer[1]
[1]Amorphyx

Overview

A peculiar templating effect is found to have a significant impact on the field-effect mobility (FET mobility) in sputtered bottom-gate top contact InGaZnO4 thin-film transistors (TFTs). By varying the gate electrode (TiAl3, Mo, AlNd0.02, or Ti) and performing DC device characterization, the linear field-effect mobility (i.e., as) is found to monotonically decrease by 20% as the surface roughness of the gate electrode increased from 0.3 to 2 nm. This trend persisted, even as the Al2O3 gate insulator thickness increased (from 5 nm to 75 nm), suggesting a strong templating effect of the underlying gate electrode on the gate dielectric and, therefore, a sensitivity to gate roughness.

Results

Atomic force microscopy (AFM) indicates that the surface topography of the gate insulator (Al2O3) is practically identical to the underlying gate electrode (TiAl3, Mo, AlNd0.02, or Ti), even as the gate insulator thickness is increased to 75 nm (Fig. 1). Importantly, the initial RMS roughness of the gate metal is transferred to the upper surface of the gate dielectric (Fig. 2a). Since this surface is also the interface between the gate-insulator and semiconductor, an increase in electron scattering is reasonable, potentially explaining the observed decrease in field-effect mobility with increased roughness (Fig. 2b).

To explain these results, we estimated the reduction in FET mobility with increasing gate roughness. The theoretical FET mobility was calculated within the relaxation time approximation (RTA), considering 2DEG electron scattering rates due to local surface roughness (SR) at the gate-insulator/semiconductor interface [1,2]; remote surface roughness (RSR) at the gate [3]; and charged impurities and phonons within the semiconductor bulk [1,2]. Nominal parameters were obtained from fitting calculated mobility to experimental data and comparing to industry-standard SPICE compact models [4] with excellent agreement (Fig. 2c). For SR and RSR scattering, a comparison was made using gaussian and exponential surface models for the autocovariance function, with better agreement using the exponential model (Figs. 3a-d) [5]. The autocovariance function represents fluctuations in surface height from mean. Both models are described by RMS roughness and correlation length, but differ in the power spectrum (i.e., the Fourier-Transform of the autocovariance) dependency on electron momentum—acutely influencing scattering rates. It is found that the observed reduction in FET mobility can be explained by an increase in SR scattering (at large gate insulator thickness) and an increase in RSR scattering (as gate insulator thickness is reduced). Interestingly, the choice of gate dielectric has a significant impact on both surface roughness scattering and remote surface roughness scattering rates, the latter being more important at smaller gate insulator thickness (Figs 3e-f). Essentially, ideal higher permittivity “high k” gate dielectrics are more effective at screening long-range scattering potentials [2], leading to a higher mobility. Thus, TFTs with smooth gate electrodes and high-k dielectrics should show reduced sensitivity to dielectric thickness scaling – a fact that has been documented in highly scaled FinFETs [6] but not in TFTs.

Significance

Increasing the mobility of IGZO TFTs is a contemporary challenge of AMOLED displays [7]. Practical arguments support replacing LTPS switching TFTs with comparable mobility IGZO TFTs, particularly to improve performance of variable image refresh mobile display technology in production [8]. Existing methods to achieve this goal are impractical, either due to cost or complexity—such as the use of ALD oxide heterostructures or double-gate TFT structures. This work is a practical step forward, supporting the use of smooth gate electrodes (e.g., amorphous metals) for improving the mobility and geometric scalability of IGZO TFTs with negligible increase to cost or complexity. Although gate-related SR and RSR scattering has been studied in silicon MOSFETs having thin gate dielectrics, we are unaware of any prior studies relating gate roughness to FET mobility in TFTs, likely because gate-dielectrics tend to be much thicker, with such templating effects to be unexpected. Given that the sputtering of insulators on metals is ubiquitous in thin-film electronics, there is also potential for generalization of these observations beyond IGZO TFTs.

References

[1] B. K. Ridley, J. Phys. C, vol. 15, p. 5899, (1982).
[2] T. Ando et al., Rev. Mod. Phys., vol. 54, p. 437, (1982).
[3] F. Gamiz et al., J. Appl. Phys., vol. 94, p. 392, (2003).
[4] M.S. Shur et al., J. Elec. Chem. Soc., vol. 144, p. 2833, (1997).
[5] S. M. Goodnick et al., Phys. Rev. B, vol. 32, p 8171 (1985)
[6] T. Matsukawa et al., IEDM, pp. 8-2 (2012)
[7] Y. Matsueda, IDCT, vol. 52, issue S2, p 615 (2021)
[8] B. You et al., SID, vol. 51, No. 1, p 676 (2020)

11:00 AM

β-Ga2O3 self-switching diodes (Student)

Mr. Glen Isaac Maciel Garcia[1], Mr. Jorge Bolio Martinez[1], Mr. Vishal Khandelwal[1], Dr. Haicheng Cao[1], Mr. Ganesh Mainali[1], Dr. Biplab Sarkar[2], Prof. Xiaohang Li[1]
[1]King Abdullah University of Science and Technology, [2]Department of Electronics and Communication Engineering, Indian Institute of Technology Roorkee, Uttarakhand 247667, India

Ultrawide bandgap (UWBG) semiconductors represent a

novel and exciting area of study within semiconductor materials, physics, devices, and applications. Among UWBG semiconductors, gallium oxide (Ga_2O_3) experienced rapid growth in research and development over the past decade. Its most stable phase, β-Ga_2O_3, has a bandgap of ~4.9 eV and can withstand extremely high fields (estimated breakdown field ~8 MV/cm), outperforming SiC and GaN. Consequently, it is regarded as a promising material for next-generation power electronics. Several devices based on the β-Ga_2O_3 phase have been extensively studied, including Schottky barrier diodes, MOSFETs, and vertical transistors [1, 2]. This work demonstrates the first β-Ga_2O_3 self-switching diode (SSD), a unipolar nanoscale nonlinear device, which reduces fabrication costs by requiring only two fabrication steps. It also helps achieve low parasitic elements that could limit operating frequency. Unlike conventional two-terminal diodes, SSDs control current flow by modulating charge within a nanochannel, either inducing or depleting the channel. The non-linear current-voltage (I-V) response of SSDs arises intrinsically from the broken device symmetry; however, surface states enhance the rectification of these devices [3]. SSDs are formed by creating two asymmetric L-shaped insulating trenches within the semiconductor layer, typically measuring between 50 and 300 nm. Fig. 1 (a) shows both a schematic of the SSD and a scanning electron microscopy image of the device, where the fabricated devices have SSDs connected in parallel. The devices are fabricated on heteroepitaxial (-201) oriented Si-doped β-Ga_2O_3 (~70 nm) on sapphire, grown using pulsed laser deposition with carrier concentration of ~2×10^{17} cm^{-3}. First, a metal hard mask is patterned using electron beam lithography, followed by BCl_3/Ar based dry etch. The remaining metal is removed, and Ti/Au contacts are sputtered and annealed at 470 °C for 60s in N_2 ambient to form ohmic contact formation. The I-V curve at room temperature (RT) for the SSDs is shown in Fig. 1(b), demonstrating diode behavior with a current density reaching 200 A/cm^2 and an Ion/Ioff ratio of ~ 103. This occurs because positive voltage counteracts the built-in field of the depletion region, reducing the interface-state-induced depletion. The devices exhibited a non-linear I-V response from 77 K to 448 K. As shown in Fig. 2, the Ion/Ioff ratio and current density at every temperature were greater than 50 and 2 A/cm^2, respectively. Additionally, a high breakdown voltage of approximately 200 V was observed for these SSDs, consistent across various devices, as shown in Fig. 3.
[1] J.Y. Tsao, Adv. Electron. Mater. 4, 1600501 (2018). [2] Andrew J. Green, James Speck, Grace Xing, et al., APL Mater. 10, 029201 (2022) [3] A. M. Song, M. Missous, P. Omling, et al., Appl. Phys. Lett. 83, 1881 (2003)

10:15 AM
Epitaxy of Highly Mismatched Alloys
Session Chairs: Nadeemulal Mahadik (Naval Research Lab), Leland Nordin (Stanford University)
ESJ 2208

10:15 AM
Bandgap Evolution in B-III-V Alloys (Student)
Ms. Qian Meng[1], Ms. Rasha El-Jaroudi[1], Ms. Corey White[1], Mr. Herbert Maczko[2], Dr. Tuhin Dey[3], Prof. Robert Kudrawiec[2], Prof. Seth Bank[4], Prof. Mark Wistey[3]
[1]The University of Texas at Austin, [2]Wroclaw University of Science and Technology, [3]Texas State University, [4]University of Texas at Austin

The incorporation of boron pnictides, with their relatively small lattice constants, into conventional III-V alloys can enable lattice-matching for near-infrared, direct-bandgap alloys to both silicon1 and III-V substrates.2,3 In other highly-mismatched alloys (HMAs), such as dilute-nitrides and dilute-bismides, the incorporation of a small amount of nitrogen or bismuth alters the resulting alloy lattice constant and perturbs the host band structure. While this reduces the bandgap energy of the alloy, it is often at the expense of degraded optical quality. The advantage of incorporating boron into III-Vs is a higher predicted solid solubility,4 which suggests that dilute-borides can be grown with better preserved material quality than is typically observed from HMAs. Surprisingly, B-III-V alloys remain relatively underexplored compared to III-V-N and III-V-Bi materials. In fact, the exploration of dilute-borides remains limited both theoretically and experimentally, which has led to inconsistencies in reported properties, such as the bandgap modulation with the addition of B.
Recently, we have demonstrated the growth of BGaAs with highly substitutional B incorporation by molecular beam epitaxy (MBE). The BGaAs alloys demonstrated increasing bandgap energy with increasing B incorporation with a notably smaller bowing parameter as compared to other HMAs, as measured by photoreflectance (PR).1,5 Here, we report a bandgap model developed for highly substitutional BGaAs, by employing density functional theory (DFT) combined with PR and ellipsometry measurements on MBE-grown BGaAs. The model aims to elucidate the increased bandgap and small bowing parameter due to the weak band anticrossing (BAC) arising from the incorporation of B atoms. BGaAs films were grown by solid-source MBE on (100) semi-insulating GaAs substrates at a growth temperature of 400°C. Bi was employed during growth as a surface surfactant. The bandgaps of the BGaAs alloys were determined by photoreflectance (PR) and ellipsometry measurements. Experimental results were then compared to ab initio simulations obtained with the density functional theory (DFT) package of the Vienna Ab initio Simulation Package (VASP) using HSE06 hybrid functionals. A set of BGaAs structures was simulated, wherein the positions of B atoms were varied for alloys with higher B concentrations where the number of B atoms was greater than one.
We found an increase in the bandgap of BGaAs with isolated B configurations using DFT calculations for structures with 0 to 6.3% B. The large electronegativity differences between B and the host GaAs induced a perturbation in the conduction band minimum (CBM) which can be described by the BAC model. However, the perturbation was smaller than is typical for a HMA. Conversely, the small size of the B atom(s) decreased the lattice constant and increased the bandgap energy of the resulting alloy. This increase outweighed the bandgap reduction caused by the perturbation from the electronegativity of B, resulting in an overall increase in the bandgap energy. We developed a bandgap model, which separates the effects of strain and electronegativity

differences, for BGaAs with isolated B atom distribution, that aligns well with DFT-calculated bandgap energies. The bandgap model was further verified by comparing the calculated bandgap energies with PR and ellipsometry measurements of MBE-grown BGaAs. This comparison demonstrated general agreement for B concentrations up to 7%. Deviations in bandgap energy for BGaAs alloys with greater B concentrations were attributed to non-isolated B configurations, such as B-B pairs or larger B clusters. In fact, localization likely caused by non-isolated B distributions was observed in temperature-dependent PR measurements at higher B concentrations.

This work was supported by the National Science Foundation (Award Nos. ECCS-1933836, DMR-1508646, and CBET-1438608). The authors also acknowledge the Learning, Exploration, Analysis, and Processing (LEAP) cluster at Texas State University for computing resources.

1 McNicholas et al. Cryst. Growth. Des. (2021); 2 El-Jaroudi et al. Appl. Phys. Lett. (2020); 3 El-Jaroudi et al. Cryst. Growth. Des. (2022); 4 Hart and Zunger. Phys. Rev. B (2000); 5 Kudrawiec et al. Mater. Res. Express (2020)

10:30 AM

Enhanced minority carrier lifetime in bulk Hydrogen-passivated InAsSbBi (Student)

Mr. Felix Estevez Hilario[1], Ms. Morgan Bergthold[1], Dr. Oleg Maksimov[2], Dr. Harish Bhandari[2], Dr. Christian Morath[3], Dr. Alexander Duchane[3], Dr. Preston Webster[3], Prof. Daniel Wasserman[1]
[1]Department of Electrical and Computer Engineering, University of Texas at Austin, Austin, TX 78758, [2]Radiation Monitoring Devices, Inc, 44 Hunt Street, Watertown, MA 02472, [3]Air Force Research Laboratory, Space Vehicles Directorate, Kirtland Air Force Base, NM 87117

High performance mid-infrared photodetectors are crucial for a range of applications in physics, chemistry, astronomy, and medicine, including molecular sensing, thermal imaging, and free space communication. HgCdTe (MCT) has been the dominant material system for both mid-infrared and long-wave infrared detection due to its bandgap tunability, low noise, and high external quantum efficiency [1]. However, due to its rather difficult epitaxial growth, and the toxicity of MCT's constituent materials, there is interest in III-V semiconductor-based photodetector architectures as alternatives to MCT, as these material structures offer i) more uniform epitaxial growth, ii) greater compatibility with existing nanofabrication techniques and facilities, and iii) significant design flexibility through heterostructure engineering. Perhaps the most promising III-V based material system is the type-II superlattice materials (T2SLs) which have been demonstrated to have broad bandgap tunability and can have relatively low Auger recombination rates [2].

A significant challenge of superlattice-based photodetectors comes from their decreased absorption coefficient resulting from the spatial separation of their electron and hole wavefunctions. Although superlattices can be integrated into resonant structures to compensate for their decreased absorption coefficient, there remains interest in the use of bulk III-V materials for mid-wave and long-wave infrared photodetection. The most suitable bulk III-V alloy for mid-infrared detection is InAsSb which can offer longer cutoff wavelengths than both InAs and InSb but which is limited by the miscibility gap and increasing lattice mismatch to other materials as the Sb percentage increases. The quaternary alloy InAsxSbyBi1-x-y has been studied as an alternative material system for mid-wave and long-wave infrared photodetectors offering broad wavelength tunability and additional flexibility in the control of strain and incorporation into other heterostructure architectures. However, the incorporation of bismuth comes at a price due to its rather low epitaxial growth temperatures (<400 ºC) in comparison to that of high quality InAs (>430 ºC) [3]. This low-temperature growth results in point defects in the crystal structure and thus deteriorates the optical quality of the semiconducting material, an effect most notably reflected in the material minority carrier lifetime. The dramatic reduction in minority carrier lifetime results in decreased collection efficiency and thus degraded detector performance. Therefore, to achieve high-quality and high quantum efficiency detector structures utilizing bulk mid-wave infrared absorbers, it is crucial to improve the minority carrier lifetime of bulk InAsSbBi.

In this work we demonstrate over extension in the minority carrier lifetimes of bulk InAsSbBi using plasma hydrogenation after a low temperature anneal of 160 ºC, from ~70 ns pre-treatment to ~170 ns post treatment, with no degradation in the material optical properties over a period of months after treatment [4]. Deuterium isotopes were used to minimize environmental contributions of hydrogen yielding surface concentrations of which quickly dropped to constant concentration of at depths up to between 1.5 and 2.5 µm, confirmed by secondary ion mass spectrometry. The hydrogen gas was diluted with argon gas giving rise to dilution ratios of 1:2 and 1:5, and we observed no significant difference in the passivated samples' minority carrier lifetimes post anneal as a function of dilution. Furthermore, we also demonstrated a improvement in the minority carrier lifetime, from ~65 ns post-treatment to ~220 ns post-anneal, when only molecular hydrogen plasma (undiluted) was present in the chamber. No enhancement of minority carrier lifetime was observed when undiluted hydrogen gas was used with no plasma. The extension of minority carrier lifetime in InAsSbBi through hydrogenation thus provides a path towards the realization of dilute-bismide-based bulk mid-IR photodetectors. Additionally, this technique may also have significant implications for other III-V based material structures for mid-wave and long-wave IR photodetection.

[1] A. Rogalski, "HgCdTe infrared detector material: History, status and outlook," Rep. Prog. Phys. 68, 2267–2336 (2005).
[2] C. H. Grein, M. E. Flatt_e, J. T. Olesberg, S. A. Anson, L. Zhang, and T. F. Boggess, "Auger recombination in narrow-gap semiconductor superlattices incorporating antimony," J. Appl. Phys. 92, 7311–7316 (2002).
[3] H. Ye, L. Li, R. T. Hinkey, R. Q. Yang, T. D. Mishima, J. C. Keay, M. B. Santos, and M. B. Johnson, "MBE growth optimization of InAs (001) homoepitaxy," J. Vac. Sci. Technol. B 31, 03C135 (2013).
[4] F. A. Estévez H., M. Bergthold, Oleg Maksimov, Harish B. Bhandari, Christian P. Morath, Alexander W. Duchane, Preston T. Webster, and D. Wasserman, "Enhanced minority carrier lifetime in bulk hydrogen-passivated InAsSbBi," Appl. Phys. Lett. 124, 021104 (2024).

10:45 AM

Improvement in Optical Quality Upon Annealing in B-III-V Alloys (Student)

Ms. Qian Meng[1], Ms. Corey White[1], Ms. Rasha El-Jaroudi[1], Dr. Tuhin Dey[2], Prof. Łukasz Gelczuk[3], Prof. Robert Kudrawiec[3], Prof. Seth Bank[4], Prof. Mark Wistey[2]
[1]The University of Texas at Austin, [2]Texas State University, [3]Wroclaw University of Science and Technology, [4]University of Texas at Austin

Incorporating atoms that are highly mismatched in size and/or electronegativity into traditional III-V alloys offers enormous design freedom for optoelectronic devices that can be lattice-matched to affordable and robust substrates including GaAs and Si. However, even highly mismatched alloys (HMAs) with a relatively small fraction of mismatched elements can be plagued by point defects or segregation that severely degrades material quality and consequently device performance as is commonly observed for III-V-N and III-V-Bi materials. The advantage of incorporating boron into III-Vs, compared with other HMAs, is a larger predicted solid solubility, suggesting that greater boron incorporation can be achieved with less degradation of the resulting alloy's material properties.1 Even so, growth challenges have led to B-III-V alloys remaining largely underexplored with previous experimental studies remaining limited to very low B concentrations.
Our group has recently grown high-quality BGa(In)As with highly substitutional B incorporation far beyond the dilute limit.2-4 Notably, the decline in optical quality with increasing B incorporation was minimal as compared to other HMAs in as-grown BGa(In)As.4 Building on this, as with other HMAs, a substantial enhancement in optical properties has been observed in both BGaAs and BInGaAs upon thermal annealing,5 likely attributed to the removal of non-radiative recombination centers originating from the low growth temperatures necessary for B incorporation.6 Here, we investigated defects in BGaAs alloys by combining density functional theory (DFT) and deep-level transit spectroscopy (DLTS) measurements to understand the mechanisms underlying the optical quality increase observed with annealing in B-III-V alloys.
BGa(In)As films were grown by solid-source molecular beam epitaxy on (100) semi-insulating GaAs substrates. Samples were progressively annealed by rapid thermal annealing for 1 minute at each temperature in 50˚C steps from 550°C to 900°C. Samples were characterized by room-temperature photoluminescence (PL) after every annealing step. Deep-level transient spectroscopy (DLTS) was used to characterize the behavior of defects in n-type BGaAs. The formation energy and band structure of defects were calculated using ab initio simulations obtained with the DFT package Vienna Ab initio Simulation Package (VASP) using HSE06 hybrid functionals. In this work, both point defects and defects complex in BGaAs were investigated.
An increase in PL intensity, nearly doubled, was observed in both BGaAs and BGaInAs films at the optimal annealing temperature (~700˚C), suggesting that the as-grown material contained several defects mitigated with thermal treatment. Indeed, DLTS analysis of as-grown n-type BGaAs and GaAs samples revealed several defects centers. The activation energies of most of the defect centers were close to native point defects and defect complexes that have been observed in low-temperature grown GaAs. However, one donor-like defect at 0.15eV was identified in all BGaAs samples but not in GaAs, indicating this trap is likely related to the B atom(s). By using DFT calculations, charge-neutral B-rich clusters close to the conduction band minimum (CBM) with energies ranging from 0.03-0.13eV were observed, aligning with the energy range of the B-related defects identified in DLTS. Similarly, defects originating from Bi clusters close to the valence band maximum were observed in III-V-Bi alloys.7 DFT calculated the formation energy for points defects and defect complexes to confirm the identity of possible defects. The accurate calculation of formation energies requires proper relaxation of charge defects, potential alignment, and image charge correction due to the finite supercell size. Initial calculations of point defects in BGaAs demonstrated good agreement with existing reports. Further calculations of possible defect complexes are in progress, aiming to provide a comprehensive identification of all of the defects observed in DLTS measurements. Detailed findings will be presented at the upcoming conference.
This work was supported by the National Science Foundation (Award Nos. ECCS-1933836, DMR-1508646, and CBET-1438608). The authors also acknowledge the Learning, Exploration, Analysis, and Processing (LEAP) cluster at Texas State University for computing resources.
1 Hart and Zunger. Phys. Rev. B. (2000); 2 McNicholas et al. Cryst. Growth. Des. (2021); 3 El-Jaroudi et al. Appl. Phys. Lett. (2020); 4 El-Jaroudi et al. Cryst. Growth. Des. (2022); 5 Meng et al. 65th Electronic Materials Conference (2023); 6 Buyanova et al. Appl. Phys. Lett. (2000); 7 Gelczuk et al. J. Phys. D: Appl. Phys. (2016).

11:00 AM

Influences of Carbon Tetrabromide (CBr4) and Tin Fluxes on GeCSn Growth

Dr. Tuhin Dey[1], Mr. Augustus Arbogast[1], Mr. Joshua Cooper[2], Dr. Thales Borrely[2], Ms. Qian Meng[3], Mr. MOHAMMED REAZ RAHMAN MUNNA[1], Mr. Khorshed Alam[1], Prof. Rachel Goldman[2], Prof. Seth Bank[4], Prof. Mark Wistey[1]
[1]Texas State University, [2]University of Michigan, [3]Microelectronics Research Center and ECE Dept., The University of Texas at Austin, [4]University of Texas at Austin

Silicon photonics would greatly benefit from a direct bandgap Group IV semiconductor that could be monolithically integrated directly within CMOS chips and operate at high processor temperatures with high reliability. Electrically pumped lasers using Ge1-xSnx or tensile strained Ge on Si have been demonstrated, but these required very high thresholds even with optical pumping or cryogenic temperatures.1,2 Adding a small fraction of C to Ge as Ge1-yCy (GeC, where y ~ 0.01) provides an alternative approach to achieve a direct bandgap with strong confinement in real space (quantum wells) due to band anti-crossing,3,4,5 as well as strong optical transitions. Our group previously demonstrated high-quality growth of GeC using custom-made6 and commercial carbon precursors with evidence of photoluminescence (PL) around 0.61 eV.7 Incorporating Sn into GeC as Ge1-x-yCySnx (GeCSn) offers additional controls in growth, mitigating local strain distortion in Ge, further increasing substitutional carbon incorporation.8 Recently, we demonstrated successful growth of high-quality GeCSn films utilizing commercially available CBr4 as the carbon precursor.9 The grown films exhibited excellent

crystalline properties and atomically flat surfaces devoid of any discernible tin droplets, secondary phases of beta-tin, or carbon-related defects such as sp3/sp2 or C=C bonds. However, subsequent Rutherford backscattering spectroscopy (RBS) measurements showed an 83% (13x) reduction of tin (Sn) content compared with equivalent carbon-free Ge1-xSnx samples. This reduction was unexpected because the dominant mechanism for loss of Sn is surface segregation as tin droplets, but no tin droplets were observed in atomic force microscopy (AFM) or scanning electron microscopy (SEM), nor was bulk Sn phase segregation detectable in x-ray diffraction (XRD). The evaporation of Sn from the surface seemed unlikely due to the low growth temperatures, <200 ºC.
This work found three distinct trends with Sn and CBr4 flux. First, the composition of carbon increased with increasing Sn flux, which shows of Sn and C have a cooperative role in growth. This is consistent with ab-initio VASP calculations showing a stable Sn-C bond when both are substituted into the Ge host lattice. Second, in contrast, increasing the CBr4 flux led to a decrease in Sn composition, i.e., a reduced sticking coefficient, which negated earlier assumptions that Sn composition can be determined from carbon-free GeSn growths at the same Sn flux. At CBr4/Sn ratios greater than 100, the measured concentration of Sn in the alloy reached a minimum of 0.1% (absolute), which is close to the thermodynamic solubility limit. Finally, the concentration of carbon reaches a plateau when the CBr4/Sn ratio is >50, suggesting an upper limit in %C, although this might possibly be extended by increased Sn flux.
These results suggest that Sn and C help reduce each other's local strains when substituted into Ge, so an increase in either helps increase the other. In contrast, the bromine in CBr4 scavenges Sn from the growth surface as volatile SnBrx, and this scavenging effect is stronger than the trend toward increasing Sn substitutional incorporation. Even so, the remaining Sn is still sufficient to increase the substitutional incorporation of C in GeCSn. Together, these suggest GeCSn may be more stable and easier to grow than either GeC or GeSn, provided the loss of Sn is taken into account.
This work was supported by the National Science Foundation (awards ECCS-1933836 and DMR-2122041 (PREM)) and AFOSR (FA9550-23-1-0458). The authors also acknowledge the Learning, Exploration, Analysis, and Processing (LEAP) cluster at Texas State University for computing resources.

11:15 AM
Observation of Low Resistance Al and Ni p-type Ohmic Contacts to Dilute GeC and GeCSn Alloys (Student)
Mr. JIBESH KANTI SAHA[1], Mr. Saif A. A. Taqy[1], Mr. Pallab K. Sarkar[1], Mr. Imteaz Rahaman[1], Mr. Augustus W. Arbogast[1], Dr. Tuhin Dey[1], Mr. Khorshed Alam[1], Mr. MOHAMMED REAZ RAHMAN MUNNA[1], Dr. Andrei Dolocan[2], Prof. Seth Bank[2], Prof. Mark
[1]Texas State University, [2]University of Texas at Austin

Germanium alloys are attractive for active photonics and high-speed transistors on silicon due to their direct bandgap and high electron and hole mobilities and their compatibility with silicon fabrication [1, 2]. The development of low resistance ohmic contacts to Ge alloys would aid development of faster and denser electronic-photonic integrated circuits (EPICs) [3] and it could also potentially lead to mid-IR photodetectors and heterojunction bipolar transistors (HBTs) and BiCMOS operating near THz speeds [4]. Ohmic metal contacts to p-doped Ge can be readily made, and with sufficiently high doping, contact resistances (Rc) are almost independent of the metal work function [5]. This work studied whether reducing the Schottky hole barrier to Ge by adding C to Ge or GeSn could reduce the contact resistance, analogous with low resistance InGaAs contacts reducing the barriers to wider bandgap GaAs or InP [6]. In this work, Ni and Al contacts were fabricated on p doped GeC grown using CBr4 as a source of monatomic carbon, along with GeCSn and Ge films and studied the two types of comparison: (a) Contacts to thick Ge with and without a thin GeC contact layer, and (b) Contacts to thick GeCSn compared with thick Ge separately for both Al and Ni contacts at several different annealing temperatures. Films were grown in an Intevac Mod Gen II MBE with a base pressure of 1×10-9 Torr. After growth, transmission line method (TLM) structures were patterned by photolithography and liftoff. TLM was used to determine the resistance of the ohmic contacts, including the contact resistance (Rc). For TLM measurements, Ni and Al contacts were evaporated onto Ga-doped (p type) Ge, Ge0.989C0.011, and Ge0.982C0.012Sn0.006 films. TLM typically requires confinement of free carriers in a relatively thin surface layer to satisfy transfer length requirements, so all samples were grown on nominally undoped GaAs to provide the necessary backside barrier. A four-point probe was utilized due to the low resistance of the samples. Selected samples were rapidly thermal annealed (RTA) for 30 seconds at various temperatures.
The actual gap spacing and variation were measured by Scanning Electron Microscope. An average edge roughness of 0.32 ± 0.10 µm was found in all the contact pads. Rapid thermal annealing significantly influenced the characteristics of the samples. Ge contacts generally increased in resistance with anneal, while those on GeCSn decreased, and those on GeC decreased before increasing again. For both Ni and Al, the contact resistances to GeC improved with RTA up to 250 °C and then again deteriorated at 350 °C. When a 40 nm p-GeC contact layer was added to p-Ge, annealed contact resistivity (Rc) dropped by 87% to 9.3×10-7 Ω-cm2 for Al but increased 32% to 2.9×10-5 Ω-cm2 for Ni. Al consistently showed lower contact resistance to GeC than Ni contacts did, with Rc as low as 9.33×10-7 Ω-cm2 with a 250 °C anneal. GeCSn films displayed ohmic behavior and low resistance to both Ni and Al contacts, both before and after annealing. As GeCSn is also likely to have a smaller bandgap, contact resistance is expected to be similar to both GeSn [7] and the GeC presented here. The specific contact resistivity decreased with increasing annealing temperature with a few exceptions. Thick films of GeCSn, with lower active doping, had contact resistivities of 4.4×10-6 Ω-cm2 for Al and 1.4×10-5 Ω-cm2 for Ni.
The addition of carbon as either GeC or GeCSn was found to reduce contact resistance relative to Ge under identical anneal conditions, including as-deposited contacts. By the above discussion we found that Al contacts were generally better than Ni, regardless of anneal, and were further improved on GeC(Sn). For Ni, on the other hand, C-containing layers had higher Rc. Annealing reduced Rc for both Ni and Al contacts to GeCSn by 4x, and 2x for Al on GeC, and 5 orders of magnitude for Ni on GeC. It is speculated that Ni-C bonds inhibit diffusion of Ni into the Ge

to form low resistance nickel germanide. For Al contacts, however, adding C as either GeC contact layers or bulk GeCSn appears to provide a significant improvement in contact resistivity compared with bulk Ge of comparable doping.

1: M. Kobayashi et al., JAP 105, 2 pp. 023702 (2009). 2: X. Sun et al., JSTQE 16,1 pp. 124-131 (2009). 3: R. Lieten et al., APL 92, 2 pp. 022106 (2008). 4: S. Ghosh et al., Physica E 115, pp.113692 (2020). 5: V. Pavan Kishore et al., APL 100, 14 pp. 142107 (2012). 6. U. Singisetti APL 93, 18 pp. 183502 (2008). 7: K.-Y. Chen et al., EDL 37,7 pp. 827-830 (2016).

10:15 AM
Materials and Quantum Applications
Session Chairs: Michael Hamilton (Auburn University), Stephanie Law (Pennsylvania State University)
ESJ 2204

10:15 AM
Kinetics of Native Oxide Formation in NbTiN Thin Films (Student)

Mr. Sami Nazib[1], Mr. Troy Hutchins-Delgado[1], Ms. Erika Sommer[1], Mr. Mark Reymatias[1], Ms. Shruti Gharde[1], Ms. Mia Baca[1], Mr. Hosuk Lee[1], Dr. Erum Jamil[1], Dr. Gennady Smolyakov[1], Dr. Angelica Benavidez[2], Dr. Tzu-Ming Lu[3], Dr. Sergei Iv
[1]Center for High Technology Materials, University of New Mexico, Albuquerque, New Mexico, [2]Center for MicroEngineered Materials, University of New Mexico, Albuquerque, NM, [3]Sandia National Laboratories, [4]Center for Integrated Nanotechnologies, Los Alamos National Laboratory, Albuquerque, NM, [5]Center for Integrated Nanotechnologies, Sandia National Laboratories

Introduction: Thin films of NbTiN are widely used in a variety of applications because of their easy fabrication into nanostructures and good chemical stability [1]. These include superconductor-insulator-superconductor (SIS) mixers for submillimeter heterodyne spectroscopy in THz telescopes, microwave kinetic inductance detectors of millimeter and sub-millimeter waves used in astronomy, superconducting nanowire single-photon detectors (SNSPDs), and Josephson junctions for single-flux quantum logic circuits. However, what is largely ignored, is the fact that those films are usually covered by a layer of native oxide that effectively reduces the thickness of the superconductor. Since the typical thickness of deposited layers is less than 10 nm, the native oxide may represent a significant fraction of total thickness, significantly affecting the device performance. To our best knowledge, aside from our work, there has been only one study published on this subject, with layers of Nb0.5Ti0.5N deposited on MgO substrates using reactive dc magnetron sputtering [2]. In this paper, we report on our investigations of native oxide formation in NbTiN thin films deposited using physical vapor deposition (PVD) on Si samples covered with Si3N4. Comprehensive characterization included atomic force microscopy (AFM), X-ray fluorescence (XRF), X-ray diffraction (XRD), X-ray reflection (XRR), and X-ray photoelectron spectroscopy (XPS).
Sample Fabrication: The fabrication process started with depositon of a 300-nm-thick Si3N4 layer using a Trion Orion III chemical vapor deposition (CVD) system. A blanket NbTiN layer of thickness varied from 3 nm to 25 nm was then deposited using DC magnetron sputtering in a Kurt J. Lesker PVD 75 system. A 3” Nb0.67Ti0.33 target was used. The chamber had a base pressure of ~2×10-7 Torr. The deposition parameters were as follows: pressure of 6 mTorr, DC deposition power of 100 W, and Ar carrier gas with 2.2% N2.
Sample Characterization: AFM measurements were performed at each stage of sample preparation, starting with the Si substrate, then after the Si3N4 layer deposition, and finally on the NbTiN film surface. AFM measurements were performed on the patterned companion samples to determine the thickness of the deposited NbTiN thin films. As an example, Fig. 1a shows the scanned area and Fig. 1b shows the corresponding height histogram, indicating a thickness of ~10.2 nm of as-deposited NbTiN for that particular sample. XRR and XRF was used to determine the relative fraction of Nb and Ti incorporated into the fabricated thin films (Figs. 2 and 3). The measurements indicate the deposited films had the composition Nb0.8Ti0.2N. XPS experiments were designed to investigate the time-dependence of native oxide formation in air under various temperatures, from room temperature to 200 ˚C. Figs. 4 and 5 show examples of angle-resolved XPS measurements of as-fabricated sample, indicating formation of TiO2 and titanium oxinitride during the PVD deposition process. The survey scans of the NbTiN thin film performed at different sample tilts shown in Fig. 4 indicate the presence of adventitious carbon in addition to native oxide. The XPS measurements were corroborated with time-dependent XRR data summarized in Table 1. Temperature-dependent oxidation experiments provide important information regarding the conditions under which the formation of native oxide can be avoided. This is especially important for CVD deposition of top SiO2 cladding directly over the SNSPDs.
Conclusions: Comprehensive characterization of NbTiN nanometer-scale films provides important insight into the process of native oxide formation. Temperature-dependent oxidation experiments provide important information regarding the conditions under which the formation of native oxide can be avoided.
Acknowledgments: The authors acknowledge financial support from the National Science Foundation under the grant OIA-2217786 “RII Track-2 FEC: Laying the Foundation for Scalable Quantum Photonic Technologies”. This work was performed, in part, at the Center for Integrated Nanotechnologies, an Office of Science User Facility operated for the U.S. Department of Energy (DOE) Office of Science by Los Alamos National Laboratory (Contract DE-AC52-06NA25396) and Sandia National Laboratories (Contract DE-NA-0003525), under the User Project #2019BU0169.
References: [1] I. Esmaeil Zadeh et al., Appl. Phys. Lett. 118, 190502, 2021. [2] L. Zhang et al., Physica C 645, 1-4, 2018.

10:30 AM
Synthesis and characterization of SmB6 thin films by chemical vapor deposition (Student)
Mr. Brendan Jordan[1], Mr. Michael Pedowitz[1], Mr. Jihun Park[1], Prof. Ichiro Takeuchi[1], Prof. Johnpierre Paglione[1], Prof. Kevin Daniels[1]
[1]University of Maryland, College Park

This work focuses on the scalable synthesis of SmB6- by chemical vapor deposition (CVD) using samarium chloride (SmCl3) and boron/boron oxide (B, B2O3) powders. SmB6 is grown at 1075°C on standard p-type [100] silicon, functionalized with nickel to catalyze the growth. The resulting films consist of rough cube-like structures with an average grain size of ~1.3 um. Samples were mechanically polished, revealing plateaus of 2-6 microns in size, which will be used to fabricate hall bars and spin valves to investigate the electrical and magnetic properties of the material. Polished samples were Ar milled at an accelerating voltage of 5keV for 35 minutes in XPS revealing conduction states according to valence band edge. Polished SmB6 films are compared to uniform sputtered SmB6 films by Raman, SEM, and XPS showing good agreement with previous thin films although currently lacking in uniformity.

10:45 AM
Electrical Transport Study of GeSn Films
Dr. Priyanka Petluru[1], Mr. Shang Liu[2], Dr. John Cain[1], Dr. Perry Grant[3], Prof. Jifeng Liu[2], Dr. Tzu-Ming Lu[1]
[1]Sandia National Laboratories, [2]Dartmouth College, [3]Air Force Research Laboratory

Group IV alloy GeSn has shown great potential as a material for electronic devices, with the incorporation of Sn in polycrystalline Ge previously having been utilized to increase the carrier mobility values [1]. Additionally, with a Sn composition of greater than 8%, GeSn has been classified as a direct bandgap semiconductor, opening the door to optoelectronic applications [2, 3]. In this work, we present a series of thin film GeSn transistors, with a Sn composition of 11%.
As part of this study, a set of GeSn (11% Sn) thin (30 nm) films was prepared by evaporating Ge and Sn on silicon and fused silica substrates through physical vapor deposition, followed by an anneal at 500 °C for crystallization. The material properties of the polycrystalline films were then analyzed with Raman spectroscopy measurements. The films grown on silicon and fused silica showed a shift in the expected position of the Ge-Ge peak normally seen at around 300.7 cm-1 [4] to 293 and 292.2 cm-1, respectively, indicating the presence of Sn in both. Following this, the films were fabricated into transistors.
Results from electrical measurements of the transistors showed that the films on both silicon and fused silica substrates froze out, at approximately 30 K and 70 K, respectively. Additionally, the drain current of both transistors was able to be modulated as a function of gate voltage, and the transistor on fused silica showed bipolar operation. The field-effect mobility values were then extracted for both transistors for a range of temperatures and drain-source voltages [5]. The mobility increases overall as a function of temperature in both transistors, which has been seen previously in polycrystalline materials such as silicon [6]. Field-effect mobility values at room temperature for the transistors on silicon and fused silica are on the order of 0.1 cm2/Vs and 1 cm2/Vs, respectively.
As these GeSn films have a Sn composition of 11%, they show further promise for optoelectronic applications. Future work will involve attempting photocurrent measurements on the transistor on fused silica, as photoluminescence has been observed from the GeSn film grown on this substrate. Since these GeSn films were not grown epitaxially, these results demonstrate their potential to be grown on substrates other than silicon.
This work was supported as part of the μ-ATOMS, an Energy Frontier Research Center funded by the U.S. Department of Energy, Office of Science, Basic Energy Sciences under award DE-SC0023412. This work was performed, in part, at the Center for Integrated Nanotechnologies, an Office of Science User Facility operated for the U.S. Department of Energy (DOE) Office of Science. Sandia National Laboratories is a multimission laboratory managed and operated by National Technology and Engineering Solutions of Sandia, LLC., a wholly owned subsidiary of Honeywell International, Inc., for the U.S. Department of Energy's National Nuclear Security Administration under contract DE-NA-0003525. The views expressed in the article do not necessarily represent the views of the U.S. DOE or the United States Government.
[1] K. Moto et al., "Improving Carrier Mobility of Polycrystalline Ge by Sn Doping," Sci. Reports, 8, 14832 (2018).
[2] B. Cao et al., "Short-Range Order in GeSn Alloy," ACS Appl. Mat. & Interfaces, 12, 57245 – 57253 (2020).
[3] S.A. Ghetmiri et al., "Direct-Bandgap GeSn Grown on Silicon with 2230 nm Photoluminescence," Appl. Phys. Lett., 105, 151109 (2014).
[4] J.H. Parker et al., "Raman Scattering by Silicon and Germanium," Phys. Rev., 155, 712 – 714 (1967).
[5] Y. Zhou et al., "Accurate Field-Effect Mobility and Threshold Voltage Estimation for Thin-Film Transistors with Gate-Voltage-Dependent Mobility in Linear Region," Adv. Elect. Mat., 9, 2200786 (2023).
[6] J.Y.W. Seto, "The Electrical Properties of Polycrystalline Silicon Films," J. Appl. Phys., 46, 5247 – 5254 (1975).

11:00 AM
Understanding the degradation of thin GaSe (Student)
Ms. Lottie Murray[1], Dr. Matthew Doty[1]
[1]University of Delaware

Photonic quantum technologies such as quantum key distribution for secure communication require controlled sources of single photons. Gallium selenide (Ga2Se2) is of interest for such applications because its 2D nature should allow it to be incorporated into a wide range of solid-state photonic devices, its transition to a direct bandgap as a function of increasing film thickness makes it less sensitive to the number of monolayers transferred onto a device, and its decrease in bandgap as a result of strain provides a mechanism to create localized emission of single photons. However, the optical signal from thin Ga2Se2 films degrades quickly. To understand this degradation, we stored exfoliated flakes of Ga2Se2 under twelve different conditions, varying air, temperature, and light exposure. We performed photoluminescence (PL) and Raman measurements at regular intervals to measure how each storage condition affected the overall optical and structural properties. We find

that degradation of the optical signal occurs under all conditions, with the majority of the degradation occurring in the first 8 hours. Differences in the degradation rate between storage conditions provide insight into the degradation mechanisms.

11:15 AM
Advancements in Time -Resolved Microwave Conductivity through Non-Resonant Coplanar Transmission Line and Interferometric Detection
Dr. Jasleen Kaur Bindra[1], Dr. Pragya Shrestha[2], Dr. Sebastian Engmann[2], Dr. Chad Cruz[2], Dr. David Gundlach[2], Dr. Jason Campbell[2]
[1]Advanced Photon Source, Argonne National Laboratory, [2]National Institute of Standards and Technology

Time-resolved microwave conductivity (TRMC) is a contactless technique used to study carrier density, transport properties, trapping phenomena, and recombination parameters in charge transport materials. Traditional cavity based TRMC methods have limitations in accuracy and frequency range and require large sample volumes. To overcome these challenges, we propose a novel approach that integrates a non-resonant coplanar transmission line and microwave interferometric detection (Fig.1). This method enhances sensitivity and eliminates the need for resonant cavities, enabling direct broadband measurement of phase-dependent changes in film conductivity (Δσ) to obtain both real (Δσ′) and imaginary (Δσ″) components of complex photoconductivity. We also demonstrate unique in operando calibration techniques by combining TRMC with transient photoconductivity (TPC) and electron spin resonance (ESR). As demonstrated by experiments on thin films of organic semiconductors P3HT: PCBM and diF TES ADT, and perovskite material MA0.85FA0.15PbI3, this integrated technique offers valuable insights into material behavior, with implications for the design and optimization of optoelectronic devices. We observe both pure electrical and mixed electrical-ionic conductivity upon optical excitation.
The microwave conductivity setup (Fig.2) utilized in this study employs a coplanar transmission line with a characteristic impedance of 50Ω (Fig.3). Thin films of the sample on glass substrates are used to couple microwave electric and magnetic fields into photosensitive thin films. TRMC measurements rely on electric field coupling to detect photoconductivity changes. Operating in transmission mode within an X-band frequency range (8−12GHz), the microwave interferometer, configured in a Mach-Zehnder setup, nulls the output when no transient photoconductivity impedance change is detected. A trombone-line microwave phase shifter in the local oscillator arm provides experimental phase control to select in-phase and out-of-phase components of Δσ. Demodulated signals are then amplified and recorded by a high-resolution oscilloscope, with sample illumination achieved using a 5ns pulsed Nd: YAG laser's second harmonic (532 nm) at a 10 Hz repetition rate and synchronized with data acquisition using an external photodiode trigger. By studying the P3HT: PCBM and MA0.85FA0.15PbI3 (Fig.4) thin films as examples, we have demonstrated that this TRMC approach can not only extract complex conductivity but also experimentally resolve the complex photoconductivity. The use of in operando ESR (Fig.5) further allows confirmation of the assignment of TRMC transients to the real or imaginary components (Fig.6). TPC (Fig.7) was used for calibration (Fig.8) to obtain the absolute conductivity of the samples (Fig.9). P3HT: PCBM films show changes in conductivity consistent with previous results of photocurrent generation. In MAFA, changes in complex conductivity related to photo-induced ionic motion, previously observed A-site cation motions, can be observed. Hence, this approach has the potential to extend the utility of TRMC measurements in organic/ionic semiconducting materials.
This work presents an innovative time-resolved microwave conductivity technique, calibrated to probe complex microwave conductivity. Leveraging a non-resonant coplanar transmission line and microwave interferometric detection, this method surpasses traditional cavity based TRMC approaches in several key aspects: (1) Sensitivity is no longer contingent on cavity loading but on broadband interferometer tuning. (2) It enables precise measurement of subtle sample photoconductivity changes post-optical excitation and facilitates exploration of extremely small sample sizes. (3) The reduced probed volume allows direct comparison with working devices, minimizing film-to-film variation effects. (4) Incorporating a phase-sensitive microwave bridge enables concurrent use of ESR and TPC measurements for absolute photoconductivity changes. (5) By concurrently measuring nearby spin standard samples with ESR, phase-dependent photoconductivity and constituent Δσ′ and Δσ components can be deduced without complex frequency dispersion analysis. This innovative approach heralds a new era in microwave conductivity investigations, offering unprecedented sensitivity and versatility.
[1] J.K. Bindra et al., 2024, Mater Today Adv, 21, 100471. [3] P.R. Shrestha et al., 2019, Anal. Chem., 91, 11108. [2] J.K. Bindra et al., 2023, J. Phys. Chem. C, 127, 4203. [4] J.P. Campbell et al., 2013, Anal. Chem., 87, 4910.

10:15 AM
Doping and Impurities
Session Chairs: Minjoo Lee (University of Illinois Urbana-Champaign), Rachel Goldman (University of Michigan)
ESJ 1224

10:15 AM
Precise Spatial Photodoping of Lateral Graphene p-n Interfaces
Dr. Son Le[1], Dr. Thuc Mai[2], Dr. Maria Munoz[2], Dr. Angela Highwalker[2], Dr. Curt Richter[2], Dr. Aubrey Hanbicki[1], Dr. Adam Friedman[1]
[1]Laboratory for Physical Sciences, [2]National Institute of Standards and Technology

Reliable and accurate spatial doping of 2-dimensional (2D) materials is important for the potential applications of this novel class of materials. Here, we present our work on spatial photo-doping of an h-BN/Graphene/h-BN heterostructure. By optically activating and deactivating the natural defect states in bulk h-BN, which act as remote doping centers for graphene, we change both the carrier

density and carrier type in graphene accurately and reversibly by several orders of magnitude. By controlling the position of a spatially resolved light source to only activate photo-dopants in selected areas of the sample, lateral doping modulation was achieved and a PNP junction (PNPJ) device was created. In-situ quantum Hall measurements were used to demonstrate the effectiveness of this doping technique and characterize the electrostatic profile of the PNPJ. This doping technique opens many possibilities to engineer novel device concepts and expand the applications of 2D heterostructures.

10:30 AM
Analysis of Lattice Damage in Post-Annealed 4H-SiC Epiwafers Implanted with High Energy Al Ions at Elevated Temperatures (Student)
Mr. Zeyu Chen[1], Ms. Qianyu Cheng[1], Ms. Shanshan Hu[1], Dr. Balaji Raghothamachar[1], Dr. Reza Ghandi[2], Ms. Stacey Kennerly[2], Mr. Charles Carlson[3], Mr. Dannie Steski[3], Prof. Michael Dudley[1]
[1]Stony Brook University, [2]GE Research, [3]Brookhaven National Laboratory

Silicon Carbide (SiC) is a semiconductor with a wide bandgap that has significant promise for power devices. Its characteristics, including wide bandgap, high breakdown voltage, and thermal stability, enable SiC devices to operate in severe conditions such as high temperature, voltage, and high frequency [1]. High voltage devices made of 4H-SiC, capable of withstanding 1.7 to 6.5 kV, are sought for in uses like hybrid systems, shipboard and power grid systems, and high-speed trains. These devices are typically produced on 4H-SiC wafers with thick epilayers to enhance breakdown voltages [2], but achieving uniform doping in such thick epilayers is challenging. One solution is to employ multi-step high energy ion implantation system established at Brookhaven National Laboratory's Tandem Van de Graaff accelerator facility [3], which can implant ions at energies up to 150 MeV. This system has been used to demonstrate medium voltage charge balance devices, 2 kV and 3.8 kV superjunction structure PIN diodes [4-6]. However, high energy ion implantation causes significant lattice strain by displacing host atoms in the epilayer, so it is crucial to characterize the strain to understand the damage induced by high energy implantation. Further the process of implantation and subsequent activation annealing must be optimized to completely heal lattice damage.
Previously, techniques such as synchrotron X-ray plane wave topography (SXPWT) and reciprocal space mapping (RSM) have been employed to determine the strain distribution within the 12 μm epilayer of a 4H-SiC epiwafer high energy implanted with 5.56 x 1013 cm-2 Al ions at room temperature. The findings reveal that the strain level in the implanted region is approximately 2.5 x 10-4 higher than in the unimplanted region [7], as depicted in Fig.1 (a). The intensity profile extracted from the topograph is fitted using Rocking Curve Analysis by Dynamical Simulation (RADS) (Fig. 1(b)), and the corresponding strain profile within the epilayer (Fig.1 (c)) also indicates a maximum strain of about 2.4 x 10-4. Therefore, high energy implantation with Al ions at room temperature can lead to substantial tensile strain. To fully recover this strain, an annealing temperature as high as 2000 °C is necessary [8]. However, such high temperatures result in the wafers having rough surfaces, which is not ideal for device fabrication. One approach to lower annealing temperature is carrying out high energy implantation at high temperatures since the dynamic annealing effect will reduce the lattice strain to some extent in the as-implanted wafer. 4H-SiC epiwafers implanted at room temperature (RT), 300 °C and 600 °C with 5 x 1016 cm-3 have been characterized by RSM, as shown in Fig. 1(d). Strain estimated from vertical peak separation are 4.1 x 10-4, 3.3 x 10-4 and 2.0 x 10-4 for wafer implanted at RT, 300°C and 600°C, respectively. The decrease strain with increasing implantation temperature indicates dynamical annealing process has been successfully triggered. These wafers will be subject to activation annealing at standard temperatures and lattice strain will be measured and analyzed. The usefulness of high temperature implantation will be evaluated from these studies and reported in this paper.

10:45 AM
Rare-earth impurities in III-V semiconductors and their alloys (Student)
Ms. Ruiqi Hu[1], Ms. Intuon Chatratin[1], Mr. Quoc Dai Ho[1], Dr. Duy Quang To[1], Dr. Garnett W. Bryant[2], Prof. Anderson Janotti[1]
[1]University of Delaware, [2]National Institute of Standards and Technology

Rare-earth impurities in semiconductors have long been studied theoretically and experimentally, with implications for both basic and applied sciences. For example, Er-doped GaAs, known for their sharp and temperature-independent 4f-intrashell-related emission near 1.55 μm, align with the lowest attenuation wavelength of silica-based optical fibers. Early experimental results suggested that Yb substitutes on the In in InP, while Er was found to occupy interstitial sites. The location of the rare-earth impurity in the lattice of the semiconductor may well be related to how it modifies the electronic and optical properties of the host material. In this presentation, we discuss the interaction between rare-earth doping and III-V semiconductors, such as AlAs, GaAs, and InAs, and their alloys. Using first-principles calculations based on hybrid density functional theory, we explore the incorporation of La, Gd, Er, and Lu into interstitial and substitutional sites of the zinc blende lattice, considering possible charge states of the impurity other than the neutral state. The choice of rare-earth impurities covers the different occupations of the 4f shell, from completely unoccupied to half occupied to fully occupied. We analyze the stability of the rare-earth impurity configuration not only through their formation energy but also through their migration barriers. Our calculations provide valuable insights into the behavior and properties of rare-earth elements as dopants in semiconductors, contributing to a better understanding of their potential to enhance the performance of III-V semiconductor devices.

11:00 AM
Vacancies and hydrogen-related defects in KTaO3 (Student)
Ms. Intuon Chatratin[1], Prof. Anderson Janotti[1]
[1]University of Delaware

Hydrogen plays an important role in semiconductor materials, particularly in most transparent conducting oxides, where it resides at interstitial sites and substitutional oxygen sites, acting as shallow donors and leading to n-type

conductivity. When forming complexes with cation vacancies, it passivates acceptor states, also enhancing n-type conductivity. Moreover, recent experiments reveal that hydrogen plays a role in the observed persistent photoconductivity (PPC) in KTaO3 at room temperature, which lasts for a very long time. In this study, we employ first-principles calculations based on hybrid density functional theory to investigate the electronic properties and stability of vacancies, hydrogen-related defects, and their interactions in KTaO3. Our results offer insights into the atomistic mechanism behind the observed PPC in KTaO3, identifying the hydrogen-related states associated with photo absorption that leads to PPC. To aid the experimental identification of the different hydrogen impurity configurations, we calculate the frequencies of local vibration modes. These findings contribute to a comprehensive understanding of the impact of hydrogen on electronic properties and persistent photoconductivity in KTaO3 and other related oxides.

11:15 AM
“No electron freezing out” in Si-doped β-Ga2O3 (010) down to 2 K
Mr. Vishal Khandelwal[1], Dr. Francesco Blanda[2], Mr. Manoj Rajbhar[2], Dr. Yi Lu[1], Dr. Xiao Tang[1], Prof. Xiaohang Li[1]
[1]King Abdullah University of Science and Technology, [2]Advanced Semiconductor Laboratory, Electrical and Computer Engineering program, CEMSE Division, King Abdullah University of Science and Technology, Thuwal 23955-6900, Saudi Arabia.

The ultrawide bandgap of β-Ga2O3 contributes to its significantly enhanced performance at high temperatures, thanks to an extremely low intrinsic carrier concentration. Further, a high-quality homoepitaxial growth with a wide range of n-type doping (1015-1020 cm-3) enables β-Ga2O3 devices to function at elevated voltages (up to 8 KV) and temperatures reaching 500°C. This makes Ga2O3 electronics applicable to power plants, gas turbines, coal mines, and aerospace systems. Additionally, the functionality of Ga2O3 devices at low temperatures can offer notable advantages, particularly in deep space missions, where its exceptional radiation hardness becomes important[1]. Therefore, it is crucial to explore the electronic properties of Ga2O3 at cryogenic temperatures up to outer space temperature (~ 2 K).
This work demonstrates the “No electron freezing out” phenomena in highly (> 1019 cm-3) and moderately (~ 1018 cm-3) doped β-Ga2O3 (010) up to 2 K. Both films show nearly temperature-independent electron concentration. The highly doped films are heavily degenerate, as confirmed by temperature-dependent Hall-effect measurements and transfer length measurement (TLM). The electron conduction in moderate-doped films is ascribed to the presence of impurity bands (IB) and variable range hopping (VRH) as described by the impurity band model and Mott’s equation. Both highly and moderately doped films show excellent crystalline quality with smooth surface morphology, as depicted in Figure 1. Electron concentration (nele.) and mobility (μ) of both films are shown in Figure 2(a) and (b). Highly doped films have nele. of ~ 2.6×1019 cm-3 at 300 K, nearly independent of temperature, whereas μ increases from 37 to 50 cm2/Vs from 300 to 2 K. These highly doped films can provide a low contact resistance, which is calculated from TLM measurement. Figure 3(a) and (b) show IV characteristics of the TLM device, depicting an ideal ohmic behavior at both 4 and 300 K. Figure 3(c) shows IV characteristics at different temperatures with TLM spacing of 50 um. The current increase with lowering the temperature is consistent with the increase in mobility as shown in Figure 2(a). Further, the contact resistivity and sheet resistance were calculated, showing a stable contact regardless of temperature.
For the moderately doped film, the nele. of ~ 2×1018 cm-3 at 300 K is nearly temperature independent whereas μ is reduced with low temperature, as shown in Figure 2(b). To understand this, the longitudinal (Rxx) and Hall (Rxy) magnetoresistance were measured in the presence of a high-magnetic field (-8≤H≤8 T). The Rxx and Hall magnetoconductance (Gxy) from 10 to 200 K is shown in Figure 4. The Rxx shows high negative magnetoresistance till 180 K, which can be a signature of the presence of impurity bands[2]. Further, an impurity band model was used to fit the Gxy following equation (1). More information can be found elsewhere[3].
This further leads to the calculation of resistivity(ρ) and Hall-coefficient (RH), shown in the RED symbol in Figure 5(a) and 5 (b). These values match exactly with the Hall-effect measurement which again confirms the presence of the impurity band. The value of RH increases till 140 K and then again decreases for T<140 K denotes the dominance of impurity band conduction at T<140K, shown in Figure 5(b). Consequently, three distinct regions for electron conduction are defined at different temperatures in Figure 5(c). The Hall-resistivity of the film follows Mott’s equation[4] for T < 180 K as shown in Figure 5(d) which shows that the variable range hopping (VRH) is the possible mechanism for electron transport in the impurity band.
This work demonstrates the potential of β-Ga2O3 (010) in low-temperature regimes which can help to design and fabricate novel Ga2O3 devices for low-temperature operation.
[1].S.J. Pearton et al., J. Appl. Phys. 124, 220901 (2018). [2] Joel et al., Phys. Status Solidi C 6, 5, 1158(2009). [3]N. Bansal et al., Phys. Rev. Lett. 109, 116804 (2012). [4]. Z. Kabilova et al., Semicond. Sci. Technol. 34 (2019).
Note: Equation 1 can not inserted here, which can be found in Abstract copy in PDF form.

10:15 AM
Wearable Electronics and Biosensors
Session Chairs: Jae-Hyun Ryou (University of Houston), Shayla Sawyer (Rensselaer Polytechnic Institute)
ESJ 1202

10:15 AM
Optical Characterization of Coal Particulate on PETG Filters Between 375nm and 1500nm Light (Student)
Mr. Nicholas Morrissey[1], Mr. Junbo Wang[2], Mr. Ryan Courtney[2], Mr. Connor Krause[2], Mr. JP Angulo[2], Dr. Candace Su-Jung Tsai[2], Dr. David Janes[3]

[1]School of Electrical and Computer Engineering and Birck Nanotechnology Center, Purdue University, West Lafayette, Indiana, [2]Department of Environmental Health Sciences, University of California Los Angeles, Los Angeles, California, [3]School of Electrical and CoSchool of Electrical and Computer Engineering and Birck Nanotechnology Center, Purdue University, West Lafayette, Indiana

While there has been advancements of the detection and monitoring of dust in a mining environment, there is still work to be done for the characterization of airborne particulate matter for an individual worker. Currently, coal mines have monitoring equipment stationed in tunnels to monitor general particulate levels and personal samplers to track exposure for individual employees on a per shift basis. There have been a possible improvement in the individual samplers with an effective particulate matter sensor made from a comb capacitor and micro-heater fabricated on polyimide film [1]. Still, while it can track the loading of a filter in an individual sampler, more can be done to distinguish between different types of dust with different exposure limits. To account for this, there needs to be another property of sampled particulate matter that can be measured to distinguish between different types such as coal dust or silica dust.
In this work, we perform a study into the optical reflectance of coal dust at different loadings on a personal sampler for a coal miner. Using the capacitive sensor, the optical measurements could be normalized and the trend from three wavelengths of light can be used to distinguish a dark material like coal from other materials like silica. With both systems, the personal sampler could provide a user more advanced warning for particulate matter exposure before reaching the legal limit during a shift. The optical measurements are made on both overloaded and calibrated mass samples on 37 mm PETG filters to characterize based on the reflective optical properties of the dust at different levels of deposition over a wavelength range between 375 nm and 1500 nm. Characteristics of coal included a low reflectance from the UV to visible spectrum, but increase in reflectance at longer wavelengths of visible and near inferred light. Using three wavelengths that characterize a coal sample, this optical characteristic can be integrated into a portable sampler. Based on these wavelengths, we encounter a linear relationship between change in reflectance and mass with order of increasing reflectivity being 405, 770, and 1450nm. This observation holds until the collected mass is below 0.1 mg. At that point, variation in the filters, housing and the mass measurements obscure any trend. With could lead to further studies of materials that could be characterized that would impact miners on the job and be tested on a physical prototype for testing.

10:30 AM
Experimental ISFET Surface Modification Validation for Streptavidin-Biotin Binding (Student)
Mr. Utku Noyan[1], Prof. Pamela Abshire[1], Prof. Sahil Shah[1]
[1]University of Maryland, College Park

Introduction
Ion-Sensitive Field Effect Transistors (ISFETs), key in biosensing, enable precise analyte measurement crucial for drug development, medical diagnostics, and environmental monitoring applications. These devices, integrated into CMOS processes, offer significant cost, size, and performance advantages relative to traditional labor-intensive assay techniques.
An integral component determining the efficiency of an ISFET is its pH-sensing layer, typically composed of materials like silicon dioxide (SiO2) or silicon nitride(Si3N4) coupled with an ion-selective substance. ISFETs can enable low-power, high-sensitivity, and label-free detection of antigens. Tailoring ISFET sensitivity and its structure for detecting specific antigens can allow optimal operation of the biosensors. In this study, we develop surface functionalization procedures for commercial ISFET devices (Winsense Co., Ltd. [1]) and report the I-V characteristics of the devices after various stages of functionalization.
Experimental Validation
The commercial ISFETs[1] have specifications of 2000 µm width, 100 µm length, and a 30nm thick Si3N4 sensing layer. The protocol to successfully bind Streptavidin-biotin conjugate onto the Si3N4 surface includes the following steps: hydroxylation (1), silanization (2), crosslinking (3), biotinylation (4), and streptavidin application. RCA Cleaning and the Oxygen Plasma Transfer produce hydroxylation of the silicon surface[2]. RCA Cleaning removes organic residues from the silicon wafer by oxidizing the silicon and leaving thin oxide on the surface. Then, to improve the surface's reactivity and remove any remaining organic contaminants, the samples were treated in an oxygen plasma for 5 min. Oxygen plasma treatment also grows a thin oxide that facilitates the creation of surface silanol groups. In the silanization stage, the hydroxylated silicon surface was immersed in APTES solution (2% APTES in 95% ethanol) for 1 h at 68 °C, then rinsed thoroughly with DI water and dried with nitrogen gas. The 3-aminopropyltriethoxysilane (APTES) is a standard method for biomolecule immobilization on silicon and silicon derivatives such as Si3N4[3]. Followed by 2.5% glutaraldehyde (GA) treatment that is used as a bi-functional crosslinking agent to the biotin by its aldehyde group[4], biotinylation is performed by soaking the wafer in 500nM biotin solution for 1 h. After each immobilization, the wafer was cleaned with 0.05% Tween-20 in PBS. In the final step, 20µg/ml Alexa Fluor 488 streptavidin was applied onto the wafer for 1 h and then washed with 0.05% Tween-20 in PBS. Alexa fluor 488 enables us to validate the recipe by fluorescence microscopy. We also analyzed threshold voltage variance between each stage using SMU and setting Vds=30mV, sweeping VG from 0.5V to 1V.
Conclusion
This study supports the experimental evidence of successful surface modification for Streptavidin-Biotin conjugation onto the Si3N4 surface with fluorescence microscopy and electrical readout. It offers potential extensions to other analyte detection scenarios and device architectures.
References:
1] L. Winsense Co., “Winsense ISFET.” [Online]. Available: http://www.winsense.co.th/item/item2.html
[2] W. Kern, “Overview and evolution of silicon wafer cleaning,” in Handbook of Silicon Wafer Cleaning Technology, 2nd ed., K. Reinhardt and W. Kern, Eds. Norwich, NY: William Andrew Publishing, Oct. 2007, ch. 1.
[3] P. Saengdee, C. Promptmas, S. Thanapitak, A. Srisuwan, A. Pankiew, N. Thornyanadacha, W. Chaisriratanakul, E. Chaowicharat, and W. Jeamsaksiri, “Optimization of 3-aminopropyltriethoxysilane functionalization on silicon nitride surface for biomolecule

immobilization," Talanta, vol. 207, p. 120305, 2020. [Online]. Available: https://www.sciencedirect.com/science/article/pii/S0039914019309385
[4] M. E. Marques, A. A. Mansur, and H. S. Mansur, "Chemical functionalization of surfaces for building three-dimensional engineered biosensors," Applied Surface Science, vol. 275, pp. 347–360, 2013, nANOSMAT 2012. [Online]. Available: https://www.sciencedirect.com/science/article/pii/S0169433212022507
[5] S. Udomsom, U. Mankong, P. Paengnakorn, and N. Theera-Umpon, "Novel rapid protein coating technique for silicon photonic biosensor to improve surface morphology and increase bioreceptor density," Coatings, vol. 11, no. 5, 2021. [Online]. Available: https://www.mdpi.com/2079-6412/11/5/595

10:45 AM

Paper-based Biosensors for the Detection of Creatinine Levels in Kidney Disease (Student)

Dr. CHIEN-HSUAN KO[1], Prof. Lung-Ming Fu[2], Prof. Soaram Kim[1]
[1]Department of Electrical and Computer Engineering, Texas A&M University, College Station, TX 77843, USA, [2]Department of Engineering Science, National Cheng Kung University, Tainan 701, Taiwan

Chronic kidney disease (CKD) has emerged as a substantial health concern in numerous nations. The World Health Organization projected that kidney illnesses rose from 13th to 10th in global mortality in 2020[1]. Kidney disease mortality jumped from 810,000 in 2000 to 1.3 million in 2019[2]. Early kidney disease symptoms are difficult to identify because the kidneys lack pain-sensitive nerves. Failure to intervene at the right time often results in permanent kidney damage. Biomarkers including creatinine, albumin, and glucose must be detected early to diagnose and treat renal diseases. Waste filtration and homeostasis regulation depend on the kidneys. Dialysis or transplantation may be needed for end-stage renal illness due to their incapacity. Creatinine, a muscle breakdown byproduct, is often used to monitor renal function. Kidneys filter blood creatinine, maintaining levels. Creatinine increases suggest renal dysfunction, usually chronic kidney disease. Regular creatinine testing can detect disorders early, allowing for timely treatment and slowing development[3].
UV-Vis Spectroscopy, High-Performance Liquid Chromatograph, Microfluidic Chip, Chronoamperometr, and Non-Enzymatic Electrochemical Sensor are used to determine Most of these procedures need expensive, skilled tools that are not disposable or portable. A disposable, portable gadget and simple approaches are needed in places with limited tools and abilities. Microfluidic Paper-based Analytical Devices (μPADs) can meet these needs. Micro paper-based analytical devices (μPAD) are a compact analytical device that incorporates all the necessary components for analytical detection, including immobilized reagents, sample conveyance, and detection systems, all integrated into a paper substrate. Filter paper or paper chromatography primarily consists of cellulose and is required as an immobilization medium. A cost-effective, portable, and disposable colorimetric approach is developed for the simultaneous determination of serum creatinine (CRE) using the Jaffe reaction. The Jaffe reaction involves the interaction of CRE with picric ions under alkaline circumstances, resulting in the formation of an orange complex. The concentration of CRE in the sample is directly related to the color intensity observed. The determination is achieved by the utilization of a system consisting of a detecting chip constructed from PET and paper substrates, and also an elaborate analysis apparatus that consists of a hot plate and a smartphone equipped with self-developed software for analyzing color intensity. The analytical apparatus can be utilized to assess renal function and aid in preventing renal failure.
This study has created a microfluidic paper-based detection device for measuring the concentration of creatinine in samples using the Jaffe Reaction. The optimization findings revealed that the reaction could be completed in the least time of 3 minutes, and the most favorable concentration for the reaction was determined to be 0.4M NaOH. The Creatinine content is determined using a colorimetric approach conducted by a custom color analysis application installed on a smartphone. The new detection system's feasibility is proved by its ability to accurately identify Creatinine concentrations within the range of 0.4–80 mg/dL. The linear relationship between the overall color intensity (Y) of the reaction complex picture and the concentration of Creatinine (X) is established by the equation Y = -1.2789X + 340.4561. The coefficient of determination (R2) has a value of 0.996. In summary, the findings demonstrate that the suggested approach provides a practical, immediate, dependable, and cost-effective alternative for point-of-care chronic kidney disease (CKD) diagnosis and monitoring in clinical settings.

Keywords：Creatinine; Paper-based Biosensors; Detection; Jaffe Reaction

[1]Sundström J, Bodegard J, Bollmann A, et al The Lancet Regional Health – Europe 2022;00:100438. doi:10.1016/j.lanepe.2022.100438
[2]World Health Organization. The top 10 causes of death. Accessed January 31, 2023.
[3] Fink, J. C., Burdick, R. A., Kurth, S. J., Blahut, S. A., Armistead, N. C., Turner, M. S., ... & Light, P. D. (1999).American journal of kidney diseases, 34(4), 694-701.

11:00 AM

Development of a Modular Bioelectronic Sensing Interface Using Escherichia coli and Dissimilatory Metal Reducing Bacteria Shewanella oneidensis MR-1

Dr. Lauren Kelly[1], Dr. MD ANARUL HOQUE[1], Dr. James Dylan Rees[1], Dr. Mattheos Koffas[1], Dr. Shayla Sawyer[1]
[1]Rensselaer Polytechnic Institute

This work presents the development of the first known modular bioelectronic sensing interface using Escherichia coli and dissimilatory metal reducing bacteria Shewanella oneidensis MR-1. The primary goal of this system is to improve the availability of low-cost, highly tunable, real time nutrient sensors for aquatic ecosystems. This system triggers the production of a measurable biocurrent by S. oneidensis MR-1 in response to a chemical quorum sensing input, an acylated homoserine lactone, that is generated by E. coli when a small target molecule of interest in the environment is detected. Synthetic biology techniques are employed to engineer the bacterial strains to enhance the sensing system in several ways. For example, the gain of

the system can be adjusted and optimized by adjusting the amount of quorum sensing signal produced by E. coli. In addition, stability of the interface can be improved through genetic regulatory feedback systems that allow for modulation of the speed of the response and improvement of the switch like behavior by minimizing variability in response to fluctuations in the system and improving bistability. Finally, genetic engineering is used to make the interface modular. The desired sensing target can be changed by genetically modifying E. coli at the front end of the system, while the backend of the system that is represented by S. oneidensis MR-1 can remain unchanged as it has been genetically engineered to only generate a biocurrent in response to the homoserine lactone from E. coli.
A genetically modified Shewanella oneidensis MR-1 OR gate developed by Graham et al. is utilized to create the backend of the bioelectronic interface [1]. E. coli is modified to respond to a small target molecule and control over the gain is investigated. Electrochemical methods including cyclic voltammetry, current measurements, and electrochemical impedance spectroscopy are explored to characterize the electrical response of the system. The bacterial strains are grown in a co-culture media and subjected to a -0.2V DC bias to activate the extracellular electron transport mechanisms of S. oneidensis MR-1. Preliminary results have successfully demonstrated the production of a measurable biocurrent signal on the order of microamps by the OR gate S. oneidensis MR-1 strain in response to a 3OC10HSL homoserine lactone input, confirming functionality of the backend of the interface. The lower limit of detection by the S. oneidensis MR-1 modified strain is also explored and the magnitude of biocurrent production as a function of homoserine lactone input was successfully measured. Scanning electron microscopy will also be employed to observe the biofilm development and interaction of the bacteria in co-culture on the electrode under an applied bias.
References: [1] A. J. Graham et al., “Transcriptional Regulation of Synthetic Polymer Networks,” 2021, bioRxiv 2021.10.17.464678.

11:15 AM
Tuning the Carbon Black content to switch Piezoelectric Behavior of P(VDF-TrFE) to Piezoresistive for Integrated Wearable Sensing Applications
Mrs. lavanya muthusamy[1], Mr. Makhluk Hossain Prio[1], Mr. Balaadithya Uppalapati[1], Dr. Goutam Koley[1]
[1]Clemson

Introduction: P(VDF-TrFE) [Poly(vinylidene fluoride-Tri fluoroethylene)] is highly attractive for wearable sensing applications due to its outstanding attributes such as excellent flexibility, self-powering capability, chemical stability, and biocompatibility. However, conventional sensing methods primarily rely on the piezoelectric effect facilitated by electric poling rather than piezoresistive behavior. This study investigated the self-poled piezoelectric and piezoresistive behavior P(VDF-TrFE)/Carbon Black (CB) composite materials, by varying the CB content within the P(VDF-TrFE) to probe their suitability for wearable sensing applications. We observed that for lower CB composition, the composite polymer exhibited self-poled piezoelectric behavior, while beyond a certain threshold composition it behaved as a piezoresistor. The concept of tuning the behavior of P(VDF-TrFE) by simply adding nanofiller into the polymer offers a simple end effective way to integrate the energy harvesting and sensing performance on the same platform, opening up promising applications for self-powered wearable sensor devices.
Device fabrication and Results: The fabrication steps of piezoelectric/piezoresistive P(VDF-TrFE)/CB composite is illustrated in Fig. 1. First, 17 wt.% P(VDF-TrFE) and carbon black was stirred with Dimethylformamide (DMF) at 60°C for 12 hours, spin coated on ITO/PET substrate at 3000 rpm for 30s. The solvent was evaporated, and the composites were then thermally treated at 140°C for 2 hours, forming a piezoelectric or piezoresistive P(VDF-TrFE)/CB thin film. We observed that 0.6 wt.% is the conduction (percolation) threshold, i.e. above this percentage composition the polymer starts to behave as a piezoresistor. At 0.6 wt.% CB, we achieved the piezoelectric output voltage of 2.74 V under 6 N force with 1 Hz excitation (measured using an oscilloscope), for a self-poled 2 × 2 cm2 film, as shown in Fig. 2. This is similar to results reported earlier [1]. We further investigated how higher carbon weight percentage tunes the piezoelectric behavior by increasing the CB content from 0.6 wt.% to 0.8 wt.%. The I-V characteristics were compared for these two composite films and the results are shown in Fig. 3. As excepted, the current can be seen to be nearly negligible (below detectable range) for the 0.6 wt.% CB composite film, which can be attributed to the random and sparse distribution of carbon particles within the matrix preventing current conduction. In contrast, significant current is observed for the 0.8 wt.% composite (Fig. 3), indicating that beyond the 0.6 wt.% CB threshold, the carbon particles started to agglomerate within the P(VDF-TrFE) matrix, making the film conductive. Conductivity was found to keep on increasing with CB at 1 wt.%; the additional results will be presented in the conference.
This level of output voltage and resistance change are sufficient for detecting subtle human motions such as finger movements, touching and wrist bending. To study the piezoresistive performance of 0.8 wt.% CB composite film with 2 × 2 cm2 active area, the fabricated piezoresistive sensor was subjected to 20 g force (which is equivalent to 0.5 Kpa), measured through commercial force sensing resistor as shown in Figs. 4(a) and (b). When a compressive force or pressure applied to the piezoresistive sensor, carbon particles in the matrix come closer together, allowing conductivity through electron hopping between nearby carbon clusters. Thus, resistance decreases and current increases in the sensor as shown schematically in Figure 5 [2,3]. The initial resistance (R) of the 0.8 wt.% carbon black piezoresistive sensor (529 Ω) decreases to 360 Ω, referred to as R0, with the change remaining pretty consistent over 9 cycles of measurement shown in Fig. 6, which underlines good repeatability. The percentage change in resistance for an applied 20 g force is calculated from the formula: . This clearly demonstrates the superior piezoresistive sensing performance, capable of detecting even small change due finger movement (sensing film put on the index finger), as shown in Fig. 7. Furthermore, the film displays high hydrophobicity and moisture resistance, making it suitable for measurements even in wet environments.
Summary and Conclusion: In summary, we have demonstrated tunable piezoelectric/piezoresistive behavior of unpoled P(VDF-TrFE)/CB composite by varying CB content for the first time. We achieved an open circuit voltage of 2.47 Vpk-pk with an output power density of 0.5 μW/cm² from a 0.6 wt.% P(VDF-TrFE)/CB piezoelectric film. On the other hand, we observed a 31% change in

resistance under an applied pressure of 0.5 kPa from a 0.8 wt.% P(VDF-TrFE)/CB piezoresistive film. Overall, the tunable characteristics of these composite films, simply by changing CB percentage, can pave the way for integrated self-power and wearable sensor devices and systems.

[1] L. Muthusamy et al. polymers., vol. 15, p. 4131, (2023) [2] Y. Wang et al. ACS Nano 2022, 16, 2, 1734–1758. [3] X. Zhano et al. Polymers 2023, 15, 1386.

10:15 AM
Novel Integration and Material Processing
Session Chairs: Robert Roberts (The University of Texas at El Paso), Dan Ewing (Dept. of Energy's Kansas City National Security Camus)
ESJ 1215

10:15 AM
GaAsSb/Si heterojunction photodiodes fabricated with epitaxial layer transfer (Student)
Ms. Manisha Muduli[1], Mr. Yongkang Xia[1], Ms. Sophie Mills[1], Dr. Seunghyun Lee[1], Prof. Shamsul Arafin[1], Prof. Sanjay Krishna[1]
[1]The Ohio State University

Silicon has been widely used in optical communications for data transfer and light detection beyond 1100 nm. However, at the telecommunication and optical communication wavelength (1300 - 1550 nm), III-V materials such as InAs, InGaAs, GaAsSb, etc. surpass the capabilities of Si. Several methods to integrate III-V materials have been studied, including wafer bonding, epitaxial growth, epitaxial layer transfer, and micro-transfer printing. Wafer bonding can impart defects such as voids and cracks in the hetero-structure interface, whereas epitaxial growth of III-V materials on Si can be challenging. Unlike the other techniques, epitaxial layer transfer does not cause interfacial defects in the III-V/Si hetero-structure. In this study, we focus on epitaxial layer transfer of GaAsSb membranes using AlAsSb sacrificial layers to make GaAsSb/Si photodiodes. GaAsSb absorbs in the telecom wavelength of 1550 nm and has a small conduction band offset with Si (<0.1 eV), which favors electron transport between GaAsSb and Si and eliminates the need for a grading layer. These properties make GaAsSb an excellent material for integrating with Si to develop high-speed avalanche photodiodes and receivers with low noise. In this study, we develop the technique to integrate GaAsSb with Si through epitaxial layer transfer. GaAsSb is grown on an InP using molecular beam epitaxy. Mesa structures of the GaAsSb membrane are then epitaxially lifted-off through substrate etching of InP and selectively etching the sacrificial layer of AlAsSb. Further, the GaAsSb mesa membrane is transfer-printed onto a Si substrate using a poly(dimethylsiloxane) (PDMS) stamp to make the GaAsSb/Si PIN diodes. The quality of the membrane post-transfer was studied through atomic force microscopy. The electronic properties of the PIN diodes were studied with current-voltage and capacitance-voltage measurements. Further, the GaAsSb-Si interface is characterized through simulations and experimentation to quantify the conduction band offset and the sheet charge density at the interface.

10:30 AM
Study on the characteristics of Si channel layer formed by recrystallization with UV nanosecond pulsed laser annealing for monolithic 3D integration (Student)
Mrs. Hyerin Shin[1], Mr. Dongmin Yoon[1], Mr. Seunghyun Baik[1], Ms. Hoonjung Oh[1], Mr. Dae-hong Ko[1]
[1]Yonsei university

As 2D integration technology approaches scaling limits, novel architectures are needed to meet the demand for advanced transistors while maintaining high performance. Vertically stacked architecture, such as the monolithic 3D (M3D), is among the most promising solutions [1,2]. The low thermal budget is essential for fabricating the upper channel layer. Furthermore, achieving lateral epitaxial growth solely through selective growth at low temperatures is challenging due to the low selectivity of silicon [3]. Therefore, we developed the lateral recrystallization process for the epitaxial channel layer by using Ultra High Vacuum Chemical Vapor Deposition (UHV-CVD) at low process temperature (≤500℃) and UV nanosecond pulsed laser (NLA).

In this research, we utilized UHV-CVD for Si layer deposition on SiO2 nano-patterned wafer. The crystalline seed with (111) facet was deposited on the Si open region while amorphous Si was formed over the SiO2 region. NLA was followed to induce liquid phase epitaxy for subsequent thermal treatment. After the epi seed was sufficiently melted by annealing with optimized conditions, lateral recrystallization from the seed to the amorphous region occurred. To understand the regrowth mechanism, Ansys simulation was conducted to analyze the thermal distribution during laser annealing. Additionally, further analyses were conducted to examine surface morphology, microstructure, and crystallinity using Scanning Electron Microscopy (SEM), Transmission Electron Microscopy (TEM), and Grazing incidence X-ray Diffraction (GI-XRD). The obtained results corroborated the regrowth mechanism as predicted by the simulation. Furthermore, we examined the effects of pattern density and the impact of multiple laser shots to gain comprehensive insights into the process of lateral recrystallization.

10:45 AM
Synthesis of Scandium Diboride Crystals Using the Laser-Diode Floating Zone Method (Student)
Mr. Daniel Harrison[1], Mr. Astrid Dzotcha Kengne[1], Mr. Ahamed Raihan[1], Mr. Evan Crites[2], Dr. Satya Kushwaha[2], Dr. Tyrel McQueen[2], Dr. Birol Ozturk[1], Dr. Michael Spencer[1], Dr. Mvs Chandrashekhar[3]
[1]Morgan State University, [2]Johns Hopkins University, [3]University of South Carolina, Columbia, USA

Scandium exhibits a boride chemistry similar to that of the transition elements and the rare earth elements [1]. The two most commonly known compounds consisting of only scandium and boron are scandium dodecaboride (ScB12) and scandium diboride (ScB2). ScB12 is more documented in literature compared to its boron deficient counterpart. But

from the little information that exists on the properties of ScB2, we hypothesize that this material could be a promising substrate for semiconductor compounds. One such property is its lattice constant, which is a close match to that of the group-III nitride semiconductor family. This close lattice match would reduce the strain and crystal defects of crystal layers grown epitaxially on this material, which would result in improved performance and reliability. Synthesizing bulk, single crystal ScB2 material would therefore allow for further research into using ScB2 as a substrate for these semiconductor materials.
In this work, we demonstrate the possibility of synthesizing ScB2 crystals using a zone melting crystal growth technique known as the laser-diode floating zone (LDFZ) method. Polycrystalline ScB2 rods were used as our feed and seed rods. A pellet of scandium (Sc) metal was placed on top of the feed rod . This effectively lowered the melting temperature, helped to establish a molten zone, created a flux of Sc to help with the crystal growth and prevented the appearance of the boron rich second phase ScB12. The experiment was done under 5 bars of pure argon gas to help suppress the evaporation of the rods at high temperatures. The maximum laser power we could reach while maintaining a stable growth was approximately 50%. This correlated to a temperature of approximately 1375°C when corrected for an emissivity of 0.5 which was estimated based on the emissivity of metal borides close to ScB2.
After several growth attempts, we found that the ideal growth direction was upwards in order to take advantage of the gravity assisted absorption of the Sc flux by the porous ScB2 rods. With this method we were able to stably grow a crystal at an average rate of 3mm/hr. The crystal grew until all the Sc flux was absorbed by the feed rod and the molten zone was eventually separated. The grown crystal was cut from the seed rod and cleaned in a solution of hydrochloric acid, hydrogen peroxide and deionized water to remove any excess Sc metal which may have been oxidized during the experiment. X-Ray Diffraction (XRD) analysis data shows that our grown crystal has intensity peaks similar to the ScB2 diffraction data found in literature.
Additional characterization and properties of the grown crystal will be presented.
This work made use of the Laser Diode Floating Zone facility of the Platform for the Accelerated Realization, Analysis, and Discovery of Interface Materials (PARADIM), which is supported by the National Science Foundation under Cooperative Agreement No. DMR-2039380.
[1]G. Levchenko et al., Preparation and some properties of ScB2 single crystals, Journal of Solid State Chemistry, Volume 179, Issue 9, 2006, p. 2949.

11:00 AM
Enabling Material and Process Integration by Combining Thermal Scanning Probe Lithography and Soft Etching
Mr. Andrea Ubezio[1], Dr. Emine Cagin[1], Mr. Andrea Vischioni[1], Dr. Jana Chaaban[1], Ms. Myriam Kaeppeli[1], Dr. Jonathan Edgeworth[2]
[1]Heidelberg Instruments Nano, [2]Moorfield Nanotechnology

Thermal Scanning Probe Lithography (t-SPL), empowered by NanoFrazor technology, is emerging as a mature and reliable direct-write nanolithography technique for fabricating nanoscale structures [1,2]. The technique is especially advantageous for integrating new materials into device applications. Operating with an ultrasharp tip, t-SPL scans the sample surface, inducing local changes through thermal stimulus. The t-SPL cantilever, featuring an ultrasharp tip with a radius of less than 10 nm, incorporates crucial elements like an integrated thermal topological sensor, electrostatic actuation, and an integrated heating element. This integration proves advantageous for generating intricate 2D and grayscale features [2,3]. In a closed-loop system, t-SPL facilitates simultaneous patterning and inspection, enabling lithography with sub-nanometer accuracy in controlling structural depth. For device fabrication with nanomaterials, t-SPL offers markerless overlay capabilities, seamlessly detecting buried nanomaterials beneath the resist system [4].
Current challenges center on integrating semiconductors, insulators, and nanomaterials like 2D flakes and nanowires into devices, employing diverse processing techniques. High-resolution etching (HRE) or lift-off (HRLO) with NanoFrazor technology can achieve sub-10 nm sizes [5] but require the use of thin (<10 nm) resist (e.g. polypthalaldehyde) and hard mask (e.g. 2 nm of SiO2) layers. However, conventional reactive ion etching (RIE) tools pose difficulties, with issues like plasma ignition and high etch rates, resulting in short and unpredictable etching processes. Processing emerging 2D materials like MoS2 and graphene with traditional RIE tools is another major issue, as the etching can damage the whole 2D layer. Integrating a soft etching tool such as the nanoETCH developed by Moorfield Nanotechnology helps address these issues effectively. The nanoETCH provides a remote plasma with low power and fine etching control crucial for graphene and other sensitive 2D materials. The tool enables substrate preparation for flake exfoliation (large-area flakes through surface conditioning), clean material patterning (graphene removal without resist residues), and defect engineering (creating defects in graphene layers), not achievable in conventional RIE tools. Notably for processes pertaining to thin resist, the absence of an ignition effect enables precise control of etching depth and process integration of these stacks in a seamless way.
Etching tests showed that the nanoETCH can offer a high control of the etch rate of PPA for high-resolution etching and lift-off processes. A mixture of N2 and O2 low-power plasma (3W) leads to a PPA etch rate of 9 nm/min and an ignition etch effect of 1 nm. Etching recipes were also successfully developed for the other materials (SiO2, PMMA, PMGI, Si) used in the fabrication of high-resolution stacks for t-SPL. Preliminary tests show a successful HRE of 40 nm lines with 60 nm half-pitch in Si substrates. Preliminary grayscale transfer results show a depth amplification of up to 3 into Si and a roughness reduction of grayscale structures by up to 60%. The etching of grayscale features was also demonstrated with SiO2 substrates. Considering the high Si:SiO2 selectivity of common etching processes, this can lead to the fabrication of highly amplified nanostructures using PPA-SiO2-Si substrates. In the presentation, we will delve into the achieved results of high-resolution, grayscale, and highly amplified etching, attained through the synergistic combination of t-SPL empowered by NanoFrazor and the soft etching capabilities offered by nanoETCH.
[1] S. Howell et al., Microsyst Nanoeng, 6, 21 (2020)
[2] N. Lassaline, J.Phys.Mater. 7 015008 (2024)
[3] N. Lassaline et al., Nature, 582, 506-510 (2020)
[4] Zheng et al., Nat Electron, 2, 17-25 (2019)

[5] Ryu et al., ACS Nano, 11, 12, 11890–11897 (2017)

11:15 AM
Fabrication of Mixed-Dimensional Heterostructures through Micro-Transfer Printing of III-V Thin Films on Monolayer Nanomaterials (Student)
Dr. Sami Znati[1], Mr. Venkatesh Deenadayalan[1], Dr. Stefan Preble[1], Dr. Parsian Mohseni[1]
[1]Rochester Institute of Technology

The heterogeneous integration of optoelectronic devices grows in cost as the critical dimensions of devices are pushed to ever smaller scales. Micro assembly technologies, such as micro-transfer printing (μTP), offer a solution as they are designed to be highly scalable and cost effective. The μTP approach also enables efficient use of growth substrates by allowing the smart integration of transferred devices (i.e., “coupons”) on the receiving “target” substrates. This process allows the fabrication of novel device architectures with reduced critical dimensions and otherwise inaccessible heterojunction configurations, including mixeddimensional heterostructure (MDH) systems composed of III-V compound semiconductors and twodimensional (2D) nanomaterials. Distinctive optoelectronic characteristics emerge in III-V/2D MDH systems owing to interlayer interactions resulting from the coupling and redistribution of charge states across the van der Waals (vdW) gap. The ability to adjust the interfacial arrangement and band alignment in pseudo-vdW materials renders them extremely appealing as heterostructures with tunable: (a) interlayer band configurations and density of states; (b) charge carrier dynamics and energy transfer efficiencies; (c) delocalized hybrid excitonic complexes; and (d) quantum emission and detection capabilities. In this work, we describe a process by which III-V device layers are released from as-grown source substrates and transferred onto 2D materials via μTP. Lattice matched InAlAs and InP epitaxial layers were grown via metalorganic chemical vapor deposition (MOCVD) on InP wafers. Transferable coupons were fabricated by deposition of a masking oxide layer and photolithographic patterning, followed by inductively-coupled plasma reactive-ion etching (ICP-RIE) to define the coupon boundaries. The InAlAs layers were released via selective etching in a phosphoric acid-based solution before being micro-transfer printed onto a range of substrates including Si, graphene, and monolayer molybdenum disulfide. To better understand the impact of printing conditions on device transfer, a design of experiments was conducted to characterize the μTP parameter space in terms of the following pick and print settings: (a) overdrive distance, or the distance during printing to which the stamp motors articulate below the surface in the vertical direction; (b) the shear distance, or the lateral distance the stamp travels during vertical withdrawal from the printing step; (c) retraction speed, or the speed at which the stamp travels from the print surface during vertical withdrawal; and (d) the overdrive speed, or the rate at which the stamp descends towards the print surface during the first phase of printing. The effect of surface van der Waals forces on the pick step of the transfer print process was investigated via a comparison between oxide-coated and oxide-free InP pick surfaces. A comparison via cross correlation of these factors provides insight into how the printing process functions from a physical and parameter space perspective. Transfer printing onto low-dimensional monolayer materials can better enable site-specific, high-throughput heterogeneous integration with the improved print yields demanded by scalable fabrication. It additionally facilitates a low complexity fabrication process for III-V/2D MDHs enabling novel device architectures with applications in optoelectronics, power devices, photovoltaics, quantum computing, nanoelectromechanical systems, and more.

11:30 AM
Lunch

1:00 PM
III-Nitride: Ferroelectric Materials and Devices
Session Chairs: Matthew Hardy (US Navy Research Laboratory), Theeradetch Detchprohm (Georgia Institute of Technology)
ESJ 0202

01:00 PM
Molecular Beam Epitaxy and Characterisation of Ferroelectric Quaternary Alloy ScAlGaN (Student)
Mr. Samuel Yang[1], Dr. Ding Wang[1], Mr. Md Mehedi Hasan Tanim[1], Dr. Danhao Wang[1], Prof. Zetian Mi[1]
[1]University of Michigan

The incorporation of rare earth elements, such as Sc and Y, into the conventional III-nitride materials AlN and GaN can transform them into ferroelectric materials while also enhancing their piezoelectric properties. These wurtzite nitride ferroelectrics have been the centre of much interest since their experimental advent via sputter deposition. Since then, advances in molecular beam epitaxy (MBE) have led to the demonstrations of high-quality monocrystalline ScxAl1-xN and ScxGa1-xN. Compared to conventional oxide ferroelectrics, these materials offer larger remanent polarisations and greater scalability, potentially into monolayer regimes. Coupled with predictions and reports of optical activeness, as well as enhanced piezoelectricity, nitride ferroelectrics show promise in revolutionising the next generation of reconfigurable electronics and optoelectronics, memories, energy harvesting systems, MEMS, and piezoelectric devices. However, many modern applications place great demand on the tuneability of material systems. For example, bandgap, band alignment, lattice parameter, and piezoelectric constant tuneability are highly desirable for electronic, optoelectronic, and acoustic devices. ScxAl1-xN and ScxGa1-xN offer some tuneability through the adjustment of Sc compositions. However, films with high Sc content suffer from the degradation of material quality and the deterioration of desirable ferroelectric and piezoelectric properties. On the other hand, the quaternary alloy ScxAlyGa1-x-yN remains largely unexplored and can serve to bridge the tuneability gap between ScxAl1-xN and ScxGa1-xN. As a first step towards realising such a tuneability bridge, a detailed investigation on the ferroelectric properties of ScxAlyGa1-x-yN is performed, focusing on Sc0.2Al0.45Ga0.35N. The samples are grown via plasma-assisted MBE on a Mo template. In-situ monitoring with reflection high-energy electron diffraction (RHEED), combined with ex-situ characterisation with atomic force microscopy (AFM) and x-ray diffractometry (XRD) confirm excellent morphology and crystallinity achieved, with a

surface rms roughness of 0.5 nm over a 25 μm2 scan area and a 0.34° (0002) plane 2q-w full-width half-maximum (FWHM). Electrical measurements reveal unambiguous ferroelectric switching with a coercive field of ~5.5 MV cm-1 at 10 kHz and a large remanent polarisation of ~150 μC cm-2. To analyse the ferroelectric switching behaviour, the time and electric field dependence of polarity reversal is quantified. The results suggest that the polarisation reversal behaviour adheres to the Kolmogorov-Avrami-Ishibashi model and follows a scheme of domain nucleation and growth. Piezoresponse force microscopy (PFM) studies further elucidate the evolution of the polarity reversal domains and support that the growth of inversion domains occurs via an in-plane motion of the domain walls. The demonstration of viable and functional ferroelectric quaternary alloy ScxAlyGa1-x-yN is the first step into an exciting dimension through which the wurtzite ferroelectrics family can be engineered for multifarious state-of-the-art electronic, optoelectronic, and acoustic devices and systems. Further studies are anticipated to extend the quaternary alloy by introducing a wide range of Sc, Al, Ga, In, and B compositions to fully bridge the gap between the corresponding ternaries.

01:15 PM
Unraveling Atomic-Scale Polarization Switching in Single Crystalline Nitride Ferroelectrics
Dr. Danhao Wang[1], Dr. Ding Wang[1], Ms. Mahlet Molla[1], Mr. Yujie Liu[1], Prof. Emmanouil Kioupakis[1], Prof. Zetian Mi[1]
[1]University of Michigan

The recent discovery of ferroelectricity in rare-earth metal-doped III-nitrides has ignited renewed interest in the ferroelectric's community, emphasizing their transformative potential in the next-generation microelectronics. The superior material parameters herald nitride ferroelectrics as potential game-changers in microelectronics, from microelectronic memory to neuromorphic computing, all while seamlessly integrating with mainstream semiconductor platforms. However, ensuring that these nitride ferroelectrics meet the stringent criteria of modern microelectronics necessitates refining various parameters including coercivity, endurance, stability, and leakage. Addressing these challenges requires more than conventional macroscopic methods; a detailed understanding at the unit cell level is pivotal. Recently, single crystalline ferroelectric nitride semiconductors have been demonstrated by utilizing molecular beam epitaxy (MBE). Their pristine crystal quality, uniform chemical composition, and congruent film-substrate orientation, coupled with atomically ordered, unambiguous interfaces, provide an optimal framework for TEM imaging and an unparalleled archetype for decoding the intricate ferroelectric phenomena endemic to this material class.
In this study, we embark on an unprecedented exploration of the intricate microstructures and ferroelectric order in Sc-III-nitride heterostructures using sub-angstrom resolution high-angle annular dark-field (HAADF) and integrated differential phase contrast (iDPC) scanning transmission electron microscopy (STEM) techniques. The robust ferroelectric properties of single-crystalline ScGaN/GaN heterostructures have facilitated direct atomic-scale resolutions of the localized polarizations within wurtzite lattices. This seminal work furnishes the inaugural atomic-scale evidence of ferroelectric polarization inversions in Sc-III nitride heterostructures. Contrasting with the inherent M-polar ScGaN/GaN structure, devices under positive voltage-poled regimes predominantly manifest a nitrogen-polar character within the ScGaN region. Intensive scrutiny of the ScGaN/GaN interface unambiguously identified an elusive "unswitched layer" in nitride ferroelectrics, a concept predicted theoretically but not observed experimentally. Moreover, sharp transitional demarcations between electrically modulated N-polar domains and their native M-polar counterparts have been discerned, offering a profound understanding of the polarization dynamics in the spatial regime. The depth of understanding achieved here heralds refined paradigms and paves avenues for the tailored development of nitride ferroelectric materials.

01:30 PM
Uncovering Wurtzite ferroelectric domain walls
Dr. Ding Wang[1], Dr. Danhao Wang[1], Ms. Mahlet Molla[1], Mr. Yujie Liu[1], Prof. Emmanouil Kioupakis[1], Prof. Zetian Mi[1]
[1]University of Michigan

Domain walls, the intrinsic atomic-scale structures that demarcate regions of differing electric polarizations within ferroelectric materials, are now under the spotlight of fervent scientific exploration. The unique electronic confinement characteristics, coupled with distinct symmetry and chemical compositions, allow these domain walls to exhibit a spectrum of electric and magnetic behaviors, a stark contrast to adjacent domains. The advent of ferroelectric domain wall devices has reimagined the design of ferroelectric devices, ushering in innovations marked by ultra-compact dimensions and pioneering designs suitable for nanoscale applications, ranging from reconfigurable transistors and memristors to biological synapses, inductors, transformers, and even forays into radio-frequency domains. The recent discovery of ferroelectricity in rare-earth doped wurtzite nitride semiconductors has ignited renewed interest in the ferroelectrics community, emphasizing their transformative potential in the next-generation microelectronics. The finesse of molecular beam epitaxy (MBE) enables these materials to be epitaxially grown layer by layer, granting unmatched control over parameters like epitaxial strain, stoichiometry, defect density, and domain architecture. Additionally, inherent defects in nitride ferroelectrics, such as nitrogen vacancies and interstitials, present a wealth of design opportunities, facilitating the manipulation of crystallographic structures and domain wall electric, spin, and orbital interactions. Yet, in spite of these promising horizons, our grasp of domain walls in nitride ferroelectrics remains nascent, necessitating a comprehensive exploration into the properties and potentials of nitride ferroelectric domain walls. In this work, leveraging sub-angstrom resolution scanning transmission electron microscopy (STEM), we demystify, for the first time, the enigmatic ferroelectric landscapes and intricate microstructures of single crystalline nitride ferroelectrics using an exemplary wurtzite ferroelectric, ScGaN. iDPC images were employed to identify the crystallographic orientation and imaging of atomic positions for lighter elements like nitrogen, and the exact atom positions have been extracted using a two-dimensional Gaussian fitting to quantify the dumbbell angle and lattice distortions. Through carefully examining the microstructures

inside a polarity-switched metal/ScGaN/n-GaN capacitor, we identify two distinct electric field-responsive inverse domain boundaries in these nitride ferroelectrics. The vertical domain walls, with antiparallel polarization, are found to be sub-nanometer thick, and are accompanied by a minor lattice expansion in the in-plane direction; whereas the horizontal domain walls, arranged in a head-to-head fashion, span a couple of monolayers, and exhibit a noticeable lattice expansion in the out-of-plane direction. These insights not only enrich our fundamental understanding of ferroelectrics, but also lay the essential groundwork for nanoscale and domain engineering of the emerging wurtzite nitride ferroelectric materials and devices.

01:45 PM
Unveiling Electronic Properties of Wurtzite Ferroelectric Domain Walls (Student)
Mr. Yujie Liu[1], Ms. Mahlet Molla[1], Dr. Ding Wang[1], Dr. Danhao Wang[1], Prof. Zetian Mi[1], Prof. Emmanouil Kioupakis[1]
[1]University of Michigan

Nitride ferroelectrics have emerged as pivotal materials in developing advanced electronic devices due to their unique properties, such as high thermal stability, large spontaneous polarization, and robustness in different environments. These characteristics make them ideal for various applications including non-volatile memory devices. Central to the functionality of these materials are the ferroelectric domain walls, whose dynamic behavior significantly influences the overall material properties. For instance, domain walls in ferroelectrics can exhibit enhanced conductivity and distinct dielectric properties, playing a crucial role in device performance and miniaturization. However, there remains a significant knowledge gap regarding the intrinsic properties of domain walls in nitride ferroelectrics, which is particularly crucial in understanding their electronic structures. Here, we apply density functional theory to determine the electronic properties of neutral and charged domain walls in nitride ferroelectrics based on the observations in experiments [1]. We explain the origin of compensation of the bound polarization charge in charge domain walls. Our findings explain the electronic properties of domain walls for nitride ferroelectric devices, paving the way for optimized device designs and new applications in the realm of electronic materials.
References:
[1] Wang, Ding, et al. “Electric-Field-Induced Domain Walls in Wurtzite Ferroelectrics.” arXiv preprint arXiv:2312.08645 (2023).

02:00 PM
Calculation of the Band Structure in Ferroelectric AlScN HEMTs
Dr. Greg Rupper[1], Dr. Brendan Hanrahan[2]
[1]U. S. Army Research Laboratory, [2]DEVCOM Army Research Laboratory

Ferroelectric materials offer nitride semiconductors a tantalizing proposition: voltage-switchable polarization. As such, Ferroelectric HEMTs have been under consideration for some time [1]. The classical oxide ferroelectrics (e.g., BaTiO3) proved difficult to integrate, but in 2019, AlScN, a wurzite nitride, was discovered to be ferroelectric [2].

Recently, there have been a number of examples of nitride-based ferroelectric HEMTS using AlScN barriers which have proposed ferroelectricity-driven threshold voltage manipulation [1], memory-window operating states [3], or state switching between E-mode and D-mode [4]. Despite these early demonstrations, there is not a full understanding of how polarization switching will interact with a polarization-driven 2DEG channel and how the charge can be managed at AlScN interfaces to allow for polarity switching. In this work, we use a self-consistent Poisson-Schrodinger equation solver to calculate the band structure, electric fields and carrier densities for a simple AlScN HEMT device.
The device that we consider in this work (shown in Fig. 1) consists of an unintentionally doped GaN layer, a 0.5nm AlN layer to form the channel at AlN/GaN interface and a layer of Al0.7Sc0.3N which replaces the layer of AlGaN that would normally be in an AlGaN HEMT. The thickness of the Al0.7Sc0.3N layer was varied from 2.5nm to 30nm. For this calculation, the AlScN is assumed to be an insulator with no charges in the AlScN later. (We note that sputtered AlScN is an insulator, however MBE grown AlScN is likely to act like a semiconductor.) The calculation was run for both the case where the AlScN polarization direction was the same as the AlN direction (normal) and the inverted polarization. Figure 2 shows the Vg dependence of the electron density in the channel. For small Vds, this density will be proportional to the drain current. Figure 3 (4) shows the resulting band diagram for the 20nm thick AlScN device with normal (inverted) polarization. To determine the polarization that will be present in the device, we need to examine the E field in the AlScN layer. Figure 5 shows the E field in the 20nm device with normal polarization. We assume a coercive field value of 4 MV/cm for the Al0.7Sc0.3N layer. When E field in the normal (inverted) polarization device is less than -4 MV/cm (more than 4MV/cm), the polarization will switch to the inverted (normal) polarization. Figure 6 shows the gate voltages where the polarization will switch polarization and the threshold voltage for the normal polarization device as a function of the AlScN layer thickness. For AlScN layer thicknesses below ~10 nm, the inverse polarization Vswitch is greater than the normal polarization Vswitch in this case, the device does not support a complete switching of the polarization when the gate voltage is between the two switching voltages. When the AlScN layer is thicker then ~10nm, there will be a range of Vg where the device operation will depend on the history of Vg. For these devices, if the polarization is inverted, then Vg will be far below the inverted devices Vth, and the device channel will be shutoff. For the normal polarization, there is a range of Vg above Vth where the device will operate like a normal HEMT, however, the device can not be operated near Vth without changing the polarization and fully shutting off the device. For this simple device, the AlScN allows switching between an off mode and a D-mode HEMT. This switchable HEMT device could be used for a class A amplifier. However, the inability to lower the gate voltage below Vth without fully switching off the device limits the ability to use such a device. Further improvements to the device design are necessary to produce devices with more flexible performance.
In conclusion we find that modeling the band structure for ferroelectric HEMTs is necessary to understand the range of useful operation of these devices. Achieving many of the goals for mixing ferroelectrics with HEMT devices, such as switching between E-mode and D-mode, will require careful

design with a full understanding of the band structure and fields within the device.
[1] Wang et al., Appl. Phys. Lett., 122, 090601 (2023).
[2] Fitchner et al., J. Appl. Phys. 125, 114103 (2023).
[3] Casamento et al., International Electron Devices Meeting pp. 11.1.1 (2022)
[4] Yong Yang et al., IEEE Electr. Device L. 44, pp 1260 (2023)

1:00 PM
Gallium Oxide Epitaxy, Processing, and Characterization
Session Chairs: Thaddeus Asel (Air Force Research Laboratory), Nidhin Kurian Kalarickal (Arizona State University)
ESJ 0224

01:00 PM
MOCVD Grown β-(Al,Ga)2O3/Ga2O3 2DEGs enabled by TEAl (Student)
Mr. Cameron Gorsak[1], Mr. Pushpanshu Tripathi[1], Mr. Joshua Buontempo[1], Dr. Jonathan McCandless[1], Mr. Chuan Chang[1], Mr. Sami Kibal[2], Ms. Katie Gann[1], Prof. Huili (Grace) Xing[1], Prof. Debdeep Jena[1], Prof. Michael Thompson[1], Prof. Hari Nai
[1]Cornell University, [2]Imperial College London

β-Ga2O3 is an attractive ultra-wide bandgap semiconductor on account of its high critical breakdown field of ~8 MV/cm, availability of large-area native substrates, and controllable n-type doping. However, compared to other wide bandgap semiconductors—SiC, and GaN, the intrinsic carrier mobility is relatively low. One potential pathway to overcome this mobility limit is through the formation of a two-dimensional electron gas (2DEG) at the interface of δ-doped β-(AlxGa1-x)2O3 and undoped β-Ga2O3 [1-5]. In this work, gallium oxide based 2DEGs were realized by growing abrupt and smooth heterojunctions using metal organic chemical vapor deposition (MOCVD) with Triethylgallium (TEGa) and Triethylaluminum (TEAl) precursors.
Previously, we and other groups have demonstrated smooth β-(AlxGa1-x)2O3 films using Trimethylgallium (TMAl) and TEGa as precursors for Al and Ga, respectively [6]. However, the growth temperature of 900 °C is too high for achieving abrupt non-compensated δ-doping profiles; to reduce the growth temperature, TMAl was replaced with TEAl as the Al precursor. Additionally, TEAl shows potentially lower carbon incorporation because it pyrolyzes via β-hydrogen elimination whereas the pyrolysis of TMAl can leave behind highly reactive methyl radicals that may incorporate into the film at lower growth temperature and/or lower oxygen to alkyl ratios.
Prior to growth, β-Ga2O3 substrates were etched in hydrofluoric acid (HF) for 30 minutes to minimize parasitic interfacial Si [7]. A β-(AlxGa1-x)2O3 back barrier is then grown to inhibit conduction of any remaining Si [8]. After growing a thick UID buffer, TEGa and TEAl precursors are jointly sent into the reactor to grow the heterojunction. Silane is used for Si doping.
We have demonstrated a 2DEG with a room temperature sheet density of ~3 x 1012 cm-2 with a mobility of > 180 cm2/Vs. Temperature dependent Hall measurements see only slight carrier freeze out of the parallel conducting top uniformly doped β-(AlxGa1-x)2O3 layer. The 2DEG reaches a peak mobility of ~ 2400 cm2/Vs.
Employing δ-doped β-(AlxGa1-x)2O3 instead of uniformly doped β-(AlxGa1-x)2O3 can potentially increase the mobility of the 2DEG channel. This will require etching and subsequent regrowth of highly doped β-Ga2O3 to the channel. Also, growing on (100) β-Ga2O3 substrates will allow for increased Al content in the fully commensurate β-(AlxGa1-x)2O3 while staying under the critical thickness for cracking [9]. Designing and growing 2DEGs with high Al content and δ-doping will enable high-voltage lateral power devices with fast switching speeds.
References
[1] Ranga, P., Bhattacharyya, A., Chmielewski, A. et al., Applied Physics Express, 14(2), 025501, (2021).
[2] Zhang, Y., Neal, A., Xia, Z. et al., APL, 112(17), (2018).
[3] Kalarickal, N. K., Xia, Z., McGlone, J. F. et al., JAP, 127(21), (2020).
[4] Joishi, C., Zhang, Y., Xia, Z. et al., IEEE Electron Device Letters, 40(8), 1241-1244, (2019).
[5] Krishnamoorthy, S., Xia, Z., Joishi, C. et al., APL, 111(2), (2017).
[6] Bhuiyan, A. F. M., Feng, Z. et al., APL, 115(12), (2019).
[7] McCandless, J. P., Gorsak, C. A., et al., arXiv:2312.06851, (2023).
[8] Ohtsuki, T., Kamimura, T., & Higashiwaki, M., IEEE Electron Device Letters, (2023).
[9] Mu, S., Wang, M., Peelaers, H., & Van de Walle, C. G., APL Materials, 8(9), (2020).

01:15 PM
Heteroepitaxy of β-Ga2O3 on GaN by MOCVD: The Impact of Nitride Polarity on β-Ga2O3 Crystalline Quality
Dr. Emma Rocco[1], Dr. Michael Liao[1], Dr. Daniel Pennachio[2], Dr. James Spencer Lundh[1], Dr. Hannah Masten[1], Dr. Marko Tadjer[3], Dr. Michael Mastro[2], Dr. Jennifer Hite[4]
[1]NRC Postdoctoral associate residing at the U.S. Naval Research Laboratory, [2]Naval Research Lab, [3]U.S. Naval Research Laboratory, [4]Department of Materials Science and Engineering, University of Florida

Ga2O3 is a promising candidate for next generation high-power and high-frequency electronics, as well as for solar-blind photodetectors and sensing applications owing to its material properties. The β-phase of Ga2O3 has an ultra-wide band gap energy of 4.8 eV and an estimated critical electric field of 8 MV/cm [1]. This leads to a high Baliga figure of merit for β-Ga2O3, that is ~4x larger than that of GaN and 10x larger than that of SiC [1].
Yet challenges remain for realizing the full potential of Ga2O3. Achieving p-type conductivity in Ga2O3 has long been the subject of both experimental and theoretical studies, with calculations predicting large effective mass and a polaronic state for holes [2]. The difficulty of achieving p-type conductivity limits the attainability of certain device structures and geometries, including homojunction p-n diodes. Additionally, the thermal conductivity of Ga2O3 is low (11-27 W/m·K), resulting in self-heating effects and in turn, degradation in device performance [1].
Heterojunction devices achieved by the epitaxial growth of Ga2O3 on GaN may allow these challenges to be overcome.

The thermal conductivity of GaN is an order of magnitude larger than Ga2O3, and high p-type conductivity has been demonstrated for Ga- and N-polar GaN. Growth of Ga2O3 on Ga-polar GaN by metal organic chemical vapor deposition (MOCVD) has recently been reported by Seo et al. [3]. With x-ray diffraction (XRD) measurements, single crystalline {-201} β-Ga2O3 was observed as well as a six-fold in-plane rotation of the grains as a result of lattice mismatch between GaN and β-Ga2O3 [3].
In the present study, we demonstrate the first epitaxial growth of β-Ga2O3 on N-polar GaN by MOCVD, and investigate the influence of GaN polarity on the heteroepitaxial crystalline quality. Ga- and N-polar unintentionally doped (UID) films were grown on nominally on-axis c-plane sapphire substrates by MOCVD using a Veeco D180 dedicated to III-nitride depositions. Following GaN growth, the samples were exposed to atmosphere. UID β-Ga2O3 was then deposited in an Agilis 500 III-oxide MOCVD to a nominal thickness of 300 nm. We will present the subsequent characterization of the β-Ga2O3 films by atomic force microscopy (AFM), XRD, scanning electron microscopy (SEM), and Raman spectroscopy. The β-Ga2O3 films grown on both N- and Ga-polar GaN exhibit a 6-fold rotation of the {-201} grains similar to the report of Seo et al. An additional 6-fold rotation is observed in XRD for the film grown on N-polar GaN. Only differences in lattice twist were observed as both films exhibited the same amount of diffuse scatter along the symmetric rocking curve direction indicating the same amount of lattice tilt distortion in either film. We will discuss the origin of this additional set of in-plane grain rotations observed for heteroepitaxial Ga2O3 on N-polar GaN.
[1] S. J. Pearton et al., “A review of Ga2O3 materials, processing, and devices,” Appl. Phys. Rev., vol. 5, no. 1, p. 011301, Jan. 2018, doi: 10.1063/1.5006941.
[2] J. Zhang, et al., “Recent progress on the electronic structure, defect, and doping properties of Ga2O3,” APL Mater., vol. 8, no. 2, p. 020906, Feb. 2020, doi: 10.1063/1.5142999.
[3] D. Seo, et al., “Heteroepitaxial Growth of Single-Crystalline β-Ga2O3 on GaN/Al2O3 Using MOCVD,” Cryst. Growth Des., vol. 23, no. 10, pp. 7090–7094, Oct. 2023, doi: 10.1021/acs.cgd.3c00318.

01:30 PM
Impact of Ga Beam Flux on Compensating Acceptors and Electron Mobility in Plasma-assisted MBE-grown β-Ga2O3
Dr. Brenton Noesges[1], Dr. Jian Li[1], Dr. Yunjo Kim[1], Dr. Adam Neal[1], Dr. Shin Mou[1], Dr. Thaddeus Asel[1]
[1]Air Force Research Laboratory

Ultra-wide band gap (UWBG) materials such as beta-gallium oxide (β-Ga2O3) have been of interest due to their high critical electric fields. β-Ga2O3 is unique among the UWBG materials because β-Ga2O3 has a native substrate growable from melt and demonstrates n-type conductivity with carrier concentration controllable between 1016 and 1020 cm-3 using shallow donors Ge, Si, or Sn. [1] However, β-Ga2O3 differs from other Ga-based semiconductors (i.e., GaN, GaAs…) where metal-rich growth conditions are utilized to improve properties and suppress the formation of Ga vacancies (VGa). Instead, β-Ga2O3 growth must balance the incorporation of Ga with the desorption of a volatile suboxide species, Ga2O where this suboxide is a limiting step when growing β-Ga2O3 via molecular beam epitaxy (MBE) with traditional Ga sources. Increased Ga2O desorption causes the growth rate of β-Ga2O3 to decrease as Ga flux is increased beyond the stoichiometric point of the material. Counter to other Ga-based semiconductors where metal-rich conditions suppress metal vacancies, the increased desorption of Ga2O under Ga-rich conditions is expected to increase the formation of VGa under Ga-rich conditions. In this work, we explore the impact of O-rich and Ga-rich conditions on electronic properties in films of β-Ga2O3 grown via plasma-assisted MBE (PAMBE). Initial results comparing two samples under O-rich and Ga-rich conditions showed a large difference in peak low-temperature mobility. The O-rich sample showed a peak low-temperature mobility of 793 cm2/V·s while Ga-rich sample peaked at only 198 cm2/V·s. The mobility and volume carrier density versus temperature data was fit using a model to extract out donor and compensating acceptor density. [1] The Ga-rich sample showed over an order of magnitude higher density of compensating acceptor compared to the O-rich sample indicating that Ga-rich conditions create increased compensating acceptors likely due to VGa formation from increased suboxide desorption. Another series of films were grown across a wider range of O- to Ga-rich conditions to further establish a trend between growth conditions and compensating acceptor density. Only Ga flux varied between samples and substrate temperature, Si source temperature and RF oxygen plasma conditions were held constant. Si concentration in each film was anti-correlated with the growth rate as expected. Conversely, compensating acceptor density increased with increasing Ga-rich conditions. The best peak low-temperature mobility occurred for the sample grown in the most O-rich conditions and mobility decreased with increasing compensating acceptor concentration. Overall, these results indicate the importance of Ga:O ratios in β-Ga2O3 films grown via MBE with conventional Ga sources. These results demonstrate how improved electronical performance can be achieved in β-Ga2O3 by growing under O-rich conditions and limiting the formation of VGa due to suboxide desorption.
[1] Neal, A. T. et al. Donors and deep acceptors in β-Ga2O3. Appl. Phys. Lett. 113, 062101 (2018).

01:45 PM
Epitaxial growth of β-(Al,Ga)2O3 films using TTBAl as Al source (Student)
Mr. Zhuoqun Wen[1], Prof. Elaheh Ahmadi[1]
[1]University of Michigan

The oxidation of Al metal source in the conventional oxide MBE requires frequent opening of the system to reload materials. To overcome this challenge, we are using a hybrid MBE which uses conventional effusion cells for Ga, and a gas source to supply Al. In this talk, we will give an overview of our custom-built gas delivery system with TTBAl as Al source and present our latest results on achieving AlGaO films with different Al compositions (1%-25%) by controlling TTBAl flow rate. Fig.1 shows the high resolution X-ray diffraction (HRXRD) 2θ-ω scan of β-(AlxGa1-x)2O3 films grown at 525 ℃ varying TTBAl flow rate, using a Ga beam-equivalent pressure (BEP) of 1×10-8 Torr, and O plasma power and flow rate of 410W and 2 sccm, respectively. By increasing the TTBAl BEP) from 1.1×10-7 Torr to 4.3×10-7

Torr, the Al incorporation increased from 1.8% to 14.9%. The Al composition can be further increased up to 25% by controlling the TTBAl flow and increasing the growth temperature. Fig. 2 demonstrates the atomic force microscopy (AFM) images of β-(AlxGa1-x)2O3 films grown at from 525 ℃ to 725 ℃, with TTBAl BEP 4.3×10-7 Torr, Ga BEP 8×10-9 Torr. The root mean square (rms) surface roughness of each sample is indicated in the figure. The sample grown under 625 ℃ has a smoothest surface under these TTBAl and Ga conditions.

02:00 PM
Excellent Si Doping Control in β-Ga2O3 (010) Films by Pulsed Laser Deposition (Student)
Mr. Vishal Khandelwal[1], Dr. Yi Lu[1], Dr. Shibin Chandroth[1], Dr. Haicheng Cao[1], Dr. Xiao Tang[1], Prof. Xiaohang Li[1]
[1]King Abdullah University of Science and Technology

The wide band gap, high breakdown strength, and extreme environment stability with the availability of native single-crystal substrate make β-Ga2O3 suitable for a diverse range of device applications. To maximize the effectiveness of β-Ga2O3 in electronic devices, two critical factors need to be addressed: firstly, utilizing native β-Ga2O3 substrates to guarantee superior crystallization quality; secondly, precisely controlling the doping level to enable its application as either a channel layer or a contact layer, depending on the specific electron concentration (nele.). Si, Sn, and Ge-doped β-Ga2O3 have been reported to achieve nele. from 1016 to 1019 cm−3 using molecular beam epitaxy, metal-organic vapor phase epitaxy, and low-pressure chemical vapor deposition. Nevertheless, the Pulsed Laser Deposition (PLD) technique has recently showcased its capability to produce high-quality Si-doped β-Ga2O3, achieving a record-high nele. up to >1020 cm-3 [1]. However, these high-conductive films are important only for the contact layer to achieve low contact resistance but are unsuitable for the device's active layer. Owing to high-quality growth with large flexibility in growth parameters in PLD, the lightly/moderately doped β-Ga2O3 films can be realized.
This work demonstrates a large range of nele. from ~1017 to >1019 cm-3 with mobility (μ) as high as ~ 59 cm2/Vs. A systematic study of PLD-grown Si-doped β-Ga2O3 (010) primarily investigated three growth schemes, GS1: Si-doped epitaxial layer without UID buffer, GS2: Varying Si-doped epitaxial layer temperature (TE) with identical buffer growth conditions, GS3: Identical Si-doped epitaxial layer growth conditions with varying buffer growth temperature (TB). Finally, a Schottky barrier diode is fabricated with PLD-grown films.
The growth scheme GS1 includes a 496 nm thick Si-doped β-Ga2O3 epitaxial layer directly grown on the Ga2O3 (010) substrate at 650 °C. The x-ray rocking curve of (020) plane, depicting Full-width half maxima (FWHM) of 105 arcsecs with root mean square (RMS) roughness of ~ 1 nm, measured by atomic force microscope (AFM) (Figure 1). Cross-sectional TEM shows perfect lattice matching of the substrate and grown film. The film shows the nele. ~ 5×1017 cm-3 and μ ~21 cm2/Vs (Table I).
For GS2, a 250 nm thick buffer layer was grown at the fixed temperature of 650 °C followed by the 300 nm Si-doped epitaxial layer grown at TE of 700, 750, and 800 °C. With higher TE, the crystal grain size and RMS roughness of the film increased attributed to improved crystallinity (Figure 2(a)). Despite the identical target as GS1, the film shows the nele. increased to 2 — 5×1018 cm-3 with μ ~ 40 cm2/Vs (Figure 2(b), Table 1). This can be due to higher Si activation efficiency and improved crystallinity respectively, compared to GS1.
In GS3, a 250 nm thick buffer layer was grown at four TB of 650, 700, 800, and 850 °C. AFM scan shows that the crystal grain size is enhanced due to higher lateral diffusion of atoms at high temperatures (Figure 3(a)). Subsequently, the Si-doped epitaxial layer was grown at the TE of 700 °C. The epitaxial film with higher TB shows a monotonic increase in μ, reaching up to 59 cm2/Vs, keeping the nele. constant at ~ 2×1018 cm-3 (Figure 3(b), Table 1). This can be attributed to bigger crystal grains or reduced grain boundaries at higher TB that will help to reduce electron scattering. Benchmarking of this growth with other growth is shown in Figure 4(a). Finally, a Schottky diode is fabricated (Figure 4(b)), showing an ideality factor of ~1.36. This work shows the precise doping control in PLD-grown Ga2O3 films for realizing high-quality Ga2O3 devices. [1]. H.M. Jeon, APL Mater. 9, 101105 (2021).

1:00 PM
Printed Electronic Materials and Devices
Session Chairs: Nathan Lazarus (University of Delaware), Gerd Grau (York University)
ESJ 2208

01:00 PM
Lathe-based Aerosol Jet Printing: A New Additive Manufacturing Method for Fabricating Conformal Electronics on 3D Curvilinear Substrates (Student)
Mr. Hansel Hobbie[1], Mr. James Doherty[2], Ms. Brittany Smith[2], Dr. Paolo Maccarini[1], Dr. Aaron Franklin[2]
[1]Department of Electrical & Computer Engineering, Duke University, [2]Duke University

Of the methods available for the additive manufacturing (AM) of electronic materials1,2, aerosol-jet (AJ) printing has proven to be a versatile option for achieving high-resolution, rapid fabrication of multi-material componentry3. AJ printing is capable of producing micron-scale structures and electronics by direct-write deposition of aerosolized inks. Thanks to the jetting nature and large standoff distance of the material deposition, AJ printing has shown particular utility in the areas of flexible and conformal printed electronics4,5. However, the conventional planar AJ printing format becomes limited for substrate geometries that are 3D and possess non-linear curvature. To overcome these limitations, we engineered a mechanism that upgrades the planar AJ printing process to lathe AJ printing – a custom method that utilizes cylindrical-coordinate orientation to print onto 3D objects of rotation (Fig. 1).
Lathe AJ printing functions by converting the linear motion of the planar printer platen into rotation about a sliding axis, onto which a substrate can easily be mounted and fixed in position underneath the print nozzle. This enables printing with full conformity around the circumference of any

rotatable object or film, thus providing a new approach to AJ printing that expands upon current capabilities. The difference between planar and lathe AJ printing approaches becomes apparent when attempting to print a conformal trace onto a cylinder where the inability to change the angle of print incidence in correlation with the curvature of the substrate causes planar printing to fail, whereas lathe printing succeeds (Fig. 2). Deposition of electronics thin films onto increasingly complex rotational objects is shown in Fig. 3, including flat substrates wrapped about a cylinder, concavities, cones, and even directly onto 3D parts. The only limitations of the system are that a substrate must be able to rotate about a given axis and be between 1 and 40 mm in outer diameter for the rotating substrate. To verify that the lathe mechanism could provide the same precision as the planar AJ printing approach, the resolution in the circumferential- (theta-) and axial-directions was tested by measuring the distances between printed microstrips and comparing them to the expected target values (Fig. 4). The almost negligible error between the target and measured pitch values all the way down to 20 µm in either print direction proves the consistent accuracy of the lathe system to planar AJ printing. After successfully prototyping the lathe mechanism, we applied the fabrication method to the unique task of installing electronic sensing capabilities directly on the surface of an esophageal catheter balloon (Fig. 5). Catheter-based electronics present an interesting AM application space but have barely been demonstrated because of the difficulty in fabricating complex designs in a practical way. The ease of fabrication with lathe AJ printing enables simple functionalization of catheters with the broad catalog of electronic materials that AJ printing is capable of depositing. Lastly, to emphasize the robustness of the lathe AJ printing technique, we fabricated electronic devices of conductive traces, capacitors, and multilayer thin-film transistors (TFTs). For the TFTs, three carbon-based materials were used – graphene, cellulose nanocrystals (CNC), and carbon nanotubes (CNTs)6. Together, these materials form fully printed CNT-TFTs, which make a completely eco-friendly, recyclable transistor when fabricated on paper (Fig. 6).
Ultimately, the work that we are presenting ranges from a full description of the lathe AJ printing mechanism and method to a complete characterization of the system's mechanical performance. Lathe AJ printing has clear implications for expanding the scope of application for AM of electronic materials as we demonstrate for fully printed electronics and catheter-based electronic sensing. Additionally, because of the versatility and scalability of the presented solution, there is potential for unlocking even more application spaces using lathe AJ printing.

01:15 PM
Exploring Form and Functionalization in Crystalline Nanocellulose Inks for Environmentally Sustainable Printed Electronics (Student)
Ms. Brittany Smith[1], Mr. Nicolas Chen[1], Mr. James Doherty[1], Dr. Aaron Franklin[1]
[1]Duke University

Printed flexible electronics show promise for providing a sustainable solution to the increasingly negative impact of electronics manufacturing and waste1. However, current print processes and inks tend to rely on hazardous solvents, extensive post-processing at high temperatures, and/or materials that are not recyclable or biodegradable. Recent work on water-based inks from nanomaterials shows that these challenges can be overcome (i.e., no hazardous chemicals, relatively low temperature processing, and all recyclable or biodegradable materials), but the resultant devices still require improvement in performance and reproducibility2,3. In this work, we investigated two new water-based inks for use in printed carbon nanotube (CNT) thin-film transistors (TFTs): nanocellulose, a biodegradable ionic dielectric, and nanoparticle gold, a recyclable conductor. We developed inks and aerosol jet printing processes for crystalline nanocellulose (CNC) and cellulose nanofibrils (CNF) with various surface modifications, including sulfate, carboxylmethylate (CM), and 2-2-6-6 tetramethylpiperidine 1-oxyl mediated oxidation (TEMPO), to gain insights into the working mechanisms of nanocellulose as an ionic dielectric. Our results reveal that the general ionic nature of the printed films is invariant with the nanostructure form or surface group through capacitor measurements, showing CNF-TEMPO yields the highest capacitance of the six types studied (Fig. 1A-C). Further, we investigated the influence of the sulfonic surface group content on capacitor performance, revealing that the sulfonation content has minimal impact on the dielectric performance. Each nanocellulose type was demonstrated as the gate dielectric for fully printed top-gated CNT-TFTs with low operating voltages (Fig. 1D-E). The average subthreshold swing (SS) of each nanocellulose type falls within 200 – 300 mV/dec, with CNC-DS (de-sulfated) devices having the lowest average SS of all the types at 224 mV/dec (Fig. 1F). For all nanocellulose types, the average off-current was below 0.05 µA/mm, the average on-current above 1 µA/mm, and the average on/off-current ratio was above 100 with CNC-DS, CNC-Reg, and CNF-CM showing the best performance (Fig. 1G). Since nanocellulose breaks down under high temperatures, the top-gate contact must be conductive with minimal post-processing to form fully printed CNT-TFTs. Therefore, as an alternative to using graphene, a novel gold ink formulation was used as the contacts for CNT-TFTs since it is a well-known recyclable material with a high market demand4. This new ink exhibited a resistance of ~5 Ω after a 1-hour sinter at 250 °C and improved the on-current and transconductance of the CNT-TFTs when compared to the graphene electrode devices (Fig. 1H-K). The impressive device performance of these printed CNT-TFTs shows promise for the use of water-based inks in environmentally sustainable printing of electronics.
1. Chandrasekaran, S., Jayakumar, A. & Velu, R. Nanomaterials vol. 12 4251 (2022).
2. Lu, S., Smith, B. N., Meikle, H., Therien, M. J. & Franklin, A. D. Nano Lett. 23, 2100–2106 (2023).
3. Williams, N. X., Bullard, G., Brooke, N., Therien, M. J. & Franklin, A. D. Nat. Electron. 4, 261–268 (2021).
4. Valayil Varghese, T. et al. ACS Mater. Au 4, 65-73 (2023).

01:30 PM
Printed Electrical Conductors: Aging and Reliability Scoping Study
Dr. Dan Ewing[1], Mr. Steven Patterson[1], Ms. Ariztbe Valladolid[1], Mr. Ryan Eickbush[1], Ms. Rebecca Hoppe[1], Mrs. Shannon Northrup[1], Mr. Michael Downey[1], Dr. Jonathan Dwyer[1], Mr. Logan Walz[1], Mr. Daniel Hartley[1], Dr. Holly Weber[1]

[1]Dept of Energy's Kansas City National Security Campus

Direct write methods, such as aerosol jet printing and direct ink write, are a new method to manufacture electronic components. Printed electronics can be printed on a variety of substrates, are low cost, can be customized for specific applications, and can add functionality like sensors to standard circuit boards. As printed electronics become adopted for electronics applications, the relationship between the printing parameters and their reliability and stability must be understood. This project will compare the aging and reliability of printed electrical traces to traditional plated copper traces.
A test board with plated copper traces of various lengths, and copper bond pads was created to directly compare electrical properties of printed and plated electrical traces. Silver traces of the same length and width as the copper traces were printed using aerosol jet and direct ink write printing processes. The first thermal aging study was for a total of 7 weeks at a temperature of 80 C, with electrical measurements and destructive physical analysis conducted after 1, 3, and 7 weeks. The second thermal aging test was conducted at 125 C for a total of 3 weeks, with electrical measurements and destructive physical analysis conducted after 1, 3, and 3 weeks.
The direct ink write traces were double the resistance of the plated copper traces, while the aerosol jet printed traces were 6-10 times the resistance of the plated traces. The DIW traces had only 20% of the traces within +/- 10% of the average resistance, while 80% of the aerosol jet printed traces were within 10% of the average resistance. After 7 weeks of aging, approximately 40% of the DIW traces failed ($\Delta R > 20\%$), while 25% of the aerosol jet printed traces failed. Scanning electron microscopy imaging of the surface of failed and functional devices did not identify a correlation between morphology or surface roughness and failure. Possible causes for variation in resistance and degradation will be discussed.
The thermal aging at 125 C of DIW traces saw an increase of 2-10 times the resistance after 1 week of aging. Additional changes in resistance were not significant in the second and third weeks of aging. In some cases, an oxide on the surface of the silver resulted in abnormally large values of resistance that were not always consistent or repeatable. Prior to aging, the DIW printed traces had improved repeatability, with at least half of the samples within 10% of the average resistance.
The DIW traces had lower resistance, but more variation in resistance and higher failure rates after aging. The aerosol jet printed traces had higher resistances, but less variation in resistance and fewer failures after aging. The results demonstrate that both direct write methods could produce reliable and stable electronic components. However, further investigation into the relationship between structure, printing process, electrical properties, and degradation mechanisms is required.

01:45 PM
Investigating Ag-Sn Transient Liquid Phase Sintering for Additive Manufacturing in Electronics (Student)
Mr. Clifton Buxbaum[1], Mr. Sebastian Winther[1], Prof. Patrick McCluskey[1]
[1]University of Maryland, College Park

Conventional manufacturing processes for electronics, especially substrate metallization, are wasteful and expensive. Substrate metallization consists of taking a fully metallized layer of material and removing the excess material to achieve the desired topology. The removal process frequently involves the use of harsh chemicals, and achieving the desired pattern requires complex equipment with unique tooling for each pattern. Depositing metal using additive manufacturing offers the potential to alleviate these challenges. The effect of material waste is reduced because metal is only deposited where needed, and each pattern is controlled by programming rather than tooling, reducing the time and cost of changing designs.
Direct ink writing has received attention for metallizing electronic substrates because the printing can be performed on low-cost equipment. The biggest challenge in direct ink writing is in the ink itself. Printing on electronic substrates typically requires pressureless sintering, and many available inks and pastes produce porous structures when sintered without pressure [1]. Of the available systems, nano-Cu and Cu-Sn pastes require atmospheric control during sintering to avoid oxidation of the print. Nano-Ag pastes do not require atmospheric control, but show limited adhesion to ceramic substrates [2][3].
This study aims to characterize the adhesion and conductivity of an Ag-Sn transient liquid phase Sintering (TLPS) paste, which can print and sinter in air, maintain good adhesion to alumina substrates, and still have good electrical resistivity, in additive manufacturing. During the process, the mixture will be heated above the melting point of Tin, which will melt, then surround and diffuse with the Silver. Preliminary results have shown good adhesion, resistivity, and printability, as shown in figures below.

02:00 PM
A Comprehensive Study of Dispense Printing: Unveiling Interactions Between Silver Flake Inks and Varied Substrates
Mr. Mohamad Kannan Idris[1], Dr. Gerd Grau[1]
[1]York University

The advancement of printed electronics is dependent on the understanding and precise control of the deposition of conductive materials on diverse substrates. This comprehensive study explores the intricacies of dispense printing, a versatile technique for fabricating intricate electronic patterns. We studied the interactions of two silver flake inks with both hydrophilic and hydrophobic surfaces, notably including Teflon—a substrate known for being challenging to print on due to its inherent hydrophobicity. This investigation depends on the understanding of key printing parameters: nozzle height, dispense pressure, and print speed, which control the ink's morphology and its interplay with the substrate, thereby influencing the outcome of the printing process. Our research rigorously examines the dispense printing process across its different phases—extrusion from the nozzle, ink spreading on the substrate, and line morphology alteration during drying. By considering these phases, we can understand how adjustments in different printing parameters influence the outcome on different substrates. The exploration uses understanding of the rheological properties of high-viscosity silver flake inks, namely NovaCentrix Metalon HPS-FG77 and Creative Materials 120-07(LPS), and their behavior under specific printing conditions. The study reveals that the substrate's wettability and the ink's viscosity are critical factors that dictate the spreading of the ink. In this work, we studied the

morphology of the lines when printed using different parameters on four surfaces with different surface wettability: glass, plasma-treated glass, Teflon, and plasma-treated Teflon. This methodology shows the different extrusion, spreading, and drying behaviors that the inks exhibit on hydrophilic and hydrophobic surfaces, underscoring the nuanced interaction between ink properties and substrate characteristics. The study shows that the dispense printing technique can work well on hydrophobic surfaces like Teflon if it is appropriately adapted to the challenges posed by the substrate's low wettability. The findings from this study also emphasize the significance of the drying and curing process, revealing that post-printing treatments have a significant effect on preserving the fidelity of the printed designs. Furthermore, our comparative analysis of different inks highlights the role of ink composition in determining printing success. The NovaCentrix ink, with its higher viscosity, demonstrates different spreading and drying behaviors compared to the Creative Materials ink, suggesting that ink selection should be tailored to the specific requirements of the substrate and the intended application. In summary, this study significantly advances the field of printed electronics by providing a deep dive into the dispense printing process's complexities. It offers actionable insights for selecting and optimizing printing parameters and ink formulations to enhance the quality and functionality of printed electronic devices. The detailed exploration of substrate-ink interactions opens new avenues for the application of printed electronics across a wider range of materials, pushing the boundaries of what is achievable in the domain of flexible and wearable electronics.

1:00 PM
Nanofabrication and Processing
Session Chairs: Pawan Tyagi (University of the District of Columbia), William Wong (University of Waterloo)
ESJ 2204

01:00 PM
Fabrication and Characterization of High-Frequency n-type Si/SiGe Fin Bulk Acoustic Resonators
Mrs. Normarieli Passalacqua Alvarado[1], Mr. Faysal Hakim[2], Dr. Keshab Sapkota[3], Dr. Aleem Siddiqui[3], Dr. Xuebin Li[4], Prof. Roozbeh Tabrizian[2], Dr. George Wang[5], Prof. Kevin Jones[1]
[1]Department of Materials Science and Engineering, University of Florida, [2]Department of Electrical and Computer Engineering, University of Florida, [3]Sandia National Laboratories, [4]Applied Materials, [5]Sandia National Laboratoories

In the realm of modern communication systems, radio frequency (RF) devices operating within the high-frequency (HF) regime (3-30 MHz) play a pivotal role. These devices find application in various domains, including shortwave broadcasting, amateur radio, skywave propagation, over-the-horizon radar (OTH), and maritime/aviation communication. The efficacy of these systems hinges significantly upon the quality factor (Q) of the devices, a parameter that influences characteristics such as frequency stability, selectivity, and energy dissipation. Conventional high-Q RF devices are often characterized by large size and power consumption, presenting challenges in integrated circuits (IC) packaging. Micro-electromechanical systems (MEMS), particularly surface acoustic wave (SAW) and bulk acoustic wave (BAW) devices, have emerged as a solution to address these challenges. MEMS exhibit the capability to provide high Q (>100,000) while maintaining a compact size, reduced weight, and lower power consumption (SWaP). Notably, film and fin bulk acoustic resonators (FBARs and FinBARs) have gained attention for their superior frequency and Q performance compared to SAW-based systems. Recent investigations highlight the suitability of single crystalline n-type silicon-based materials for MEMS fabrication. This choice is attributed to their ability to resonate in the HF regime and sustain oscillations, thanks to the thermo-resistive (piezoresistive effect) property exhibited by n-type Si under direct current (d.c.) application. Moreover, Si/SiGe heterostructures have recently garnered attention for their enhanced electrical properties, including larger current gain, better output conductance, and reduced noise margins, when compared to purely Si devices. The present study aims to advance this technology by fabricating high-frequency n-type Si/SiGe FinBARs and comprehensively characterizing their electrical and acoustic properties. The fabrication process starts with the epitaxial growth of a multilayered structure with alternating single crystalline n-type Si and SiGe layers via chemical vapor deposition (CVD) on silicon-on-insulator (SOI) wafers. Subsequent steps include the deposition of a piezoelectric and electrode material. Additionally, to induce electrical excitation, a through hole via is patterned followed by the deposition of a conducting material. To achieve a range of targeted frequencies (3-30 MHz), fins with varying widths (5-200 μm) are patterned. Finally, the device is released by removing the underlying substrate and buried oxide layer. Characterization of the multilayered structure and device is conducted using transmission and scanning electron microscopy. The Q factor of the devices are determined through optical excitation induced by ultrashort pulsed outputs from a titanium-sapphire laser system. Moreover, a vector network analyzer (VNA) is employed to identify the device’s resonance modes and to extract their frequency responses. Successful device fabrication is confirmed via a series of optical and SEM images. Preliminary computational studies support the thermo-electrical response of n-type Si layers, resonating in the high-frequency regime with a peak at 25 MHz.

01:15 PM
Focused Ion Beam Milling of Ta/Co/NiFe Magnetic Tunnel Junction based Molecular Spintronics Device (Student)
Mr. Hayden Brown[1], Dr. Eva Mutunga[1], Dr. Pawan Tyagi[2]
[1]University of the District of Columbia, [2]University of the district of Coulombia

In the realm of molecular spintronics, the fabrication of magnetic tunnel junctions (MTJs) using traditional techniques often faces challenges in achieving the desired precision and uniformity. This study introduced an advanced method utilizing focused ion beam (FIB) milling, specifically employing Gallium ions, to enhance the fabrication of

Ta/Co/NiFe/AlOx/NiFe magnetic tunnel junction-based molecular spintronics devices (MTJMSD). Our research aims to refine the fabrication process, focusing on the junction area, to improve the interaction between ferromagnetic electrodes (FMEs) and molecular transport channels. Operation of current MTJMSD configuration requires a 2 nm insulating layer where defects can arise and short-circuit the device [1]. Having a molecule bridge greater than 2 nm is challenging, so maintaining a short separation between FMEs while incorporating an insulating layer of 5 – 10 nm will minimize the chance of a short circuit while facilitating molecular connection. Plasma ion etching requires careful study to implement as problems like over-etching and lack of uniformity can occur [2]. This limitation becomes particularly pronounced in the context of MTJs, where the precision of the junction area is paramount. To address these challenges, our approach leverages the high-resolution capabilities of Gallium Ion FIB milling. This technique allows for precise etching of the junction area, enhancing the interface between FMEs and the insulating barrier, a critical factor for the optimal performance of MTJMSDs [3]. In our methodology, the FIB dose was varied from 4.1E-12 to 8.8E-11 pC/μm² to investigate its impact on etching depth within the FME layers. Key parameters such as beam energy, current, diameter, and overlap percentage were kept constant to isolate the effects of the FIB dose. We observed that the FIB etch depth exhibited a linear scaling with dosage, highlighting the precision and predictability of the FIB milling process. We achieved precise and uniform milling depths from 1 to 28 nm, a testament to the efficacy of FIB milling in achieving controlled etching at the nanoscale. This research demonstrates a marked improvement in the precision and control of MTJ fabrication and underscores the potential of Gallium Ion FIB milling as a transformative technique in the manufacturing of advanced molecular spintronics devices.

01:30 PM

Development and Characterization of a Tunnel Junction Chemical Sensing (TJCS) device for Neurochemical Detection with a Focus on Dopamine Sensing. (Student)

Mr. Pius Suh[1], Dr. Pawan Tyagi[2]
[1]University of the District of columbia, [2]University of the district of Coulombia

This paper presents the intricate development and comprehensive characterization of a Tunnel Junction Chemical Sensing (TJCS) device, specifically engineered for the detection of neurochemicals, with a primary focus on dopamine. The sensitivity and specificity of neurochemical detection are paramount in diagnosing and understanding a myriad of neurological disorders. Our TJCS device, based on a Magnetic Tunnel Junction (MTJ) structure, employs a sophisticated layering of Ta-NiFe (top electrode), AlOx (insulator), and Silicon (bottom electrode), each material chosen for its unique properties that contribute to the device's overall performance.
The fabrication of the MTJ involves a meticulous process, beginning with the Silicon substrate known for its excellent electronic properties and compatibility with semiconductor processing techniques. An ultra-thin AlOx layer (~2nm) is naturally oxidized to form the tunnel barrier, a critical component for achieving a high tunnel magnetoresistance (TMR) ratio. This ratio is pivotal in amplifying the sensitivity of the device to neurochemical stimuli. The Ta-NiFe layer, serving as the top electrode, completes the MTJ structure, ensuring robustness and contributing to the device's high sensitivity.
The characterization of the TJCS device demonstrates its remarkable potential in dopamine detection. The presence of dopamine induces a discernible change in the tunneling current, attributable to the interaction between the dopamine molecules and the AlOx barrier. This interaction subtly alters the electron tunneling dynamics, leading to a measurable modulation in the device's electrical properties. The TJCS device's response to varying concentrations of dopamine is meticulously recorded, highlighting its capability for not only qualitative but also quantitative neurochemical analysis.
The TJCS device marks a significant breakthrough in the neurochemical detection field, particularly for dopamine. Its innovative design, coupled with the high TMR effect and precise fabrication process, sets new benchmarks for sensitivity and specificity in neurochemical analysis, promising profound implications in both clinical diagnostics and neurological research domains.

01:45 PM

The Effect Of The Dimension Of Ferromagnetic Electrodes On The Magnetic Properties Of The Magnetic Tunnel Junction Based Molecular Spintronics Devices

Ms. Uzma Amir[1], Dr. Pawan Tyagi[2], Mr. Christopher D'Angelo[3]
[1]University of the District of columbia, [2]University of the district of Coulombia, [3]University of the District of Columbia

To investigate the impact of different dimensions of ferromagnetic (FM) electrodes and magnetic molecules, the magnetic tunnel junction based molecular spintronics device (MTJMSD) approach offers unprecedented opportunities. MTJMSD is formed by placing magnetic molecular channels along the exposed sides of a magnetic tunnel junction, with molecules appearing in the form of a ring around the tunnel barrier. However, the information about the dimensions of the FM electrodes physical dimensions and their effects on the magnetic properties of MTJMSD is limited. This paper will provide insight about the impact of FM electrode widths. Molecular spin channels that form strong coupling Heisenberg type exchange coupling coupled the spin properties at two FM electrodes. The effect of FM electrode and molecular channel coupling was investigated. We investigated spatial autocorrelation and magnetic susceptibility of the different parts of MTJMSD and overall device. We have studied the effect of FM electrode dimensions using continuous spin Monte Carlo Simulation (MSC) algorithm that has produced useful insights about the experimental observations. The effect of FM electrode dimension was strongly dependent on the magnetic molecule coupling with the two ferromagnetic electrodes. The spatial correlation of the magnetic molecular spin with FM electrode spins is found to be dependent on the FM electrode thickness of the FM electrodes. Additionally, local and global magnetic susceptibility calculations are performed to explore the switching potential of MTJMSD in multiple states. This study provides valuable insights into the intricate interplay between FM electrode dimensions and the magnetic properties of MTJMSD, advancing our understanding of molecular spintronics applications.

02:00 PM
Low Interface Defects (~ 10^10 cm^-2eV^-1) Solution Processed Charge Trapping Oxide (Student)
Mr. Atul Sachan[1], Prof. Sandip Mondal[2]
[1]Ph. D Research Scholar, IIT Bombay, India, [2]Assistant Professor, IIT Bombay

Introduction: The charge-trapping oxide is the heart of non-volatile storage memories that can be electrically programmed and erased has been used in a wide range of electronic devices, ranging from smartphones and laptop computers to industrial robots and self-driving cars [1]. This work demonstrates fully solution-processed charge-storing oxide grown using Aluminium Oxide Phosphate (ALPO). A metal oxide semiconductor (MOS) has been fabricated using solution-processed ALPO that are capable of storing charges of NT (ALPO) ~1.72×1013 cm-2 and simultaneously exhibit low leakage current density of 7.78×10-9 A/cm2 with a low interface trap density (DIT) of 9.96×1010 cm-2eV-1. The DIT plays a critical role in determining the performance of memory devices. High DIT leads to degraded device performance and increased power consumption, limiting the scalability of flash memory devices.
Device Fabrication: Solution-processed MOS [2] with structures (Al/ALPO/Si) were fabricated to test the memory behavior of oxide. These devices have been fabricated on Si wafers by spin coating of ALPO and followed by annealing at 275 °C for 1 hr in normal room environment. Circular top electrodes (Al) were fabricated using a shadow mask through thermal evaporation.
Result and Discussion: The devices (Al/ALPO/p-Si) were characterized through capacitance-voltage (CV) measurement at a high frequency of 1 MHz with a small signal of 50 mV (Fig. 1a). A change in flat band voltage is observed (ΔVFB) ~ 11.4 V and (ΔVFB) ~ 5 V at constant sweep voltage for different gate oxide thickness of around 90 nm and 30 nm respectively. This ΔVFB w.r.t to the thickness of the gate oxide remain constant because the electric field is inversely proportional to the thickness of the gate oxide (Fig. 1b). The significant amount of increase in ΔVFB from 2.3 V to 11.4 V because of the sweep voltage increases from ± 5 V to ± 15 V (Fig. 1c). Therefore, the number of trapped charges increases from 6.84×1011 cm-2 to 3.06×1012 cm-2 (Fig. 2a). The increase in trap charges is due to an enhancement in the electric field, which considerably increases the number of injected charges into the deep-level defects in ALPO [3]. Fig. 2b shows the results as a function of , or band bending. To calculate , a graphical or numerical differentiation of vs. VG was used. CIT() was determined using equation (1), as shown below [4].
Once CIT is determined from equation (1), DIT can be calculated using equation (2), where Cox is the maximum capacitance per unit area calculated from the high frequency CV curve, and Csi denotes the silicon surface capacitance per unit area, which varies accordingly . Remarkably, with a DIT value at the mid-gap region of 9.96×1010 cm-2eV-1, the ALPO exhibits an interface trap density closer to that of SiO2. As we increase the gate sweep voltage there is increase in the trap density as shown in Fig. 2c. Beyond 15 V, (electric field ~ 1.25 MVcm-1) due to which it leads to increase in charge loss that significantly increases the leakage current from 1.8×10-8 A/cm2 to 15.6×10-8 A/cm2, thus there is a reduction in the hysteresis window (Inset Fig. 2c). At room temperature there is variation in the leakage current density from 7.78×10-9 A/cm2 to 3.78×10-8 A/cm2. Thinner the barrier, the higher the probability of tunneling, leading to increased leakage currents (Fig. 3a). The band diagram of devices has been realized to understand the underlying mechanism of the charge trapping with an electron affinity and band gap of ALPO of EA(ALPO) = 1.35 eV, Eg(ALPO) = 7.6 eV respectively (Fig. 3b). This configuration signifies equilibrium under zero gate bias, where the fermi level aligns with the mid-gap energy levels. At Vg < 0, the energy band experiences bending and depleting charges towards the Si-ALPO interface and injecting the charges to the deep level traps (Fig. 3c) [4]. During inversion, while Vg > 0, the stored charges get ejected to metal gate from Si-ALPO interface, which leads to the elimination of charges from the huge deep level traps (Fig. 3d).
Conclusion: We grown solution-processed ALPO at low-temperature (~ 275 °C), highly useful for flexible charge-trapping memory devices applications. The ALPO based-MOS device characteristics have been explained using band diagram that are useful for predicting the reliability of devices.
The authors thank to Nanofabrication Centre (IIT-BNF) at IIT Bombay, Mumbai, India.

1:00 PM
SiC Materials, Characterization, and Devices
Session Chairs: Nadeemulah Mahadik (Naval Research Lab), Patrick Lenahan (Penn State University)
ESJ 1224

01:00 PM
Comparison between epitaxial and implanted aluminum-doped 4H-SiC
Dr. Suman Das[1], Dr. Daniel Lichtenwalner[2], Dr. Shane Stein[1], Dr. Jae-Hyung Park[1], Dr. Philipp Steinmann[1], Dr. Sei-Hyung Ryu[3]
[1]Research Scientist, [2]Manager Process Development Engineering, [3]Director Research Science

Silicon carbide is one of the most promising semiconductors for fabricating power devices. It can be doped via epitaxially grown p- or n-type dopants, or by ion implantation. Although ion implantation has its own disadvantages like implant damage [1,2], and energy state creation [2,3], it is typically necessary for power device fabrication. A rigorous study comparing the key difference between the two types of doping would be helpful for a better understanding of the

possible effects of damage or trap generation due to ion implantation.
In this work, a comparison between epitaxially-doped and implanted Aluminum (Al) is performed to compare the electrical behavior obtained using the two types of doping procedures. Al dopant is either implanted up to 1 um deep in a box profile and activated near 1600 oC, or epitaxially grown on 150 mm Si-face on n-type 4H-SiC (0001), 4 degree off-axis wafers. To study the electrical characteristics, square van der Pauw structures (1 cm×1 cm) were made, shown schematically in Fig. 1 (a, b). To obtain ohmic contacts, a high dose of Al (>5×1019) was implanted at four corners of the van der Pauw structures, and Ni contacts were deposited and annealed at high temperature. The samples were then diced, and 4-point probe resistance and Hall measurements were conducted to obtain resistivity, carrier concentration, and Hall mobility. Thereafter, dopant activation percentage and ionization energy levels are calculated using a one or two-level charge neutrality model, as discussed below.
Figure 2 shows the resistivity versus temperature curve for different implanted and epitaxial grown Al-doped samples. For the implanted samples resistivity is higher at room temperature and increases at a faster rate as temperature drops. An epi doping of 2×1017 cm-3 shows lower resistivity than a 2.5×1017 cm-3 implanted sample. In Fig. 3, carrier concentration is shown as a function of temperature. Here the 2x1017 cm-3-doped epi is seen to reach its maximum ionization level at a faster rate with higher values compared to the comparable implanted samples. Figure 4 shows the comparison of mobilities for differently doped samples. Counter-intuitively, the data shows that the epi 2×1017 sample shows higher mobility at lower temperatures compared to an implanted doping of 1×1017 cm-3.
The carrier concentrations are then modeled using a two-level charge neutrality model, with assigned specific ionization energies to each level as shown in Fig. 5. The epitaxially grown Al sample fits perfectly with the model after applying a Hall scattering factor correction [4,5] with a single ionization energy of 230 meV, and 100% dopant activation. However, to properly fit the implanted Al sample data with the calculated data, two different ionization energies (~240 meV shallow energy state, and ~360 meV deep energy state) are needed as shown in Fig. 6 for the implanted 1×1017 cm-3 sample. The deep energy level seems to appear specifically due to Al ion implantation. Earlier research indicates that these states could be deep hole traps [1-3] named DI defects [2]. Table I summarizes the ionization energies and fraction of atoms present at each energy state (α). Al implanted SiC behaves differently than epitaxially grown SiC doped with Al; and therefore, these two types of Al doped SiC need to be treated differently for modelling. The activation percentages and ionization energies extracted from the data will be useful to understand ion implantation effects better and for proper calibration of Technology Computer Aided Design (TCAD) models for electrical simulations of 4H-SiC-based devices.
[1] L. Patrick and W. J. Choyke, Phys. Rev. B 5, 3253, (1972)
[2] L. Storasta et al., Appl. Phys. Lett. 78, 46 (2001)
[3] K. Kawahara et al., J. App. Physics 108, 033706, (2010)
[4] G. Pensl et. Al., Mat. Sc. Forum, 433-436, (2003),
[5] Koizumi, Suda, and Kimoto, J. Appl. Phys. 106, 013716 (2009)

01:15 PM
Microstructural Analysis of Different Stacking Faults in 180um Thick SiC epitaxial layers
Dr. Nadeemulah Mahadik[1], Dr. Robert Stahlbush[2], Mr. David Scheiman[2]
[1]Naval Research Lab, [2]U.S Naval Research Laboratory

Silicon carbide (4H-SiC) devices with blocking voltage rating up to 3.3kV have been successfully commercialized [1]. Two key factors for this are the availability of lower cost, high quality SiC substrates, and the availability of low defect epitaxial layers with a thickness of up to 30 mm. SiC devices also have the potential to outperform Si devices for higher voltage applications beyond 6.5kV due to lower power dissipation and superior thermal conductivity [2]. For this, thicker epitaxial layers are required for higher blocking voltage. In-grown stacking faults (IGSF) can be generated during epitaxial growth of SiC and can have a more complex nature in thick epitaxial layers [3]. These IGSFs can cause device leakage and can also result in surface defects that may influence oxide reliability in SiC MOSFETs. Hence, it is essential to investigate their formation and microstructure. In this work, we perform investigation of IGSFs that were formed during different times of epitaxial growth, analyze their microstructure and identify possible formation mechanisms using ultraviolet photoluminescence (UVPL) imaging and X-ray topography (XRT).
For this work we used, 180µm thick SiC epitaxial layers with n-doping of 5x1014 cm-3. This was commercially grown on 4H-SiC substrates with a 20mm thick highly n-doped buffer layer. UVPL extended defect mapping of the 150mm diameter wafer was performed on a custom setup with 355nm laser excitation. The 660-1000nm luminescence images were collected using a cooled CCD detector. Additionally, spectra; UVPL mapping of selected defects were carrier out with several bandpass filters Whole wafer XRT was performed on the Rigaku XRTmicron system using reflection, transmission and section topography. Section topography was performed on selected sample IGSF regions to investigate defect evolution and propagation with depth. Multiple Bragg conditions were used in each geometry to analyze defect types and Burgers vectors.
Overall in the wafer, there were almost no BPDs that had propagated from the substrate to the epitaxial layer due to implementation of widely known mitigation strategies such as hydrogen etching, conversion in buffer layer, etc. However, new sources of BPDs are introduced during epitaxial growth, such as inclusions due to fall downs and other BPD loops. Custom BPD counting software was employed to obtain statistics on BPD density in the wafers. Almost 50% of the wafer was found to be BPD-free, which is remarkable for SiC wafers with such high thickness epitaxial layers. IGSFs of various sizes were observed in the wafers as shown in Fig 1. This indicates that they did not form at the substrate / epitaxial interface but at a later stage during epitaxial growth. They also appeared to have different microstructure. Many of them were a Frank-type IGSF, but there were others that also had a Shockley component. This was observed using multi-vector XRT imaging of the same defect regions as shown in Fig. 2 where the XRT contrast indicates presence of multiple components of fault vectors for different faults. Further details from spectral UVPL will be shown to determine the various fault types in more detail from their emission spectra. Additionally, depth resolved

section XRT will be shown to investigate their origins in the epitaxial layer and determine what led to their formation.
[1] D. Xing et al., pp 1-6, 2020 WiPDA Asia, doi.org/10.1109/WiPDAAsia49671.2020.9360270.
[2] J. Wang, et. al., IEEE Industrial Electronics Magazine, 3, 16-23, (2009).
[3] N. A. Mahadik, et. Al., Scripta Materialia 235, 115598, (2023).

01:30 PM
Analysis of Inclusions and Associated Dislocation Configurations in 4H-SiC Wafers through Synchrotron X-Ray Topography (Student)
Ms. Qianyu Cheng[1], Mr. Zeyu Chen[1], Ms. Shanshan Hu[1], Dr. Balaji Raghothamachar[1], Prof. Michael Dudley[1]
[1]Stony Brook University

The blooming of electronic and optoelectronic devices industries leads semiconducting materials to a rapidly expanding role in contemporary high technology society. Among all semiconductors, silicon carbide (SiC) as a superior wide bandgap material has been the focus of worldwide research during the recent decades. SiC is steadily replacing conventional semiconducting materials owing to its outstanding properties such as larger bandgap, higher electron saturation velocity and thermal conductivity [1, 2], which enables its wide application in high-frequency, high-temperature, and high-power device fabrication. The key to maintain the performance of this excellent material is manufacturing large-scale, high-quality, polytypic stable SiC substrate wafers. Therefore, understanding the nature and origins of crystallographic defects within SiC is a major research pursuit since those can induce degradation that challenges device reliability while achieving high performance [3]. Synchrotron X-ray topography (XRT) [4, 5] is a powerful characterization technique that has been widely applied in semiconductor materials research as a non-destructive method to generate high-resolution X-ray images of the internal structure of a crystal. Crystallographic defects and structural features are then revealed as topographic contrast features that can be identified applying contrast formation mechanisms. Extensive studies on the observation of various dislocation configurations, stacking faults and low angle grain boundaries have been carried out in this manner. In this study, we focus on hexagonal features observed optically on a 6-inch 4° off-axis 4H-SiC substrate wafer that presents correlated topographic contrasts in synchrotron XRT recorded through both transmission and grazing-incidence geometries. These hexagonal features are identified as inclusions as topographs reveal the generation of large strain fields associated with them. The activation of prismatic slip is found to be induced by the presence of inclusions as both regular (9keV) and high energy (18keV) grazing-incidence topographs show threading edge dislocation (TED) slip bands expand from inclusions along <11-20> directions. Basal plane dislocation (BPD) half loops are also observed associated with inclusions. Using ray-tracing simulation technique based on orientation contrast mechanism [6,7], inclusion contrast will be simulated and compared to X-ray topograph images to estimate the strains induced. This will provide insights on the stresses that induce basal and prismatic slip.
Reference:
[1] Matsunami, H., Current SiC technology for power electronic devices beyond Si. Microelectronic Engineering, 2006. 83(1): p. 2-4.
[2] Codreanu, C., et al., Comparison of 3c SiC, 6h SiC and 4H SiC MESFETs performances. Materials Science in Semiconductor Processing, 2000. 3: p. 137-142.
[3] Neudeck, P.G., Electrical Impact of SiC Structural Crystal Defects on High Electric Field Devices. Materials Science Forum, 2000. 338-342: p. 1161-1166.
[4] Tanner, B.K. and D.K. Bowen, Synchrotron X-radiation topography. Materials Science Reports, 1992. 8(8): p. 371-407.
[5] Lang, A.R., The early days of high-resolution X-ray topography. Journal of Physics D: Applied Physics, 1993. 26(4A): p. A1.
[6] Huang, X.R., et al., Superscrew dislocation contrast on synchrotron white-beam topographs: an accurate description of the direct dislocation image. Journal of Applied Crystallography, 1999. 32(3): p. 516-524.
[7] Dudley, M., X.R. Huang, and W. Huang, Assessment of orientation and extinction contrast contributions to the direct dislocation image. Journal of Physics D: Applied Physics, 1999. 32(10A): p. A139.

01:45 PM
Frank dislocations generation and behavior investigation in PVT-grown 4H-SiC crystals (Student)
Ms. Shanshan Hu[1], Mr. Zeyu Chen[1], Ms. Qianyu Cheng[1], Dr. Balaji Raghothamachar[1], Prof. Michael Dudley[1]
[1]Stony Brook University

With wide band gap, high thermal conductivity, and high breakdown field, silicon carbide, typically 4H-SiC, has steadily become the material of choice for next generation high-power electronic devices[1]. However, the presence of defects especially dislocations, such as micropipes (MPs), threading screw dislocations (TSDs), threading edge dislocations (TEDs), basal plane dislocations (BPDs), and Frank dislocations, are hindering the widespread application of 4H-SiC device due to their harmful effects on the reliability of high-performance SiC power devices. In particular, Frank dislocations are particularly deleterious since Frank SFs and Shockley-Frank SFs associated with Frank dislocations can lead to increased reverse leakage current for p-n and Schottky diodes[2]. Formation of Frank dislocations is related to deflection of TSDs/TMDs by the overgrowth of macro-steps during the PVT crystal growth process[3]. Deflection processes can reduce dislocation content in the growing crystal, but it is desirable to limit it to early stages of growth near boule edges and minimize it in the middle of the boule to maximize yield. A more detailed understanding of these deflection processes is needed to optimize Frank dislocations generation and behavior inside the 4H-SiC crystals.
In this study, axial wafers from several 6 in. 4° off-axis (0001) boules of SiC grown by PVT method are prepared and characterized by synchrotron X-ray topography. 000 12 back reflection images reveal Frank dislocations have black contrast on one side and white contrast on the other side (Figure1). The distribution of Franks dislocations is related to the as-grown surface shape of the boule. The region with larger angle between the surface of the boule and the basal plane encourages larger macrostep formation (Figure2) and

thus Frank dislocation generation. A detailed analysis is being carried out to establish a relationship between the angle between the as-grown surface and basal plane and the incidence of Frank dislocation generation. This will enable determining a critical angle for deflection. Seed and as grown sides of the boules will also be corelated to reveal generation and behavior of Frank dislocations during crystal growth.
References:
[1] G. Dhanaraj, K. Byrappa, V. Prasad, M. Dudley: Springer handbook of crystal growth. Springer, 2010.
[2] H. Tsuchida, M. Ito, I. Kamata, M. Nagano, Formation of extended defects in 4H SiC epitaxial growth and development of a fast growth technique. physica status solidi (b) 246 (2009), 1553-1568.
[3] M. Dudley, F. Wu, H. Wang, S. Byrappa, B. Raghothamachar, G. Choi, S. Sun, E. Sanchez, D. Hansen, R. Drachev, Stacking faults created by the combined deflection of threading dislocations of Burgers vector c and c+ a during the physical vapor transport growth of 4H–SiC. Applied Physics Letters 98 (2011), 232110.

02:00 PM
Mitigation of BPD Faulting Using H2 Etches for Pulsed Power Applications
Dr. Rachael Myers-Ward[1], Dr. Nadeemulah Mahadik[1], Dr. Michael Liao[2], Dr. Geoffrey Foster[3], Dr. Samuel White[3], Dr. Jenifer Hajzus[1], Dr. Daniel Pennachio[1], Dr. Andrew Koehler[3]
[1]Naval Research Lab, [2]U.S Naval Research Laboratory, [3]US Naval Research Laboratory

Basal plane dislocations (BPDs) have been a concern for SiC high-voltage bipolar devices for many years as they source Shockley-type stacking faults in the presence of an electron-hole plasma and reduce minority carrier lifetimes [1]. There has been much focus on the reduction of BPD densities including pre-growth treatments [2], growth interrupts [3], and proton implantation [4]. It has been demonstrated that with sufficient carrier injection, BPDs from the highly doped buffer layer or substrate can expand and propagate into the drift layer [5], causing device failure. Therefore, a technique is needed to prevent BPD faulting during high carrier injection for high peak, pulsed power applications. In this paper, we use an in-situ H2 etch process to mitigate BPD faulting under high-power UV exposure at 12 kW/cm2, which is equivalent to ~1x1019 cm-3 carrier injection in the substrate.
Intentionally doped (ID) n-type (~ 5x1015 cm-3) epitaxial layers were grown on 4° off-axis substrates in a horizontal hot-wall chemical vapor deposition reactor using the standard chemistry of silane (2% in H2) and propane. Growth was conducted at 1620 °C, 100 mbar, and a C/Si of 1.55. A 6 µm buffer layer (n-type ~ 2x1018 cm-3) was grown prior to the ID drift layer. A H2 etch was performed at different stages of the growth to determine its impact on BPD faulting. The etch was conducted at 1665 °C and 70 mbar for 50 min, either before the buffer layer (BL), after the BL, or both before and after the BL. A fourth sample was grown with a H2 etch prior to the BL and a growth interrupt after the BL. The growth interrupt consisted of reducing the temperature to 1000 °C in H2 and immediately ramping back to the growth temperature, after which the ID drift layer was grown. A control sample was grown without any etches or growth interrupt. Ultraviolet photoluminescence (UVPL) imaging was used to identify the BPD faulting behavior after epitaxial growth, and before and after UV stressing.
When exposing the control sample to 300 W/cm2, the BPDs present in the BL faulted after 420 s of UV exposure and continued to propagate throughout the drift layer. For the sample with a H2 etch between the BL and ID drift layer, only the pre-existing BPDs in the drift layer faulted at 300 W/cm2, and no BPDs from the BL faulted after > 1240 s. Similar results were found for the sample grown with a H2 etch before and after the BL. When these two H2 etched samples (etched before and after the BL, and etched after the BL) were stressed at an increased UV exposure of 1 kW/cm2, again, no faulting of BL or substrate BPDs were observed after 1900 s. With 10X higher power density (12 kW/cm2), BPD faulting from the substrate occurred for both of the H2 etched samples. However, for the sample with just a single H2 etch between the BL and drift layer, the density of additional BPD faulting was ~ 200 BPDs/cm2, whereas when the H2 etch was performed before and after the BL, the density of newly faulted BPDs was only ~ 50 BPD/cm2. For the sample grown with a H2 etch before and a growth interrupt after the BL, BPDs did not expand at 12 kW/cm2. Carrier concentration was simulated as a function of epitaxial layer depth for the various UV laser powers. At the highest power density, the injected carrier concentration is higher than the doping of all the layers, which should lead to recombination induced BPD faulting in the substrate, BL and ID epilayer. We propose that H2 from the H2 etch and growth interrupt pin the BPDs and prevent them from expanding. This level of suppression of BPD expansion, to our knowledge, has not been demonstrated before at these power densities.
[1] J.P. Bergman, et al., Mater. Sci. Forum Vol. 353-356, 299 (2001).
[2] N.A. Mahadik et.al., Mater Sci Forum 858, 233 (2016).
[3] R. E. Stahlbush, et al., Appl. Phys. Lett. 94, 041916 (2009).
[4] M. Kato, et al., Sci. Rep., 12, 18790 (2022).
[5] N.A. Mahadik, et. al., Appl. Phys. Lett., 100, 042102 (2012).

1:00 PM
Materials for Memory and Computation
Session Chairs: Susan Fullerton (University of Pittsburgh), Eric Seabron (Howard University)
ESJ 1202

01:00 PM
Phase Change Chalcogenides for Functional Photonics and Electronics: Advanced Materials, Metrology, and Devices
Prof. Eric Seabron[1], Mr. Robert Coleman[1]
[1]Howard University

Significant strides in information processing technologies,

such as Integrated Microwave Photonics, Neuromorphic Computing, and Quantum Photonics, have been realized through the advancement of functional light-matter-heat interactions and electron transport phenomena enabling innovative device capabilities. Phase Change Chalcogenide materials (PCMs) have emerged as a promising material platform enabling active wavefront manipulation in free space optics, analog tuning in photonic integrated circuits, and reconfigurability in microwave electronics. Their intriguing functionality stems from non-volatile, reversible changes in material properties resulting from thermally induced amorphous-crystalline phase transitions, notably exhibiting a substantial contrast in conductivity and permittivity across a broad electromagnetic spectrum. Despite their attractive and promising attributes, the energy-efficient, robust, and CMOS-compatible electrical reconfigurability of PCMs has been elusive and is particularly challenging to achieve for both electronic and photonic platforms. This presentation delves into the challenges and opportunities of integrating PCMs into functional photonics, optoelectronics, electronic memristors, and memcapacitors. Various methods for lowering the phase transition temperature and improving the cyclability of PCMs by engineering their chemical composition and physical structure are discussed in detail. In support of these efforts, we have also developed advanced methods for nanoscale characterization of PCMs using Scanning Near-Field Optical Microscopy (SNOM) and Multiphoton Confocal Microscopy (MCM) in tandem with Electron Microscopy techniques. Both MCM and SNOM provide a strategic advantage for in situ metrology, by analyzing the functional behavior of PCMs during cycling by inducing thermal phase transitions using the microscope's laser source or patterned electrical microheaters. Additionally, we will propose several device platforms with strong mode confinement, enabling the co-integration of PCMs with significantly reduced volume fractions crucial for reducing overall power consumption. The primary objective of this talk is to showcase recent progress in advancing PCMs for functional electronic and photonic devices, aiming to deepen our understanding of new materials, device failure, novel transport physics, and intriguing nanoscale light-matter-heat phenomena.

01:15 PM
Entropy-stabilized oxide memristors
Prof. Sieun Chae[1], Dr. Sangmin Yoo[2], Prof. Emmanouil Kioupakis[2], Prof. Wei Lu[2], Prof. John Heron[2]
[1]Oregon State University, [2]University of Michigan

Memristor arrays have emerged as a promising hardware platform for efficient machine learning tasks. Traditional amorphous oxide-based memristor materials, however, suffer from device stochasticity and a lack of tunability which hinder applications requiring adaptive networks. Here I will present a study on tunable carrier transport and dynamics in single crystalline (MgCoNiCuZn)O entropy-stabilized oxide (ESO) thin films. We find that the ESO undergoes composition tunable hopping conduction in agreement with the composition dependent point defect formation and electronic structure from first principles calculations. Notably, the transport is bulk and non-filamentary. Pulsed measurements reveal a low resistance state with a short, composition-tunable retention time that can be harnessed for memristor function via temporal data processing. We interpret the carrier dynamics in terms of voltage modulated filling of deep level defects states that are controlled by composition as predicted by theory. The precise tunability of carrier transport in this ESO make it an excellent candidate for "task specific" neural network systems with record energy efficiency for temporal data processing.

01:30 PM
Understanding the Interplay of Device Geometry on the Temporal Response of Lithium Intercalation Synapses for Enhanced Neural Computation Beyond the Cross-bar Architecture (Student)
Mr. Timothy McCrone[1], Dr. Aheli Ghosh[1], Mr. Alex Weidenbach[1], Dr. Bill Zivasatienraj[1], Prof. William Doolittle[2]
[1]Georgia Institute of Technology, School of Electrical and Computer Engineering, [2]Georgia Institute of Technology

Memristors are a category of devices that can perform compute-in-memory operations like a synapse [1]. But most memristive devices are not capable of implementing the temporal dynamics that occur in the brain. Lithium-ion intercalation memristors can implement these temporal dynamics including time, phase, frequency, and magnitude sensitivity [2]. One of these memristors is lithium niobite ($LiNbO_2$). $LiNbO_2$ is attractive due to its low power <100 mV operation, wide dynamic range of 9000%, and linear programming behavior. Prior work on $LiNbO_2$ has shown the ability to change the speed of operation of the memristor statically by adjusting the dimensions of the device and dynamically by Li intercalation [2]. Likewise, by varying the device geometry, both the absolute resistance and the dynamic range of the resistance change can be engineered [2,3]. The diverse temporal dynamics – specifically the ability to have volatile and non-volatile memristors within the same material/chip - and unique low voltage/high dynamic range characteristics have been shown to enable lifetime self-learning without the need to directly access each memristor via use of non-crossbar memristor arrays that more accurately mimic mammalian neural pathways [3]. Understanding the electrical behavior of the programming phenomenon in these devices and how the material continues to scale is the key to understanding their potential as a solution. These devices are shown here to have an initial cycle clockwise hysteresis behavior that switches to a counterclockwise behavior with ~100x current increase on all further cycling. After this initial cycle, the devices see a substantial increase in conductivity for positive voltages that matches the expected behavior for a positive voltage driving Li^+ into the lithium soluble Ag electrode, increasing conductivity. Likewise, a negative voltage drives Li^+ back into the channel, decreasing conductivity. The change in behavior after initial cycling suggests an initial impediment to Li^+ permeation into the Li-soluble electrode, the existence of a change of chemistry/phase at the electrode interface or within the channel itself. After initial cycling, a minimum programming voltage is found to scale with device length. As the length of the device is changed this programming threshold decreases from 750 mV to <100 mV in smaller devices. This scaling behavior indicates a dependence on the electric field. In addition, this programing threshold is observed to decrease only slightly with temperature, indicating neither diffusion nor the thermal activation of Li^+ is the primary origin of the thresholding mechanism. The

testing at temperatures as high as 150°C also indicates that LiNbO2 is stably programmable over a wide range of temperatures. While it has already been shown that the programming voltages and resistance ranges vary drastically depending on electrode chemistry, the lack of significant temperature dependence suggests a programing mechanism independent of thermal activation, possibly ion drift through a vacancy rich channel [4]. The fully analog behavior of this programming response is also shown in both the programming and deprogramming directions with a hysteresis that scales with the magnitude of the input which can be controlled through either voltage or current compliance. Finally, during deprogramming, a unique temporal response, negative differential resistance (NDR), is observed. In addition, this NDR feature disappears as the device is programmed and deprogrammed at higher frequencies, indicating a relation to ion dynamics, possibly ionic momentum. This thorough investigation of the features of the programming and deprogramming of LiNbO2 memristors produces insight into Li+ intercalation memristors that will drive further research into their opportunities in neuromorphic computing.

[1] S, Chen et al. Adv. Mater. 35, 2301924 (2023)
[2] A. Ghosh et al. IEEE Transactions on Electron Devices. 70, 2, 776-781 (2023)
[3] B. Zivasatienraj et al. Frontiers in Neuroscience. 17 1153183 (2023)
[4] A. Ghosh et al. ECS J. Solid State Sci. Technol. 9 055018 (2020)
[5] A. Ghosh, Adaptive Oxide Based Low-Power Memristive Devices for Neuromorphic Computing

01:45 PM

Bit Error Rate Probability of Single and Multi Level Cell Flash Memory (Student)

Mr. Dharmendra Kumar Singh[1], Dr. Arjun Shetty[2], Prof. Sandip Mondal[3]
[1]Ph. D Research Scholar, IIT Bombay, [2]Intel Corporation Santa Clara, California, United States, [3]Assistant Professor, IIT Bombay

Solid state memories are the heart of current semiconductor technology as they store high volume data for computational purpose. The NAND flash-based storage system are the most suitable solution to store high volume data in the solid state drives due to its compact size, lower power requirement, higher storage density and faster program/read/erase operation cycle [1]. Memory technology is constantly striving to store higher density data in smaller form factors with reduction of cost. Such requirements can be fulfilled by 3D NAND flash memory due to its layered structure where memory layers are placed vertically in stack. On the other hand, the 2D NAND flash memories are horizontal in nature. Stacking of memory layers in 3D NAND flash also leads to bit errors with variation in irradiation dose [2]. Data is getting stored in digital format in 2D NAND as well as 3D NAND flash but bits are getting effected by gamma irradiation when technology nodes differs [3]. In this paper we have monitored bit flipping behaviour of 2D-NAND Single Level Cell (SLC) as well as 3D NAND multi-level cell (MLC) memory at high temperatures. At higher temperatures, there is charge loss from the floating gate and from de-trapping of traps in the tunnelling oxide. This charge loss can eventually lead to a bit flip in the stored data.

To see the impact of temperature variation on bits flipping of commercial 2D and 3D NAND flash memory we have taken initial 50 blocks. We have used 3D flash memory (MT29F256G08CBCBBWP-10: B which is 256 Gbit MLC) for experiment. Likewise, we have considered 2D-NAND (29F4G08ABADA, 4-Gbit SLC) for comparison with 3D NAND memory device. Before starting the experiment, we have performed five program/Erase (P/E) cycles to initialise 50 fresh blocks on both type of memory devices. Both chips were baked at 120° C for 7 hours with read outs taken after every hour. After every hour of baking, the chip was taken out from the hot plate and it was kept for 20 minutes cooling at room temperature then the measurement was performed. In this experiment, block wise bit flipping recorded with the help of data acquisition system fig.2 (a) including TSOP 48 socket for holding raw NAND Flash chip, FT2232H mini module microcontroller which is controlling flow of various operations inside memory and PC.
Fig.1 (a) represents floating gate-based transistor which have tunnel oxide, floating gate, gate oxide and control gate P type Silicon substrate. Based on voltage applied different operations like read/write/erase has been performed but there is leakage of charges occurred during charge de-trapping which creates errors in the bit.Fig.1 (b) represents schematic view of 3D NAND flash memory, it has number of columns in which all the cells are getting connected in series string form. Due to complex structure it shows more leakage inside dielectric material. In Fig.2 (b) and (c) we observe increase in mean bit error rates (BER) with respect to baking time in 2D NAND as well as 3D NAND Flash memory but 3D NAND is showing opposite behaviour than 2D NAND flash memory. Fig.3 (a) and (b) shows block wise BER variation during 0 hour to 7 hours of baking in 2D and 3D NAND respectively. In this figure we can clearly depict that 3D NAND flash memory shows more bit flipping probability in order to compare with 2D NAND Flash memory. Here in fig. 3 (c) shows block wise variation when we are taking BER ratio of 2D and 3D NAND Flash memory, here in 7th hours of baking bit error probability is reached at highest level.
In conclusion, we can conclude that 3D NAND flash memory shows more bit variation than 2D NAND flash memory and we need to more powerful firmware software inside controller to correct these bits flipping inside 3D NAND flash memory. This analysis is too beneficial for satellite communication application where massages are getting transmitted through different layers of atmosphere.

02:00 PM

Quantum Enhanced Josephson Junction Field-Effect Transistors for Logic Applications

Dr. Wei Pan[1], Dr. Aaron Muhowski[2], Dr. Bill Martinez[1], Dr. Courtney Sovinec[1], Dr. Juan Mendez[1], Dr. Denis Mamaluy[1]
[1]Sandia National Laboratories, [2]Sandia National Labs, Albuquerque, NM 87185, USA

The need of data centers for cloud and network computing has dramatically increased power consumption. In 2014, data centers in the U.S. consumed an estimated 70 billion kWh, representing about 1.8% of total U.S. electricity consumption [“United States Data Center Energy Usage Report," published in June 2016 and supported by the Federal Energy Management Program of the U.S. Department of Energy]. Worldwide, the International Energy

Agency estimates that currently about 1% of all global electricity is used by data centers. It is expected that by 2030 the electricity use of information and communications technology may exceed 20% of all global electricity. The microelectronics industry has been focusing on aggressively shrinking the size of logic and memory devices to reduce power consumption. However, this scaling is going to eventually stop as we approach the fundamental materials limit. Moreover, the power dissipation due to the increased number of transistors is also expected to be a limiting factor for processor performance.

Superconducting computing has been suggested as a promising approach for low-energy, power-efficient circuit applications. Moreover, using superconducting interconnects can further reduce power consumption. Josephson junction field-effect transistors (JJFET, Fig. 1a) have recently emerged as a promising candidate for superconducting computing. JJFETs are particularly useful for low power consumption applications as they are operated with, in the superconducting regime, zero voltage drop across its source and drain. Feasibility of using JJFETs for logic operations has been explored [1]. Moreover, high noise margin has been demonstrated for the logic inputs [2]. Compared to single flux quantum approach, JJFET circuits can use designs similar to conventional silicon MOSFETs [1].

For JJFETs to perform logic operations, the gain-factor (αR) value must be larger than 1. Here

αR = dIc/d(Vg–Vt) x πΔ/Ic, Δ is the superconducting gap, Vg the gate bias voltage, Vt the threshold voltage. Ic ∝ exp(-L/ξc) is the critical supercurrent, where L is the channel length and ξc the carrier coherence length [3]. In a conventional JJFET, ξc ∝ (Vg–Vt)0.5 (Fig. 1b), and thus dIc/d(Vg–Vt) is small (Fig. 1c). This translates to a requirement of superconducting transition temperature of ~ 400K for αR larger than 1, far exceeding any recorded critical temperatures. As such, it is impossible to use conventional JJFETs for logic operations.

Device and Results

Here, we propose a novel type of JJFET based on quantum phase transition, such as the excitonic insulator (EI) transition in a type-II InAs/GaSb heterostructure [4], for low-energy, power-efficient logic applications. The nature of the collective phenomenon in the EI quantum phase transition can provide a sharp transition of the supercurrent states (e.g., ξc ∝ (Vg–Vt)5 and dIc/d(Vg–Vt) very large, as shown in Figs. 1b and 1c, respectively) which will enable αR larger than 1 with an easy-to-achieve superconducting transition temperature of ~ 40K. In this talk, we will present some preliminary results demonstrating that indeed the gain factor in these quantum enhanced JJFETs can be greatly improved, thus making them a promising candidate for logic applications.

Fig. 2a shows a JJFET made of a zero-gap InAs/GaSb heterostructure with tantalum (Ta) as the source and drain electrodes. The superconducting critical current in the JJFET is zero when Vg-Vt ≤ 0.23V, but sharply jumps to a finite value at Vg-Vt = 0.24V and then increases slowly as Vg-Vt continues to increase (Fig. 2b). The gain factor is calculated to be ~ 0.06. Though still less than 1, it is already more than 50 times larger than that recently reported in a conventional JJFET made of InAs quantum wells [5]. With further optimization, a sharper excitonic insulator transition can be achieved. Together with a higher superconducting transition temperature, a large gain factor can be expected.

References

[1] F. Wen et al., IEEE Transactions on Electron Devices 66, 5367 (2019).
[2] S.R.S. Raman et al., IEEE Transactions on Applied Superconductivity 31, 1800105 (2021).
[3] D.J. Frank, Cryogenics 30, 996 (1990).
[4] W. Yu et al., New J. Phys. 20, 053062 (2018).
[5] F. Wen et al., IEEE Transactions on Electron Devices 68, 1524 (2021).

2:15 PM
Coffee Break
ESJ Building

2:45 PM
Contacts to III-N Semiconductors
Session Chairs: Matthew Hardy (US Navy Research Laboratory), Theeradetch Detchprohm (Georgia Institute of Technology)
ESJ 0202

02:45 PM
Deconstructing the Zr/Al/Mo/Au Ohmic Contact to AlN-rich AlGaN (Student)
Mr. Nathan Banner[1], Mr. Abdullah Mamun[2], Mr. Tariq Jamil[2], Dr. Asif Khan[2], Dr. Suzanne E. Mohney[1]
[1]Pennsylvania State University, [2]University of South Carolina, Columbia, USA

Aluminum nitride is an emerging semiconductor for power electronics due to its extreme bandgap of 6.1 eV and high thermal conductivity.1 Now that AlN has been successfully doped,2,3

there is potential for a paradigm shift in power electronics for the grid, transportation, and other high-temperature, high-power applications. AlxGa1-xN with a high fraction of AlN, or high x, is also technologically important.4,5 Without low-resistance ohmic contacts, extreme bandgap semiconductors cannot be exploited. This study investigates the resistance of contacts to n-type AlxGax-1N with high x and the role of contact metallurgy. Inspired by prior work to “deconstruct” Ti/Al-based contacts to n-GaN,6,7 we investigated the previously reported Zr/Al/Mo/Au8–10 contact on AlxGa1-xN with x = 0.66–0.83 using the circular transfer length method and also examined the metallurgy of contacts to AlN. Zirconium is an interesting metal for contacts to AlN-rich compositions because Zr reacts with AlN at lower temperatures than some other metals, while Al, Mo, and Au are predicted to be unreactive with AlN based on thermodynamics. Preparing Zr/Al stacks without the Mo/Au cap, we found that Al-rich contacts (with a 1:4 ratio of Zr:Al) became ohmic on AlxGax-1N with x = 0.67 after annealing at 800 °C, while Zr-rich contacts did not become ohmic even after annealing as high as 1150°C, highlighting the continuing importance of Al in the contacts to AlxGax-1N with

high x. Moreover, the thickness of Au in the capping layer also played a role in both the contact morphology and the required temperature to form ohmic contacts AlxGax-1N with x = 0.66-0.67. An annealing temperature of 700 °C was optimal for the Au-rich contact, while a higher temperature of 950 °C was needed when the Au cap was thin, despite both contacts having nearly the same specific contact resistance once they became ohmic (3-4 x 10-4 Ohm-cm2). Based on an examination of the contact morphology and relevant phase diagrams, we have formed a hypothesis that contacts that undergo partial melting can be prepared using much lower annealing temperatures. The best contact in this study to date was the Zr/Al/Mo/Au contact with layer thicknesses of 15/100/35/100 nm on AlxGax-1N with x = 0.67, which yielded a specific contact resistance of 3 x 10-4 Ohm-cm2.
Distribution Statement A: Approved for public release distribution unlimited (DCN# 0543-1699-24).

03:00 PM
Evidencing Low Ohmic Contacts on n-type AlN with Contact Resistivity at 10-3 Ω·cm2 Level
Dr. Haicheng Cao[1], Mr. Mingtao Nong[1], Dr. Xiao Tang[1], Dr. Biplab Sarkar[2], Prof. Ying Wu[1], Prof. Xiaohang Li[1]
[1]King Abdullah University of Science and Technology, [2]Department of Electronics and Communication Engineering, Indian Institute of Technology Roorkee, Uttarakhand 247667, India

Achieving low ohmic contact resistivity in AlGaN with high Al content, especially in AlN, remains a considerable challenge due to the inherently very low carrier concentration in these materials. To date, the most successful strategy has been the creation of an AlxGa1-xN gradient on top of AlN films during metalorganic chemical vapor deposition (MOCVD). This approach, however, is highly dependent on the specific condition of MOCVD equipment and requires precise control over processing parameters, including the Ga-Al gradient and Si-precursor flow. Alternatively, adjustments on the metal side, rather than the nitride film side, offer a more facile method. These adjustments involve selecting primary contact layer (e.g. Vanadium, thin SiNx) to minimize contact barrier, along with employing the Rapid Thermal Annealing (RTP) process to generate nitrogen vacancies at the AlN/metal interface for creating additional donor states. Despite considerable efforts with these strategies, while ohmic contacts have been achieved, contact resistivities have consistently remained above 10-1Ω·cm2, far from the effectiveness of the Ga-gradient method. In this research, we propose a comprehensive solution that includes modified contact metal configurations and severe annealing condition to successfully achieve AlN ohmic contact with a low contact resistivity at the 10-3 Ω·cm2 level, offering a straightforward method for attaining low ohmic contact resistance in n-AlN. In this research, AlN is grown on sapphire substrates in the (0001) orientation using metal-organic vapor phase epitaxy. The epitaxial structure consists of 1.1um undoped AlN and 250nm Si-doped AlN. Two types of ohmic contact metal stacks were used: TiAlTiAu and TiAlTi. Metal stacks were prepared by sputtering and subjected to RTP in an N2 atmosphere, with temperatures ranging from 800°C to 950°C and durations from 30 to 120 seconds. Contact characteristics were determined using the circle linear transmission line method (CTLM) with a 150 μm diameter and contact spacing of 10~60 μm, as shown in Fig. 1(a).

Fig. 1(b-c) depict the surface morphology of the two differently annealed ohmic metal stacks measured by atomic force microscopy (AFM). Noted that a relatively flatter surface morphology was observed in the sample with TiAlTi contacts, which is preferable for electronic devices. The I-V characteristics of TiAlTiAu and TiAlTi metal stacks at different annealing condition are shown in Fig. 2(a-b). The specific contact resistivity, evaluated based on the linear region, is presented in Fig. 2(c). Evidently, all the contacts exhibit moderate Schottky behavior. While the I-V characteristics of TiAlTi metal stacks, compared to that of TiAlTiAu, become less rectifying with a significant increase in current. In the TiAlTiAu metal stack, a minimum specific contact resistivity of ~0.37Ω·cm2 is achieved at 900°C for 60 seconds. For the TiAlTi metal stacks, the IV characteristics become less rectifying when the annealing temperature is increased to 950°C. By extending the annealing time to 90 seconds, the I-V characteristics become less resistive, achieving a minimum contact resistivity of 2.3×10-3Ω·cm2. Furthermore, AlN Schottky barrier diodes (SBD) were fabricated using the optimal conditions for the two ohmic contact metal stack, as shown in Fig. 2(d). It illustrates that superior ohmic contacts notably decrease the SBD's on-resistance and operation voltage. HAADF STEM images and EDXS profiles of the samples under optimized RTP conditions for the two metal stacks were analyzed. As depicted in Fig. 3, Ti-N phase formation was observed at the interfaces of both metal stacks, indicating N extraction. However, compared to TiAlTi, a thick layer of Al-N was observed at the interface in the TiAlTiAu metal stacks. The thick interfacial Al-N layer is likely the main cause of the higher contact resistance in TiAlTiAu metal stacks, as it impedes carrier tunneling and N extraction. Fig. 4(a) benchmarks our best contact resistivity results against previous reports, demonstrating our significant advantage.
In conclusion, a record low contact resistivity of 2.3×10-3 Ω·cm2 ohmic contact on n-AlN was demonstrated. These results represent a significant milestone in the development of AlN ohmic contacts, presenting the potential for more efficient devices in high-power electronic applications.
References
[1] Y. Yang et al., Solid-State Electronics, vol. 208, 2023. [2] H. K. Cho et al., IEEE Photonics Technol. Lett., vol. 35, no. 17, p. 915-918, 2023. [3] C. J. Zollner et al., Crystals, vol. 11, no. 8, 2021. [4] L. Sulmoni et al., Photonics Research, vol. 8, no. 8, 2020. [5] H. K. Cho et al., Semiconductor Science and Technology, vol. 35, no. 9, 2020. [6] N. Nagata et al., Physica status solidi c, vol. 14, no. 8, 2016. [7] A. G. Baca et al., Applied Physics Letters, vol. 109, no. 3, 2016. [8] R. France et al., Applied Physics Letters, vol. 90, no. 6, 2007. [9] N. Yafune et al., Japanese Journal of Applied Physics, vol. 50, no. 10R, 2011. [10] H. Tokuda et al., Applied Physics Express, vol. 3, no. 12, 2010.

03:15 PM
Revolutionizing P-Type GaN: An Innovative Approach to Achieve High-Doping Efficiency and Low-Contact Resistance for GaN Devices
Ms. Haley Dishman[1], Mr. Owen Meilander[1], Prof. Mona Ebrish[1]
[1]Vanderbilt University

The poor quality of selective doping in GaN impacts its electrical contacts, and the inability to create abrupt junctions

limits the device structures that can be realistically fabricated. This work explores an innovative method to attain high-doping efficiency and eventually achieve low-contact resistance with GaN substrates, especially p-type contact. The approach is based on the diffusion of Mg-dopant by annealing under metastable conditions. Figure 1 illustrates the process flow for this selective doping approach to achieve P-type GaN. The process flow entails the sputtering of Mg and AlN onto GaN, subsequent diffusion of Mg into GaN, and culminates in the removal of the AlN cap while adding metal contacts. The Mg layer was introduced via sputtering, followed by an Aluminum Nitride (AlN) incapsulating layer. This was confirmed using a scanning electron microscopy (SEM) image in Figure 2, which indicates the presence of Mg as the darkest section on a GaN substrate with an AlN cap layer on top. The sputtering conditions were studied in prior work to ensure a layer of ~15nm of Mg is deposited at room temperature. The AlN layer protects the Mg from oxidizing before the diffusion and activation while safeguarding the GaN substrate from decomposing during the meta-stable anneal. Rapid Thermal Annealing, carried out in an N2 ambient at ~900℃, is used to diffuse the Magnesium. A chemical etch was used post-annealing to remove the AlN layer. Several etching processes were explored to ensure a complete removal of the AlN layer. These processes were compared using energy-dispersive X-ray spectroscopy (EDS). The STEM EDS image in Figure 3 presents promise as Mg has been successfully diffused into GaN prior to the removal of AlN. Electrical characterization is under investigation to evaluate the carrier concentration. Additional electrical characterization, such as Circular Transmission Line Measurement (CTLM), will be used to identify the specific contact resistance. Furthermore, other characterization techniques, such as secondary ion mass spectrometry (SIMS), will also be used to quantify the diffusion depth of Mg in GaN further under our annealing conditions. This alternative selective doping technique provides crucial insight into the effectiveness of the selective doping approach and its potential for enhancing the performance of GaN-based devices. The EDS results for each step are illustrated in Figure 4. The Al Etchant with TMAH is as effective as KOH and AZ-400K, leaving behind 0% of the AlN cap. The post-anneal analysis reveals that Mg diffuses into the sample, and any remaining material on the surface is removed with cap removal processes. The presented work explores a cutting-edge process to achieve high-doping efficiency and low-contact resistance for p-type GaN.

03:30 PM
Schottky Diodes to GaN Prepared by Atomic Layer Deposition (Student)
Mr. Jacob W. Clark[1], Mr. Nathan Banner[2], Mr. Nicholas Redwing[1], Dr. Bangzhi Liu[1], Mr. CHAN WEN CHIU[1], Dr. Thomas J. Larrabee, Sr.[1], Prof. Jennifer L. Gray[1], Dr. Suzanne E. Mohney[1]
[1]Pennsylvania State University, [2]Penn State University

Conductive metal nitrides are candidates for high-temperature, high-power Schottky diodes to n-type GaN. One of the metal nitrides in thermodynamic equilibrium with GaN that also has a high work function is Mo2N. Using bis (tertbutylimido) bis (dimethylamino) molybdenum, either a remote N2-H2 plasma [1] or NH3 was used as the co-reactant to deposit a conductive metallization. ALD offers an advantage over sputter deposition because deep levels can be created in GaN from the direct plasma during sputter deposition. ALD also has an edge over electron beam evaporation because it is difficult to control the stoichiometry of nitride compounds during e-beam evaporation. Both types of ALD processes resulted in layers that contained some carbon, but the layers were good conductors, and there is significant solubility of MoC in Mo2N. Thermal ALD resulted in diodes with a Schottky barrier height of 0.69 eV and an ideality factor of 1.06 before annealing, while the remote-plasma process resulted in nonideal diodes with high reverse currents. However, after annealing in N2 at 600 °C, diodes prepared by both methods offered similar Schottky barrier heights (0.84 eV by thermal ALD and 0.87 eV by remote-plasma ALD). Surprisingly, the diodes prepared with the remote-plasma process were more ideal after annealing. When making measurements at room temperature, an ideality factor near 1.02 is expected due to image force lowering and was measured after annealing diodes prepared using the remote-plasma process. After annealing diodes prepared by thermal ALD, the ideality factor became 1.04. Cross-sectional transmission electron microscopy suggests a thin interfacial layer in the diodes prepared by thermal ALD, which may be the origin of the modest non-ideality. Capacitance-voltage measurements as a function of frequency shed provide more insight on the role of the interfacial layer. The authors gratefully acknowledge the support of ONR (LJ Petersen) through N00014-22-1-2462. Distribution Statement A: Approved for public release distribution unlimited (DCN# 0543-1697-24).

2:45 PM
Gallium Oxide Epitaxy, Processing, and Characterization
Session Chairs: Thaddeus Asel (Air Force Research Laboratory), Nidhin Kurian Kalarickal (Arizona State University)
ESJ 0224

02:45 PM
In-situ Deep Patterned Etching of beta -Ga2O3 using Triethylgallium (Student)
Mr. Nabasindhu Das[1], Mr. Abishek Katta[1], Mr. Advait Gilankar[1], Dr. Will Brand[2], Dr. Fikadu Alema[2], Dr. Andrei Osinsky[2], Dr. Nidhin Kurian Kalarickal[1]
[1]Arizona State University, [2]Agnitron Technology Incorporated

β-Ga2O3 is a highly promising ultra-wide band gap semiconductor for power switching applications thanks to its high critical breakdown field strength (8 MV/cm) and availability of bulk substrates. For commercial power device applications, it is crucial to develop processing technologies for β-Ga2O3 capable of realizing 3-D device architectures such as trench Schottky barrier diodes (SBDs), trench MOSFETs, and FinFETs. An essential aspect of such technology is a highly controllable and low damage etching process. Several dry and wet etch techniques have been documented in β-Ga2O3 with various limitations like surface damage and angled sidewalls. We had previously reported on the use of metal organic (MO) precursors like triethylgallium (TEGa) as an effective in-situ etchant for β-Ga2O3, capable of achieving high etch rates (>8 micron/hr)

and smooth surface morphology (~2 nm). In this work, we study deep patterned etching of β-Ga2O3 using the same method on (001) and (010) oriented β-Ga2O3 substrates for fabrication of 3-D structures like fins and trenches and characterize electrical properties of the etched surface.
The 'in-situ TEGa etching' was carried out in an Agnitron Agilis 100 oxide MOCVD reactor. TEGa is used as the MO precursor for etching, which undergoes pyrolysis, depositing Ga adatoms on the substrate surface. The etching process proceeds by the formation of volatile gallium suboxide (Ga2O) via the reaction between Ga and Ga2O3 [1]. For patterned etching, a SiO2 hard mask deposited using PECVD is used, which is subsequently patterned using optical lithography and etched using BOE. The patterned samples were etched at a substrate temperature of 800 and TEGa flow of 18 mol/min for 80 minutes. Etch depth was measured using both Dektak profilometry and AFM to be ~ 4 micron. Due to the conformal nature of MOCVD deposition, Ga adatoms are also deposited on the etched sidewalls, resulting in appreciable lateral etching. To investigate the anisotropic dependence of lateral etch rate, we fabricated spoke wheel structures comprising of fins oriented along important crystallographic directions. Post etching, these structures were observed under SEM to measure lateral etch rates. The lowest lateral etch rate was observed for [010] fins on (001) beta-Ga2O3 substrates and for the [001] fins on the (010) beta-Ga2O3 substrate. This anisotropic variation was also confirmed through tapered spoke-wheel structures which were specifically designed with varying fin-widths to magnify the effect of lateral etch rate. Lateral etching combined with vertical etch allows us to successfully fabricate sub-m fins with smooth sidewalls. [010] fin arrays were patterned on (001) beta-Ga2O3 substrate and [001] fin arrays were patterned on (010) beta-Ga2O3 substrate with vertical sidewalls and high aspect ratios (AR) of around 8.
For electrical characterization of the etched beta-Ga2O3 substrate surface, Ni SBDs were fabricated on etched and non-etched surfaces (masked region) after Ga etching. In addition, control Ni SBDs were also fabricated on a separate β-Ga2O3 epilayer sample, which did not undergo Ga etching. Capacitance-Voltage (CV) measurements showed no difference in net donor concentration on the etched surface when compared to the non-etched surface, confirming the damage free nature of the etch process. However, the non-etched surface showed a reduction in Schottky barrier height (0.96 V) by ~ 0.2 V, when compared to etched (1.19 V) Schottky diodes. Diode I-V characteristics also confirm the lowered Schottky barrier height on the non-etched surface, along with higher resistance due to the thicker epilayer under the non-etched surface. Reverse IV measurements of the diodes showed low leakage current for diodes fabricated on the etched-surface, and elevated leakage for diodes fabricated on non-etched surface due to lower Schottky barrier height. However, no significant change in the hard breakdown voltage was observed (~200 V).
In summary, this study demonstrates the feasibility of damage free patterning of high aspect ratio structures using 'in-situ MOCVD etching using TEGa' and lays the groundwork for future advancements in β-Ga2O3 vertical and lateral three-dimensional devices.

03:00 PM
Impact of Remote Hydrogen Plasma on Ga2O3 Carrier Density and Mobility (Student)
Mr. Carlos DeLeon[1], Mr. Lingyu Meng[1], Mr. Daram Ramdin[1], Mr. Jade Cowsky[1], Prof. Hongping Zhao[1], Prof. Leonard Brillson[1]
[1]The Ohio State University

Gallium Oxide (Ga2O3) is an increasingly important semiconductor for high power electronics due to its ultra-wide bandgap. The most commercially common growth technique to produce Ga2O3 is through Molecular Organic Chemical Vapor Deposition (MOCVD) in which one can produce high quality films at a fast growth rate. However, the presence of impurities such as carbon and hydrogen during MOCVD growth can negatively impact electrical properties [1]. The goal of this project is to identify effects of both C and H on the electrical properties of Ga2O3 [2,3,4] and to identify possible methods of controlling their effects. Remote Hydrogen Plasma (RHP) is a technique that can passivate, rearrange, and reconfigure defects within the film in a non-destructive fashion.
Depth Resolved Cathodoluminescence (DRCLS) in conjunction with room temperature Hall measurements were used to measure Ga2O3 samples with differing C content that underwent RHP exposure with increasing time. Carrier density of both samples increased and then remained constant as exposure time increased while mobility in both samples were observed to decrease and remained constant with time.
From our previous studies, the 3.8 eV defect is thought to be H – related, results which are supported by our RHP studies. However, the difference in C content across different samples also reveals that the defect is likely C - related. After an hour of RHP exposure, the high C sample experienced a 14% increase near surface of the 3.8 eV defect, while the low C sample showed only a negligible percent change near surface. The carrier concentration increases by 20% for the high C sample while mobility decreases by 20%. The carrier concentration and mobility for low C sample has negligible change after 1 hour of RHP exposure. This suggests the 3.8 eV defect has a significant impact on electrical properties, while several other deep level defects we observed defects did not track with changes with electrical properties.
When exposed to RHP for an additional 2 hours, the electrical properties of both samples experience negligible change while deep level defects we observed at hv = 2.5 eV, 3.6 eV, and 3.8 eV, changed significantly. This suggests a complex interplay between H incorporation and defect – H complex formation within Ga2O3. Further experiments are in progress to understand the exact role of H and C in Ga2O3 and to extend the RHP passivation of C through full Ga2O3 epilayer thicknesses.
[1]: Sai Mu, Mengen Wang, Joel B. Varley, John L. Lyons, Darshana Wickramaratne, and Chris G. Van de Walle Phys. Rev. B 105, 155201.
https://doi.org/10.1103/PhysRevB.105.155201
[2]: Lingyu Meng, A F M Anhar Uddin Bhuiyan, Hongping Zhao. Appl. Phys. Lett. 5 June 2023; 122 (23): 232106.
https://doi.org/10.1063/5.0153626
[3]: Yuan et al., Fundamental Research, Volume 1, Issue 6, 2021, Pages 697-716,
https://doi.org/10.1016/j.fmre.2021.11.002

[4]: N. Ma, N. Tanen, A. Verma, et al., Appl. Phys. Lett. 109 (21) (2016) 212101. http://dx.doi.org/10.1063/1.4968550

03:15 PM
Cracking in β-(AlxGa1-x)2O3 films on (010) β-Ga2O3 substrates: Characterization and Modelling (Student)
Mr. Dorian Luccioni[1], Dr. Kenny Huynh[1], Dr. Michael Liao[1], Mr. Kaicheng Pan[1], Mr. Brandon Carson[1], Ms. Lezli Matto[1], Dr. James Spencer Lundh[2], Dr. Marko Tadjer[3], Dr. Kohei Sasaki[4], Dr. Keita Konishi[4], Dr. Hannah Masten[2], Dr. Jennifer
[1]University of California, Los Angeles, [2]NRC Postdoctoral associate residing at the U.S. Naval Research Laboratory, [3]U.S. Naval Research Laboratory, [4]Novel Crystal Technology, Inc., [5]Department of Materials Science and Engineering, University of Florida, [6]Advanced Photon Source, Argonne National Laboratory

Relaxation in the form of cracking was observed in higher Al content or thicker epitaxially grown (010) β-(AlxGa1-x)2O3 films – along the primary [001] and secondary [100] cleavage directions – in a systematic study with films ranging from 50 to 400 nm thick, with varying composition (x = 0.10 to 0.15). Strain management in lattice-mismatched systems can manifest in different ways; typically, misfit dislocations are observed, but in this case, cracking is the dominant mechanism. Large diffuse scatter arcs in symmetric (020) reciprocal space maps (RSM) were found to be dependent on the orientation of the diffracted X-ray beam; the observed “wing-like” features, around the substrate and epilayer, were maximized with the beam aligned perpendicular to the dominant crack direction and minimized with the beam aligned in parallel. Samples that did not exhibit cracking did not show this behavior.
In the literature, diffuse scatter in XRD data has been shown but not discussed, especially when the diffuse scattering deviates from the ω scanning axis, indicating that the in-plane localized strain-relaxation via the formation of cracks causes out-of-plane strain changes in the tilted regions. In this work, a combination of triple-axis X-ray diffraction (XRD), X-ray topography (XRT), transmission electron microscopy (TEM), and atomic force microscopy (AFM) were used to develop a cracking model that describes the origin of the “wing-like” diffuse scatter features with material behavior. XRT revealed that increasing film thickness and Al content caused increases in crack density throughout the film. During cracking, the epilayer and the substrate undergo some localized in-plane strain relaxation, resulting in a decrease in curvature with increasing crack density. To accommodate the change in geometry, the epilayer and substrate produce an out-of-plane strain in the affected regions, due to volume conservation, which results in an increase in interplanar spacing in the out-of-plane direction and the tilting of lattice planes.
This model and the symmetric (020) RSMs can be combined to produce cross-section profiles of the lattice planes in the cracked material. From this, lattice relaxation was found to extend around 300 nm from the crack edges, comparable to prior studies regarding strain distribution in cracked epilayers, while the fully strained inter-crack spacing is on the order of microns. This limited extent of strain relaxation explains why, despite cracking, asymmetric (422) RSMs still reveal that the epilayer remains fully strained with respect to the substrate. The model is capable of predicting the average crack geometry and density from RSMs. The distortion profile caused by the cracking-induced relaxation was ascertained, and a better understanding of this behavior is the first step to developing mitigation strategies for this desirable material system.

03:30 PM
Investigation of Thermal Stability and Phase Transitions of α-, κ(ε)-, and γ-Ga2O3 Epitaxial Films via Annealing and In-Situ XRD (Student)
Mr. Jingyu Tang[1], Dr. Kunyao Jiang[1], Prof. Robert Davis[1], Prof. Lisa Porter[1]
[1]Carnegie Mellon University

Gallium oxide (Ga2O3) has been characterized by four universally accepted polymorphs: α-, β-, γ-, and κ(ε)-Ga2O3. Among these polymorphs, β-Ga2O3 is the thermodynamically stable phase. All other polymorphs convert to β-Ga2O3 upon heat treatment. While β-Ga2O3 has attracted the most attention for its potential in high-power electronics and optoelectronics applications, the thermodynamically metastable polymorphs are beginning to receive considerable interest. For example, α-Ga2O3, with its highest bandgap among all Ga2O3 polymorphs, is a promising alternative for high-power electronics applications. κ(ε)-Ga2O3, with its high predicted spontaneous polarization, shows promise as a potential ferroelectric material. γ-Ga2O3 has demonstrated properties such as photoluminescence, photocatalysis, and room-temperature ferromagnetism. However, due to their inherent thermal instability, the maximum application temperatures of these metastable polymorphs are uncertain.
In this study, in-situ high-temperature x-ray diffraction (HT-XRD) was used to characterize α-, κ(ε)-, and γ-Ga2O3 epitaxial films through annealing at increasing temperatures under both air (500 - 900 °C) and vacuum (500 - 1500 °C, ~2×10-5 Torr) conditions. The epitaxial films included α-Ga2O3 films grown on (0001) Al2O3 via halide vapor phase epitaxy (HVPE) by Kyma Technologies, and κ(ε)-Ga2O3 and γ-Ga2O3 films grown on (0001) Al2O3 and (100) MgAl2O4 substrates via metal-organic chemical vapor deposition (MOCVD), respectively. To minimize the impact of film thickness and substrate-induced strain on thermal stability, the film thicknesses were controlled to be ~1μm and their relaxation was validated by reciprocal space maps (RSMs). Samples were held at each temperature for 1hr at increments of 25 °C while the XRD data was acquired at each temperature. For films annealed in air, the XRD results show the first detectable changes in phase at approximately 550 ℃, 825 ℃ and 575 ℃, respectively, for α-, κ(ε)-, γ-Ga2O3 films. Strong crystallographic orientation relationships (ORs) were observed before and after the phase transition: (0006) α-Ga2O3 // (-201) β-Ga2O3, (002) κ(ε)-Ga2O3 // (310) and (-201) β-Ga2O3, and (400) γ-Ga2O3 // (400) β-Ga2O3. In contrast, the minimum temperatures at which detectable phase changes occurred for α-, κ(ε)-, γ-Ga2O3 films annealed in vacuum were 1325 ℃, 1450 ℃ and 1350 ℃, respectively, while keeping the same ORs observed in air.

03:45 PM
Photoluminescence study on MgGa2O4 thin films grown by molecular beam epitaxy (Student)
Mr. Tianchen Yang[1], Mr. Chengyun Shou[1], Mr. Abdullah

Almujtabi[1], Mr. Quazi Sanjid Mahmud[1], Mr. Edward Zhu[2], Mr. Yuan Li[1], Prof. Jianlin Liu[1]
[1]University of California Riverside, [2]University of California, Riverside

As a promising ultrawide bandgap oxide semiconductor material in the spinel family, magnesium gallate (MgGa2O4) with a bandgap around ~5.0 eV exhibits great potential for deep UV optoelectronic applications. Apart from reports on bulk materials grown by CZ and a few epitaxial films grown by MOCVD or PLD methods, MgGa2O4 thin films grown by MBE are seldom reported. Besides, few studies reveal the photoluminescence (PL) properties of MgGa2O4 thin films. In this effort, MgGa2O4 thin films were grown by using oxygen plasma-assisted MBE under different substrate temperatures ranging from 300 to 600 ºC. The atomic ratios of Mg, Ga, and O were measured by energy-dispersive X-ray spectroscopy (EDX). The lattice structures were investigated by X-ray diffraction (XRD). Thin film absorbance and transmittance spectra were measured using a high-performance UV-Vis-NIR spectrophotometer. Bandgap around 5.0 eV was achieved, and all samples have the transmittance over 80% in the visible spectral range. Power and temperature-dependent PL studies were performed on film grown under a substrate temperature of 600ºC. Room temperature PL deconvolution was performed to reveal the different luminescence energy band emissions and a schematic model illustrating the estimated defects energy levels was given. Relationship between the peak position, intensity and temperature for each emissions band were analyzed as well.

2:45 PM
Additive Manufacturing and 3D Devices
Session Chairs: William Scheideler (Dartmouth College), Jung-Bin Ahn (Texas A&M University)
ESJ 2208

02:45 PM
3D Woven Liquid Metal Litz Wire for MHz Functionality (Student)
Mr. Md Saifur Rahman[1], Dr. Anand Tiwari[1], Mr. Simon Agnew[1], Prof. William Scheideler[1]
[1]Dartmouth College

The emergence of wearable electronics that adapt to the human body has opened new frontiers in the fields of the Internet of Things (IoT), mechanical sensing, and healthcare monitoring. Central to the functionality of such devices are mechanically flexible and stretchable materials such as gallium (Ga) base room temperature liquid metals (LM). LM-based flexible devices deform via stretching, torsion, and compression. While DC resistance to these deformations is known, their high-frequency alternating current (AC) high-frequency response is unexplored. Through extensive Finite Element Analysis (FEA) and experimentation, we investigated the complex interplay between the 3D geometry of liquid metal conductors and their conductance of RF signals. These led to the discovery of several energy-efficient approaches to enhance LMs performance in wearable sensors and in inductive coils for wireless power transfer.
First, we report a new method of high-frequency AC-enhanced resistive mechanical sensing that leverages the deformability of liquid metals (LM) to enhance low-power detection (100x lower than DC) of biomechanical stimuli in wearable electronics. The mechanism behind this improvement is the modulation of the AC skin effect, which induces current crowding at the surface of an LM conductor. Here, we apply 1-50 MHz excitation in combination with DC sensing to pinpoint mechanical deformations such as stretching in-plane and compression out-of-plane that are otherwise indistinguishable via DC resistive sensing alone. Second, we consider the design of LM-based stretchable air-core magnetics with an emphasis on trace geometry and RF performance. Specifically, we investigate inductive coils that are crucial for communication and power transfer in flexible electronics systems. While such coils provide mechanical conformability, their electromagnetic performance falls short compared to conventional rigid copper wires, resulting in lossy radio frequency (RF) characteristics. To address this, we introduce multistranded three-dimensional (3D) woven 'litz' transmission lines to augment the resonant RF performance by combating the AC skin effect and proximity effect. Simulations and experiments unveil an impressive 80% increase in the Quality Factor (Q) with the interwoven LM litz wires, surpassing the performance of standard liquid metal wires. Furthermore, we present a fabrication methodology for stretchable coils that demonstrates the capability to maintain a high Q (>30) even under significant biaxial strain, outperforming previously reported LM coils. The versatility of this approach is exemplified through the 3D printing of four-terminal 'choke' inductors optimized for RF filtering and inductance tunability, overcoming limitations associated with planar fabrication. These findings provide valuable insights into designing and implementing 3D-printed magnetics, paving the way for a diverse range of electromagnetic device applications.

03:00 PM
ANALYSIS OF DIFFERENT MICROFLUIDIC STRUCTURES IN PACKAGES FABRICATED USING METAL ADDITIVE MICROFABRICATION FOR THE THERMAL MANAGEMENT OF SEMICONDUCTOR DIES.
Dr. Bhushan Lohani[1], Mr. Ryan Price[2], Mr. Peter Sanchez[2], Dr. Robert Roberts[2]
[1]Pennsylvania State University, [2]The University of Texas at El Paso

This abstract presents a study examining the hydrodynamic and thermal efficiencies of three distinct micro-pin-fin structures and three microchannel structures on metal additively microfabricated packages designed for semiconductor package-level thermal management. The aim is to comparatively assess these structures to identify the optimal microfluidic design. The packages were fabricated using Direct Metal Laser Sintering (DMLS), demonstrating the potential of additive manufacturing for developing microfluidic packages and integrating them with cleanroom microfabricated semiconductor dies. By enabling fluid flow

through the proposed microfluidic structures within the package, efficient heat dissipation from the semiconductor dies is achieved, enhancing functionality and operational characteristics of the overall integration. This embodies the concept of heterogeneous integration, facilitating the integration of components fabricated through diverse processes.
The ongoing trend toward miniaturizing microsystems, aimed at cramming more of them into compact and high-performance dies, has led to localized heat generation, known as hotspots, within the chips. These hotspots result in increased die temperature, adversely impacting reliability, performance, and lifespan. To fully leverage the benefits of miniaturization, effective thermal management of devices is imperative. Commonly used system-level cooling methods like copper heat exchangers, fins, and fans rely on conductive heat transfer through interfaces, but they suffer from higher thermal resistance, increased hardware size and costs.Die-level thermal management systems, such as microfluidic channels and micro pin-fins located on the back end of the die, offer efficiency through direct cooling, but they complicate overall die fabrication. To harness the benefits of these methods without imposing undue strain on the die, this abstract proposes innovation in package, which is mostly used for die connectivity. Integrating microfluidic structures into the package enables effective package-level thermal management. However, these microfluidic structures need to be optimized to have the least hydrodynamic resistance and better thermal efficiency. This abstract introduces metal additively microfabricated packages with leads and die pads, showcasing different microfluidic pin-fin structures (as depicted in Figure 1) and comparing their thermal efficiency. The DMLS system uses a CAD file, slicing it into layers and fabricating them through sequential melting and fusing of metal powder until the structure is built. In this study, the DMLS system utilized 3D CAD files (depicted in Figure 1) to microfabricate final packages (shown in Figure 2) using 316L steel powder. Figures 1 and 2 depict six packages with shared leadframes but showcasing various microfluidic designs: circular pin-fin (CPF), square pin-fin (SPF), and teardrop pin-fin (TDPF) for micro pin-fins in (P1), (P2), and (P3) respectively, and Serpentine Straight Microfluidic Channel (SSMFC), Parallel Straight Microfluidic Channel (PSMFC), and Serpentine Wavy Microfluidic Channel (SWMFC) for microchannels in (C1), (C2), and (C3) respectively. This research aims to experimentally determine the most efficient structure among them in terms of flow resistance and thermal efficiency. From the pictures it is clear that the leadframe and die holder are fabricated on a support plate, which serves as a temporary fixture during integration. This plate will be subsequently removed, isolating the leads. This process is demonstrated in Figure 3, illustrating the proposed integration, and Figure 4 (c), showing the backside of the final system with the leads isolated. In Figure 4(a), the package (test sample) is depicted with an integrated die and extended inlet/outlet, while (b) showcases the corresponding test setup. Figures 5 and 6 illustrate that SWMFC experiences the lowest flow resistance and outperforms others in thermal performance for similar pump power. In Figures 7 and 8 demonstrates that TDPF has the lowest flow resistance and outperforms other structures in thermal performance for similar pump power. TDPF was able to reduce thermal resistance from 5.25°C/W for a conventional non-microfluidic package to 0.9°C/W.

03:15 PM
Electroless Nickel Plating Application on Additive Manufacturing Metal Components As-Built, ChemPolished (cp), and ElectroPolished (ep) Exploration. (Student)
Mr. Pablo Sanchez[1], Dr. Pawan Tyagi[2]
[1]University of the District of columbia, [2]University of the district of Coulombia

Additive manufacturing has multiple advantages for the electronics sector. These include the capacity to produce complex geometries and intricate designs, quick prototyping that enables electronics designers to test and refine ideas, customization, reduced material waste, and the integration of various materials that encourages innovative and productive manufacturing techniques. In the electromagnetic industry, AM also facilitates on-demand production, innovates coil and antenna designs, and optimizes weight and heat dissipation. assisting in the development of customized and more effective solutions for electromagnetic components and devices. Similarly, its benefits in the heat transfer sector include the fusion of various materials, heat transfer topology optimization, effective heat exchanger manufacturing, decreased mass, enhanced fluid flow regulation, and creative heat exchanger design. These advantages contribute to the creation of thermal management solutions that are more successful and efficient. The current study investigates electroless nickel plating and surface finishing techniques such as ChemPolishing (CP) and ElectroPolishing (EP) for postprocessing on additively manufactured stainless-steel samples. Existing additive manufacturing (AM) technologies generate metal components with a rough surface that typically exhibit fatigue characteristics, resulting in component failure and undesirable friction coefficients on the printed part. Small cracks formed in rough surfaces at high surface roughness regions act as a stress raiser or crack nucleation site. As a result, the direct use of as-produced parts is limited, and smoothening the Surface presents a challenge. Previous research has shown that CP ChemPolishing has a significant advantage in producing uniform, smooth surfaces regardless of size or part geometry. EP Electropolishing has a high material removal rate and an excellent surface finishing capability. Electropolishing, on the other hand, has some limitations in terms of uniformity and repeatability. On additively manufactured stainless-steel samples, electroless nickel deposition has a higher plating potential. Nickel has excellent wear resistance, and nickel-plated samples are more robust as scratch resistant than not plated samples when tested for scratch resistance. This research uses medium-phosphorus (6-9% P) and high-phosphorus (10-13% P). The L9 Taguchi design of experiments (DOE) was used to optimize the electroless nickel deposition experiments. The mechanical properties of as-built and nickel-coated additive manufacturing (AM) samples were investigated using a standard 5 N scratch test and the adhesion test ASTM B-733 thermal shock method. The KEYENCE Digital Microscope VHX-7000 was used to examine the pre- and post-processed surfaces of the AM parts. The complete scratch and Design of Experiment (DOE) analysis was performed using the Qualitek-4 software.

Keywords: Taguchi design of experiments, additive manufacturing, chem polishing, electropolishing, electroless nickel plating, hardness, crack nucleation.

03:30 PM
INVESTIGATION OF POLYMER MICROSTRUCTURE PYROLYSIS FOR ROBUST 3D PRINTED CARBON MEMS (Student)
Mr. Ryan Price[1], Mr. Peter Sanchez[1], Mr. Jorge Ochoa[1], Mr. Gabriel Saucedo[1], Dr. Robert Roberts[1]
[1]The University of Texas at El Paso

Advances in additive manufacturing using 2-Photon Polymerization (2PP) has enabled the shrinkage of conventional MEMS devices especially in biomedical engineering [1]. It can also be seen in [1–3], Carbon MEMS (C-MEMs) have a wide host of applications with excellent electrical/mechanical properties and are biocompatible. Extending 2PP by taking microstructures printed of photoresist resins and pyrolyzing them at different temperatures, allows the tuning of the resulting carbon structures where low temperatures below 600 Celsius provide non-conductive glassy carbon [3–5]. To test the effects of pyrolysis on large structures with complex details and high aspect ratios a conical needle array, as seen in Figure 1, was printed using 2PP. At time of publication, a relief map logo, rendered as seen in Figures 2 and 3, with finer detail is being studied.
A review of prior works has revealed a gap in knowledge with respect to gaining a good yield of repeatable quality (C-MEMs) parts from 2PP polymers. [6] provides details and a model of shrinkage and hints at how exposure parameters impact the resulting carbon structures. The temperatures at which thermal decomposition begins are well documented in [3–5] which explain the difficulties of generating conductive carbons at lower pyrolysis temperatures as seen in [7]. The needles of [1] are interesting from the standpoint of having varied shape over length while [5,6] dig deeper into the complex shapes and overhangs. It is seen that there is a large swath of research into specific applications currently without a generic solution. The workflow for this process is illustrated in Figure 4. An array of micro-needle arrays was printed using IP-S resin on an ITO glass slide with a NanoScribe Photonic Professional GT2 using a 25x objective. These samples were then cleaned by submergence in PGMEA for 25 minutes before a 5 minute dip in IPA. Once fully developed, these parts were then diced apart using an Emblaser 2 laser cutter with the assistance of some Kapton tape as a thermal target. A single micro-needle array, now on a 2mm square, is then placed inside of an MTI OTF-1200X tube furnace on top of a ceramic holder and conditions inside the furnace are then varied. The first set of experiments were done with pure Argon gas, the second set of experiments used Nitrogen gas, a third set of experiments used a forming gas consisting of 3% Hydrogen with balance Argon, and a fourth set of experiments used trace Argon atmosphere under a 4 millitorr vacuum. Samples were then imaged with an JOEL IT200 Scanning Electron Microscope with a few select samples destructively analyzed using a LabRAM HR Evolution Raman Spectrometer. Observations of final resistivity were conducted with a Keithley 2400 SMU using a Kelvin probe arrangement.
This work investigated the growing knowledge base that exists for the technique of template pyrolysis using structures printed using 2-Photon Polymerization. Figure 5 presents a representative sample of a successful pyrolysis run. A pleasant surprise was discovered that most samples could be degassed/diffused at 300 Celsius for 15 minutes. A second notable observation is that convective versus radiative heating impacts the structure of the resulting carbon with convective heating modes preferred. The resin was found to melt before pyrolysis with direct radiative heating in our experimental setup. Several key data points in the prior works were able to be replicated, onset of carbonization was confirmed to be close to 450ºC after initial difficulties in preventing parts from melting. The results of the Raman study also show that there is a chemical change as seen in Figure 6. Many prior works had focused on higher Raman Shifts where this study fills in some knowledge with changes in the lower spectral range. This means that the results of several research groups are confirmed to be valid and that the experimental procedures used in this study were also able to be validated. The impact this investigation has is in the lessons learned in replicating the results and tuning the process parameters to search for more optimal solutions that do not require complex modeling, or tight controls of the exposure parameters used in 2PP. Furthermore, continuing research into these carbon form techniques is currently being explored to enable multi-material selective carbon structures, with the hope that selective activation of the resulting carbon is not only possible but that the non-conductive carbon would provide excellent dielectric properties. Applications of these structures would then not be limited to the obvious supercapacitor technologies but would be expandable to sensor elements, chemically selective filaments, Carbon MEMS, and print in place carbon based electronics.

03:45 PM
3D PolyJet-printed flexible coil for wireless power transfer application (Student)
Ms. Chia Ying Kuo[1], Dr. Jung-Bin Ahn[1], Dr. Byungseok Yoo[2], Prof. Nathan Lazarus[3], Prof. Soaram Kim[1]
[1]Texas A&M University, [2]University of Maryland, College Park, [3]University of Delaware

Driven by the demand for wearable technologies, the field of flexible electronics has seen substantial progress, especially in developing flexible inductors for power electronics and communication systems. Flexible inductors have progressed from 2D thin film constructs to 3D printed geometries. While these 3D models improve inductance and quality factors through intricate helical designs, they encounter production challenges in preserving mechanical reliability and reactive properties after assembly [1, 2]. Lazarus group has reported diverse fabrication methods for 3D inductors with deformable coil components and polymeric matrix. The group used an stereolithography (SLA) 3D printer to directly construct a polymeric matrix with built-in microchannels, subsequently filled with liquid metal to complete the inductors [3].
In this work, we suggest a straightforward method to obtain stretchable and deformable 3D inductors using a PolyJet-type 3D printer, capable of printing with multiple materials of varying properties and combinations thereof, with customized material properties. Two 3D printable polymers with different mechanical properties, Vero rigid and Agilus 30, were employed to obtain a polymeric matrix with microchannels. Vero rigid offered a rigid feature while Agilus

30 was employed to impart flexibility and softness to the matrix. Figure 1 illustrates the design of solenoid and toroid inductors, which incorporate microchannels and access channels within the Agilus 30-based soft matrix, following the structure design principles established in Lazarus's prior work [3]. After 3D printing the polymeric matrices, the water-soluble supports in the channels were washed away. The access channels created for the microchannel cleansing were closed by using UV curable resin with similar material properties to Agilus 30. The inductor fabrication was finalized by injecting liquid metal (Eutectic Gallium Indium, Sigma-Aldrich) into the microchannels. The electrical performance evaluation of each inductor under strain and bending conditions was conducted using an Agilent 4294A precision impedance analyzer, measuring the reactive parameters through a frequency range from 1 to 200 MHz. Figure 2 displays the consistent performance of the reactive parameters across various deformations, affirming the stable reactive properties of the inductors and underscoring their suitability for flexible power interfaces in wearable and mobile devices. The congruence of these results with those reported in Lazarus's work [3] suggests that our method retains the essential reactive properties while providing the mechanical flexibility.

The 3D flexible inductor was further applied to wireless power transmission. To enhance the applicability in wireless power transmission systems, the coil was redesigned into a cylindrical configuration with five turns, resembling the commonly used transformers in power systems (as depicted in Figure 3). The 3D-printed coil achieved an inductance of 1.2 μH and was designated as the receiving coil. In parallel, a six-turn cylindrical copper coil with a self-inductance of 2.3 μH was fabricated to serve as the transmitter coil. To synchronize the mutual inductance, capacitors of 18 pF and 33 pF were connected in parallel to the transmitter and receiver coils, respectively. These modifications aimed to create LC resonant circuits with closely matched resonant frequencies. Employing the resonant frequency formula $f = 1/(2\pi\sqrt{LC})$, where L represents coil inductance and C the capacitance of the connected capacitor, we calculated the resonant frequencies f to be approximately 24.74 MHz for the transmitter and 25.29 MHz for the receiver, demonstrating a near-resonant condition intended to optimize power transfer. When a 7 V peak-to-peak, 25 MHz sinusoidal voltage was applied to the transmitter, a 4.92 V peak-to-peak voltage was measured across the transmitter coil (Figure 4b) due to the impedance mismatch with the function generator. Proper alignment (Figure 4a) with the receiver coil resulted in a resonant voltage of 4.2 V peak-to-peak as shown in Figure 4c. This equates to a 14.63 % voltage drop from transmitter to receiver.

These findings reveal the feasibility of employing 3D-printed coils in the development of flexible devices for wireless power transmission, with particular relevance to wearable electronics and soft robotics that require soft, flexible components capable of safe wireless charging.

2:45 PM
Nanostructured Materials and Devices
Session Chairs: Kris Bertness (National Institute of Standards and Technology), Parsian Mohseni (Rochester Institute of Technology)
ESJ 2204

02:45 PM
Electrolyte-Gated Junctionless III-V Nanowire Transistors: A TCAD-Based Evaluation (Student)
Mr. Muhammad Islam[1], Mr. Nithil Manimaran[1], Dr. Alireza Abrand[1], Mr. Wyatt Morrell[1], Prof. Ahmad Kirmani[1], Prof. Ke Xu[1], Prof. Parsian Mohseni[1]
[1]Rochester Institute of Technology

Transistor scaling is critical to sustaining the historical pace of increased logic device density and improved performance per chip. However, continued scaling faces major obstacles such as managing the exponential rise in gate tunneling leakage current, controlling short channel effects, and variability at nanometer dimensions. To overcome the leakage challenges, the adoption of a high-κ dielectric solution reduces carrier mobility. However, high-κ dielectric-based gate stacks present other obstacles, including bias temperature instability, complex processing and integration, challenge of achieving high-quality interfaces, and ensuring material stability without undesirable reactions. As an alternate, electric double layer (EDL) gating using ion conducting electrolytes enables ultra-high charge carrier densities (i.e., > 1014 cm-2), which exceed the capability of oxide dielectrics before reaching breakdown. They also open novel routes toward tuning exotic materials properties such as superconductivity, by leveraging the high EDL capacitance even at low gate voltages (i.e., < 1 V). To date, significant progress has been made using EDL gating on two-dimensional (2D) semiconductors. However, fabricating integrated circuits using 2D transistors and scaling devices to nanoscale dimensions, while ensuring their thermal stability and long-term reliability, remains challenging. On the other hand, III-V semiconductors (i.e., InxGa1-xAs) offer higher carrier mobilities, compositionally tunable bandgaps, and ease of integration with silicon by leveraging nanostructure epitaxial growth. Their excellent transport properties enable high frequencies and power efficiencies unattainable by silicon, making them highly attractive candidates for next-generation electronics and photonics. In this work, we simulate the operation and performance of electrolyte-gated junctionless III-V nanowire (NW) transistors composed of compositionally-graded InxGa1-xAs channels. To mimic the EDL induced at the electrolyte/semiconductor interface, we add a 1 nm interfacial oxide layer to prevent charge transfer between the electrolyte and channel regions. We optimize the channel configuration by tuning the heterostructured InxGa1-xAs NW composition and doping profile, followed by device simulations under fixed and bias-dependent conduction band and valence band effective density of states. The simulations are performed using Silvaco's ATLAS 2D device simulation tool considering a drift-diffusion transport model with field-dependent, Lombardi CVT and concentration-dependent mobility model with Fermi-Dirac carrier statistics. Device scaling is tested for NW channels ranging from 20 to 100 nm in diameter, and 200 to 1000 nm in gate length. We benchmark the EDL double-

gated device structure against a conventional HfO2-gated device structure. We demonstrate an Ion/Ioff ratio of 106 for the EDL-gated device, with subthreshold slope of 61.2 mV/dec, and threshold voltage of 0.52 V, operating at a low drain voltage of 0.3 V. This represents two orders of magnitude improvement in Ion/Ioff ratio and ~30 mV/dec reduction in subthreshold slope compared to conventional junctionless oxide-gated NW transistors, demonstrating that EDL gating provides improved electrostatic integrity. An experimental process flow for the fabrication of the simulated devices will be presented. Future works include the integration of quantum mechanical confinement effects for thinner NW channels and full three-dimensional modeling to mimic the NW geometry with gate-all-around configuration. This work is anticipated to advance energy-efficient edge-computing and neuromorphic computing applications.

03:00 PM
Rapid Material Characterization with Scanning Microwave Microscopy for High-Throughput Material Discovery (Student)
Ms. Atefeh Ghafari[1], Mr. Jaemin Shin[1], Prof. Christopher Hinkle[1], Prof. Jonathan Chisum[1]
[1]Department of Electrical Engineering, University of Notre Dame

This paper presents a detailed analysis of Scanning Microwave Microscopy (SMM) for rapid material characterization, with applications in high-throughput material discovery. We explore the use of SMM within the high-frequency range of 1-10 GHz, aiming to determine key properties vital for the development of high-frequency microelectronics, such as dielectric constant, doping concentration, loss tangent, and conductivity [1]. Figure 1 illustrates our SMM setup, which combines an Atomic Force Microscope (AFM) with a Vector Network Analyzer (VNA). The microwave signal propagates to the AFM tip where it probes the material under test (MUT). We employed a circuit model, also depicted in Figure 1, to analyze tip-sample interactions and correlate the measured reflection coefficient S11 with the electrical properties of the MUT.
To evaluate the sensitivity of the SMM system, we measured various known materials, focusing on detecting local conductivity or carrier density variations. Figure 2(a) illustrates the system's proficiency in differentiating materials with slight conductivity differences, using a set of doped silicon samples with high conductivity (HC) ranging from 10 to 20 S/m, and low conductivity (LC) ranging from 0.1 to 0.2 S/m. Figure 2(b) presents a histogram of the S11 amplitude over ten frequency scans, highlighting the variations in measurements. The observed S11 data indicates that the system can detect larger variations in conductivity compared to within-sample variations, confirming its sensitivity to subtle changes. We further tested the repeatability of the SMM setup by changing measurement locations on a known homogeneous sample. As shown in Figure 2(c, d), the variance in the same material at different sites ("Point 1", "Point 2", and "Point 3") is minor compared to the variance between distinct materials but still larger than the variance for a single location on the samples. At each site, the SMM was lifted from the sample and landed at a new location, where ten frequency scans were recorded. Having characterized the stability of the SMM using a known doped Si sample, Figure 2(e, f) demonstrates the system on a custom-designed material, amorphous indium oxide doped with tungsten (IWO). The difference between high conductivity (HCD) and low conductivity (LCD) is smaller but still significant. This measurement confirms that for materials of interest, differentiation is possible.
The measured data can be fed into an AI/ML tool to correlate with parameters like conductivity and doping. Prior calibration of the SMM ensures the AI/ML tool focuses on significant features rather than systematic measurement errors. To this end, we investigate the modified short-open-load (mSOL) [2] calibration method. The traditional Short-Open-Load (SOL) calibration method requires a well-defined port (e.g, a coaxial cable) and readily manufactured impedance standards--the "Short", "Open", and "Load" standards. However, in the SMM setup there is no conventional port at the MUT and it is difficult, and sometimes not possible, to fabricate SOL standards. mSOL uses only capacitive loads as standards which is more suitable for SMM measurements as short and load configurations often resemble capacitive loads in series with the SMM tip. To evaluate the effectiveness of mSOL, we developed an electromagnetic (EM) simulation model of the SMM system and simulated the calibration of various complex loads, analyzing the percent error between the calibrated and expected S11 values. It was found that if the tip-to-MUT capacitance Ct, is within the range bounded by C1, C2, and C3 and the range is small relative to Ct, error is reduced. For new material systems, MUT capacitance is not known a priori, so it may be necessary to develop new calibration kits. In order to guide the design of custom calibration kits we used the EM simulation model to explore the parasitic electromagnetic environment around the tip including tip Ct, stray Cs, and ground-return Cg capacitances. Our findings in Figure 3 indicate that the size of the calibration pads in the calibration kit significantly determines the relative importance of the ground-return capacitance, Cg, impacting measurement accuracy. It is desirable that a tip/cantilever be designed such that Cg >> Ct so that Cg can be ignored (because it is in series), resulting in the simplified equivalent circuit in Figure 3(b). This simulation model is useful for understanding the validity of calibration, the design of new calibration kits, and even the design of new SMM probes.

03:15 PM
Functionalized Bioelectronic Materials for Multiplexed Leukocytes Enumeration Enabled by Machine Learning
Dr. Brandon Ashley[1], Dr. Jianye Sui[1], Dr. Mehdi Javanmard[1], Dr. Umer Hassan[1]
[1]Rutgers University

Functionalized bioelectronic materials finds many biomedical applications. Here, we present out work in developing biomedical platform where multiplex biomarker detection is enabled by functionalized bioelec- tronic materials. Bioelectronic materials in particular impedance-sensitive Janus polystyrene microparticles (MOJPs) with different electrical properties were utilized for targeting different biomarkers in complex sample matrices. MOJPs can be coated with different metal oxide layers (aluminum oxide, hafnium oxide, titanium oxide, etc.) with different thicknesses (5-30 nm) which makes them distinguishable at different probing frequencies. Re- cently, we have shown the target application for leukocyte multiplex detection. Hydrogel

microparticles were probed at different frequencies to generate unique electrical signatures. Once these particles are functionalized with specific antibodies, they can target different corresponding leukocyte antigens which were detected in a microfluidic impedance cytometer. We tested the multiplexing system with human blood samples collected from the patients.

03:30 PM
Perovskite Nanofiber Developed as the Matrix of Electrochemical Amyloid β Immunosensor
Mr. Antonio S Garcia[1], Mr. Bryson Core[1], Dr. Gibin George[1], Dr. Zhiping Luo[1], Dr. Shubo Han[1]
[1]Department of Chemistry, Physics and Materials Science, Fayetteville State University, Fayetteville, NC 28301, USA

Amyloid β protein (Aβ) is the main component of neuritic plaques in Alzheimer's disease (AD), the most common neurodegenerative disorder afflicting more than 50 million people in the world. The accumulation of Aβ has been considered as the molecular driver of Alzheimer's pathogenesis and progression1. Quantification of trace amount Amyloid β (Aβ) is informative for pre-clinical diagnosis of Alzheimer's disease (AD)2, in which nanomaterials-based electrochemical immunosensor is a promising method due to the high sensitivity3, 4. Besides other advantages of nanomaterials as the biosensor matrix, perovskite nanomaterials showed more strengths, such as tunable surface conformation and high biocompatibility5. In this work, electrospun perovskite nanofibers were fabricated for the development of an electrochemical immunosensor for Aβ detection in urine samples.
La0.75Sr0.25(NiCo)0.5O3 (LSCNO) was prepared following our earlier work6. Briefly, electro-spinnable solution containing the stoichiometric quantities of metal salts and gel forming medium was used to prepare precursor composite fibers by electrospinning, and then LSCNO was prepared by calcining the precursor composite fibers above the degradation temperature of the volatile components, finally the product was characterized by scanning electron microscopy (SEM), transmission electron microscopy (TEM) and energy dispersive spectrum (EDS). The nanostructured sensor matrixes were chemically modified with amino groups by using aminosilane (APTES), and then were immersed in a crosslinking solution 1-ethyl-3-(3-dimethylaminopropyl) carbodiimide (EDC) and N-hydroxysuccinimide (NHS) to obtain active surface with well-distributed carboxyl functional groups for anti-Aβ binding. Next, anti-Aβ was immobilized to the nanostructure surface, followed by blocking the free carboxyl ends by binding bovine serum albumin (BSA). Electrochemical immunosensors were then tested for Aβ solutions by using cyclic voltammetry (CV) and electrochemical impedance spectroscopy (EIS). Analytical performance such as dynamic and linear range, detection limit, and lower quantification limit were tested for the designed Aβ sensors. Aβ solutions containing interfering substances were detected by CV and EIS for the immunosensors. To evaluate the practical applications of the immunosensors to body fluids, the spike recoveries, and precisions of different Aβ concentrations in body fluid samples were studied by standard addition methods. The detection limit of the prepared LSCNO-based Aβ immunosensor is 10 pg/L, a level that can be used for AD early diagnosis. The sensor is free of any redox mediator, such as potassium ferricyanide due to electroactive and catalytic transition elements in LSCNO matrix acting as the same role, which not only simplified the analytical procedure, but also improved the sensor stability and prevented Aβ from further aggregation during the analytical process.

03:45 PM
Continuous Liquid Metal Printing of 2D Transparent Conductive Oxide Flexible Bioelectrodes (Student)
Mr. Md Saifur Rahman[1], Dr. Anand Tiwari[1], Prof. William Scheideler[1]
[1]Dartmouth College

Indium tin oxide (ITO) is a ubiquitous transparent conducting oxide (TCO) with applications in touch screens, solar cells, and smart windows. However, conventional ITO fabrication methods often rely on expensive vacuum deposition processes that produce brittle films unsuitable for flexible electronics. This study presents a pioneering approach utilizing continuous liquid metal printing (CLMP) to achieve scalable, high-performance, and transparent 2D ITO layers compatible with polymer substrates. By leveraging the low melting point of an indium-tin (In-Sn) alloy, we achieve spontaneous oxide growth at low temperatures, following Cabrera-Mott oxidation kinetics. A roller with precise control deforms the molten alloy that simultaneously grows and deposits the thin skin oxide layer onto surfaces via van der Waals adhesion across large areas (approximately 1200 cm^2) in mere seconds. The printing parameters, including deposition temperature, speed, and substrate choice, are employed to precisely tune the film properties, such as thickness, conductivity, and transparency. Furthermore, the fabrication technique demonstrates remarkable scalability, boasting high throughput capabilities of up to 30 meters per minute, with less than 0.6 nm print-to-print variability in film thickness (Figure 1).
These large-scale printed ITOs are characterized by a suite of material and mechanical characterization tools to determine their fitness as flexible, transparent bioelectrodes. Utilizing high-resolution Scanning Electron Microscopy (SEM), we unveil a distinctively flake-like grain growth with an average size of 55 nm (Figure 1). Under ideal conditions, these grain morphologies result in a film exhibiting superior conductivity (1400 S/cm) compared to any previously reported solution-processed or printed ITO films. We explore the crystalline characteristics of these nanoscale oxide films on plastic substrates (170˚C to 290˚C) using X-ray Diffraction (XRD), revealing key InOx cubic phases, such as (222) and (400) planes (Figure 2). We assess the flexibility of these printed ITO layers in comparison to sputtered ITO electrodes on plastic substrates, highlighting their ultrathin nature that provides significantly enhanced strain tolerance during cyclic bending (Figure 2). Moreover, we subject these flexible 2D ITO electrodes to test their film hardness and adhesion strength, which are crucial due to susceptibility to interfacial degradation from skin conformability and wear. They exhibit superior scratch resistance and adhesion strength in tape tests compared to commonly used bioelectrodes such as PEDOT: PSS and Gold (Au) film (Figure 3). Lastly, we demonstrate the practical application of these electrodes in a single-lead system for capturing electrocardiogram (ECG) signals and accurately measuring heart rate (Figure 3). These findings underscore the high potential of continuous liquid metal printing in harnessing metal oxides to refine and amplify the electronic properties of ITO beyond the current standards for low-temperature processed metal oxides.

2:45 PM
SiC Materials, Characterization and Devices
Session Chairs: Nadeemulal Mahadik (Naval Research Lab), Patrick Lenahan (Penn State University)
ESJ 1224

02:45 PM
Bulk 3C-SiC synthesis with Laser Diode Floating Zone (Student)
Mr. Ahamed Raihan[1], Mr. Daniel Harrison[2], Mr. Astrid Dzotcha Kengne[1], Mr. Evan Crites[3], Dr. Satya Kushwaha[3], Dr. Mvs Chandrashekhar[4], Dr. Birol Ozturk[1], Dr. Tyrel McQueen[3], Dr. Michael Spencer[1]
[1]Morgan State University, [2]Department of Electrical and Computer Engineering, Morgan State University, U.S.A, [3]Johns Hopkins University, [4]University of South Carolina, Columbia, USA

In recent years silicon carbide (SiC) has evolved as a widely recognized material in semiconductor industry. SiC exhibits great heat conductivity (λ), high breakdown voltage (EB), high charge carrier saturation velocity (Vs). SiC has applications for automotive power electronics, energy efficient and high-density power electronics with high switching frequency, and quantum computing. SiC exists forms in many different polytypes. The most common polytypes are 3C (cubic), 4H and 6H (both alpha). Most industrial applications utilize the 4H-SiC substrates because of the higher electron mobility. However, there are several specialized applications such as single photon sources, optical switching, and use as a cubic GaN seed for which 3C-SiC is ideally suited. Physical vapor transport (PVT) technique is the most widely used method to synthesis 4H-SiC. However, in this work, a Liquid Solid (LS) melting zone synthesis technique is utilized using Laser diode floating zone furnace to create single crystal 3C-SiC. Figure-1(a) demonstrates a side view of the molten zone, where graphite rod is used as feed from the bottom and 3C-SiC seed is provided from the top. In addition, 300mg of silicon crystal piece is placed on top of feed rod to create the melting zone at lower temperature. The dimensions of seed crystal are 1 mm x 2mm x 50mm which is diced from a 3C-SiC wafer commercially grown. The laser diodes were focused in the top and bottom part of seed and feed rod respectively to establish a small molten zone by connecting the two rods slowly. Figure 1(b) shows the liquid molten zone is formed where both rods are connected. During the whole process the top and bottom rod were constantly rotating at the same speed. Once stable molten zone is established, the top rod slowly pulled upward allowing the molten zone to move up, as showed in figure 1(c). Figure 1(d) shows, as the material solidifies it becomes part of the single crystal rod of 3C-SiC, which is the newly grown 3C-SiC part. The solidifying liquid may form multiple domain boundary in the initial phase. The thermodynamics of the system ultimately will select a single domain and single crystal will grow.
Figure 2 shows the initial X-ray diffraction results on potential growth of 3C-SiC with a characteristic peak at 35.7o, which is (111) plane. The FWHM is calculated by a gaussian fit around the (111) peak. The calculated FWHM is 0.302o, that suggests good crystalline growth. The estimated crystal grain size utilizing the Scherrer equation, which is 27.47 nm.

03:00 PM
Using a Convolutional Neural Network with Ultraviolet Photoluminescence Images to Map Defects on SiC Wafers
Dr. James Gallagher[1], Dr. Michael Mastro[1], Dr. Nadeemulah Mahadik[1], Dr. Karl Hobart[1], Dr. Travis Anderson[1]
[1]Naval Research Lab

Semiconductor manufacturing has been enhanced by the adoption of machine learning (ML) models particularly for mature materials such as silicon (Si) which are massed produced in foundries. However, for less mature materials such as wide bandgap semiconductors, the scarcity of manufacturing foundries and the high production costs makes obtaining large datasets difficult particularly in academic and small-scale laboratory setting they are typically studied. Silicon carbide (SiC) and Gallium Nitride (GaN) are prominent wide bandgap semiconductors, which exemplify this scenario, where dislocations defects are common and their impact on semiconducting device quality is not well studied.
Though it is possible to write a conventional computer program to quantify the defects, it can be challenging to achieve as many of the wafer scale techniques for detecting defects rely on subtle changes in signal and may have inconsistent intensities. Therefore, the algorithm may need to be changed with each sample. ML, on the other hand, requires obtaining good data for training, with the best algorithm selectable through hyperparameter optimization, which is more feasible today with faster computing speeds. In this study, we demonstrate ability to count defects on a SiC wafer wide bandgap semiconductors by employing ultraviolet photoluminescence (UVPL) imaging on a wafer scale to detect various dislocations. Through the cataloging of treading and screw dislocation locations in 50 small (~ 1 mm2) UVPL images, we successfully trained a machine learning model using TensorFlow software, showcasing its ability. This breakthrough advances defect detection capabilities for SiC and other thin film technologies with defects detectible by direct imaging. Additionally, it enables the application of ML models for defect detection in smaller laboratory settings where resources are limited.

03:15 PM
Investigating CVD Graphene Barriers for Remote Epitaxy of SiC
Dr. Daniel Pennachio[1], Dr. Jenifer Hajzus[1], Dr. Rachael Myers-Ward[1]
[1]Naval Research Lab

Remote epitaxy (RE) is a relatively new growth technique that utilizes 2D material as a release layer for epilayer transfer of conventional, non-2D material. [1] This technique requires uniform, single-to-few monolayer thick 2D material in order for the potential fields from the underlying substrate to penetrate the release layer and direct the epitaxial alignment. Most current remote epitaxial experiments rely on

transferred 2D material as a release layer, but this can introduce defects, such as tears and contamination, and also reduces scalability of the process. This work focuses on developing methods for in situ grown graphene release layers for RE of SiC epilayers on SiC(0001) starting substrates. This material system is uniquely suited for RE, as the graphene release layer can be grown epitaxially on the SiC substrate. The cost savings from substrate reuse after RE-enabled film transfer is also significant due to the expense of SiC substrates. In addition, thin, isolated SiC layers or SiC layers on insulators are promising systems for photonic devices and RE is a promising technique to produce these structures in a cost-effective manner without the damage associated with traditional epilayer transfer techniques such as controlled cleaving or ion implantation. Growing SiC on graphene is, however, challenging due to the high-temperature hydrogen-containing chemical vapor deposition (CVD) SiC growth environment, which will easily damage or remove graphene. This study investigates in situ propane-based CVD growth of graphene barriers for single-run SiC/graphene/SiC(0001) RE and focuses on growth methods to reduce damage to the graphene barrier.

For this study, a growth window for propane-based graphene CVD was established. Graphene films with minimal defects were produced by growing at 1620 °C in 20 slm H2 with 20 sccm propane flow. Raman spectral maps found that these conditions produced predominantly single-monolayer (ML) films on on-axis 6H-SiC(0001) substrates and 2-3 ML films on 4° off-axis 4H-SiC(0001) substrates. These films exhibited increased uniformity compared to epitaxial graphene growth via solely thermal Si sublimation, as determined by atomic force microscopy (AFM) and Raman spectral maps. Using the established optimal graphene boundary layer growth conditions, SiC remote epitaxial growths were conducted to study the effect of growth temperature, precursor C/Si ratio, and growth rate on hot-wall CVD SiC RE crystalline quality. Nomarski optical microscopy, scanning electron microscopy (SEM), and AFM found low growth rate SiC deposition at 1620°C with a C/Si ratio of 1.55 to have the smoothest surface morphology and fewest polytype inclusions. RE SiC crystalline quality appeared to be correlated to growth rate, with lower growth rates producing smoother films with fewer polytype inclusions. This study found single-crystalline polytype-pure SiC epilayers could be grown on 4° off-axis CVD graphene/4H-SiC(0001) substrates. Cross-sectional transmission electron microscopy (TEM) of some RE growth interfaces in this study exhibited non-uniform patches of multilayer graphitic carbon, motivating further study of this growth system to improve graphene boundary uniformity and SiC epilayer quality.

[1] Kim, Y., Cruz, S., Lee, K. et al. Nature 544, 340–343 (2017).

03:30 PM

Demonstration of Metal/3C-SiC/Silicon Bipolar UV Phototransistor (Student)

Ms. Mafruda Rahman[1], Dr. Muhammad Ali Johar[2], Dr. kannan vasudevan[2], Dr. Gary Tompa[2], Dr. Mvs Chandrashekhar[1]
[1]University of South Carolina, Columbia, USA, [2]Structured Materials Industries, Inc.

Silicon carbide (SiC) is a polytypic semiconductor currently used in power electronics. Recently 3C-SiC has been found to have high thermal conductivity 500W/mK1. Further interest in low-cost 3C-SiC/Si has been driven by quantum sensing systems to realize single photon emitters in 3C-SiC from defect/impurity state transitions. These “flying qubits” 2 have long coherence lengths for practical quantum systems by integrating other components such as microdisk resonators.2 To have fully integrated quantum systems, a high-performance photodetector is required. Previously, we have shown that high detectivity can be obtained in 4H-SiC photodetectors by using Schottky emitter/collector bipolar phototransistors,3 simplifying fabrication and overall device design, while similar Schottky electrode approaches have been successful in other materials.4

In this paper, we translate this approach to a metal/3C-SiC/Si Schottky electrode phototransistor. The large band offset at the 3C-SiC/Si heterojunction of 1.7 eV is suitable for good photodiode performance,5 owing to lower dark currents. Here, we improve photodiode performance by introducing bipolar gain. We measure the performance of our 3C-SiC phototransistors under different light wavelengths and report on the responsivity, response speed, and leakage current at different metal stack thicknesses of the device. The epitaxial layer (3C-SiC) grown on a p-Si substrate (MSE Supplies, Tucson, AZ) is 300nm thick. The Schottky contact was made by the metal stack of Ti/Au (5/20 nm), patterned with a photolithography lift-off process. Another sample with Ti/Au (2.5/10) was also made (Fig. 1a). Our dark current I-V results indicate that the 3C-SiC epilayer is n-doped, as shown by the positive polarity rectification with ideality n=2 of the metal/3C-SiC diode (Fig. 2a). Clear photocurrent response is seen under illumination with monochromatic light from 300-700nm (Fig. 2b).

E-h pairs created in the 3C-SiC base, photoelectrons in the base lower the barrier for hole transport from the p-Si substrate to the metal electrode. Larger photoresponsivity is observed for positive voltage, where the metal/3C-SiC junction is the emitter, with the large area p-Si/3C-SiC junction being the collector. For negative voltage, the small area Schottky junction is the collector, leading to lower absolute photocurrent, although when normalized for device area, the performance is comparable to the positive voltage Schottky emitter polarity. In both polarities, the photoresponse began increasing around the 3C-SiC bandgap ~2.3eV suggesting that band-to-band transitions are responsible for the observed photocurrent. Responsivity increased from <1A/W near 0V to >102A/W (Fig. 3) indicating the clear presence of photoconductive gain. Given that the hole transit time through the base is in the ps range for 10V bias, and that 3C-SiC is an indirect gap semiconductor with s recombination time, such high gains are advantageous for high gain devices at low light intensities. Initial results indicate response times in the ms range, which will be measured in greater detail. By introducing defect states in the 3C-SiC bandgap, bipolar photocurrent gain at the telecommunication wavelength of 1550nm may be realized.

03:45 PM

Investigation of high-order silane based SiGe epitaxy in ultra-high vacuum chemical vapor deposition process

Mr. Dongmin Yoon[1], Mrs. Hyerin Shin[2], Mr. Seokmin Oh[2], Mr. Seonwoong Jung[2], Mr. Dae-hong Ko[2]
[1]Yonsei univeristy, [2]Yonsei university

In the semiconductor industry, single-crystalline Si and SiGe are fundamental materials primarily produced through epitaxial growth on single-crystalline Si substrates via chemical vapor deposition. The performance of single-crystalline Si-based transistors has traditionally enhanced through 2-dimensional (2D) scaling, but this method has reached its physical and electrical limits. Innovative stacked device designs, such as 3D complementary field-effect transistors, are being developed to overcome these challenges. These designs require a low thermal budget during the processing of the upper device layers to avoid damaging the lower layers [1]. Moreover, unit processes aimed at significantly improving the electrical performance, for example, source/drain contact epitaxy to achieve low contact resistivity of sub 10-9 Ω.cm2, also call for low-temperature processes due to their placement in the post-gate stage of device fabrication [2]. These needs have prompted the proposal of high-order silanes (SinH2n+2, n≥2) as potential alternatives to conventional Si precursors, such as SiHCl3, SiH2Cl2, and SiH4. High-order silanes are preferred because their Si-Si bonds have lower bond energy, making them easier to decompose at low temperatures and leading to faster growth rates than with conventional precursors. This study explores the epitaxial growth of SiGe films using Si2H6, Si3H8, and Si4H10 under ultra-high vacuum chemical vapor deposition conditions. We investigated how changing the flow rates of each Si precursor affects the growth characteristics. We observed the SiGe films' Ge concentration and growth rate under varying growth conditions. We also observed the crystallinity and surface morphology of each film. Our results show that using high-order silanes is feasible for low-temperature SiGe epitaxy.

2:45 PM
Materials for Memory and Computation
Session Chairs: Susan Fullerton (University of Pittsburgh), Eric Seabron (Howard University)
ESJ 1202

02:45 PM
Enhancement hysteresis in transparent MOS device (Student)
Dr. Moumita Indra[1], Mr. Atul Sachan[1], Prof. Sandip Mondal[2]
[1]Indian Institute of Technology Bombay, [2]Assistant Professor, IIT Bombay

Modern electronic systems increasingly depend on flash memory, a type of non-volatile data storage system utilizing Metal-Oxide-Semiconductor (MOS) device technology. Recently, there has been growing demand for transparent memory, necessitating the development of cost-effective, sol-gel spin-coating techniques suitable for large-area electronics. Although there are reports of transparent memory technology using transparent dielectrics as channel layers, many of them are involved sophisticated ultra-high vacuum techniques or high-temperature deposition. Furthermore, some memory devices are limited to being UV-erasable and electrically programmable. In this study, we present a solution-processed Metal-Oxide-Semiconductor (MOS) device utilizing aluminum oxide phosphate (ALPO) and Indium-Gallium-Zinc-Oxide (IGZO) dielectrics.
All of the inorganic starting materials, specifically the powdered Al(OH)3, were dissolved in water to create the ALPO [Al2O3-3X (PO4)2X] precursor solution (resistivity: 18 MΩ cm). This mixture was mixed with 2 mol equivalents of HCl and a sufficient quantity of H3PO4 to achieve a concentration of P:Al ratio 0.5. The solution was stirred for approximately 24 hours at 90 °C in a water bath to ensure homogeneous density. The IGZO synthesis was conducted using with 18 MΩ DI water in normal lab environment. The sol-gel IGZO (70:15:15) was prepared with 0.070 M (315.87 mg) of Indium nitrate hydrate [In(NO3)·xH2O], 0.015 M (57.54 mg) Gallium nitrate hydrate [Ga(NO3)·xH2O], 0.015 M (66.94 mg) Zinc nitrate hexahydrate [Zn(NO3)2·xH2O] in anhydrous 2-methoxyethanol (2-ME) to yield the 0.3 M of metal ion concentration. The solution was stirred at 80ºC for one hour.
We fabricated two different devices: Device 1 with only ALPO and Device 2 with ALPO+IGZO (Device 2) as dielectric layers as shown in Fig 1. We used RCA cleaned low-doped (NA ~ 4×1015cm-3) p-type Si wafer (Single side polished, Orientation: <100>, resistivity ranging from 4.0 to 7.0 Ohm-cm) of thickness 275 µm. Each sample was cleaned for one minute (60 sec) in O2 plasma using a Plasma Asher. For the Device 1, ALPO is deposited by spin-coating on the Si wafer at 4000 RPM for 30 seconds. The spin-coating procedure was repeated twice to deposit two layers of ALPO. After deposition, the substrates were annealed at temperature 275°C. Indium-Tin-Oxide (ITO) of 50 nm was deposited as a top contact by Sputter Orion with a Shadow Mask to create the top contacts. The bottom metal contact was made using silver paste. For Device 2, an additional single layer of IGZO was deposited on top of the ALPO layers using same spin coating process and annealed at 110°C. The same top and bottom contacts as in Device 1 were applied.
We have measured capacitance as a function of voltage for both devices under different voltage sweeps as shown in Figure 2 and also noted the hysteresis window. We observed hysteresis window increases with voltage. The oxide capacitance (Cox) for Device 1 was found at 51.3 pF and 51.6 pF for 10 V and 20V respectively; whereas in case of Device 2, it was at 48.6 pF and 46.2 pF at voltage 5V and 20V respectively.

03:00 PM
Growth of Novel 2D Ferromagnet MnxSey by Chemical Vapor Deposition (Student)
Ms. Jennifer DeMell[1], Mr. Elias Kallon[2], Prof. Kevin Daniels[2]
[1]Laboratory for Physical Sciences, [2]University of Maryland, College Park

Theory predicts that MnxSey is strongly magnetic thin film with a high TC of nearly 250 K and stability in ambient conditions, unlike many other leading 2D ferromagnets.1 Despite the material’s suitability as a large-scale, high TCmagnetic thin film, much is still unknown and the crystallographic phases of thin-film MnxSey and their properties are still not well understood. In this work, we demonstrate the growth of novel 2D ferromagnet MnxSey in a three-chamber chemical vapor deposition system using Se

and MnCl2 precursor powders in an argon- and hydrogen-rich atmosphere on a sapphire substrate. A thorough characterization is performed with Raman spectroscopy, atomic force microscopy, and scanning electron microscopy. We observe a distinct Raman peak at 255 cm-1 using a 532 nm laser excitation source with a 14 mW spot power, which has been reported previously in the literature as the A1g Mn-Se stretching mode.2 AFM measurements show flake nucleation heights of around 15 µm. Finally, we discuss the primary parameters impacting crystal nucleation, focusing on the impact of the argon/hydrogen atmospheric ratio.

03:15 PM

Controlling the nanoscale heat flow in phase change memory with Sb2Te3/TiTe2 superlattices (Student)

Mr. Seppe Van Dyck[1], Dr. Kiumars Aryana[2], Mr. Md. Rafiqul Islam[2], Mr. William Riffe[2], Prof. Patrick Hopkins[2], Prof. Christophe Detavernier[1]
[1]Ghent University, [2]University of Virginia

Introduction
The heralded widespread implementation of computing on the edge and in the cloud partly relies on a new type of memory often called storage-class or non-volatile memory. Among the candidate technologies currently being researched to fill this place is phase change memory (PCM). Phase change memory cells offer very fast read and write, are very scalable and robust. Their functioning is based on a set of materials, called phase change materials with a specific set of properties. They can exist in multiple solid phase, typically crystalline and amorphous, where each phase has distinct optical and electrical properties. Because of this, data can be read out by simply measuring an electrical resistance. Writing data, i.e. changing the phase, happens through short current pulses that heat up the material in order to crystallize or melt-quench it in the desired phase. This makes this an energy-hungry technology and reducing its energy consumption is still one of the biggest challenges faced. Finding materials or architectures with a very low thermal conductivity can reduce the power consumption by preventing the created heat from dissipating into the surroundings. A good PCM material should therefore have a low thermal conductivity in both its crystalline and amorphous phase, but this is rarely the case for typical phase change materials such as Ge2Sb2Te5 (GST). These typically exhibit a relatively low thermal conductivity in the amorphous phase that increases drastically upon crystallization [1]. As superlattices of different kinds are currently being studied to improve PCM performance, it begs the question how the thermal conductivity of this structure holds up compared to bulk materials. More specifically, we will study Sb2Te3/TiTe2 superlattices, a material system first proposed by Shen et al. in reference [4]. After deposition and structural characterization of these superlattices, the thermal transport properties are examined using time-domain thermoreflectance (TDTR).
Time-Domain Thermoreflectance
TDTR is a laser-based pump-probe technique that can be used to accurately measure the thermal conductivity of thin-films [2], its working principle is sketched in figure 3. Samples are prepared with a metal transducer layer whose role it is to absorb the pump laser, heating up the surface. The reflection of the probe beam is then used to measure the evolution of the surface temperature. By fitting a model of the sample to the recorded transient response, the thermal conductivity can be extracted. As this technique does not require physical contact with the sample, it can be performed in situ during heating under an inert atmosphere. This is ideal for studying how the thermal conductivity evolves during an anneal of the superlattices, visualizing the phase change.
Results
All samples are created through magnetron co-sputtering from elementary pure targets, which creates planarly texturized layers upon anneal. This is verified through in situ and ex situ XRD, which can be seen in figure 1 and 2. The prominence of the 00L family of peaks is indicative of a strong crystalline texture of the films, while satellite peaks confirm the superlattice structure [3]. Three types of superlattice are created, as shown in figure 4. Both materials in the Sb2Te3/TiTe2 superlattice fulfil a different role: Sb2Te3 is the phase change material, while TiTe2 is added as a thermal insulation that stays unchanged during cycling. In figure 4 16 periods of the three types of superlattice are compared to a sample containing only the phase change material: 80nm of Sb2Te3. At room temperature we see that the relative composition of the superlattices has little effect on the as-deposited thermal conductivity. This can be explained by the high thermal resistance of the amorphous Sb2Te3 sub-layers that dominate the stack. While heating up, the thermal conductivity of all superlattices increases, analogous to the Sb2Te3 sample. When cooling back down, on the other hand, values for the superlattices decrease again, showing a lower thermal conductivity, even in the crystalline phase. We can see that for the sample with a 5nm Sb2Te3 – 3nm TiTe2 period, there is almost no contrast between its as-deposited and annealed state. This might indicate that the superlattice's added interfaces not only introduce a thermal resistance, but also influence the phonon population, leading to the low thermal conductivity contrast that is observed.
K. Aryana et al., Nat. Commun. 12, 774 (2021).
D. Cahill, MRS Bull. 43, 782 (2018).
M. Noh et al., Science 270, 1181 (1995).
J. Shen et al., ACS Appl. Mater. Interfaces 11, 5336 (2019).

03:30 PM

Memory effect in CdTe nanoparticles (Student)

Mr. Himanshu Marothya[1], Dr. Vishwas Acharya[2], Mr. Atul Sachan[1], Prof. Sandip Mondal[3]
[1]Ph. D Research Scholar, IIT Bombay, India, [2]Indian Institute of Technology, Bombay, [3]Assistant Professor, IIT Bombay

Non-volatile memories are the most widely used memory devices for permanent storage of data due to their capability of storing data for a long time. Conventional Flash memory devices use Floating-Gate (FG) memory cells but have reliability problems related to the leaking of electrons from continuous FG. Nanoparticles (NPs) based memory devices overcome this reliability problem due to discrete charge storage inside NPs. In this work, we have explored a fully solution-processed CdTe nanoparticle-based memory device that has an excellent memory window of ~8V. Simulations of fabricated devices are also performed using Sentarus TCAD Software that are well aligned with experimental data.

03:45 PM
In-situ Growth of {-201} Fiber-textured β-Ga2O3 Semiconductor Tape for Flexible Thin-Film Transistor
Dr. Xiao Tang[1], Dr. Haicheng Cao[1], Mr. Vishal Khandelwal[1], Mr. Saravanan Yuvaraja[1], Prof. Xiaohang Li[1]
[1]King Abdullah University of Science and Technology

Beta-phase gallium oxide (β-Ga2O3) is an emerging semiconductor material with an ultra-large bandgap of 4.8 eV, high critical field strength (8 MV/cm), and robust thermal/chemical stability. It is promising in various applications, such as deep ultraviolet optoelectronics, thin-film transistors (TFT), and hazardous gas sensors, due to its unique and excellent properties.1 The devices should be deposited on flexible templates to accommodate these electronics for portable and real-time uses. Currently, the most used flexible templates are based on polymers, including polyimide, polyether sulfone, and polycarbonate. In general, such polymer materials are lightweight and low-cost with robust deformability and have been readily adopted in the fabrication of diverse organic semiconductor materials.2 However, their low thermal stability limits their processing temperature to ~250℃. Additionally, β-Ga2O3 manifests semiconducting properties only when sintered above 500℃ due to an oxygen deficit. Hence, polymer templates are inappropriate for the deposition of β-Ga2O3 thin films. Alternatively, the “lift-off-paste” technique appears to realize the fabrication of β-Ga2O3-channeled flexible electronics; that is, single-crystalline β-Ga2O3 thin films are first routinely deposited on conventional rigid substrates and then lifted off and pasted on the mentioned polymer flexible substrates. Despite the high quality of the produced flexible electronics, the low output and reproducibility make the lift-off-paste technique yet ideal for actual large-scale production.2 In this context, there is a demand to explore flexible substrates with high thermal stability that allow for the direct deposition of β-Ga2O3 thin films. Hastelloy is a superalloy material comprising nickel, molybdenum, tungsten, and chromium and has a super-high thermal stability of up to 1100℃. Tape made of Hastelloy has been widely commercialized and exhibits excellent deformation. With this consideration, we adopt Hastelloy tape as a flexible substrate for the in-situ deposition of β-Ga2O3 thin films.3,4
Hastelloy tape is first coated with an insulating/planarization layer comprising SiOx and Al2Ox. On top of the Al2Ox layer, the β-Ga2O3 thin films are grown via pulsed laser deposition (PLD) and have a fabric texture with an out-of-plane preferred orientation along <–201>. Based on a 10-cm-long β-Ga2O3 coated tape, for the first time, dozens of transistors with a top-gate configuration are fabricated using β-Ga2O3 as the channel layer. The picture of the twisted flexible transistor tape and the cross-section microscopic images are shown in figure 1. Out of the 48 tested transistors, 35 exhibit clear on-off transition behavior. The representative transistor displays an on current of 4 μA at a gate voltage (VGS) of 10 V, drain voltage (VDS) of 10 V, threshold voltage of approximately -2.75 V, and subthreshold swing of 650 mV/dec. The high critical field strength of β-Ga2O3 results in the breakdown voltage of the transistors reaching 116 V. The representative results are shown in Figure 2. A fatigue test was also performed on the patterned β-Ga2O3 flexible tape, indicating that the transistors have a robust mechanical property with no significant degradation of the electrical performances after 20,000 bending cycles (Figure 3).
We believe this work provides a novel flexible platform for high temperature in situ growth of various inorganic semiconductors. Moreover, it paves the way for complementary metal-oxide-semiconductor transistor operation in flexible display and circuit technologies in the future.

2:45 PM
Heterointegration of WBG/UWBG Semiconductors
Session Chairs: Robert Roberts (The University of Texas at El Paso), Mona Ebrish (Vanderbilt University)
ESJ 1215

02:45 PM
Direct wafer bonding of GaN on AlN for thermal management and power device applications (Student)
Mr. Kaicheng Pan[1], Dr. Kenny Huynh[1], Dr. Man Li[1], Dr. Yijun Ge[1], Prof. Timothy Fisher[1], Prof. Yongjie Hu[1], Prof. Mark Goorsky[1]
[1]University of California, Los Angeles

Direct wafer bonding of Gallium Nitride and Aluminum Nitride is presented in this study. The choice of the GaN-AlN material pair has multiple benefits. First, due to their small coefficient of thermal expansion mismatch and the high thermal conductance of AlN, AlN can function as a thermal management layer for GaN power devices. Second, the strong spontaneous polarization at both GaN and AlN surfaces gives rise to large net polarization charge difference, which leads to the generation of 2D electron gas or a 2D hole gas at the interface depending on the orientation of the GaN and AlN wafers.[1] In this work, we chose direct wafer bonding over epitaxial growth because the epitaxial buffer layer or critical thickness limits the GaN film thickness grown on AlN, which may lead to misfit dislocations and poor crystal quality. Also, strain-free layers can be achieved by wafer bonding, eliminating the strain induced piezoelectric stress that negatively impacts the polarization.[2]
For bonding, 2” GaN and 2” AlN wafers were polished using processes based on our earlier work to produce sub-nanometer roughness GaN [3] and bonded after standard cleaning and immersion in a (NH4)2S solution. The samples were rinsed, dried and pressed Ga- to N-face (AlN). Under moderate pressure (~50 kPa) and room temperature bonding was initiated. A significant fraction of the surfaces bonded, except for a couple of triangular regions associated with growth sector boundaries in the GaN. Subsequent annealing up to 800 C° was performed to strengthen the bond and to test the structure for high temperature stability. Similar CTE values between GaN and AlN at high temperatures allow for high temperature annealing without debonding or cracking. The GaN substrate was then grinded and subjected to CMP to as thin as 200 nm to realize the intention of having a thin film of GaN on AlN. High resolution X-ray Diffraction rocking curves and RSMs, transmission

electron microscopy and time-domain thermal reflectance measurements confirm high crystalline quality.
High resolution transmission electron microscopy shown in Figure 2(a) reveals complete crystallinity across the interface. However, only a ~1.5 nm interfacial region is observed, which is suspected to be caused by reconfiguration of the interface after a total anneal of 350 °C 22 hours, 600 °C 1 hour, and 800 °C 1 hour. No thicker amorphous or oxide interfacial layer commonly found in other bonding methods (surface activated bonding, plasma treatment, or other interfacial layers) [4-7] are observed in this study. High resolution X-ray diffraction measurements indicated a strain-free layer with good crystal quality, and minimal subsurface damage was induced in the GaN thin film during thinning. The thermal boundary conductance is ~250 MW/m2K, measured by time domain thermal reflectance, shown in Figure 2(b). This high TBC value supports the concept of an AlN thermal management layer via wafer bonding.
This project is funded by the DARPA Program: “Doping-enhanced thermal transport at WBG semiconductor interfaces.”
[1] Hobart, Karl D., et al. U.S. Patent Application No. 17/731,289, (2023)
[2] del Alamo, Jesús A., et al. Microelectronics reliability 49.9-11 (2009): 1200-1206.
[3] S. Hayashi, et al., J. Electrochem. Soc., 155(2), p.H113 (2007)
[4] M.E. Liao, et al., ECS Trans., 86(5), 55 (2018)
[5] V. Dragoi, et al., ECS Trans., 86(5), 23 (2018)
[6] Y. Xu, et al., Ceram. Int., 45, 6552 (2019).
[7] F. Mu, et al., Appl. Surf. Sci., 416, 1007 (2017)

03:00 PM

Understanding the breakdown-field capability of narrow band gap (p-Si)/ultra-wide band gap (n-Ga2O3) heterojunction p-n diode (Student)

Mr. Shuwen Xie[1], Mr. Md Tahmidul Alam[1], Dr. Jiarui Gong[1], Mr. Qinchen Lin[1], Dr. Moheb Sheikhi[1], Mr. Jie Zhou[1], Dr. Fikadu Alema[2], Dr. Andrei Osinsky[2], Prof. Shubhra Pasayat[1], Prof. Zhenqiang Ma[1], Prof. Chirag Gupta[1]
[1]University of Wisconsin-Madison, [2]Agnitron Technology Incorporated

In recent years, β-Ga2O3 has emerged as a promising candidate for the next generation of ultra-wide bandgap material. With a large bandgap (4.8 eV), high critical electric field (Ec) (8 MV/cm), and high Baliga’s figure of merit, β-Ga2O3 can potentially enable power electronics that exceed high voltage performance of silicon carbide (SiC) and gallium nitride (GaN) [1]. The lack of p-type capability in Ga2O3 necessitates hetero-integration. P-type Silicon is a reasonable choice for hetero-integration as the Si/Ga2O3 heterojunction high voltage device may be on-chip compatible to conventional CMOS gate drivers. In addition, while Si/Ga2O3 heterojunction combines materials narrow and ultra-wide band gap, it is intriguing to investigate its breakdown mechanism and it’s limitations. In this work, we demonstrate a Si/(001) Ga2O3 heterojunction p-n diode with a breakdown voltage of 752 V corresponding to a breakdown field of > 2 MV/cm (6x higher than Si breakdown field) fabricated using semiconductor grafting.

A 2-inch (001) β-Ga2O3 epitaxial wafer was used to fabricate the heterojunction diode. An 8.2 μm thick, ~1.4×1016 cm-3 Si-doped epitaxial layer was grown on a n-type substrate using halide vapor phase epitaxy (HVPE). A silicon on insulator (SOI) wafer with a 185 nm-thick device layer heavily doped with boron (~1x1020 cm-3) was used as the p-type material. Fig. 1 (a-f) shows the Si/(001)-Ga2O3 heterojunction p-n diode fabrication process flow. The SOI wafer was first patterned and immersed in Hydrofluoric acid (HF) to etch away the sacrificial SiO2 layer. The released Si NM was then picked up using a PDMS stamp and transferred on to the Ga2O3 wafer. It is noted that even though no foreign ultra-thin oxide (UO) layer was inserted at the interface between Si and Ga2O3 intentionally, the surface nonstoichiometric GaOx and possible native oxide on the released Si layer are expected to have served the double-side passivation functions as the UO layer used in general grafting approach. Rapid thermal annealing (RTA) was performed to bond the NM and substrate. Reactive-ion etching (RIE) isolation was performed to form mesa of 50 μm diameter, and p-ohmic (Al/Ni) and n-ohmic (Ti/Ni) metal was deposited at the top and back side of the wafer using E-beam evaporation.
The diode showed a breakdown voltage (Vbr) of ~752 V, shown in Fig. 2, which is one of the highest breakdown voltage reported for Si/(001) Ga2O3 heterojunction diode to date. The specific on resistance (Ron,sp) was measured to be 7.02 mΩ·cm2, corresponding to a power figure of merit of ~80.6 MW/cm2. The average peak electric field (Em) was calculated to be >2 MV/cm near breakdown, higher than the Ec of Si (~0.3 MV/cm) [2]. The heavily doped p-Si depletion width was estimated to be ~1 nm at breakdown, significantly smaller than the electron mean free path [3], therefore, the depletion region in Si is not enough for the p-side injected electrons to be accelerated and acquire enough energy to result in avalanche behavior in Silicon. In addition, the depletion width at Ga2O3 side is much longer than Si, which leads to a higher possibility for the electron impact ionization to happen at the Ga2O3 side. Catastrophic breakdown is confirmed by optical microscope inspection, with delamination observed on Ga2O3 surface, shown in Fig. 3. The on–off ratio was 2.28 × 107 at –4 and 4 V, and the ideality factor was 1.58. C-V scanning between -4 V and 0 V was performed with no hysteresis observed, shown in Fig. 4. The built-in voltage (Vbi) was extracted to be ~1.12, and turn-on voltage (Von) to be ~1.23 V. Further optimization of the fabrication process to improve the interface quality and edge termination in our future studies could lead to a higher performance Si/Ga2O3 heterojunction diode.
Acknowledgment: The work was partially supported by DARPA H2.
[1] Mastro, Michael A., et al. ECS Journal of Solid State Science and Technology 6.5 (2017): P356. [2] Xue, Chunlai, et al. 2009 6th IEEE International Conference on Group IV Photonics. IEEE, 2009. [3] Gergely, G., et al. Vacuum 48.7-9 (1997): 621-624.

03:15 PM

Fabrication and characterization of heterogeneous pn and Schottky diodes made with bonded GaN membranes

Dr. Eric Blanton[1], Dr. Stefan Nikodemski[1], Dr. Nicholas Glavin[1], Dr. Michael Snure[1]
[1]Air Force Research Laboratory

To achieve higher performance microwave and power devices, heterogeneous heterojunctions are being explored that extend potential heterojunction combinations beyond that allowed by traditional growth techniques [1]. In particular, the ability to build heterostructures with bonded GaN and other III-N's is desirable to optimize performance in devices, e.g. hot electron transistors and heterojunction bipolar transistors. However, GaN membrane production/processing as well as interface quality challenges must be solved before the benefits of this technology are realized. To this end, we have fabricated a series of pn and Schottky junctions using transferred n-GaN membranes: n--GaN-p+-Si and n-GaN-p-GaN pn junctions and n-GaN-graphene Schottky junctions. IV-T, CV, and transmission electron microscopy were used to understand the transport mechanisms across and potential defect-related issues at the interface. To achieve the freestanding GaN layers, Si-doped GaN was grown by MOCVD on BN-on-sapphire templates before being separated from the growth substrate. Stressed Ni spalling was used to facilitate fracture at the weak BN van der Waals (vdW) interface [2]. The ~2um thick GaN layer was thinned from the backside using a Cl-based dry etch before the Ga-face was vdW bonded to the secondary substrate.

03:30 PM
Lapping and Chemical Mechanical Polishing of wide and ultra-wide bandgap semiconductors (Student)
Mr. Kaicheng Pan[1], Dr. Kenny Huynh[2], Prof. Mark Goorsky[2]
[1]UCLA, [2]University of California, Los Angeles

Optimization of surface preparation of wide and ultrawide bandgap semiconductors is presented in this study. The surface optimization recipes of single crystal Gallium Nitride and Aluminum Nitride wafers are not well established and lead to suboptimal surface roughness, which create obstacles for further integration and application of the material. For example, the as-received single crystal AlN wafers from wafer suppliers show around 3 nm RMS on both sides, and the N-face of single crystal GaN wafers usually are unpolished and show ~1 μm RMS. Thus, Chemical Mechanical Polishing becomes a critical and necessary tool to produce atomically smooth surface (<1 nm RMS) for epitaxy and wafer bonding purposes. In this study, the N-face and the Al-face of the AlN were successfully polished to <1 nm RMS roughness on a Logitech PM5 polishing machine using chemistry based on our previous work with GaN CMP [1]. Diluted sodium hypochlorite solution was used for the N-face of AlN and a combination of diluted citric acid and sodium hypochlorite solution was used for the Al-face of AlN. The sodium hypochlorite solution oxides the N-face of the wafer, creating a mechanically weaker oxidation layer that can be polished with the mechanical abrasion of the polishing pad, achieving the desired smoothing and planarization of the surface. Furthermore, for the more chemically inert Al-face, the combination of citric acid and sodium hypochlorite solution was proven effective for oxidizing and polishing the surface. Similarly, the rough N-face of GaN was also successfully polished to sub-nanometer roughness from 1 μm RMS roughness using first 9 μm particle size alumina slurry, Chemlox polishing fluid, and finally sodium hypochlorite solution. Atomic force microscope scans in Figure 1 show the comparison between as-received and polished surfaces. These atomically smooth surfaces achieved on GaN and AlN wafers pave the way for direct wafer bonding and epitaxial growth on both III- and N-face, providing opportunities to explore thermal and electrical properties of different surface combinations.
Controlled roughening of the surface is also important for effective heating of the wafer for applications such as MBE growth. The originally smooth N-face (~2 nm RMS roughness) of AlN was successfully and uniformly roughened to 500 nm RMS roughness with peak to valley distance as deep as 2.4 μm. Due to the hardness of the AlN wafers, large particle size (45 μm) diamond lapping paste and high pressure (40 kPa) were used. Figure 2 shows the atomic force microscope and the optical image of the roughened AlN surface. However, an increase in wafer curvature was observed for the roughened wafer. The flattening of the curved wafer by annealing under growth-like conditions will be presented. [2]
This work is supported by the Office of Naval Research through a MURI Program.
[1] S. Hayashi, et al., J. Electrochem. Soc., 155(2), p.H113 (2007)
[2] Wang, Y., et al., ECS Journal of Solid State Science and Technology 10.4 (2021): 045010.

03:45 PM
p-GaAsn-Ga2O3 heterojunction diode with breakdown voltage of ~800V (Student)
Mr. Shuwen Xie[1], Dr. Moheb Sheikhi[1], Mr. Shining Xu[1], Mr. Md Tahmidul Alam[1], Mr. Jie Zhou[1], Prof. Luke Mawst[1], Prof. Zhenqiang Ma[1], Prof. Chirag Gupta[1]
[1]University of Wisconsin-Madison

In recent years, β-Ga2O3 has shown great potential in power electronics due to its high breakdown field (~8 MV/cm), wide bandgap (~4.8 eV), and decent electron mobility.[1] β- Ga2O3 based Schottky diode, vertical and lateral field effect transistors of high breakdown voltage have been reported, and their extraordinary breakdown performance is promising for high voltage applications.[2] However, due to the large effective mass of holes, valence band structure, and the lack of shallow p-type dopant in β-Ga2O3, p-type conductivity in β-Ga2O3 is considered extremely challenging. One alternative way to overcome this issue is using semiconductor grafting technology to hetero-integrate a p-type material nanomembrane (NM) with Ga2O3, which has shown great potential in recent years.[3-4] Here, using semiconductor grafting technology, we hetero-integrated a p-type GaAs NM with n-type Ga2O3 to create a heterojunction diode which showed a breakdown voltage of ~800V. By taking advantage of the InGaAsP alloy system, a wide variety of GaAs-Ga2O3 based high voltage HBT can be further developed, making this material platform very attractive.
The fabrication process was illustrated in Fig. 1. A GaAs epitaxial wafer was grown with metal-organic chemical vapor deposition (MOCVD). A 400 nm p-GaAs NM layer (Zn, 1×1018 cm-3) was grown on a 500nm thick unintentionally doped AlAs sacrificial layer. The wafer was patterned and immersed in diluted Hydrofluoric acid (HF) to etch away the sacrificial AlAs layer and release the NM. The NM was then picked up with PDMS and transferred onto a n-type β-Ga2O3 epitaxial wafer with 8.2 μm epitaxial layer (Si,

9×1015 cm-3) grown on a 600 μm substrate (Sn, 6.2×1018 cm-3) with hydride vapor phase epitaxy (HVPE). In this case, the surface GaOx of the Ga2O3 wafer functions as both the double-side passivation and quantum tunneling layer, without a foreign ultra-thin dielectric layer required to be inserted at the interface as shown in general grafting approach.[5] A low temperature RTA was performed to bond the NM and the wafer, followed by ICP-RIE GaAs mesa patterning. The p-ohmic metal (Ti/Ni: 30 nm/100 nm) with diameter 25 μm was deposited with e-beam evaporation on top of the GaAs mesa. The n-ohmic metal (Ti/Ni: 50 nm/200 nm) was deposited on the backside of the Ga2O3 wafer. The fabricated p-GaAs/n-Ga2O3 heterojunction diode of 25 μm diameter showed a breakdown voltage of ~800 V, shown in Fig. 2. The specific on resistance was calculated to be 5.06 mΩ·cm2, corresponding to a power figure of merit of 126.5 MW/cm2. At high reverse bias, an extremely low leakage of ~1.77 nA current was observed. The average peak electric field was calculated to be 1.60 MV/cm. The turn on voltage of the diode was determined to be around 1.91 V at threshold current density of 10-1 A/cm2, with an on-off ratio to be 6×106 at –4/4 V. The ideality factor was extracted to be approximately 1.34 indicating reasonable interface quality. By managing the peak electric field with suitable edge termination techniques, higher breakdown voltage can be expected, shown in Fig. 3. In addition, by taking advantage of the InGaAsP alloy system, a wide variety of GaAs-Ga2O3 based high voltage HBT can be further developed.

Acknowledgment: The work was partially supported by DARPA H2.

[1] Mastro, Michael A., et al. ECS Journal of Solid State Science and Technology 6.5 (2017): P356. [2] Yang, Jiancheng, et al. IEEE Electron Device Letters 38.7 (2017): 906-909. [3] Liu, Dong, et al. arXiv preprint arXiv:1812.10225 (2018). [4] Xie, Shuwen, et al. IEEE Electron Device Letters (2024). [5] Gong, Jiarui, et al. arXiv preprint arXiv:2305.19138 (2023).

4:30 PM
Panel Discussion: Future Careers in Electronic Materials
Session Chair: Adrienne Stiff-Roberts (Duke University)
ESJ 0202

Panel Members:
Dr. Kris Bertness, National Institute of Standards and Technology (NIST)
Dr. Hemant Dixit, Wolfspeed
Dr. Nadeemullah Mahadik, U.S. Naval Research Laboratory
Prof. Jamie Phillips, University of Delaware
Prof. Shayla Sawyer, Rensselaer Polytechnic Institute

6:00 PM
EMC 2024 Conference Dinner
Stamp Student Union Building, Grand Ballroom

TECHNICAL PROGRAM

FRIDAY

JUNE 28, 2024

8:00 AM
Registration Opens
ESJ Building, Ground Level

8:30 AM
Growth of Group III-Nitrides
Session Chairs: Russell Dupuis (Georgia Institute of Technology), Theeradetch Detchprohm (Georgia Institute of Technology)
ESJ 0202

08:30 AM
Electrical Conductivity of Si-doped AlN on Sapphire: Effects of Various Growth Conditions
Dr. Haicheng Cao[1], Mr. Mingtao Nong[1], Dr. Xiao Tang[1], Prof. Chehao Liao[1], Mr. Vishal Khandelwal[1], Prof. Ying Wu[1], Prof. Xiaohang Li[1]
[1]King Abdullah University of Science and Technology

Semiconductors with larger bandgaps are increasingly crucial due to rapid advancements in power device technology [1]. Among them, Aluminum nitride (AlN), with its ultra-wide bandgap (6-6.2eV), high breakdown field, thermal conductivity, and its seamless integration with nitride-based devices has attracted extensive interest. To date, the epitaxial growth of high-quality doped AlN via MOCVD has predominantly been conducted on native AlN substrates to mitigate dislocation densities. However, the limited size and prohibitive cost of native AlN substrates necessitate exploring the growth of high-quality doped AlN on alternative substrates for commercial viability. Therefore, our study focuses on MOCVD growth of doped AlN epitaxy on sapphire substrate, and aims to examine the relation between epitaxial conditions, surface morphology, defects, and AlN film conductivity on sapphire substrate.
In our research, we grew a 636nm undoped AlN layer and a 500nm Si-doped layer (Si: 4.6×1018 cm-3) on an AlN template on sapphire. We primarily investigated two critical growth conditions: temperature (1100°C to 1300°C) and V/III ratio (1000 to 5000), using a single quarter of a substrate for each individual condition to eliminate the impact of substrate differences. Cathodoluminescence (CL) spectra and Circular Transmission Line Measurement (CTLM) method were used to characterize the defect and conductivity of the Si-doped AlN, respectively. During CL characterization, the acceleration voltage was precisely maintained at 4 keV to ensure all the signals are from the Si-doped layer.
The full width at half maximum (FWHM) of the rocking curves on AlN (002) and (102) orientations (Fig. 2 (h-k)) show crystallization and dislocation density to be largely unaffected by varying growth conditions. However, atomic force microscopy (AFM) images (Fig. 2 (a-c)) revealed that increased growth temperatures led to a morphological shift from bilayer to macro-step flow due to a reduced aluminum surface supersaturation [2]. Higher temperatures also resulted in decreased conductivity (Fig. 3 (a)), rendering Si-doped AlN non-conductive at 1300°C. CL spectra in Fig. 3 (g) show the emergence of Al vacancy-Si (VAl-Si) complex peaks at higher temperatures, indicating the formation of VAl-Si complexes that lead to Si compensation and reduced conductivity. At 1300°C, the VAl-Si peak shift to higher energies, suggesting the creation of high-order VAl-nSi complexes [3] and further increased resistivity. Temperature-dependent conductivity measurements (Fig. 3 (b)) indicated no significant change in Si ionization energy in AlN, implying a dominant role for deep state (Si-DX) centers [4].
With increasing V/III ratios, surface morphology comparisons (Fig. 2 (d-g)) show 3D growth features with increased roughness and enhanced nAlN conductivity (Fig. 3 (c)). CL spectra variations (Fig. 3 (h)) reveal a strong relationship between conductivity and reduced carbon defect (CN) peak intensity, as evidenced by the decrease of CN (an acceptor center). Moreover, the ionization energy of Si remained consistent across different V/III ratios (Fig. 3 (d)), with Si-DX centers still predominant.
Overall, this study is crucial in demonstrating the interdependence between Si-doped AlN epitaxial conditions on sapphire and factors like conductivity, surface morphology, and defects, providing essential insights for the cost-effective heteroepitaxial growth of AlN-based power devices.

08:45 AM
Crack-Free AlN Film Exceeding 1-µm Thickness Epitaxially Grown on Si Substrate (Student)
Mr. Muhammad Aqib[1], Dr. Mina Moradnia[1], Dr. Mihee Ji[2], Dr. Vijay S. Parameshwaran[2], Dr. Wendy L. Sarney[2], Dr. Sara Pouladi[1], Dr. Nam-In Kim[1], Dr. Gregory A Garrett[2], Dr. Anand V Sampath[2], Dr. Rebecca Forrest[1], Prof. Jae-Hyun Ryou[1]
[1]University of Houston, [2]Army Research Laboratory

Ultra-wide bandgap AlN and AlxGa1-xN materials offer many advantageous properties, including excellent thermal and chemical stability, high dielectric breakdown voltage, bandgap energies corresponding to the deep ultraviolet spectrum, excellent electromechanical conversion, and high surface acoustic velocity. For such device applications, relatively thick and high-quality AlN layers are needed in buffer and device epitaxial structures. Relatively thick AlN films have been epitaxially grown on sapphire, SiC, and native AlN substrates. However, the growth of high-quality, thick-film, and crack-free epitaxial AlN materials on cost-effective large-area Si substrates consistently encounters numerous technical challenges. Achieving thick AlN films on Si substrates is primarily hindered by crack formation in the epitaxial film, arising from significant mismatches in lattice and thermal expansion parameters, which results in strain accumulation during the epitaxial growth and cooling-down process. Most thick (e.g., > 400 nm) AlN films on Si grown by molecular beam epitaxy (MBE) or metalorganic chemical vapor deposition (MOCVD) ended up with crack formation along the cleavage planes. In this presentation, we propose a method to address the technical challenge of crack formation in relatively thick AlN films. Specifically, we examined different interlayers that satisfy the following requirements: (1) Its crystalline structure has an epitaxial

relationship with both the AlN layer and Si substrate; (2) it can mitigate the in-plane tensile strain in AlN or convert the strain status to in-plane compressive strain; (3) it is sufficiently ductile, and hence has very high cleavage energy, to not form cracks even with large in-plane tensile strain exerted from the substrate; and (4) the interlayer can be partially relaxed so that the strain from the substrate is not conveyed to the AlN layer. Among the possible candidates, we used Au to test the hypothesis that ductile epitaxial interlayers modify the strain in AlN and prevent crack formation. We demonstrated that the strain in a 1.5-μm thick AlN layer deposited by sputtering and MBE was modified by the ductile Au interlayer and prevented the formation of cracks, as evidenced by surface and cross-sectional characterization by X-ray diffraction, transmission electron microscopy, and atomic force microscopy. The control sample with the same AlN thickness but without the Au interlayer had cracks. These findings hold significant promise for advancing the field of ultrawide-bandgap semiconductor materials, with potential applications in electronic, optoelectronic, sensing, and energy device applications.

09:00 AM
Semi-metallic conductivity in N-polar Al-rich AlGaN on C-face 4H-SiC by Molecular Beam Epitaxy (Student)
Mr. Shubham Mondal[1], Mr. Pat Kezer[2], Mr. Md Mehedi Hasan Tanim[1], Dr. Ding Wang[1], Prof. John Heron[1], Prof. Emmanouil Kioupakis[1], Prof. Zetian Mi[1]
[1]University of Michigan, [2]University of Michigan, Ann Arbor

Recent technological focus on III-Nitride semiconductors revolves around ultra-wide bandgap materials, particularly AlGaN. This material stands out for its direct tunable ultrawide-bandgap, large breakdown field, low intrinsic carrier concentration, and the ability to be doped both n and p-type. In heavily doped semiconductors like AlGaN, achieving extremely low resistivity poses a significant challenge. The development of high performance wide-bandgap AlGaN channel transistors with high current densities and reduced Ohmic losses necessitate extremely highly doped, high Al content AlGaN epilayers for regrown source/drain contact regions. In this work, we demonstrate the achievement of semi-metallic conductivity in Silicon (Si) doped N-polar Al0.6Ga0.4N grown on C-face SiC substrates by Molecular Beam Epitaxy (MBE). The epitaxially grown films show smooth surface morphology, with an r.m.s roughness of only ~ 0.25 nm and optimization of growth conditions have led to the identification of a growth window for the effective suppression of compensating defects, as evidenced from PL spectroscopy. Owing to the highly efficient doping, Mott transition to the semi-metallic state has been achieved in this work, with an exceptionally high free electron concentration of ~ 1.8 × 1020 cm-3 as obtained from Hall measurements in the standard van-der Pauw configuration, with a high mobility of 34 cm2/V·s, leading to a room temperature resistivity of only ~ 1 mΩ·cm. Temperature-dependent Hall measurements show that the electron concentration, mobility and sheet resistance do not depend on temperature, clearly indicating dopant Mott transition to a metallic state, wherein the activation energy (Ea) falls to 0 meV at this high value of Si doping for the AlGaN films. The achievement of semi-metallic conductivity Si doped in N-polar high Al content AlGaN lays the groundwork for advancing wide bandgap electronic and optoelectronic devices.

09:15 AM
Evolution of AlN: from 1 nm Nitridation to 2 μm of Molecular Beam Epitaxy
Dr. Michael Liao[1], Mr. Dorian Luccioni[1], Dr. Kenny Huynh[1], Dr. Yekan Wang[1], Ms. Lezli Matto[1], Prof. Habib Ahmad[2], Dr. Zhan Zhang[3], Prof. William Doolittle[2], Prof. Mark Goorsky[1]
[1]University of California, Los Angeles, [2]Georgia Institute of Technology, [3]Advanced Photon Source, Argonne National Laboratory

The structural evolution of AlN from ~1 nm nitridation on (0001) sapphire followed by up to 2 μm of molecular beam epitaxial growth is studied using laboratory triple-axis X-ray diffraction, synchrotron X-ray diffraction, and high-resolution transmission electron microscopy. First, the sapphire substrates are annealed in a nitrogen atmosphere at 1175 °C to achieve a terrace-and-step surface. Nitridation is performed on the annealed sapphire substrates at 200 °C to form a ~1.6 nm thick (0001) AlN layer, which is followed by AlN growth ranging from thicknesses of ~4 nm up to ~2 μm at 800 °C. After each AlN growth, ~80 nm Al was deposited at 200 °C. The structures are important for understanding the role if interfacial defects on thermal transport across AlN interfaces.
Cross-sectional transmission electron microscopy images of the ~1.6 nm AlN from nitridation show only one orientation (0001) of AlN. Synchrotron X-ray symmetric measurements reveal that the rocking curve width is ~30”. The (0001) orientation is maintained during subsequent AlN growth. This contrasts with AlN growths on sapphire without nitridation, where islands of AlN exhibited two dominant orientations (0001) and (1012) [1]. We show that the nitridation of (0001) sapphire enables only (0001) AlN to form. In other words, the nitridation hinders the nucleation of other AlN orientations and produces less defective AlN|Al2O3 heterointerfaces. Both triple-axis laboratory and synchrotron measurements show that for all thicknesses of AlN, the symmetric rocking curves exhibit two-peak components. Two-peak-component rocking curves have been reported by studies that nitridated at 950 °C [2], but the characteristics of the components were not determined. Additionally, it has been shown that nitridation at lower temperatures (200 °C) results in structurally and chemically homogeneous AlN [3]. By observing how each X-ray rocking curve component behaves at different symmetric reflections [4], i.e., (0002) vs (0004), we are able to ascertain that one component is attributed to lattice tilt (~30” across all samples) and the other component is due to lateral coherence length (which generally increases with increasing AlN thickness). Studying the structural evolution of AlN from nitridation to growth is an essential step towards understanding the role of structural characteristics on thermal transport across heterointerfaces.
The authors would like to acknowledge the support from the Office of Naval Research through a MURI program, grant No. N00014-18-1-2429.
References
[1] J.R. Heffelfinger, et al., J. Appl. Phys., 85(1), 466 (1999).
[2] J. Wang, et al., Scientific Reports, 7, 42747 (2017).

[3] G. Namkoong, et al., J. Vac. Sci. Technol. B, 20, 1221 (2002).
[4] R. Chierchia, et al., J. Appl. Phys., 93(11), 8918 (2003).

09:30 AM
Strain Accumulation and Relaxation on Crack Formation in Epitaxial AlN Films on Si (111) Substrate (Student)
Mr. Muhammad Aqib[1], Dr. Sara Pouladi[1], Dr. Mina Moradnia[1], Mr. Rheno Paul Rajesh Kumar[1], Dr. Nam-In Kim[1], Prof. Jae-Hyun Ryou[1]
[1]University of Houston

Aluminum nitride (AlN) belongs to the Group III-nitride (III-N) semiconductor family and exhibits ultrawide bandgap (UWBG) energy, significant thermal conductivity, high critical electric field, notable piezoelectricity, offers a great technological potential for high-temperature, high-power, and high-voltage electronics, piezoelectric sensing and energy harvesting, and deep UV (DUV) photonics. It is desirable to epitaxially grow relatively thick aluminum nitride (AlN) films and device structures on economically viable, large-area silicon (Si) substrate for manufacturing cost reduction, achieve monolithic integration of AlN and Si, and an easy layer-transfer process. However, the epitaxial growth of a crack-free thick layer of AlN on a Si substrate is reported to be extremely challenging. For example, cracks typically formed in the AlN layer with thickness exceeding ~200-300 nm in most chemical vapor epitaxy carried out higher than 1000 °C and in any AlN layers thicker than ~1 µm. Although the experimental results are characterized in terms of mismatches in lattice constants and thermal expansion coefficients between AlN and Si, detailed calculations to estimate the conditions of crack formation have not been performed. In the present study, we employ Griffith theory of brittle fracture, elastic strain energy, and the role of the threading dislocations estimated from Mathews-Blakeslee model of misfit dislocations for the estimation of strain accumulation and relaxation for the epitaxial growth of AlN on Si (111) substrate. The strain energy increases with the thickness of the layers, as predicted, but drops significantly with increasing growth temperature. Then, the relationship between strain energy and cleavage energy in thick AlN layers grown on Si substrates was investigated. It is noted that one can grow a crack-free layer of AlN on Si substrate as long as the strain energy is lower than that of cleavage energy otherwise it leads to crack formation in the layer. Also, the strain energy and formation of misfit dislocations play a critical role in the cleavage formation in AlN growth. After the detailed calculations, we then compared the estimated theoretical results with experimental results reported in the literature. We also suggest a possible pathway to grow crack-free AlN thick layers on Si (111) substrate using new buffer layers between AlN and Si. These findings have important implications for the design and fabrication of AlN-based devices and highlight the need for careful control of the growth conditions to minimize strain and improve the quality of AlN films on Si substrates.

8:30 AM
Optoelectronic Devices
Session Chair: Kyle McNicholas (MIT Lincoln Laboratory)
ESJ 0224

08:30 AM
Effect of Varying Period Structure on Tunneling Current in AlInAsSb Digital Alloys (Student)
Ms. Ellie Wang[1], Mr. J. Andrew McArthur[1], Ms. Hannaneh Karimi[2], Mr. Patrick Devaney[1], Prof. Joe Campbell[2], Prof. Seth Bank[1]
[1]University of Texas at Austin, [2]University of Virginia

AlxIn1-xAsySb1-y (referred to as AlInAsSb) grown as a digital alloy on GaSb substrates has been shown to offer numerous advantages for optoelectronic devices operating at near- to mid-infrared wavelengths. The material system has a tunable direct bandgap over a wide compositional range, large conduction band offsets, and low excess noise due to nearly single carrier-initiated impact ionization with impact ionization coefficient ratios as low as k = 0.01 [1-2]. Accordingly, a number of advanced detectors using AlInAsSb have been reported, such as 2-µm separate absorption, charge, multiplier avalanche photodiodes (APDs) [3] and staircase APDs [4,5]. So far, AlInAsSb has been grown using relatively standard parameters, with a 10 monolayer thick period strain-balanced to a GaSb substrate, and only the aluminum composition being varied to adjust the bandgap. However, there are several degrees of freedom in the growth space that can also be explored, such as the period thickness and the constituent binary thicknesses for a given composition, all of which can affect material properties. Using this design freedom to explore different digital alloy period compositions could potentially help to improve photodetector performance characteristics such as interband tunneling current, a key component of the dark current, especially in the narrow bandgap absorber regions.
Here we present variational design studies calculating the interband tunneling current of different variations of the AlInAsSb digital alloy on GaSb. The interband tunneling matrix elements of 30 nm digital alloy regions with varying period structures and average aluminum contents (Al%) were calculated using a self-consistent Schrodinger-Poisson solver. These were then used to simulate the tunneling current under varying applied electric fields up to 420 kV/cm. Tunneling current densities were first calculated for varying aluminum compositions, Al% from 30% to 70%, while maintaining a constant period thickness of 10 monolayers. As expected, the tunneling current trended inversely with increasing aluminum composition, which is consistent with the increased effective bandgap [1]. Predicted tunneling currents for varying period thicknesses, from 5 monolayers to 20 monolayers at a constant Al% of 30%, showed a weaker dependence upon effective bandgap [6]. Consequently, when the period thickness and aluminum composition were simultaneously varied to hold the absorption cutoff at a ~2 µm wavelength, the predicted tunneling currents decreased significantly at elevated period thickness and Al%, suggesting a potential avenue for mitigating dark currents. Samples were grown by solid-source molecular beam epitaxy and effective bandgaps corresponding to ~2 µm cutoff wavelength were confirmed with optical absorption and photoluminescence spectroscopy. Further experimental studies of the effects of varying the structure of the digital alloy period on the tunneling current are underway and will be presented at the

conference. This work was supported by the Army Research Office (W911NF22P0067), the National Science Foundation Designing Materials to Revolutionize and Engineer our Future (NSF DMREF, DMR-2118787), and Northrop Grumman.
References
[1] Maddox, et al. Crystal Growth 2016 [2] Woodson, et al. APL 2016 [3] Ren, et al. JLT 2017 [4] Martyniuk, et al. App Phys Rev 2014 [5] Jones, et al. Nature Photonics 2020 [6] McArthur, et al. 65th EMC. (2023)

08:45 AM
Suppressing AlInAsSb Avalanche Photodiode Dark Currents by Tuning the Absorption Region (Student)
Mr. J. Andrew McArthur[1], Dr. Adam Dadey[2], Ms. Ellie Wang[1], Ms. Hannaneh Karimi[2], Prof. Joe Campbell[2], Prof. Seth Bank[1]
[1]University of Texas at Austin, [2]University of Virginia

Near- to mid-infrared photodetection is primarily dominated by the HgxCd1-xTe (MCT) materials platform. Its bandgap flexibility and low excess-noise properties are ideal for high-sensitivity avalanche photodiodes. Several challenges like toxicity concerns, manufacturing yield, and cooling requirements, however, are spurring the search for alternative material platforms. III-Vs offer robust manufacturing capabilities, higher temperature operation, and fewer toxicity concerns. Especially when employed in a separate absorption charge multiplication (SACM) avalanche photodiode (APD), performance metrics of III-V devices are rapidly approaching MCT at elevated temperatures. Further improvements in gain- bandwidth products, efficiencies, and dark current suppression in devices could see III-V SACM APDs unseat MCT as the photodetector of choice in this wavelength range.
AlxIn1-xAsySb1-y digital alloys (here referred to as AlInAsSb) grown strain-balanced to GaSb substrates are a promising candidate as an infrared APD material. AlInAsSb on GaSb possesses a widely tunable compositional range, as well as advantageous band offsets and low-noise impact ionization properties at room temperature [1]. Additionally, the digital alloy nature of the material provides benefits for bandgap and compositional gradings—key for SACM APDs. The material has been used to demonstrate low-noise, high-gain SACM photodetectors with cutoff wavelengths spanning 1.55 to 3.5 µm [2-3]. The room temperature performance of these SACMs can rival state-of-the-art MCT detectors [4]. Further work shows that a device with a thinner absorption region displays significantly reduced dark currents by limiting absorber band-to-band tunneling [5]. Despite the work on AlInAsSb SACM APDs, little experimental work has been done to optimize device geometries and material properties. Relative thicknesses of absorber and multiplier regions, as well as changes in the digital alloy period, can have key impacts on the dark current densities, external quantum efficiencies, and impact-ionization gain. The questions remain— what are the key trade-offs as the absorber thickness changes? Are there any local optimal points to exploit? What band engineering mechanisms or tunable material properties are in place to recover trade-offs in performance?
Here we report a comprehensive study on the effect that AlInAsSb SACM layers have on the APDs and materials approaches to further improve device performance. Photodiode devices have been grown, fabricated, and characterized with absorber and multiplier regions ranging an order of magnitude in thickness. Current-voltage (I-V) and external quantum efficiency (EQE) characterization reveal a 100-nm absorber, for example, exhibits dark currents approximately half of the previously reported 200-nm absorber device. It is worth noting that the previously published latter device already featured record low dark currents for III-V detection at 2 µm. The EQE, however, is reduced by a factor of ~10—an important tradeoff for certain applications. These and more device results will be explored in depth at the conference, as well as potential avenues to recovering EQE by tuning the digital alloy material that would curb the deleterious effects of a thinner absorber. This work was supported by the Army Research Office (W911NF22P0067) and Northrop Grumman.
References:
[1] Maddox, et al. Crystal Growth 2016 [3] Dadey, et al. APL Photonics 2023 [5] Chen, et al. Nature Photonics 2022 [2] Ren, et al. APL 2016 [4] Jones, et al. Nature Photonics 2020

09:00 AM
The Electro-absorption effect in InGaAs and GaAsSb p-i-n photodiodes (Student)
Ms. Yifan Liu[1], Dr. Xiao Jin[1], Ms. Hyemin Jung[2], Mr. SeungHyun Lee[2], Dr. Faezah Harun[3], Prof. Jo Shien Ng[1], Prof. Sanjay Krishna[2], Prof. John P.R. David[1]
[1]University of Sheffield, [2]The Ohio State University, [3]Universiti Kuala Lumpur British Malaysian Institute

GaAsSb has been recently shown to be a direct band-gap semiconductor compatible with InP substrates and capable of absorbing light at telecommunication wavelengths much like InGaAs. Both these ternary alloys have a bandgap energy of ~0.75 eV. In opto-electronic devices, these materials are often subjected to built-in or externally applied electric fields with potentially significant changes to their absorption properties. This research examines the changes in the absorption coefficient spectrum under electric fields up to 200kV/cm in InGaAs and GaAsSb, addressing the gap in existing literature on field-dependent absorption properties in these materials.
Two p-i-n diode structures, P1 (InGaAs) and P2 (GaAsSb), were epitaxially grown and fabricated into mesa diodes with optical windows. Measurements of current-voltage, capacitance-voltage, and optical responsivity were conducted as a function of reverse bias.
The background doping was found to be low at ~ 1015 cm-3 in the intrinsic region of both structures, suggesting that the electric field is fairly uniform. For InGaAs and GaAsSb, modelling shows that band-to-band tunnelling dominates the reverse dark currents at electric fields above 250kV/cm and 220kV/cm, respectively, with avalanche multiplication becoming apparent as the electric fields increase further. Photocurrent measurements as a function of wavelength and reverse bias were used to determine the influence of the electro-absorption effect in these two materials. Absorption coefficients (a) were extracted after accounting for the surface reflectivity and the minimal influence from the wider bandgap cladding layers. For both InGaAs and GaAsSb, a increases with electric fields beyond 1650 nm. When subject to an electric field of 200 kV/cm, InGaAs has a = 91 cm-1 at 2000 nm with a dark current density of 2 mA/cm2, while GaAsSb has a =66 cm-1 absorption with a dark current

density of 6 mA/cm2. Conversely, at 1600nm under the same electric field, the a decreases from 7113cm-1 to 4983 cm-1 in InGaAs and from 7107 cm-1 to 5560cm-1 in GaAsSb. The observed electro-absorption characteristics of InGaAs and GaAsSb are strikingly similar, reflecting their similar band structures and effective masses.
This work was partially supported by the Advanced Component Technology (ACT) Program of NASA's Earth Science Technology Office (ESTO) under Grant No. 80NSSC21K0613

09:15 AM
Influence of Growth Temperature on Defect States in GaAs0.51Sb0.49 pin Diodes on InP
Ms. Rachel Adams[1], Ms. Hyemin Jung[1], Mr. Nathan Gajowski[1], Dr. Seunghyun Lee[1], Prof. Sanjay Krishna[1], Dr. Steven Ringel[1]
[1]The Ohio State University

Low noise avalanche photodiodes (APDs) able to detect in the 1550 nm wavelength are incredibly important for photonic devices. A material of interest for the absorber in APDs is GaAs0.51Sb0.49 because of its high quantum efficiency, being lattice matched to InP, and the low conduction band offset with a silicon multiplier [1,2]. To improve the performance of GaAsSb based APDs, an understanding of any defects that act as traps within the detector material is needed. This work establishes a baseline defect spectrum for n-GaAs0.51Sb0.49 samples grown in a RIBER Compact 21 DZ system molecular beam epitaxy (MBE) system on InP at two different growth temperatures: one optimized and one non-optimized [2]. Additionally, this work compares the trap concentration with the minority carrier lifetime. The distribution of traps was determined using deep level transient spectroscopy (DLTS), while the minority carrier lifetime was measured using transient microwave reflectance (TMR).
Multiple 200-μm diameter diodes were screened with current-voltage (IV) and capacitance-voltage (CV) measurements to ensure high quality devices. All the scans performed showed consistent and high-quality devices with strong rectification and good forward bias linearity making them suitable for defect spectroscopy measurements. With the quality of the test diodes established, DLTS measurements were performed on multiple devices to ensure good statistics in the results. Two defect states were observed, with each revealing a strong dependence on growth temperature. The Arrhenius plot for these spectra determined the activation energies were at EC – 0.21 eV and EC – 0.40 eV. The optimized growth temperature sample had a 100x lower concentration than the non-optimized sample.
Previous work reported the SRH lifetime of UID GaAs0.51Sb0.49 lattice matched to InP to be 20.5 6.3 μs [3]. The focus of this work was to measure the SHR lifetime of the two different growth temperature samples and determine any correlations between the lifetime and the DLTS results. It was determined that the SRH lifetime was 18.7 ± 2.5 μs for the optimized sample, and 9.6 ±1.1 μs for the non-optimized sample. This suggests that the EC – 0.40 eV trap, which is the dominant trap in the bandgap and is close to midgap, has a potential role as a lifetime-limiting trap in n-GaAs0.51Sb0.49.
In summary, a comprehensive investigation of the bandgap states in MBE-grown n-GaAs0.51Sb0.49 samples grown on InP at two different temperatures was performed using DLTS. Two traps were detected in the GaAs0.51Sb0.49, at Ec – 0.40 eV and Ec – 0.21 eV. These two states were detected in both samples, with the optimized sample having a 100x lower concentration than the non-optimized sample. The dominant Ec – 0.40 eV trap appears to lower the SRH recombination lifetime as there was a decrease in the minority carrier lifetime of the non-optimized sample. This strongly suggests that there is a correlation between growth temperature, trap concentration, and minority carrier lifetime, all which affects device performance.
REFERENCES
[1] S. Krishna, et al., IEEE J. Quantum Electron, 58, 4500207 (2022).
[2] H. Jung, et al., Appl. Phys. Lett., 122, 221102 (2023).
[3] A. M. Arquitola, et. al., AIP Advances 13(8), (2023).

09:30 AM
InGaAlAs/InAlAs on InP Avalanche Photodiodes For Near-Infrared LIDAR Imaging
Dr. Nuha Ahmed-Babikir[1], Prof. Jamie Phillips[1], Dr. Martin H.Ettenberg[2], Dr. Ye Xu[2], Dr. Matthew Peart[2]
[1]University of Delaware, [2]Princeton Infrared Technologies

Avalanche photodiodes (APDs) are desirable in many detection applications due to their high signal to noise ratios derived from the inherent gain mechanism of the impact ionization process. The near-infrared (NIR) region is of importance for many applications, including light detection and ranging (LIDAR) imaging systems based on Nd:YAG lasers at 1.06 μm. At this wavelength, established APD material technologies have significant shortcomings: silicon has low optical absorption and corresponding quantum efficiency, InGaAs/InP has limited gain, and HgCdTe requires significant cooling, has higher associated cost and lower yield and uniformity. In this work, we explore a separate absorption, grading, charge, and multiplication (SAGCM) APD device based on InGaAlAs absorption and InAlAs gain regions lattice matched to InP. These materials and the SAGCM architecture leverage strong optical absorption and minimization of bulk dark current in the absorber, design of the electric field profiles to minimize band-to-band tunneling and maximize desired impact ionization, and use of InAlAs multiplication layers for improved impact ionization, higher breakdown field, and lower excess noise. We report on NIR-APDs with a wavelength cutoff of ~1.4 μm and high gain >100 utilizing separate quaternary In0.53Ga0.321Al0.15As absorber and In0.52Al0.48As multiplication regions. The planar device structure is based on an n-type material stack grown by molecular beam epitaxy (MBE) and zinc diffusion for p-type junction formation. Material thickness, alloy composition, and doping were designed based on drift-diffusion modeling including Selberherr impact ionization, Shockley-Read-Hall (SRH) recombination, Auger recombination, concentration dependent mobility, and Fermi Dirac statistics. The dark-light current-voltage (I-V) characteristics of the measured devices exhibit clear reach-through and breakdown behavior that are defining characteristics of the SAGCM APD device. Simulated and measured dark-light I-V curves at room temperature demonstrate strong qualitative agreement, where differences in the reach-through and breakdown (Vbr) voltages, and sharpness of turn-on characteristics can be attributed to variability in doping levels, graded doping profile, and accuracy of simulation models for recombination mechanisms. Simulated electric field profiles near Vbr

indicate a high electric field > 4.5x105 V/cm in the In0.52Al0.48As multiplication/gain region and low electric field in the absorber region and corresponding low measured dark current density (0.6 μA/cm2) at the reach-through voltage (300 K) due to suppressed high field induced tunneling in the absorber region. The APD has a responsivity of 0.5 A/W at 1.06 μm illumination measured at unity gain bias point at room temperature. Temperature dependent dark-light I-V characteristics were measured from ~80 K to room temperature using a closed cycle cryogenic probe station. The dark current density shows an Arrhenius relationship with two distinct regions with activation energies of 0.07 eV (T< 160K) and 0.4 eV (T>160K). The small activation energy at T<160 K suggests that trap assisted transport is the limiting factor for dark current. At higher temperatures, the activation energy of 0.4 eV corresponds to approximately half the bandgap of the quaternary absorber, indicating that the dominant recombination mechanism is SRH limited behavior corresponding to generation-recombination within the absorber region. Vbr increased from 35 V at 80 K to 44 V at 260 K and is attributed to increased phonon scattering rates with temperature. The temperature dependence of Vbr has a low coefficient of 30 mV/K in comparison to ~80 mV/K reported for APDs with InP multiplication regions due to the InAlAs impact ionization coefficients and design of the optimum gain region thickness. The low temperature dependence of Vbr in these devices utilizing InAlAs gain regions in comparison to InP and other gain materials make this APD design particularly useful for high gain stability over a wide temperature range. InAlAs alloys on InP provide an attractive APD gain region with low temperature dependence of breakdown voltage and highly manufacturable materials and device technology. In summary, we demonstrate a SAGCM InGaAlAs-InAlAs APD on highly producible InP platform with a 1.4 μm cutoff, high gain, and low temperature dependent behavior.

8:30 AM
Hybrid Organic/Inorganic Devices and Molecular Electronics
Session Chairs: Suprem Das (Kansas State University), Pawan Tyagi (University of the District of Columbia)
ESJ 2208

08:30 AM
Synthesis and Characterization of MAPbBr3 Perovskites for Radiation Detection Applications (Student)
Ms. Alexandria Ragsdale[1], Ms. Shea Tonkinson[1], Dr. Maya Narayanan Kutty[1], Mx. Mega Frost[1], Mr. Melvin Foster[1], Mr. Kaleab Ayalew[2], Prof. Thomas J. Rotter[1], Dr. Alexander Barzilov[2], Dr. Adam Hecht[1], Prof. Ganesh Balakrishnan[1]
[1]Center for High Technology Materials, University of New Mexico, Albuquerque, New Mexico, [2]University of Nevada Las Vegas, Las Vegas, Nevada

High resolution, room temperature radiation detection is of utmost importance, with applications in national security, nuclear nonproliferation, and medical physics. A typical high-resolution solid-state detector crystal, Ge, has a high carrier mobility () and lifetime (□) for both electrons and holes, and a small band gap ~ 0.6 eV which increases the counting statistics and improves energy resolution, but requires operation at cryogenic temperatures to reduce thermal noise. High energy resolution room temperature solid state detectors allow much more ease of use by removing the cooling constraints. The leading solid state room temperature detector material is CdZnTe (CZT), with a band gap of ~ 1.6 eV (depending on composition), which eliminates cooling needed to reduce thermal noise, but still has reasonable counting statistics for good resolution. The □ and □ values are lower than for Ge and, very importantly, the □□ product for holes is ~1000 times poorer, leading to an asymmetric charge induction efficiency across a CZT based detector. While this can be compensated for by multiple electrode arrangements, this is still a fundamental material issue and reduces counting statistics vs. a dual carrier detector.
Methylamunium lead halide pervoskites (MAPBX3), such as MAPbBr3, have emerged as an attractive candidate for ionizing radiation detection over CZT. MAPbBr3 has a greater band gap (~2.2 eV) compared to CZT and is expected to have excellent charge carrier transport properties with high resistivity (>107 □*cm), low density of defects, and low-cost synthesis and processing of large crystal sizes from solution. However, their air/moisture instability and the presence of toxic lead are barriers for their further development into commercial products.
In our study, we carry out device and material characterizations of MAPbBr3 pervoskite crystals grown at UNLV. Extensive surface and compositional analysis of the crystals are performed using Nomarski optical contrast microscopy, SEM/EDS, and photoluminescence measurements. Nomarski images ofthe crystals show a polished surface. The diffraction pattern gathered through TEM is shown in Fig 1.The presence of phase segregation in the growth of the perovskite crystals did not seem to be present, and this is further confirmed through TEM images, Fig. 2. Sample #OH3 was used from TEM imagery and shows single crystalline behavior. In the EDS analysis, we confirm that the perovskites are MAPbBr3.
A 2151 Femtowatt Silicon Photoreceiver, Lock-in amplifier, and monochromator-based setup were used to measure photoluminescence of the perovskites in the 300-1050nm visible spectrum. The roughest MAPbBr3 sample, #OH2B, has the most visible defects on the surface and produced a PL peak ~532nm. The sample #OH3B has a smoother surface and produced the greatest PL peak ~536nm. Lastly, sample# OH6B, produced the lowest PL peak ~528nm. The PL spectra for these samples is seen in Fig. 3.

08:45 AM
Trenched bottom electrode based molecular devices with gate electrode: Process and applications of promising spintronics molecular devices.
Dr. Erwan Peigney[1], Dr. Pawan Tyagi[1]
[1]University of the District of Columbia

In conventional silicon-based microelectronic devices, high-speed information processing and high-density data storage rely on electronic switches. These devices operate by controlling the transport between the source and drain through the application of electric field stimuli to a gate terminal. At a molecular scale, creating a gate-controlled

device remains very challenging even after three decades [1]. It is crucial to strictly insulate the gate from the molecule and the source/drain electrodes. This ensures that the gate terminal exclusively establishes an electrostatic coupling with the molecule, ultimately minimizing gate leakage and maximizing the electric field reaching the molecule. Several approaches have been attempted for the fabrication of solid-state single-molecule transistors [2–5]. Nevertheless, the fabrication process suffers of numerous limitations resulting in a notably low device yield of 10%.
A recent patent introduced an innovative approach to fabricating gate-controlled molecular devices, utilizing standard microfabrication techniques, equivalent to CMOS devices [6]. This method is well-suited for integration into existing manufacturing industries. The process incorporates photolithography, deposition of thin layers through sputtering and argon etching. This invention specified two locations for the gate, both relying on the creation of a trench: (a) below the bottom electrode and (b) encapsulated within the drain (cf. Figure 1a) and b)). The molecules are then placed along the exposed side edges of the trench.
The current work focuses on implementing and optimizing the process for fabricating trenched bottom electrode-based molecular devices with gate electrodes, as described in Dr. Tyagi's patent [6]. Complete devices were topologically and electrically characterized using an AFM and home-made I-V testing setup, respectively. The I-V testing method revealed a CMOS behavior in the elaborated devices, expected to exert an electric field influencing the molecular device states during current flow between the source and drain electrical connections. Particular attention has been given to the impact of insulation layer thickness, aiming to enhance the electric field and minimize leakage current.
[1] G. Ke, C. Duan, F. Huang, and X. Guo, Electrical and Spin Switches in Single-Molecule Junctions, InfoMat 2, 92 (2020).
[2] W. Liang, M. P. Shores, M. Bockrath, J. R. Long, and H. Park, Kondo Resonance in a Single-Molecule Transistor, Nature 417, 6890 (2002).
[3] J. A. Mol, C. S. Lau, W. J. M. Lewis, H. Sadeghi, C. Roche, A. Cnossen, J. H. Warner, C. J. Lambert, H. L. Anderson, and G. A. D. Briggs, Graphene-Porphyrin Single-Molecule Transistors, Nanoscale 7, 13181 (2015).
[4] J. Park et al., Coulomb Blockade and the Kondo Effect in Single-Atom Transistors, Nature 417, 722 (2002).
[5] H. Song, Y. Kim, Y. H. Jang, H. Jeong, M. A. Reed, and T. Lee, Observation of Molecular Orbital Gating, Nature 462, 1039 (2009).
[6] P. Tyagi, Trenched Bottom Electrode and Liftoff Based Molecular Devices, US10833162B2 (10 November 2020).

09:00 AM
Modification of Conjugated Polymers with Indigo Dye to Enhance their Optoelectronic Properties: An Experimental and Computational Study
Dr. ufana Riaz[1], Dr. Neetika Singh[2]
[1]North carolina central university, [2]Jamia Millia Islamia

With the aim to design dye incorporated polymers to enhance their extent of conjugation and optoelectronic characteristics, the present work reports indigo dye incorporated polyaniline (Indigo-PANI), poly(1-naphthylamine) (Indigo-PNA), poly(o-phenylenediamine) (Indigo-POPD), polypyrrole (Indigo-PPy), and polythiophene (Indigo-PTh) synthesized via ultrasound-assisted method. The chemical structures were theoretically computed using Gaussian 09 software using density functional theory (DFT) by applying Becke, 3-parameter, Lee–Yang–Parr method (B3LYP) with 6-311G (d) basis set. The band gap energies were theoretically computed to be 1.25 eV for Indigo-PANI, 1.13 eV for Indigo-PNA, 1.03 eV for Indigo-POPD,1.2 eV for Indigo-PPy, 1.04 eV for Indigo-PTh respectively. The experimental as well as theoretical vibrational spectra were found to be in close agreement and confirmed the successful incorporation of Indigo dye in PANI, PNA, POPD, PPy and PTh. The theoretical electronic spectra of geometry optimized structures were simulated via time-dependent density-functional theory (TD-DFT) using 6-311G (d) basis set and the results were compared with the experimental ultraviolet-visible (UV-vis) spectra. The experimental data was found to be in good agreement with the theoretical electronic transitions and showed variations in the electronic properties upon incorporation of Indigo dye. The morphology was investigated by X-ray diffraction (XRD) and scanning electron microscopy (SEM) studies. The XRD studies confirmed semi-crystalline morphology and SEM studies revealed formation of flaky and elongated rods like structures. The thermogravimetric analysis (TGA) confirmed that the polymers were thermally stable up to 300oC. Fluorescence studies revealed emission ranging between 500 nm to 700 nm which could be utilized to design imaging probes via facile route.

09:15 AM
Synthesis and characterization of yttrium ferrite nanoparticle incorporated PVDF-TPU composite
Dr. SUSHRISANGITA SAHOO[1], Dr. Abhinav Yadav[2], Mr. Gautam Chandrasekhar[2], Prof. Vijaya Rangari[2]
[1]Department of Material Science and Engineering, Tuskegee University, AL, 36088, [2]Department of Material Science and Engineering, Tuskegee University, AL, 36088, USA

The development of poly(vinylidene fluoride) (PVDF) based flexible film for mechanical energy harvesting and piezoelectric measurement became a recent trend in material science due to its application potentiality in wearable electronics, actuators and biomedical applications. Improvement of piezoelectric and other functional properties of pure PVDF can be attained by enhancement of polar β-phase through composite preparation. Composite of PVDF/ nanoparticles were well studied in the literature [1,2]. In this work, we prepared a ternary composite of PVDF, thermoplastic polyurethane (TPU) and yttrium ferrite (YFO) with varying concentration of YFO. First, YFO nanoparticles were synthesized by nanoagitator bead milling for 3 hr. The orthorhombic phase formation of YFO is confirmed from the room temperature XRD spectrum. About 30 wt% TPU was added to PVDF in DMF solvent for the preparation PVDF-TPU composite film by doctor blade apparatus. Then 1, 3, 5 and 7 wt% of YFO is added PVDF-TPU for preparation of ternary composites. The structural characterization of composites was carried out using XRD pattern. The XRD pattern of pure PVDF, TPU and PVDF-TPU is also stacked in the same graph for better comparison. The peak at 18.3o and 20.2o in the XRD pattern of all the ternary composites including PVDF-TPU indicate the (0 2 0) and (1 1 0)/(2 0 0) planes corresponding to γ and β electroactive phase of

PVDF, respectively. The small hump at 26.5o observed in the XRD spectra for 1 and 5 wt% of YFO in PVDF-TPU corresponds to the (0 2 1) planes of α-phase of PVDF. The crystalline peaks of YFO became more prominent with increase in wt% of YFO in PVDF-TPU matrix. The FTIR band at 764 and 840 cm-1 represents the α- and β-phase, whereas the band at 812 and 1234 indicates the γ-phase of PVDF, respectively [3]. The band at 1533 and 1735 cm-1 represents the -CONH and C=O characteristic band of TPU. Another two bands at 2971 and 3365 cm−1 also observed corresponding to C-H and N-H stretching band of TPU. The electroactive phase content is calculated using Beer-Lambert law and found to be highest i.e. 68% for 3wt% of YFO in PVDF-TPU composite. The addition of 1 and 3 wt% of YFO may facilitate the reorientation of dipoles inside the composite resulting initial improvement of electroactive phase. Further increase in YFO content may loses the polarizability to improve electroactive phase content [4]. The TGA result of all the studied composites undergoes a three-step thermal degradation with a peak max temperature of 340 oC, 420 oC and 474 oC. The first step begins with onset temperature of 327 oC and the second step at 400 oC indicate the degradation due to the cleavage of urethane bond and soft segments of TPU respectively. The third degradation at high temperature with onset temperature around 460 oC is due to the dehydrofluorination in PVDF [5]. The melting point, glass transition and recrystallization temperatures of the composites were determined using the DSC analysis. The melting peak occur at around 172 oC corresponding to the β-phase of PVDF, the small step at ~90 oC represents the glass transition of hard segment of TPU and peak at 135 oC in the cooling curve indicates the recrystallization temperature of PVDF.

Acknowledgement:
Authors would like to acknowledge the financial support from NSF PREM #1827690 and NSF MRI grants: 2117242.

Reference:

[1] Nano to micrometer range particle size effect on the electrical and piezoelectric energy harvesting performances of hydroxide mediated crosslinked PVDF composites, Abhishek Sasmal, Sourav Maity, Payel Maiti, A. Arockiarajan, Shrabanee Sen Chemical Engineering Journal 468 (2023) 143794

[2] Efficient energy harvesting enabled by large-area piezoelectric PVDF-based composite film enhanced by carbon nanotubes Xinyue Yang, Yuanhui Li, Huiling Guo, Shibing Xiao, Chongxiao Yuan, Chao Zhang, Huajun Sun Ceramics International 50 (2024) 12185–12194

[3] Electroactive phases of poly(vinylidene fluoride): Determination, processing and applications, P.Martins, A.C. Lopes. S. lanceros-Mendez Progress in Polymer Science 39 (2014) 683-706

[4] Stretchable nanofibers of polyvinylidenefuoride (PVDF)/ thermoplastic polyurethane (TPU) nanocomposite to support piezoelectric response via mechanical elasticity Nader Shehata, Remya Nair, Rabab Boualayan, Ishac Kandas, Abdulrzak Masrani, Eman Elnabawy, Nada Omran, MohammedGamal, Ahmed H. Hassanin Scientifc Reports 12 (2022) 8335

[5] Thermoplastic polyurethane-carbon black nanocomposite coating: Fabrication and solid particle erosion resistance Mengyao Dong, Qiang Lia, Hu Liua, Chuntai Liua, Evan K. Wujcikc, Qian Shaod, Tao Dinge, Xianmin Maif, Changyu Shena , Zhanhu GuoPolymer 158 (2018) 381–390

09:30 AM

Realization of Self-poled, flexible P(VDF-TrFE) energy harvester using PDMS/Carbon Black Electrostatic Interaction Layer

Mrs. lavanya muthusamy[1], Dr. Goutam Koley[1], Mr. Makhluk Hossain Prio[1], Mr. MD SOHANUR E HI RAJU[1]
[1]Clemson

Introduction

Piezoelectric materials have gained widespread recognition for their ability to extract energy from the surrounding environment, utilizing their inherent self-powering abilities to extract energy from the surrounding environment. Furthermore, piezoelectric materials can be made into thin films with high flexibility. These characteristics make them an outstanding alternative to current state-of-the-art technologies, which face challenges related to low energy density, and bulk systems. Recently, the development of piezoelectric nanocomposites, achieved by dispersing nanoparticles within a flexible matrix, has exhibited a significant breakthrough in wearable sensing applications[1-4]. The electrostatic interaction between the surface charge of nanofillers and dipoles of piezoelectric materials (CH2 & CF2) arranges the dipoles in one direction, eliminating the requirement for poling. In this study, a self-poled P(VDF-TrFE) energy harvester has been successfully developed for the time, utilizing a highly charged PDMS/Carbon black layer in between two P(VDF-TrFE) layers. As a result, the integration of this highly charged PDMS/Carbon black electrostatic interaction layer between the two P(VDF-TrFE) layers not only enhances the energy harvesting efficiency but also significantly reduces the overall burden on energy consumption.

Device fabrication and Results

A Schematic representation of the overall fabrication process is shown in Fig. 1. First, 17 wt.% P(VDF-TrFE) solution was prepared by mixing the P(VDF-TrFE) powder and Dimethylformamide(DMF) at 60 °C for 12 h. Then, 5 wt.% CB particles were dissolved in toluene and mixed with PDMS. As prepared P(VDF-TrFE) solution was dropped on the glass substrate to obtain 30 μm thickness. After crystallizing the P(VDF-TrFE) film at 140 °C, the PDMS/CB solution was spin-coated on the P(VDF-TrFE) layer at 3000 rpm for 30s. Once the PDMS was cured, the PDMS/CB and P(VDF-TrFE) layer was peeled off from the glass substrate and attached to the bottom electrode. Subsequently, the top P(VDF-TrFE) layer was dropping cast and crystallized at 140 °C. Finally, the top electrode was established to further accomplish the electrical characterization. As illustrated in Fig. 2, the static charges from the homogeneously dispersed carbon black (CB) in the PDMS layer interact with dipoles closest to the surface of the P(VDF-TrFE) in both directions, aligning them unidirectionally. Subsequently, the remaining dipoles align accordingly, and the collected charges are then gathered through the electrodes. To compare the effect of the PDMS/CB layer, the unpoled P(VDF-TrFE) and tri-layer film structures (active area of 2 × 2 cm2) were subjected to the same 6 N force from the external shaker with 1 Hz excitation. The voltage and current generated by the respective devices were plotted in Fig. 3 (a-d). The tri-layer energy harvester demonstrated promising output performances when the device was subjected to

approximately 6 N force and produced the maximum open circuit voltage of 6.8 V pk-pk and short circuit current of 3.8 µA pk-pk current, which was able to provide a 10-fold larger output voltage than that of pure PVDF piezoelectric polymer (0.7 V pk-pk). Additionally, the as-fabricated self-poled tri-layer energy harvester exhibited output power and maximum power density of 13.2 µW and 3.3 µW/cm2 , respectively. Additionally, this device produces a maximum output voltage of 7.68 V pk-pk for finger imparting. We previously reported a nanocomposite-based energy harvester that directly incorporates CB particles into the P(VDF-TrFE) matrix and achieved a maximum peak – peak output voltage of 3 V with an output power of 2.25 µW[4]. Compared to previous studies, Carbon black is a cheap and widely available material, so it is cost- effective[5,6]. This innovation contributes to a more sustainable and efficient energy utilization in wearable sensing applications.

Summary and Conclusion

In summary, we demonstrated that self-poled, cost effective, and highly flexible P(VDF-TrFE) energy harvester by employing PDMS/CB as a sandwich layer in between two P(VDF-TrFE) layers for the first time. We achieved an open circuit voltage of 6.8 Vpk-pk and a maximum current of 3.8 µA pk-pk with an output power density of 3.3 µW/cm2 . We thankfully acknowledge the financial support for this work from National Science Foundation Grant# ECCS - 1809891.

[1] Y Tian et al, Nano energy, Vol.101, P.107556,(2022) [2] N. Bhadwal et al, Nanomaterial, Vol. 13,24 3170(2023) [3] M. Soha et al, RSC Adv, Vol.13,P. 370-387 (2023) [4] L. Muthusamy et al. polymers., vol. 15, p. 4131, (2023) [5] L. Yaqoob et al., composite B, vol. 159, p. 259, (2019). [6] L.Yaqoob et al, Appl Surf , vol. 405, P. 420-426,(2017).

8:30 AM
Transitional Metal Dichalcogenide and h-BN Synthesis and Devices
Session Chairs: Soaram Kim (Texas A&M University), Kevin Daniels (University of Maryland)
ESJ 2204

08:30 AM
Electrical Transport of High-Quality CVD-Grown MoSe2 Nanoribbons (Student)
Mr. Leo Sun[1], Ms. Ona Ambrozaite[2], Prof. Thomas Kempa[2], Prof. Thomas Murphy[1], Dr. Adam Friedman[3], Dr. Aubrey Hanbicki[3]
[1]University of Maryland, College Park, [2]Johns Hopkins University, [3]Laboratory for Physical Sciences

Two-dimensional (2D) materials such as transition metal dichalcogenides are excellent candidates for creating novel nano-electronic and photonic devices. Previous research indicates that the edge states of MoS2 could strongly influence its conductivity, and the 2D honeycomb structure enables different electronic performance along the zigzag and armchair edges. Understanding and controlling the conductivity is essential in devices like field effect transistors that use MoS2 as the channel. To date, transport along edge states of MoSe2 nanoribbons, which have substantially reduced dimensionality relative to 2D crystals, has not been explored. In this project, we used chemical vapor deposition (CVD) to synthesize MoSe2 nanoribbons through directed growth on phosphine (PH3)-treated Si substrates. This approach yields directed growth of monolayer MoSe2 to form high aspect ratio (>7) nanoribbons. Tip-enhanced photoluminescence (TEPL) is used to probe the optical properties of the edge and surface of the MoSe2 nanoribbons. To perform electronic transport measurements, we used e-beam lithography to pattern contacts on the nanoribbons in a Hall bar configuration with the side contacts at the edges and tips of the nanoribbons. The influence of edge states on the electrical performance of MoSe2 nanoribbons was investigated by conductivity and Hall transport measurements. Current flow in the transverse and longitudinal directions of the nanoribbon was compared to analyze the importance of edge states on MoSe2 nanoribbon conductivity.

08:45 AM
Seeking an Ion Beam Substitute for Neutron Irradiation in the Monolayer 2D Semiconductor MoS2
Mr. Mark Reymatias[1], Dr. John Cain[1], Dr. Taisuke Ohta[1], Dr. Christopher Smyth[1]
[1]Sandia National Laboratories

Radiation-tolerant, multi-functional electronic materials are needed to meet the growing demand for resilient and agile electronics in extreme environments. Recent work in 2D transition metal dichalcogenides (TMDs), suggests that these materials exhibit high radiation tolerance in addition to their favorable electronic properties,1-7 due in part to their significantly reduced radiation interaction cross section compared to conventional electronic materials. Neutron irradiation effects in TMD electronics must be characterized to evaluate their feasibility in numerous real-world applications. However, neutron irradiation effects have not yet been explored in TMD devices. The orders of magnitude lower interaction cross sections exhibited by neutrons compared to ions and the scarcity of neutron sources necessitate an ion beam surrogate for neutron irradiation in TMDs.
Here, we present a direct comparison of neutron and ion irradiation effects in the monolayer 2D semiconductor MoS2. Both large area MoS2 monolayers and back-gated MoS2 transistors are irradiated under neutron and ion beams. Neutron irradiation was carried out in the Annular Core Research Reactor (ACRR) at Sandia National Laboratories and a 2 MeV Fe2+ ion beam was employed for ion irradiations. The chemistry and relative Fermi level position of MoS2 monolayers was measured before and after irradiations ex-situ from the radiation environment using X-ray photoelectron spectroscopy (XPS). The strain and relative changes in carrier concentration were measured using Raman spectroscopy. Transfer and output characteristics of the monolayer MoS2 transistors were measured before and after irradiations ex-situ from the radiation environment under high vacuum in a Lakeshore probe station.

Any changes in chemistry and relative Fermi level position after neutron exposure are below the limit of XPS detection (Figure 1). Raman spectroscopy reveals the neutron irradiation causes a slight increase in hole concentration on the order of 1012 cm-2 and negligible change in strain. The neutron irradiation causes a mobility reduction of ~50% and a VT shift of +8 V, which are relatively minor changes considering the relatively high neutron fluence (Figure 2). Effects of the 2 MeV Fe2+ beam at multiple fluences on chemistry and electronic transport in MoS2 monolayers will also be discussed.

This work was supported by a Laboratory Directed Research & Development program at Sandia National Laboratories. Sandia National Laboratories is a multimission laboratory managed and operated by National Technology & Engineering Solutions of Sandia, LLC, a wholly owned subsidiary of Honeywell International, Inc., for the U.S. DOE's National Nuclear Security Administration under contract DE-NA-0003525. The views expressed in the article do not necessarily represent the views of the U.S. DOE or the United States Government. This work was performed, in part, at the Center for Integrated Nanotechnologies, an Office of Science User Facility operated for the U.S. Department of Energy (DOE) Office of Science.

1J. Jiang et al., Nature, vol. 616, pp. 470-475, 2023
2C. X. Zhang et al., IEEE Transactions on Nuclear Science, vol. 61, no. 6, pp. 2862-2867, 2014
3A. J. Arnold et al., ACS Applied Materials & Interfaces, vol. 11, no. 8, pp. 8391-8399, 2019/02/27, 2019
4O. Ochedowski et al., Journal of Applied Physics, vol. 113, no. 21, p. 214306, 2013
5T.-Y. Kim et al., ACS Nano, vol. 8, no. 3, pp. 2774-2781, 2014/03/25, 2014
6P. Dhakras et al., IEEE Transactions on Nuclear Science, vol. 65, no. 1, pp. 53-57, 2018
7C. S. Smyth, et al., Journal of Materials Research, vol. 37, no. 17, pp. 2723-2737, 2022

09:00 AM

Evaluating the Dielectric and Piezoelectric Response of 2D SnSe Thin Films (Student)

Mr. Joshua Wahl[1], Mr. Jonathan Chin[1], Mr. Marshall Frye[1], Dr. Lauren Garten[1]
[1]Georgia Institute of Technology

SnSe is predicted to exhibit a piezoelectric coefficient greater than other known 2D material [1], but piezoelectricity will only occur when SnSe is scaled down to the monolayer limit, becoming the non-centrosymmetric Pmn21 phase. Previously, we have developed a molecular beam epitaxy (MBE) growth approach that provides layer control down to the monolayer limit while maintaining stoichiometry to access the piezoelectric phase of SnSe [2]. This work describes the electrical and piezoelectric characterization of those SnSe thin films compared to exfoliated layers. The layer thickness and grain morphology were determined by atomic force microscopy. Then lateral and van der Pauw contacts were deposited by e-beam lithography for conductivity and Hall measurements respectively. The piezoelectric response was determined using e11 biaxial flexure measurements. The in-plane strain was calculated using the Stoney formula from the out-of-plane displacement measured by a laser doppler vibrometer. Determining the piezoelectric coefficient is the first step towards 2D SnSe piezotronics and piezoelectric energy harvesters.

[1] Fei, Ruixiang, et al. "Giant Piezoelectricity of Monolayer Group IV monochalcogenides: SnSe, SNS, Gese, and Ges." Applied Physics Letters, vol. 107, no. 17, 2015, https://doi.org/10.1063/1.4934750.
[2] Chin, Jonathan R., et al. "Self-limiting Stoichiometry in SnSe Thin Films." Nanoscale, vol. 15, no. 23, 5 June 2023, pp. 9973–9984, https://doi.org/10.1039/d3nr00645j.

09:15 AM

Self-limiting stoichiometry in SnSe thin films (Student)

Mr. Jonathan Chin[1], Mr. Marshall Frye[1], Mr. Ian Graham[1], Mr. Derrick Shao-Heng[1], Dr. Maria Hilse[2], Dr. Jeffrey Shallenberger[2], Dr. Mengyi Wang[2], Dr. Nadire Nayir[2], Dr. Yung Shin[2], Dr. Ke Wang[2], Prof. Stephanie Law[2], Prof. Adri van Du
[1]Georgia Institute of Technology, [2]Pennsylvania State University

Tin selenide (SnSe), when scaled down to the monolayer limit, transitions from the centrosymmetric Pnma space group to the non-centrosymmetric Pmn21 space group [1] enablinga piezoelectric response in monolayer SnSe that is otherwise unavailable in its bulk form. However the strong van der Waals forces between layers in SnSe make it difficult to isolate a single layer via mechanical exfoliation. Therefore, we have developed a molecular beam epitaxy (MBE) deposition approach for SnSe which enables layer control while maintaining stoichiometry. Thin films of SnSe, that were grown on (100) magnesium oxide (MgO) in ultrahigh vacuum at 280 ± 5 °C. These films were grown over a range of Sn:Se flux ratios from 1:1 to 1:5, yet maintained a predominantly 1:1 Sn:Se stoichiometry. Figure 1 displays the consistent growth of the {200} family of the planes of SnSe for five different flux ratios [2]. With increasing Se concentration, the primary change is in the crystallographic orientation with the emergence of the (311) plane for a 1:5 ratio. These results highlight a strong self-limiting effect on stoichiometry for a broad range of Sn:Se flux ratios. ReaxFF molecular dynamics (MD) simulations demonstrate how excess selenium accumulates into distinct Se clusters that have weak interactions with the SnSe particles, thereby restricting alterations in stoichiometry. Further support for the self-limiting nature of SnSe is given by the Raman spectra in Figure 2, which shows predominantly SnSe. During the initial stages of growth a small amount of SnSe2 is observed; however, after several SnSe layers are grown, the Raman response reflects only SnSe, indicating that no additional SnSe formed. The Raman results are corroborated by the presence of a minor second phase of SnSe2 that occurs for flux ratios of 1:5 for films with similar thicknesses; the second phase does not increase with greater amounts of Se, suggesting that the Se supply is self-limiting. This is important because SnSe2 is not piezoelectric, so the self-limiting nature of SnSe grants control over the film stoichiometry, providing an avenue for the growth of wide scale SnSe for electrical devices.

[1] W. Fang, L.-C. Zhang, G. Qin, Q.-B. Yan, Q.-R. Zheng, and G. Su, "Layer dependence of geometric, electronic and piezoelectric properties of SnSe," arXiv [cond-mat.mtrl-sci], 06-Mar-2016.

[2] J. R. Chin et al., “Self-limiting stoichiometry in SnSe thin films,” Nanoscale, Jun. 2023.

09:30 AM
Selective Area Epitaxy of van der Waals Materials on Semiconductor Substrates (Student)
Mr. Ryan Trice[1], Ms. Molly McDonough[1], Prof. Adri van Duin[1], Prof. Stephanie Law[1]
[1]Pennsylvania State University

Two-dimensional (2D) van der Waals (vdW) materials are interesting for a variety of applications ranging from optoelectronics and photocatalysis to energy storage and topological devices. However, vdW materials synthesized using common techniques like chemical or physical vapor deposition often have a high density of growth-related defects. The primary types of defects that are typically observed are grain boundaries, twin defects, pyramidal growth, and spiral defects. While pyramidal growth can be minimized through higher growth temperatures, grain boundaries, twin defects, and spiral defects are much harder to overcome. For many applications, especially in electronics and optics, these defects lead to non-radiative recombination, electron scattering, and other undesirable effects. To control the formation of these defects and to create single grain crystals of vdW materials, we used selective area epitaxy (SAE) to grow Bi2Se3 thin films. SAE is a technique in which thin films nucleate and grow in defined areas on a wafer. This is done through use of a patterned mask where growth conditions are selected such that the film will only nucleate inside the exposed pattern. This removes the need for etchants after deposition of the vdW material allowing for more pristine crystalline materials. Further, from this growth of Bi2Se3 in confined areas, we can explore various growth conditions to see what effects the Bi2Se3- nucleation and growth processes allowing us to be understand the growth of vdW materials.
In this talk, we will describe SAE growth of Bi2Se3 on Si (111) substrates using a SiO2 mask. The mask was deposited onto a 10x10mm Si (111) substrate by atomic layer deposition. Etching of the SiO2 mask was done with standard photolithography techniques and a direct write laser beam lithography system, and the SiO2 was removed from selected areas using a wet chemical etch, resulting in micron-scale holes of various shapes and sizes. The processed substrates were then loaded into a molecular beam epitaxy chamber for growth of the Bi2Se3 film. From this investigation, we found that a lower substrate temperature resulted in significantly more Bi2Se3 nuclei forming. Second, we found that a higher Bi flux ending at the same total Bi deposition (i.e twice the rate of growth and half the time) resulted in an increased number of nucleation sites. Third, we determined that ultra-high vacuum annealing of the Si (111) substrate and SiO2 mask to 850°C prior to growth promoted a significantly higher nucleation density of the Bi2Se3 nuclei on the substrate and mask surfaces. Fourth, we observed that the shape and size of the mask openings influenced the quality and defect density of the Bi2Se3 film. Specifically, we have observed that a triangular opening, that was aligned with the growth direction of Bi2Se3, produced a more coalesced film. Further studies will focus on using different masking materials and shifting the growth to nano-scale holes.

8:30 AM
Ferroelectrics and Structural Defects
Session Chairs: Christian Wetzel (Rensselaer Polytechnic Institute), Len Brillson (The Ohio State University)
ESJ 1224

08:30 AM
Exploring the Energetics of Domain Walls in Wurtzite Ferroelectrics (Student)
Ms. Mahlet Molla[1], Mr. Yujie Liu[1], Dr. Danhao Wang[1], Dr. Ding Wang[1], Prof. Zetian Mi[1], Prof. Emmanouil Kioupakis[1]
[1]University of Michigan

III-nitrides such as AlN and GaN have high carrier mobilities and light-emitting efficiency that have enabled their wide application in semiconductor devices. Furthermore, the discovery of ferroelectricity in this class of materials has expanded the range of their technological applications. In this work, we provide an atomic-scale understanding of the switching mechanisms and domain energetics that is critical to integrating ferroelectric wurtzites into devices. Using Density Functional Theory (DFT), we are able to uncover the atomic configurations of domain walls observed experimentally in representative ferroelectric nitride, ScGaN. We are able to confirm the presence of a vertical and horizontal domain wall both in experiment and theory by comparing the atomic distances of their respective configurations (Figures 1 and 2). In addition, we find that the atomic configurations at charged domain walls enable a high charge density at the interface due to the presence of dangling bonds, which compensate for the large polarization discontinuity and stabilize these interfaces without the formation of defects. We further analyze the nature of these dangling bonds by examining their energetics and the nature of their electronic structure. Our findings provide insights into the switching mechanism of III-nitrides and lay the groundwork for innovative applications.

08:45 AM
Controlling dislocation motion in semiconductors using an electric field
Prof. Yu Zou[1]
[1]University of Toronto

Dislocation motion, an important mechanism underlying crystal plasticity, is critical for the hardening, processing and application of a wide range of structural and functional materials. For decades, the movement of dislocations has been widely observed in crystalline solids under mechanical loading. However, the goal of manipulating dislocation motion via a non-mechanical field alone remains elusive. Here we present real-time observations of dislocation motion controlled solely by using an external electric field in single-crystalline zinc sulfide—the dislocations can move back and forth depending on the direction of the electric field. We reveal the non-stoichiometric nature of dislocation cores and determine their charge characteristics. Both negatively and positively charged dislocations are directly resolved, and

their glide barriers decrease under an electric field, explaining the experimental observations. This study provides direct evidence of dislocation dynamics controlled by a non-mechanical stimulus and opens up the possibility of modulating dislocation-related properties.

09:00 AM
Probing qubits in silicon carbide using Multislice electron ptychography
Dr. Junghwa Kim[1], Mr. Aaditya Bhat[2], Prof. James LeBeau[1]
[1]Department of Materials Science and Engineering, Massachusetts Institute of Technology, [2]Department of Materials Science and Engineering, Massachusetts Institute of Technology, Cambridge, MA 02139 USA

With well-established growth and device engineering platforms, silicon carbide (SiC) has been extensively employed in the fabrication of high-frequency, high-temperature, and high-power applications [1]. Additionally, the wide band gap characteristic of SiC serves as the matrix for hosting deep-level defects, holding a significant platform for quantum technologies [2]. For example, transition metal dopants (e.g. vanadium, erbium) in SiC emerge as promising candidates for telecom quantum networks, emitting at and near telecom wavelengths [3]. However, identifying these defects/defect complexes remains a key challenge for practical utilization. This highlights the need for atomic resolution methods to probe these defects within their local environment. While conventional scanning transmission electron microscopy (STEM) with focal-series high-angle annular dark field (HAADF) imaging has been employed to identify heavy transition metal impurities [4], it requires extremely thin samples (around or less than 10 nm) with pristine surfaces and it is challenging to extract local structural features. These limitations necessitate the development of a new approach.
In this presentation, we will discuss the direct observation and quantification of individual erbium (Er) dopants within a 3D volume of 4H-SiC using multislice electron ptychography, as illustrated in Figure 1. Utilizing multislice electron ptychography provides several advantages, offering the capability to characterize these defects with extreme in-plane spatial resolution and depth resolution along the beam direction [5]. By identifying outliers in the reconstructed object phase, we highlight the detection of Er dopants and Si/C vacancies, as well as prospects for identifying defect complexes. Our findings reveal that integrating multislice ptychography and quantification can be an excellent method for detailed quantification of spin centers for quantum computing applications.
[1] T. Kimoto and Y. Yonezawa, Mater. Sci. Semicond. Process. 78, 43-56, 2018
[2] W. F. Koehl, et al. Nature 479, 84-87, 2011
[3] G. Wolfowicz et al. Sci. Adv. 6, eaaz1992, 2020
[4] G. Saito et al. Ultramicroscopy 175, 97-104, 2017
[5] Z. Chen et al. Science 372, 826, 2021
[6] The authors acknowledge funding from AFOSR (FA9550-22-1-0370). This work was carried out in part using the facilities at MIT.nano.

09:15 AM
Imaging Point Defects and Implantation Damage in Silicon Carbide using Multislice Electron Ptychography (Student)
Mr. Aaditya Bhat[1], Dr. Junghwa Kim[1], Prof. James LeBeau[1]
[1]Department of Materials Science and Engineering, Massachusetts Institute of Technology

Long coherence times, telecom wavelength emission and high fidelity electrical readout have been demonstrated for spin qubits in SiC [1]. These spin qubits are based on a variety of spin active point defects such as divacancies and transition metal substitution-vacancy complexes. Understanding the formation and transformations of these defects is key to implementing multi-qubit systems. Additionally, implantation induced structural defects, such as stacking faults and damage, and subsequent annealing must be considered since they affect coherence and defect interactions [3]. Relating the optical properties to specific defects is, however, challenging as methods typically used, such as confocal photoluminescence (PL) and optically detected magnetic resonance (ODMR), do not directly resolve the structural defects present. Recent advances in scanning transmission electron microscopy (STEM), and multislice ptychography in particular, have overcome prior limitations and robust 3D structure characterization of point defects is now possible [2].
In this presentation we go beyond conventional STEM to map point defects and their complexes in SiC using multislice electron ptychography. First using microscopy simulations and ptychographic reconstructions, we will show that the relevant point defects can indeed be identified using a combination of suitable imaging and reconstruction parameters. Subsequently we compare these results to experimental reconstructions of ion implanted and annealed samples. Furthermore, multimodal characterization of lattice damage due to ion implantation using multislice ptychography and annular dark field imaging, and resulting challenges in identifying point defects are considered. Finally, we discuss implications for fabrication of spin qubits in SiC and strategies for effective characterization using microscopy [4].
References
[1] S. Castelletto and A. Boretti. Silicon carbide color centers for quantum applications. J. Phys. Photonics, 2(2):022001, Mar. 2020.
[2] Z. Chen, Y.-T. Shao, Y. Jiang, and D. Muller. Three-dimensional imaging of single dopants inside crystals using multislice electron ptychography. Microanal, 27(S1):2146–2148, Aug. 2021.
[3] Z. He, Z. Xu, M. Rommel, B. Yao, T. Liu, Y. Song, and F. Fang. Investigation of ga ion implantation-induced damage in single-crystal 6H-SiC. Journal of Micromanufacturing, 1(2):115–123, Nov. 2018.
[4] The authors acknowledge funding from FA9550-22-1-0370. This work was carried out in part using the facilities at MIT.nano and MIT SuperCloud. We thank the Awschalom group at the University of Chicago for providing ion implanted and annealed silicon carbide samples.

8:30 AM
Solar Cell Materials and Devices
Session Chairs: Deidra Hodges (Florida International University), Mark Wistey (Texas State University)
ESJ 1202

08:30 AM
Growth of Hexagonal ScFeO3 for Bulk Photovoltaic Effect Optoelectronics
Mr. Marshall Frye[1], Dr. Lauren Garten[1]
[1]Georgia Institute of Technology

The bulk photovoltaic effect (BPE) -a mechanism of charge separation within a polar material- has potential for next generation photovoltaics however, the power conversion efficiencies of BPE photovoltaics is limited by the wide bandgap (>3 eV) and low photocurrents of many established polar materials.1 Polar materials with inherently narrow bandgaps and high photocurrents are critically needed to increase the efficiency of BPE-based photovoltaics. Hexagonal rare-earth ferrites are a class of polar materials that fit these criteria. Specifically, the polar hexagonal phase of ScFeO3 (h-SFO) is predicted to have a high BPE photocurrent and a bandgap of 1.2 eV. Unfortunately, this phase is in competition with multiple other polymorphs that are similar in energy, making stabilization complex.
In this study we describe the stabilization of the metastable P63cm hexagonal phase of ScFeO3 by pulsed laser deposition (PLD). We investigate the role of epitaxy on the phase formation pathway by growing ScFeO3 on an array of substrates with different lattice matching namely: (0001) sapphire, (0001) GaN, (111) SrTiO3, and (111) Pt. Phase-pure h-SFO was stabilized on the (0001) sapphire substrates, while the other substrates showed mixed phase or the ground-state phase of ScFeO3. XRD phi scans, Figure 1, show that the hexagonal phase of ScFeO3 films grew epitaxially on the c-plane sapphire which was unusual given the 17% lattice mismatch between the film and substrate.2 Beyond the effect of substrate, we also find that temperature is a determining factor for stabilizing the hexagonal phase with increasing the temperature of deposition resulting in increasing concentration of the hexagonal phase. Temperature dependent x-ray diffraction on films of ScFeO3 deposited on c-plane Al2O3 at room temperature shows similar trends. With increasing temperature, the initial formation of the bixbyite phase was observed, followed by a transition to the hexagonal phase; the hexagonal phase remained stabilized once cooled to room temperature.
Once the hexagonal phase was established, we characterized the optical and electronic properties of the thin films to test the candidacy of h-SFO as a photovoltaic material. Through UV-Vis spectroscopy and photoluminescence measurements we find that h-SFO has a narrow bandgap (1.4-1.6 eV), which would increase solar conversion efficiency. Furthermore, we characterize the charge carrier mobilities and dielectric response in h-SFO thin films. This study highlights the potential of hexagonal ScFeO3 for use in solar energy harvesting devices.

References:
1. Frye, M. B. & Garten, L. M. Reaching the Potential of Ferroelectric Photovoltaics. Acc. Mater. Res. 4, 906–909 (2023).
2. Disseler, S. M. et al. Magnetic Structure and Ordering of Multiferroic Hexagonal LuFeO3. Phys. Rev. Lett. 114, 217602 (2015).

08:45 AM
Preparation of the Alloys of the CuBiS2 – CuInS2 System and Their Characterization
Prof. Barys Korzun[1]
[1]The City University of New York, BMCC, 199 Chambers St., New York, NY 10007, U.S.A. 2Long Island University, 1 University Plaza, Brooklyn, New York, NY 11201, U.S.A.

Copper indium disulfide (CuInS2) is one of the promising chalcopyrite-like compounds that can be used in thin films solar cells but its energy band gap should be adjusted to the optimum value for the photovoltaic conversion, which is approximately 1.35 eV under AM1.5 conditions. An obvious approach for such reduction of the CuInS2 band gap consists of combining CuInS2 in alloys with other ternary compounds that have a lower band gap, for instance, CuBiS2 compound. The aim of the present paper is to prepare alloys of the CuBiS2 – CuInS2 system, investigate phase equilibria and to determine the limits of solubility in this system using X-ray powder diffraction (XRPD), differential thermal analysis (DTA), and scanning electron microscopy (SEM) combined with energy-dispersive X-ray spectroscopy (EDX).
Alloys of the CuBiS2 - CuInS2 system were synthesized by melting the mixture of the constituent chemical elements. In addition to the initial CuBiS2 and CuInS2 ternary compounds, 9 alloys were obtained in the system (CuBiS2)1-x - (CuInS2)x with a molar part of CuInS2 x equal to 0.05, 0.15, 0.25, 0.375, 0.50, 0.625, 0.75, 0.85, and 0.95. The X-ray studies of alloys were carried out using monochromatic Cu Ka-radiation (1.54018 Å, step size 0.01 º, counting time 10 s). The Rietveld analysis of the X-ray powder diffraction data was done using the FullProf software. SEM-EDX data were obtained using a Leo 1455VP scanning electron microscope and a Hitachi TM 3000 tabletop scanning electron microscope (Hitachi High-Technologies, Clarksburg MD, USA). The EDX data was processed using Quantax70 X-ray microanalysis software (Bruker, Berlin, Germany). The DTA measurements were performed by means of equipment specially designed and constructed for measurements up to temperatures of 1573 K. The presence of phase transformations and their temperatures were determined with an accuracy of 2 K for the phase transition temperature. Powdered samples (typical mass 1 g) were placed in evacuated silica capsules with Al2O3 used as a reference material. DTA was run on samples that were heated at the constant rate of 2-3 K/min. The temperatures of the sample and the reference materials were determined with Pt/90%Pt-10%Rh thermocouples.
It was found that the phase relations in the (CuBiS2)1-x(CuInS2)x
system are characterized by a limited solubility at room temperature. The lack of complete solubility can be explained by the fact that the crystal structures of the starting ternary compounds CuBiS2 and CuInS2 are different. The

limitations of the noncongruent melting of CuBiS2 and existence of three polymorphic modifications in CuInS2 on the formation of solid solutions in the CuBiS2 – CuInS2 system are also discussed.

09:00 AM
Formation of off-stoichiometric AgGaTe2 and application to solar cells. (Student)
Mr. Tatsuya Sasaki[1], Prof. Masakazu Kobayashi[1]
[1]Waseda University

AgGaTe2, chalcopyrite I-III-VI2 compound, has a band gap energy close to that of sunlight and exhibits a high optical absorption coefficient. It is also attracting attention as an environmentally friendly material because it does not contain Se nor In. AgGaTe2 thin films have been formed by the close-space sublimation method and fabricated into solar cell devices with a structure of Glass/Mo/p-AgGaTe2 /n-ZnIn2S4 /ZnO: Al1). In the past, the close-space sublimation method was performed using Ga2Te3 powder source, and the obtained AgGaTe2 layer was about 20% Te-rich from the stoichiometry. Recent studies have shown that AgGaTe2 thin films with near stoichiometry could be formed when GaTe source powder was used.2) CIGS solar cells with chalcopyrite structure has known to exhibit around 20% of the conversion efficiency when using about 20% Ga-rich layers3). So, tuning the AgGaTe2 thin film from stoichiometric to Ga-rich composition would lead to higher conversion efficiencies. Therefore, two methods of achieving Ga-rich AgGaTe2 thin films were examined. They are namely increasing the diffusion/deposition time, and using a source material with a composition more Ga-rich than GaTe. Ga:Te=80:20 source material was prepared in this study and used as the source materials. After thin films were formed, X-ray diffracion θ-2θ measurements were performed. When diffusion/deposition time was increased from 10 to 45 minutes, the FWHM of the AgGaTe2-originated peak around 24.9° was increased and the Ga-rich AgGa5Te8 originated peak was appeared with a 30% of the AgGaTe2 diffraction intensity. On the other hand, when Ga:Te=80:20 source material was used, AgGaTe2 and AgGa5Te8 was observed and the AgGaTe2 peak was split into two. The new peak is presumed to be Ag3Ga5Te9.The diffraction intensities of AgGa5Te8 and Ag3Ga5Te9 were increased to the similar level of the AgGaTe2 peak. The reason why the diffraction peaks were appeared in the order of AgGaTe2→AgGa5Te8→Ag3Ga5Te9 is under investigation. This may be related to the fact that the unit cell of AgGa5Te8 is about four times larger than that of AgGaTe2 with a similar crystallographic structure, but Ag3Ga5Te9 owns a quite different structure. AgGaTe2 is a ternary compound, which has more compositionally flexible than elemental materials and binary compounds. Therefore, a certain volume of AgGa5Te8 may have been included in the chalcopyrite structure. Further increase of Ga caused the defect introduction and formation of another compound like Ag3Ga5Te9. Solar cells were fabricated using the Ga-rich thin films. The solar cell using a layer with about 30% AgGa5Te8 included in AgGaTe2 showed Voc of 0.43[V], and Jsc of 10.1[mA/cm2]. From these results, extended diffusion/deposition times as well as the use of Ga:Te = 80:20 source materials were effective to fabricate Ga-rich AgGaTe2 thin films and the use of these film is effective to increase the efficiency of AgGaTe2 solar cell.

This work was supported in part by a Waseda University Grant for Special Research Projects and was partly carried out at the Joint Research Center for Environmentally Conscious Technologies in Materials Science at ZAIKEN, Waseda University.
1) A.Uruno, and M. Kobayashi, AIP Advances, 8, 115023 (2018)
2) G. Park and M. Kobayashi, Physical Status Solidi a, 2300548 (2023)
3) P. Jackson, D. Hariskos, E. Lotter, S. Paetel, R. Wuerz, R. Menner, W. Wischmann and M. Powalla, Progress in Photovoltaics Vol.19, pp 894-897,(2011)

09:15 AM
AlGaAsP distributed Bragg reflectors for GaAsP/Si solar cells (Student)
Mr. Brian Li[1], Mr. Adrian Birge[1], Ms. Bora Kim[1], Mr. Xizheng Fang[1], Dr. Minjoo Lee[1]
[1]University of Illinois Urbana-Champaign

As silicon solar cells approach their efficiency limit of 29.4% 1, epitaxial growth of III-V/Si tandem cells gives a potential path to stable devices with efficiencies greater than 30% while leveraging the low-cost and manufacturing scale of Si. 1.7 eV GaAs0.77P0.23 (hereafter GaAsP) has been extensively studied for two-junction (2J) III-V/Si cells, with record 2J efficiencies of 23-25% 2,3. A major limiting factor to further efficiency improvement is insufficient carrier collection, measured by quantum efficiency (QE), in the GaAsP cell due to threading dislocations from lattice-mismatched growth on Si. To reduce carrier loss from dislocations, a rear-surface distributed Bragg reflector (DBR) could be added to reflect transmitted photons with energies near the band-edge back into the GaAsP cell, increasing carrier generation and QE. Semiconductor-based DBRs use alternating high- and low-refractive-index layers to provide strong reflection around a central wavelength λc with layer thicknesses of λc/4n, where n is the refractive index. In addition to their ubiquitous application in vertical cavity surface-emitting lasers, DBRs are widely used for space-based III-V cells to maintain QE as the cells degrade due to electron and proton irradiation. In this work, we present the design and growth of metamorphic (Al)GaAsP DBRs for the first time.
All of the materials in this work were grown by molecular beam epitaxy with effusion cells for Ga and Al and valved cracker sources for As and P. The growth substrates were (001) GaP/Si templates from NAsPIII-V GmBH consisting of 40 nm of GaP grown pseudomorphically on a Si wafer. The DBRs were deposited on 2.1 µm-thick GaAsP graded buffers, significantly thinner than our typical > 3 µm buffers, to accommodate the extra DBR thickness while avoiding cracking due to thermal expansion mismatch. The buffer consists of 500 nm GaP, a 1300 nm compositionally graded region consisting of 100 nm GaAsyP1-y steps, and a 300 nm GaAs0.77P0.23 capping layer. Next, DBRs were grown by alternating GaAsP and AlxGa1-xAsP with x = 0.4 or 0.8. The DBRs targeted 700 nm, near the band-edge of GaAs0.77P0.23, with 20 pairs of high/low-index layers for a total DBR thickness of ~2 µm. TDD was measured with electron channeling contrast imaging (ECCI) on both the buffer and DBR surfaces, while reflectance profiles for the DBRs were both simulated in TFCalc software and experimentally measured.

The buffer had a TDD of ~1×107 cm-2 from defect counting of several ECCI images, a sufficiently low value to achieve high-performance GaAsP 1J cells and on par with devices in the literature; the average TDD on top of the DBRs was similar to the buffer alone. For the GaAsP/AlxGa1-xAsP DBRs, the experimental reflectance spectra (measured in air) had peak values of 80 and 94% for x = 0.4 and x = 0.8, respectively, with the higher index contrast of Al0.8Ga0.2AsP providing a significant improvement in both peak reflectance and reflectance bandwidth. The experimental spectra also matched our simulations closely, with the experimental reflectance slightly higher due to over-estimation of parasitic absorption in the simulated GaAsP layers. Lastly, early cell simulations show enhanced QE with the added DBRs, enabling a tandem cell efficiency improvement of as much as 1.1%. In summary, we grew (Al)GaAsP DBRs on thinned buffers with reasonable TDD values for high-efficiency GaAsP solar cells and reflectance profiles closely matching simulated values, and also showed simulated improvements in QE. At the conference, we plan to present Al0.2Ga0.8AsP/Al0.8Ga0.2AsP DBRs without the parasitic absorption of GaAsP and further refinements to our simulations of the effects of DBRs on solar cell performance.
1 Richter, A. et al. IEEE J. Photovoltaics 3, 1184–1191 (2013) 2 Lepkowski, D. L. et al. Sol. Energy Mater. Sol. Cells 230, 1–9 (2021) 3 Fan, S. et al. Cell Reports Phys. Sci. 1, 100208 (2020)

09:30 AM
Translucent Solar Cells Fabricated with Nanosecond Pulsed Laser Beams
Mr. Ashif Chowdhury[1], Prof. Heayoung Yoon[1]
[1]University of Utah

Translucent solar cells offer a promising option for building-integrated photovoltaic technologies (BiPV), capable of generating substantial electrical power while allowing some sunlight to pass through to the building. Among various designs, architectures using perforated microstructures enable adjustable transparency. However, conventional lithography and etching processes are limited in the scalability of these cells to PV module levels.
This work explores a rapid patterning technique utilizing a nanosecond laser beam (λ = 355 nm) to create microhole arrays on commercial Si solar cells. In our prototype cells, this method produces a hexagonally arranged array of microholes (≈ 22 μm in diameter), with a microhole spacing of 10's of μm to 100's μm. The array, measuring 20 mm × 7 mm, is created in under 7 seconds. Photovoltaic analysis of cells with 120 μm spacing (transparency ≈ 1 %) shows retention of over 93 % of the initial short-circuit current density (Jsc), with the open-circuit voltage (Voc) and fill factor (FF) maintaining 85 % and 80 % of their initial values, respectively. This suggests that most damage is localized near the junction region. Electron microscopy reveals a SiOx layer beneath the Si surface, likely formed by reactions with ambient oxygen. We will address optimizing the process to reduce laser-induced damage at the junction and remove surface debris to boost device performance.

9:45 AM
Coffee Break
ESJ Building

10:15 AM
Growth of Group III-Nitrides
Session Chairs: Russell Dupuis (Georgia Institute of Technology), Theeradetch Detchprohm (Georgia Institute of Technology)
ESJ 0202

10:15 AM
Epitaxial Growth of Multichannel AlScN/GaN Heterostructures by Molecular Beam Epitaxy (Student)
Mr. Thai-Son Nguyen[1], Mr. Chandrashekhar Savant[1], Prof. Huili (Grace) Xing[1], Prof. Debdeep Jena[1]
[1]Cornell University

AlScN is a promising ultrawide bandgap semiconductor material with lattice-matching and high-k capabilities strongly desired for GaN electronics. Molecular beam epitaxy (MBE) and metal organic chemical vapor deposition (MOCVD) have been employed to create single-channel AlScN/GaN HEMT heterostructures [1, 2, 3] with two-dimensional electron gases (2DEGs) of electron densities surpassing 2 × 1013/cm2, electron mobilities exceeding 1500 cm2/V.s, and sheet resistances below 250 Ω/□ [2]. HEMTs fabricated using these heterostructures exhibit remarkable performance characteristics, such as a current density greater than 3 A/mm [4] and an output power exceeding 8 W/mm at 30 GHz [3]. Ferroelectric AlScN barrier layers enable ferroelectric gating effects, enabling FerroHEMTs [4] with the potential for high-speed, high-power reconfigurable single-channel transistors. But multichannel AlScN/GaN heterostructures have not been reported. Compared to AlN, AlGaN, or AlInN barriers, AlScN is lattice matched to GaN at approximately 9-11% Sc, thereby allowing for enhanced conduction band offset and superior 2DEG confinement without suffering from strain-induced structural degradation. Additionally, AlScN possesses a stronger spontaneous polarization than AlGaN and AlInN, suggesting the potential for thinner stacks and higher total sheet charge densities in AlScN/GaN multichannel structures.
We report the MBE growth and transport properties of multichannel AlScN/GaN multichannel heterostructures in this work. Near lattice-matched (11-12% Sc) composition was targeted for AlScN barriers. Samples of five-channel AlScN/GaN and AlScN/AlN/GaN were grown on GaN-on-sapphire templates with AlScN barrier thickness of 10 nm and various GaN channel thicknesses between 20 nm and 50 nm. 2 x 2 μm area atomic force micrographs showed smooth surfaces with root-mean-square (RMS) roughness measuring below 1 nm. Both AlScN/GaN and AlScN/AlN/GaN heterostructures were pseudomorphically grown onto the GaN substrate as verified by reciprocal space mapping (RSM). Sharp interfaces were achieved by MBE and the barrier thicknesses were precisely controlled, as confirmed by X-ray diffraction (XRD) analysis. These five-channel heterostructures consistently exhibited total sheet charge densities of approximately 1 × 1014/cm2, among the highest carrier densities ever reported for multichannel GaN

HEMT structures. By incorporating an AlN interlayer or adjusting the thickness of the GaN channel, electron mobility up to 583 cm2/V.s and sheet resistance as low as 106 Ω/□ were measured. Temperature-dependent Hall effect measurements conducted between 10 K and 300 K showed less than 15% carrier freezeout and confirmed the presence of multiple 2DEGs. The total sheet charge density also scaled with the number of AlScN/GaN periods and layer thicknesses, highlighting the strong tunability of transport properties of such AlScN/GaN multichannel structures. This study demonstrates the versatile capability of AlScN/GaN multichannel heterostructures to provide exceptionally high sheet charge density for forthcoming high-power GaN electronics.

[1] M. T. Hardy et al., Epitxial ScAlN Grown by Molecular Beam Epitaxy on GaN and SiC Substrates, Appl. Phys. Lett. 110, 162104 (2017).
[2] J. Casamento et al., Transport Properties of Polarization-Induced 2D Electron Gases in Epitaxial AlScN/GaN Heterojunctions, Appl. Phys. Lett. 121, 192101 (2022).
[3] S. Krause et al., AlScN/GaN HEMTs Grown by Metal-Organic Chemical Vapor Deposition With 8.4 W/mm Output Power and 48 % Power-Added Efficiency at 30 GHz, IEEE Elec. Dev. Lett., 44 (1), 17-20 (2023).
[4] J. Casamento et al., FerroHEMTs: High-Current and High-Speed All-Epitaxial AlScN/GaN Ferroelectric Transistors, 2022 International Electron Devices Meeting 11.1.1 – 11.1.4 (2022).

10:30 AM

Epitaxial Growth of High ScN Fraction ScAlN on (111) Si

Dr. Matthew Hardy[1], Dr. Eric Jin[1], Dr. Neeraj Nepal[1], Dr. Brian Downey[1], Dr. Vikrant Gokhale[1], Dr. Scott Katzer[1], Dr. Virginia Wheeler[1]
[1]U.S. Naval Research Laboratory

ScAlN thin films have attracted significant attention due to their factor of five increase in piezoresponse over AlN for ScxAl1-xN compositions of x = 0.43 [1], leading to potential applications in 5G filters and RF electronics. Epitaxial growth of ScAlN on Si opens up the potential for use of mature microelectromechanical systems (MEMS) processing technology, particularly under-cut etching for released acoustoelectric devices.

In this work, we demonstrate the growth of ScxAl1-xN layers on AlN nucleation layers (NL) on 100-mm (111) Si wafers with x up to 0.40 using molecular beam epitaxy. Optimization of the total group-III to group-V (III/V) ratio of the AlN NL is critical to avoid polycrystalline domain formation in the very thin AlN layer (≤ 10 nm) while avoiding pitting of the substrate and Si incorporation due to silicide formation. III/V ratios of 0.5 and 0.8 show broadening of the layer spots in reflection high-energy electron diffraction (RHEED) as well as formation of ring segments suggesting a broadening of domain orientation. III/V ratio > 1 shows streaky RHEED, but atomic force microscopy (AFM) indicates etching of the underlying Si substrate and suggests an Al-silicide formation. III/V of 0.93 gives a streaky RHEED pattern with slight spot-modulation and no apparent etching of the Si substrate. Sc0.40Al0.60N layers overgrown on the AlN NL show similar behavior, with ring segments present during the AlN NL propagating through the ScAlN layer in the case of lower AlN III/V ratio, with no polycrystalline features evident in ScAlN film grown on optimized AlN.

Similarly, III/V ratio plays a critical role in the growth of high ScN fraction ScxAl1-xN. Several samples were grown at low substrate temperatures (410 °C), varying both the Sc and Al flux to allow changes in the III/V ratio for a fixed composition, but resulting in changes to the metal-flux-limited growth rate. At low III/V ≤ 0.8, rings appear in the RHEED pattern suggesting the presence of polycrystalline domains. Similar samples grown on SiC substrates show a yellow tint, suggesting the presence of a non-wurtzite phase. At III/V around 0.95, the rings disappear leaving a spotty wurtzite RHEED pattern free of extraneous features. At III/V ≥ 1.0 the RHEED pattern broadens and forms indistinct dual-ring-segments. Similar samples grown on SiC show a gray tint to the film. This is the first demonstration of both a lower and upper bound to the high ScN fraction growth space, as well as identification of characteristic RHEED patterns and is distinct from the III/V ratio behavior at low ScN fraction (x ≤ 0.2).

A ScAlN/AlN/Si sample grown using the optimized AlN and ScAlN III/V ratios, having a 10-nm AlN NL, a 20-nm graded 0.32 → 0.40 ScAlN nucleation layer, and a 100-nm Sc0.40Al0.60N layer, shows a clean wurtzite RHEED pattern throughout growth, an 0002 X-ray diffraction full-width at half maximum of 1.1°, and an rms roughness of 0.57 nm. Neither the AFM height image or the phase image show any indication of anomalously oriented grains (AOGs) over a 5 × 5 nm2 scan. Such thin, high structural and phase purity films are well suited to high frequency RF MEMS applications.

[1] M. Akiyama, K. Kano, and A. Teshigahara, Appl. Phys. Lett., 95, 162107 (2009).

10:45 AM

Growth and Characterization of AlInN/GaN Superlattices (Student)

Mr. HAOTIAN XUE[1], Mr. Elia Palmese[1], Mr. Ben Sekely[1], Dr. Brian Little[1], Dr. Fred Kish[1], Dr. John Muth[1], Dr. Jonathan Wierer[1]
[1]North Carolina State University

III-nitride semiconductors have had successes in optoelectronic and electronic devices. Of the ternaries in this family, AlInN is the least explored and implemented in devices. AlInN is attractive because it can be lattice-matched to GaN, has a wider bandgap and higher electric field at breakdown, has a high refractive index contrast compared to GaN, and has high polarization fields to create 2-dimensional electron gases. However, AlInN is challenging to implement because of growth limitations that lead to poor surface morphology at thicknesses greater than 50 nm, even with the best-known growth conditions. Island growth dominates, and mounds form in alignment with the step-like surface of the underlying GaN. Pits originating from the substrate or within the AlInN grow as the layer thickness increases. Usually, AlInN thicknesses are limited to ~300nm before the surface becomes too rough or pitted to be of use. This work presents data on near-lattice-matched AlInN/GaN superlattices (SLs) with superior morphology than thick (bulk) AlInN layers [1].

The SLs and bulk AlInN are grown by metalorganic chemical vapor deposition in a Taiyo Nippon Sanso Co. reactor. The layers are grown on free-standing GaN and GaN-on-sapphire substrates. The SL samples consist of 20 or 100 pairs of ~3nm thick AlInN and ~1nm thick GaN layers (80nm or 400nm thick) at varying temperatures and pressures. The

layer thicknesses are chosen to prevent defects from forming and achieve an SL consisting predominately of AlInN to retain its desirable properties. For comparison, bulk layers of AlInN are grown at the same thicknesses. All samples are grown in an N2 ambient with a V/III ratio of ~1.44×104 and are unintentionally doped. The growth temperature and pressure are constant for all layers to avoid temperature or pressure ramping and growth interruptions.
Growth conditions are explored to find optimum conditions. The Al1-xInxN indium content decreases linearly (x=0.2-0.15) with increasing temperatures (775-800°C), the same behavior as bulk AlInN. The SLs grown at pressures between 20-40kPa exhibit step-like surface morphology, while at 10kPa and 50kPa they roughen. There is also a decrease in the AlInN growth rate (3.6-2.5nm/min) with increasing pressure (10-50kPa) and higher indium content at higher pressures. A pressure of 30kPa is chosen for the following growth results.
The SLs suppress island growth and pit formation that occurs in bulk AlInN and exhibit superior morphology with lower roughness. The 20-period SLs and GaN-on-sapphire substrates exhibit extremely smooth surfaces with atomic force microscope (AFM) scans showing root mean square (RMS) roughness of 0.3nm and atomic steps closely resembling the underlying GaN layers. Pits caused by threading dislocations are present with a density of ~1.36×108 cm-2, comparable to the dislocation density of the substrates before growth. The bulk AlInN control sample shows the typical small mounds aligning to the atomic edges of the underlying GaN with an RMS~0.65 nm. Increasing to 100 periods slightly increases pit sizes, but stepped surfaces remain.
AlInN/GaN 20-period SLs grown on free-standing GaN substrates have excellent surfaces with nearly linear atomic steps, matching the step morphology of the underlying GaN. Pits are only observed in the larger 20μm×20μm AFM scans and are formed from the pits in the underlying GaN substrate. Transmission electron microscope images show a highly periodic SL with consistent composition and slight layer intermixing.
The SL also exhibits interesting optical properties. The refractive index versus wavelength measured by ellipsometry of the AlInN/GaN SL shows a weighted value between those of AlInN and GaN at ~3:1, matching the thickness of each layer. Light emission via cathodoluminescence from the AlInN/GaN SL grown on GaN substrates is observed with a peak at ~317 nm from transitions in quantum states within the thin SL GaN layers.
[1] H. Xue, et al., "Growth and Characterization of AlInN/GaN Superlattices," J. of Crystal Growth (2024). 10.1016/j.jcrysgro.2024.127567

11:00 AM
Misfit Dislocation Management in a 1D FACELO AlGaN/GaN Heterostructure (Student)
Mr. Michael Carter[1], Mr. Jack Almeter[1], Dr. Shashwat Rathkanthiwar[1], Dr. Ronny Kirste[2], Dr. Seiji Mita[2], Prof. Ramón Collazo[1], Prof. Zlatko Sitar[1]
[1]North Carolina State University, [2]Adroit Materials

AlGaN is a primary candidate for use in next-generation optoelectronic devices, owing in part to the tunable, direct bandgap from GaN (3.4 eV) to AlN (6.4 eV). Among other issues, AlGaN device performance has historically been limited by dislocations and other defects. As a path to mitigate high dislocation densities in AlGaN/sapphire, growth on native GaN and AlN substrates was suggested. However, even in these cases the lattice mismatch present during AlGaN epitaxy, which may be up to 1.2% for Al0.5Ga0.5N on (0001) GaN/AlN substrates, would require a spacing of approximately 26 nm between edge-type misfit dislocations (MDs) to fully relieve strain. In the standard growth orientation of (0001), dislocation glide from the growth surface to the interface is only possible via slip systems with relatively high Peierls barriers. Thus, formation of the necessary MD array is hindered, ultimately leading to strained psuedomorphic growth, epilayer cracking, or a high density of short MDs, which contribute two threading dislocations (TDs) each in the epilayer. Since TDs are known sources of leakage current and non-radiative recombination, forming a more coherent array of long MDs is desirable.
Semipolar growth has shown promise in producing well defined MD arrays, owing to the favorable stress state for edge dislocation slip in the (0001) plane. However, availability of semipolar native substrates is low and growth often results in surface degradation. Facet controlled epitaxial lateral overgrowth (FACELO), has been shown to grow thick, crack-free, relaxed AlGaN layers in (0001) growth orientation. To do this, FACELO produces {11-22} facets, which are used as semipolar growth surfaces for the desired AlGaN epilayer composition. The AlGaN epilayer is then fully planarized to return to a (0001) growth orientation.
In this study, we analyze via cross-section and plan-view transmission electron microscopy (TEM) semipolar {11-22} AlGaN/GaN interfaces formed during FACELO. This analysis is conducted to confirm the formation of an ordered array of long MDs relieving epitaxial lattice strain on the {11-22} interface, determine causes and prevalence of MD threading from the interface, and identify areas for further refinement of FACELO, such as at the coalescence boundaries. As a case study, we use a one-dimensionally-patterned maskless FACELO on a freestanding GaN substrate with a >5 μm thick, relaxed Al0.35Ga0.65N epilayer. The TD density in the epilayer is also measured and discussed in terms of the MD density. Use of a (11-22) plan-view TEM sample reveals novel information about the MDs formed during this growth method, including average length and overall arrangement on the interface. The measured spacing of 23 nm between MDs in this view direction is shown to agree well with the predicted value of 19 nm. Using the standard invisibility criterion in TEM to determine the Burgers vector shows that the MD array is edge type with b = ⅓<11-20>. The plan-view TEM analysis additionally reveals the average length of a MD along the interface to be >1 μm. The TD density is measured directly via cross-section TEM and found to be ~109 cm-2, primarily resulting from coalescence boundaries and areas of incomplete FACELO with (0001) Al0.35Ga0.65N/GaN interfaces. The TD density is also estimated from the MD length and density measured in the plan-view TEM sample and found to be 109-1010 cm-2. Contrasted with the localized and roughly equal TD density measured in cross section, this data suggests that the TDs produced from the MD array experience termination or annihilation to reduce their density in the epilayer. Thus, we conclude that the primary source of TDs in FACELO is not the MD array. This study demonstrates the potential of FACELO to produce high quality AlGaN epitaxial films and motivates further refinement of growth parameters to reduce dislocations associated with other interfaces and coalescence boundaries and increase average MD length. Additionally, this study provides a basis for analysis of other geometries of FACELO structures, specifically two-

dimensionally patterned FACELO which has been shown to biaxially relieve lattice strain.

10:15 AM
Optoelectronic Devices
Session Chair: Kyle McNicholas (MIT Lincoln Laboratories)
ESJ 0224

10:15 AM
Heteroepitaxial Integration of Embedded Visible InP Quantum Dot Lasers on SiN/Si Photonic Integrated Circuits (Student)
Mr. Yiteng Wang[1], Dr. Christopher Heidelberger[2], Dr. Jason Plant[2], Dr. Cheryl Sorace-Agaskar[2], Dr. Dave Kharas[2], Dr. Pankul Dhingra[1], Dr. Paul Juodawlkis[2], Dr. Minjoo Lee[1]
[1]University of Illinois Urbana-Champaign, [2]MIT Lincoln Laboratory

Heterogeneous integration of visible lasers with low-loss SiN waveguides is attractive for on-chip photonic applications such as quantum computing, biosensing and displays.1-3 Direct epitaxial growth of III-V devices on complementary metal–oxide–semiconductor (CMOS)-compatible SiN/Si photonic integrated circuits (PICs) leverages the maturity of Si manufacturing with the potential for high-density integration of optical gain. Quantum dots (QDs) are a promising gain medium for semiconductor lasers on Si substrates due to their great dislocation tolerance, thermal stability, and optical feedback immunity.4-5 Recently, several groups have demonstrated near- to mid-infrared III-V lasers on patterned Si PICs by direct epitaxial growth.6-8 We earlier proposed a scheme for butt-coupling III-V gain, detection, and modulation with SiN passives with the III-V devices grown in pockets.9 In this work, we demonstrate the first visible-spectrum InP QD lasers directly grown on SiN/Si PICs with room-temperature (RT), continuous-wave (CW) operation at low threshold current density and mW-level power output.
The PIC structure consists of SiN waveguides and SiO2 clads with a total thickness of 6 µm, fabricated at Lincoln Laboratory on 200 mm Ge-on-Si (001) with a 6° offcut and a threading dislocation density of ~2-3×107 cm-2. After cutting into coupons, metal-organic chemical vapor deposition (MOCVD) was used for selective growth of a 3.2 µm n-GaAs buffer in dry-etched pockets that expose the surface of the Ge layer. The coupons are then transferred to UIUC for non-selective molecular beam epitaxy (MBE) growth of InP QD lasers. Post-growth rapid thermal annealing (RTA) was performed at 850 °C for 4 minutes to improve the optical quality of the active region without damaging the Ge layer (Tmelt, Ge = 937 °C). The polycrystalline layer on top of the SiO2 was removed by a combination of dry and wet etching before Fabry-Perot edge-emitting laser fabrication. Next, narrow ridges (2.6 – 9.6 µm wide, ~ 3 µm tall) were defined by Cl-based ICP-RIE etching, with their sidewalls passivated by PECVD-deposited SiO2. Lastly, contact metals were deposited, and the sample was manually cleaved into 4 mm long Fabry-Perot lasers for device testing.
Micro-photoluminescence (micro-PL) shows the QD emission at ~740 nm after RTA, and Nomarski images confirm there is no cracking or other RTA-induced damage. The RT CW light-current (L-I) measurements show threshold current densities of 580 and 750 A/cm2 for 2.6 and 4.6 µm-wide ridge lasers, respectively; the 2.6-µm ridge laser reaches 10 mW output from a single facet. Overall, the performance of the embedded narrow-ridge lasers is comparable to our previous broad-area lasers on unpatterned GaAs/GaP/Si (threshold of 670 A/cm2 with > 10 mW output power)10. T-dependent L-I testing shows CW lasing up to 50 °C with characteristic temperature T0 = 51 K. With the demonstration of visible lasers grown within SiN PICs, future work will focus on efficient butt-coupling of the laser light into SiN waveguides to enable on-chip visible light applications.
[1] J. Wang et al. Nat. Photonics 2020, 14 (5), 273–284.
[2] K. De Vos et al. Opt. Express 2007, 15 (12), 7610.
[3] H. Hamada et al. Fiber and Integr. Opt. 2015, 34 (5–6), 259–281.
[4] P. Dhingra et al. Appl. Phys. Lett. 2020, 117 (18), 181102.
[5] H. Huang et al. APL Photonics 2020, 5 (1), 016103.
[6] C. Shang et al. Light Sci. Appl. 2022, 11 (1), 299.
[7] W. Wei et al. Light Sci. Appl. 2023, 12 (1), 84.
[8] A. Remis et al. Light Sci. Appl. 2023, 12 (1), 150.
[9] C. Heidelberger et al. 2021 IEEE Photonics Conference (IPC), 2021, pp 1–2.
[10] P. Dhingra et al. Optica 2021, 8 (11), 1495.

10:30 AM
Effects of Molecular Beam Epitaxy Selective Area Growth Techniques on III-V Optical Quality (Student)
Mr. Byron Aguilar[1], Ms. Ashlee Garcia[1], Dr. Alec Skipper[1], Dr. Daniel Ironside[1], Prof. Seth Bank[2]
[1]Chandra ECE Department, The University of Texas at Austin, [2]University of Texas at Austin

An all-molecular beam epitaxy (MBE) approach to selective area epitaxy (SAE) enables the creation of novel optoelectronic devices through integration of metal and dielectric microstructures in III-V semiconductors. The encapsulation of patterned dielectrics and metals in III-V semiconductors could unlock opportunities for integrating high contrast photonic structures, site-controlled quantum emitters and laterally structured plasmonic layers into MBE-grown devices.1,2 Furthermore, utilizing an all-MBE approach would enable further advancement due to its high layer precision and non-equilibrium growth conditions.3 However, the challenge of integration via MBE regrowth is its historically poor deposition selectivity as compared with other epitaxial growth techniques.3 Deposition occurs on the amorphous mask surface rather than only in the seeding III-V windows, which leads to a build-up of adatoms that results in the formation of polycrystalline material.4 Therefore, to achieve selective growth of high quality, single crystalline III-V and mitigate polycrystalline formation on the mask surface, conditions outside of the ideal III-V growth regime, specifically high growth temperatures and low deposition rates, are required.5 Furthermore, fabrication of the mask for prior to regrowth requires reactive ion etching (RIE) or an acid etch, which can damage the initial epitaxial surface.6

Combined, these non-idealities could potentially result in poor surface morphology and optical quality.
Here, we explore the influence of selective area epitaxy conditions on the structural and optical quality of MBE-grown materials. Previously, we reported the first demonstration of III-V encapsulation of low-aspect ratio features by MBE; periodic supply epitaxy (PSE) was paired with planar coalescence to promote selective lateral growth and then restore the interface for continued growth.7,8 To embed the SiO_2 structures, selective lateral growth was performed with 300 cycles of PSE at ~630 °C and a 50% duty cycle (30s Ga deposition followed by a 30s interruption) at a rate of 0.25 μm/hr under a 65× As_4/Ga overpressure. After which, 2 μm of continuous growth at 570 °C restored the growth interface. Via atomic force microscopy, it was observed that the restored surface had a room-mean-square roughness of 3 to 7nm. To further assess the influence of the encapsulation process on the material quality of the semiconductor, we grew a thin $In_{0.15}Ga_{0.85}As$/GaAs type-I quantum well (QW) on top of GaAs with embedded 25nm tall SiO_2 gratings of varying pitches. This was then compared to an identically grown structure on a GaAs wafer without the embedded gratings. The peak photoluminescence (PL) responses of the samples were within 2× of that of the control, indicating that the underlying SAE-grown GaAs interface was of comparable quality, as non-radiative defects would result in intensity reduction.9 Experiments are currently underway to explore the imposed limits of various MBE SAE techniques and necessary fabrication steps on material quality. By examining the influence of high temperatures, low deposition rates and PSE interruption times as well as the sensitivity to damage from etching, we can maximize optical performance and produce high quality surface morphology for selective area regrowth applications. This work was supported by the National Aeronautics and Space Administration (NASA) through the Quantum Pathways Institute (Award 80NSSC22K0287), the National Science Foundation (ECCS-1926187), and Lockheed Martin.
[1] J.E. Bowers et al., Optical Fiber Communication Conference (2017). [2] A.M. Skipper et al., Applied Physics Letters (2022) [3] U.W. Pohl, Epitaxy of Semiconductors: Physics and Fabrication of Heterostructures, Springer (2020). [4] S.C. Lee et al. J. Cryst. Growth (2016). [5] S.C. Lee et al., J. of Appl. Phys. (2002). [6] J. Rossabi et al., Surface and Interface Analysis of Microelectronic Materials Processing and Growth (1989). [7] F.E. Allegretti et al., J. Cryst. Growth (1995). [8] D.J. Ironside et al., Progress in Quantum Electronics (2021). [9] J. Christen, Advances in Solid State Physics, Springer (1990).

10:45 AM
Molecular Beam Epitaxy Selective Area Regrowth of High Aspect Ratio Microstructures for Mid-Infrared Optoelectronics (Student)
Ms. Ashlee Garcia[1], Mr. Byron Aguilar[2], Mr. William Doyle[1], Mr. Yiteng Wang[3], Dr. Daniel Ironside[1], Dr. Alec Skipper[1], Ms. Morgan Bergthold[4], Dr. Minjoo Lee[5], Prof. Daniel Wasserman[4], Prof. Seth Bank[6]
[1]Chandra ECE Department, The University of Texas at Austin, [2]The University of Texas at Austin, [3]University of Illinois, [4]Department of Electrical and Computer Engineering, University of Texas at Austin, Austin, TX 78758, [5]University of Illinois Urbana-Champaign, [6] University of Texas at Austin

A molecular beam epitaxy (MBE) approach to selective area epitaxy (SAE) of III-V semiconductors enables the seamless integration of metals, dielectrics, and high-quality crystalline semiconductors. This technique has the potential to advance novel optoelectronic structures, such as high-contrast photonics, site-controlled quantum emitters, stacked pixel detectors, and photonic integrated circuits. While SAE by metal organic chemical vapor deposition has been widely successful due to its high material deposition selectivity, an SAE MBE method could enable further advances through its high layer precision and access to non-equilibrium growth conditions1,2.
However, MBE SAE has been historically difficult to achieve under conventional growth conditions as a result of its poor III-V deposition selectivity. This leads to an aggregation of adatoms on the amorphous surface which results in the formation of polycrystalline material on the mask surface.2-7 Despite many efforts to expand selectivity by modulating the group-III and -V fluxes2,4,5, modeling growth mechanisms3,6, or utilizing hydrogen-assisted MBE7, the accessible growth window remains quite narrow necessitating high growth temperatures and low growth rates. Successful selective growth techniques rely on minimizing the interaction of the adatoms with the surface of the amorphous structure by enhancing desorption off the mask surface and/or diffusion to the crystal growth window.2-7 For this reason, surface roughness and defects can even further restrict the MBE selective growth regime by lowering the barrier for polycrystal nucleation.8 This presents a particularly challenging barrier for applications requiring microns-tall high-aspect-ratio dielectric structures, such as mid- and long-wave infrared high-contrast photonics9-11 and aspect ratio trapping of threading dislocations for metamorphic growth12, due to the innately rough surfaces produced by plasma-enhanced chemical vapor deposition (PECVD) of thick films.13
To enable fully selective growth of such structures, a MBE-compatible surface restoration technique is required. Hydrogen silsesquioxane (HSQ) is an inorganic flowable oxide that has been utilized to create high quality planar SiO_2 interfaces which are vacuum compatible and stable at high temperatures once cured.14,15 Here we demonstrate HSQ as an effective solution to aid MBE regrowth selectivity for the design of novel device and optical structures by mitigating the surface roughness of micron-scale dielectric features. Integrating the HSQ surface planarization with a 100 nm layer of HSQ in the fabrication of 2 μm tall features demonstrated a significant decrease in film roughness from a root-mean-square roughness of 3.95 nm to 0.98 nm. GaAs selective regrowth of 2 μm tall SiO_2 features fabricated with this approach was performed; a significant improvement in selectivity was observed as compared to the un-planarized features with no polycrystalline material formation on SiO_2 bars <10 μm wide alongside a commensurate 30 increase in achievable feature aspect ratio (1:3 10:1). Experiments are currently underway to extend this approach to regrowth of InAs to access wavelengths in the mid-wave infrared regime and demonstrate the complete encapsulation of high aspect ratio dielectric microstructures via the all-MBE regrowth technique. This work was supported by the National Aeronautics and Space Administration (NASA) through the Quantum Pathways Institute (Award 80NSSC22K0287), the National Science Foundation (ECCS-1926187), and Lockheed Martin.

[1] D.J. Ironside et al., J. Cryst. Growth (2019). [2] F.E. Allegretti et al., J. Cryst. Growth (1995). [3] S.C. Lee et al. J. of Appl. Phys. (2002). [4] Y. Horikoshi. J. Cryst. Growth (1999). [5] S. Yokoyama et al. J. Cryst. Growth (1989). [6] Aseev et al. Nano Lett. 2019. [7] T. Sugaya et al. Jpn. J. Appl. Phys. (1992). [8] M. Ohring, The Material Science of Thin Films, Academic Press (1992). [9] Jun Wang et al. 2017 Laser Phys. Lett. 14 125801. [10] C. J. Chang-Hasnain et al. Adv. Opt. Photon., Sep 2012. [11] S. S. Wang et al. Appl. Opt., May 1993. [12] J.Z. Li et al. Appl. Phys. Lett. 91 (2) (2007). [13] M. R. Amirzada et al. Appl Nanosci (2016). [14] F. Salmassi et al, Appl. Opt. (2006). [15] C.-C. Yang et al., J. Mater. Chem. (2002).

11:00 AM

Demonstration of InAs Quantum Dots-in-a-Well Photonic Crystal Surface Emitting Lasers (PCSELs) by Epitaxial Regrowth (Student)

Ms. Subhashree Seth[1], Dr. Kevin J. Reilly[1], Mr. Fatih Furkan Ince[1], Dr. Akhil Kalapala[2], Mr. Chhabindra Gautam[2], Prof. Thomas J. Rotter[1], Dr. Zhongue Liu[2], Dr. Sadhvikas Addamane[3], Prof. Weidong Zhou[2], Prof. Ganesh Balakrishnan[1]
[1]Center for High Technology Materials, University of New Mexico, Albuquerque, New Mexico, [2]Department of Electrical Engineering, The University of Texas at Arlington, Arlington, TX, [3]Center for Integrated Nanotechnologies, Sandia National Laboratories

Self-assembled Quantum dot (QD) gain media-based lasers have attracted considerable attention due their low sensitivity to operating temperature and record-low threshold current densities. InAs Stranski-Krastanov QD based edge emitting lasers (EELs), vertical cavity surface emitting lasers (VCSELs) or vertical external cavity surface emitting lasers (VECSELs) have been demonstrated with excellent performance. In this study, we demonstrate a QD based optically-pumped photonic crystal surface emitting laser (QD-PCSEL). While the QD-PCSEL can be fabricated using wafer bonding or by creating a photonic crystal (PC) that is exposed to the surface, in this case we are making use of an epitaxial regrowth process which results in a buried PC region between the laser's waveguide and upper clad layers. The epitaxial process is performed using a solid source molecular beam epitaxy reactor (MBE) and begins with an initial growth containing the bottom Al0.3Ga0.7As cladding layer and the GaAs waveguide including the QD active region. In the next step, the wafer is removed from the reactor and the PC layer is patterned by electron beam lithography (EBL) and is etched into the semiconductor using an inductively coupled plasma (ICP) dry etcher. Lastly, we perform the epitaxial regrowth of the top cladding and a top contact layer. The most crucial step before growing the top clad layer is thermal removal of the gallium oxide under arsenic overpressure which can alter (>6000C) the QD gain media as well as lasing emission by causing a blue shift in photoluminescence and narrowing of PL emission of self-assembled QDs [1-3]. In our study, we incorporate a dot-in-well (DWELL) design as the active region, which is a modification of the InAs QD active region and involves the inclusion of the QDs in a InxGa1-xAs quantum well (QW). The DWELL active region is stable under the regrowth process with no change to the emission wavelength and is key to the realization of this laser. The PCSEL is tested by optical pumping and we present both light-input light-output (LL) and spectrum measurements.
M.-Y. Hsu, and G. Lin, "Quantum-Dot Photonic-Crystal Surface-Emitting Lasers with Bottom Distributed Bragg Reflector," Photonics 5, (2018).
T.-S. Chen, Z.-L. Li, M.-Y. Hsu, G. Lin, and S.-D. Lin, "Photonic crystal surface emitting lasers with quantum dot active region," J. Lightwave Technol. 35(20), 4547–4552 (2017).
L.-R. Chen, K.-B. Hong, K.-C. Huang, C.-L. Liu, W. Lin, and T.-C. Lu, "Study of an epitaxial regrowth process by MOCVD for photonic-crystal surface-emitting lasers," Cryst. Growth Des. 21(6), 3521–3527 (2021).
This work was performed, in part, at the Center for Integrated Nanotechnologies, an Office of Science User Facility operated for the U.S. Department of Energy (DOE) Office of Science by Los Alamos National Laboratory (Contract 89233218CNA000001) and Sandia National Laboratories (Contract DE-NA-0003525).

11:15 AM

Optical and morphological study of local-droplet etched quantum dots

Dr. Sadhvikas Addamane[1], Prof. Oleg Mitrofanov[1], Dr. Prasad Iyer[1], Dr. Ashish Chanana[2], Mr. Casey Timms[3], Ms. Chloe Marzano[3], Dr. Darryl Shima[4], Prof. John Schaibley[3], Dr. Marcelo Davanco[2], Prof. Ganesh Balakrishnan[4], Dr. Igal Brener[1
[1]Center for Integrated Nanotechnologies, Sandia National Laboratories, [2]National Institute of Standards and Technology, [3]University of Arizona, [4]Center for High Technology Materials, University of New Mexico, Albuquerque, New Mexico

Self-assembled III-V quantum dots (QDs) are essential building blocks for various optoelectronics applications including lasers, detectors, and quantum light sources. Among III-V QDs, local-droplet etched (LDE) QDs have recently emerged as a viable alternative to widely-used Stranki-Krastanov (S-K) In(Ga)As QDs, specifically for single- and entangled-photon sources. The LDE method allows for the realization of unstrained, pure, and uniform QDs with low fine structure splitting, short radiative lifetime, and long spin coherence times. Since their conceptualization, considerable research has been conducted to reveal details of the LDE growth mechanism, and the structural and optical properties of the QDs. However, a comprehensive analysis of the growth process and the growth conditions required to obtain high-quality LDE QDs hasn't been widely reported. In this work, we investigate the effect of different growth conditions (temperature, flux, and thickness) on the structural properties, (size, shape, and density) and consequentially on the optical characteristics (emission wavelength, linewidth, brightness etc.) of LDE QDs.
The samples analyzed here are grown using molecular beam epitaxy on (100)-oriented GaAs substrates. The epitaxial stack consists of GaAs LDE QDs grown at the center of a 140nm-thick Al0.4GaAs membrane and on top of a 500nm Al0.75GaAs sacrificial layer. The QDs are grown in three distinct steps: deposition of group-III droplets, formation of shallow nanoholes, and in-filling of nanoholes with the QD material. In each of these steps, a wide variety of growth conditions are explored, and separate samples are

grown for each different condition. The structural properties of the QDs are analyzed using various microscopy techniques, including atomic force microscopy and transmission electron microscopy. For emission characteristics, photoluminescence (PL) measurements are carried out at 4K. PL imaging is used to locate embedded QDs for spectrum measurements and estimate areal density. This presentation will introduce the background behind LDE QDs, and the experimental process followed. Most of it will highlight the results showing a strong correlation between optical and structural characteristics of the QDs and the epitaxial growth conditions.

[1] Y. Arakawa, et al., Appl. Phys. Rev. 7, 2 (2020).
[2] S.F.C da Silva, et al. Appl. Phys. Lett. 119, 12 (2021).

Acknowledgements: This work was performed, in part, at the Center for Integrated Nanotechnologies, an Office of Science User Facility operated for the U.S. Department of Energy (DOE) Office of Science by Los Alamos National Laboratory (Contract 89233218CNA000001) and Sandia National Laboratories (Contract DE-NA-0003525).

10:15 AM
Oxide UV Photodetectors and Other Devices
Session Chairs: Hari Nair (Cornell University), Esmat Farzana (Iowa State University)
ESJ 2208

10:15 AM
Significantly enhanced and dark current suppressed β-Ga2O3 based DUV self-powered photodetector by ion implantation process
Dr. Kishor Upadhyaya[1], Mrs. Fatimah Alreshidi[1], Ms. Hadeel Alamoudi[1], Mr. Duarte Esteves[2], Mr. Marco Peres[2], Dr. Katharina Lorenz[2], Prof. Iman Roqan[1]
[1]Semiconductor and Spectroscopy laboratory, King Abdullah University of Science and Technology, [2]Instituto Superior Técnico, Campus Tecnológico e Nuclear

Self-powered solar-blind deep UV (DUV) photodetectors (PDs) have a wide range of potential applications especially, ultra-wide band gap semiconductor, Ga2O3 based devices are to be one of the most promising candidates for such applications. It has been reported earlier that Sn dopants can be used to modify the electrical properties of Ga2O3 however the role of Sn implantation and post-annealing in enhancement of the PD characteristics has not been reported so far. We hereby report a systematic study of the effect of Sn+ ion implantation under different conductions and post-annealing of β-Ga2O3 epilayers grown by pulsed laser deposition on their electric, structural, and optical properties as well as the performance of DUV PD device. X-ray diffraction (XRD) studies reveal that the orientation of the obtained films is along the (-201) plane and the crystal quality shows improvement due to post-annealing while no implantation related damages are observed. UV-Vis spectroscopy studies show a decrease in the bandgap with the implantation dosage due to introduction of shallow donor states below the conduction band. High-resolution transmission electron microscopy (HR- TEM) and secondary ion mass spectroscopy (SIMS) reveal that the depth of implantation region is up to ~160nm from the surface consisting of smaller crystallite sizes due to implantation effect, while RBS studies reveal the damage recovery post-annealing. Raman studies reveal that vacancies are formed in octahedral Ga2O3 chains due to the substitution of Sn+ ions at Ga sites because of implantation which might play an important role in enhancing the optical and electrical properties. PD devices based on as-grown β-Ga2O3 form Schottky contacts with significant dark current, whereas the PDs fabricated using annealed and Sn+ ion implanted β-Ga2O3 films form ohmic contacts with almost no dark current. Photo transport studies show enhanced responsivity and detectivity of PD based on implanted samples by 20 and 105 times, respectively compared to those based on as grown samples under 244 (UV- C) illumination. In addition to that fast rise and fall time, high self-powered photodetection under 0V bias has been observed for all implanted devices. We discuss the enhancement mechanism in light of suppression of persistent photoconductivity due to annealing and implantation. This is the first report on a study of significantly enhanced self-powered solar-blind DUV PD devices fabricated via Sn+ ion implanted (post-annealed) β-Ga2O3.

10:30 AM
Highly Textured Sn Doped β-Ga2O3 Epilayers for Economic Solar-Blind Ultraviolet Photodetectors with High Responsivity
Mr. Nathan Episcopo[1], Dr. Debabrata Das[1], Dr. Ramana Chintalapalle[1]
[1]The University of Texas at El Paso

The ongoing progress of contemporary civilization has led to the gradual enhancement of state-of-the-art photodetector configurations, resulting in economic, miniaturized, and superior performance. Moreover, solar-blind photodetectors utilizing ultrawide bandgap semiconductors have garnered significant attention due to their extensive perspective in military, civilian, and astronomical sectors. These photodetectors are expected to exhibit strong photosensitivity, fast response time, and simple fabrication steps. In this context, we report highly textured Sn-doped β-Ga2O3 thin film-based metal-semiconductor-metal type deep-UV photodetector using a commercially acceptable magnetron sputtering method. Here, the effect of Sn is bidirectional, as a dopant to increase the electrical conductivity and as a surfactant at the growth front to assist the stabilization of highly textured β-Ga2O3 epilayers on sapphire substrate. Simple growth and fabrication steps are chosen intentionally to illustrate a trivial way to demonstrate an economic photodetection strategy without compromising the device performance. In-depth structural, morphological, chemical, and optical characterizations have been done to optimize the best configuration for further device fabrication and testing. Under transient triggering circumstances, a fast response time of around 500 ms is reported, accompanied by a responsivity of approximately 60.5 A/W. The detectivity, external quantum efficiency, and photo-to-dark current ratio values are reported as 1.6×1013 Jones, 2.8×104 %, and 17.4, respectively. According to recent literature reports on sputtered Ga2O3 deep-UV photodetectors, the overall device performance is in the top 80%. The low cost and simplistic fabrication process for solar-blind UV

photodetection represents a novel contribution to the field. This approach holds significant implications for the development of electronics capable of functioning in extreme environments and exhibits substantial potential for enhancing low-cost UV photodetector technology.

10:45 AM
Kappa/beta gallium oxide type-II phase heterojunction for self-powered deep ultraviolet photodetection. (Student)
Mrs. Patsy Miranda Cortez[1], Dr. Yi Lu[1], Dr. Xiao Tang[1], Mr. Zhiyuan Liu[1], Mr. Vishal Khandelwal[1], Dr. Shibin Chandroth[1], Prof. Xiaohang Li[1]
[1]King Abdullah University of Science and Technology

This study demonstrates the β-Ga2O3/κ-Ga2O3 phase heterojunction, a type-II III-oxide heterojunction. The experiment reveals a sharp interface and significant band offsets of 0.65 eV for and 0.71 eV for . This unique band alignment shows promise for self-powered deep ultraviolet (DUV) detection. The fabricated heterojunction photodetector exhibits higher responsivity (17.8 mA/W) under DUV illumination and zero external bias compared to bare β-Ga2O3 and κ-Ga2O3 photodetectors. This work highlights the potential of the β-Ga2O3/κ-Ga2O3 heterojunction for Ga2O3-based technologies.
Ultrawide bandgap Ga2O3 is a highly promising material for advanced electronic applications. Among its multiple polymorphs, the β-phase with a bandgap of 4.85 eV has been widely studied due to its stability under atmospheric conditions. The κ-phase, is the following more stable and has a slightly larger bandgap. Integrating different Ga2O3 phases to create "phase heterojunctions" can result in unique junction properties stemming from variations in bandgap and electron affinity. Previous studies indicated a potential band offset at the β-Ga2O3/κ-Ga2O3 junction, suggesting a type-II band alignment. These phase heterojunctions hold great potential for applications in photodetectors, solar cells, and photocatalytic water splitting where one promising application is the self-powered detection of solar-blind DUV signals. In this study, we used pulsed laser deposition to grow β-Ga2O3 on κ-Ga2O3, creating a phase heterojunction with a type-II band alignment confirmed by multiple characterizations. This heterojunction facilitated efficient electron-hole separation and enabled self-powered DUV detection.
The XRD patterns of the β-phase/κ-phase Ga2O3 (Figure 1(a)) confirms the presence of κ-Ga2O3 and β-Ga2O3 characteristic peaks. The cross-section TEM image of the β-phase/κ-phase Ga2O3 film (Figure 1(b)), reveals the interface between the κ-Ga2O3 thin film and the sapphire substrate, with epitaxially grown β-Ga2O3 on top while the high-resolution TEM image (Figure 1(c)), clearly shows the crystal models for the monoclinic β-Ga2O3 structure (Figure 1(d)) and orthorhombic κ-Ga2O3 (Figure 1(e)). These results confirm the stacked phase heterostructure. Employing the binding energy of core levels of Ga 3d and O 1s (Figure 2(a)) obtained from XPS measurements, and the optical bandgap values for β-Ga2O3 and κ-Ga2O3 (4.94 eV and 5.0 eV, respectively) obtained from the UV-Vis spectra (Figure 2(b)), and are estimated to be approximately 0.65 eV, and 0.71 eV, respectively. This confirms the type-II band alignment for the β-Ga2O3/κ-Ga2O3 heterojunction (Figure 2(c)).
Under 0 bias, the fabricated quasi vertical β-Ga2O3/κ-Ga2O3 junction PD, shows a peak current of approximately -0.24 nA with DUV illumination (Figure 3(a)). Under various bias conditions, the PD exhibits high sensitivity to DUV light, as photocurrent (Iphoto) is more than three orders of magnitude higher than the dark current (Idark) for each value (Figure 3(b)), furthermore, the IV curve is not symmetric for positive and negative values due to respective changes in the depleted region and the built in potential. This confirms the presence of the phase heterojunction and interfacial electric field. Figure 3(c) presents the photoresponsivity of the β-Ga2O3/κ-Ga2O3 junction PD under different biases. The photoresponsivity can reach approximately 43.7 A/W at 5 V and 169 A/W at 10 V, indicating its significant potential for applications in solar-blind detection.

11:00 AM
Phase Transition and Bandgap Engineering of MgSnO Thin Films for Solar-blind Ultraviolet Photodetector Applications (Student)
Mr. Chengyun Shou[1], Mr. Tianchen Yang[1], Mr. Theodore Yang[1], Mr. Abdullah Almujtabi[1], Mr. Yuan Li[1], Mr. Quazi Sanjid Mahmud[1], Prof. Jianlin Liu[1]
[1]University of California Riverside

Transparent conducting oxide (TCO) semiconductors have high transmittance in the visible light range and are often used in displays, solar cells, and other optoelectronic devices. Among these TCO semiconductors, tetragonal rutile structure tin oxide (SnO2) has been applied in many areas such as gas sensors, glass coating, and transparent electrodes. However, due to its relatively small bandgap (3.6 eV), it is difficult to realize SnO2-based deep ultraviolet (UV) applications, including solar-blind photodetection of light with a wavelength below 280 nm, which requires a semiconductor of a bandgap of ~4.4 eV or larger. To extend SnO2-based optoelectronic applications into deep ultraviolet solar-blind wavelength range. In this research, MgSnO alloy thin films were grown on c-sapphire using plasma-assisted molecular beam epitaxy. As Mg composition is between 0 and ~24.4 at. %, MgSnO films exhibit rutile structure. The lattice constants increase as Mg composition increases. MgSnO films become amorphous as Mg composition exceeds 24.4 at. %, and eventually become rock-salt structure as Mg composition exceeds 45.9 at. %. The optical bandgap of MgSnO increases with the increase of Mg composition. To explore the photodetection performance of these MgSnO thin films, MSM photodetectors were fabricated by patterning an interdigitated Pt (20 nm)/Au (100 nm) electrode on the films. When Mg composition increases, both the dark current and photocurrent of the devices decrease. Current fitting was also performed on rutile and amorphous sample to understand the current transport mechanism. High responsivities were observed for all MgSnO MSM devices, suggesting that MgSnO thin films are promising for deep-UV solar-blind photodetection and other photonic and electronic applications.

11:15 AM
Usage of Albrecht model for simulation of β-Ga2O3-/NiOx super junction devices for ultrawide bandgap electronics
Mr. Jose Manuel Taboada Vasquez[1], Mr. Glen Isaac Maciel Garcia[2], Mr. Mritunjay Kumar[2], Dr. Biplab Sarkar[3], Prof.

Xiaohang Li[2]
[1]Advanced Semiconductor Laboratory, Electrical and Computer Engineering program, CEMSE Division, King Abdullah University of Science and Technology, Thuwal 23955-6900, Saudi Arabia., [2]King Abdullah University of Science and Technology, [3]Department of Electronics and Communication Engineering, Indian Institute of Technology Roorkee, Uttarakhand 247667, India

Wide bandgap semiconductors (WBG) are integral to various technological applications, enhancing performance while reducing size. In recent years, β-Ga2O3 has been studied thoroughly and is now considered a promising semiconductor for high-power applications. two primary challenges persist: the absence of p-type dopants for β-Ga2O3 and the complication of simulating these structures due to its low mobility. P-type NiOx has been recently studied to complement n-type β-Ga2O3 on different p-n hetero-junctions. [1]
This work demonstrates the simulation of Superjunction (SJ) diodes made of β-Ga2O3 /NiOx, which benefit from the Reduced Surface Field (RESURF) effect. This effect allows the electric field to be dispersed across the vertical and horizontal regions of the device, resulting in an expanded depletion region compared to other structures. By using SILVACO Technology Computer-Aided Design (TCAD) simulations and enabling additional calculation parameters on semiconductors, such as the Albrecht Model for Low Field Mobility, it was possible to determine the electric field distribution of SJ diodes [2].
For comparison, a standard PIN device was also simulated. Figure 1 illustrates the device design structure and the carrier concentrations used for the simulation. Table 1 presents the distinct simulation parameters for NiOx and β-Ga2O3. The electric field distribution at 0 V, 500 V, 1000 V, and 1500 V is depicted in Figure 2. As seen, the depletion region in the SJ diode is extended across all the vertical and horizontal regions of the low-doped β-Ga2O3 region, broadening the electric field and reducing it at higher voltages. For comparison, the simulations were conducted up to 3400 V, where both devices achieved the theoretical breakdown field of the β-Ga2O3. However, Figure 3 displays the maximum recorded electric field on the devices at various voltages, clearly indicating the superior distribution of the electric field in the SJ device compared to the PIN junction device. The results of this work are promising and motivating for device design strategies of future β-Ga2O3 /NiOx SJ diodes.

10:15 AM
Transition Metal Dichalcogenide and h-BN Synthesis and Devices
Session Chairs: Soaram Kim (Texas A&M University), Kevin Daniels (University of Maryland)
ESJ 2204

10:15 AM
Extraordinary tunnel electroresistance in layer-by-layer engineered van der Waals ferroelectric tunnel junctions
Dr. Qinqin Wang[1]
[1]University of Maryland, College Park

The ability to engineer potential profiles of multilayered materials is critical for designing high-performance tunneling devices such as ferroelectric tunnel junctions (FTJs). FTJs comprise asymmetric electrodes and a ferroelectric spacer, promising semiconductor platform-compatible logic and memory devices. However, the traditional FTJs consisting of metal/oxide/metal multilayer heterostructures can only exhibit the modest tunneling electroresistance (TER, usually <106), which is fundamentally undermined by the unavoidable defect states and interface trap states. Here, we constructed van der Waals (vdW) FTJs by a layered ferroelectric CuInP2S6 (CIPS) and graphene. Owing to the gigantic ferroelectric modulation of the chemical potentials in graphene by as large as ~1 eV, we demonstrated a giant TER of 109. While inserting just a monolayer MoS2 between CIPS/graphene, the off state is further suppressed, leading to >1010 TER. Our discovery opens a new solid-state paradigm where potential profiles can be unprecedentedly engineered in a layer-by-layer fashion, fundamentally strengthening the ability to manipulate electrons' tunneling behaviors and design advanced tunneling devices.

10:30 AM
Electric-field-sensitive polymer electrolytes for non-volatile doping of two-dimensional field-effect transistors
Prof. Susan Fullerton[1], Mr. Dnyanesh Sarawate[1], Ms. Priscilla Prem[1], Prof. Ke Xu[2], Prof. Eric Beckman[1]
[1]University of Pittsburgh, [2]Rochester Institute of Technology

Solid polymer electrolyte gating provides access to regimes of transport in two-dimensional (2D) materials that would otherwise be inaccessible using conventional gate dielectrics. The enabling mechanism is the formation of an electric double layer (EDL) at the electrolyte/2D material interface that creates large fields (~V/nm) and therefore induces large p- and n-type carrier densities in 2D materials (~1013-1014 cm-2). In this work, we demonstrate a new type of solid polymer electrolyte wherein the electric field created by the ions serves a dual purpose: driving ions to the channel surface to induce heavy doping, and driving chemical reactions that "lock down" the ions at the interface, thereby providing channel doping that persists even after the gate bias is removed (i.e., non-volatile doping). Specifically, the polyethylene oxide (PEO)-based co-polymer is designed with field-sensitive reactive groups to crosslink the polymer and therefore arrest ion mobility, disallowing the ions from diffusing away from the channel surface once the gate is grounded.

We demonstrate the non-volatile doping of graphene FETs using a field-sensitive polymer electrolyte by applying positive programing gate voltages (VG ≥ +2 V), and then monitoring the Dirac point shift and change in ON/OFF current. VG ≤ +2 V showed no non-volatile doping effect; however, programming at VG ≥ 2 V leads to a non-volatile, n-type shift in the minimum conduction current, and an increase in the ON/OFF. Applying negative programming after positive programming shifts the device less n-type, likely due to counter-doping, however the device retains a higher ON/OFF ratio and steeper subthreshold swing than

the undoped device. Dual-gated devices are also measured where the electrolyte gate is used to set the doping, then the contacts are grounded, and the temperature is decreased below the glass transition temperature of the electrolyte. Transfer measurements are taken using the backgate. This approach immobilizes the ions in the bulk, thereby isolating the electrical impact of the “locked” ions at the interface. Although the concentration of ions in these initial tests is approximately ten times lower than typical for a solid polymer electrolyte, the non-volatile doping density is on the order 1012 cm-2 based on shifts in the Dirac point. This is ten times greater than the intrinsic carrier density. Sheet carrier densities measured by Hall effect and chemical/physical characterization of the polymer electrolyte will be presented for electrolytes with higher salt concentration. The work is supported by the National Science Foundation (NSF, U.S.) under Grant No. ECCS-EPMD-2132006.

10:45 AM
Growth and characterization of two-dimensional hexagonal boron nitride on Ni (111) substrates by using diborane and ammonia in molecular beam epitaxy (Student)
Mr. Yuan Li[1], Mr. Quazi Sanjid Mahmud[1], Mr. Chengyun Shou[1], Mr. Abdullah Almujtabi[1], Mr. Edward Zhu[2], Mr. Tianchen Yang[1], Prof. Jianlin Liu[1]
[1]University of California Riverside, [2]University of California, Riverside

Two-dimensional (2D) hexagonal boron nitride (h-BN) plays a significant role in next generation van der Waals (vdW) electronic and optoelectronic devices, and controllable and reliable growth is essential for its wide range of applications. Here, we carried out molecular beam epitaxy (MBE) growth of 2D h-BN on Ni (111) substrates by using diborane (B2H6, 5% in H2) and ammonia (NH3) as the sources. It was found that with the increased flow rate ratio of B (B2H6) to N (NH3), the morphology of h-BN flakes tends to evolute from concave triangle to isosceles triangle, to convex triangle or polygon, corresponding with B and N terminations, induced by different hydrogenation level during the growth. With the increase of hydrogenation, the edge attachment and diffusion energy barrier is increased, making it difficult for h-BN flakes to continue to grow horizontally. The substrate engineering of Ni (111) surface catalytic effect can be further tuned by incorporated with silicon atoms using Si2H6 gas treatment prior to the film growth. The samples were analyzed using scanning electron microscopy, X-ray photoelectron spectroscopy (XPS), atomic force microscopy (AFM), ultraviolet-visible (UV-vis) spectroscopy, Raman spectroscopy, Fourier-transform infrared spectroscopy (FT-IR), X-ray diffraction (XRD), and electron backscatter diffraction (EBSD). Metal-insulator-metal (MIM) interdigital devices were fabricated based on transferred h-BN samples, demonstrating a strong deep ultraviolet (DUV) response. Our work reveals the influence of hydrogen and silicon on the catalytic effect of Ni in the MBE growth of monolayer h-BN and provides an effective way to control the morphology and quality of the 2D h-BN films.

11:00 AM
Vibrational Characteristics of Rare Earth Element based Two Dimensional MXenes
Mr. Joshua Abbott[1], Ms. Vanessa Morris[2], Dr. Binod Rai[3], Dr. Daniel Autrey[2], Dr. Bhoj Gautam[1]
[1]Department of Chemistry, Physics and Materials Science, Fayetteville State University, Fayetteville, NC 28301, USA, [2]Department of Chemistry, Physics, & Materials Science, Fayetteville State University, Fayetteville, NC 28301, USA, [3]Savannah River National Labortory

Two-dimensional materials based on transition metal carbides and nitrides called MXenes offer a unique combination of metallic conductivity, hydrophilicity, and structural diversity and are recognized as multifunctional nanomaterials. In this work, we synthesized i-MAX (Er1/3Mo2/3)2C MXene from (Er1/3Mo2/3)2AlC i-MAX phase. (Er1/3Mo2/3)2C MXene was synthesized by adding (Er1/3Mo2/3)2AlC powders into the LiF/HCl solution and was etched for 7 days. We used X-ray diffraction (XRD) and Raman spectroscopy to characterize the structural and vibrational properties of (Er1/3Mo2/3)2C. We observed several XRD peaks in the scan range 5-50°. After LiF/HCl etching of (Er1/3Mo2/3)2AlC, the (002) peak broadens and is shifted towards a smaller angle (10.5°) compared to the unetched (Er1/3Mo2/3)2AlC (12.9°), indicating removal of Al from (Er1/3Mo2/3)2AlC. In addition, the peak at 39° is vanishingly small as compared to (Er1/3Mo2/3)2AlC suggesting more complete removal of Al. Raman measurement on (Er1/3Mo2/3)2C MXene shows the several bands in 100-800 cm−1 range. The band ~145 cm-1 is highly suppressed when excited with 532 nm laser in comparison to 785 nm laser. In addition, the number of peaks above 250 cm-1 decreases with an increase in laser excitation wavelength suggesting that Raman resonance effect is occurring with 532 nm laser excitation. Our results provide important information regarding the vibrational characteristics of rare earth element based i-MXenes.

10:15 AM
Doping and Transport
Session Chairs: Len Brillson (The Ohio State University), Christian Wetzel (Rensselaer Polytechnic Institute)
ESJ 1224

10:15 AM
Hole transport analysis in p-type N-polar GaN (Student)
Mr. Masahiro Kamiyama[1], Dr. Shashwat Rathkanthiwar[1], Mr. Cris Quinones[1], Dr. Seiji Mita[2], Dr. Pramod Reddy[2], Dr. Ronny Kirste[2], Prof. Ramón Collazo[1], Prof. Zlatko Sitar[1]
[1]North Carolina State University, [2]Adroit Materials

Thanks to its wide and direct bandgap, high saturation

velocity, high critical electric field, and n- and p-type doping capability, gallium nitride (GaN) has proven itself as an essential semiconductor for a range of power, RF, and optoelectronic device technologies. Understanding the electrical transport properties and transport-limiting scattering mechanisms in doped GaN films is of significance

in designing next-generation devices. Hall effect measurement is an established technique to measure fundamental electrical properties such as resistivity, carrier concentration and mobility. While there have been several reports on electron transport in n-type GaN, systematic Hall effect studies on hole transport in p-type GaN are limited due to the complications related to anisotropy and non-parabolicity in the valence band structure. These complications lead to the deviation of the Hall scattering factor (rH) from its ideal value of unity, especially at high temperatures and high acceptor concentrations. The assumption of a rH value of unity at high temperatures often leads to an overestimation of the extracted NA to values much larger than the actual doping concentration, obviously an anomalous result. The deviation of rH value from unity also leads to the deviation of the experimentally measured Hall mobility from the theoretical drift mobility. Indeed, only a few attempts to fit theoretical drift mobility to Hall mobility have been reported in the p-GaN literature, and reasonable fitting has not been achieved. Thus, accurate knowledge of rH is crucial for analysis of Hall effect measurements.
In this study, we comprehensively investigate the electrical characteristics in p-type N-polar GaN as a function of process supersaturation and Mg doping concentration and develop a methodology for analysis of Hall effect measurements. Two sets of Mg-doped N-polar GaN samples were grown by metalorganic chemical vapor deposition. In the first set, the Mg doping concentration was fixed at 1019 cm-3, and the compensation level was varied by changing the V/III ratio (process supersaturation) during the growth. The second set was grown using low compensation (high supersaturation) growth conditions where the Mg doping concentration was varied from 3x1018 to 4x1019 cm-3. Next, Hall measurements were performed in a wide temperature range of 220-770 K to measure resistivity and Hall coefficient values. A charge balance model based on Fermi Dirac statistics and charge neutrality equation was developed to extract the acceptor (NA) and donor (ND) concentrations from temperature-dependent Hall coefficients. The value of rH was extracted as a function of temperature by understanding the deviation of experimentally measured hole concentration to the theoretical value. The experimentally measured Hall mobility was modified to the experimental drift mobility using these values and fitted by the theoretical drift mobility. The fittings for the two sets of samples revealed distinct features. First, the mobility values for the different samples converged at high temperatures. The mobility values showed a monotonic decrease at higher temperatures pointing to the dominance of phonon-limited scattering mechanisms. Second, the mobility values for the different samples diverged at low temperatures. The fittings revealed dislocation scattering to be the limiting scattering mechanism for hole transport. Interestingly, the trap occupancy which governs the number of donor-like trap states per unit c-lattice translation of a dislocation was found to vary as a function of compensation level and Mg doping concentration. In general, the number of trap states decreased as a function of supersaturation and increased as a function of Mg doping concentration. For all the samples, the donor concentration (ND) obtained using the hole concentration analysis was found to be in good agreement with oxygen impurity concentration measured by SIMS and the donor-like trap concentration along dislocations obtained from the mobility analysis.

10:30 AM
Enhanced Be Dopant Incorporation and the Role of In Surfactant in MOCVD GaN:Be
Mr. Benjamin McEwen[1], Dr. Vincent Meyers[1], Mr. Alireza Lanjani[1], Ms. Shadi Omranpour[1], Mr. Oleksandr Andrieiev[2], Mr. Mykhailo Vorobiov[2], Prof. Denis Demchenko[2], Prof. Michael Reshchikov[2], Prof. F. Shahedipour-Sandvik[1]
[1]Department of Nanoscale Science and Engineering, University at Albany, [2]Department of Physics, Virginia Commonwealth University

In recent years, beryllium doping in III-nitrides has been the subject of much research due to evidence that it gives rise to the shallowest known acceptor in the material system. Despite the successful realization of p-type AlN using Be dopant1, conductive p-type GaN:Be has still never been shown reliably or reproducibly. In MOCVD-grown GaN:Be, poor incorporation efficiency may be at least partially to blame. Additionally, the small atomic size of Be makes the formation of Beint more favorable than interstitials of other dopants such as Mg. One potential way to improve incorporation efficiency and prevent the formation of Beint is by using a surfactant species during growth. Indium is a common surfactant for GaN growth and has been used to improve the material quality of N-polar GaN2 as well as the activation efficiency of Mg in p-GaN3. To date, the use of In surfactant in GaN:Be has not been shown experimentally. However, first principles calculations have indicated that Be incorporates more efficiently into Ga sites when the GaN surface is In-terminated during growth4. Due to the highly volatile nature of In at common MOCVD growth temperatures (>900 °C), little-to-no In incorporates into the GaN.
In this study, GaN:Be was grown by MOCVD with varying amounts of trimethylindium (TMIn) introduced into the growth chamber to provide In surfactant. We investigate the impact of In surfactant on material quality, as determined by X-ray diffraction (XRD) and atomic force microscopy (AFM), as well as on the incorporation and activation efficiency of Be in GaN. Low-temperature photoluminescence (PL) studies revealed strong Be-related PL bands, including the yellow band at 2.15 eV assigned to the deep state of the BeGa acceptor and the peak at 3.38 eV attributed to the shallowest, yet unidentified, acceptor in GaN. Despite a wide range of TMIn flow values, little impact on material quality is observed. However, modest differences in Be acceptor formation are found as a result of In surfactant. The increase in Be and Be-related acceptor formation is discussed, and potential paths forward to combine multiple methods of improving p-type activity in GaN:Be are presented.
(1) Ahmad, H.; Lindemuth, J.; Engel, Z.; Matthews, C. M.; McCrone, T. M.; Doolittle, W. A. Adv. Mater. 2021, 33 (42). https://doi.org/10.1002/adma.202104497.
(2) Aisaka, T.; Tanikawa, T.; Kimura, T.; Shojiki, K.; Hanada, T.; Katayama, R.; Matsuoka, T. Jpn. J. Appl. Phys. 2014, 53 (8). https://doi.org/10.7567/JJAP.53.085501.
(3) Chen, Y.; Wu, H.; Yue, G.; Chen, Z.; Zheng, Z.; Wu, Z.; Wang, G.; Jiang, H. Appl. Phys. Express 2013, 6 (4). https://doi.org/10.7567/APEX.6.041001.

(4) Northrup, J. E. Appl. Phys. Lett. 2001, 78 (19), 2855–2857. https://doi.org/10.1063/1.1368369.

10:45 AM
Mercury-probe based electrical characterization of β-Ga2O3
Dr. Jian Li[1], Dr. Yunjo Kim[1], Dr. Adam Charnas[1], Dr. Brenton Noesges[1], Dr. Prescott Evans[1], Dr. Adam Neal[1], Dr. Thaddeus Asel[1], Mr. Cameron Gorsak[2], Ms. Kathy Azizie[2], Prof. Michael Thompson[2], Prof. Hari Nair[2], Prof. Darrell Schlom[2
[1]Air Force Research Laboratory, [2]Cornell University, [3]University of Michigan, [4]University of California, Los Angeles

To facilitate the lab-to-fab transition of the β-Ga2O3 technology, advancement of techniques is being called for to characterize the electrical properties of the materials at multiple stages of development including bulk crystal, substrate, epitaxy, dielectrics, and interfaces. Ideally, the characterization techniques should be non-destructive in nature, i.e., the material under test retains no permanent physical and chemical alterations after the characterization. The materials in this presentation represent to the following types of wafers: bare substrates, an epitaxial layer on an insulating substrate, an epitaxial layer on a conducting substrate, and a dielectric layer on a conducting epitaxial layer or substrate.
We develop characterization methodology for the investigation of the electrical properties (Figure 1) spanning across a wide spectrum of the β-Ga2O3 material technology: epitaxy and doping (carrier density profile, Schottky barrier height); electronic transport and breakdown (mobility, resistivity, epi-layer thickness, breakdown voltage and field); bulk defects (type, emission/capture time, energy, capture cross-section, density profile); dielectrics (dielectric constant, ferroelectricity, thickness); dielectric/semiconductor interface (density of states thereof, fixed charges, flat band voltage). The above set of electrical properties are quantitatively determined through a suite of electrical measurements (Figure 1): capacitance-voltage hysteresis, current-voltage, admittance spectroscopy, isothermal capacitance transient spectroscopy, conducted with or without the assistance of optically exciting the material under test. All the above experiments are to be carried out on a commercial off-the-shelf mercury probe apparatus that enables electrically characterization of the β-Ga2O3 material under test in a non-destructive fashion, i.e., without permanent metal deposition.
JVL, YK, ARC, BAN, PEE, TJA, ATN, and SM acknowledge funding support from AFOSR lab task No. 23RXCOR017 (P.O.: Dr. Ken Goretta). CAG, KA, MOT, HPN, and DGS acknowledge funding support from AFOSR Center of Excellence (No. FA9550-18-1-0529). CAG acknowledges support from the National Defense Science and Engineering Graduate (NDSEG) Fellowship. EA and ZW were supported by AFOSR (P.O.: Dr. Ali Sayir) through Program No. FA9550-20-1-0045, NSF under Grant No. 2043803, and DARPA under Grant No. N660012214032.

11:00 AM
Using Near-Zero Field Magnetoresistance Measurements as a Tool for Defect Analysis in Silicon Photovoltaics (Student)
Mr. Elijah Allridge Allridge[1], Dr. Patrick Lenahan[1], Mr. Chirag Mule[2], Dr. Paul Stradins[3]
[1]Penn State University, [2]Colorado University of Mines, [3]National Renewable Energy Lab

We propose to apply a new technique that could help researchers and industry engineers in the development of longer lasting, more efficient silicon solar cells: near-zero field magnetoresistance (NZFMR). NZFMR is related to electrically detected magnetic resonance (EDMR), which itself is a derivative of electron paramagnetic resonance (EPR). The two latter techniques have been used extensively over the past several decades to probe the atomic scale defects in all kinds of semiconductor devices and materials, with EDMR specifically having been used extensively to solve reliability problems in silicon, silicon carbide, and silicon dioxide based devices, as well as devices based on more exotic materials [1,2]. However, EDMR and classical EPR require large, water cooled magnets, complex microwave circuitry and plumbing, as well as a host of supporting equipment that put it out of reach for many labs in university and industrial settings.
NZFMR eliminates the need for microwaves entirely, and reduces the need for very large magnetic fields, while providing much of the same information that can be derived from the other two techniques. NZFMR relies on a quasi-static magnetic field being swept across the device under test. As the field sweeps through zero, deep level paramagnetic defects within the device see a dramatic change in spin-dependent recombination and spin-dependent trap assisted tunneling. At zero field, the electrons in these deep-level charge traps experience only the fields due to nearby nuclear magnetic moments [3]. While the mechanisms behind NZFMR are not 100% understood, there has been recent success in extracting information from multiple material systems from the nuclear hyperfine interactions involved.
The devices tested were fabricated by the national renewable energy lab (NREL), with a structure based on a passivated silicon wafer with doped polycrystalline silicon grown all around. The devices explored had minor changes in the fabrication process, such as introduced nitrogen or boron budgeted oxygen precipitation. There were noticeable differences in the base electrical characteristics from the different devices, and the preliminary results from the NZFMR measurements showed very large differences in the strength of the signal while in the dark under modest forward biasing (50-400 mV) at room temperature, with the strength of the signal being largely bias dependent, and decreasing relative to the total DC current through the device.
While we are not yet at a point where we can comfortably identify the structure of the active defects from the NZFMR spectra, NZFMR still provides useful information, at least allowing for grouping devices with similar defect populations together.
[1] S.J. Moxim et al., 2020 IIRW Proceedings, DOI: 10.1109/IIRW49815.2020.9312868.
[2] C.J. Cochrane et al., 2011 ISDRS Proceedings, DOI: 10.1109/ISDRS.2011.6135142.
[3] E.B. Frantz et al., Appl. Phys. Lett., vol. 119, 2021, DOI: 10.1063/5.0066640.

11:15 AM
Nanoscale electrical conductance and leakage currents in etched and selective-area regrown GaAs pn junctions (Student)
Mr. Tae-Hyeon Kim[1], Dr. Alec Skipper[2], Prof. Seth Bank[3], Prof. Edward Yu[1]
[1]The University of Texas at Austin, [2]University of California, Santa Barbara, [3]University of Texas at Austin

Junction leakage currents play a critical role in a wide range of semiconductor devices. For vertical pn and pin type junction structures such as diodes or photodetectors, electrical conduction at device peripheries due to etch damage during fabrication of mesa structures has been identified as one of the major sources of leakage current. Selective-area growth, in which epitaxial layers are grown on a semiconductor substrate within cavities etched into an electrically insulating thin film, offers a potential approach for reducing sidewall leakage currents by eliminating the need for etching in formation of device mesa structures. We have used scanning capacitance microscopy (SCM) and conductive atomic force microscopy (CAFM) to characterize local carrier distributions and electrical current flow in mesa-etched and selective-area regrown GaAs pin junction structures grown by MBE. For the latter, periodic supply epitaxy (PSE), a technique which regularly interrupts the group III flux to enhance adatom mobility, was used to ensure selective growth of the diode structures in windows opened in a silicon dioxide thin film that was deposited on an n-type GaAs wafer. Mesa diodes were fabricated using conventional UV photolithography and a phosphoric acid wet etch on a sample grown under the same conditions on a standard n-type GaAs wafer. SCM measurements confirm the expected distribution of dopants in the mesa-etched structures, and reveal carrier spillover effects that lead to unusual contrast observed in SCM imaging near the etch-exposed regions of the pn junction. CAFM studies indicate that wet etch-induced defect states are present on the etched surfaces of mesa structures, and that these defects lead to increased local electrical conductivity that could contribute to sidewall leakage in etched mesa diode devices. CAFM characterization of GaAs pin junction structures grown within holes etched into a SiO2 layer by selective-area regrowth reveals the presence of an annular low-conductivity region in the vicinity of the GaAs-SiO2 interface that could act to suppress current flow at the edges of pn junction diode device structures fabricated from selective area-regrown material. Together, these studies provide new insights into the origin of sidewall leakage currents in mesa-etched GaAs pn junction diodes, and their suppression in selective-area regrown devices.

10:15 AM
Solar Cell Materials and Devices
Session Chairs: Deidra Hodges (Florida International University), Mark Wistey (Texas State University)
ESJ 1202

10:15 AM
Transforming Magnetic Metal into Semiconductor: Spin Solar Cell Phenomenon on Single Molecule Magnet(SMM) Impacted CoFeB based Magnetic Tunnel Junctions
Dr. Pawan Tyagi[1], Dr. Marzieh Savadkoohi[2], Mr. Pius Suh[2], Dr. Daniel Gopman[3], Dr. F. Jose Martinez[4]
[1]University of the district of Coulombia, [2]University of the District of columbia, [3]National Institute of Standards and Technology, [4]University of Valencia

The spin photovoltaic field is an exciting field of research that harvests electron spin, instead of charge, of solar energy harvesting. The single-molecule magnet (SMM) transformed conventional magnetic tunnel junction(MTJ), a memory device used in present-day computers, into solar cells[1]. For the first time, we demonstrated the electronic spin-dependent solar cell effect on an SMM-transformed MTJ under unpolarized white light(Fig.1)[2]. In our MTJ, CoFeB was present on both sides of the MgO tunnel barrier. We produced cross-junction-shaped MTJ with the two exposed junction edges where the physical gap between two electrodes was less than the length of to-be-bridged SMM spin channels. Along the exposed edges, we bridged SMM between the two CoFeB electrodes across the insulating barrier and observed that SMM channels yielded a region of long-range magnetic ordering around molecular junctions. Our SMM possessed a hexanuclear [Mn6(μ3-O)2(H2N-sao)6(6-atha)2(EtOH)6] [H2N-saoH = salicylamidoxime, 6-atha = 6-acetylthiohexanoate] complex and thiols end groups to form bonds with metal films. SMM impacted MTJ and started exhibiting the solar cell effect, yielding ≈80 mV open circuit voltage and ≈10mA/Sq.cm saturation current under one sun radiation. The Kelvin Probe AFM(KPAFM) study provided direct evidence that SMM has transformed the electronic properties of the MTJ's electrodes over several thousand times more areas than molecular junction areas at room temperature (Fig. 2). The decisive factor in this study depends on successfully forming SMM spin filtering channels between two dissimilar ferromagnets- without that, SMM and MTJ are conventional materials.
References:
[1] P. Tyagi and C. Riso, "Molecular spintronics devices exhibiting properties of a solar cell," Nanotechnology, vol. 30, p. 495401, 2019/09/19 2019.
[2] M. Savadkoohi, D. Gopman, P. Suh, C. Rojas-Dotti, J. Martínez-Lillo, and P. Tyagi, "Spin Solar Cell Phenomenon on a Single-Molecule Magnet (SMM) Impacted CoFeB-Based Magnetic Tunnel Junctions," ACS Applied Electronic Materials, 2023/05/31 2023.

10:30 AM
Optimization of Pb-free Highly Efficient Cs2AgInBr6 Double Perovskite Solar Cells: A Numerical Investigation using SCAPS (Student)
Mr. Mahir Abrar[1], Mrs. Ishrat Jahan Biswas[1], Mrs. Srabanti Datta[1], Dr. Deidra Hodges[1]
[1]Florida International University

Halide perovskite solar cells have emerged as the most rapidly advancing photovoltaic (PV) technology in the realm of research and development. [1] The first scholarly work elucidating the potential of halide perovskites in the realm of PV energy conversion was brought to light in 2009. [2] The researchers showed a power conversion efficiency (PCE) of 3.8% by using hybrid organic-inorganic halide perovskite CH3NH3PbI3 as a photosensitizer within a dye-sensitized solar cell architecture. As of the composition of this

manuscript, the pinnacle of certified efficiency stands at 26.1%, a remarkable achievement. (according to NREL's best research cell efficiencies chart) [3].
Notwithstanding the notable optoelectronic characteristics exhibited by lead-based perovskite solar cells (PSCs), their extensive application is impeded by the dependence on toxic lead (Pb) and limited stability. Consequently, scholars are directing their efforts toward identifying alternatives with reduced toxicity, aiming to uphold elevated efficiency levels and fortify stability. Pb-free Double Perovskite Solar Cells (DPSCs) have attracted considerable scholarly scrutiny in recent years due to their potential as a promising absorber layer within the device architecture, coupled with their cost-effectiveness, outstanding stability, and superior performance. The impediment to the commercialization of Perovskite solar cells (PSCs) persists due to the incorporation of lead and non-biodegradable toxic materials. This study delves into the exploration of a non-toxic inorganic material, Cs2AgInBr6 by using SCAPS-1D software. Multiple parameters, including thickness and operating temperature, for the perovskite absorber layer (Cs2AgInBr6) were optimized. The influence of various electron transport layers (ETLs) and hole transport layers (HTLs) on the device performance was also thoroughly examined. The simulation outcomes reveal that, at an optimal absorber layer thickness of 600 nm, the Double Perovskite Solar Cell (DPSC) using Ag/Cu2O/Cs2AgInBr6/ZnSe/FTO attains a peak efficiency of 22.03% with solar spectrum at AM 1.5.

10:45 AM
Investigation of a Simplified Metamorphic Buffer Approach in GaAs(y)P(1-y) Alloys (Student)
Ms. Lauren Kaliszewski[1], Prof. Tyler Grassman[1]
[1]The Ohio State University

Recent advances in high-quality GaP/Si templates have enabled considerable advances in contemporary III-V/Si integration efforts [1],[2], but excess threading dislocation densities (TDD) resulting from the often large total lattice mismatches for many integrated III-V/Si optoelectronic designs are still an issue. The most common method for accommodating this lattice mismatch is through the use of a metamorphic step-graded buffer (SGB). However, SGBs are often less than ideal due to needing to be several microns thick. The large thermal expansion mismatch between Si and III-V compounds institutes total III-V film thickness limits to avoid epilayer cracking, and thus thick SGBs leave little room for optimal device design. Recent successes have been achieved with an SGB alternative based thermal cyclic annealing (TCA) and a novel asymmetric graded filter (ASG). GaAs-on-Si virtual substrates with TDD as low as 2×106 cm-2 have been created with this approach using a simple InxGa1-xAs ASG [3]. And much larger lattice mismatches have also been bridged, including GaSb-on-Si virtual substrates [4]; while the TDD was much higher (9.8 x 107 cm-2), the fact that this was accomplished over a mismatch of ~12% with a buffer structure of < 3 µm is intriguing. Nonetheless, while this approach has been reasonably effective for binary III-V compounds on Si, its efficacy on more complex alloys is unknown. As such, we focus here on the use of ternary GaAsyP1-y buffers.
The III-V/Si heteroepitaxial structures created for this work were grown via metalorganic chemical vapor deposition (MOCVD) and are comprised of 1.0 µm of n-GaAsyP1-y on a GaP/Si virtual substrate, produced in-house following our previously developed processes [5]. Each sample was subjected to a 7-cycle, 400-800°C in-situ TCA. For GaAs (4.1% misfit vs. Si) and GaAs0.75P0.25 (3.2% misfit) samples, the growth rate was 0.5 µm/hr. GaAs0.6P0.4 samples (2.6% misfit), being closer to a 50:50 alloy composition, and thus anticipated peak alloy hardening, were produced across a range of growth rates: 1 µm/hr, 0.5 µm/hr, and 100 nm at 0.1 µm/hr followed by 900 nm at 0.2 µm/hr — these samples are referenced herein as GaAs0.6P0.4A, GaAs0.6P0.4B, and GaAs0.6P0.4C respectively. Sample characterization was performed via atomic force microscopy (AFM) for surface morphology, X-ray diffractometry (XRD), and SEM-based electron channeling contrast imaging (ECCI) for TDD measurement. By comparing the GaAs0.6P0.4 and GaAs-0.75P0.25 samples to GaAs, both within this sample set and from [3], we aim to better understand the dislocation dynamics, along with the competing roles of lattice mismatch and alloy hardening of the ternary alloy versus that of the binary. Comparative AFM analysis (see Figure 1) from as-grown and post-TCA 0.5 µm/hr samples reveals that the surface roughness trended opposite of the lattice mismatch, with GaAs the smoothest (Rq = 9.7 nm RMS) and GaAs0.6P0.4B the roughest (Rq = 25 nm). Considering the different GaAs0.6P0.4 samples, roughness was found to trend with growth rate: GaAs0.6P0.4A (1.0 µm/hr) was roughest at 37 nm RMS and GaAs0.6P0.4C (0.1-0.2 µm/hr) the smoothest 10.7 nm RMS. These results may suggest a significantly slower surface diffusivity of P adatoms (or precursor fragments) than As, which leads to continued roughening following the initial Stranski-Krastanov morphology early in the growth; such roughnesses are not observed when using well-designed SGBs, which typically show smooth, step-flow growth (albeit with underlying micron-scale cross-hatch). When considering resultant pre- and post-TCA TDD of GaAs0.6P0.4B versus GaAs (see Figure 2), the TCA was found to be considerably less effective for the ternary alloy, reaching only 2×108 cm-2 after two full rounds of TCA, whereas the GaAs sample reached nearly 1×107 cm-2 with identical treatment. The 10× worse TDD for GaAs0.6P0.4B (versus < 2× worse starting difference) than GaAs indicates a significantly lower dislocation reduction efficacy for the ternary alloy. This is most likely due to some combination of reduced dislocation glide velocity based entirely on both composition (i.e. GaP is ~100× slower than GaAs) and alloy hardening (i.e. further glide reduction), as well as lower total misfit / effective stress (i.e. a driver for dislocation glide). This work is ongoing; we intend to focus on completing additional TCAs on the GaAs0.75P0.25 and GaAs0.6P0.4 samples, as well as implement GaAsyP1-y ASG filters to determine their efficacy, as well.
[1] D. L. Lepkowski, et al., Sol. Energy Mater. 230, 111299 (2021); https://doi.org/10.1016/j.solmat.2021.111299.
[2] Fan, Shizahao, et al., Cell Reports Physical Science, 1, 100208 (2020), https://www.cell.com/cell-reports-physical-science/pdf/S2666-3864(20)30223-X.pdf.
[3] Shang, Chen, et al., Physica Status Solidi, 218, 2000402 (2021), https://doi.org/10.1002/pssa.202000402.
[4] Yeon, Eungbeom, et al. ACS Applied Materials & Interfaces, 15, 55965 (2023), https://doi.org/10.1021/acsami.3c10979.
[5] J.T. Boyer, et al., Journal of Crystal Growth, 571, 126251 (2021), https://doi.org/10.1016/j.jcrysgro.2021.126251

11:00 AM
Thin Film Deposition of Two-Dimensional Hybrid Perovskite in Inert Gas by Resonant Infrared Matrix-Assisted Pulsed Laser Evaporation (RIR-MAPLE) (Student)
Mr. Joshua Ayeni[1], Prof. Adrienne Stiff-Roberts[1]
[1]Department of Electrical & Computer Engineering, Duke University

This study investigates the influence of background pressure in resonant infrared matrix-assisted pulsed laser evaporation (RIR-MAPLE) on the properties of phenylethyl ammonium lead iodide ((PEA)2PbI4) films, focusing on the morphology, crystallinity, and composition. (PEA)2PbI4 is a two-dimensional hybrid organic-inorganic perovskite that can serve as a passivation layer to enhance efficiency and stability solar cells, featuring three-dimensional hybrid perovskite active regions [1]. Also, (PEA)2PbI4 can serve as the active region for light emitters. This versatility is due to its high absorption coefficient, long carrier life, low defect concentration, and shallow defect energy levels [2-3]. RIR-MAPLE, a variation of the pulsed laser deposition method, is beneficial for depositing (PEA)2PbI4 owing to its gentle deposition approach. RIR-MAPLE employs a low-energy Er:YAG laser with a peak wavelength of 2.94 μm [4]. By resonant absorption of the laser energy, a frozen matrix solvent (monoethylene glycol) is sublimated from the target, which contains the hybrid perovskite precursor solutions. As a result, organic and inorganic precursor droplets are transferred to the substrate for eventual nucleation and growth of the hybrid perovskite polycrystalline film. RIR-MAPLE is compatible with a variety of substrates and is applicable to a wide range of hybrid organic-inorganic materials, including those with immiscible components that can be challenging to deposit using conventional solution processing [5]. Although RIR-MAPLE has demonstrated success in depositing different hybrid perovskite films [6, 7], it is not known how film deposition could change under an inert environment, as opposed to the active vacuum conditions typically used during film growth. Determining the impact of an inert gas background pressure on (PEA)2PbI4 film properties could reveal improved material properties and ease vacuum requirements, thereby facilitating scale-up of RIR-MAPLE for industrial application.
Thin films were prepared by RIR-MAPLE deposition from lead iodide and phenethyl ammonium iodide precursors solutions at various background pressures, ranging from active vacuum (10-5 Torr) to 300 mTorr (nitrogen gas atmosphere). Film crystallinity was analyzed by X-ray diffraction (XRD), which was also used to determine grain size by Williamson-Hall analysis. Film morphologies were analyzed by scanning electron microscopy (SEM) and optical properties were investigated using UV-Vis absorbance and photoluminescence (PL) spectroscopies. XRD patterns reveal slight crystal rearrangement under different background pressures leading to variations in the full width at half maximum (FWHM) linewidth in the (002) peak. Additionally, a perovskite-solvent intercalation peak emerges at background pressures exceeding 250 mTorr (Figure 1a, indicated by arrow). Similarly, crystallite size increases with increasing background pressure until reaching a peak value at 250 mTorr (Figure 1b). These observations imply that background pressure higher than 250 mTorr is detrimental to film quality. Furthermore, film deposition in an inert environment provides an approach to increase crystallite grain size, which is important for improving electronic properties. The morphology of the films grown under active vacuum, for both as-grown and annealed films, have similar features to those grown at 250 mTorr (Figure 2). In addition, there are no observable differences in the absorbance and PL spectra of the films (Figure 3), suggesting that variations in background pressure do not notably affect the optical properties. This study will further investigate the impacts of an inert gas environment on (PEA)2PbI4 surface composition by X-ray photoelectron spectroscopy, surface roughness by atomic force microscopy, and electrical properties by current density-voltage measurements.

11:15 AM
Photovoltaic-Powered Monarch Butterfly Migration Tracker
Dr. Abhilasha Kamboj[1], Mr. Gordy Carichner[2], Prof. David Blaauw[2], Prof. Jamie Phillips[1]
[1]University of Delaware, [2]University of Michigan, Ann Arbor

Monarch butterflies make an annual multi-generational round trip between Southern Canada/Northern USA to Central Mexico. The Monarch population has drastically declined due to loss of milkweed fostering habitat, pesticides, climate change. The recent data estimated a huge decline from 100s of millions in 1990s to only few millions in 2024 with a decrease of 95%. Various conservation efforts have been taking place to protect the monarchs. Tracking a species is one important part to understand the habitat during the migration, the effect of weather conditions and human interventions. Given the size of butterflies, the weight (< 75mg) and size (mm-scale) of a tracker needs to be taken into account while ensuring long-distance monitoring. To that end, our team at University of Delaware and the University of Michigan have developed a wireless sensor that is powered through solar harvesting. The sensor consists of temperature and light sensor, RF transceiver for communication, chip sized battery, 16 kb memory and processor where the assembly is thinned to size and weight that can be handled by an average monarch butterfly. To power the system, a millimeter-scaled device with 8 GaAs photovoltaics in series is used that would harvest energy from the sun. The previous version of GaAs PV system employed proved effective in the power generation for light levels as low as 500 lux [1,2]. However, the prolonged darker days (sub-500 lux) impacted the lifetime of the tracker. To that end, we have developed a new design for the photovoltaic to improve the energy harvesting at lower lux levels and utilize them in the future systems. The PV structure is grown by IQE plc on a semi-insulating GaAs substrate. The growth structure from the bottom to top is as follows: 400 nm thick p-doped Al0.3Ga0.7As barrier layer, 1 μm thick n+-GaAs bottom contact, 150 nm thick n+ Al0.3Ga0.7As BSF layer, 3 μm thick n GaAs, 500 nm thick p+ GaAs, 30 nm p+ Al0.8Ga0.2As window layer and finally a 200 nm p++GaAs top contact layer. In an 8-cell PV module, 530 x 590 μm2 PV cells are arranged in series where bottom contact of a PV cell is electrically connected to top contact of next PV cell through metal interconnects. The PV mesas are defined with a chemical etch to GaAs bottom contact and then, each PV is isolated with etch to SI-GaAs layer with a 20 μm trench width between adjacent PV cells. The wet etch chemistry

consists of a 1:1:1 ratio of H3PO4/H2O2/H2O. The top (Ti/Pt/Au) and bottom (Ni/Ge/Au/Ti/Pt/Au) metal contacts are deposited respectively. The mesas are passivated and isolated with a 75 nm thick SiNx deposited using PECVD and via holes are etched to expose the metal contacts. And finally, a 1 μm thick metal stack of Ti/Al/Ti/Au interconnects are deposited at the exposed metal contacts to connect the 8 PV cells in series. The fabricated PV devices are mounted on and wirebonded to a leadless chip carrier and their voltage dependent currents are measured under dark and illuminated conditions at room temperature.

The series of 8-PV cell module show a turn-on at ~ 5.8V. For illuminated case, a tungsten halogen lamp (T = 3200 K) with an estimated luminance of 10s of klux was used to illuminate the PV devices. The measured current density for bright conditions is ~ 11 μA/mm2 with maximum power output at 5.8 V being ~ 155 μW. The battery charging requires output voltage over 5V and has a charge capacity of 18μAhr with operating voltage of ~ 3.9V. Under bright conditions, the PV series module very well meet the battery's demand. The near future work includes measuring and calculating the quantum efficiency of the PV devices and the power output at different light conditions and determine the effectiveness of the GaAs photovoltaics under low light conditions of 500 lux or under. While this study on PV cells is for a biological tracking application, the similar energy harvesting capabilities open doors to numerous future applications in mm and sub-mm scale systems.

References:

E. Moon et al…, J. Phillips, Journal of Photovoltaics, Vol. 10, No. 6, 2020

I. Lee et al…, D. Blaauw, MobiCom '21, 517-530, 2021

Author Index